

Remote Sensing and Digital Image Processing

Yifang Ban *Editor*

Multitemporal Remote Sensing

Methods and Applications



Remote Sensing and Digital Image Processing

Volume 20

Series Editor

Freek D. van der Meer, Faculty of Geo-Information Science and Earth Observation (ITC), Department of Earth Systems Analysis, University of Twente, Enschede, The Netherlands

EARSeL Series Editor

Anna Jarocińska, Department of Geoinformatics, Cartography and Remote Sensing, Warsaw University, Poland

Editorial Advisory Board

Michael Abrams, NASA Jet Propulsion Laboratory, Pasadena, CA, U.S.A.

Paul Curran, City University London, U.K.

Arnold Dekker, CSIRO, Land and Water Division, Canberra, Australia

Steven M. de Jong, Department of Physical Geography, Faculty of Geosciences, Utrecht University, The Netherlands

Michael Schaepman, Department of Geography, University of Zurich, Switzerland

EARSeL Editorial Advisory Board

Mario A. Gomarasca, CNR - IREA Milan, Italy

Martti Hallikainen, Helsinki University of Technology, Espoo, Finland

Håkan Olsson, Swedish University of Agricultural Sciences, Umeå, Sweden

Eberhard Parlow, University of Basel, Switzerland

Rainer Reuter, Carl von Ossietzky University of Oldenburg, Germany

More information about this series at <http://www.springer.com/series/6477>

Yifang Ban

Editor

Multitemporal Remote Sensing

Methods and Applications



Springer

Editor
Yifang Ban
Division of Geoinformatics
KTH Royal Institute of Technology
Stockholm, Sweden

ISSN 1567-3200 ISSN 2215-1842 (electronic)
Remote Sensing and Digital Image Processing
ISBN 978-3-319-47035-1 ISBN 978-3-319-47037-5 (eBook)
DOI 10.1007/978-3-319-47037-5

Library of Congress Control Number: 2016958196

© Springer International Publishing AG 2016

Chapters 15 and 16 are published with kind permission of the Her Majesty the Queen Right of Canada. This work is subject to copyright. All rights are reserved by the Publisher, whether the whole or part of the material is concerned, specifically the rights of translation, reprinting, reuse of illustrations, recitation, broadcasting, reproduction on microfilms or in any other physical way, and transmission or information storage and retrieval, electronic adaptation, computer software, or by similar or dissimilar methodology now known or hereafter developed.

The use of general descriptive names, registered names, trademarks, service marks, etc. in this publication does not imply, even in the absence of a specific statement, that such names are exempt from the relevant protective laws and regulations and therefore free for general use.

The publisher, the authors and the editors are safe to assume that the advice and information in this book are believed to be true and accurate at the date of publication. Neither the publisher nor the authors or the editors give a warranty, express or implied, with respect to the material contained herein or for any errors or omissions that may have been made.

Cover illustration: NASA's Earth Observing Systems, courtesy of NASA Earth Observatory (<http://earthobservatory.nasa.gov/IOTD/view.php?id=81559>).

Printed on acid-free paper

This Springer imprint is published by Springer Nature
The registered company is Springer International Publishing AG
The registered company address is: Gewerbestrasse 11, 6330 Cham, Switzerland

Preface

The idea for this book was conceived at the 1st International Workshop on Temporal Analysis of Satellite Images that I organized in Mykonos, Greece during May 23–25, 2012. The workshop was announced only a few months earlier when the EARSeL Special Interest Group on Temporal Analysis of Satellite Images was established and I became the co-chair. The organizing committee was expecting 30–40 participants for a one and half day event. We were pleasantly surprised, however, that the workshop attracted over 100 participants from 28 countries with 100 presentations covering a variety of topics. This clearly demonstrated strong interests in multitemporal analysis from the remote sensing community. Two months later on July 23, 2012, the Landsat program celebrated its 40th anniversary and then Landsat-8 was launched on Feb. 11, 2013, marking two significant milestones in multitemporal remote sensing.

In 2012, the world also witnessed natural disasters striking across the globe, from flooding, hurricanes and earthquakes to droughts, heat waves and wildfires, killing thousands and inflicting billions of dollars in property and infrastructural damage. Furthermore, our planet is facing unprecedented environmental challenges including rapid urbanization, deforestation, pollution, loss of biodiversity, sea-level rising, melting polar ice-caps and climate change. With its synoptic view and repeatability, remote sensing offers a powerful and effective means to observe disaster damages and monitor our changing planet at local, regional and global scale. Since the launch of Landsat-1 in 1972, numerous Earth Observation satellites have been launched providing huge volumes of multitemporal data. Significant progress has been made to develop methods and techniques for multitemporal analysis, change detection and time series processing. A wide range of applications has been conducted to monitor global environmental changes and to assess disaster damages. It became apparent that a book on multitemporal remote sensing was overdue to provide an overview of the methods and techniques developed and to showcase a variety of application examples. With the enthusiastic support from the authors, the book proposal was submitted and approved by Springer in late 2013.

The chapters in this book are contributed by leading scientists in multitemporal remote sensing from around the world. I would like to express my sincere gratitude

to all authors for their commitment to this endeavor and for their patience in the long process. I would also like to thank all reviewers for volunteering their time to review the chapters and for their constructive comments and suggestions that helped to improve the chapters. Special thanks to the former Book Series Editor of EARSeL, André Marcal, and to the former Chairman of EARSeL, Ioannis Manakos for their support to the book project. Many thanks to Dorothy Furberg and Jan Haas for proofreading and language editing selected chapters.

I am grateful to my family for their enduring love and support. I am also thankful to my parents for their love and strong commitment to my education. Special thanks to my father who changed the subject in my university application to Computer Cartography at Nanjing University that lead me to remote sensing where I found my true passion.

Stockholm, Sweden
July, 2016

Yifang Ban

Contents

1 Multitemporal Remote Sensing: Current Status, Trends and Challenges	1
Yifang Ban	
2 Change Detection Techniques: A Review	19
Yifang Ban and Osama Yousif	
3 Change Detection in Urban Areas: Spatial and Temporal Scales	45
Paolo Gamba and Fabio Dell'Acqua	
4 Change Detection in Multitemporal Hyperspectral Images	63
Lorenzo Bruzzone, Sicong Liu, Francesca Bovolo, and Peijun Du	
5 Object-Based Change Detection in Urban Areas Using Multitemporal High Resolution SAR Images with Unsupervised Thresholding Algorithms	89
Osama Yousif and Yifang Ban	
6 Fusion of Multitemporal Spaceborne SAR and Optical Data for Urban Mapping and Urbanization Monitoring	107
Yifang Ban and Alexander Jacob	
7 Post-classification Change Detection in Arctic Glaciers by Multi-polarization SAR	125
Vahid Akbari, Anthony P. Doulgeris, and Torbjørn Eltoft	
8 Interferometric SAR Multitemporal Processing: Techniques and Applications	145
Daniele Perissin	
9 TIMESAT for Processing Time-Series Data from Satellite Sensors for Land Surface Monitoring.....	177
Lars Eklundh and Per Jönsson	

10	PhenoSat – A Tool for Remote Sensing Based Analysis of Vegetation Dynamics	195
	Arlete Rodrigues, André R. S. Marcal, and Mário Cunha	
11	Temporal Techniques in Remote Sensing of Global Vegetation	217
	Aleixandre Verger, Sivasathivel Kandasamy, and Frédéric Baret	
12	Soil Moisture Dynamics Estimated from MODIS Time Series Images	233
	Thomas Gumbrecht	
13	Temporal Analysis of Remotely Sensed Land Surface Shortwave Albedo	255
	Tao He and Shunlin Liang	
14	Observing the Response of Terrestrial Vegetation to Climate Variability Across a Range of Time Scales by Time Series Analysis of Land Surface Temperature	277
	Massimo Menenti, H.R. Ghafarian Malamiri, Haolu Shang, Silvia M. Alfieri, Carmine Maffei, and Li Jia	
15	A Review of Multitemporal Synthetic Aperture Radar (SAR) for Crop Monitoring	317
	Heather McNairn and Jiali Shang	
16	An Approach for Determining Relationships Between Disturbance and Habitat Selection Using Bi-weekly Synthetic Images and Telemetry Data	341
	Nicholas D. A. Brown, Trisalyn Nelson, Michael A. Wulder, Nicholas C. Coops, Thomas Hilker, Christopher W. Bater, Rachel Gaulton, and Gordon B. Stenhouse	
17	Multitemporal Remote Sensing for Inland Water Bodies and Wetland Monitoring	357
	Yeqiao Wang, Shuhua Qi, and Jian Xu	
18	Global Land Surface Water Mapping and Analysis at 30 m Spatial Resolution for Years 2000 and 2010	373
	Xin Cao, Jun Chen, Anping Liao, Lijun Chen, and Jin Chen	
19	Multitemporal Remote Sensing of Coastal Waters	391
	Susanne Kratzer, Krista Alikas, Therese Harvey, José María Beltrán-Abaunza, Evgeny Morozov, Sélima Ben Mustapha, and Samantha Lavender	
20	Monitoring Long-Term Disaster Recovery – Space and Ground Views	427
	Tuong-Thuy Vu and Daroonwan Kamthonkiat	

Contributors

Vahid Akbari Earth Observation Laboratory, Department of Physics and Technology, University of Tromsø – The Arctic University of Norway, Tromsø, Norway

Silvia M. Alfieri Department of Geoscience and Remote Sensing, Faculty of Civil Engineering, Delft University of Technology, Delft, The Netherlands

Institute for Mediterranean Agricultural and Forest Systems (ISAFOM), Naples, Italy

Krista Alikas Department of Remote Sensing, Tartu Observatory, Tartumaa, Estonia

Yifang Ban Division of Geoinformatics, KTH Royal Institute of Technology, Stockholm, Sweden

Frédéric Baret EMMAH-UMR 1114 – INRA UAPV, Avignon, France

Christopher W. Bater Forest Management Branch, Forestry Division, Alberta Agriculture and Forestry, Edmonton, AB, Canada

José María Beltrán-Abaunza Department of Ecology, Environment and Plant Sciences, Stockholm University, Stockholm, Sweden

Francesca Bovolo Center for Information and Communication Technology, Fondazione, Bruon Kessler, Trento, Italy

Nicholas D. A. Brown Department of Geography and Environmental Studies, Carleton University, Ottawa, ON, Canada

Lorenzo Bruzzone Department of Information Engineering and Computer Science, University of Trento, Trento, Italy

Xin Cao State Key Laboratory of Earth Surface Processes and Resource Ecology, Beijing Normal University, Beijing, China

Jin Chen State Key Laboratory of Earth Surface Processes and Resource Ecology, Beijing Normal University, Beijing, China

Jun Chen National Geomatics Center of China, Beijing, China

Lijun Chen National Geomatics Center of China, Beijing, China

Nicholas C. Coops Integrated Remote Sensing Studio, Department of Forest Resources Management, University of British Columbia, Vancouver, BC, Canada

Mário Cunha Faculdade de Ciências da Universidade do Porto, Department of GAOT & Centro de Investigação em Ciências Geo-Espaciais, Universidade do Porto, Porto, Portugal

Fabio Dell'Acqua Department of Electrical, Computer and Biomedical Engineering, University of Pavia, Pavia, Italy

Anthony P. Doulgeris Earth Observation Laboratory, Department of Physics and Technology, University of Tromsø – The Arctic University of Norway, Tromsø, Norway

Peijun Du Department of Geographical Information Science, Nanjing University, Nanjing, China

Lars Eklundh Department of Physical Geography and Ecosystem Science, Lund University, Lund, Sweden

Torbjørn Eltoft Earth Observation Laboratory, Department of Physics and Technology, University of Tromsø – The Arctic University of Norway, Tromsø, Norway

Paolo Gamba Department of Electrical, Computer and Biomedical Engineering, University of Pavia, Pavia, Italy

Rachel Gaulton School of Civil Engineering and Geosciences, Newcastle University, Newcastle upon Tyne, UK

Thomas Gumbrecht Karttur AB, Stockholm, Sweden

Therese Harvey Department of Ecology, Environment and Plant Sciences, Stockholm University, Stockholm, Sweden

Tao He Department of Geographical Sciences, University of Maryland, College Park, MD, USA

Thomas Hilker (Deceased Sep 5, 2016) Department of Geography and Environment, University of Southampton, Southampton, UK

Alexander Jacob Division of Geoinformatics, KTH Royal Institute of Technology, Stockholm, Sweden

Li Jia Institute of Remote Sensing and Digital Earth (RADI, CAS), Beijing, China

Per Jönsson Group for Materials Science and Applied Mathematics, Malmö University, Malmö, Sweden

Daroonwan Kamthonkiat Department of Geography, Faculty of Liberal Arts, Thammasat University, Bangkok, Thailand

Sivasathivel Kandasamy CCRS, Ottawa, ON, Canada

Susanne Kratzer Department of Ecology, Environment and Plant Sciences, Stockholm University, Stockholm, Sweden

Samantha Lavender Pixalytics Ltd, Plymouth, Devon, UK

Shunlin Liang Department of Geographical Sciences, University of Maryland, College Park, MD, USA

State Key Laboratory of Remote Sensing Science, School of Geography, Beijing Normal University, Beijing, China

Anping Liao National Geomatics Center of China, Beijing, China

Sicong Liu Department of Information Engineering and Computer Science, University of Trento, Trento, Italy

Carmine Maffei Department of Geoscience and Remote Sensing, Faculty of Civil Engineering, Delft University of Technology, Delft, The Netherlands

H. R. Ghafarian Malamiri Department of Geoscience and Remote Sensing, Faculty of Civil Engineering, Delft University of Technology, Delft, The Netherlands

Yazd University, Yazd, Iran

André R. S. Marcal Faculdade de Ciências da Universidade do Porto, Department of Matemática & INESC TEC, Universidade do Porto, Porto, Portugal

Heather McNairn Agriculture and Agri-Food Canada, Ottawa, ON, Canada

Massimo Menenti Department of Geoscience and Remote Sensing, Faculty of Civil Engineering, Delft University of Technology, Delft, The Netherlands

Institute of Remote Sensing and Digital Earth (RADI, CAS), Beijing, China

Evgeny Morozov Department of Ecology, Environment and Plant Sciences, Stockholm University, Stockholm, Sweden

NIERSC, St. Petersburg, Russia

Selima Ben Mustapha Department of Ecology, Environment and Plant Sciences, Stockholm University, Stockholm, Sweden

Institut Maurice-Lamontagne, Pêches et Océans Canada, Mont-Joli, Québec, Canada

Trisalyn Nelson School of Geographical Sciences and Urban Planning, Arizona State University, Tempe, AZ, USA

Daniele Perissin Lyle School of Civil Engineering, Purdue University, West Lafayette, IN, USA

Shuhua Qi Ministry of Education's Key Laboratory of Poyang Lake Wetland and Watershed Research, School of Geography and Environmental Science, Jiangxi Normal University, Nanchang, Jiangxi, China

Arlete Rodrigues Faculdade de Ciências da Universidade do Porto, Department of GAOT & Centro de Investigação em Ciências Geo-Espaciais, Universidade do Porto, Porto, Portugal

Haolu Shang Department of Geoscience and Remote Sensing, Faculty of Civil Engineering, Delft University of Technology, Delft, The Netherlands

Institute of Remote Sensing and Digital Earth (RADI, CAS), Beijing, China

Jiali Shang Agriculture and Agri-Food Canada, Ottawa, ON, Canada

Gordon B. Stenhouse Foothills Research Institute, Hinton, AB, Canada

Aleixandre Verger CREAf, Cerdanyola del Vallès, Catalonia, Spain

Tuong-Thuy Vu Department of Physics, International University, Vietnam National University HCMC, Ho Chi Minh City, Vietnam

Yeqiao Wang Department of Natural Resources Science, University of Rhode Island, Kingston, RI, USA

Ministry of Education's Key Laboratory of Poyang Lake Wetland and Watershed Research, School of Geography and Environmental Science, Jiangxi Normal University, Nanchang, Jiangxi, China

Michael A. Wulder Canadian Forest Service (Pacific Forestry Centre), Natural Resources Canada, Victoria, BC, Canada

Jian Xu Ministry of Education's Key Laboratory of Poyang Lake Wetland and Watershed Research, School of Geography and Environmental Science, Jiangxi Normal University, Nanchang, Jiangxi, China

College of Chemistry and Chemical Engineering, Jiangxi Normal University, Nanchang, Jiangxi, China

Osama Yousif Division of Geoinformatics, KTH Royal Institute of Technology, Stockholm, Sweden

Chapter 1

Multitemporal Remote Sensing: Current Status, Trends and Challenges

Yifang Ban

Abstract Our planet is facing unprecedented environmental challenges including rapid urbanization, deforestation, pollution, loss of biodiversity, sea-level rising, melting polar ice-caps and climate change. With its synoptic view and the repeatability, remote sensing offers a powerful and effective means to observe and monitor our changing planet at local, regional and global scale. Since the launch of Landsat-1 in 1972, numerous Earth Observation satellites have been launched providing large volumes of multitemporal data acquired by multispectral, hyperspectral, passive microwave, synthetic aperture radar (SAR), and LiDAR sensors. This chapter first presents an overview of the Earth Observation sensors and trends in multitemporal observation capacity. Then the current status, challenges and opportunities of multitemporal remote sensing are discussed. Finally the synopsis of the book is provided covering a wide array of methods and techniques in processing and analysis of multitemporal remotely sensed images as well as a variety of application examples in both land and aquatic environments.

1.1 Introduction

Our planet is facing unprecedented environmental challenges including rapid urbanization, deforestation, pollution, loss of biodiversity, sea-level rising, melting polar ice-caps and climate change, just to name a few. The conversion of Earth's land surface to urban areas is one of the most irreversible human impacts on the global biosphere. It hastens the loss of highly productive farmland, affects energy demand, alters the climate, modifies hydrologic and biogeochemical cycles, fragments habitats, and reduces biodiversity (Seto et al. 2011). Deforestation, on the other hand, is a growing problem in the world's rain forests and has many negative effects on the environment including the loss of habitat for millions of species, the lessening of carbon sink, soil erosion and flooding, among others. Melting of the Arctic glaciers and ice-caps as well as rising of sea-level not only are manifestation

Y. Ban (✉)

Division of Geoinformatics, KTH Royal Institute of Technology, Stockholm, Sweden
e-mail: yifang@kth.se

of climate change but also have serious environmental consequences. Therefore, effective methods and tools are of critical importance to map, monitor and analyze environmental changes and evaluate their impact in a timely and reliable manner.

With its synoptic view and the repeatability, remote sensing offers a powerful and effective means to observe and monitor our changing planet at local, regional and global scale. Since the launch of Landsat-1 in 1972, numerous Earth Observation (EO) satellites have been launched providing large volumes of multitemporal data acquired by multispectral, hyperspectral, passive microwave, synthetic aperture radar (SAR), and LiDAR sensors. The increasing number of Earth Observation systems presents enhanced capability to acquire multitemporal data of the Earth surface with improved spectral, spatial, radiometric and temporal resolutions. Such new scenario significantly increases our ability to observe, monitor and predict the dynamics of natural and anthropogenic processes, thus helps to improve our understanding of environmental/climate changes and to support sustainable development.

In this chapter, the Earth Observation sensors and trends in multitemporal observation capacity are presented first. Then the current status, challenges and opportunities of multitemporal remote sensing are discussed. Finally the synopsis of the book is provided.

1.2 Multitemporal Earth Observation Satellites

The first Landsat, launched on July 23, 1972, marked a new era for Earth observations. Since then, seven Landsat satellites have been successfully launched providing data continuity for long-term observation and monitoring of regional and global change. By the end of 2013, a total of 197 earth observing polar orbiters were successfully launched and nearly 50 % were still operational. The number of launches of polar orbiting Earth Observation satellites per year also increased, especially in the past decade (Fig. 1.1). For examples, on 1st August 1972 there was one mission in orbit; by 1st August 1982 the number of satellites had increased to eight, by 1st August 1992 there were twenty such missions, by 1st August 2002 there were thirty-nine and by 1st August 2012 eighty-three. Out of the 197 satellites, only 19 missions carry SAR imagers (Belward and Skøien 2015).

The 44-year archive of the Landsat program is the most extensive, longest-running record of Earth observations from space. Through the Landsat open archives program, the long-term satellite time series data have been freely available since 2008 (Wulder et al. 2012). Free imagery enables reconstruction of the history of Earth's surface back to 1972, chronicling both anthropogenic and natural changes during a time when our population doubled and the impacts of climate change became noticeable (Woodcock et al. 2008). The Earth Resources Observation and Science (EROS) Center at USGS provided approximately 25,000 Landsat images in 2001, the prior record for annual distribution, at a price of \$600 per scene. By comparison, EROS distributed approximately 2.5 million images for free in 2010.

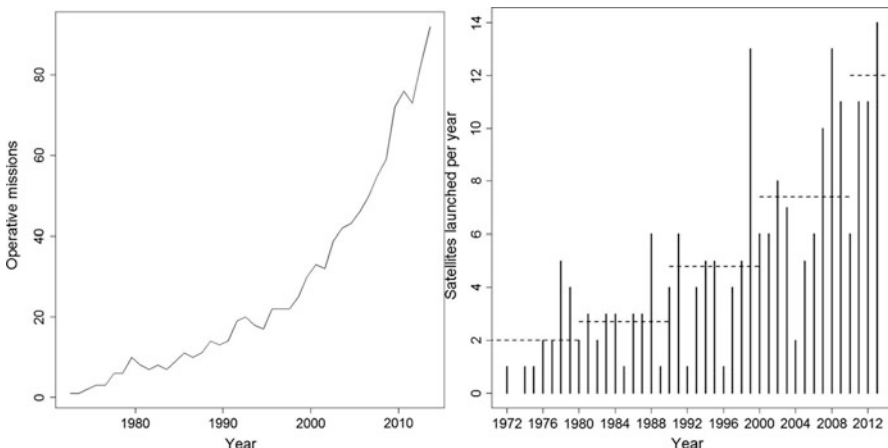


Fig. 1.1 The number of near-polar orbiting, land imaging civilian satellites. *Left:* # of operational satellites/year as of 1st August 1972 to 2013; *Right:* # of launches per year. The horizontal dotted lines denote the average number launched per decade (1970s–2010s) (Belward and Skøien 2015)

As a result of the free data policy, combined with notable advancements in technical capacity to analyze large datasets for long-term and large area investigations and applications, Landsat data are experiencing more widespread use by an ever increasing range of end users in a variety of disciplines (Wulder et al. 2012). This is reflected in the increasing number of publications as shown in the next section. One important application example is the production of bi-temporal global land cover maps at 30 m resolution for 2000 and 2010 that are also open access (Chen et al. 2014).

Multitemporal coarse-resolution satellite data (typically 250 m–1 km) have had a ‘free-and-open’ data policy for many years, the longest-standing example being the Advanced Very High Resolution Radiometer (AVHRR) data from the NOAA satellites (Belward and Skøien 2015). The satellite sensors at coarse resolution offer daily observations at global scales and provide the best possibility for cloud-free observations (Lasaponara and Lanorte 2012). In fact, AVHRR NDVI time series (1981–2015) were the first long time-series available for monitoring temporal changes and dynamic processes of Earth surface. The launches of Moderate Resolution Imaging Spectroradiometer (MODIS) on board Terra (2000–present) and Aqua (2002 to present) were another significant milestones in multitemporal remote sensing as they provide time series data in 36 spectral bands imaging the entire Earth’s surface every 1–2 days. The availability of the large volume time series data at 25 m resolution quickly expended the development of times series methodology and applications (Eklundh and Jönsson 2015), as reflected in the number of publications described in next section. Other time series data at coarse resolution include SPOT-4/5 Vegetation (1998–2013), PROBA Vegetation (Follow-on to Vegetation, 2013–present), SeaWiFS (1997–2010), Suomi-NPP VIIRS (2012–present) (Pinzon and Tucker 2014) as well as ENVISAT Medium Resolution Imaging Spectrometer

(MERIS, 2002–2012). These time series data provide consistent, long-term satellite records to monitor trends in land surface dynamics as well as processes occurring in the oceans and the lower atmosphere.

The launch of SPOT-1 in 1986 marked a new era of commercialized Earth observation at high-resolution, i.e., 10 m and 20 m for panchromatic and multispectral images respectively. Since then, three generations of SPOT satellites have been launched with improved spatial resolution to 1.5 m for panchromatic and 6 m for multispectral images. Compared to Landsat data, however, SPOT images were much less used in multitemporal analysis primarily due to their higher-costs. The trend of increasing spatial resolution is apparent in the emergence of ‘very high’ resolution classes benefited from the declassified spy satellite technology. With the launch of IKONOS, the first commercial very high resolution satellite in 1999, panchromatic and multispectral images at spatial resolutions of 1 m and 4 m became available. The spatial resolutions are further improved by QuickBird (0.65 m/2.62 m), WorldView-1/2 (0.46 m/1.84 m), GeoEye-1 (0.46 m/1.84 m), Pleiades-1A/1B (0.5 m/2 m). The highest resolutions were reached by WorldView-3 at 31 cm panchromatic resolution and 1.24 m multispectral resolution in 2014. Very high resolution multitemporal data enable new, strategic and challenging applications, such as monitoring illegal excavations in archaeological areas (Lasaponara and Lanorte 2012), precision farming, detailed disaster damage assessment and urban mapping, among others. However, the use of very high resolution data for multitemporal analysis are rather limited as reflected in the low number of publications (see next section) due to their high cost. Figure 1.2 shows then number of multispectral and panchromatic sensors at different spatial resolutions on board near-polar orbiting, land imaging civilian satellites per year (Belward and Skøien 2015).

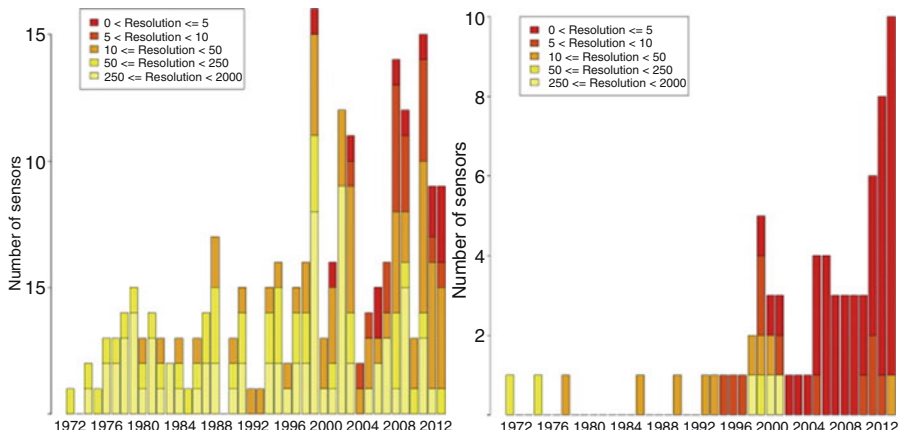


Fig. 1.2 Number of multispectral (Left) and panchromatic (Right) sensors at different spatial resolutions on board near-polar orbiting, land imaging civilian satellites per year (Belward and Skøien 2015)

One of the latest developments in the optical remote sensing is the use of the CubeSat concept in Earth Observation. Since 2014, Planet Labs have launched over 100 small satellites with the objective of having 150 satellites in a sun synchronous orbit by the end of 2016 collecting the entire land mass of the Earth every day at 3–5 m resolution in Red, Green, Blue and Near Infrared wavelengths (Planet Labs 2015). Terra Bella (formerly Skybox Imaging)'s SkySat-1/-2 are microsatellites carrying a two-dimensional sensor array capable of providing 0.9 m resolution imagery in red, green, blue, near-infrared and panchromatic bands as well as the first-ever commercial high-resolution video (1.1 m resolution) of Earth from a satellite (Terra Bella 2016). These data offer the potential to monitor land surface changes at high-spatial and high-temporal resolution, but cost is an obvious issue.

The first SAR imaging system is the Seasat mission, launched by the U.S. in 1978 with a L-band SAR at 25 m resolution on board. As the mission duration is only 105 days, Seasat SAR data had very little use in multitemporal remote sensing. The first multitemporal SAR dataset became available with the launch of the European Space Agency's ERS-1 in 1991 with C-VV SAR at 30 m resolution on board. This is followed by the launches of Russia's ALMAZ-1B S-band SAR at 30 m resolution in 1991 and Japan's JERS-1 L-band SAR at 18 m resolution in 1992. These early SAR sensors are in single frequency, single polarization, single incidence-angle and single resolution. The launch of Canada's RADARSAT-1 in 1995 marked the beginning of high-resolution SAR systems with multiple beams at various spatial resolutions (8 m–100 m). To provide data continuity, ESA launched ERS-2 in 1995 with the same sensor and ENVISAT in 2002 with C-band SAR in dual-polarization and multiple beam modes and resolutions. ESA's ERS SAR and ENVISAT ASAR data have been most used for multitemporal SAR remote sensing, as reflected in the number of publications (see next section). Another data continuity mission is Japan's Phased Array type L-band Synthetic Aperture Radar (PALSAR) in 2005, also with multiple beams and resolutions (10–100 m). Very high resolution SAR data became available with the launch of RADARSAT-2 with ultra-fine beam C-band SAR at 3 m resolution in 2007. Another advanced feature of RADARSAT-2 SAR is to acquire data in fully polarimetric mode at 10 m resolution, in addition to the continued multi-beam multi-resolution modes of RADARSAT-1. The highest resolution SAR became available in 2007 with the launches of Italy's CosmoSkymed and Germany's TerraSAR, both in X-band at 1 m resolution. Another advance is the launch of TanDEM-X in 2010 providing high-resolution SAR interferometry (InSAR) data for multitemporal applications from monitoring land subsidence to glacier retreats.

Time series data from very coarse resolution (25–50 km) passive microwave scatterometer have also been available since the early 1990s, including ERS-1/-2 scatterometer (SCAT), European Meteorological Operational Satellites (MetOp) Advanced Scatterometer (ASCAT), and NASA Quick Scatterometer (QuikSCAT). These data are mainly used to derive soil moisture, wind speed and direction, and for sea ice monitoring. Multitemporal thermal infrared data, on the other hand, are mainly from Landsat sensors, AVHRR, MODIS and AATSR. They have been

used to analyze multiannual to multidecadal LST patterns as well as hotspots and anomalies in the context of urban heat islands and long-burning underground coal fires, etc. However, the analysis of time series of convincing length is rare in these contexts (Kuenzer et al. 2015).

One of the significant developments in multitemporal remote sensing is the open access to big EO data at high-spatial and temporal resolutions. With the recent launches of ESA Sentinel-1A/B and Sentinel-2A, multitemporal SAR and optical data in 10 m and 20 m resolution with 6-day global coverage become freely available. The images acquired by the Sentinel satellites represent an enormous amount of data: whereas ENVISAT provided 0.3 terabyte (TB) per day, each Sentinel-1 provides 1.8 TB/day, with Sentinel-2 s providing 1.6 TB and Sentinel-3 s providing 0.6 TB (Showstack 2014). Processing and mining such huge volume of data presents both challenges and opportunities in multitemporal remote sensing.

1.3 Multitemporal Remote Sensing: Trend, Challenges and Opportunities

As discussed in the previous section, a large number of new spaceborne remote sensing systems have been launched in the past two decades. The enhanced capability to acquire multitemporal data of the Earth surface with improved spatial, spectral, radiometric and temporal resolution have significantly increased the interest in multitemporal remote sensing, time series processing and applications. As a result, various methods and algorithms have been development for change detection (e.g., Bruzzone and Prieto 2000; Lu et al. 2004; Bovolo and Bruzzone 2005; Gamba et al. 2006; Bovolo and Bruzzone 2007a, b; Ban and Yousif 2012; Yousif and Ban 2013; Liu et al. 2015) and time series analysis (e.g., Roerink et al. 2000; Jönsson and Eklundh 2004; Galford et al. 2008; Pinzon and Tucker 2014; Hermosilla et al. 2015; Kuenzer et al. 2015; Müller et al. 2015). Multitemporal remote sensing have been used for a wide range of applications including urban mapping (e.g., Gong et al. 1992; Gamba and Harold 2009; Pesaresi et al. 2013; Ban et al. 2015), urbanization monitoring (e.g., Taubenböck et al. 2012; Haas et al. 2015) and environmental impact assessment (e.g., Güneralp and Seto 2013; Haas and Ban 2014), Crop monitoring (e.g., Shao et al. 2001; Bouvet et al. 2009; McNairn et al. 2014), deforestation (e.g., Skole and Tucker 1993; Rignot et al. 1997; Tucker and Townshend 2000; Achard et al. 2002; Hansen et al. 2013), desertification (e.g., Yang et al. 2005; Dawebait and Morari 2012), flooding (e.g. Martinez and Le Toan 2007), biodiversity monitoring (e.g., Turner et al. 2003; Kuenzer et al. 2014; Skidmore et al. 2015), land cover mapping (e.g., Anderson et al. 1976; Friedl et al. 2002; Bontemps et al. 2011; Ban and Jacob 2013; Chen et al. 2015) and change detection (e.g., Bruzzone and Serpico 1997; Zhu and Woodcock 2014), vegetation dynamics (Olsson et al. 2005; Hilker et al. 2014), land surface dynamics (e.g., Liang 2004; Kuenzer et al. 2015), natural disasters and hazards (Tralli et al. 2005; Bovolo and

Bruzzone 2007a; Gamba et al. 2007; Vu and Ban 2010), coastal monitoring (Arnone and Parsons 2005; Kratzer et al. 2008), Retreat of glaciers and ice shelves (e.g., Rignot 2001; Rack and Rott 2004; Rignot et al. 2014), as well as sea ice monitoring (e.g, Eriksson et al. 2010; Mahmud et al. 2016). Multitemporal remote sensing has demonstrated its enormous capability and potential for environmental change monitoring at various scales.

Driven by the increasing interests in studying the dynamics of environmental changes, improved sensor technology and image processing techniques as well as open data policy, the remote sensing community has witnessed a substantial increase in multitemporal remote sensing research, development and applications in the past two decades. As shown in Fig. 1.3, the number of journal articles (including review articles) on change detection has been increasing rapidly since 2000. Similar trends are observed when search for number of journal articles (including review articles) on multitemporal remote sensing or time series. This period coincides with the launches of high-spatial or high-temporal resolution optical satellite systems, advanced spaceborne SAR sensors, the development of innovative multitemporal image processing and analysis techniques as well as open access to Landsat data archive. The most relevant peer-reviewed journals for multitemporal remote sensing, change detection and time series analysis are presented in Table 1.1. It is apparent that all major remote sensing journals have published articles on these subjects. The top five journals are International Journal of Remote Sensing, Remote Sensing of Environment and IEEE Transactions on Geoscience And Remote Sensing, Remote Sensing, and IEEE Journal of Selected Topics in Applied Earth Observations and Remote Sensing (JSTARS). Started in 2009 and 2008 respectively, Remote Sensing

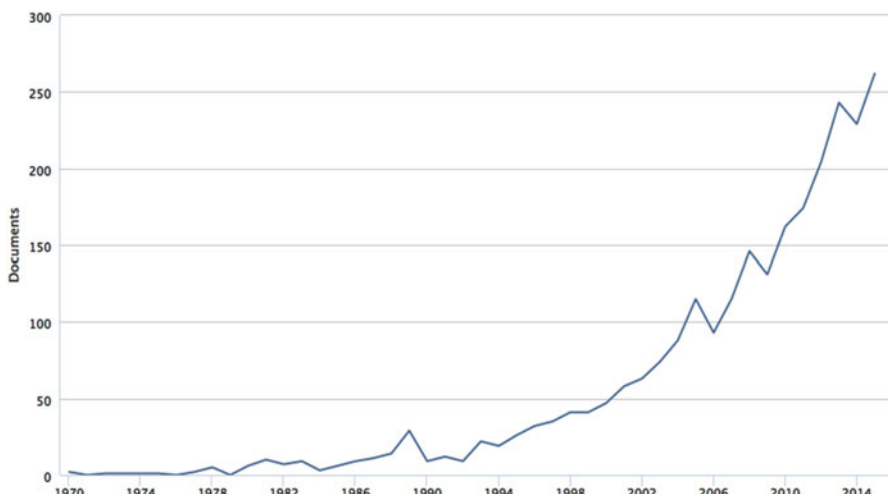


Fig. 1.3 The number of articles (including review articles) per year on change detection derived from a Scopus search on July 15, 2016, by the author

Table 1.1 Literature search results using Scopus on ‘Multitemporal Remote Sensing’, ‘Change Detection’, ‘Remote Sensing Time Series’

Number of journal papers on multitemporal remote sensing	Number of journal papers on remote sensing + change detection	Number of journal papers on remote sensing + time series
<i>International Journal of Remote Sensing</i> (299)	<i>International Journal of Remote Sensing</i> (432)	<i>Remote Sensing of Environment</i> (427)
<i>IEEE Transactions on Geoscience and Remote Sensing</i> (242)	<i>Remote Sensing of Environment</i> (403)	<i>International Journal of Remote Sensing</i> (277)
<i>Remote Sensing of Environment</i> (213)	<i>IEEE Transactions on Geoscience And Remote Sensing</i> (262)	<i>Remote Sensing</i> (191)
<i>Remote Sensing</i> (135)	<i>Remote Sensing</i> (165)	<i>IEEE Transactions on Geoscience And Remote Sensing</i> (150)
<i>IEEE Journal of Selected Topics in Applied Earth Observations and Remote Sensing</i> (78)	<i>IEEE Geoscience and Remote Sensing Letters</i> (128)	<i>IEEE Journal of Selected Topics in Applied Earth Observations and Remote Sensing</i> (97)
<i>International Journal of Applied Earth Observation and Geoinformation</i> (58)	<i>IEEE Journal of Selected Topics in Applied Earth Observations And Remote Sensing</i> (124)	<i>International Journal of Applied Earth Observation and Geoinformation</i> (74)
<i>ISPRS Journal of Photogrammetry and Remote Sensing</i> (57)	<i>Photogrammetric Engineering And Remote Sensing</i> (106)	<i>ISPRS Journal of Photogrammetry and Remote Sensing</i> (63)
<i>IEEE Geoscience and Remote Sensing Letters</i>	<i>ISPRS Journal of Photogrammetry And Remote Sensing</i> (88)	<i>IEEE Geoscience and Remote Sensing Letters</i> (53)
<i>Journal of Applied Remote Sensing</i> (36)	International Journal Of Applied Earth Observation And Geoinformation (65)	<i>Journal of Applied Remote Sensing</i> (38)
<i>Canadian Journal of Remote Sensing</i> (35)	Journal of Applied Remote Sensing (62)	<i>Canadian Journal of Remote Sensing</i> (37)
<i>Photogrammetric Engineering and Remote Sensing</i> (31)	Canadian Journal of Remote Sensing (55)	<i>Photogrammetric Engineering and Remote Sensing</i> (37)

Note: The search was conducted on July 15, 2016. A total of 2290 papers on ‘multitemporal remote sensing’, 3188 papers on ‘remote sensing + change detection’ and 3694 papers on ‘remote sensing + time series’ were found

and JSTARS, the two new journals, have managed to reach the top five. A number of special issues on multitemporal analysis or time series analysis have been published in these top journals except in *Remote Sensing of Environment*.

Figure 1.4 shows the Scopus search of publications for multitemporal optical data using the Keyword ‘Multitemporal’ or ‘Change Detection’ or ‘Time Series’ + ‘EO optical sensor/satellite’, All publications include all journal articles, review articles,

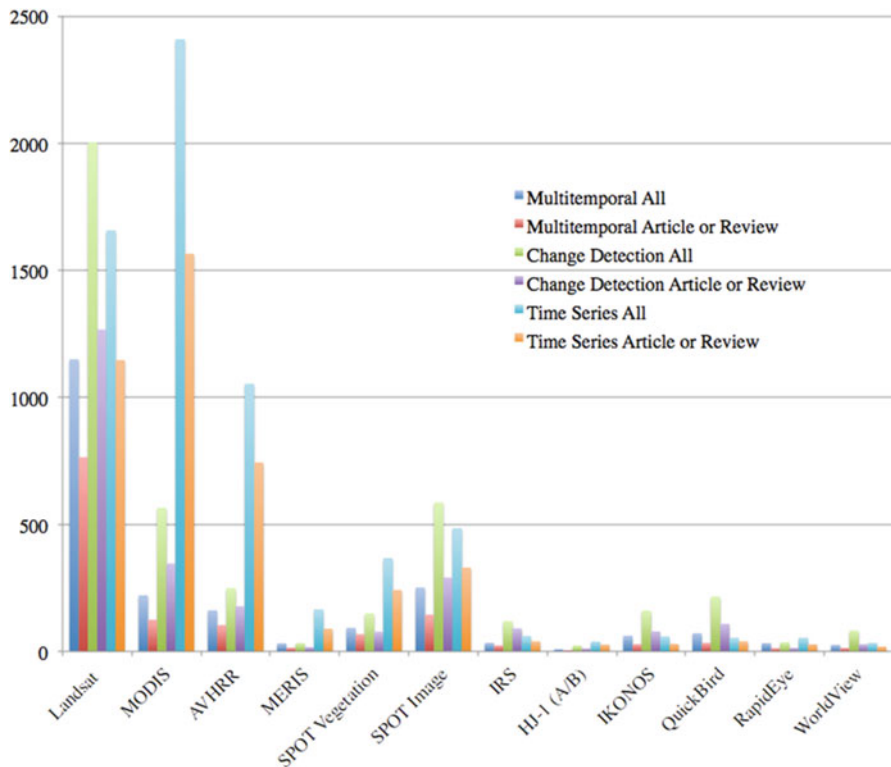


Fig. 1.4 Optical sensors: Scopus search of publications using the keyword ‘Multitemporal’ or ‘Change Detection’ or ‘Time Series’ + EO sensor/satellite’, all publications include all journal articles, review articles, books, book chapters, conference papers, conference reviews, editorials, and letters. Article or review only includes journal articles and reviews

books, book chapters, conference papers, conference reviews, editorials, and letters. Article or Review only includes journal articles and reviews. With its longest time-series, Landsat has the highest numbers of publications for ‘multitemporal’ and ‘change detection’, significantly more than other EO sensors. However, MODIS has the top hit for ‘time series’ while Landsat in the second place and AVHRR in the third place. This could be attributed to that MODIS time series have been freely available since 2000 while Landsat’s open data policy was only in place since 2008. Fewer publications were found on MERIS and SPOT Vegetation in comparison to MODIS. In spite of the high costs of SPOT images, the number of publications on ‘change detection + SPOT image’ gained number two place indicating interests high-resolution data in change detection methodology and applications. Limited number of publications on very high resolution sensors was due to their high costs while the low number of publications on IRS and HJ-1 data is due to their availability and accessibility.

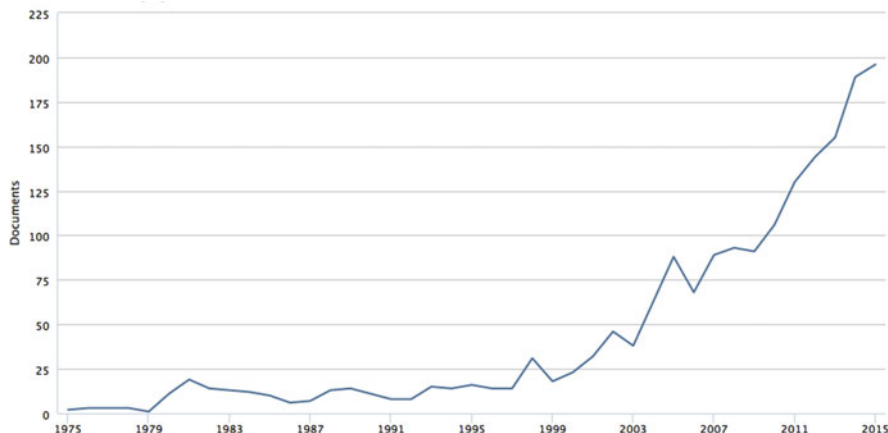


Fig. 1.5 Number of publications per year from Scopus search for ‘Change Detection’ and ‘Landsat’

Figure 1.5 Shows that the number of publications per year from Scopus search for ‘Change Detection’ and ‘Landsat’. It shows that the number of publications per year using Landsat for change detection/multitemporal analysis is relatively low in the early years. Since the launch of Landsat-7 in 1999 with a new panchromatic band at 15 m spatial resolution, the number of publications increased significantly, especially after the Landsat free data policy in 2008, the publications per year experienced exponential growth, from approx. 90 in 2009 to approx. 200 in 2015.

Scopus search of publications for multitemporal SAR data using the Keyword ‘Multitemporal’ or ‘Change Detection’ or ‘Time Series’ + EO sensor/satellite’ is presented in Fig. 1.6. The total number of publications for SAR are much lower than optical data. With its longest SAR time series, ERS holds the top places for ‘Multitemporal’ and ‘Time Series’ as well as ‘change detection’ in journal and review articles. RADARSAT has the highest hit for all papers on ‘change detection’, second place in ‘multitemporal’ and third place in ‘time series’. ENVISAT ASAR holds the second place for ‘time series’. Compared to the top three, both ALOS PALSAR and TerraSAR-X also have good number of publications indicating interests in multitemporal L- and X-band SAR analysis and applications.

Multitemporal remote sensing has emerged as a new frontier for Earth observations. With the increasing number of Earth Observation systems with enhanced capacities and free access to terabytes and petabytes of multitemporal data with global coverage, the remote sensing community is presented with major challenges and ample opportunities. Big data analytics paradigm needs to be introduced to image processing and analysis frameworks, novel processing and data mining methods are necessary to handle longer and denser time series data, effective change detection techniques need to be developed to process VHR multispectral, SAR, hyperspectral images and for cross-sensor change detection. Data fusion methods need to be advanced to integrate multi-sensor multi-resolution data. Multi-scale

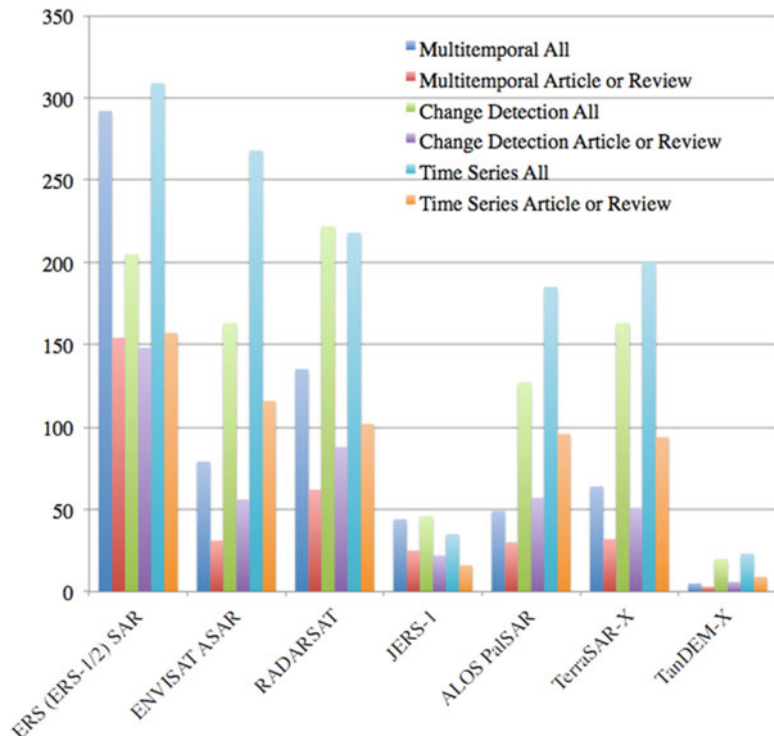


Fig. 1.6 SAR: Scopus search of publications using the keyword ‘Multitemporal’ or ‘Change Detection’ or ‘Time Series’ + EO sensor/satellite’, all publications include all journal articles, review articles, books, book chapters, conference papers, conference reviews, editorials, and letters. Article or review only includes journal articles and reviews

analysis with a holistic approach is necessary for monitoring environmental changes from micro-level to macro-level. In addition, cloud-based data repository and processing such as Google Earth Engine could also facilitate global environmental change monitoring, with Global Forest Watch (Davis and Thau 2014) as an excellent example. Last but not least, new applications are expected to emerge from these new datasets, technological developments and paradigm shifts.

1.4 Synopsis of the Book

The book intends to provide an overview of a wide array of methods and techniques in processing and analysis of multitemporal remotely sensed images as well as a variety of application examples covering both land and aquatic environments. A broad range of multitemporal datasets is used in the methodology demonstrations and application examples. Multispectral and hyperspectral data include Landsat,

ASTER, HJ-1, MODIS, AVHRR, MERIS, SPOT Vegetation, SeaWiFS and Hyperion while SAR data include ERS, ENVISAT, Sentinel-1A, RADARSAT, ALOS PALSAR, TerraSAR-X and TanDEM-X. Passive microwave data is also used.

Chapter 1 provides a synopsis of Earth Observation sensors and trends in multitemporal observation capacity as well as the current status, challenges and opportunities of multitemporal remote sensing. Chapters 2, 3, 4, 5, 6 and 7 are focused on change detection. First, Chap. 2 provides a comprehensive review of the recent development in change detection techniques using both optical and SAR images. Various aspects of change detection processes were presented including data preprocessing, change image generation and change detection algorithms. Major challenges for change detection are also identified. Chapter 3 provides a detailed analysis of a number of the issues arising from urban change detection. Specifically, the role of very high resolution sensors and their relevance with respect to either fast or slow changes in human settlement is analyzed. The possibility to exploit long temporal sequences of coarser resolution data is also explored. Chapter 4 addresses the multiple-change detection problem in multitemporal hyperspectral remote sensing images in an agricultural landscape. First, an analysis of the concept of “change” is given from the perspective of pixel spectral behaviors, taking into account the intrinsic complexity of the hyperspectral data. Then a hierarchical change-detection approach is presented aiming at detecting multiple-change information in an unsupervised way. Satisfactory results obtained on both simulated and real bi-temporal Hyperion images confirm the effectiveness of the proposed hierarchical method. Chapter 5 investigates object-based unsupervised change detection in Beijing and Shanghai using very high resolution SAR images. Three thresholding algorithms, i.e., the Kittler-Illingworth algorithm, the Otsu method, and the outlier detection technique, are tested and compared. Promising results are presented and limitations are revealed. Chapter 6 evaluates multitemporal spaceborne SAR and optical data for urban land cover mapping and urbanization monitoring using KTH-SEG and KTH-Pavia Urban Extractor. The results indicate that carefully selected multitemporal SAR dataset and its fusion with optical data could produce nearly as good classification accuracy as the whole multitemporal dataset. The results also show that urban areas as well as small towns and villages could be well extracted using multitemporal Sentinel-1A SAR data while major urban areas could be well extracted using a single-date single-polarization SAR image. The results clearly demonstrate that multitemporal SAR data are cost-and time-effective way for monitoring spatiotemporal patterns of urbanization. Chapter 7 presents a processing chain for post-classification change detection in Arctic glaciers using multi-polarization SAR images. The method consists of terrain correction, segmentation using an unsupervised contextual non-Gaussian clustering algorithm, consistency analysis of the segmentation algorithm, post-classification change detection. A series of dual polarization C-band ENVISAT ASAR images over the Kongsvegen glacier, Svalbard, are used for demonstration.

The basic theory of SAR interferometry and Multi-Temporal InSAR is discussed in Chap. 8. InSAR is potentially a very powerful technology to estimate DEMs and ground movement, however, InSAR is affected by important limitations such

as decorrelation, phase ambiguity and atmospheric biases. Multi-Temporal InSAR techniques offer a series of tools for lessening InSAR limitations, making it possible to process and analyze displacement time series, and also to precisely estimate ground elevation.

Chapters 9, 10, 11, 12, 13 and 14 present various processing and analysis methods for coarse-resolution time series with a focus on monitoring vegetation and land surface dynamics. Chapter 9 presents TIMESAT, a software package for processing time-series data from coarse resolution satellite sensors for land surface monitoring using asymmetric Gaussian fits, double-logistic fits, and Savitzky-Golay filtering. Example applications using TIMESAT are also given including phenology and phenological variations; ecological disturbances; vegetation classification and characterization; agriculture applications; climate applications; and for improving remote sensing signal quality. Chapter 10 presents PhenoSat, another software tool that extracts phenological information from satellite-based vegetation index time-series. The main characteristics and functionalities of PhenoSat are evaluated using multi-year NDVI derived from SPOT VEGETATION and NOAA AVHRR with six fitting methods: cubic splines, piecewise-logistic, Gaussian models, Fourier series, polynomial curve-fitting and Savitzky-Golay. The results show that PhenoSat is capable to extract phenological information consistent with reference measurements, and to adapt to different vegetation types, and different satellite data sources. Chapter 11 compares six methods to improve the temporal coherence and continuity of leaf area index (LAI) time series. A dedicated approach combining the local temporal smoothing gap filling (TSGF) filter with a climatology gap filling technique is then developed. This method constitutes the basis of the algorithm for the operational production of continuous and smooth time series of biophysical variables from VEGETATION data within the European Copernicus Global Land Service. Chapter 12 attempts to define metrics relevant for capturing the soil moisture dynamics from an annual series of wetness estimates derived from global MODIS images. Different algorithms for both smoothing and gap-filling the time series are tested with the results compared to in-situ data. Metrics capturing the global surface wetness phenology for 2011, extracted after smoothing using a simplified locally weighted scatterplot smoothing (LOWESS) model, are presented at a spatial resolution of 500 m for the calendar year 2011. Chapter 13 first discusses the potential and limitations of long-term time series analyses of land surface albedo using satellite-derived surface albedo products such as GLASS, GlobAlbedo, MERIS, MODIS. Then this chapter presents some recently developed methods to detect sensor change, to reduce data gaps, and to improve data consistency and accuracy of existing satellite products, followed by a case study on the temporal analysis of regional long-term land surface albedo changes. Chapter 14 analyzes vegetation response to climate variability using time series analysis of land surface temperature in two different spectral regions: Thermal Infrared (TIR) observations of land surface temperature to study the thermal behavior of the land surface in response to weather and climate; and 37 GHz observations of the polarization difference in brightness temperature to retrieve the fractional abundance of water-saturated soil. Two methods are applied to identify and remove anomalous

observations (outliers) and to fill the resulting gaps: Harmonic ANalysis of Time Series (HANTS) and the Multichannel Singular Spectrum Analysis (M-SSA). Three applications of time series of land surface temperature are presented: (a) monitoring of spectral thermal admittance of the land surface; (b) estimation and mapping of air temperature and (c) monitoring of thermal load to assess the risk of forest fires.

Chapter 15 provides a comprehensive review of multitemporal SAR for crop monitoring. First, SAR's response to crop type and conditions are discussed, then SAR for crop classification and acreage estimation is presented. Temporal trends in SAR's response and sensitivity to crop phenology is then discussed and sensitivity of SAR to crop bio-physical properties including LAI, canopy biomass and crop height are presented. Chapter 16 highlights the opportunities and the challenges for integrating wildlife location data with high spatial and temporal resolution landscape disturbance datasets, available from remotely sensed imagery. The 16-day outputs from the Spatial Temporal Adaptive Algorithm for mapping Reflectance Change (STAARCH) disturbance maps are integrated with grizzly bear (*Ursus arctos*) telemetry data. The results indicate that males and females avoided same-year disturbances, while male bears were most likely to avoid recently disturbed areas in summer. When intra-year (disturbances mapped at a 16-day time-step) analysis of disturbance was compared to traditional annual time-step analysis, annual aggregation of disturbance data resulted in an increase in the observed selection of same-year disturbed habitat, although change was not statistically significant ($\alpha 0.05$). The use of low-temporal resolution disturbance data to evaluate short-term impacts on wildlife is cautioned and the need for further development of probabilistic- and model-based techniques for overcoming spatial-temporal differences between datasets is highlighted.

Chapters 17, 18 and 19 present applications of multitemporal remote sensing in coastal and aquatic environment. Chapter 17 summarizes remote sensing applications in water and wetland monitoring, in particular in the topics of monitoring water quality, water surface areas and water fluctuation in wetland areas. The chapter then introduces two cases of monitoring studies in the Poyang Lake, the largest fresh water lake in China, in terms of monitoring of fluctuation and variation of water surface areas using MODIS data product, and monitoring of variation of natural wetlands corresponding to the changing water levels of Poyang Lake using Landsat data. Chapter 18 describes a bi-temporal study of global land surface water in China's Global Land Cover Mapping project. Through collection and processing of Landsat TM/ETM+, China's HJ-1 satellite imagery and other remotely sensed data, global water layers in 2000 and 2010 were extracted using a pixel-, object- and knowledge-based approach. Based on the GlobeLand30-Water 2000/2010 products, the spatial distribution patterns and temporal fluctuation trends of land surface water at global scale are analyzed in the chapter. Chapter 19 addresses some of the recent developments in marine coastal remote sensing with regards to the evaluation of water quality using spaceborne multitemporal data. First, a general introduction to marine remote sensing is provided. Then the chapter reports the recent results from remote sensing of several coastal and aquatic environments, including (1).

the Baltic Sea, that is optically dominated by the absorption of light by coloured dissolved organic matter (CDOM), and during summer months, by high standing stocks of filamentous cyanobacteria; (2). the Bay of Biscay in the north-eastern Atlantic Ocean west of France, which is an area highly influenced by river discharge and dinoflagellate blooms, and (3). a coastal area in the eastern Beaufort Sea in the Canadian Arctic that is influenced by a pool of CDOM. The chapter concludes with a synthesis on merging of satellite data from different ocean colour missions and discusses the limitations for coastal applications.

Chapter 20 investigates the integration of multitemporal medium resolution satellite images with socio-economic field data for monitoring recovery of the tsunami-affected areas in Phanga, Thailand. Multitemporal landuse/landcover maps were produced using a supervised classification of ASTER images. Socio-economic data was analyzed to obtain information related to the recovery process on the ground. The two datasets presented a good agreement in detection of the recovery of tourism and expansion of agricultural activities. The rehabilitation of mangrove forest could be observed, but it was not possible to confirm whether a building was newly built. To some extent, the integration of ASTER images and ground data proved useful in providing a clear picture of the recovery process in an area like Phang Nga, Thailand.

References

- Achard F, Eva HD, Stibig H-J, Mayaux P, Gallego J, Richards T, Malingreau J-P (2002) Determination of deforestation rates of the world's humid tropical forests. *Science* 297(5583):999–1002. doi:[10.1126/science.1070656](https://doi.org/10.1126/science.1070656)
- Anderson JR, Hardy EE, Roach JT, Witmer RE (1976) A land use and land cover classification system for use with remote sensor data. United States Government Printing Office, Washington, 964, 28p
- Arnone RA, Parsons AR (2005) Real-time use of ocean color remote sensing for coastal monitoring. In: *Remote sensing of coastal aquatic environments*. Dordrecht, Springer, pp 317–337
- Ban Y, Jacob A (2013) Object-based fusion of multitemporal multiangle ENVISAT ASAR and HJ-1B multispectral data for urban land-cover mapping. *IEEE Trans Geosci Remote Sens* 51(4):1998–2006
- Ban Y, Yousif OA (2012) Multitemporal spaceborne SAR data for urban change detection in China. *IEEE J Select Topic Appl Earth Observ Remote Sens (JSARS)* 5(4):1087–1094
- Ban Y, Jacob A, Gamba P (2015) Spaceborne SAR data for global urban mapping at 30 m resolution using a robust urban extractor. *ISPRS J Photogrammet Remote Sens Spec Issue Glob Land Cov Map* 103:28–37
- Belward AS, Skøien JO (2015) Who launched what, when and why; trends in global land-cover observation capacity from civilian earth observation satellites. *ISPRS J Photogramm Remote Sens* 103:115–128. <http://dx.doi.org/10.1016/j.isprsjprs.2014.03.009>
- Bontemps S, Defourny P, van Bogaert E, Arino O, Kalogirou V, Perez JR (2011) GlobCover 2009, products description and validation report. European Space Agency/Universite' Catholique de Louvain, Frascati/Louvain-la-Neuve
- Bouvet A, Le Toan T, Lam DN (2009) Monitoring of the rice cropping system in the Mekong delta using ENVISAT/ASAR dual polarisation data. *IEEE Trans Geosci Remote Sens* 47(2):517–526

- Bovolo F, Bruzzone L (2005) A detail-preserving scale-driven approach to change detection in multitemporal SAR images. *IEEE Trans Geosci Remote Sens* 43:2963–2972. doi:[10.1109/TGRS.2005.857987](https://doi.org/10.1109/TGRS.2005.857987)
- Bovolo F, Bruzzone L (2007a) A split-based approach to unsupervised change detection in large-size multitemporal images: application to tsunami-damage assessment. *IEEE Trans Geosci Remote Sens* 45:1658–1670. doi:[10.1109/TGRS.2007.895835](https://doi.org/10.1109/TGRS.2007.895835)
- Bovolo F, Bruzzone L (2007b) A theoretical framework for unsupervised change detection based on change vector analysis in the polar domain. *IEEE Trans Geosci Remote Sens* 45:218–236. doi:[10.1109/TGRS.2006.885408](https://doi.org/10.1109/TGRS.2006.885408)
- Bruzzone L, Prieto DF (2000) Automatic analysis of the difference image for unsupervised change detection. *IEEE Trans Geosci Remote Sens* 38:1171–1182
- Bruzzone L, Serpico SB (1997) An iterative technique for the detection of land-cover transitions in multitemporal remote-sensing images. *IEEE Trans Geosci Remote Sens* 35(4):858–867
- Chen J, Ban Y, Li S (2014) China: open access to earth land-cover map. *Nature* 514(7523):434–434
- Chen J, Chen J, Liao A, Cao X, Chen L, Chen X, He C, Han G, Peng S, Lu M, Zhang W, Tong X, Mills J (2015) Global land cover mapping at 30 m resolution: a POK-based operational approach. *ISPRS J Photogramm Remote Sens* 103:7–27
- Davis C, Thau D (2014) Monitoring the world's forests with global forest watch. <https://maps.googleblog.com/2014/02/monitoring-worlds-forests-with-global.html>
- Dawelbait M, Morari F (2012) Monitoring desertification in a Savannah region in Sudan using Landsat images and spectral mixture analysis. *J Arid Environ* 80:45–55
- Eklundh L Jönsson P (2015) Chapter 7: TIMESAT: a software package for time-series processing and assessment of vegetation dynamics, pp 141–158. In: *Remote sensing time series: revealing land surface dynamics*. Springer, Cham, 441pp
- Eriksson LEB, Borenäs K, Dierking W, Berg A, Santoro M, Pemberton P, Lindh H, Karlson B (2010) Evaluation of new spaceborne SAR sensors for sea-ice monitoring in the Baltic Sea. *Can J Remote Sens* 36:S56–S73. doi:[10.5589/m10-020](https://doi.org/10.5589/m10-020)
- Friedl MA, McIver DK, Hedges JCF, Zhang XY, Muchoney D, Strahler AH, Woodcock CE, Gopal S, Schneider A, Cooper A, Baccini A, Gao F, Schaaf C (2002) Global land cover mapping from MODIS: algorithms and early results. *Remote Sens Environ* 83(1–2):287–302
- Galford GL, Mustard JF, Melillo J, Gendrin A, Cerri CC, Cerri CEP (2008) Wavelet analysis of MODIS time series to detect expansion and intensification of row-crop agriculture in Brazil. *Remote Sens Environ* 112(2008):576.587
- Gamba P, Harold (2009) Global mapping of human settlement: experiences, datasets, and prospects. CRC Press, Boca Raton, 374 pp
- Gamba P, Dell'Acqua F, Lisini G (2006) Change detection of multitemporal SAR data in urban areas combining feature-based and pixel-based techniques. *IEEE Trans Geosci Remote Sens* 44:2820–2827. doi:[10.1109/TGRS.2006.879498](https://doi.org/10.1109/TGRS.2006.879498)
- Gamba P, Dell'Acqua F, Trianni G (2007) Rapid damage detection in the Bam area using multitemporal SAR and exploiting ancillary data. *IEEE Trans Geosci Remote Sens* 45:1582–1589. doi:[10.1109/TGRS.2006.885392](https://doi.org/10.1109/TGRS.2006.885392)
- Gong P, Marceau DJ, Howarth PJ (1992) A comparison of spatial feature extraction algorithms for land-use classification with SPOT HRV data. *Remote Sens Environ* 40(2):137–151
- Güneralp B, Seto KC (2013) Futures of global urban expansion: uncertainties and implications for biodiversity conservation. *Environ Res Lett* 8(1):014025
- Haas J, Ban Y (2014) Urban growth and environmental impacts in Jing-Jin-Ji, the Yangtze River Delta and the Pearl River Delta. *Int J Appl Earth Obs Geoinf* 30:42–55
- Haas J, Furberg D, Ban Y (2015) Satellite monitoring of urbanization and environmental impacts—a comparison of Stockholm and Shanghai. *Int J Appl Earth Obs Geoinf* 38:138–149, <http://dx.doi.org/10.1016/j.jag.2014.12.008>
- Hansen MC, Potapov PV, Moore R, Hancher M, Turubanova SA, Tyukavina A, Thau D, Stehman SV, Goetz SJ, Loveland TR, Kommareddy A, Egorov A, Chini L, Justice CO, Townshend JRG (2013) High-resolution global maps of 21st-century forest cover change. *Science* 342(6160):850–853. doi:[10.1126/science.1244693](https://doi.org/10.1126/science.1244693)

- Hermosilla T, Wulder MA, White JC, Coops NC, Hobart G (2015) An integrated Landsat time series protocol for change detection and generation of annual gap-free surface reflectance composites. *Remote Sens Environ* 158:220–234. doi:<http://dx.doi.org/10.1016/j.rse.2014.11.005>
- Hilker T, Lyapustin AI, Tucker CJ, Hall FG, Myneni RB, Wang Y, Bi J, de Moura YM, Sellers PJ (2014) Vegetation dynamics and rainfall sensitivity of the Amazon. *Proc Natl Acad Sci U S A* 111(45):16041–16046
- Jönsson P, Eklundh L (2004) TIMESAT—a program for analyzing time-series of satellite sensor data. *Comput Geosci* 30(8):833–845
- Kratzer S, Brockmann C, Moore G. Using MERIS full resolution data to monitor coastal waters – a case study from Himmerfjärden, a fjord-like bay in the northwestern Baltic Sea. *Remote Sens Environ* 112(5):2284–2300. ISSN 0034–4257. <http://dx.doi.org/10.1016/j.rse.2007.10.006>
- Kuenzer C, Ottinger M, Wegman M, Wikelski M (2014) Earth observation satellite sensors for biodiversity monitoring: potentials and bottlenecks. *Int J Remote Sens* 35(18):6599–6647
- Kuenzer C, Dech S, Wagner W (eds) (2015) Remote sensing time series: revealing land surface dynamics. Springer, Cham. 441pp
- Lasaponara R, Lanorte A (2012) Forward: satellite time series analysis international journal of remote sensing, special issue: satellite time series analysis: from local analysis to a global view. 33:15, 4649–4652
- Liang S (2004) Quantitative remote sensing of land surfaces. Wiley, Hoboken, 534 pages
- Liu S, Bruzzone L, Bovolo F, Zanetti M, Du P (2015) Sequential spectral change vector analysis for iteratively discovering and detecting multiple changes in hyperspectral images. *IEEE Trans Geosci Remote Sens* 53:4363–4378. doi:[10.1109/TGRS.2015.2396686](https://doi.org/10.1109/TGRS.2015.2396686)
- Lu D, Mausel P, Brondízio E, Moran E (2004) Change detection techniques. *Int J Remote Sens* 25(12):2365–2401. doi:[10.1080/0143116031000139863](https://doi.org/10.1080/0143116031000139863)
- Mahmud MS, Howell SEL, Geldsetzer T, Yackel J (2016) Detection of melt onset over the northern Canadian Arctic Archipelago sea ice from RADARSAT, 1997–2014. *Remote Sens Environ* 178:59–69. <http://dx.doi.org/10.1016/j.rse.2016.03.003>
- Martinez J-M, Le Toan T (2007) Mapping of flood dynamics and spatial distribution of vegetation in the Amazon floodplain using multitemporal SAR data. *Remote Sens Environ* 108(3):209–223. doi:[10.1016/j.rse.2006.11.012](https://doi.org/10.1016/j.rse.2006.11.012)
- McNairn H, Kross A, Lapen D, Caves R, Shang J (2014) Early season monitoring of corn and soybeans with TerraSAR-X and RADARSAT-2. *Int J Appl Earth Obs Geoinf* 28:252–259
- Müller H, Rufin P, Griffiths P, Siqueira AJB, Hostert P (2015) Mining dense Landsat time series for separating cropland and pasture in a heterogeneous Brazilian savanna landscape. *Remote Sens Environ* 156:490–499
- Olsson L, Eklundh L, Ardö J (2005) A recent greening of the Sahel—trends, patterns and potential causes. *J Arid Environ* 63(3):556–566
- Pesaresi M et al (2013) A global human settlement layer from optical HR/VHR RS data: concept and first results. *IEEE JSTARS* 6(5):2102–2131
- Pinzon JE, Tucker CJ (2014) A non-stationary 1981–2012 AVHRR NDVI3g time series. *Remote Sens* 6:6929–6960. doi:[10.3390/rs6086929](https://doi.org/10.3390/rs6086929)
- Planet Labs (2015) Planet Labs at a glance: satellite operations and data pipeline overview. In: *ESA living planet symposium*, Prague, Czech Republic
- Rack W, Rott H (2004) Pattern of retreat and disintegration of the Larsen B ice shelf, Antarctic Peninsula. *Ann Glaciol* 39(1):505–510
- Rignot E (2001) Evidence for rapid retreat and mass loss of Thwaites Glacier, West Antarctica. *J Glaciol* 47(157):213–222
- Rignot E, Salas WA, Skole DL (1997) Spaceborne imaging radar MissionMapping deforestation and secondary growth in Rondonia, Brazil, using imaging radar and thematic mapper data. *Remote Sens Environ* 59(2):167–179. [http://dx.doi.org/10.1016/S0034-4257\(96\)00150-2](http://dx.doi.org/10.1016/S0034-4257(96)00150-2)
- Rignot E, Mouginot J, Morlighem M, Seroussi H, Scheuchl B (2014) Widespread, rapid grounding line retreat of Pine Island, Thwaites, Smith and Kohler glaciers, West Antarctica from 1992 to 2011, *Geophys Res Lett.* accepted for publication. doi:[10.1002/2014GL060140](https://doi.org/10.1002/2014GL060140)

- Roerink GJ, Menenti M, Verhoef W (2000) Reconstructing cloudfree NDVI composites using Fourier analysis of time series. *Int J Remote Sens* 21(9):1911–1917
- Seto KC, Fragkias M, Güneralp B, Reilly MK (2011) A meta-analysis of global urban land expansion. *PLoS One* 6(8):e23777. doi:[10.1371/journal.pone.0023777](https://doi.org/10.1371/journal.pone.0023777)
- Shao Y, Fan X, Liu H, Xiao J, Ross S, Brisco B, Brown R, Staples G (2001) Rice monitoring and production estimation using multitemporal RADARSAT. *Remote Sens Environ* 76(3):310–325
- Showstack R (2014) Sentinel satellites initiate new era in Earth observation. *Eos* 95(26):239–240
- Skidmore AK, Pettorelli N, Coops NC, Geller GN, Hansen M, Lucas R, Mücher CA (2015) Environmental science: agree on biodiversity metrics to track from space. *Nature* 523(7561):403–405. doi:[10.1038/523403a](https://doi.org/10.1038/523403a)
- Skole D, Tucker C (1993) Tropical deforestation and habitat fragmentation in the Amazon—satellite data from 1978 to 1988. *Science* 260:1905–1910
- Taubenböck H, Esch T, Felbier A, Wiesner M, Roth A, Dech S (2012) Monitoring urbanization in mega cities from space. *Remote Sens Environ* 117:162–176
- Terra Bella (2016) <https://terrabella.google.com>. Accessed on 10 July 2016
- Tralli DM, Blom RG, Zlotnicki V, Evans DL (2005) Satellite remote sensing of earthquake, volcano, flood, landslide and coastal inundation hazards. *ISPRS J Photogramm Remote Sens* 59(4):185–198
- Tucker CJ, Townshend JRG (2000) Strategies for monitoring tropical deforestation using satellite data. *Int J Remote Sens* 21(6 & 7):1461–1471
- Turner W, Spector S, Gardiner N, Fladeland M, Sterling E, Steininger M (2003) Remote sensing for biodiversity science and conservation. *Trend Ecol Evol* 18:306–314
- Vu TT, Ban Y (2010) Context-based mapping of damaged buildings from high-resolution optical satellite images. *Int J Remote Sens* 31(13):3411–3425
- Woodcock CE, Allen R, Anderson M, Belward A, Bindschadler R, etc (2008) Free access to Landsat imagery. *Science* 320(5879):1011–1011
- Wulder MA, Masek JG, Cohen WB, Loveland TR, Woodcock CE (2012) Opening the archive: how free data has enabled the science and monitoring promise of Landsat. *Remote Sens Environ* 122:2–10, ISSN 0034–4257, <http://dx.doi.org/10.1016/j.rse.2012.01.010>
- Yang X, Zhang K, Jia B, Ci L (2005) Desertification assessment in China: an overview. *J Arid Environ* 63(2):517–531
- Yousif O, Ban Y (2013) Improving urban change detection from multitemporal SAR images using PCA-NLM. *IEEE Trans Geosci Remote Sens* 51:2032–2041. doi:[10.1109/TGRS.2013.2245900](https://doi.org/10.1109/TGRS.2013.2245900)
- Zhu Z, Woodcock CE (2014) Continuous change detection and classification of land cover using all available Landsat data. *Remote Sens Environ* 144(25):152–171

Chapter 2

Change Detection Techniques: A Review

Yifang Ban and Osama Yousif

Abstract With its synoptic view and the repeatability, satellite remote sensing can provide timely, accurate and consistent information about earth's surface for cost-effective monitoring of environmental changes. In this chapter, recent development in change detection techniques using multitemporal remotely sensed images were reviewed. The chapter covers change detection methods for both optical and SAR images. Various aspects of change detection processes were presented including data preprocessing, change image generation and change detection algorithms such as unsupervised and supervised change detection as well as pixel-based and object-based change detection. The review shows that significant progress has been made in the field of change detection and innovative methods have been developed for change detection using both multitemporal SAR and optical data. Attempts have been made for change detection using multitemporal multisensor/cross-sensor images. The review also identified a number of challenges and opportunities in change detection.

2.1 Introduction

Change detection is the process of identifying differences in the state of an object or phenomenon by observing it at different times (Singh 1989). With its synoptic view and the repeatability, satellite remote sensing can provide timely, accurate and consistent information about earth's surface for cost- and time-efficient monitoring of environmental changes. This information is vital to the management of natural resources, the conservation of ecosystems and biodiversity as well as decision support for sustainable development.

Change detection using multitemporal remote sensing imagery plays a crucial role in numerous fields of applications. Examples include urbanization (e.g. Ban and Yousif 2012; Taubenböck et al. 2012), deforestation (Achard, et al. 2002;

Y. Ban (✉) • O. Yousif

Division of Geoinformatics, KTH Royal Institute of Technology, Stockholm, Sweden
e-mail: yifang@kth.se

Desclée et al. 2006; Vollmar et al. 2013), desertification (e.g., Yang et al. 2005; Dawelbait and Morari 2012), flooding (e.g. Martinez and Le Toan 2007; Martinis et al. 2011), disaster monitoring (Bovolo and Bruzzone 2007a; Gamba et al. 2007) and glacier change monitoring (Akbari et al. 2014). The wide spread use of remotely sensed images in change detection can be attributed to their wide geographic coverage and availability in a wide range of spatial, spectral, and temporal resolutions.

A number of change detection methods and algorithms have been developed and tested over the past decades. These algorithms have focused on various aspects of the change detection processes, for examples, analysis and estimation of image registration noise (Bovolo et al. 2009; Marchesi et al. 2010), speckle reduction in the context of change detection (e.g., Dekker 1998; Yousif and Ban 2013), unsupervised change detection (e.g., Bovolo and Bruzzone 2007b), extraction of detailed from-to change information using post-classification comparison algorithm (e.g., Alphan et al. 2008), change detection by fusion techniques to merge multiple difference images (Du et al. 2012), change detection using multi-channel SAR images (e.g., Moser and Serpico 2009), change detection using polarimetric SAR images (e.g., Conradsen et al. 2003; Sabry 2009), spatio-contextual change detection (e.g., Bruzzone and Prieto 2002; Moser and Serpico 2009; Yousif and Ban 2014), change detection by combining feature-based and pixel-based techniques (e.g., Gamba et al. 2006), object-based change detection (e.g., Desclée et al. 2006; Bontemps et al. 2008; Qin et al. 2013; Yousif and Ban 2015), and the fusion of SAR and optical images for change detection (e.g., Poulain et al. 2011; Ban et al. 2014).

The detection of changes using multitemporal remotely sensed images, however, is complex due to uncertainties in the measured phenomenon, limitations in the ability of the imaging sensors to measure the ground changes, the noise inherent in the imaging process, compatibility of images from different sensors and the uncertainties in the change detection process as well as phenology, soil moisture, sun angles etc. The specific characteristics of remotely sensed images including sensor characteristics (radar or optical), resolution (spatial, spectral, radiometric and temporal), noise and distortions in imagery and the characteristics of the phenomenon under study need to be carefully considered when selecting change detection algorithm. Owing to the complexity, no single method exists that can handle all types of change detection problems. Different applications call for different approaches, and different types of remotely sensed data require sensor-specific considerations. The development of new remote sensing systems that can produce higher quality images, i.e., with better spatial, spectral, radiometric and temporal resolution, will also require the development of new techniques.

In this chapter we review recent development in change detection techniques using multitemporal remote sensing image. The chapter covers various aspects of change detection including data preprocessing, change images generation and change detection algorithms including unsupervised thresholding and supervised classification as well as pixel- and object-based approaches. Figure 2.1 presents the change detection workflow.

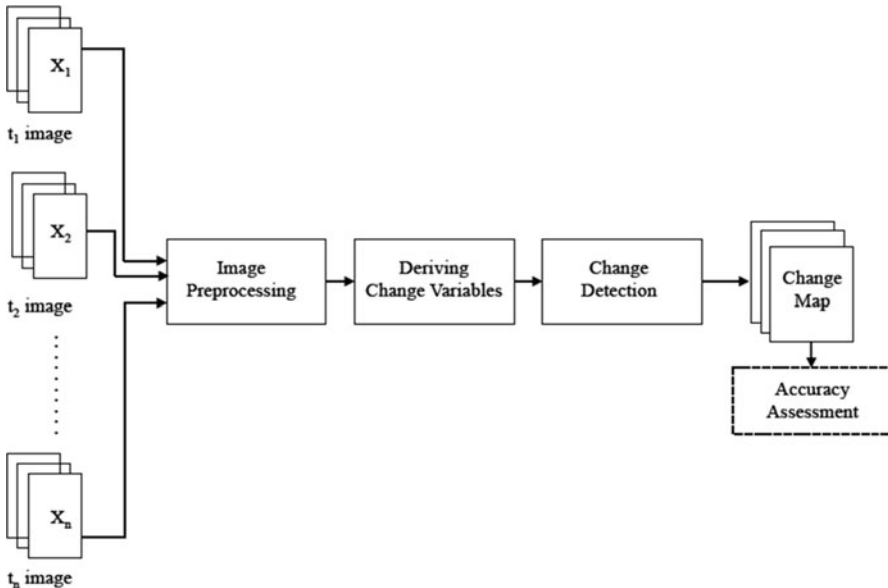


Fig. 2.1 The change detection workflow

2.2 Change Detection Preprocessing

2.2.1 Geometric and Radiometric Correction

For a successful change detection analysis, the multitemporal images should be preprocessed to ascertain that they are radiometrically and spatially comparable. The first preprocessing step aims at making the multitemporal images radiometrically comparable. Ideally, a ground object should show the same brightness values if no change has occurred. In reality, measured intensities are to a high degree sensitive to change in acquisition geometry and atmospheric condition. Radiometric conditions can be influenced by many factors such as different imaging seasons, different solar angles, different meteorological conditions, etc. Acquisition geometry, such as sensor viewing angle, local incident angle, and solar orientations in the case of optical image acquisition, can have a significant effect on the acquired image. This is also true for radar image as radar return from the ground is quite sensitive to the local incident angle. Atmospheric conditions have a serious impact on the measured intensity when using optical remotely sensed images. Therefore, it is usually necessary to carry out radiometric correction before change detection (Leonardo et al. 2006). Absolute atmospheric correction or image-to-image normalization is often used to reduce the negative impact of the atmosphere and make the multitemporal optical images comparable. Absolute atmospheric correction converts digital numbers to scaled surface reflectance. It

requires information about the atmospheric condition during image acquisition, which is not always easy to obtain. Image-to-image normalization consists of the linear transformation of the spectral characteristics of the image to be corrected to match those of a base (or reference) image (Gao et al. 2010). de Carvalho et al. (2006) developed a radiometric normalization technique that searches for highest quality invariant features. Velloso et al. (2002) proposed to use artificial neural network to automatically perform a nonlinear image-to-image normalization. SAR has the advantage of being less affected by atmospheric condition. Nevertheless, SAR images should be calibrated if a proper change detection analysis is to be conducted. SAR image calibration calculates the radar cross section (or backscatter coefficient if area correction is applied). Calibration allows the comparison of radar images with different resolutions, transmitted power and processing gains (Oliver and Quegan 2004).

Geometric correction is accomplished by image-to-image registration or image orthorectification in mountainous areas, and in urban areas for very high resolution images (Boccardo et al. 2004) (Fig. 2.2). This process ensures that corresponding pixels in the multitemporal images refer to the same geographic location. Image-to-image registration is often carried out by manually selecting ground control points. Automatic techniques, with different levels of success, also exist. Image-to-image registration is particularly difficult when the analysis involves high spatial resolution images, or when the images contain high frequency components (e.g., edges and linear features). Inaccurate image-to-image registration is one of the main sources of errors in change detection analysis, and can lead to a significant degradation in accuracy (Dai and Khorram 1998; Townshend et al. 1992). Compared to pixel-based, object-based change detection proved to be less sensitive to image-to-image registration errors (Chen et al. 2014; 2012). While very high resolution optical images have geometric distortions, radar images are affected by different types of distortions, i.e. relief displacement including foreshortening, layover, and variations in the ground resolution along the range direction. Therefore, it is necessary to perform orthorectification on these images using satellite orbital models and a DEM either using ground control points or automatically (Marsetic et al. 2016).



Fig. 2.2 High resolution images in Shanghai *Left:* GeoEye-1 image; *Right:* TerraSAR-X image

2.2.2 SAR Speckle Filtering for Change Detection

Coherent processing of synthetic aperture radar (SAR) data makes images susceptible to speckles, the salt and pepper appearances of SAR image because of the existence of many scatterers within the resolution cell (Fletcher et al. 2007). Speckle in SAR images complicates image interpretation by reducing the effectiveness of image segmentation and classification (Lee et al. 1994). Change detection based on multitemporal SAR images are affected by speckle. Dekker (1998) has shown that speckle increases false and missed alarm rates when thresholding the SAR ratio image. In the context of unsupervised change detection Bazi et al. (2005) attributed the increase in the overlap between changed and unchanged classes in the 1D feature space to the existence of speckle.

In SAR-based change detection, the traditional strategy for eliminating the effect of speckle is to filter the individual SAR images before the comparison. Usually, an adaptive filter is iteratively applied to the SAR image until a satisfactory result is obtained. For examples, Moser and Serpico (2006) found that the best change map is obtained by filtering the individual SAR images twice using the Gamma MAP filter. Bazi et al. (2005) proposed an automatic method to estimate the optimum number of filtering iterations to be applied to SAR images. The method is based on analysis of the behavior of a criterion function that is related to the average classification error. However, Dekker (1998) found that ratioing filtered SAR images causes the accumulation of individual filter errors and consequently the degradation of the quality of the change variable. The author suggested filtering the change image (e.g., the ratio image) rather than the individual SAR image. In Yousif and Ban (2013), the negative effects associated with using a local adaptive filters in change detection, e.g., the erosion of fine geometric details, were addressed by using the nonlocal means denoising algorithm. There, the algorithm was applied directly to the change variable (i.e., the modified ratio image) in order to prevent the accumulation of individual filter errors and to reduce the computational burden.

The effects of speckle can also be reduced during the classification phase, i.e., no speckle filtering is required. Moser and Serpico (2009) developed an unsupervised change detection algorithm, in which the use of the MRF model successfully helped in reducing the impact of speckle. Similarly, Yousif and Ban (2014) extended the traditional MRF-based algorithm to include a nonlocal constraint that helps reducing the negative impact of speckle and maintain fine geometric details in the image.

2.3 Deriving Change Variables from Multitemporal Remote-Sensing Images

One of the essential steps in change detection analysis is the comparison of multitemporal remote sensing images. The aim of this step is to generate a change image that increases the contrast between changed and unchanged areas. A change

map can then be generated by thresholding or classifying the change image using either supervised or unsupervised techniques.

2.3.1 Driving Change Variables from Multitemporal Optical Images

A comprehensive review of the mathematical operators that can be used to compare multitemporal optical remote sensing images (Fig. 2.3) was provided by Lu et al. (2004). These operators include image differencing, image ratioing, image regression and change vector analysis (CVA). Berberoglu and Akin (2009) found image ratioing to be effective in reducing topographic effects such as variation in illumination and shadowing. However, image ratioing produces relatively poor results compared to image differencing and CVA for detecting changes in the Mediterranean land use/cover using Landsat images. Change vector analysis is an extension of the concept of image differencing, and for given multi-date pairs of spectral measurements, it computes spectral change vectors and compares their magnitudes to a specified threshold criterion (Malila 1980). He et al. (2011) extended the CVA technique to include textural information layers. Bovolo and Bruzzone (2007b) found that the use of CVA magnitude does not utilize all the information contained in the multispectral multitemporal difference image. They suggested transforming the spectral change vector from the Cartesian to the polar coordinate system, in which they developed rigorous statistical distributions for the magnitude and the direction random variables. Liu et al. (2015a) used CVA to extract change information from multitemporal hyperspectral images. They proposed a novel hierarchical scheme by considering spectral change information to identify the change classes having discriminable spectral behaviors. In a similar manner, Liu et al. (2015b) proposed a sequential CVA technique that used an iterative hierarchical scheme for discovering and detecting different kinds of changes from multitemporal hyperspectral images. Thonfeld et al., (2016) proposed a modified version of CVA, i.e., robust change vector analysis (RCVA), that can mitigate radiometric and geometric distortions by taking into consideration neighboring pixels.



Fig. 2.3 Optical image pair in Shanghai, *Left:* 2000 IKONOS image; *Right:* 2009 GeoEye-1 image

Comparison of multitemporal optical remote sensing images can also be carried out in a new transformed space instead of in the raw data domain defined by the observed multitemporal images. A simple example is differencing multitemporal normalized difference vegetation index (NDVI) images, where the measured intensities in each image, i.e. red and near infrared values, are first transformed to the NDVI space (Latifovic and Pouliot 2014; Lyon et al. 1998). Similarly, Cakir et al. (2006) transformed each individual image in the multitemporal dataset to a component space using correspondence analysis. The difference image is then constructed in this new space.

2.3.2 *Driving Change Variables from Multitemporal SAR Images*

Comparison of multitemporal SAR images (Fig. 2.4) is commonly carried out using the ratio operator (Moser and Serpico 2006; Rignot and van Zyl 1993; Xiong et al. 2012). Ratio-related operators have also been used to compare SAR images, including the log-ratio (Bazi et al. 2005; Bovolo et al. 2013; Marin et al. 2015) and the normalized mean-ratio (Ma et al. 2012). The ratio image is known for its robustness with respect to the SAR multiplicative radiometric errors (Bazi et al. 2005). The detection of changes in SAR ratio images can be performed equally well in regions with high and low levels of intensity (Rignot and van Zyl 1993). Bujor et al. (2003) compared different types of parameters to quantify temporal changes based on SAR images and found the ratio operator to be especially suitable for the detection of step-like changes. Hou et al. (2014) proposed a Gauss log-ratio operator for the comparison of multitemporal SAR images. This comparison operator applies a low-pass filtering to the logarithmically transformed SAR images.

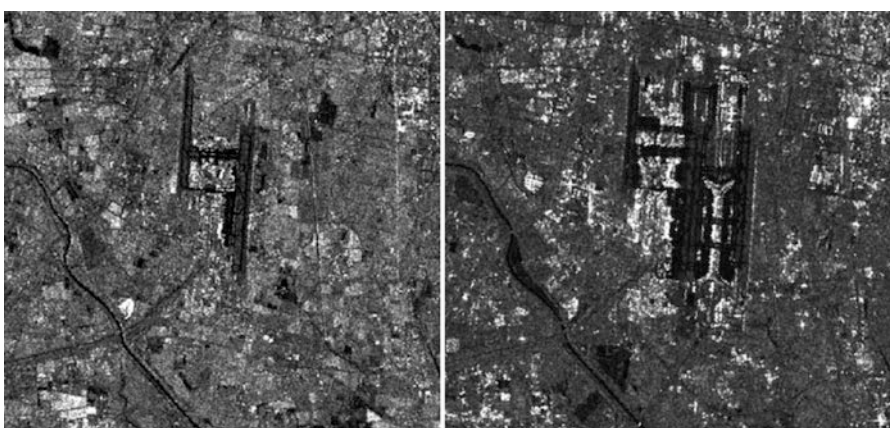


Fig. 2.4 Beijing international airport, *Left*: 1998 ERS-2 SAR image; *Right*: 2008 ENVISAT ASAR image

Image differencing is then applied to the filtered images. Hachicha and Chaabane (2010) suggested two different types of change indicators that were developed based on the assumption that SAR amplitudes are Rayleigh distributed. The first indicator (Rayleigh ratio detector) works per pixel and uses first-order statistics, while the second one, the Rayleigh Kullback-Leibler divergence, utilizes higher order statistics for the comparison.

The comparison of multitemporal SAR images can also be carried out using similarity measures (Chatelain et al. 2007; Cui et al. 2016). These measures have been used extensively in the field of automatic image-to-image registration as a mean of quantifying similarity in the spatial domain. In the context of change detection analysis, given two co-registered images, similarity measures can be used to quantify temporal rather than spatial similarity (Alberga 2009). The strength of similarity measures lies in the fact that the estimation of the change indicator takes into account the pixel and its neighbourhood in contrast to traditional arithmetic operators, which work per pixel and normally ignore the contextual information (Inglada and Mercier 2007).

In SAR-based change detection, it is common to transform the SAR change variable (e.g., the ratio image) to a new transformed space. The new space preferably allows for effective mitigation of speckle and preservation of geometric details. In Bovolo and Bruzzone (2005) for example, the change variable was decomposed into many scale-dependent images using a wavelet transform. Each wavelet transformed image is a tradeoff between detail preservation and noise suppression. A suitable scale is selected to classify each pixel based on global and local statistics. Similarly, Celik (2010a) used a dual-tree complex wavelet transform to decompose the log-ratio image into different scales. The change maps generated at each scale using the expectation maximization algorithm are then combined using logical operators. Finally, it worth mentioning the approach proposed in (Gong et al. 2016), where no image comparison step was required. Instead a binary change map was generated by submitting the multitemporal SAR images to a deep neural network classifier.

2.4 Pixel-Based Change Detection

2.4.1 *Unsupervised Change Detection Algorithms*

Unsupervised change detection algorithms have the advantage that no prior knowledge about the study area (i.e., training data) is required. An unsupervised change detection algorithm usually produces a binary change map that shows changed versus unchanged areas. The main disadvantage of this type of algorithms is the lack of detailed from-to change information.

There are several techniques for unsupervised change detection using multitemporal images. Bruzzone and Prieto (2000a) developed two unsupervised change detection methods. The first method automatically selects the decision threshold that minimizes the probability of error. The second method analyses the difference

image by taking into consideration the spatio-contextual information included in the neighbourhood of each pixel. Celik (2010b) considered unsupervised change detection to be an intensive search for a change mask that optimizes a minimum mean square (MSE) criterion function. The genetic algorithm is used to search for this optimum mask—that is, the change map. Celik (2009) used the PCA technique to map local neighbourhoods in the difference image to a higher dimensional space defined using non-overlapping image blocks. The k-means algorithm was then used to automatically separate the changed from the unchanged areas. Bruzzone and Prieto (2002) proposed an unsupervised change detection algorithm in which a Parzen estimate was used to model the likelihood function of the observations. Hao et al. (2014) proposed an unsupervised change detection approach based on the expectation-maximization-based level set method. Quin et al. (2014) develop an automatic change detection technique that was especially designed for the analysis of a SAR time series. In Liu et al. (2015a) different classes of change were automatically extracted from multitemporal hyperspectral images using the expectation maximization algorithm. Li et al. (2015) combined fuzzy c-mean algorithm with nearest neighbor rule to automatically extract change information from SAR images.

The minimum error thresholding algorithm proposed by Kittler and Illingworth (1986) has been used extensively in change detection. This algorithm, developed based on Bayesian decision theory, is known to be a fast and effective thresholding tool. Melgani et al. (2002) used the algorithm successfully thresholding a change variable derived from multispectral images. To deal with the non-Gaussian nature of the SAR amplitude and intensity images, the algorithm was generalized by Bazi et al. (2005) and Moser and Serpico (2006). There, different types of density-function models suitable for describing the statistics of the changed and unchanged classes in a SAR change image were proposed. Essentially, the algorithm assumes the existence of one object (i.e., one typology of change) and one background. Bazi et al. (2006) successfully applied the algorithm to a case in which more than one typology of change existed in the study area—that is, to a case with more than one threshold. The main drawback of the multithreshold version of the Kittler-Illingworth algorithm is its high computational complexity. Ban and Yousif (2012) developed a modified ratio operator that takes into account both positive and negative changes to derive a change image. A generalized version of Kittler-Illingworth minimum-error thresholding algorithm was then used to classify the change image into change and no change classes. Various probability density functions, i.e., Log normal, Generalized Gaussian, Nakagami ratio, and Weibull ratio were investigated to model the distribution of the change and no change classes. The results showed that Kittler-Illingworth algorithm applied to the modified ratio image is effective in detecting urban changes using SAR images. To apply this approach over large urban areas, Hu and Ban (2014) developed an automatic approach to threshold the log-ratio change indicator whose histogram may have one mode or more than one mode. A bimodality test is performed to determine whether the histogram of the log-ratio image is unimodal or not. If it has more than one mode, the generalized Kittler and Illingworth thresholding algorithm

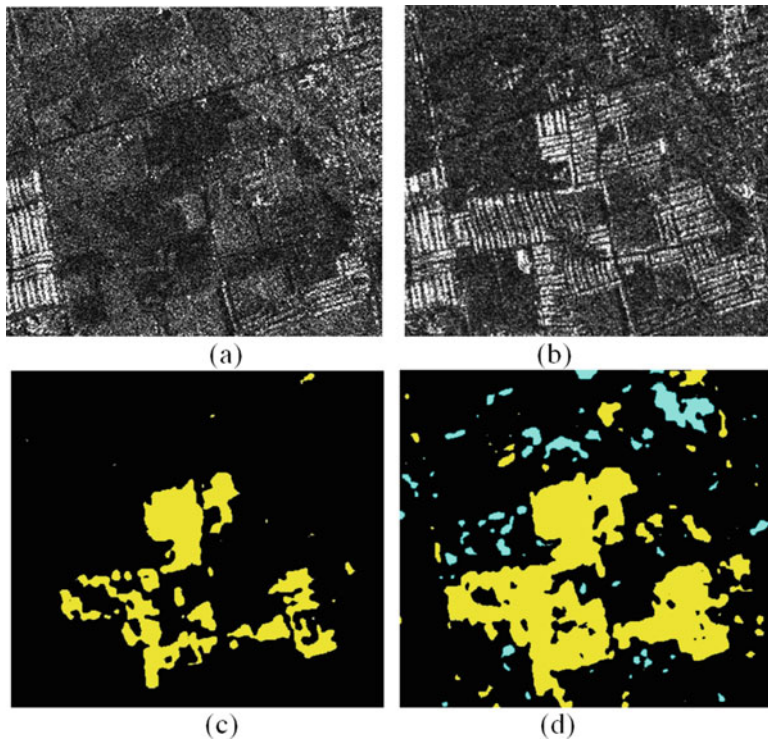


Fig. 2.5 Change detection results in Toronto. (a) RADARSAT-1 SAR image on August 18, 2002. (b) RADARSAT-2 SAR image on August 22, 2008. (c) Change map produced by direct application of Generalized Gaussian. (d) Change map produced by the approach of Hu and Ban (2014). Positive changes are in yellow and negative changes are in cyan

based on the generalized Gaussian model is used to detect the optimal thresholds. If it is unimodal, the log-ratio image is divided into small regions and a multi-scale region selection process is carried out to select regions that are a balanced mixture of unchanged and changed classes. Results obtained from multitemporal SAR images of Toronto and Beijing demonstrate the effectiveness of the proposed approach (Fig. 2.5).

2.4.2 Supervised Change Detection Algorithms

Traditionally, supervised change detection is carried out using post-classification comparison logic. It consists of classifying each image in the multitemporal dataset independently using the same classification scheme. The detailed from-to change information can then be extracted by comparing the classified images on a pixel-by-pixel basis. Yuan et al. (2005) applied the method to a series of Landsat images

in order to study the dynamics of the land-cover change over the Twin Cities Metropolitan Area. Del Frate et al. (2008) used post-classification-comparison to extract change information from multitemporal SAR images. Instead of using the maximum likelihood classifier, the authors used an artificial neural network for the classification of each SAR image. In Castellana et al. (2007) the accuracy of the change detection process is improved by combining supervised post-classification logic with an unsupervised change detection algorithm.

Supervised change detection is not restricted to post-classification comparison logic. For example, Volpi et al. (2013) investigated supervised change detection using two techniques—namely, multidate classification and analysis of difference image. To address the problem of high intraclass variability the authors suggested using a support vector machine (SVM) classifier. Similarly, in Nemmour and Chibani (2006) urban growth in the Algerian capital was extracted from Landsat multitemporal images using SVM classifier.

The main drawback with the supervised change detection method is the need for high-quality training data to classify each image in the multitemporal dataset. This turns out to be rather difficult to achieve, especially for older images. Many semisupervised change detection algorithms have been developed that require only a limited amount of ground truth information or limited interaction from the analyst (Moser et al. 2002; Roy et al. 2012).

2.4.3 Context-Based Change Detection Algorithms

Contextual information plays an essential role in image understanding and analysis (Li 2009). In change detection, spatio-contextual information can be used at different levels of analysis. For example, spatio-contextual information may be utilized at the image-comparison stage; Im and Jensen (2005) used spatio-contextual information to extract change images (i.e., correlation, slope, and intercept images) from multitemporal optical remote sensing images. In an attempt to reduce the negative impact of speckle noise, Gong et al. (2012a) developed a comparison operator (i.e., neighbourhood-based ratio) that uses neighbouring pixels in the comparison process.

The most common use of spatio-contextual information in image analysis, however, is during classification rather than in the image comparison. Ghosh et al. (2007) used a Hopfield-type neural network that takes spatial correlation between neighbouring pixels into consideration to carry out an unsupervised change detection. Markov random field provides a rigorous statistical framework for modeling the contextual information in image analysis. It has been used extensively in the field of image classification (Garzelli 1999; Tso and Olsen 2005), in multisource image classification (Cossu et al. 2005; Solberg et al. 1996), and in change detection (Bruzzone and Prieto 2000a, 2002; Kasetkasem and Varshney 2002).

Moser and Serpico (2009) developed an unsupervised change-detection algorithm specifically tailored for the analysis of multichannel-multitemporal SAR images. In that work the MRF model is used not only to model the spatio-contextual information but also to provide a framework for the fusion of the change information extracted from each SAR ratio channel. Similarly, Moser et al. (2007) developed an MRF-based change detection algorithm for the analysis of multichannel-multitemporal SAR images. In that study, the multichannel change image was transformed using Fisher transformation. Kasetkasem and Varshney (2002) pointed out that transformations such as image differencing, destroy the MRF properties of the image. Instead, they suggested a change detection algorithm in which the observed multitemporal images and the required change map are modeled using MRF. Wang et al. (2013) developed an unsupervised change detection algorithm for multitemporal SAR images that utilizes a triplet Markov field. Baselice et al. (2014) developed an MRF-based change detection algorithm for high resolution complex SAR data. Each complex SAR image in the multitemporal dataset is modelled using Markov random field hyperparameters. The hyperparameters maps are compared using similarity measure.

Contextual information can also be modeled using conditional random field (CRF). Unlike MRF, this model relaxes the assumption of conditional independence of the observations. Zhou et al. (2016) proposed a method based on CRF and region connection constraint to extract change information from high resolution images. To extract change information from images with different resolutions, Hoberg et al. (2015) CRF was extended to model temporal interactions.

2.5 Object-Based Change-Detection Algorithms

Although most of the available change detection algorithms are pixel-based, change detection has also been approached using object-based logic (Zhong and Wang 2006; Berberoglu and Akin 2009; Jovanović et al. 2010; Bin et al. 2013; Rasi et al. 2013; Son et al. 2015; Janalipour and Mohammadzadeh 2016). Image segmentation techniques subdivide the image into meaningful homogeneous regions (i.e., objects) based not only on the spectral property, but also possibly on the shape, texture, and size properties. In object-based techniques the contextual information is exploited in the segmentation phase rather than during classification or change detection analysis. For high-resolution imagery, object-based analysis could also help reducing the computational complexity. Moreover, object-based change detection proved to be less sensitive to images coregistration errors.

The resort to object-based analysis was triggered by the increasing availability of high spatial resolution imagery. With these images, the use of pixel-based classification or change detection algorithms often leads to low-accuracy and rather noisy results. Object-based change detection, on the other hand, was recognized as offering unique approaches for exploiting high resolution imagery, to capture

meaningful detailed change information while suppress noise in change detection results in a systematic and repeatable manner (Chen et al. 2012; Hussain et al. 2013). A number of studies have investigated object-based change detection using optical data (e.g., Hall and Hay 2003; Desclée et al. 2006; Bontemps et al. 2008). However, object-based change detection using SAR data has been very limited. Only one study was found by Yousif and Ban (2015) investigating the unsupervised object-based urban change detection with high-resolution TerraSAR-X imagery. The results indicate that, compared with pixel-based, the object-based approach helps in improving the quality of the produced change maps.

2.5.1 Segmentation Strategies for Change Detection

With the development of several powerful segmentation techniques and software tools entirely devoted to image segmentation, e.g., eCognition, a commonly used commercial software and KTH-SEG, an edge-aware region growing and merging algorithm. (Ban and Jacob 2013), several new segmentation possibilities in the context of change detection arose. Remote sensing change detection, by default, involves at least two images that are acquired over the same geographic area at different times. Consequently, there are two possible segmentation strategies. The first one consists of the independent segmentation of each image in the multitemporal dataset. A consequence of this technique is the creation of sliver polygons when comparing the segmented images. The main advantage of this approach is that it allows the inclusion of objects' geometrical properties and topological relationships in the change detection analysis (Blaschke 2005). Hazel (2001) developed a change detection framework, where a new image is segmented separately and then compared with an existing site model.

The second strategy, known as multistage segmentation, dominates the object-based change detection literature (Bontemps et al. 2008; Desclée et al. 2006; Hall and Hay 2003; Im et al. 2008). It involves the segmentation of all images in the multitemporal dataset in one step. The result is objects that are spectrally, spatially, and temporally homogeneous (i.e., no sliver polygon). Because of the fixed geometrical extent of objects, there is a limited ability to utilize objects' geometric relationships in the change detection analysis.

2.5.2 Objects Comparison and Change Map Generation

From certain perspective, the difference between pixel and segment representations of an image is merely of the used spatial unit/scale. In light of this view, most pixel-based comparison techniques are readily transferable to the object-based analysis. Instead of pixel intensity, object's mean intensity can simply be used as a feature

for image analysis tasks. Comparison of multitemporal objects can then be carried out using conventional mathematical operators usually used in pixel-based change detection (e.g. differencing, ratioing . . . etc.). This logic is especially simple to apply when multiday segmentation strategy is used. Hall and Hay (2003) for example, compared the multitemporal objects using the absolute value of differenced image. Nielsen (2007) developed a pixel-based change detection algorithm for multi- and hyperspectral imagery that enhances the change information using multivariate alteration detection (MAD) transformation. Niemeyer et al. (2008) successfully extended this algorithm to the object-based case, where in addition to the spectral information the analysis also considered objects geometric features.

Similar to image comparison techniques, most of pixel-based thresholding/classification algorithms can directly be applied to segmented images. Post-classification comparison logic can be applied to extract change information using object-based paradigm. Walter (2004) and Zhou et al. (2008) successfully extracted detailed change information by comparing images classified using the object-based technique instead of per-pixel classification. Similarly, Anders et al. (2013) applied object-based post-classification comparison to obtain a detailed from-to geomorphological change information using multitemporal LiDAR-based digital terrain model (DTM). Im and Jensen (2005) developed a pixel-based change detection algorithm that extracts the detailed from-to change information using multiday composite image classification logic. Im et al. (2008) successfully extended this algorithm to the object-based case. To avoid the error accumulation associated with the post classification comparison method, Qin et al. (2013) performed supervised object-based change detection using the multiday composite logic.

Unsupervised change detection algorithms have also been used extensively in object-based change detection. Hall and Hay (2003) for example, applied the Otsu method to threshold an object-based change image constructed using image differencing technique. Desclée et al. (2006) proposed an automatic object-based change detection algorithm, in which objects are compared using image differencing technique. The final change map is generated using outlier detection technique, where the changed objects are conceived as outliers disturbing the statistical distribution of the unchanged objects. Similarly, Bontemps et al. (2008) developed an automatic algorithm based on outlier detection technique to extract environmental changes from SPOT vegetation time series images. Their main target was to exploit the temporal dependence information in the time series to model intra- and inter-annual changes. In Yousif and Ban (2015), three different unsupervised thresholding algorithms, i.e., Kittler-Illingworth algorithm, Otsu method, and outlier detection technique, were used to threshold the change image and generate a binary change map. Two TerraSAR-X SAR images acquired over Shanghai in August, 2008, and September, 2011, were used to test the methods. The results show that the three unsupervised thresholding algorithms performed equally well (Fig. 2.6).

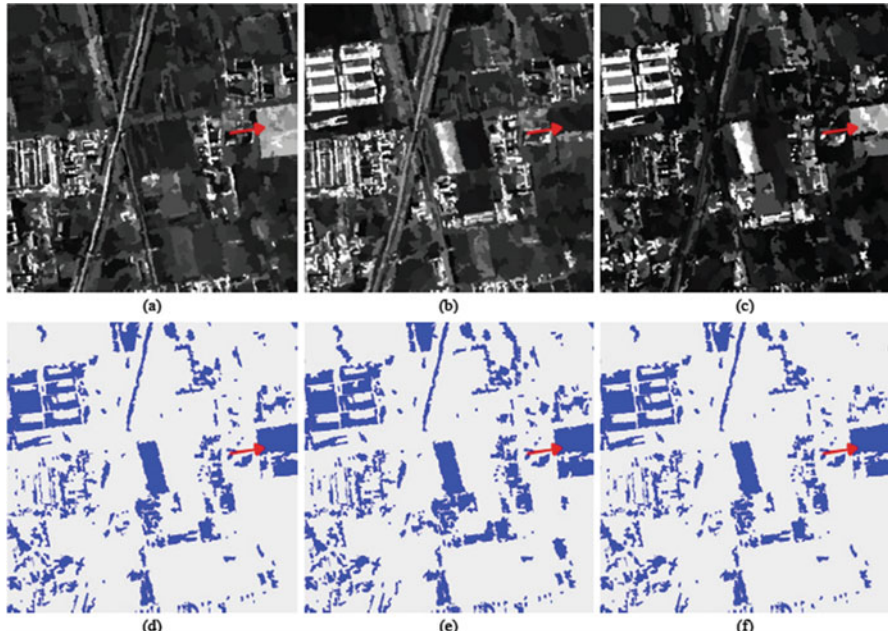


Fig. 2.6 Beijing object-based change detection (a) date I image, (b) date II image, (c) modified ratio image, and change maps produced using (d) Kittler-Illingworth algorithm, (e) Otsu method, (f) Outlier detection technique

2.6 Data Fusion for Change Detection

In remote sensing the ultimate goal of image fusion is to enhance the final product in light of the intended application: visual image interpretation, classification or change detection. Remote sensing image fusion typically involves different types of images—for instance, images with different spatial or spectral resolutions—and in many cases involves images with different modalities as in the fusion of SAR and optical images.

In change detection analysis, the fusion of SAR and optical data is important from two perspectives. First, on many occasions the limited availability of data forces the generation of a change indicator through the comparison of an image pair acquired over the same area but with different modalities. Although the images were acquired with sensors that have different modalities, they are two different representations of the same physical reality and consequently can be compared (Inglada and Giros 2004). Recently, similarity measures have played an essential role in performing such complicated image comparison. Mercier et al. (2008), for example, successfully used Kullback-Leibler divergence to compare an ERS SAR image with a SPOT image. In a similar line, Liu et al. (2014) proposed a

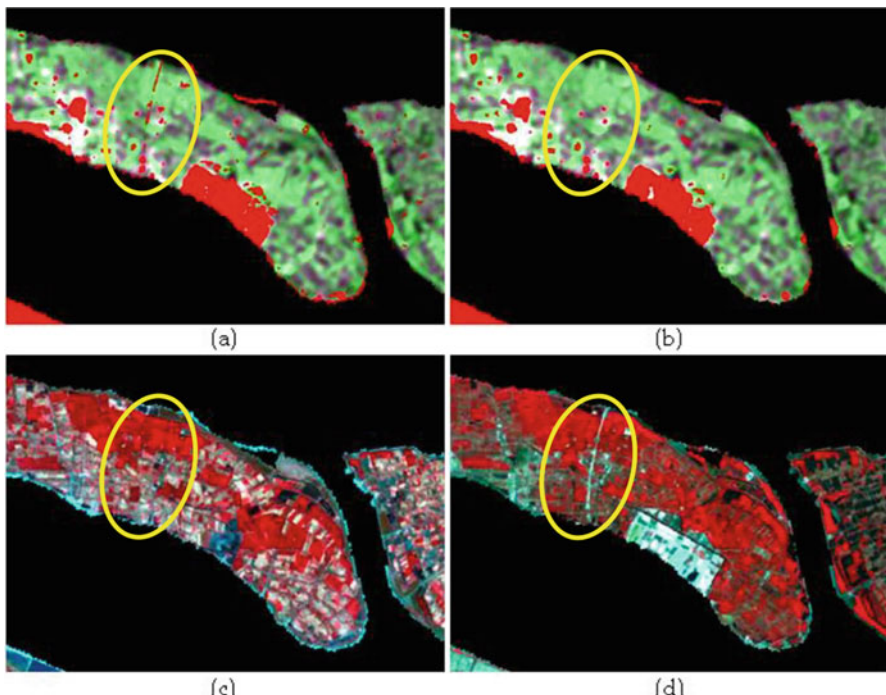


Fig. 2.7 Detected changed areas in yellow, overlaid in a false color composite using (a) SAR & Optical combined solution, (b) SAR modified ratio with log normal solution, (c) 1999 Landsat image, & (d) 2008 Landsat image (Ban et al. 2014)

multidimensional evidential reasoning approach to extract change information from heterogeneous multitemporal images.

Second, single-source multitemporal images (i.e., optical or radar) are known for their limited capacity to provide exhaustive documentation of changes that have occurred on the ground. Unlike optical, SAR images have a very high temporal resolution. The existence of speckle, however, impedes the accurate identification of shapes and edges. Optical images show more detail and allow the detection of sharp edges and region boundaries (Orsomando et al. 2007). Change detection analysis can benefit from the complementary nature of the change information represented by each type of data—that is, by SAR and by optical multitemporal datasets. In an attempt to improve the quality of the binary change map, Bruzzone and Prieto (2000b) proposed an unsupervised change detection approach that uses consensus theory to integrate many change variables. Ban et al. (2014) demonstrated that the fusion of both optical and SAR data could improve change detection (Fig. 2.7). In this research, a multidimensional change image was constructed by combining SAR and optical change variables. An iterative classification strategy is then adopted to separate changed and unchanged classes.

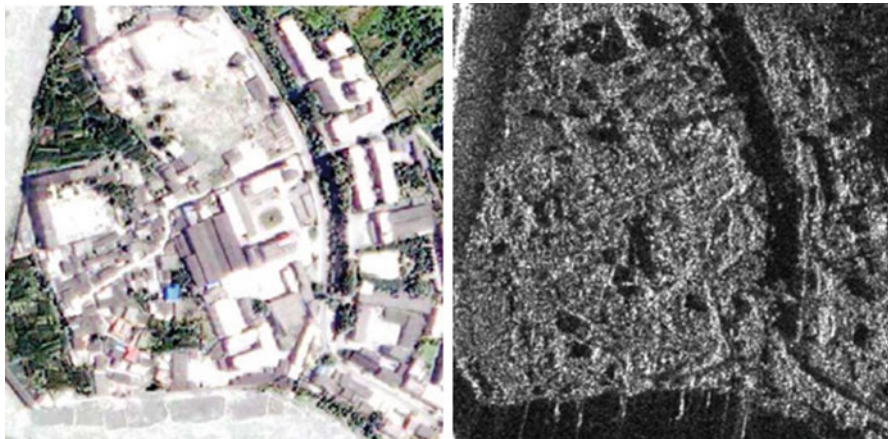


Fig. 2.8 Image subset of 2008 Sichuan earthquake, *Left*: QuickBird image before earthquake; *Right*: COSMO-SkyMed image after earthquake (Brunner et al. 2010)

Fusion in remote sensing analysis is not restricted to images with different resolution or modalities; it is also extended to include the fusion of different types of information extracted from the same source. Gong et al (2012b) improved the quality of the final change indicator through the fusion of different change variables extracted from the same multitemporal dataset using different comparison operators. The authors claimed that the mean-ratio image emphasizes changed areas in the scene, while the log-ratio image more reflects the background information, the unchanged areas. Consequently, two change variables were constructed using the mean-ratio and log-ratio operators. Each change variable can then be decomposed into low- and high-frequency components using a wavelet transform. The fusion of the change variables is performed in the wavelet domain, where different rules were developed for the low- and high-frequency components. It is worth mentioning that the same wavelet-based fusion approach was adopted by Ma et al. (2012), where different fusion rules were used. In a similar way, Hou et al. (2014) fused two change images produced using the Gauss log-ratio and log-ratio comparison operators. In contrast, Du et al. (2013) each band in the multispectral image was used to generate a change map. A final change map is generated by fusion at the decision level.

For cross-sensor change detection, Brunner et al. (2010) presented a novel method that detects buildings destroyed in an earthquake using pre-event VHR optical imagery (QuickBird and WorldView-1) and post-event detected VHR SAR imagery (TerraSAR-X and COSMO-SkyMed). They demonstrated the feasibility and the effectiveness of the proposed method for a heavily damaged in the Sichuan earthquake of May 12, 2008. Figure 2.8 shows the complexity and challenges using very-high resolution cross-sensor imagery for change detection.

2.7 Concluding Remarks

The chapter covers change detection methods for both optical and SAR images. Various aspects of change detection processes were reviewed including data pre-processing, change image generation and change detection algorithms. In terms of preprocessing, absolute or relative radiometric corrections are necessary for change detection using multitemporal optical imagery. Geometric correction and image co-registration in high-accuracy are critical for all images. Orthorectification are mandatory for SAR images in mountainous regions and all very-high resolution data in urban areas. Speckle filtering is also important for SAR-based change detection. In terms of change image generation, most commonly used operators for optical data are image differencing, image regression, change vector analysis and NDVI differencing. For SAR images, image ratio, log ratio and similarity measures are often used. In terms of change detection algorithms, unsupervised and supervised change detection as well as pixel-based and object-based approaches were used. The review shows that significant progress has been made in the field of change detection and innovative methods have been developed for change detection using both multitemporal SAR and optical data. Attempts have been made for change detection using multitemporal multisensor/cross-sensor images.

In the past decade, many advanced Earth Observation systems have been launched with increased spatial, spectral, radiometric and/or temporal resolutions. With the recent launches of Sentinel-1A, -1B and -2A, multitemporal SAR and optical data with the globe coverage in every 6 days become freely available. They provide excellent opportunity to develop novel methods and algorithms for operational applications and to expand to new applications. The review also identified the following challenges and opportunities:

- First, the change detection methods developed are still at research and development stage, with very few operational application examples. Operational methods and algorithms need to be developed to support environmental monitoring and sustainable decision-making.
- Second, most of the studies used relatively small study areas and datasets, but to support global change research, change detection at global or regional scale is necessary. Global land cover mapping (GLC), for example, took several years to complete with significant cost, it would be more time- and cost-efficient to update the GLC maps using change detection.
- Third, with the availability of huge volume of optical and SAR imagery, big data analytical paradigm need to be introduced to change detection in order to handle the multitemporal big EO data.
- Forth, new generation of satellite data at very high resolution demands the development of robust processing techniques for change detection in VHR multispectral, SAR, hyperspectral images and their fusion.
- Fifth, long time series (44 years for satellite optical or cross sensor imagery and 25 years for spaceborne SAR data) require the development of novel processing and data mining methods.

References

- Achard F, Eva HD, Stibig H-J, Mayaux P, Gallego J, Richards T, Malingreau J-P (2002) Determination of deforestation rates of the world's humid tropical forests. *Science* 297(5583):999–1002. doi:[10.1126/science.1070656](https://doi.org/10.1126/science.1070656)
- Akbari V, Doulgeris A, Eltoft T (2014) Monitoring glacier changes using multitemporal multipolarization SAR images. *IEEE Trans Geosci Remote Sens* 52:3729–3741
- Alberga V (2009) Similarity measures of remotely sensed multi-sensor images for change detection applications. *Remote Sens* 1:122–143. doi:[10.3390/rs1030122](https://doi.org/10.3390/rs1030122)
- Alphan H, Doygun H, Unlukaplan YI (2008) Post-classification comparison of land cover using multitemporal Landsat and ASTER imagery: the case of Kahramanmaraş, Turkey. *Environ Monit Assess* 151:327–336. doi:[10.1007/s10661-008-0274-x](https://doi.org/10.1007/s10661-008-0274-x)
- Alwashe MA, Bokhari AY (1993) Monitoring vegetation changes in Al Madinah, Saudi Arabia, using Thematic Mapper data. *Int J Remote Sens* 14:191–197
- Anders NS, Seijmonsbergen A, Bouten W (2013) Geomorphological change detection using object-based feature extraction from multi-temporal LiDAR data. *IEEE Geosci Remote Sens Lett* 10:1587–1591. doi:[10.1109/LGRS.2013.2262317](https://doi.org/10.1109/LGRS.2013.2262317)
- Ban Y, Jacob A (2013) Object-based fusion of multitemporal multi-angle ENVISAT ASAR and HJ-1 multispectral data for urban land-cover mapping. *IEEE Trans GeoSci Rem Sens* 51(4):1998–2006
- Ban Y, Yousif O (2012) Multitemporal spaceborne SAR data for urban change detection in China. *IEEE J Sel Top Appl Earth Obs Rem Sens* 5(4):1087–1094
- Ban Y, Yousif O, Hu H (2014) Fusion of SAR and optical data for urban land cover mapping and change detection. *Glob Urban Monit Assess Earth Obs* 353
- Baselice F, Ferraioli G, Pascazio V (2014) Markovian change detection of urban areas using very high resolution complex SAR images. *IEEE Geosci Remote Sens Lett* 11:995–999. doi:[10.1109/LGRS.2013.2284297](https://doi.org/10.1109/LGRS.2013.2284297)
- Bazi Y, Bruzzone L, Melgani F (2005) An unsupervised approach based on the generalized Gaussian model to automatic change detection in multitemporal SAR images. *IEEE Trans Geosci Remote Sens* 43:874–887. doi:[10.1109/TGRS.2004.842441](https://doi.org/10.1109/TGRS.2004.842441)
- Bazi Y, Bruzzone L, Melgani F (2006) Automatic identification of the number and values of decision thresholds in the log-ratio image for change detection in SAR images. *IEEE Geosci Remote Sens Lett* 3:349–353. doi:[10.1109/LGRS.2006.869973](https://doi.org/10.1109/LGRS.2006.869973)
- Berberoglu S, Akin A (2009) Assessing different remote sensing techniques to detect land use/cover changes in the eastern Mediterranean. *Int J Appl Earth Obs Geoinf* 11:46–53. doi:[10.1016/j.jag.2008.06.002](https://doi.org/10.1016/j.jag.2008.06.002)
- Bin W, Jian Y, Zhongming Z, Yu M, Anzhi Y, Jingbo C, Dongxu H, Xingchun L, Shunxi L (2013) Parcel-based change detection in land-use maps by adopting the holistic feature. *IEEE J Sel Top Appl Earth Obs Remote Sens*. Early Access Online
- Blaschke T (2005) Towards a framework for change detection based on image objects. *Gött Geogr Abh* 113:1–9
- Boccardo P, Borgogno Mondinoa E, Giulio Tonolo F, Lingua A (2004) Orthorectification of high resolution satellite images. In: Proceedings, ISPRS 35th congress, Istanbul.
- Bontemps S, Bogaert P, Titeux N, Defourny P (2008) An object-based change detection method accounting for temporal dependences in time series with medium to coarse spatial resolution. *Remote Sens Environ* 112:3181–3191. doi:[10.1016/j.rse.2008.03.013](https://doi.org/10.1016/j.rse.2008.03.013)
- Bouziani M, Goita K, He D-C (2010) Automatic change detection of buildings in urban environment from very high spatial resolution images using existing geodatabase and prior knowledge. *ISPRS J Photogramm Remote Sens* 65:143–153
- Bovolo F, Bruzzone L (2005) A detail-preserving scale-driven approach to change detection in multitemporal SAR images. *IEEE Trans Geosci Remote Sens* 43:2963–2972. doi:[10.1109/TGRS.2005.857987](https://doi.org/10.1109/TGRS.2005.857987)

- Bovolo F, Bruzzone L (2007a) A split-based approach to unsupervised change detection in large-size multitemporal images: application to tsunami-damage assessment. *IEEE Trans Geosci Remote Sens* 45:1658–1670. doi:[10.1109/TGRS.2007.895835](https://doi.org/10.1109/TGRS.2007.895835)
- Bovolo F, Bruzzone L (2007b) A theoretical framework for unsupervised change detection based on change vector analysis in the polar domain. *IEEE Trans Geosci Remote Sens* 45:218–236. doi:[10.1109/TGRS.2006.885408](https://doi.org/10.1109/TGRS.2006.885408)
- Bovolo F, Bruzzone L, Marchesi S (2009) Analysis and adaptive estimation of the registration noise distribution in multitemporal VHR images. *IEEE Trans Geosci Remote Sens* 47(8): 2658–2671
- Bovolo F, Marin C, Bruzzone L (2013) A hierarchical approach to change detection in very high resolution SAR images for surveillance applications. *IEEE Trans Geosci Remote Sens* 51:2042–2054. doi:[10.1109/TGRS.2012.2223219](https://doi.org/10.1109/TGRS.2012.2223219)
- Brunner B, Lemoine G, Bruzzone L (2010) Earthquake damage assessment of buildings using VHR optical and SAR imagery. *IEEE Trans Geosci Remote Sens* 48(5):2403–2420
- Bruzzone L, Prieto DF (2000a) Automatic analysis of the difference image for unsupervised change detection. *IEEE Trans Geosci Remote Sens* 38:1171–1182
- Bruzzone L, Prieto DF (2000b) Unsupervised change detection in multisource and multisensor remote sensing images. In: Proceedings. IEEE 2000 international geoscience and remote sensing symposium. Presented at the IGARSS 2000, vol 6, pp 2441–2443. doi:[10.1109/IGARSS.2000.859602](https://doi.org/10.1109/IGARSS.2000.859602)
- Bruzzone L, Prieto DF (2002) An adaptive semiparametric and context-based approach to unsupervised change detection in multitemporal remote-sensing images. *IEEE Trans Image Process* 11:452–466
- Bujor FT, Nicolas J-M, Trouve E, Rudant J-P (2003) Application of log-cumulants to change detection on multi-temporal SAR images. In: IEEE international geoscience and remote sensing symposium. Presented at the IGARSS 2003, vol 2, pp 1386–1388
- Bujor F, Trouve E, Valet L, Nicolas J-M, Rudant J-P (2004) Application of log-cumulants to the detection of spatiotemporal discontinuities in multitemporal SAR images. *IEEE Trans Geosci Remote Sens* 42:2073–2084. doi:[10.1109/TGRS.2004.835304](https://doi.org/10.1109/TGRS.2004.835304)
- Cakir HI, Khorram S, Nelson SAC (2006) Correspondence analysis for detecting land cover change. *Remote Sens Environ* 102:306–317. doi:[10.1016/j.rse.2006.02.023](https://doi.org/10.1016/j.rse.2006.02.023)
- Castellana L, D'Addabbo A, Pasquariello G (2007) A composed supervised/unsupervised approach to improve change detection from remote sensing. *Pattern Recogn Lett* 28:405–413. doi:[10.1016/j.patrec.2006.08.010](https://doi.org/10.1016/j.patrec.2006.08.010)
- Celik T (2009) Unsupervised change detection in satellite images using principal component analysis and k-means clustering. *IEEE Geosci Remote Sens Lett* 6:772–776. doi:[10.1109/LGRS.2009.2025059](https://doi.org/10.1109/LGRS.2009.2025059)
- Celik T (2010a) A Bayesian approach to unsupervised multiscale change detection in synthetic aperture radar images. *Signal Process* 90:1471–1485. doi:[10.1016/j.sigpro.2009.10.018](https://doi.org/10.1016/j.sigpro.2009.10.018)
- Celik T (2010b) Change detection in satellite images using a genetic algorithm approach. *IEEE Geosci Remote Sens Lett* 7:386–390. doi:[10.1109/LGRS.2009.2037024](https://doi.org/10.1109/LGRS.2009.2037024)
- Chatelain F, Tourneret J-Y, Inglada J, Ferrari A (2007) Bivariate gamma distributions for image registration and change detection. *IEEE Trans Image Process* 16:1796–1806
- Chen G, Hay GJ, Carvalho LMT, Wulder MA (2012) Object-based change detection. *Int J Remote Sens* 33:4434–4457. doi:[10.1080/01431161.2011.648285](https://doi.org/10.1080/01431161.2011.648285)
- Chen G, Zhao K, Powers R (2014) Assessment of the image misregistration effects on object-based change detection. *ISPRS J Photogramm Remote Sens* 87:19–27
- Conradsen K, Nielsen AA, Schou J, Skriver H (2003) A test statistic in the complex wishart distribution and its application to change detection in polarimetric SAR data. *IEEE Trans Geosci Remote Sens* 41:4–19. doi:[10.1109/TGRS.2002.808066](https://doi.org/10.1109/TGRS.2002.808066)
- Cossu R, Chaudhuri S, Bruzzone L (2005) A context-sensitive bayesian technique for the partially supervised classification of multitemporal images. *IEEE Geosci Remote Sens Lett* 2:352–356. doi:[10.1109/LGRS.2005.851541](https://doi.org/10.1109/LGRS.2005.851541)

- Cui S, Schwarz G, Datcu M (2016) A benchmark evaluation of similarity measures for multitemporal SAR image change detection. *IEEE J Sel Top Appl Earth Obs Remote Sens* 9:1101–1118. doi:[10.1109/JSTARS.2015.2486038](https://doi.org/10.1109/JSTARS.2015.2486038)
- Dai X, Khorram S (1998) The effects of image misregistration on the accuracy of remotely sensed change detection. *IEEE Trans Geosci Remote Sens* 36:1566–1577
- Dawelbait M, Morari F (2012) Monitoring desertification in a Savannah region in Sudan using Landsat images and spectral mixture analysis. *J Arid Environ* 80:45–55
- de Carvalho O, Guimaraes R, Gomes R, de Carvalho A, da Silva N (2006) Normalization of multi-temporal images using a new change detection method based on the spectral classifier. In: IEEE international conference on geoscience and remote sensing symposium, 2006. IGARSS 2006. Presented at the IEEE international conference on geoscience and remote sensing symposium, 2006. IGARSS 2006, pp 771–774. doi:[10.1109/IGARSS.2006.198](https://doi.org/10.1109/IGARSS.2006.198)
- Dekker RJ (1998) Speckle filtering in satellite SAR change detection imagery. *Int J Remote Sens* 19:1133–1146
- Del Frate F, Pacifici F, Solimini D (2008) Monitoring urban land cover in Rome, Italy, and its changes by single-polarization multitemporal SAR images. *IEEE J Sel Top Appl Earth Obs Remote Sens* 1:87–97. doi:[10.1109/JSTARS.2008.2002221](https://doi.org/10.1109/JSTARS.2008.2002221)
- Deng J-S, Wang K, Li J, Deng Y-H (2009) Urban land use change detection using multisensor satellite images. *Pedosphere* 19:96–103. doi:[10.1016/S1002-0160\(08\)60088-0](https://doi.org/10.1016/S1002-0160(08)60088-0)
- Desclepere B, Bogaert P, Defourny P (2006) Forest change detection by statistical object-based method. *Remote Sens Environ* 102:1–11. doi:[10.1016/j.rse.2006.01.013](https://doi.org/10.1016/j.rse.2006.01.013)
- Du P, Liu S, Gamba P, Tan K, Xia J (2012) Fusion of difference images for change detection over urban areas. *IEEE J Sel Top Appl Earth Obs Remote Sens* 5:1076–1086. doi:[10.1109/JSTARS.2012.2200879](https://doi.org/10.1109/JSTARS.2012.2200879)
- Du P, Liu S, Xia J, Zhao Y (2013) Information fusion techniques for change detection from multi-temporal remote sensing images. *Inf Fusion* 14:19–27. doi:[10.1016/j.inffus.2012.05.003](https://doi.org/10.1016/j.inffus.2012.05.003)
- Fletcher K, European Space Agency, European Space Research and Technology Centre, ESTEC (2007) InSAR principles: guidelines for SAR interferometry processing and interpretation. ESA Publications Division, ESTEC, Noordwijk, the Netherlands
- Gamba P, Dell'Acqua F, Lisini G (2006) Change detection of multitemporal SAR data in urban areas combining feature-based and pixel-based techniques. *IEEE Trans Geosci Remote Sens* 44:2820–2827. doi:[10.1109/TGRS.2006.879498](https://doi.org/10.1109/TGRS.2006.879498)
- Gamba P, Dell'Acqua F, Trianni G (2007) Rapid damage detection in the bam area using multitemporal SAR and exploiting ancillary data. *IEEE Trans Geosci Remote Sens* 45:1582–1589. doi:[10.1109/TGRS.2006.885392](https://doi.org/10.1109/TGRS.2006.885392)
- Gao F, Masek JG, Wolfe RE, Tan B (2010) Normalizing Landsat and ASTER data using MODIS data products for forest change detection. In: Geoscience and remote sensing symposium (IGARSS), 2010 IEEE international. Presented at the Geoscience and Remote Sensing Symposium (IGARSS). 2010 IEEE International, pp 3206–3209
- Garzelli A (1999) Classification of polarimetric SAR images using adaptive neighbourhood structures. *Int J Remote Sens* 20:1669–1675. doi:[10.1080/014311699212678](https://doi.org/10.1080/014311699212678)
- Ghosh S, Bruzzone L, Patra S, Bovolo F, Ghosh A (2007) A context-sensitive technique for unsupervised change detection based on Hopfield-Type neural networks. *IEEE Trans Geosci Remote Sens* 45:778–789. doi:[10.1109/TGRS.2006.888861](https://doi.org/10.1109/TGRS.2006.888861)
- Gong M, Cao Y, Wu Q (2012a) A neighborhood-based ratio approach for change detection in SAR images. *IEEE Geosci Remote Sens Lett* 9:307–311. doi:[10.1109/LGRS.2011.2167211](https://doi.org/10.1109/LGRS.2011.2167211)
- Gong M, Zhou Z, Ma J (2012b) Change detection in synthetic aperture radar images based on image fusion and fuzzy clustering. *IEEE Trans Image Process* 21:2141–2151. doi:[10.1109/TIP.2011.2170702](https://doi.org/10.1109/TIP.2011.2170702)
- Gong M, Zhao J, Liu J, Miao Q, Jiao L (2016) Change detection in synthetic aperture radar images based on deep neural networks. *IEEE Trans Neural Netw Learn Syst* 27:125–138. doi:[10.1109/TNNLS.2015.2435783](https://doi.org/10.1109/TNNLS.2015.2435783)
- Grey W, Luckman A, Holland D (2003) Mapping urban change in the UK using satellite radar interferometry. *Remote Sens Environ* 87:16–22. doi:[10.1016/S0034-4257\(03\)00142-1](https://doi.org/10.1016/S0034-4257(03)00142-1)

- Hachicha S, Chaabane F (2010) Comparison of change detection indicators in SAR images. In: 8th European conference on synthetic aperture radar. EUSAR 2010, pp 1–4
- Hall O, Hay GJ (2003) A multiscale object-specific approach to digital change detection. *Int J Appl Earth Obs Geoinf* 4:311–327. doi:[10.1016/S0303-2434\(03\)00010-2](https://doi.org/10.1016/S0303-2434(03)00010-2)
- Hao M, Shi W, Zhang H, Li C (2014) Unsupervised change detection with expectation-maximization-based level set. *IEEE Geosci Remote Sens Lett* 11:210–214
- Hazel GG (2001) Object-level change detection in spectral imagery. *IEEE Trans Geosci Remote Sens* 39:553–561. doi:[10.1109/36.911113](https://doi.org/10.1109/36.911113)
- He C, Wei A, Shi P, Zhang Q, Zhao Y (2011) Detecting land-use/land-cover change in rural–urban fringe areas using extended change-vector analysis. *Int J Appl Earth Obs Geoinf* 13:572–585. doi:[10.1016/j.jag.2011.03.002](https://doi.org/10.1016/j.jag.2011.03.002)
- Hoberg T, Rottensteiner F, Feitosa RQ, Heipke C (2015) Conditional random fields for multitemporal and multiscale classification of optical satellite imagery. *IEEE Trans Geosci Remote Sens* 53:659–673. doi:[10.1109/TGRS.2014.2326886](https://doi.org/10.1109/TGRS.2014.2326886)
- Hou B, Wei Q, Zheng Y, Wang S (2014) Unsupervised change detection in SAR image based on gauss-log ratio image fusion and compressed projection. *IEEE J Sel Top Appl Earth Obs Remote Sens. Early Access Online.* doi:[10.1109/JSTARS.2014.2328344](https://doi.org/10.1109/JSTARS.2014.2328344)
- Hu H, Ban Y (2014) Unsupervised change detection in multitemporal SAR images over large urban areas. *IEEE J Selected Top Appl Earth Obs Remote Sens* 7(8):3248–3261. doi:[10.1109/JSTARS.2014.2344017](https://doi.org/10.1109/JSTARS.2014.2344017)
- Hussain M, Chen D, Cheng A, Wei H, Stanley D (2013) Change detection from remotely sensed images: from pixel-based to object-based approaches. *ISPRS J Photogramm Remote Sens* 80:91–106
- Im J, Jensen JR (2005) A change detection model based on neighborhood correlation image analysis and decision tree classification. *Remote Sens Environ* 99:326–340
- Im J, Jensen JR, Tullis JA (2008) Object-based change detection using correlation image analysis and image segmentation. *Int J Remote Sens* 29:399–423. doi:[10.1080/01431160601075582](https://doi.org/10.1080/01431160601075582)
- Ingla J, Giros A (2004) On the possibility of automatic multisensor image registration. *IEEE Trans Geosci Remote Sens* 42:2104–2120. doi:[10.1109/TGRS.2004.835294](https://doi.org/10.1109/TGRS.2004.835294)
- Ingla J, Mercier G (2007) A new statistical similarity measure for change detection in multitemporal SAR images and its extension to multiscale change analysis. *IEEE Trans Geosci Remote Sens* 45:1432–1445. doi:[10.1109/TGRS.2007.893568](https://doi.org/10.1109/TGRS.2007.893568)
- Janalipour M, Mohammadzadeh A (2016) Building damage detection using object-based image analysis and ANFIS from high-resolution image (Case study: BAM earthquake, Iran). *IEEE J Sel Top Appl Earth Obs Remote Sens* 9:1937–1945
- Jovanović D, Govđedarica M, Đorđević I, Pajić V (2010) Object based image analysis in forestry change detection. In: International symposium on intelligent systems and informatics. Presented at the SISY 2010, pp 231–236. doi:[10.1109/SISY.2010.5647487](https://doi.org/10.1109/SISY.2010.5647487)
- Kasetkasem T, Varshney PK (2002) An image change detection algorithm based on Markov random field models. *IEEE Trans Geosci Remote Sens* 40:1815–1823
- Kittler J, Illingworth J (1986) Minimum error thresholding. *Pattern Recogn* 19:41–47
- Latifovic R, Pouliot D (2014) Monitoring cumulative long-term vegetation changes over the Athabasca oil sands region. *IEEE J Sel Top Appl Earth Obs Remote Sens. Early access online.* doi:[10.1109/JSTARS.2014.2321058](https://doi.org/10.1109/JSTARS.2014.2321058)
- Lee JS, Jurkevich L, Dewaele P, Wambacq P, Oosterlinck A (1994) Speckle filtering of synthetic aperture radar images: A review. *Remote Sens Rev* 8(4):313–340
- Leonardo P, Francisco G, Jose A, Sobrino JC, Jimenez M, Haydee K (2006) Radiometric correction effects in Landsat multi-date/multi-sensor change detection studies. *Int J Remote Sens* 2:685–704
- Li SZ (2009) Markov random field modeling in image analysis, 3rd edn. Springer, London
- Li HC, Celik T, Longbotham N, Emery WJ (2015) Gabor feature based unsupervised change detection of multitemporal SAR images based on two-level clustering. *IEEE Geosci Remote Sens Lett* 12:2458–2462. doi:[10.1109/LGRS.2015.2484220](https://doi.org/10.1109/LGRS.2015.2484220)

- Liu Z, Mercier G, Dezert J, Pan Q (2014) Change detection in heterogeneous remote sensing images based on multidimensional evidential reasoning. *IEEE Geosci Remote Sens Lett* 11:168–172. doi:[10.1109/LGRS.2013.2250908](https://doi.org/10.1109/LGRS.2013.2250908)
- Liu S, Bruzzone L, Bovolo F, Du P (2015a) Hierarchical unsupervised change detection in multitemporal hyperspectral images. *IEEE Trans Geosci Remote Sens* 53:244–260. doi:[10.1109/TGRS.2014.2321277](https://doi.org/10.1109/TGRS.2014.2321277)
- Liu S, Bruzzone L, Bovolo F, Zanetti M, Du P (2015b) Sequential spectral change vector analysis for iteratively discovering and detecting multiple changes in hyperspectral images. *IEEE Trans Geosci Remote Sens* 53:4363–4378. doi:[10.1109/TGRS.2015.2396686](https://doi.org/10.1109/TGRS.2015.2396686)
- Lu D, Mausel P, Brondízio E, Moran E (2004) Change detection techniques. *Int J Remote Sens* 25:2365–2401. doi:[10.1080/0143116031000139863](https://doi.org/10.1080/0143116031000139863)
- Lyon JG, Yuan D, Lunetta RS, Elvidge CD (1998) A change detection experiment using vegetation indices. *Photogramm Eng Remote Sens* 64:143–150
- Ma J, Gong M, Zhou Z (2012) Wavelet fusion on ratio images for change detection in SAR images. *IEEE Geosci Remote Sens Lett* 9:1122–1126. doi:[10.1109/LGRS.2012.2191387](https://doi.org/10.1109/LGRS.2012.2191387)
- Malila WA (1980) Change vector analysis: an approach for detecting forest changes with Landsat. *LARS Symposia. Paper 385.* http://docs.lib.psu.edu/lars_symp/385
- Marchesi S, Bovolo F, Bruzzone L (2010) A context-sensitive technique Robust to registration noise for change detection in VHR multispectral images. *IEEE Trans Image Process* 19(7):1877–1889
- Marin C, Bovolo F, Bruzzone L (2015) Building change detection in multitemporal very high resolution SAR images. *IEEE Trans Geosci Remote Sens* 53:2664–2682. doi:[10.1109/TGRS.2014.2363548](https://doi.org/10.1109/TGRS.2014.2363548)
- Marsetic A, Ostir K, Fras MK (2016) Automatic orthorectification of high-resolution optical satellite images using vector roads. *IEEE Trans Geosci Remote Sens* 53(11):6035–6047
- Martinez J-M, Le Toan T (2007) Mapping of flood dynamics and spatial distribution of vegetation in the Amazon floodplain using multitemporal SAR data. *Remote Sens Environ* 108(3):209–223. doi:[10.1016/j.rse.2006.11.012](https://doi.org/10.1016/j.rse.2006.11.012)
- Martinis S, Twele A, Voigt S (2011) Unsupervised extraction of flood-induced backscatter changes in SAR data using Markov image modeling on irregular graphs. *IEEE Trans Geosci Remote Sens* 49:251–263. doi:[10.1109/TGRS.2010.2052816](https://doi.org/10.1109/TGRS.2010.2052816)
- Melgani F, Moser G, Serpico SB (2002) Unsupervised change-detection methods for remote-sensing images. *Opt Eng* 41:3288–3297
- Mercier G, Moser G, Serpico SB (2008) Conditional copulas for change detection in heterogeneous remote sensing images. *IEEE Trans Geosci Remote Sens* 46:1428–1441. doi:[10.1109/TGRS.2008.916476](https://doi.org/10.1109/TGRS.2008.916476)
- Moser G, Serpico SB (2006) Generalized minimum-error thresholding for unsupervised change detection from SAR amplitude imagery. *IEEE Trans Geosci Remote Sens* 44:2972–2982. doi:[10.1109/TGRS.2006.876288](https://doi.org/10.1109/TGRS.2006.876288)
- Moser G, Serpico SB (2009) Unsupervised change detection from multichannel SAR data by Markovian data fusion. *IEEE Trans Geosci Remote Sens* 47:2114–2128. doi:[10.1109/TGRS.2009.2012407](https://doi.org/10.1109/TGRS.2009.2012407)
- Moser G, Melgani F, Serpico SB, Caruso A (2002) Partially supervised detection of changes from remote sensing images. In: *IEEE international geoscience and remote sensing symposium. Presented at the IGARSS 2002, vol 1, pp 299–301.* doi:[10.1109/IGARSS.2002.1025019](https://doi.org/10.1109/IGARSS.2002.1025019)
- Moser G, Serpico S, Vernazza G (2007) Unsupervised change detection from multichannel SAR images. *IEEE Geosci Remote Sens Lett* 4:278–282. doi:[10.1109/LGRS.2007.890549](https://doi.org/10.1109/LGRS.2007.890549)
- Nemmour H, Chibani Y (2006) Multiple support vector machines for land cover change detection: an application for mapping urban extensions. *ISPRS J Photogramm Remote Sens* 61:125–133. doi:[10.1016/j.isprsjprs.2006.09.004](https://doi.org/10.1016/j.isprsjprs.2006.09.004)
- Nielsen A (2007) The regularized iteratively reweighted MAD method for change detection in multi- and hyperspectral data. *IEEE Trans Image Process* 16:463–478. doi:[10.1109/TIP.2006.888195](https://doi.org/10.1109/TIP.2006.888195)

- Niemeyer I, Marpu PR, Nussbaum S (2008) Change detection using object features. In: Blaschke T, Lang S, Hay GJ (eds) Object-based image analysis, Lecture notes in geoinformation and cartography. Springer, Berlin/Heidelberg, pp 185–201
- Oliver C, Quegan S (2004) Understanding synthetic aperture radar images. SciTech Publishing, Raleigh
- Orsomando F, Lombardo P, Zavagli M, Costantini M (2007) SAR and optical data fusion for change detection. Urban Remote Sens Joint Event 2007:1–9
- Poulain V, Ingla J, Spigai M, Tourneret J-Y, Marthon P (2011) High-resolution optical and SAR image fusion for building database updating. IEEE Trans Geosci Remote Sens 49:2900–2910. doi:[10.1109/TGRS.2011.2113351](https://doi.org/10.1109/TGRS.2011.2113351)
- Qin Y, Niu Z, Chen F, Li B, Ban Y (2013) Object-based land cover change detection for cross-sensor images. Int J Remote Sens 34:6723–6737. doi:[10.1080/01431161.2013.805282](https://doi.org/10.1080/01431161.2013.805282)
- Quin G, Pinel-Puyssegur B, Nicolas J-M, Loreaux P (2014) MIMOSA: an automatic change detection method for SAR time series. IEEE Trans Geosci Remote Sens 52:5349–5363. doi:[10.1109/TGRS.2013.2288271](https://doi.org/10.1109/TGRS.2013.2288271)
- Rasi R, Beuchle R, Bodart C, Vollmar M, Seliger R, Achard F (2013) Automatic updating of an object-based tropical forest cover classification and change assessment. IEEE J Sel Top Appl Earth Obs Remote Sens 6:66–73. doi:[10.1109/JSTARS.2012.2217733](https://doi.org/10.1109/JSTARS.2012.2217733)
- Rignot EJ, van Zyl JJ (1993) Change detection techniques for ERS-1 SAR data. IEEE Trans Geosci Remote Sens 31:896–906
- Roy M, Ghosh S, Ghosh A (2012) Search-based semi-supervised clustering algorithms for change detection in remotely sensed images. In: Annual IEEE India conference. Presented at the INDICON 2012, pp 503–507. doi:[10.1109/INDCON.2012.6420670](https://doi.org/10.1109/INDCON.2012.6420670)
- Sabry R (2009) A new coherency formalism for change detection and phenomenology in SAR imagery: a field approach. IEEE Geosci Remote Sens Lett 6:458–462. doi:[10.1109/LGRS.2009.2016359](https://doi.org/10.1109/LGRS.2009.2016359)
- Singh A (1989) Review Article Digital Change Detection techniques using remotely-sensed data. Int J Remote Sens 10(6):989–1003. doi:[10.1080/01431168908903939](https://doi.org/10.1080/01431168908903939)
- Solberg AH, Taxt T, Jain AK (1996) A Markov random field model for classification of multisource satellite imagery. IEEE Trans Geosci Remote Sens 34:100–113
- Son NT, Chen CF, Chang NB, Chen CR, Chang LY, Thanh BX (2015) Mangrove mapping and change detection in Ca Mau Peninsula, Vietnam using landsat data and object-based image analysis. IEEE J Sel Top Appl Earth Obs Remote Sens 8:503–510. doi:[10.1109/JSTARS.2014.2360691](https://doi.org/10.1109/JSTARS.2014.2360691)
- Taubenböck H, Esch T, Felbier A, Wiesner M, Roth A, Dech S (2012) Monitoring urbanization in mega cities from Space. Remote Sens Environ 117:162–176
- Thonfeld F, Feilhauer H, Braun M, Menz G (2016) Robust Change Vector Analysis (RCVA) for multi-sensor very high resolution optical satellite data. Int J Appl Earth Obs Geoinfor 50:131–140. doi:[10.1016/j.jag.2016.03.009](https://doi.org/10.1016/j.jag.2016.03.009)
- Townshend JRG, Justice CO, Gurney C, McManus J (1992) The impact of misregistration on change detection. IEEE Trans Geosci Remote Sens 30:1054–1060. doi:[10.1109/36.175340](https://doi.org/10.1109/36.175340)
- Tso B, Olsen RC (2005) A contextual classification scheme based on MRF model with improved parameter estimation and multiscale fuzzy line process. Remote Sens Environ 97:127–136. doi:[10.1016/j.rse.2005.04.021](https://doi.org/10.1016/j.rse.2005.04.021)
- Velloso MLF, de Souza FJ, Simoes M (2002) Improved radiometric normalization for land cover change detection: an automated relative correction with artificial neural network. In: Geoscience and remote sensing symposium, 2002. IGARSS'02. 2002 IEEE international. Presented at the geoscience and remote sensing symposium, 2002. IGARSS'02. 2002 IEEE international, vol 6, pp 3435–3437. doi:[10.1109/IGARSS.2002.1027207](https://doi.org/10.1109/IGARSS.2002.1027207)
- Vollmar M, Rasi R, Beuchle R, Simonetti D, Stibig H-J, Achard F (2013) Combining Landsat TM/ETM+ and ALOS AVNIR-2 satellite data for tropical forest cover change detection. IEEE J Sel Top Appl Earth Obs Remote Sens 6:102–109. doi:[10.1109/JSTARS.2013.2241017](https://doi.org/10.1109/JSTARS.2013.2241017)

- Volpi M, Tuia D, Bovolo F, Kanevski M, Bruzzone L (2013) Supervised change detection in VHR images using contextual information and support vector machines. *Int J Appl Earth Obs Geoinfor* 20:77–85. doi:[10.1016/j.jag.2011.10.013](https://doi.org/10.1016/j.jag.2011.10.013)
- Walter V (2004) Object-based classification of remote sensing data for change detection. *ISPRS J Photogramm Remote Sens* 58:225–238. doi:[10.1016/j.isprsjprs.2003.09.007](https://doi.org/10.1016/j.isprsjprs.2003.09.007)
- Wang F, Wu Y, Zhang Q, Zhang P, Li M, Lu Y (2013) Unsupervised change detection on SAR images using triplet Markov field model. *IEEE Geosci Remote Sens Lett* 10:697–701. doi:[10.1109/LGRS.2012.2219494](https://doi.org/10.1109/LGRS.2012.2219494)
- Xiong B, Chen Q, Jiang Y, Kuang G (2012) A threshold selection method using two SAR change detection measures based on the Markov random field model. *IEEE Geosci Remote Sens Lett* 9:287–291. doi:[10.1109/LGRS.2011.2166149](https://doi.org/10.1109/LGRS.2011.2166149)
- Yang X, Zhang K, Jia B, Ci L (2005) Desertification assessment in China: an overview. *J Arid Environ* 63(2):517–531
- Yousif O, Ban Y (2013) Improving urban change detection from multitemporal SAR images using PCA-NLM. *IEEE Trans Geosci Remote Sens* 51:2032–2041. doi:[10.1109/TGRS.2013.2245900](https://doi.org/10.1109/TGRS.2013.2245900)
- Yousif O, Ban Y (2014) Improving SAR-based urban change detection by combining MAP-MRF classifier and nonlocal means similarity weights. *IEEE J Sel Top Appl Earth Obs Remote Sens* 7:4288–4300. doi:[10.1109/JSTARS.2014.2347171](https://doi.org/10.1109/JSTARS.2014.2347171)
- Yousif O, Ban Y (2015) Object-based urban change detection using high resolution SAR images. 2015 Joint Urban Remote Sensing Event (JURSE), Lausanne, pp 1–4. doi:[10.1109/JURSE.2015.7120502](https://doi.org/10.1109/JURSE.2015.7120502)
- Yuan F, Sawaya KE, Loeffelholz BC, Bauer ME (2005) Land cover classification and change analysis of the Twin Cities (Minnesota) Metropolitan Area by multitemporal Landsat remote sensing. *Remote Sens Environ* 98:317–328. doi:[10.1016/j.rse.2005.08.006](https://doi.org/10.1016/j.rse.2005.08.006)
- Zhong P, Wang R (2006) Object detection based on combination of conditional random field and Markov random field. In: 18th international conference on pattern recognition, 2006. ICPR 2006. Presented at the ICPR 2006, pp 160–163. doi:[10.1109/ICPR.2006.876](https://doi.org/10.1109/ICPR.2006.876)
- Zhou W, Troy A, Grove M (2008) A comparison of object-based with pixel-based land cover change detection in the Baltimore Metropolitan area using multitemporal high resolution remote sensing data. In: IEEE international geoscience and remote sensing symposium. Presented at the IGARSS 2008, p IV-683-IV-686. doi:[10.1109/IGARSS.2008.4779814](https://doi.org/10.1109/IGARSS.2008.4779814)
- Zhou L, Cao G, Li Y, Shang Y (2016) Change detection based on conditional random field with region connection constraints in high-resolution remote sensing images. *IEEE J Sel Top Appl Earth Obs Remote Sens*, pp 1–1. doi:[10.1109/JSTARS.2016.2514610](https://doi.org/10.1109/JSTARS.2016.2514610)

Chapter 3

Change Detection in Urban Areas: Spatial and Temporal Scales

Paolo Gamba and Fabio Dell'Acqua

Abstract Urban areas are a challenging environment because of their ever changing structure and the different temporal behaviors and spatial patterns. In this chapter a detailed analysis of some of the questions arising from the use of remotely sensed data in urban area for change detection are addressed. Specifically, the role of very high resolution sensors and their relevance with respect to either fast or slow changes in human settlement is analyzed, with specific stress on rapid mapping in specific sites (hotspots), e.g. for post-disaster damage assessment. Similarly, the possibility to exploit long temporal sequences of coarser resolution data is also explored and discussed, since the availability of huge archives is nowadays a reality that may be used to look for interesting interrelationships between urban area pattern changes and environmental changes, at both the local (town), regional and global level. Examples related to a so-called “hypertemporal” sequences of EO data are offered, and show the great potentials of these data sets.

3.1 Introduction

Change detection is an image processing technique that implies the availability of images acquired at sufficiently different dates and the ability to detect all the significant changes that occurred between two of these dates. **Change detection using Earth Observation (EO) data for any specific application** induces some additional constraints on the general statement above, specifically in two ways.

- Temporal resolution, i.e. the largest time difference between two acquired images that can still be considered “enough”, as per the previous definition, to detect a change in one or more elements of the urban area. Temporal resolution is defined by the airborne or spaceborne EO sensor used, but also by the specific change that is the focus of the analysis.
- Spatial resolution, i.e. the level of geographical details required to be able to detect a change that happened, obviously related to the geographical scale of the

P. Gamba (✉) • F. Dell'Acqua

Department of Electrical, Computer and Biomedical Engineering, University of Pavia, Pavia, Italy
e-mail: paolo.gamba@unipv.it

changing event, the size of the change results that we may want to observe, and the “significance” of these details with respect to the specific urban structures whose changes we want to track. Once again, a suitable (range of) spatial resolution depends on the sensors but also on the change to be tracked.

Specifying to change detection in urban areas, therefore, requires the definition of the spatial scale of the change (by means, for instance, of the size of the objects that are affected by the change) as well as the temporal scale of the same change. Specifically, for the spatial scale the change may be considered at the scale of the whole urban area, at the block or road/infrastructure network scale, at the building/road element scale. Roughly speaking, these scales correspond to spatial resolutions in the range between 100 and 10 m, from 10 to 5 m, from 2.5 to less than 1 m. Temporal scales correspond to a wide range of situations, too. Trend analysis for urban areas may require temporal samples for various years, a few months or even a few days/hours, depending on the structure that is monitored (e.g., urban extents, land uses and road traffic, respectively).

3.2 Urban Changes at Different Spatial and Temporal Scales

There is a clear connection between spatial and spectral resolution of EO data and the mapping task they can be used for. As graphically represented in Fig. 3.1, different sensors and data sets support (very) different mapping tasks in urban areas. For instance, for urban extent mapping purposes (from local up to the global scale), single-band optical and/or radar data are enough, while building outlines may be recognized only in VHR data sets. **Please note that in Fig. 3.1 “very high spatial**

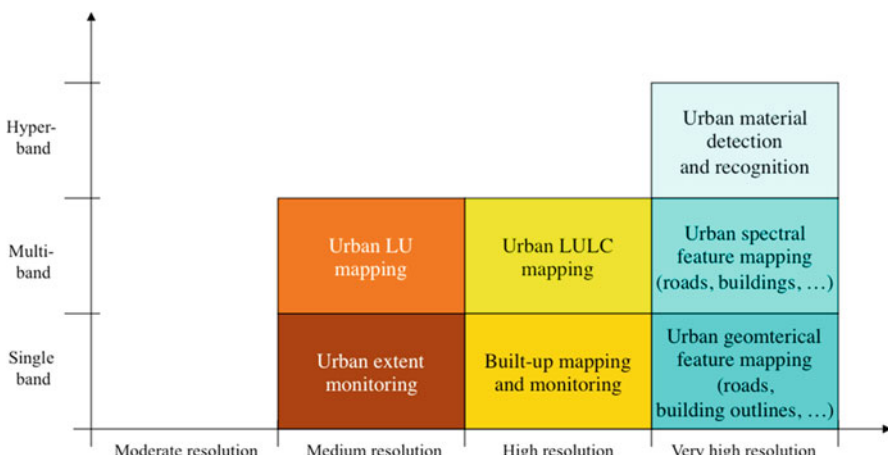


Fig. 3.1 Graphical representation of urban mapping task related to the spectral and spatial resolutions of the EO data sets at hand

resolution” means a pixel posting of 1 m or less, “high resolution” from 3 to 5 m, “medium resolution” from 10 to 100 m, and “moderate resolution” more than 100 m (typically 250, 500 or 1000 m).

By adding the temporal dimension to the graph in Fig. 3.1, additional options arise, according to the temporal behavior of the phenomenon to be investigated. Sudden events, like natural disasters, require fast sampling during selected time period, while long-term events, like urbanization, or land use changes, can be monitored with a less dense time sequence of EO data sets, and with the correspondingly useful spatial resolution (e.g., single band medium resolution and multi-band high resolution, according to the figure above).

The combination of spectral, spatial and temporal requirements determines in turn some constraints on the data sets and the algorithms that can be used. In this chapter, after a preliminary survey of the technical literature on urban change detection, we focus on a couple of examples, i.e. site-specific sudden change detection mapping and long-term city-wide trend analysis. In the following, therefore, first a brief overview of the most common approaches presented in technical literature for change detection for site-specific (or “hotspots”) and long-term trend analyses is offered. Then, some specific examples of processing chains and algorithmic solutions to the these two problems in urban areas exploiting their specific spatial and temporal scales are introduced and discussed.

3.2.1 Hotspot Change Detection

Hotspot monitoring is an application of urban change detection mainly devoted to the characterization of short-term changes in well-defined areas. It is very similar, in this sense, to pollution detection or fire detection or deforestation detection. As a matter of fact, it is usually an unsupervised change detection problem, where we are interested more to know that a change took place than to understand what change happened. Sometimes the amount of change is enough to provide the user with a reasonable interpretation (e.g., the amount of damages after a disaster can be used to infer areas in need of more help). Sometimes, instead, there is a requirement of a more precise classification of the changes, and the above mentioned assumption is no longer true. In any case, if no particular requirement is posed on the changes are to be detected, pixel-based or parcel-based unsupervised techniques comparison methods are enough to reveal extent and location of changes in the observed area. This is especially true when using medium resolution satellites, which provide low-cost data that may be co-registered and corrected using very standard techniques already available in common off the shelf (COTS) software. Indeed, even for sudden changes medium resolution sensors (like those on board of Landsat-8 and in the future on the Sentinel missions by ESA) are good enough to detect changes in urban areas under surveillance. Instead, while the analysis of the actual change requires very high resolution (VHR) imagery. As a matter of fact, when the focus is on particular locations and urban (infra)structures, VHR data are mandatory. In this

case more specific area surveillance techniques, suited to the task of this particular target detection, can provide direct and better results. This is the reason why in this section we treat both “generic” unsupervised change detection approaches and area surveillance methods.

Unsupervised change detection may be obtained by very simple combinations of the raw images at two dates. The combination depends on the sensor characteristics, and is usually prone to errors due to misregistration and miscalibration. Basic methods comprise differencing or ratioing (the latter is better if SAR data is used) as in Rignot and van Zyl (1993). Alternatively, indexes may be extracted from data, like the Normalized Difference Vegetation Index (NDVI). Similarly, in Zha et al. (2003) a new index is proposed, namely the Normalized Difference Built-up Index (NDBI), which seems to be a better descriptor than NDVI for urban areas. This index exploits the fact that urban areas and barren soil shows a far larger increment in digital number values from band 4 to band 5 (Medium Infrared) for Landsat TM. A comparison with Max Likelihood results shows that NDBI provides better results. A slightly more complex method is Change Vector Analysis (CVA), since it allows tracking how the change **affected each band**, and thus recognizing what happened. In Johnson and Kasischke (1998) CVA is applied to some examples, among which the monitoring of urban expansion near Seattle. A maximum likelihood classification allows then extracting information on the nature of the change. Finally, in Grey et al. (2003) a very interesting analysis of multi-temporal SAR sequence using interferometric measures is discussed. The paper shows that it is possible to detect changes in built areas using satellite SAR data and differencing the coherence between SAR images. Results are validated against GIS land map layers in the UK Cardiff area.

Even if these simple methods may be effective, they usually require thresholds, and this may be a subjective matter, unless some automatic or semi-automatic approach is developed. This has been done in Bruzzone and Fernandez Prieto (2000a), where the Bayesian theory is used to automatically determine the correct threshold to be applied to a difference image. In particular, this image is analyzed by considering the spatial-contextual information included in the pixel neighborhood, relying on Markov Random Fields (MRF's) to exploit inter-pixel class dependency contexts. An iterative method based on the Expectation-Maximization (EM) algorithm is used to estimate the statistical terms that characterize the distributions of the changed and unchanged pixels in the difference image. The authors report to have made experiments on both satellite and airborne multi-spectral data: results appear to be good, and the robustness of the algorithm against noise is highlighted. An extension of this work is presented in Bruzzone and Fernandez Prieto (2000b), where a more application-oriented tool for monitoring land-cover changes is proposed. The proposed technique relies on the definition of the unsupervised change-detection problem in terms of the Bayes rule for minimum cost (BRMC), which in turn allows the generation of change-detection maps in which the more critical type of error is minimized according to end-user requirements.

A different unsupervised but equally adaptive technique is proposed in Bruzzone and Serpico (1997), the Selective use of multi-spectral Information (SMI). In

this approach, even if a land cover change may be visible only in some spectral bands, all the bands are considered. Those where the change is not detectable are used to identify pixels affected by registration noise and pixels belonging to other non-investigated changes. In Bruzzone and Fernandez Prieto (2000c) a technique based on “adaptive parcels” (small homogeneous regions shared by both original images) is presented. The adaptive nature of parcels allows spatial-contextual information to be exploited so that noise may be reduced without damaging the boundaries of changed areas. In addition, the characterization of parcels with a set of different features allows identifying different land cover changes. In Bruzzone and Fernandez Prieto (2002) an adaptive semi-parametric technique for the unsupervised estimation of the statistical terms associated with the gray levels of changed and unchanged pixels in a difference image is presented. Statistical estimation and spatial/contextual information are jointly considered to generate the change map. Similarly, in Kasetkasem and Varshney (2002) the authors exploit the spatial correlation between adjacent pixels using Markov Random Fields. They find that the method is particularly robust against noise and misregistration. Experiments are on simulated an actual images of the San Francisco Bay area.

Finally, some very specific methods have been proposed in technical literature for area surveillance. One of them is Carlotto (1997), where methods for modeling and detecting general patterns of change associated with construction and other kinds of activities that can be observed in remotely sensed imagery are presented. They include a new nonlinear prediction technique for measuring changes between images and temporal segmentation and filtering techniques for analyzing patterns of change over time. Another, very interesting, example is Hazel (2001). Here objects are first extracted from each image to be analyzed, and a site model is built; then, site models extracted from different images are compared and the differences highlighted. Besides robustness against misregistration, this method provides higher-level information and potentially allows some degree of scene understanding; moreover, addition of more imagery helps to perfect the model and thus tends to improve detection results. Finally, Smits and Meyer (2000) investigate a method that can be used to characterize and understand the spatial behavior of change by decomposing the change intensity image into a tree of entities called echelons. Such a tree can be extremely helpful in discovering connections between changes.

3.2.2 Detailed Urban Change Information from Long Temporal EO Series

For medium and **long-term** urban change detection, the temporal sampling of polar orbit satellites with environmental and scientific mission is almost ideal. The possibility to acquire one image per month on a long time span, which is Landsat legacy, is indeed invaluable in this respect, and the analysis can be complemented using SAR data from ESA satellites (ERS-1 and 2 and ENVISAT), as well as

those operated by JAXA and the Canadian Space Agency (the RADARSAT family). Following well-established techniques in EO data interpretation technical literature, when more data sets are available over the same area at different dates, even not from the same satellite, a change detection map can be drawn by cross-checking the land use maps obtained at different dates. **This operation, however, may not always be possible, because land covers easily classified in one image type (e.g., optical images) are sometimes very difficult to extract from another type (e.g., radar images), and vice versa.** Another way of accomplishing the same task, but mostly in case there are more data sets from the same sensor/satellite, is that of directly classifying multi-temporal images.

The very basic approach (Madhavan et al. 2001) corresponds to a previous classification step and a pixel by pixel post-classification comparison. A slightly different approach is proposed in Clapham (2003), relying on continuum-based classification, i.e. classification maps based on variables that assume values in a continuum, like percent impervious land surface and percent canopy cover. This allows better understanding each change, but requires a final step to assign changes to classes again. **A post-classification change detector tailored to the “built-up” class may be found in Zhang (2001).** It uses multi-spectral (Landsat TM) together with panchromatic optical satellite data (SPOT pan), and performs a heavy post-classification processing in order to improve the accuracy, especially for the “built-up” class. The processing is based on three steps: a co-occurrence matrix-based filtering for separating buildings from noise, an axis-oriented linking and segmentation for a complete extraction of urban and water areas, and finally mathematical morphology operations for improving the classified green areas. The differences are detected by comparison with the same results on earlier data; the authors report an accuracy of about 86 % on detection of new buildings and state that big buildings (10–20 m) can be individually detected. Finally, there are papers such as Xiuwan (2002) and Sunar (1998) comparing different methods vs. Post-classification comparison, showing its problems but also its strength with respect to unsupervised techniques. In Xiuwan (2002), for instance, the authors provide a comparison of many methods, rather than a single method. Post-classification is used, and the importance of ancillary data (possibly integrated into a GIS) is stressed. Emphasis is put, like for other post-classification methods, on improving single date classification performance.

When the temporal sequence come from the same sensor/satellite, urban land use change can be detected and classified by means of a supervised classification of multi-temporal data, either original raw data or transformed ones. A first example is Li and Yeh (1998), where the authors use principal component analysis of optical Landsat multi-temporal images to overcome the problems related to obtaining from-to class information. Tested on urban areas in Dongguan, close to Hong Kong, the method has showed superior performance with respect to conventional post-classification comparison, both in terms of accuracy and of limited overestimation of land use change. In Seto et al. (2002), Tasseled Caps is instead used, since it provides 3 bands virtually independent from the observed scene. After normalization and transformation, data are classified using a Bayesian supervised classifier and a hier-

archical approach that leads directly to 9 change classes. A final image segmentation approach is used to discard “salt-and pepper” noise in the final classification map. The accuracy is very precisely assessed and provides very good results for most of the change classes, showing that the method is reliable and precise.

A very interesting point of view has been added to this series of works by Smits and Annoni (2000), where the user requirement are explicitly introduced in the change detection chain. The first point raised by the paper is that region-based change detection is usually required by the final user, while the above mentioned methods are mainly pixel-based. Second, a cost function taking into account the user requirements is often the key for a successful acceptance of the final change map. This consideration leads us quite naturally to the topic of the integration of GIS and remote sensing data. An interface to and from GIS layer is usually essential for providing information that is valuable for final users, especially in urban areas. This may lead to a direct comparison of one date classification to a GIS layer, like in Prol-Ledesma et al. (2002), or to drive the classification by means of the already considered GIS layer (Jansen and Molenaar 1995; Smits and Annoni 1999; Smit and Fuller 2001).

As an algorithmic note to this overview, most of the examples discussed above deal with the comparison of a couple of images at a time. This is the most direct definition of change detection and can be enough to adapt to the different time scales of different events in urban areas. However, the availability of more and more data sets and the possibility to model the temporal process using information extracted from images for more dates has been also explored (Almeida et al. 2003; Xia and Yeh 2000).

3.3 Sudden Change Detection in SAR Images Using “ad hoc” Indexes

One of the most important problems related to urban change detection is the recognition of sudden changes that may happen due to a natural or human-induced disaster, but also because of a specific change in a given site, as mentioned above. Without extensively treating the problem of damage assessment after earthquakes (which is thoroughly analyzed in Dell’Acqua and Gamba 2012), we would like to focus in the following on sudden detection in case of natural/man-made disasters using “ad hoc” indexes. In this section, therefore, the focus is more on the spatial scale and resolution, while the punctual nature of the event requires images that are as temporally close as possible to it.

As a matter of fact, it is usually expected that a sudden change induces an extensive change in the appearance of the objects in EO data, but this is not always the case. Changes depend on the phenomenon, on the spatial resolution and on the type of sensor providing the data. Sometimes, for instance, it is easier to spot a change in the pattern of more buildings than the change on a building-by-building comparison. This is particularly true when dealing with SAR data, where

the combination of materials and geometry defines the backscattering pattern in a given area. Therefore, although it is recognized that change detection application require the most detailed imagery available, the best way to process these data and achieve a (semi) automatic detection of the change is not always corresponding to an analysis at the pixel level.

For SAR imagery related to urban area, for instance, it has been demonstrated in Gamba et al. (2011) that the use of textural feature is helpful to extract urban extents, and specifically a combination of different scales of texture is important. In that work it was highlighted that the best result to extract extents from high resolution and very high resolution SAR imagery is obtained when combining c-occurrence matrix textural features (Haralick et al. 1973) and Local Indicator of Spatial Association (LISA, Sokhal and Thompson 2006) features. The latter ones, in particular, describe very well the chessboard patterns that may appear in urban area due to the intertwines high backscattering and mirror-like reflectance phenomenon due to the simultaneous presence of buildings (corner reflectors) and road (flat surfaces). The same methodologies can be used for change detection, but with different.

On the last point the most recent results include an analysis of LISA indicators for building level change detection, when very local damages occur due to peculiar and spatially limited event. LISA indicators (the Moran index, the Geary index and the Getis-Ord index) describe together the positive and negative autocorrelation effects of SAR backscatters in urban areas. Specifically, Moran's index evaluates the similarity between the neighbors of a pixel by comparing its value with the average local value, and describes local homogeneity. On the contrary, Geary's index identifies areas of high contrast, providing a measure of local dissimilarity, while Getis-Ord index G_i is useful to identify "outliers", i.e. values very different from the surroundings. The latter is represented by means of the following formula

$$G_i = \frac{\sum w_{ij}x_j}{\sum x_j} \quad (3.1)$$

where x_i is the generic pixel value at the i -th position, and w_{ij} are the elements of a weight matrix, here set to either '0' or '1' according the so called "Rook's case".

The examples considered here refer to an event occurred on 7th June, 2012 in Conversano, south Italy, where a gas explosion caused the complete collapse of a three-story building in the densely built-up area of the village center. The damage inflicted to the surrounding buildings was, though, hardly visible to an external observer as noticed in the pictures published on the news. In this case the damage was assumed to be visible in very high resolution radar images, due to the substantial shape change of the target, but very complex to detect, because of the surrounding environment. Moreover, the limited spatial extent of the damage would ease fair comparisons between backscattering patterns of damaged and non-damaged buildings in real-world cases. By considering the above mentioned Getis-Ord LISA indicator, and looking at the patterns averaged on the building shape for the area, it is possible to obtain a first interpretation of a TerraSAR-X

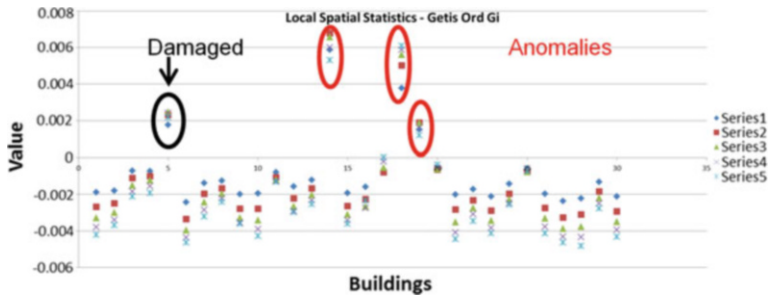


Fig. 3.2 Getis-Ord patterns for damaged and undamaged building in the Conversano (Italy) event using the LISA Getis-Ord textural index

scene covering the whole village. The quantitative results are shown in Fig. 3.2, where the damaged building has a distinct behavior, different from most of the other undamaged ones. By using this indicator, however, some false positive could also show up, as visible in the figure, but the majority of the area will reveal the lack of any change.

3.4 “Hypertemporal” Sequences

The second example of urban change detection in this chapter refers to a very different temporal scale than the one discussed in the previous section, and also to a different target with respect to the required spatial resolution to match its extents. Specifically, the idea is to classify the temporal behavior of urban areas (as a whole, or at the block level) by considering a sequence of datasets covering the same area. Since the temporal datasets available tends to be made by long sequence of information from the same sensors, which may be considered as bands of the same image, this idea has been introduced in Gamba et al. 2008, and these sequence have been labeled as “hypertemporal”, by similarity with hyperspectral imaging, where a lot of bands help to discriminate targets via their spectral behaviors on several tens of wavelengths. Examples of the same idea already existing in technical literature (in addition to those mentioned by the end of the hotspot section) are Yang and Lo (2002) and Masek et al. (2000), where respectively the land use/land cover change data of Atlanta metropolitan area over 25 years have been extracted, by using a time series of Landsat MSS and TM images, and the dynamics of urban growth in the Washington DC metropolitan area in the period from 1973 to 1996 have been studied from Landsat observations.

The main idea, following Gamba et al. (2008), is that a hypertemporal data series $X_n, n \in \{1, \dots, N\}$ is a long enough sequence of consistent data sets directly from the sensor or obtained by processing EO data, with $N \gg 1$. For each of the pixel with geographical position (i, j) , $X_n(i, j)$ has the meaning of its temporal. In

order to be able to work on these sequences, a few pre-processing steps must be guaranteed:

- first of all, since the “bands” of this hyperspectral image are not acquired simultaneously, their alignment must be ensured by means of a multitemporal co-registration;
- second, the data at different dates is temporally correlated in some portions of it, both in the spatial and in the temporal terms; they can (and must) be subject to de-noising and/or feature reduction steps. In Gamba et al. (2008), for instance, a multitemporal speckle filter like in Quegan and Yu (2001) was considered, while in case of an optical sequence techniques like Principal Component Analysis of Minimum Noise Fractions may be considered more suitable.

A graphical representation of a typical processing procedure for a hypertemporal data set (very similar to the one for an hyperspectral image) is thus proposed in Fig. 3.3.

Although the procedure in the previous figure refers to an analysis at the pixel level, the same approach may be considered at a very different spatial scale by considering the possibility to include information about “objects” in the target area, whose changes are more relevant than those detected at the pixel scale. Moreover, in a per-segment approach, there is no need for a precise denoising of the hyper-temporal sequence, since the same effect could be achieved by means of the spatial analysis (e.g., a simple spatial average). If a segmentation map is available, the first step of the procedure should be to substitute pixel values with segment values for any of the bands of the hyper-temporal sequence. Please note however that the significance of these measures for each segment would be best where boundaries have been extracted in accordance to some consistent segmentation procedure based on the original EO data itself. If the boundary information is obtained from an independently extracted GIS layer, the analysis at the segment level may be less significant.

An example considering a sequence of SAR images over the town of Pavia, Italy, and using a GIS layer determining boundaries between homogeneous portions of the town with respect to building types and land uses, is proposed in Fig. 3.4.

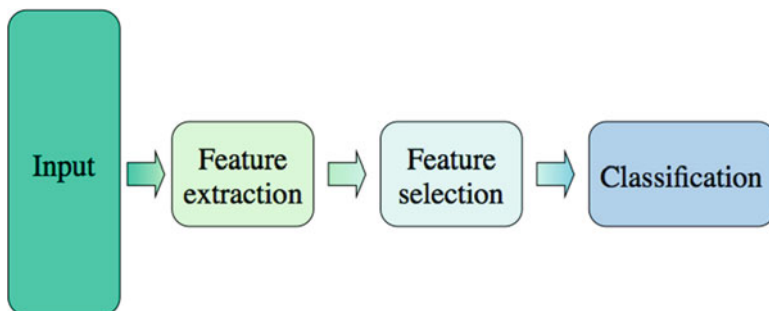


Fig. 3.3 Graphical representation of the main processing steps of the hypertemporal data processing chain

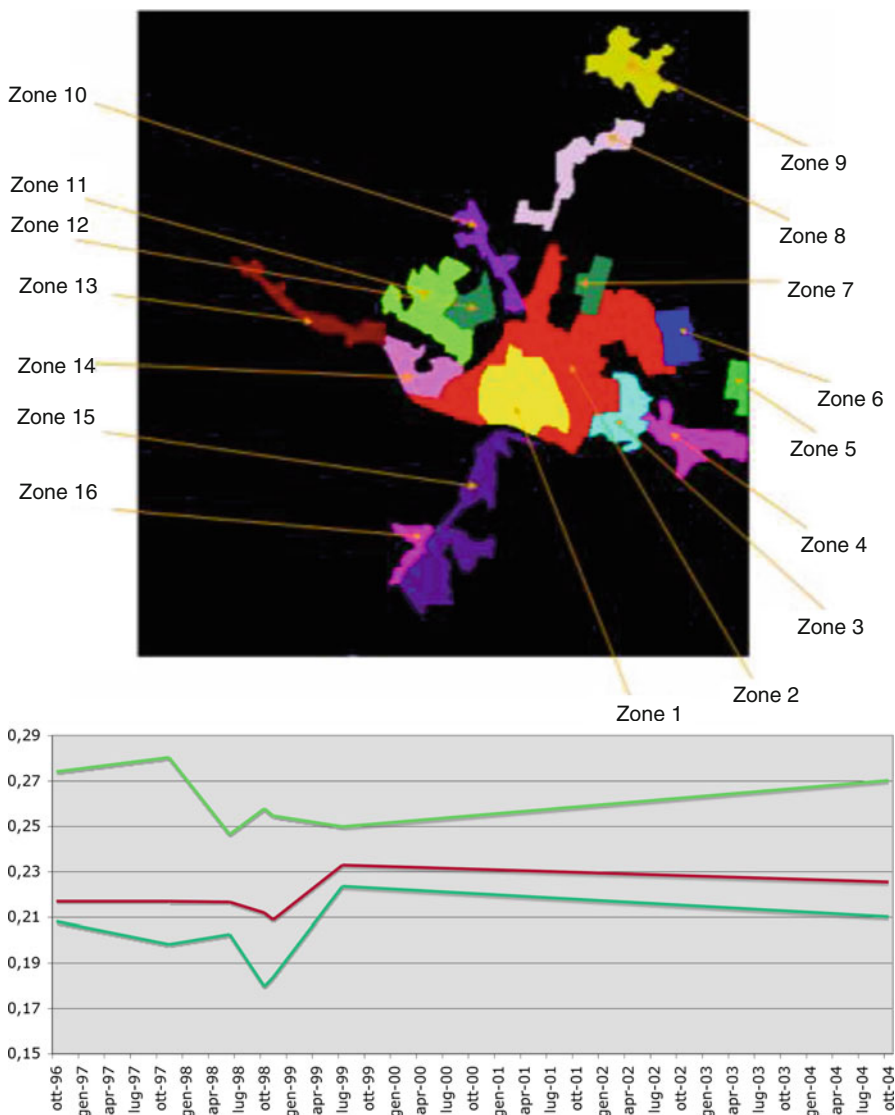


Fig. 3.4 Per-segment analysis of a hypertemporal ERS SAR data sequence for Pavia (Italy), from 1996 to 2004. The different temporal evolution of the mean backscattered value for a few segments depicted in the *bottom* graph reflects the substantially stable situation in the town, with the exception of segment n. 11

Specifically, in this case a sequence of 7 SAR images collected by the ERS-1 and 2 satellites in a time range of 8 years, between 1996 and 2004, is considered. After a precise co-registration, the spatial segmentation of the sequence and thus the per-segment index computation is obtained by considering the above mentioned GIS of the test area. In Fig. 3.4 the different segments are highlighted by different colors, and their temporal pattern is depicted by using the same color, to visually show the match. As for the index, a simple per-segment average of the backscattered value is used as a way to analyze the temporal behavior of each portion of the town. This index strictly related with the presence of strong scattering (double bounce) effects, which in turn are highly correlated in urban areas with buildings and other artificial built-up structures. As clearly visible, the index shows a substantial stability, and no actual change can be detected, apart from the sudden drop in the average value for all segments due to the flooding event in 1998. As for the general trend, it denotes in general a slight decrease, but with the exception of segment 11, whose tendency to increasing values from 1999 on is due to the construction of the new site for the Engineering School of the University.

A different example for this hypertemporal sequence framework is the classification of urban evolution patterns using Landsat data. The idea is that Landsat provides a continuous and interesting monitoring of land use patterns, and can be used to monitor, at the global level, urbanization and its change in time. Besides the variability in different geographical areas, here we focus on the possibility to extract different time behaviors, discriminating areas that, for instance, became urbanized at different dates. The results shown in the following are obtained therefore by means of a processing chain composed **of** the following two steps:

1. urban extent extraction at different dates using the Normalized Difference Spectral Vector (NDSV);
2. unsupervised multitemporal classification of the stack of urban extent maps at different dates to discriminate among different temporal patterns.

The first step follows the approach proposed in Trianni and Angiuli (2013). The NDSV has been proposed as a mean to group existing normalized different indexes (such as the normalized difference vegetation index – NDVI, the normalized difference water index – NDWI, and the normalized difference Built-up index – NDBI). The idea is to include in one single vector all the possible normalized indexes that can be computed starting from a Landsat 5 or 7 image, considering therefore 6 bands and 15 possible combinations (the dual ones are not considered as their result is the same with opposite sign). As a result, each pixel is characterized by a set of values that have been at this point “labeled” only partially, and whose full potential is still to be explored. By looking at a standard calibrated Landsat scene, it can be demonstrated that urban areas exhibit a NDSV spectral signature that is basically “flat” across all indexes, and can be discriminated from other classes by

their distinct behavior in this new “multispectral” 15-dimensional space. The NDSV can be therefore well exploited to extract human settlement extents, by applying a classifier such as the Spectral Angle Mapper classifier in the original version, that captures the differences in multispectral vectors and is robust with respect to difference in illumination. Due to the unavailability of this classifier in the analysis framework that was used for the implementation, and according to our experience, we considered instead, with very similar results, a Classification and Regression Trees (CART) supervised procedure.

The second step instead exploits a very basic K-means or ISODATA unsupervised classifier. The input of the classifier is the multi-temporal stack of human settlement extents extracted from the previous step, and thus a set of binary (urban/non-urban) images where each pixel reflects the pattern of urbanization in the corresponding scene portion. To avoid or at least reduce as much as possible errors in classification, the training set of the previously described NDSV classification procedure are selected by jointly considering the first and the last images in the stack, to ensure a selection of areas that belong to the same land use along the whole sequence. Moreover, since misclassifications are expected, the assumption that urban areas tend to become bigger and do not shrink is considered. Although not completely accurate in time, for the time period considered by our satellite archives, corresponding to one of the biggest push into urbanization of the human history, this is a quite reasonable assumption. In terms of our algorithms, it translates into a set of masking operation implemented on the time sequence of extracted human settlement extents maps in reverse order. In other words, the extents at one date are constrained by those obtained at a later date and cannot extend beyond them.

The overall chain is implemented in Google Earth Engine (2013), which provides a powerful and very flexible platform to analyze multiple remote sensing data sets, including the whole collection of NASA/USGS Landsat imagery, by being able to run processing steps on Google’s dedicated cloud storage and computational hardware.

Results for the city of São Paulo by means of the implemented version of the above mentioned algorithm are proposed in Fig. 3.5, and correspond to a sequence of 36 Landsat-5 images from 1992 to 2010, selected every other year with the criterion of a cloud cover of less than 1% of the scene, and combined into yearly composites. Note that the area in purple in the final multi-temporal classification corresponds to the core part of the city, which did not change during the time period of this analysis, while the other shades, from purple to blue, highlight different time behaviors. Specifically, the areas in the center of São Paulo show changes in the typology of built-up elements, that in turn show up as different colored patterns in the hypertemporal combined map.

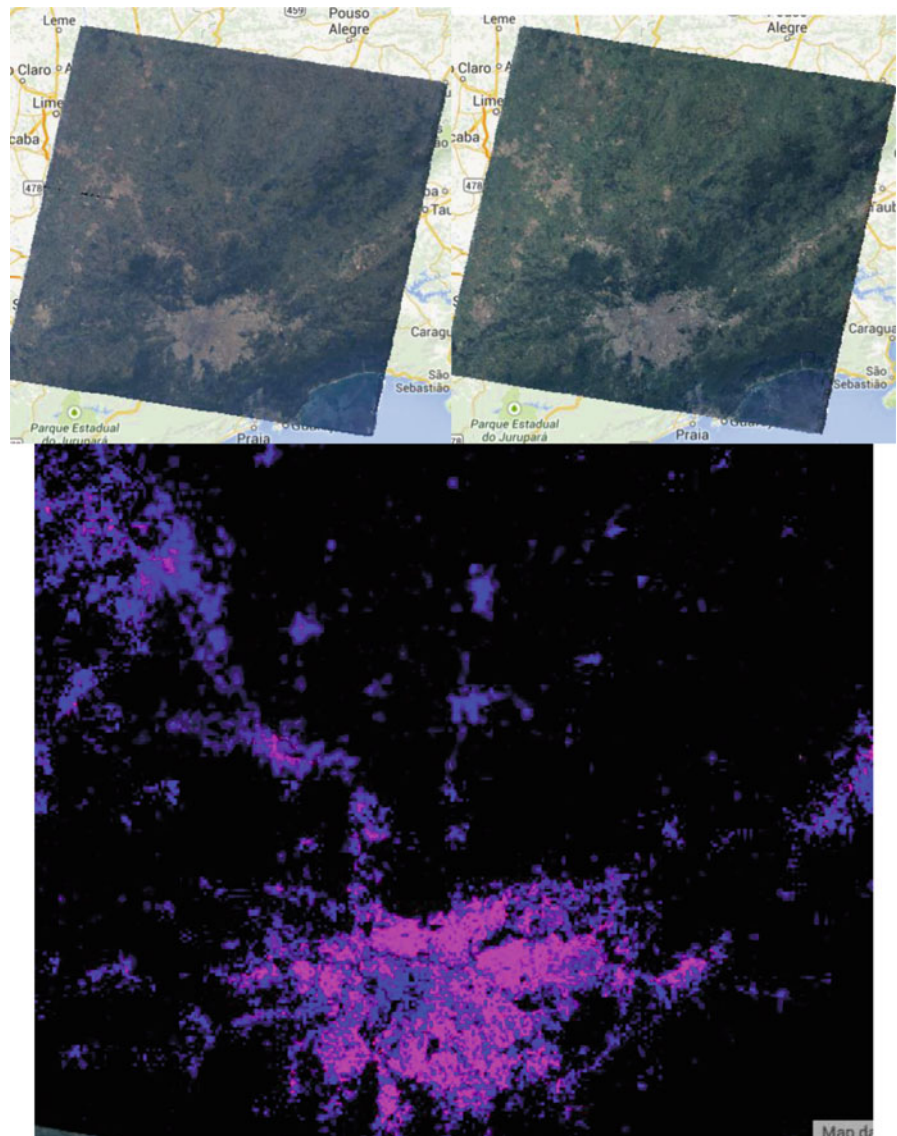


Fig. 3.5 Analysis of a hypertemporal sequence of Landsat data for the city of São Paulo (Brazil), from 1992 (left top image) to 2010 (right top image). The different temporal patterns for the urbanization obtained from a stack of 36 images are shown with different colors in the bottom map (see the text for a more detailed explanation and analysis)

3.5 Conclusions

The techniques and examples presented in this chapter may be summarized, according to the authors' vision, in the following points:

- Spatial and temporal scales are, in general, equally important in urban area monitoring. Although this statement is somehow a trivial one, it is still not always considered. Examples may be studies working on damage extraction using image with a wrong spatial/temporal sampling, or change detection approaches not matching the temporal scale of the event.
- In this sense, a second important point is that the selection of relevant scales is problem-dependent. This is a less trivial sentence, and data processing algorithms should consider it as well. A "change detection" technique not always fits the temporal change, although it may fit the same data for a different detection problem. An example is urban sprawl monitoring using SAR coherence, which makes sense because of the long time span of this change, while the same approach applied to urban hotspots would not work and would require additional steps like a dedicated spatial filtering routine.
- A definitely more interesting outcome of the researches discussed in this chapter is that the combined use of relevant spatial and temporal scales in urban areas is a feature-dependent (object-dependent) problem. According to the application, different features/objects are affected by the change to be detected, and the selection of the target object includes a priority on the spatial and temporal scale to be considered.
- The most important challenge to be met by using EO data in urban area to capture their changes and monitor at different scales their evolution is thus that they do not capture enough scales to be useful by themselves. The most important aspect is that some a priori or associated information is required, and some sort of fusion at the information or decision level is required. For instance, damage mapping at the block level proved (Dell'Acqua and Polli 2011) to be more effective when information about where damaged areas may happen is included at the global city scale, usually obtained by running vulnerability/exposure models of the area.

References

- Almeida CM, Batty M, Vieira Monteiro AM, Camara G, Silveira Soares-Filho B, Coutinho Cerqueira G, Lopes Pennachin C (2003) Stochastic cellular automata modeling of urban land use dynamics: empirical development and estimation. *Comput Environ Urban Syst* 27:481–509
- Bruzzone L, Fernandez Prieto D (2000a) Automatic analysis of the difference image for unsupervised change detection. *IEEE Trans Geosci Remote Sens* 38(3):1171–1182
- Bruzzone L, Fernandez Prieto D (2000b) A minimum-cost thresholding technique for unsupervised change detection. *Int J Remote Sens* 21(18):3539–3544
- Bruzzone L, Fernandez Prieto D (2000c) An adaptive parcel-based technique for unsupervised change detection. *Int J Remote Sens* 21:817–822

- Bruzzone L, Fernandez Prieto D (2002) An adaptive semi-parametric and context based approach to unsupervised change detection in multitemporal remote-sensing images. *IEEE Trans Image Process* 11(4):452–466
- Bruzzone L, Serpico SB (1997) Detection of changes in remotely sensed images by the selective use of multi-spectral information. *Int J Remote Sens* 18:3883–3888
- Carlotto MJ (1997) Detection and analysis of change in remotely-sensed imagery with application to wide area surveillance. *IEEE Trans Image Process* 6(1):189–202
- Clapham WB Jr (2003) Continuum-based classification of remotely sensed imagery to describe urban sprawl on a watershed scale. *Remote Sens Environ* 86:322–340
- Dell'Acqua F, Gamba P (2012) Remote sensing and earthquake damage assessment: experiences, limits and perspectives. *Proc IEEE* 100(10):2876–2890
- Dell'Acqua F, Polli DA (2011) Post-event only VHR radar satellite data for automated damage assessment: a study on COSMO/SkyMed and the 2010 Haiti earthquake. *Photogramm Eng Remote Sens* 77:1037–1043
- Gamba P, Trianni G, Lisini G (2008) Hypertemporal SAR sequences for monitoring land cover dynamics. In: Proceedings of 2008 IEEE Radar conference, Rome, 25–29 May 2008, pp 1416–1420
- Gamba P, Aldrighi M, Stasolla M (2011) Robust extraction of urban area extents in HR and VHR SAR images. *IEEE J Sel Top Appl Earth Obs Remote Sens* 4(1):27–34
- Google Earth Engine (2013) <http://earthengine.google.org>. Accessed 15 Feb 2014
- Grey WMF, Luckman AJ, Holland D (2003) Mapping urban change in the UK using satellite radar Interferometry. *Remote Sens Environ* 87:16–22
- Haralick R, Shanmugam K, Dinstein I (1973) Textural features for image classification. *IEEE Trans Syst Man Cybern* 3:610–621
- Hazel GG (2001) Object-level change detection in spectral imagery. *IEEE Trans Geosci Remote Sens* 39(3):553–561
- Janssen LLF, Molenaar M (1995) Terrain objects, their dynamics and their monitoring by the integration of GIS and remote sensing. *IEEE Trans Geosci Remote Sens* 33(33):749–758
- Johnson RD, Kasischke ES (1998) Change vector analysis: a technique for the multi-spectral monitoring of land cover and condition. *Int J Remote Sens* 19(3):411–426
- Kasetkasem T, Varshney PK (2002) An image change detection algorithm based on Markov random field models. *IEEE Trans Geosci Remote Sens* 40(8):1815–1823
- Li X, Yeh AGO (1998) Principal component analysis of stacked multi-temporal images for the monitoring of rapid urban expansion in the Pearl River Delta. *Int J Remote Sens* 19(8): 1501–1518
- Madhavan B, Kubo S, Kurisaki N, Sivakumar TVLN (2001) Appraising the anatomy and spatial growth of the Bangkok Metropolitan area using a vegetation-impermeable-soil model through remote sensing. *Int J Remote Sens* 22(5):789–806
- Masek JG, Lindsay FE, Goward SN (2000) Dynamics of urban growth in the Washington DC metropolitan area, 1973–1996, from Landsat observations. *Int J Remote Sens* 21(18): 3473–3486
- Prol-Ledesma MR, Uribe-Alcantara M, Diaz-Molina O (2002) Use of cartographic data and Landsat TM images to determine land use change in the vicinity of Mexico City. *Int J Remote Sens* 23(9):1927–1933
- Quegan S, Yu JJ (2001) Filtering of multichannel SAR images. *IEEE Trans Geosci Remote Sens* 39:2373–2379
- Rignot EJM, van Zyl JJ (1993) Change detection techniques for ERS-1 SAR data. *IEEE Trans Geosci Remote Sens* 31(4):896–906
- Seto KC, Woodcock CE, Song C (2002) Monitoring land-use change in the Pearl River Delta using Landsat TM. *Int J Remote Sens* 23(10):1985–2004
- Smith GM, Fuller RM (2001) An integrated approach to land cover classification: an example in the Island of Jersey. *Int J Remote Sens* 22(16):3123–3142
- Smits PC, Annoni A (1999) Updating land-cover maps by using texture information from very high-resolution Space-Borne imagery. *IEEE Trans Geosci Remote Sens* 37(3):1244–1254

- Smits PC, Annoni A (2000) Toward specification-driven change detection'. *IEEE Trans Geosci Remote Sens* 38(3):1484–1488
- Smits PC, Meyer W (2000) Echelon approach to characterize and understand spatial structures of change in multi-temporal remote sensing imagery. *IEEE Trans Geosci Remote Sens* 38(5):2299–2309
- Sokal RR, Thomson BA (2006) Population structure inferred by local spatial autocorrelation: an example from an Amerindian tribal population. *Am J Phys Anthropol* 129:121–131
- Sunar F (1998) An analysis of changes in a multi-date data set: a case study in the Ikitelli area, Istanbul, Turkey. *Int J Remote Sens* 19(2):225–235
- Trianni G, Angiuli E (2013) Urban mapping in Landsat images based on normalized difference spectral vector. *IEEE Geosci Remote Sens Lett* 11(3):661–665
- Xia L, Yeh AG (2000) Modelling sustainable urban development by the integration of constrained cellular automata and GIS. *Int J Geogr Inf Sci* 14:131–152
- Xiuwan C (2002) Using remote sensing and GIS to analyse land cover change and its impacts on regional sustainable development. *Int J Remote Sens* 23(1):107–124
- Yang X, Lo CP (2002) Using a time series of satellite imagery to detect land use and land cover changes in the Atlanta, Georgia metropolitan area. *Int J Remote Sens* 23(9):1775–1798
- Zha J, Gao J, Ni S (2003) Use of normalized difference built-up index in automatically mapping urban area from TM imagery. *Int J Remote Sens* 24(3):583–594
- Zhang Y (2001) Detection of urban housing development by fusing multisensor satellite data and performing spatial feature post-classification. *Int J Remote Sens* 22(17):3339–3355

Chapter 4

Change Detection in Multitemporal Hyperspectral Images

Lorenzo Bruzzone, Sicong Liu, Francesca Bovolo, and Peijun Du

Abstract Multitemporal hyperspectral images provide very detailed spectral information that directly relates to land surface composition. This results in the potential detection of more spectral changes than those visible in the traditional multispectral images. However, the process of extracting changes from hyperspectral images is very complex. This chapter addresses the multiple-change detection problem in multitemporal hyperspectral remote sensing images by analyzing the complexity of this task. An analysis of the concept of “change” is given from the perspective of pixel spectral behaviors, in order to formalize the considered problem. A hierarchical change-detection approach is presented, which aims to identify the possible changes occurred between a pair of hyperspectral images. Changes having discriminable spectral behaviors in hyperspectral images are identified hierarchically by following a top-down structure in an unsupervised way. Experimental results obtained on simulated and real bi-temporal images confirm the validity of the proposed hierarchical change detection approach.

Parts of contents in this chapter are taken from: S. Liu, L. Bruzzone, F. Bovolo and P. Du, “Hierarchical change detection in multitemporal hyperspectral images,” *Geoscience and Remote Sensing, IEEE Transactions on*, vol.53, no.1, pp:244–260, 2015.

L. Bruzzone (✉) • S. Liu

Department of Information Engineering and Computer Science, University of Trento, Via Sommarive 5, Povo, 38123 Trento, Italy

e-mail: lorenzo.bruzzone@unitn.it; sicongliu.rs@gmail.com

F. Bovolo

Center for Information and Communication Technology, Fondazione Bruno Kessler, Via Sommarive 18, Povo, 38123 Trento, Italy

e-mail: bovolo@fbk.eu

P. Du

Department of Geographical Information Science, Nanjing University, Nanjing, China
e-mail: dupjrs@126.com

4.1 Introduction

Global change is a big challenge for the whole human society in the twenty-first century. Accordingly, how to effectively monitor and comprehensively understand the changes is important for the sustainable development of human society. As one of the interesting topics in global change study, detection of anthropogenic and natural impacts on land surface is essential. To enable a whole monitoring and evaluation of changes occurred on the ground, both long term and short term observations are required. The conventional monitoring approach is mainly conducted by field investigation, which is usually time costly and labour expensive. Due to the revisit property of polar Earth Observation (EO) satellites, remote sensing images can be regularly acquired in a given geographical area at different times. Therefore, multitemporal remote sensing images become an important data source to detect the land surface changes in wide geographical areas, representing an effective alternative to the conventional field investigation.

For an effective exploitation of multitemporal remote sensing images, Change Detection (CD) techniques are required that automatically discover and detect the changes occurred between two (or more) images (Bruzzone and Bovolo 2013). Automatic CD techniques have been widely used in various remote sensing applications (e.g., ecosystem monitoring, urban area study, disaster monitoring) (Coppin and Bauer 1996; Ridd and Liu 1998; Marin et al. 2014). However, most of the available CD methods are designed for the analysis of multitemporal images acquired by multispectral (MS) remote sensing sensors (Coppin and Bauer 1996; Ridd and Liu 1998; Du et al. 2012a; Singh 1989). With the launch of a new generation of hyperspectral (HS) sensors onboard of satellites (e.g., PRISMA, HISUI, ENMAP), in the future, satellite multitemporal HS images are expected to become more available for CD. Differently from the traditional MS sensors, HS sensors measure the solar reflected radiation in a wide wavelength spectrum (e.g., 400–2500 nm), but at narrow spectral intervals (e.g., 10 nm). For a given pixel on the HS image, a near-continuous spectral signature can be obtained over the whole range of wavelengths. Therefore, HS images can point out very small variations in their spectral signature along the temporal direction. Thus makes it possible to identify changes that are usually not detectable with MS data. However, those latent variations are often hidden inside strong changes and highly mixed with each other. Thus available CD methods fail in detecting and separating them. This makes the change analysis more complex and challenging, especially when ground truth data are not available (i.e., unsupervised approaches should be employed). Therefore, it is important and necessary to define novel CD techniques capable to exploit the intrinsic properties of HS images and to meet the requirements of practical CD applications.

After an overview about CD methods developed for HS images, in this chapter we focus the attention on methods that exploit the difference image. The difference image (computed by subtracting pixel by pixel in spectral channels) carries multiple change information. Thus the behavior of spectral signatures in the hyperspectral

difference domain results in a fine modeling of different kinds of changes, which is not possible with MS images. To better understand this concept let us consider an example. Let us consider a vegetated field affected by land-cover changes. On the one hand, MS images can highlight strong changes, which are class transitions that significantly affect the spectral signature (e.g., vegetation to land covers like water, built-up areas, soil). However within such strong changes, other changes may be observed that correspond to slightly different realizations of the strong change itself. In a given vegetation change class there might be more change contributions due to different factors (e.g., difference on the vegetation growth status, density, water content). These kinds of changes show small spectral differences with respect to those of the strong change they are associated with. Such differences are usually localized in specific parts of the spectrum, which are difficult to be recognized from the rough spectral representation typical of MS images. On the other hand, these subtle changes become detectable in HS images due to the detailed representation of the spectral signatures. Moreover, if calibrated data are available, it is possible to obtain the explicit semantic meaning of the class transition (“from-to”) for a change by matching the spectral signature of each single date with the standard reference spectra in spectral libraries. However, in the reality, reference samples are often not available. Therefore, the design of effective unsupervised CD methods that are independent from ground truth data availability is highly attractive in real applications.

In this chapter, we analyze and define the concept of “change” in HS images from the spectral signature point of view. Then a hierarchical unsupervised CD approach is present that is suitable to identify different kinds of changes between two HS images (Liu et al. 2015). The developed CD method: (1) addresses the problem of multiple-change detection; (2) makes adequate use of the detailed spectral information in HS data; and (3) is unsupervised.

The outline of this chapter is as follows. Section 4.2 gives an overview of CD techniques presented in the literatures for both MS and HS images. Moreover, it addresses and formalizes the concept of changes in the HS case. The proposed CD method based on the hierarchical clustering is described in Sect. 4.3. Experimental results on the different data sets are shown in Sect. 4.4. Finally, Sect. 4.5 draws the conclusion.

4.2 Change Detection in Hyperspectral Images

4.2.1 *Overview of CD Techniques*

For decades, many CD techniques have been proposed for addressing the CD problem (Bruzzone and Bovolo 2013; Coppin and Bauer 1996; Ridd and Liu 1998; Du et al. 2012a; Lu et al. 2004; Radke et al. 2005). From the application purpose, these techniques can be divided into those for binary and for multiple change

detection. Binary CD methods consider only the presence/absence of change, ignoring the possible different class transitions. Thus all kinds of changes present on the ground are considered as a single general change class. For multiple change detection, the aim is not only to detect the changes, but also to identify different kinds of changes among each other. From the methodological point of view, the CD techniques can be clustered into two main groups: supervised and unsupervised. Supervised CD methods are based on supervised classification schemes having the available prior knowledge for training a classifier. This is the case of post-classification comparison (PCC) (Castellana et al. 2007), joint-classification of multi-date images (Soares and Hoffer 1994), compound classification (Bruzzone and Serpico 1997), classification of differential features (Nemmour and Chibani 2006) and sub-pixel level change identification (Du et al. 2014). Some other methods are designed based on partially unsupervised (Bruzzone and Cossu 2002) or semisupervised learning (Demir et al. 2012). Note that such supervised CD methods were mainly developed for MS images but are applicable to HS images as well. However, when dealing with HS data, more attention should be devoted to define effective classification systems that: (i) are suitable to the analysis of high-dimensional data and overcome the Huges phenomenon (i.e., with a fixed number of training samples, the predictive power of a classifier reduces as the dimensionality increases) (Hughes 1968), and (ii) can effectively exploit informative features thus enhancing change detectability. Although supervised CD methods generally outperform the unsupervised ones in detecting land-cover transitions, the process of collecting reference data for multitemporal images is always time costly and often unfeasible. Thus unsupervised methods are more attractive from the real application point of view.

For the unsupervised category, several methods have been proposed for binary CD (Bruzzone and Serpico 1997; Bruzzone and Prieto 2000a; Bruzzone and Prieto 2000b; Celik 2010; Du et al. 2012b; Du et al. 2013; Hégarat-Mascle and Seltz 2004; Ghosh et al. 2011). From the methodological point of view, they can be categorized into thresholding-based and clustering-based techniques. In (Bruzzone and Prieto 2000b), the problem of binary CD was solved automatically by modeling the statistical distribution of classes and incorporating spatial-context information, thus significantly improved the previous works that are mainly based on manual thresholding (Bruzzone and Serpico 1997; Bruzzone and Prieto 2000a). Some other techniques were designed to improve the CD performance by using optimized computation algorithms (Celik 2010), ensemble learning schemes (Du et al. 2012b), data fusion approaches (Du et al. 2013) and multi-feature strategies (Hégarat-Mascle and Seltz 2004). Clustering algorithms have been used for solving the same binary CD problem as well (Ghosh et al. 2011). However, a more challenging goal is to distinguish among multiple changes. Some attempts based on transformation, multivariate analysis, etc., have been done to address this kind of problems in (Canty and Nielsen 2006a; Canty and Nielsen 2006b). A simple yet effective method named Compressed Change Vector Analysis (C^2VA) was recently proposed in (Bovolo et al. 2012), which was developed based on the polar Change Vector Analysis (CVA) approach (Bovolo and Bruzzone 2007). In C^2VA the considered multiple-

change detection problem is represented in a magnitude-direction 2-D domain generated by a lossy compression (potentially ambiguous) procedure. Thus both the change detection and change separation can be easily implemented within the 2-D domain, without relying on any band selection which might result in loss of change information. C²VA has proved to be effective in different CD applications with MS images (Bruzzone and Bovolo 2013; Bovolo et al. 2012). However, the problem becomes more complex and challenging (and the efficiency of these methods is reduced) when HS images are considered. This is mainly due to the ambiguity that generated when compressing a high dimensional feature space into only two components, and also to the potentially critical situation when too many changes are present.

The relatively few works present in the literature on the topic of CD in HS images are based on: (1) transformation methods (Schaum and Stocker 2004; Schaum and Stocker 1998; Nielsen 2007; Ortiz-Rivera et al. 2006; Liu et al. 2012); (2) spectrum analysis methods (Adar et al. 2011; Du et al. 2004, 2005, 2007; Vongsy and Mendenhall 2011), and (3) other techniques (Meola et al. 2007, 2011; Vongsy et al. 2012; Eismann et al. 2008). Covariance equalization and cross covariance (chronochrome) are two commonly used linear transformation algorithms (Schaum and Stocker 1998, 2004). They identify changes in the transformed space by subtracting feature vectors. Another type of transform-based methods represent the images in a new transformed feature space, where the change information is concentrated into fewer components, thus reducing the data dimensionality and noise, and focusing on the components that are related to the specific changes of interest. Multivariate Alteration Detection (MAD) method, which is based on the Canonical Correlation Analysis (CCA), was first introduced in (Frank and Carty 2003) to solve vegetation CD problems by using multitemporal HS images in an unsupervised way. Then it was extended to an iterative reweighted procedure (IR-MAD) in (Nielsen 2007). Other attempts like Temporal-PCA (TPCA) and Independent Component Analysis (ICA) can be found in (Ortiz-Rivera et al. 2006; Liu et al. 2012). After a given transformation, one (or several) component(s) can be selected for change identification. The spectrum analysis based CD methods take advantage of the detailed spectral signature in HS images. On the one hand, the distance and similarity measurements can be used to detect the difference between the considered pixel spectral signatures at two times [e.g., Spectral Angle Measure (SAM), Spectral Information Divergence (SID) and Spectral Correlation Measure (SCM) (Adar et al. 2011; Du et al. 2004; Vongsy and Mendenhall 2011)]. On the other hand, spectral analysis can be done by using linear unmixing techniques (Du et al. 2005), change vector analysis after radiometric normalization (Du et al. 2007). Other works have been also developed to explore the CD problem from different perspectives: model-based methods by formulating the CD as a statistical hypothesis test (Meola et al. 2011); CD based on tensor-factorization and PCA (Du 2012). Moreover, there are some other works focusing on the external factors that affect the CD performance, which include limiting image parallax errors (Vongsy et al. 2012), studying vegetation and illumination variation (Meola et al. 2007), and addressing diurnal and seasonal variations (Eismann et al. 2008). These factors may introduce

errors into the CD process and thus decrease the detection accuracy, which should be limited as much as possible in real applications.

4.2.2 Challenges for CD in HS Images

Due to the intrinsic properties of HS images, the CD problem is more challenging than that in MS images. The main challenges are from both the data and the CD techniques. From the data itself the challenges are as follows:

- (a) High dimensionality. It involves challenges in data handling, including storage volume and computing bottle necks, which are actually common problems for all HS data processing tasks (i.e., classification, change detection, target recognition). For CD task, the main difficulty is to effectively extract changes from a high dimensionality feature space. Methods developed for MS images, like CVA or C²VA (Bovolo et al. 2012; Bovolo and Bruzzone 2007), may fail to give a proper change representation after compression of a high dimensional data, thus decrease the CD accuracy.
- (b) Redundant information. Indeed, the spectral information of the adjacent bands in HS images results in a non-negligible redundancy. Moreover, a reduction of the signal-to-noise ratio (SNR) of the spectral signal is obtained when the spectral resolution increases (Dalponte et al. 2009). Thus information in a single HS band becomes more sparse and implicit, which may reduce the discriminability of a detector.
- (c) Accurate data pre-processing. An accurate pre-processing phase (e.g., radiometric correction, image co-registration) is required for CD in HS images, which may significantly affect the final CD accuracy.

Other problems and challenges arise from the methodological point of view. We can observe that:

- (i) Most of the existing unsupervised CD methods directly compare and analyze the difference of pixel radiance values, ignoring the rich near-continuous spectrum information that is the peculiar property of HS data. The high-dimensionality and redundant information in HS data makes the changes more implicit and difficult to be identified: changes become more mixed and less separable. Thus the identification of the number of changes and their discrimination boundaries become a critical problem.
- (ii) Most of CD approaches present in the literature for HS images focus on either binary CD (Vongsy and Mendenhall 2011; Du et al. 2005) or the detection of specific changes [e.g., (Nielsen 2007; Liu et al. 2012; Du et al. 2007; Frank and Carty 2003; Du 2012)]. Still there is less method that addresses the challenging problem of detecting multiple changes simultaneously (which can be very important especially when unexpected changes occur on the ground). Moreover, some methods still rely solely on change magnitude information

(Nielsen 2007; Liu et al. 2012; Frank and Canty 2003), neglecting the direction information (and thus the whole spectrum information) for discriminating different changes.

- (iii) Although the transformation-based methods (e.g., MAD, IR-MAD, TPCA) allow us to detect multiple changes (Canty and Nielsen 2006b; Ortiz-Rivera et al. 2006; Frank and Canty 2003), the application of transformation to high-dimensionality data results in a high computation cost, in a difficult interpretation of all components and in a qualitative and ambiguous description of change classes, especially for subtle changes.
- (iv) Definition and description of the detected changes are still rough. Although the unsupervised approaches are not capable to provide the “from-to” land-cover transition information, it is necessary to define methods that are able to differentiate the detected changes related to the complex different land-cover transitions.
- (v) The existing methods try to extract all changes directly from the original data space or from a transformed feature space relying only on a single operation (e.g., transformation, differencing), which increases the difficulties of separating multiple change classes and thus affects the detection accuracy.

4.3 Analysis of the Change Concept in Multitemporal HS Images

Our aim is to develop a method that is able to identify all class transitions having discriminable spectral behaviors either globally or locally in the spectrum of multitemporal HS images. These class transitions are defined as *change endmembers*.

First it is important to understand the concept of “change” in multitemporal HS images and its relationship with the concept of endmember. The very high spectral resolution makes it possible to detect many differences in the spectral signatures of pixels acquired in a scene of interest. Note that such differences may occur at different spectral resolution levels or spectral detail scales.

Let us consider two HS images X_1 and X_2 with size $P \times Q$, acquired over the same geographical area at times t_1 and t_2 , respectively. To analyze the behaviors of spectral differences between the two images, the HS difference image X_D is computed by subtracting multitemporal images from each other pixel by pixel (Bovolo et al. 2012).

$$X_D = X_2 - X_1 \quad (4.1)$$

Let x_i be a Spectral Change Vector (SCV) with spatial position i ($i = 1, \dots, P \times Q$) in X_D , $x_i \in X_D$. In such image each pixel is characterized by a SCV that shows as many elements as the spectral channels in the original HS images. Each element assumes values that depend on whether a change occurred or not for a specific

wavelength, and on the kind of change. Therefore, we use SCV signatures that are related to the land-cover class transitions to formalize the considered problem.

Generally speaking, a pixel can belong to the class of changed pixels Ω_c or the one of unchanged pixels ω_n according to its SCV magnitude ρ_i (Bovolo and Bruzzone 2007).

$$\rho_i = \sqrt{\sum_{b=1}^B (x_i^b)^2} \quad (4.2)$$

where B denotes the number of spectral channels of the HS images (i.e., the dimensionality of SCVs), and x_i^b is the b -th spectral difference in x_i . Figure 4.1a shows a qualitative example of the expected behavior of the X_D magnitude. Unchanged pixels show a SCV magnitude close to zero (blue mode in Fig. 4.1a), and their SCV signatures have all spectral components close to 0 (see the blue signature in Fig. 4.1b). Changed pixels have high magnitude values (red mode in Fig. 4.1a), and their SCV signature have one or more components that are far from 0. It is worth noting that in the 1-D magnitude domain usually all changes contribute to a single class Ω_c , and different kinds of change cannot be separated (see Fig. 4.1a). A finer analysis of SCV behaviors points out that Ω_c may include contributions from several change classes (see red and green signatures associated in Fig. 4.1b) depending on how the specific kind of change impacts on the spectral signature. Thus SCVs can be preliminary separated into *major changes*. Major changes mainly depend on the land-cover class transitions and have a large spectral difference with respect to no-change class and among each other. Usually, major changes can be easily and directly identified as they significantly affect a large portion of their SCVs. In many cases they can be also detected from MS images. As shown in Fig. 4.1c, each major change (i.e., ω_{C_1} and ω_{C_2}) produces statistically significant different spectra compared with each other and with the class of ω_n . Within each major change, depending on the data, it is possible to detect other clusters of pixels

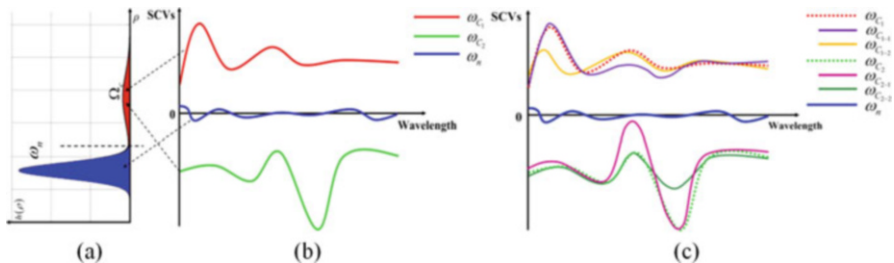


Fig. 4.1 Qualitative illustration of (a) the statistical distribution of the magnitude of SCVs [$h(\rho)$]; the sample spectra on SCVs of major and subtle change classes that defined in multitemporal HS images: (b) major changes; (c) subtle changes (solid line) within the given major changes (dotted line)

having significant statistical differences in some specific parts of the spectrum. Such clusters are defined as *subtle changes*. Subtle changes have SCVs similar to a major change, but differ from it in small portions of the spectrum. In Fig. 4.1c, subtle changes ω_{C_1-1} and ω_{C_1-2} belong to the same major change ω_{C_1} , whereas ω_{C_2-1} and ω_{C_2-2} belong to ω_{C_2} . It happens only if a fine sampling of the spectral signature is available as it is in HS images. If the sampling is poor as in the case of MS images, they cannot be detected.

On the basis of the above discussion $\Omega_c = \{\omega_{C_1}, \omega_{C_2}, \dots\}$ is the set of major changes, i.e., changes that affect a large part of the spectrum and that have statistical properties significantly different from each other. Each major change may include subtle changes (i.e., $\omega_{C_1} = \{\omega_{C_1-1}, \omega_{C_1-2}, \dots\}$ and $\omega_{C_2} = \{\omega_{C_2-1}, \omega_{C_2-2}, \dots\}$) whereas others may not (i.e., $\omega_{C_3} = \emptyset$). By iteratively applying the reasoning to each subtle change it is possible to isolate changes having statistical homogeneity at different spectral resolution. Each major or subtle change that cannot be split anymore is defined as *change endmember*.¹ Accordingly, pixels associated with a specific change endmember have the same (or very similar) spectral behaviors in the SCV domain and thus can be clustered into a same group. Let $\Omega_e = \{e_1, e_2, \dots, e_E\}$ be the set of E possible change endmembers. Let e_n be the endmember associated to no-changed pixels. Thus the problem that we need to address is related to the identification and separation of change endmembers from each other and from unchanged pixels. We assume that the considered images are all radiometrically corrected, thus change endmembers are only related to the application and the end-user. Note that the external factors (e.g., illumination conditions, seasonal effects) might have impacts on the detected change endmembers, but will not be identified as one of them due to its low change magnitude.

4.4 Hierarchical Technique for the Detection of Multiple Changes in Hyperspectral Images

According to the aforementioned discussion and definitions, we illustrate a hierarchical CD method for detecting changes in HS images and separating them into different change endmembers. The method mainly consists of three steps: (i) pseudo-binary change detection to initialize the process and extract general changes Ω_c ; (ii) change endmember detection based on hierarchical spectral change analysis; and (iii) generation of the CD map by merging endmember clusters. The block scheme of the hierarchical CD approach is illustrated in Fig. 4.2.

¹Note that the definition of change endmember is conceptually different from the definition of endmembers in spectral unmixing. In the latter case, endmembers are the spectral signatures of pure classes that result combined in mixed pixels due to the limited spatial resolution of the acquisition sensor.

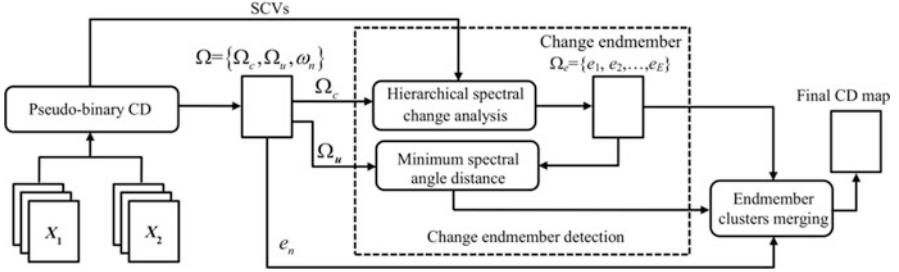


Fig. 4.2 Block scheme of the hierarchical change-detection approach to multitemporal hyperspectral images

4.4.1 Pseudo-Binary Change Detection

This step is based on the analysis of the SCVs magnitude according to traditional binary CD techniques. However it is referred as pseudo-binary because the output has three classes: change (Ω_c), no-change (ω_n) and an uncertainty buffer class (Ω_u), where the class of changes (Ω_c) is used to initialize the hierarchical analysis in the next step. Thus the magnitude ρ is a 1-D feature that compressed from the whole B-D feature space. The rationale behind this choice is: (1) to simplify and avoid any feature selection procedure; (2) to exploit the contribution of all portions of the spectrum. If noisy bands are detected in the pre-processing (e.g., due to atmosphere absorption) they can be neglected.

Changed (Ω_c) and unchanged (ω_n) pixels are separated into two groups according to a threshold value T_ρ computed on the magnitude ρ . Bayesian decision theory is applied to find this threshold (Bruzzone and Prieto 2000b). Expectation Maximization (EM) algorithm is used for estimating the class statistical parameters (i.e., the class prior probabilities, the mean values and variances) in an unsupervised way (Bruzzone and Prieto 2000b). Note that Ω_c and ω_n classes are assumed to be Gaussian distributed, as widely done in binary CD with MS images. This demonstrated to be a good approximation also for HS images (Bruzzone and Bovolo 2013; Bovolo et al. 2012; Bovolo and Bruzzone 2007). The approximation is acceptable as this is only a preliminary step.

In order to reduce the possible thresholding errors and obtain conservative results that do not propagate significant errors in the next steps, a margin δ is set on the threshold T_ρ computed on the histogram $h(\rho)$ of the magnitude ρ (see Fig. 4.3) and three classes are defined: (1) *class of uncertain pixels* (Ω_u), on which it is not possible to take a reliable decision at this level of the processing. These pixels will be analyzed and reclassified according to the generated endmembers; (2) *class of changed pixels* (Ω_c), which includes pixels having a high probability to be changed, but without any information on their kind. The problem of the multiple changes identification will be addressed in the next step by the developed hierarchical method; (3) *class of no-changed pixels* (ω_n), which only contains pixels having a

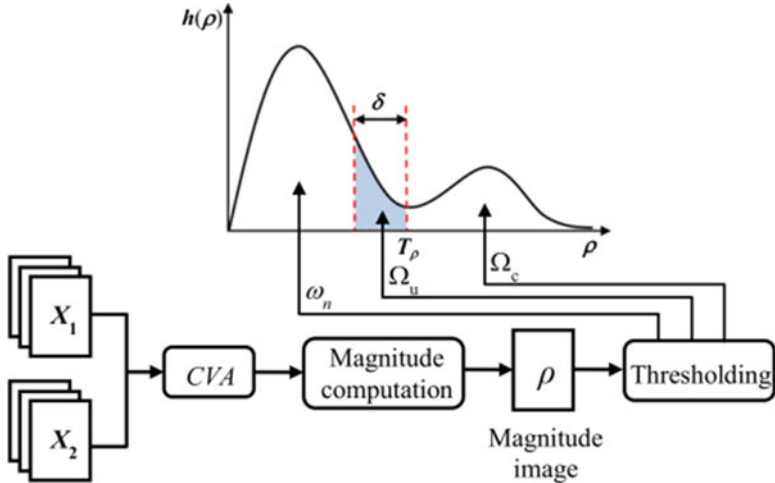


Fig. 4.3 Block scheme of the pseudo-binary CD step used for initializing the tree structure

high probability to be unchanged. These pixels are treated as a pure no-change class endmember due to their low magnitude. Thus for a given SCV x_i in X_D , a label is assigned according to the following rule:

$$x_i \in \begin{cases} \Omega_c, & \text{if } \rho_i \geq T_\rho \\ \Omega_u, & \text{if } T_\rho - \delta \leq \rho_i < T_\rho \\ \omega_n, & \text{if } \rho_i < T_\rho - \delta \end{cases} \quad (4.3)$$

where ρ_i is the SCV magnitude of the considered x_i . Figure 4.3 illustrates the flowchart of the pseudo-binary CD step.

4.4.2 Hierarchical Spectral Change Vector Analysis (HSCVA)

In this step, we focus on the classes of changed (i.e., Ω_c) and uncertain (i.e., Ω_u) pixels obtained in the previous step in order to identify the change endmembers. The problem can be addressed by automatically clustering different change classes. However, the problem of multiple-class separation in HS images is much more difficult than in MS images. This is due to the following issues: (1) the high spectral resolution makes the spectrum more sensitive to changes, thus a high number of changes might be detected; and (2) subtle changes within major changes are always difficult to be identified directly from Ω_c . These problems decrease the detectability of all the hierarchy of changes directly from the data in one shot, and limit the effectiveness of clustering methods.

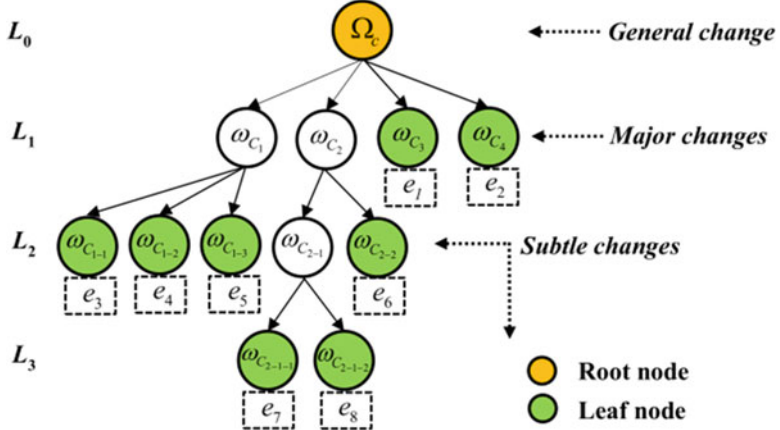


Fig. 4.4 Example of the hierarchical tree for the detection of change endmembers with tree depth $D = 4$ and identified leaves ($K = 8$)

To overcome these problems, the idea of *Hierarchical Spectral Change Vector Analysis* (HSCVA) is employed (see Fig. 4.4 for a qualitative example of hierarchy). The hierarchical structure is modeled by a tree of changes defined to drive the analysis. Let L_d be a generic level in the tree structure with $d = 0, 1, \dots, D-1$. The depth of the tree is D (e.g., $D = 4$ in Fig. 4.4). The main idea is to start from the root node in the top level (i.e., L_0) that represents the general change class Ω_c identified in the pseudo-binary CD step) and gradually separate different kinds of change into child nodes by selectively exploiting the spectral information. At the first level (i.e., L_1) of the hierarchy the priority is given to identify the major changes that have significant spectral difference among each other. Within each child node, subtle changes (if any) are detected and separated. This process is iterated until all change endmembers (i.e., leaf nodes of the tree) are found.

Let us consider Ω_c in the root node. To model the spectral homogeneity of all the considered changed pixels in Ω_c , a similarity measure based on the Spectral Angle Distance (SAD) (Plaza et al. 2004) is used. The SAD ϑ is computed between each x_i in Ω_c , and a reference spectral signature S_{Ω_c} calculated as the average of all the x_i in Ω_c , i.e.,

$$\vartheta(x_i, S_{\Omega_c}) = \arccos \left(\frac{\sum_{b=1}^B x_i^b S_{\Omega_c}^b}{\sqrt{\sum_{b=1}^B (x_i^b)^2} \sqrt{\sum_{b=1}^B (S_{\Omega_c}^b)^2}} \right), \quad x_i \in \Omega_c \quad (4.4)$$

x_i^b and $S_{\Omega_c}^b$ are the b -th component in \mathbf{x}_i and S_{Ω_c} , respectively. For each \mathbf{x}_i , the smaller $\vartheta(x_i, S_{\Omega_c})$, the higher the similarity with the reference spectrum and vice versa. For a pure change endmember we expect that all SCVs have very similar spectral behaviors, thus resulting in a small standard deviation of the similarity measure. Thus to verify the homogeneity of Ω_c we compare the standard deviation value $\sigma_{\vartheta_{\Omega_c}}$ of $\vartheta(x_i, S_{\Omega_c})$ with a threshold value T_σ . If $\sigma_{\vartheta_{\Omega_c}}$ is smaller than T_σ , the change class is considered to be homogeneous and a change endmember is detected. In this case, the process will be in convergence and the tree only has a single node. Otherwise the change class is considered as inhomogeneous and likely to contain more kind of changes. Therefore the hierarchical decomposition starts.

To distinguish major changes in Ω_c , Principal Component Analysis (PCA) and clustering algorithm are used. Any other transformation technique can be considered as well. Note that PCA is applied only to the \mathbf{x}_i belonging to Ω_c . Thus we optimize the representation of the changes. Then the clustering algorithm is applied to the subset of transformed Principal Components (PCs) that includes more than 95 % of change information to reject the noise and redundant information. This choice also reduces the computational complexity. Let \mathbf{P} be the image with selected M ($M < B$) PCs and let \mathbf{P}_i be the vector characterizing spatial position i ($i = 1, \dots, P \times Q$) in \mathbf{P} , $\mathbf{P}_i \in \mathbf{P}$. An effective clustering technique should be used to correctly identify the major change classes inside Ω_c , addressing the following two issues: (1) identification of the number of major changes; (2) modeling and clustering the multiple change information.

To this end, the adaptive x -means algorithm is used to automatically find an optimal number of major changes and generate reliable clustering results in an unsupervised framework (Pelleg and Moore 2000; Ishioka 2005). Differently from the popular k -means method, x -means adaptively searches on a range of k values and aims to find the best clustering model according to the Bayesian Information Criterion (BIC) (Pelleg and Moore 2000). BIC identifies an adequate tradeoff between simplicity of the model (number of parameters) and quality of fit. It analyzes the maximum likelihood-based models of a given data distribution. We adopt the algorithm proposed in (Ishioka 2005), which is an expansion of the original x -means, and modified it in order to satisfy our requirements. A given range $U = [k_0, k_0 + t]$ is first defined to initialize the x -means. This is the only input parameter to the algorithm. k_0 denotes the lower bound for the number of major changes k , and t is a constant value to control the upper bound. Then M -dimensional PCs of Ω_c are given as input to the x -means clustering and the method is initialized by applying k -means with $k = k_0$. We assume that all kinds of change approximately follow the Gaussian distribution. The BIC value of each generated cluster is then compared with the joint BIC value of its split into two clusters, and the clusters associated with the smaller value are selected (the smaller BIC value the better the fitting) (Pelleg and Moore 2000). An additional merging operation is applied if necessary to ensure that the final output number of clusters is within the defined range U (Ishioka 2005). After applying the x -means clustering, the final output includes: (1) the optimal number k of major changes; (2) the detected major

changes in Ω_c (i.e., the level L_1 of the hierarchical tree structure). Note that BIC is just one of the choices for the model selection. However, it is a reliable criterion especially for normal distributions. Other test criteria such as Akaike Information Criterion (AIC) and Minimum Description Length (MDL) may also be used (Hu and Xu 2004; Tu and Xu 2012).

To define a reliable range U for the clustering process, the initial number of classes should be identified, which is the lower bound k_0 ($k_0 \geq 2$) in the x -means. k_0 should be small enough to include the minimum number of change classes that can be directly recognized. To obtain a reliable initial number of this parameter, we apply a method based on the analysis of the compressed change direction representation proposed in (Bovolo et al. 2012). Instead of directly computing the angular distance in the original feature space, it was computed on the selected M -dimensional PCs of Ω_c as follows:

$$\varphi(\mathbf{P}_i) = \arccos\left(\frac{1}{\sqrt{M}} \left(\sum_{m=1}^M P_i^m / \sqrt{\sum_{m=1}^M (P_i^m)^2} \right)\right) \quad (4.5)$$

where $\varphi(\mathbf{P}_i)$ is the compressed change direction of \mathbf{P}_i , and P_i^m is the m -th component of vector \mathbf{P}_i . In this way we emphasize in the direction variable only the possible changes associated with Ω_c . The first PCs can properly model the changes that we are looking for. Thus the modes of the obtained distribution on the compressed change direction $\varphi(\mathbf{P}_i)$ can be recognized as the initial number k_0 of major changes existing in Ω_c (see Fig. 4.5). The upper bound of the range U is defined by adding a small integer bias value t to k_0 . t is in the order of few units and takes into account the intrinsic uncertainty of defining k_0 by analyzing $\varphi(\mathbf{P}_i)$.

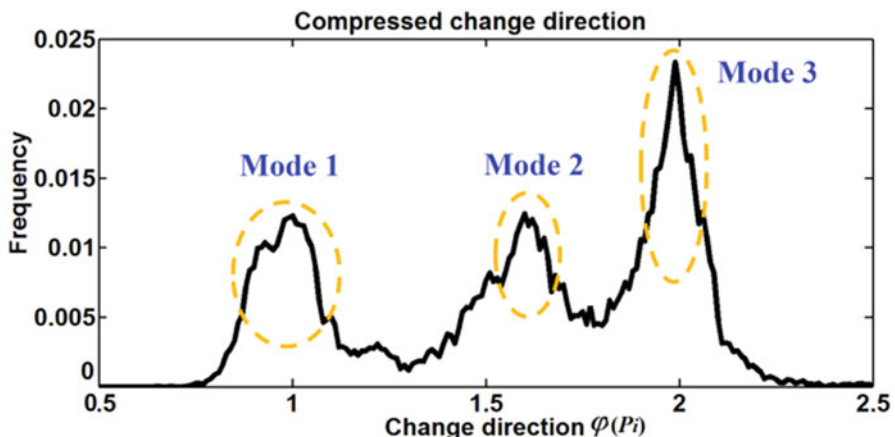


Fig. 4.5 Example of definition of the initial cluster number (k_0) analyzing of the compressed change direction

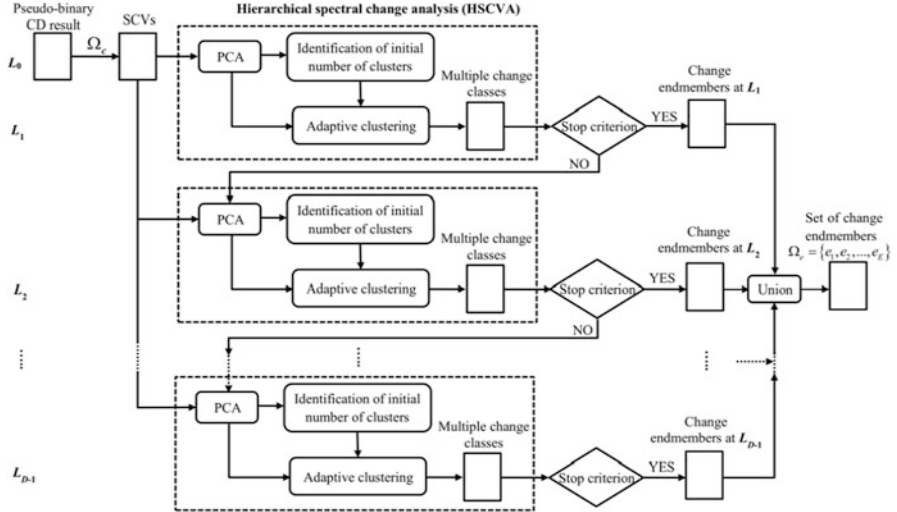


Fig. 4.6 Block scheme of the HSCVA step in the hierarchical change-detection approach

Once the major changes in Ω_c have been recognized and separated by using the adopted clustering algorithm, the root node splits into different child nodes at L_1 in the tree. Each node corresponds to one major change class (i.e., $\omega_{C_1}, \omega_{C_2}, \dots$). For each of them, the spectral homogeneity of SCVs is tested according to (4.4). For example, if we consider the first child node associated to class ω_{C_1} . The SAD of ω_{C_1} is computed as $\vartheta(x_i, S_{\omega_{C_1}})$ for each $x_i \in \omega_{C_1}$. If for a given node convergence is not reached then all the above operations (i.e., PCA, x -means, homogeneity evaluation) are iterated by considering only the SCVs of pixels x_i in the considered node (e.g., ω_{C_1}). Once all the nodes at L_1 are processed, the algorithm moves to the next level. The hierarchical decomposition is applied to each node in every level of the tree until the convergence is reached for all of them (see Fig. 4.6). The homogeneous condition of each node is evaluated according to the similarity measures in (4.4). The leaf node of each branch corresponds to a change endmember in $\Omega_e = \{e_1, e_2, \dots, e_E\}$. Note that at convergence change endmembers might appear at different levels of the tree. The block scheme of this step is shown in Fig. 4.6.

4.4.3 Generation of the Change-Detection Map

After identifying E change endmembers $\Omega_e = \{e_1, e_2, \dots, e_E\}$, pixels in the uncertain class Ω_u derived in the pseudo-binary CD step are considered. These pixels are assigned to one of the change endmembers or to the no-change class on the basis of spectral similarity. SAD (4) is computed between the SCV x_i ($x_i \in \Omega_u$) and the reference spectra S_e (i.e., the average spectrum of each detected change endmember

in Ω_e and of the no-change endmember e_n). Then x_i is assigned to the class with the minimum distance value, i.e.,

$$x_i \in \arg \min_{e_j \in \{\Omega_e, e_n\}} \{\vartheta(x_i, S_{e_j})\} \quad (4.6)$$

where $\vartheta(x_i, S_{e_j})$ denotes the SAD between x_i ($x_i \in \Omega_u$) and a given reference spectrum S_{e_j} . The final CD map is generated by merging the results obtained in the three sets of changed, uncertain and unchanged pixels (see in Fig. 4.6).

4.5 Experimental Results and Discussion

The hierarchical CD approach has been applied to two HS data sets, including one synthetic bi-temporal HS data set and a pair of real bi-temporal images. The pseudo-binary CD step was conducted firstly and three clusters (Ω_c , Ω_u and ω_n) were generated. The value δ was set such that the Ω_u class includes 25 % of the pixels in ω_n . After obtaining the general change class Ω_c , T_σ was set to drive the decomposition of the root node and to build the hierarchical tree for change endmember detection. T_σ is a user dependent parameter and controls the level of spectral homogeneity of the detected change endmembers. The smaller the T_σ , the higher the homogeneity level is and thus the number of change endmembers, and viceversa. In practical applications, the threshold should be selected taking into account the desired sensitivity to subtle changes. In our experiments trials were carried out with different values of T_σ , achieving different trade-offs in terms of endmember homogeneity.

After the initialization of Ω_c (i.e., root node of the tree), the identification of multiple change endmembers was done by using the HSCVA. The initial number of k_0 was defined based on the compressed change direction, and t was set equal to 3 to define the upper bound of U . The final CD map was obtained when all change endmembers were generated and the pixels in Ω_u were assigned to one of them or to the no-changed endmember. The results obtained by HSCVA method were compared with the ones obtained by the popular unsupervised k -means and fuzzy C-means (FCM) clustering methods. The two reference methods were applied to the subset of PCs selected by the HSCVA method for the root node, i.e., the ones that contain most of the information for Ω_c . The class number k of k -means and FCM was fixed on the basis of the HSCVA method outcome. In this way, we give clear advantage to the reference techniques that have not the intrinsic capability to estimate the number of expected change endmembers. This choice implicitly penalizes the HSCVA method. To reduce the uncertainty due to the random initialization in two reference methods, we ran them 200 times. The final accuracy was calculated as the average over 200 trials.

To evaluate the CD results both quantitative and qualitative assessments were carried out for each of the considered data sets. For the synthetic data set, the

quantitative assessment was based on the CD accuracy (i.e., endmember accuracy and kappa accuracy) and error indices obtained according to the reference map. In addition, the average endmember distance has been computed to assess the average endmember separability. To this end, pair-wise Bhattacharyya distance was computed among all the pairs of change endmembers. For two generic detected change endmembers e_α and e_β ($\alpha, \beta \in [1, E]$ and $\alpha \neq \beta$), the Bhattacharyya distance $B_{\alpha, \beta}$ is calculated as follows:

$$B_{\alpha, \beta} = \frac{1}{8} (\mu_\alpha - \mu_\beta)^T \left\{ \frac{\Gamma_\alpha + \Gamma_\beta}{2} \right\}^{-1} (\mu_\alpha - \mu_\beta) + \frac{1}{2} \ln \left\{ \frac{|(\Gamma_\alpha + \Gamma_\beta)/2|}{|\Gamma_\alpha|^{1/2} |\Gamma_\beta|^{1/2}} \right\} \quad (4.7)$$

where μ_α and μ_β denote the mean vectors, Γ_α and Γ_β represent the covariance matrices of change endmembers α and β , respectively. The higher distance the better the class separability, and viceversa. The average pairwise Bhattacharyya distance computed on all pairs of change endmembers indicates the overall class separability. In this chapter, we will refer to it as multi-class Bhattacharyya distance.

The CD results were also analyzed qualitatively by comparing: (1) the obtained CD maps; (2) the 2-D scatterplots of change endmembers in the feature space (i.e., the first PC versus the second PC on Ω_c); and (3) the spectral signatures of all the detected change endmembers in X_D with the ones obtained with reference techniques.

4.5.1 Simulated Hyperspectral Data Set

The first data set is taken from a real-world database of HS images, which includes images acquired by a commercial HS camera (Nuance FX, CRI Inc.) (Chakrabarti and Zickler 2011). The considered image has 31 narrow wavelength bands. The bandwidth is approximately 10 nm in a wavelength range from 420 nm to 720 nm, covering mainly the visible spectrum region. The selected image is an outdoor scene in the Harvard University with a size of 1392×1040 pixels (see Fig. 4.7a). To simulate the change targets and build the synthetic dataset, eight tiles were extracted from the original image (X_1) over all the spectral bands (see highlighted rectangles in Fig. 4.7a). They correspond either to different materials on the wall in the scene or to the same material but under different illumination conditions. Tiles were inserted into disjoint areas on a copy of the original image to generate a simulated image (X_2) showing two kinds of changes that are associated to: (1) the material transitions; and (2) the same material transitions but affected by different illumination conditions. By doing this, we simulated the subtle changes and increased the complexity of the considered problem. The same simulation setup was conducted three times by varying the position of tiles, thus generating three simulated multitemporal datasets. Each one is composed of X_1 and one among the three simulated X_2 . Figure 4.7b

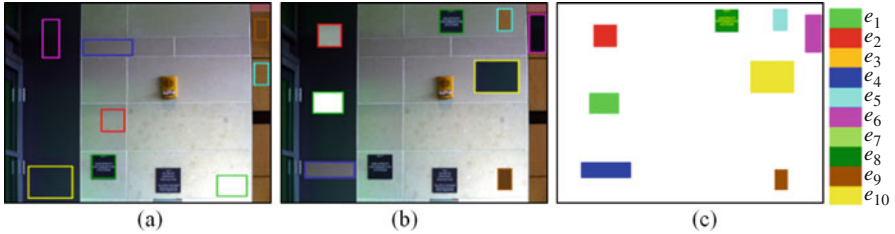


Fig. 4.7 Original HS image (a) acquired by the Nuance FX HS camera (X_1); (b) one of the simulated image (X_2) with changes; (c) Reference map (10 changes in *different colors*, no-change class in *white color*)

Table 4.1 Average kappa accuracy and multi-class Bhattacharyya distance obtained by the three considered methods on the simulated data sets

Method	Average k	Average multi-class Bhattacharyya distance
PCA k -means	0.9772 ± 0.0007	5.28
PCA FCM	0.9002 ± 0.0012	5.03
HSCVA	0.9930 ± 0.0009	5.91

shows one of the simulated images, and Fig. 4.7c presents the corresponding change reference map, which includes 10 change endmembers. The performance indices for this data will be presented as the average values over the three simulated data sets.

In this case the pseudo-binary CD step was neglected as the general change class Ω_c is explicitly defined by the change simulation step. Thus we directly focused on the pixels in Ω_c and tried to identify different change endmembers inside it. Performance is assessed quantitatively on the three reference maps. The final performance indices are given as the average accuracy over the three simulated datasets. Experimental results were obtained by fixing $T_\sigma = 0.05$ for all the three image pairs. The average kappa accuracy (k) and the average multi-class Bhattacharyya distance obtained by the three considered methods are shown in Table 4.1. As one can see, the HSCVA method obtained both the highest kappa accuracy and the highest average Bhattacharyya distance.

Let us now analyze one of the three simulated cases in greater detail (see Fig. 4.7). In this case, the complete tree has a structure with 3 levels and 14 nodes, where 10 of them are leaf nodes identified as change endmembers. The CD maps obtained by the HSCVA and the reference ones are shown in the first row of Fig. 4.8. Figure 4.8a–c reports the results of the HSCVA method, the reference k -means and FCM, respectively. Figure 4.8d shows the reference map. Each color corresponds to a specific detected change endmember, whereas the unchanged pixels are in white. In the second row, 2-D scatterplots of the detected change classes are shown in the feature space of first two PCs extracted from pixels in Ω_c . The spectral behaviors of the change endmembers in the SCV domain are presented in row 3. Tiles extracted from the whole CD maps are illustrated and further compared in row 4. Accuracies and error indices obtained according to the reference data are summarized in Table 4.1.

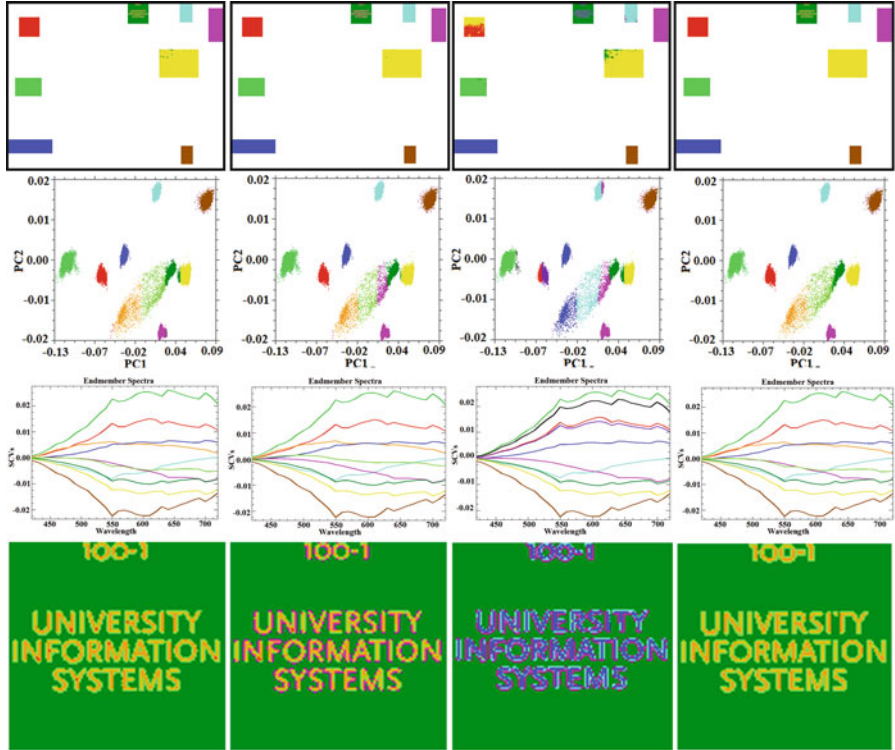


Fig. 4.8 CD results obtained on the simulated HS data set. Results provided by: (a) HSCVA, (b) k -means, and (c) FCM, (d) ground truth. From up to down, each row represents: (1) CD maps (or reference map); (2) 2-D scatterplots of change classes in the feature space; (3) SCV signatures of detected changes; (4) a subset from results in (1)

As one can see from Fig. 4.8, the HSCVA method detected the expected changes on this simulated data set accurately. In particular, it identified properly all the change classes in a hierarchical way. However, it was not affected by the problem on minority classes. The subtle changes with small amount of pixels (e.g., change of letters and their edges) were also detected in a precise way (see row 4 in Fig. 4.8). On the contrary, despite the conventional k -means and FCM received as input the true number of change endmembers, their results were less accurate. This demonstrates the advantages of using the hierarchical analysis structure. A visual comparison of scatterplots confirms the better results produced by the proposed method with respect to the other techniques. The two reference methods obtained in overall good performance, but showed a higher error rate for some change endmembers. By comparing the SCV signatures of changes detected by the three methods [Fig. 4.8 row 3 (a)-(c)] with the one of reference change map [Fig. 4.8 row 3 (d)], we can observe: (1) higher similarity between results of the HSCVA method and the

Table 4.2 Endmember and kappa accuracy, number of detection errors and multi-class Bhattacharyya distance obtained by three considered methods on one of the simulated data sets

Method	k	Tot. errors (pixel)	Multi-class Bhattacharyya distance
PCA k -means	0.9770	1367	5.49
PCA FCM	0.9007	2218	4.93
HSCVA	0.9933	650	6.22

reference spectra; and (2) different kinds of change (i.e., change endmembers) have discriminable spectral behaviors in the SCV domain [see row 3 (a) in Fig. 4.8], thus indicating the effectiveness of the HSCVA method in separating change information. The reference techniques detected some wrong change endmembers. For example, in the result of the FCM there are two couples of change endmembers with very similar spectral signatures. The first couple is represented by red and purple signatures, and the second is given by green and sienna signatures in Fig. 4.8c row 3. These changes were wrongly detected by the FCM method even by fixing the correct number of input classes.

The above analysis is confirmed by the numerical results in Table 4.2. We can observe that: (1) the hierarchical method outperformed reference approaches in terms of kappa accuracy and number of errors. The kappa accuracy is the highest among the three (i.e., 0.9933 compared to 0.9770 for k -means and 0.9007 for FCM). The total error of the HSCVA method (i.e., 650 pixels) is significantly smaller than the ones of reference methods (i.e., 1367 pixels for k -means and 2218 pixels for FCM); (2) the multi-class Bhattacharyya distance values indicate that the HSCVA approach achieves the highest class separability (i.e., 6.22) with respect to two clustering methods (i.e., 5.49 in k -means and 4.93 in FCM, respectively).

4.5.2 Hyperion Satellite Images of an Irrigated Agricultural Area

The second data set is made of a pair of real bi-temporal HS remote sensing images having a size of 211×396 pixels. These images were acquired by the Hyperion sensor mounted onboard the Earth Observing-1 (EO-1) satellite on May 1st, 2004 (X_1) and May 8th, 2007 (X_2). Figure 4.9a, b shows a false color composite of the two images. The study area covers an irrigated agricultural land of Hermiston city in Umatilla County, Oregon, United States. Land-cover changes include the transitions among the crops, soil, water and other land-cover types. The changes occurred in the cropland are mainly due to the vegetation water content that affected the irrigation condition in the field (see the circles on the image, which correspond to the radius of the irrigation system), and to the difference of the crop growth situation. The original Hyperion images contain 242 spectral bands, wavelength ranges are from 350 nm to 2580 nm, with a spectral resolution of 10 nm and a

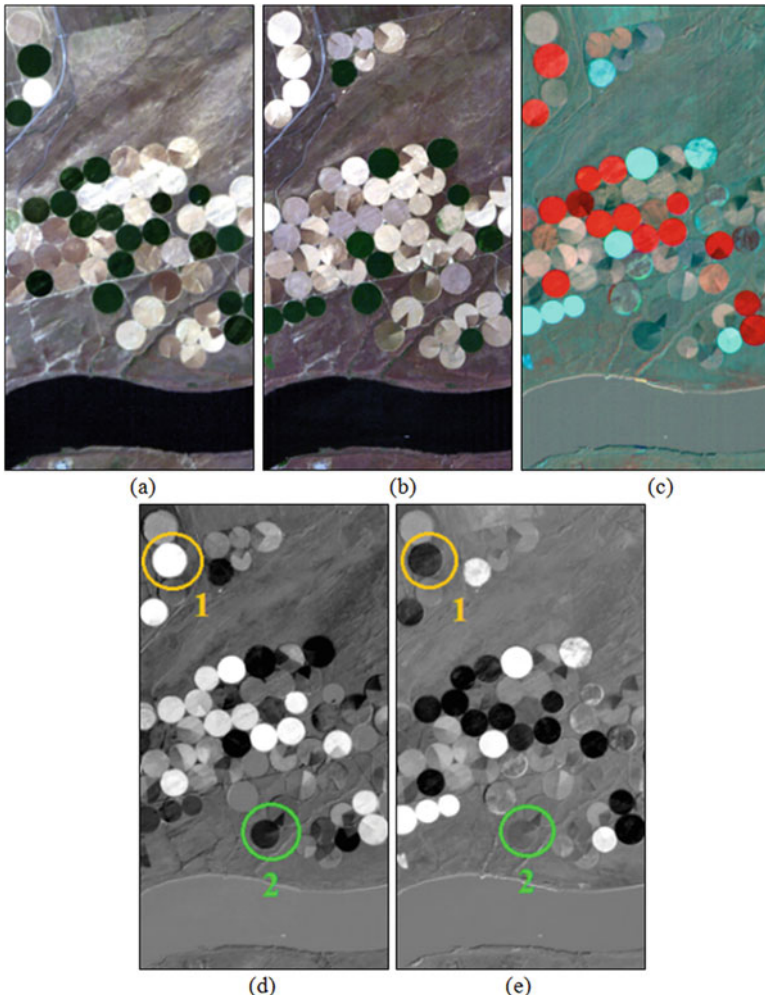


Fig. 4.9 Hyperion images acquired on an irrigated agricultural area. The original images acquired in (a) 2004 (X_1) and (b) 2007 (X_2); (c) composite three SCVs channels (R: 1729.70 nm, G: 1023.40 nm, B: 752.43 nm); single SCVs channel of (d) band 30 (650.67 nm) and (e) band 40 (752.43 nm)

spatial resolution of 30 m. Pre-processing was applied to the images, including bad stripes repairing, atmospheric corrections, and image co-registration with a residual error of 0.5 pixels. Radiometric correction was conducted to mitigate differences in illumination conditions and their impact on the CD process, thus reducing changes that are mainly irrelevant to the application and the end-users. In addition, we removed the uncalibrated bands (according to the prior knowledge on the Hyperion sensor), the overlapped redundant bands and the noisiest bands

due to low SNR values (Beck 2003). It should be noted that even if we removed the noisiest bands and uncalibrated bands, the selected channels include both clean and partially noisy bands, which still maintain the complexity of the data. Finally, 159 pre-processed bands (i.e., 8–57, 82–119, 131–164, 182–184, 187–220) were selected for performing the CD task. However, no ground truth samples are available for this data set. Thus the validation of results is done mainly in a qualitative way. Figure 4.9c represents a false color composite of spectral channels in X_D . Different colors indicate possible kinds of change classes, whereas gray areas represent the unchanged pixels. The same change class can be described differently in different wavelengths (e.g., see Fig. 4.9d, e where the same kind of change is highlighted in orange and green circles and has different behaviors in bands 30 and 40 of X_D). Accordingly the two examples given in Fig. 4.9 do not fully describe the complexity of the problem.

In this case the threshold T_σ was set to 0.13. The HSCVA method detected 15 change endmembers as leaf nodes in the hierarchical tree, which includes 4 levels and 20 nodes. Figure 4.10 illustrates CD results obtained by (a) the hierarchical method, (b) the k -means, and (c) the FCM. From row 1 to row 3 the figure shows the CD maps, the 2-D scatterplots in the two-dimensional feature space (i.e., the first two PCs extracted from pixels in Ω_c), and the SCV signatures of all the detected changes, respectively. For the hierarchical approach the 15 change endmembers are represented with different colors, whereas the no-change pixels are in white. For the two reference methods, the change clusters are also shown in different colors, but it is not possible to establish a direct correspondence among the legend given for the HSCVA method in Fig. 4.10, and the colors used for the reference methods. Also in this case the number of clusters for the k -means and the FCM was fixed on the basis of the result produced by the HSCVA technique.

The hierarchical CD approach obtained satisfactory results detecting change endmembers (validated by the detailed photointerpretation) and separating them according to the defined spectral homogeneity level. In greater detail, we can observe that: (1) The HSCVA method detected change endmembers due to the hierarchical analysis. On the contrary, two reference methods (that identify all the changes in a single step) ignore the intrinsic hierarchy of the change information in HS images. This increased the errors in the detection of change classes. (see also Fig. 4.10 row 1, where the hierarchical method detects changes with a higher homogeneity than the two reference methods). (2) All the considered methods are able to discriminate multiple changes, but with different performance on the change separability of change endmembers. The multi-class Bhattacharyya distance values were 4.12 (HSCVA), 3.78 (k -means) and 3.65 (FCM). The HSCVA method obtained the highest separability among all the detected change endmembers. (3) The generated spectra of change endmembers point out the spectral differences in the SCV domain, which illustrate the change separability of the different considered methods.

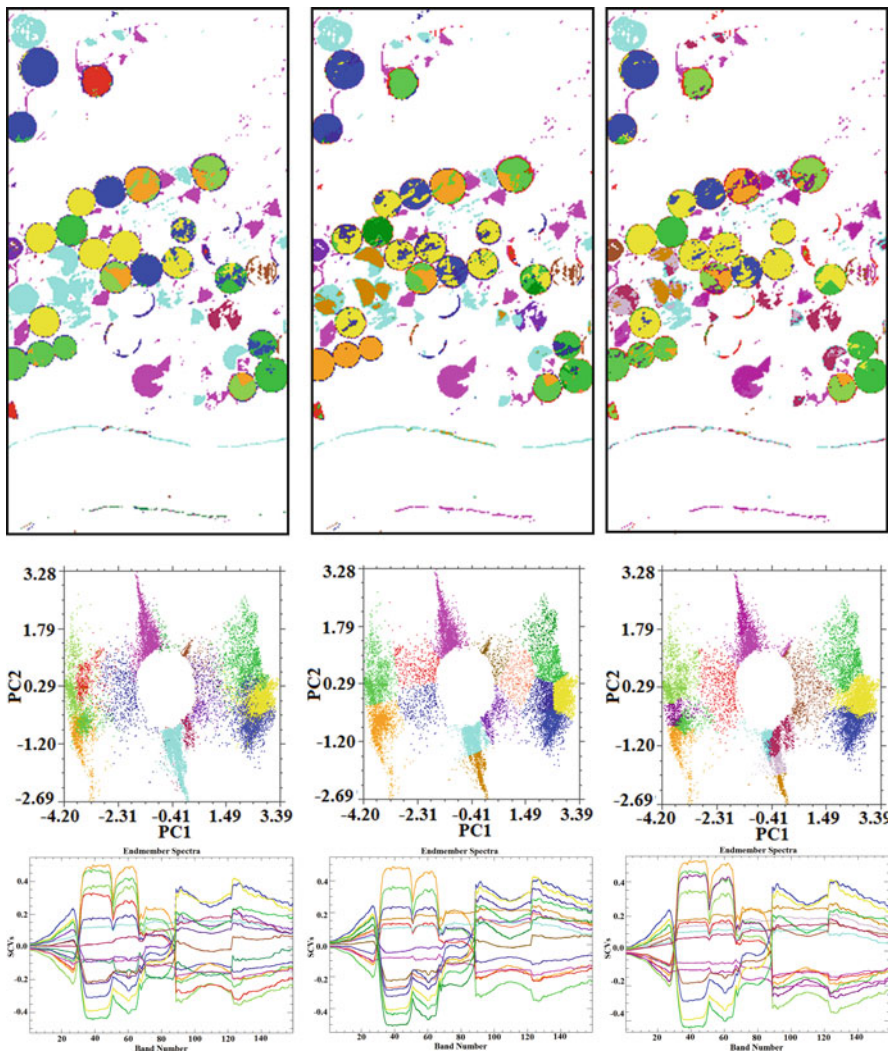


Fig. 4.10 CD results obtained on the real Hyperion HS images on an agricultural area. Results provided by (a) the HSCVA, (b) the k -means, and (c) the FCM. From row 1 to row 3: (1) change-detection maps; (2) 2-D scatterplots of all change classes in the feature space by using the first two PCs computed on pixels in Ω_c ; (3) spectra of the detected changes in the SCV domain. The legend only applies to the HSCVA method results

4.6 Conclusion

This chapter focused on the problem of change-detection in multitemporal hyperspectral images. In more details, taking into account the intrinsic complexity of the HS data, a proper definition of the concept of “change” in HS images is

given and together with the concept of change endmembers. A hierarchical spectral change analysis approach has been presented that aims at detecting and identifying multiple-change information in an unsupervised way. The hierarchical analysis can identify the discriminable spectral change endmembers from coarse to fine level (major change, subtle change and finally change endmembers) leading to a better model, whereas the reference methods are based on a single processing step only. In this way, we progressively decompose the complex problem into several specific sub-problems, focusing on each specific portion of the multiple-change information. This makes it possible to discover the difference among similar changes by decreasing the difficulty of detection.

Satisfactory results obtained on both simulated and a pair of real bi-temporal HS remote sensing images confirm the effectiveness of the proposed hierarchical method.

As future development of this work, we plan to: (i) consider in the hierarchical approach also the spatial information in order to increase the robustness and the accuracy of the CD results; (ii) define alternative method for the identification of change endmembers; (iii) validate the CD-HS results on data sets for which an exhaustive ground truth is available.

Acknowledgements This work was carried out in the framework of the project “Very high spatial and spectral resolution remote sensing: a novel integrated data analysis system”, funded by the Italian Ministry of Education, University and Research (Ministero dell’Istruzione, dell’Università e della Ricerca – MIUR) as a research program of relevant national interest (Programmi di Ricerca di Rilevante Interesse Nazionale – PRIN 2012).

References

- Adar S, Notesco G, Brook A, Livne EA (2011) Change detection over Sokolov open-pit mining area, Czech Republic, using multi-temporal HyMAP data (2009–2010). In: Proceedings of the SPIE 8180, image and signal processing for remote sensing XVII, 81800 T
- Beck R (2003) EO-1 User Guide
- Bovolo F, Bruzzone L (2007) A theoretical framework for unsupervised change detection based on change vector analysis in the polar domain. *IEEE Trans Geosci Remote Sens* 45(1):218–236
- Bovolo F, Marchesi S, Bruzzone L (2012) A framework for automatic and unsupervised detection of multiple changes in multitemporal images. *IEEE Trans Geosci Remote Sens* 50(6):2196–2212
- Bruzzone L, Bovolo F (2013) A novel framework for the design of change-detection systems for very-high-resolution remote sensing images. *Proc IEEE* 101(3):609–630
- Bruzzone L, Cossu R (2002) A multiple cascade-classifier system for a robust a partially unsupervised updating of land-cover maps. *IEEE Trans Geosci Remote Sens* 40(9):1984–1996
- Bruzzone L, Prieto DF (2000a) A minimum-cost thresholding technique for unsupervised change detection. *Int J Remote Sens* 21(18):3539–3544
- Bruzzone L, Prieto D (2000b) Automatic analysis of the difference image for unsupervised change detection. *IEEE Trans Geosci Remote Sens* 38(3):1170–1182
- Bruzzone L, Serpico S (1997) An iterative technique for the detection of land-cover transitions in multitemporal remote-sensing images. *Geosci Remote Sens IEEE Trans on* 35(4):858–867
- Canty MJ, Nielsen AA (2006a) Visualization and unsupervised classification of changes in multispectral satellite imagery. *Int J Remote Sens* 27(18):3961–3975

- Canty MJ, Nielsen AA (2006b) Multivariate alteration detection (MAD) and MAF postprocessing in multispectral, bitemporal image data: new approaches to change detection studies. *Int J Remote Sens* 27(18):3961–3975
- Castellana L, D'Addabbo A, Pasquarello G (2007) A composed supervised/unsupervised approach to improve change detection from remote sensing. *Pattern Recogn Lett* 28(4):405–413
- Celik T (2010) Change detection in satellite images using a genetic algorithm approach. *IEEE Geosci Remote Sens Lett* 7(2):386–390
- Chakrabarti A, Zickler T (2011) Statistics of real-world hyperspectral images. In: Proceedings of the IEEE conference on Computer Vision and Pattern Recognition (CVPR)
- Coppin P, Bauer M (1996) Digital change detection in forest ecosystems with remote sensing imagery. *Remote Sens Rev* 13:207–304
- Dalponte M, Bruzzone L, Vescovo L, Gianelle D (2009) The role of spectral resolution and classifier complexity in the analysis of hyperspectral images of forest areas. *Remote Sens Environ* 113:2345–2355
- Demir B, Bovolo F, Bruzzone L (2012) Detection of land-cover transitions in multitemporal remote sensing images with active-learning-based compound classification. *IEEE Trans Geosci Remote Sens* 50(5):1930–1941
- Du Q (2012) A new method for change analysis of multi-temporal hyperspectral images. In: IEEE Proceedings of the 4th WHISPERS, Shanghai
- Du YZ, Chang CI, Ren H, Chang C, Jensen J (2004) New hyperspectral discrimination measure for spectral characterization. *Opt Eng* 43(8):1777–1786
- Du Q, Wasson L, King R (2005) Unsupervised linear unmixing for change detection in multitemporal airborne hyperspectral imagery. In: IEEE International Workshop on MultiTemp, Biloxi, USA
- Du Q, Younan N, King R (2007) Change analysis for hyperspectral imagery. In: IEEE International Workshop on MultiTemp, Belgium
- Du P, Liu S, Bruzzone L, Bovolo F (2012) Target-driven change detection based on data transformation and similarity measures. In: 2012 IEEE international geoscience and remote sensing symposium, Munich, Germany
- Du P, Liu S, Gamba P, Tan K, Xia J (2012b) Fusion of difference images for change detection over urban areas. *IEEE J Sel Top Appl Earth Obs Remote Sens* 5(4):1076–1086
- Du P, Liu S, Xia J, Zhao Y (2013) Information fusion techniques for change detection from multi-temporal remote sensing images. *Inf Fusion* 14(1):19–27
- Du P, Liu S, Liu P, Tan K, Cheng L (2014) Sub-pixel change detection for urban land-cover analysis via multi-temporal remote sensing images. *Geo-spatial Inf Sci* 17(1):26–38
- Eismann MT, Meola J, Stocker A, Beaven S, Schaum A (2008) Hyperspectral change detection in the presence of diurnal and seasonal variations. *IEEE Trans Geosci Remote Sens* 46(1):237–249
- Frank M, Canty M (2003) Unsupervised change detection for hyperspectral images. In: Proceedings of the 12th JPL Airborne earth science workshop, NASA Technical Reports Server (NTRS), Pasadena, USA
- Ghosh A, Mishra NS, Ghosh S (2011) Fuzzy clustering algorithms for unsupervised change detection in remote sensing images. *Inf Sci* 181(4):699–715
- Hégarat-Mascle SL, Seltz R (2004) Automatic change detection by evidential fusion of change indices. *Remote Sens Environ* 91(3–4):390–404
- Hu X, Xu L (2004) Investigation on several model selection criteria for determining the number of cluster. *Neural Inform Process – Lett Rev* 4(1):1–10
- Hughes GF (1968) On the mean accuracy of statistical pattern recognizers. *IEEE Trans Inf Theory* IT-14:55–63
- Ishioka T (2005) An expansion of x-means for automatically determining the optimal number of clusters—progressive iterations of k-means and merging of the clusters. In: IASTED international conference on computational intelligence. ACTC Press, Calgary, Canada

- Liu S, Bruzzone L, Bovolo F, Du P (2012) Unsupervised hierarchical spectral analysis for change detection in hyperspectral images. In: Proceedings of the 4th WHISPERS, Shanghai
- Liu S, Bruzzone L, Bovolo F, Du P (2015) Hierarchical change detection in multitemporal hyperspectral images. *IEEE Trans Geosci Remote Sens* 53(1):244–260
- Lu D, Mause P, Brondízio E, Moran E (2004) Change detection techniques. *Int J Remote Sens* 25(12):2365–2401
- Marin C, Bovolo F, Bruzzone L (2014) Rapid and accurate damage detection in built-up areas combining stripmap and spotlight SAR images. In: IEEE international geoscience and remote sensing symposium, Québec City, Québec, Canada
- Meola J, Eismann M, Barnard K, Hardie R (2007) Analysis of hyperspectral change detection as affected by vegetation and illumination variation. In: Proceedings of the SPIE, Orlando, US
- Meola J, Eismann M, Moses R, Ash J (2011) Detecting changes in hyperspectral imagery using a model-based approach. *IEEE Trans Geosci Remote Sens* 49(7):2647–2661
- Nemmour H, Chibani Y (2006) Multiple support vector machines for land cover change detection: an application for mapping urban extensions. *ISPRS J Photogramm* 61(2):125–133
- Nielsen A (2007) The regularized iteratively reweighted MAD method for change detection in multi- and hyperspectral data. *IEEE Trans Image Proc* 16(2):463–478
- Ortiz-Rivera V, Vélez-Reyes M, Roysam B (2006) Change detection in hyperspectral imagery using temporal principal components. In: Proceedings of the SPIE, algorithms and technologies for multispectral, hyperspectral, and ultraspectral imagery XII
- Pelleg D, Moore AW (2000) X-means: extending K-means with efficient estimation of the number of clusters. In: In Proceedings of the seventeenth international conference on machine learning (ICML '00), San Francisco, CA, USA
- Plaza A, Martinez P, Perez R, Plaza J (2004) A quantitative and comparative analysis of endmember extraction algorithms from hyperspectral data. *IEEE Trans Geosci Remote Sens* 42(3):650–663
- Radke RJ, Andra S, Al-Kofahi O, Roysam B (2005) Image change detection algorithms: a systematic survey. *IEEE Trans Image Process* 14(3):294–307
- Ridd MK, Liu JJ (1998) A comparison of four algorithms for change detection in an urban environment. *Remote Sens Environ* 63(2):95–100
- Schaum A, Stocker A (1998) Long-interval chronochrome target detection. In: Proceedings of the International Symposium on Spectral Sensing Research, 1997, pp 1760–1770
- Schaum A, Stocker A (2004) Hyperspectral change detection and supervised matched filtering based on covariance equalization. *Proc Spie Int Soc Opt Eng* 5425:77–90
- Singh A (1989) Digital change detection techniques using remotely-sensed data. *Int J Remote Sens* 10(6):989–1003
- Soares V, Hoffer RM (1994) Eucalyptus forest change classification using multi-data Landsat TM data. *Proc SPIE* 2314:281–291
- Tu S, Xu L (2012) A theoretical investigation of several model selection criteria for dimensionality reduction. *Pattern Recogn Lett* 33(9):1117–1126
- Vongsy K, Mendenhall M (2011) A comparative study of spectral detectors. In; Proceedings of the 3rd WHISPERS, Lisbon, Portugal
- Vongsy K, Mendenhall M, Eismann M, Peterson GL (2012) Removing parallax-induced changes in hyperspectral change detection. In IEEE international geoscience and remote sensing symposium, Munich, Germany

Chapter 5

Object-Based Change Detection in Urban Areas Using Multitemporal High Resolution SAR Images with Unsupervised Thresholding Algorithms

Osama Yousif and Yifang Ban

Abstract With the recent launches of optical and SAR systems that are capable of producing images in very high resolution, the quantification of temporal changes can be achieved with unprecedented level of details. However, very high resolution data presents new challenges and difficulties such as the strong intensity variations within land cover classes thus the noisy appearance of change map generated by pixel-based change detection. This has led to the development of object-based approaches that utilize image segmentation. For unsupervised change detection, on the other hand, automatic thresholding algorithms provided a simple yet effective technique to produce a binary change map. Thresholding techniques have been used successfully for pixel-based change detection using medium resolution SAR images. They have also been used for object-based change detection using high resolution optical imagery. However, they have not been tested in the context of object-based change detection using high resolution SAR images. Therefore, this chapter investigates the potential of several thresholding techniques for object-based unsupervised detection of urban changes using high resolution SAR images. To avoid the creation of sliver polygons, the multiday image segmentation strategy is adopted to produce image objects that are spectrally, spatially, and temporally homogeneous. A change image is generated by comparing objects multitemporal mean intensities using the modified ratio operator. To threshold the change image and generate a binary change map, three thresholding algorithms, i.e., the Kittler-Illingworth algorithm, the Otsu method, and the outlier detection technique, are tested and compared. Two multitemporal datasets consisting of TerraSAR-X images acquired over Beijing and Shanghai are used for evaluation. Quantitative and qualitative analyses reveal that the three algorithms achieved similar results. The three algorithms achieved Kappa coefficients around 0.6 for the Beijing dataset and 0.75 for the Shanghai datasets. The analysis also reveals the limitation of the mathematical comparison operator in accentuating the difference between the changed and the unchanged

O. Yousif (✉) • Y. Ban

Division of Geoinformatics, KTH Royal Institute of Technology, Stockholm, Sweden
e-mail: osama.yousif@abe.kth.se

class, thus calls for the development of more sophisticated object-based change image generation mechanisms capable of reflecting all types of changes in the complex urban environment.

5.1 Introduction

Change detection using multitemporal remote sensing imagery plays an essential role in numerous fields of applications. Examples include urbanization (Ban and Yousif 2012), deforestation (Desclée et al. 2006), flooding (Moser and Serpico 2006), wetland mapping (Nielsen et al. 2008), and disaster monitoring and damage assessment (Bovolo and Bruzzone 2007). The wide spread of remotely sensed images in change detection can be attributed to their wide geographic coverage and availability in a wide range of spatial, spectral, and temporal resolutions. In recent years, a great deal of attention has been dedicated to change detection based on multitemporal SAR images due to SAR's independence of solar illumination and atmospheric conditions (Ban and Yousif 2012; Moser and Serpico 2009). Various SAR based change detection methods have been developed including unsupervised change detection (Bazi et al. 2005; Melgani et al. 2002; Hu and Ban 2014), spatio-contextual change detection (Yousif and Ban 2014), and speckle filtering and geometric detail preservation (Dekker 1998; Yousif and Ban 2013).

Recently, unsupervised change detection using automatic thresholding algorithms has gained a lot of popularity. These techniques analyze the change image (e.g., ratio or differenced image) in order to generate a binary change map that shows changed versus unchanged class. Example of these algorithms include Kittler-Illingworth (Kittler and Illingworth 1986), Otsu (1975), and Huang and Wang's fuzzy thresholding method (Huang and Wang 1995). These algorithms do not require training data (i.e., automatic), and are known for being very fast since, in most cases, the analysis only considers the histogram of the input image. Because of their simplicity, automatic thresholding algorithms have been used widely in change detection analysis using medium resolution optical (Melgani et al. 2002), and SAR images (Ban and Yousif 2012; Bazi et al. 2005; Moser and Serpico 2006), where the analysis has been carried out at the pixel level.

Recent technological developments led to the design and launch of several optical and SAR systems (e.g., QuickBird, IKONOS, RADARSAT-2, COSMO-SkyMed, and TerraSAR-X) capable of producing images in very high resolution. Using these data, the quantification of temporal changes can be achieved with unprecedented level of details. Nevertheless, very high resolution data presents new challenges and difficulties. One example is the strong intensity variations within land cover classes. This phenomenon is responsible of the noisy appearance of change map generated by applying pixel-based techniques to high resolution images, and has led to the development of object-based approaches that utilize image segmentation techniques.

Segmentation subdivides image into meaningful homogeneous regions/objects based not only on the spectral properties, but also on shape, texture, and size (Ban et al. 2010; Qin et al. 2013). The object-based paradigm allows the contextual information to be exploited in the segmentation phase rather than during the classification/change detection analysis. For high resolution imagery, object-based analysis can significantly help reducing the computational load. Compared to pixel-based techniques, object-based change detection proved to be less sensitive to image coregistration errors (Chen et al. 2012, 2014).

Several studies have shown the potential of object-based change detection approaches. In (Walter 2004; Zhou et al. 2008), for example, the detailed from-to change information was extracted by comparing images classified using object-based technique. Niemeyer et al. (2008) developed an algorithm that enhance change information at the object level using multivariate alteration detection transformation. Desclée et al. (2006) proposed an unsupervised object-based change detection algorithm that utilizes outlier detection technique. Similarly, Bontemps et al. (2008) developed an automatic change detection technique for the extraction of change information from SPOT vegetation time series. Using SAR images, Ye et al. (2013) developed an object-based change detection algorithm that fuses several change maps generated at different segmentation scales. In a similar line, Xiaoxia et al. (2013) proposed change detection algorithm for multitemporal POLSAR images that utilizes unitemporal segmentation strategy.

On the one hand, unsupervised thresholding algorithms have been used to extract change information from medium resolution SAR images (e.g. ERS-2 SAR, ENVISAT ASAR... etc.), where the analysis is often conducted at the pixel level (Adam and Ban 2009; Moser and Serpico 2006). On the other hand, object-based techniques have been used to extract change information from high resolution optical images (Desclée et al. 2006; Im et al. 2008). This study, therefore, investigates the object-based unsupervised detection of urban changes using multitemporal high resolution TerraSAR-X images. In particular, three unsupervised thresholding algorithms, i.e., Kittler Illingworth, Otsu, and outlier detection, will be investigated. The Kittler-Illingworth algorithm is common in pixel-based change detection using either optical or SAR multitemporal images. The outlier detection technique, on the other hand, has been used in object-based change detection using optical images (Bontemps et al. 2008; Desclée et al. 2006). Otsu method has also been used for pixel-based change detection using optical images (Melgani et al. 2002), however, its application in change detection based on SAR images is not common. All three algorithms have not been tested in the context object-based change detection using very high resolution SAR images.

This chapter is organized in five sections. The next section describes the methodology in detail. A description of the test datasets is given in Sect. 5.3. Results are discussed in Sect. 5.4 and conclusions are drawn in Sect. 5.5.

5.2 Methodology

In this section the change detection workflow (Fig. 5.1) based on a combination of image segmentation and automatic thresholding techniques, is presented. The subsections describe the steps involved in more details.

5.2.1 Preprocessing

The first step in change detection analysis is the accurate coregistration of the multitemporal images. Inaccurate image-to-image registration can cause a significant degradation of the accuracy of the change detection analysis. The TerraSAR-X images used in this study are enhanced ellipsoid corrected product (EEC). EEC generation includes the use of a medium resolution digital elevation model to correct for terrain induced distortions (Roth et al. 2004). As a result, this product has high positional accuracy. Visual analysis of the images reveals that image-to-image registration is not necessary.

SAR images are affected by speckle. The presence of speckle affects the extraction of useful information from SAR images. A despeckling step is therefore necessary before segmentation. In this study an enhanced Lee filter with a 7×7 pixel window is used to filter each image in the multitemporal dataset.

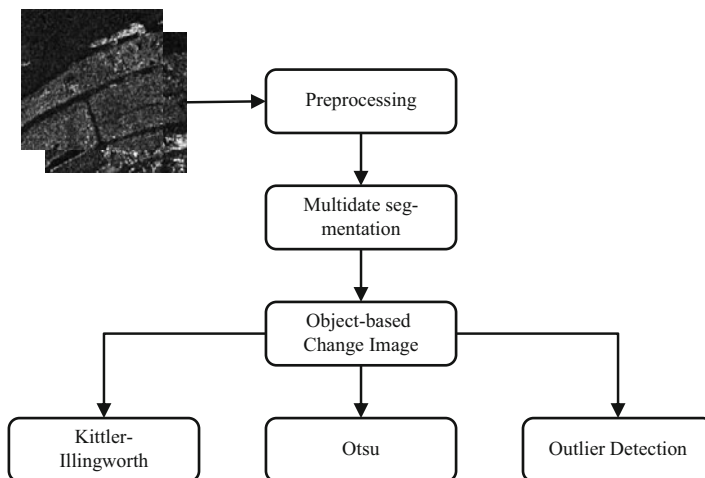


Fig. 5.1 A work flow for object-based unsupervised change detection using high spatial resolution SAR imagery

5.2.2 Segmentation

Segmentation subdivides the image into meaningful homogeneous regions. For change detection analysis, there are two types of segmentation strategies. The first one consists of segmenting, separately, each image in the multitemporal dataset. A consequence of this technique is the creation of sliver polygons when comparing the segmented images. Sliver polygons can complicate the change detection analysis. With this approach, however, objects can be compared not just in terms of their spectral properties (e.g., object's mean intensities), but also geometrically (e.g., objects areas and perimeters). In the second strategy, known as multidate segmentation (Desclée et al. 2006), all images in the multitemporal dataset are stacked and segmented together in one step. This technique results unique object layout (i.e., no sliver polygons). With this segmentation technique, the difference between object- and pixel-based change detection is merely of the used spatial scale. Most existing pixel-based change detection techniques can simply be extended to the object-based case.

Because of the involved simplicity, the multidate image segmentation approach is adopted in this work (Desclée et al. 2006; Qin et al. 2013). The multitemporal image segmentation is carried out using the *Multiresolution* segmentation algorithm (eCognition™). The *Multiresolution* algorithm is a bottom-up region growing segmentation technique that takes into consideration the objects spectral and geometrical properties. For more information about this algorithm the reader is referred to (Baatz and Schäpe 2000; Benz et al. 2004).

5.2.3 Change Image Generation

After image segmentation, the next step is to compare the multitemporal objects in order to generate an object-based change image that emphasizes the contrast between the changed and the unchanged areas. Due to speckle statistical characteristics, multitemporal SAR images are often compared using the ratio, or a ratio related (e.g., log-ratio) operator (Rignot and van Zyl 1993). Here, a version of the ratio operator, known as modified ratio, will be used. Let the average intensities of an object i at the first and second date images be I_{i1} and I_{i2} , respectively. The modified ratio operator computes the intensity of change r_i as:

$$r_i = \frac{\max(I_{i1}, I_{i2})}{\min(I_{i1}, I_{i2})} \quad (5.1)$$

The modified ratio operator clusters both positive and negative changes together, allowing the use of a single threshold to separate changed and unchanged classes (Ban and Yousif 2012). Positive and negative changes refer to changes that induce intensity increase and intensity decrease over time, respectively.

5.2.4 Thresholding

Thresholding involves the selection of an optimum threshold that can be applied to a change image in order to generate a binary change map. According to (5.1), objects with modified ratio less than the estimated threshold are considered unchanged, while those with greater values are assumed to be changed. Several techniques exist to estimate the unknown threshold. In this work, three algorithms will be considered, i.e., Kittler-Illingworth, Otsu method, and outlier detection. All algorithms considered are unsupervised techniques in the sense that no training phase is required.

5.2.4.1 Kittler-Illingworth Algorithm

This algorithm has been developed to separate an object from a background in a generic image (Kittler and Illingworth 1986). The algorithm assumes that the probability distribution of the input image is a mixture of two populations (e.g., changed and unchanged classes). If the classes' density functions and prior probabilities are known, then Bayesian decision theory can be used to estimate an optimum threshold that minimizes the average classification error. Since these quantities are unknown in an unsupervised context, the algorithm uses histogram fitting to estimate the unknown probabilities and an optimum threshold that can be used to binarize the input image.

Let $h(r)$ be the normalized histogram of the modified ratio image $r \in [r_1, r_2, \dots, r_L]$, where L indicates the number of levels used to construct the histogram. Let $p_u(r|\omega_u)$ and $p_c(r|\omega_c)$ be the conditional probability density functions of the unchanged (ω_u) and the changed class (ω_c), respectively, while $P_u(\omega_u)$ and $P_c(\omega_c)$ are their corresponding prior probabilities. The histogram of the change image provides an approximation of its probability distribution. This in turn is considered to be a mixture of two distributions, i.e., $h(r) \approx P(r) = p_u(r|\omega_u)P_u(\omega_u) + p_c(r|\omega_c)P_c(\omega_c)$.

Each possible value of the threshold $r_T \{r_T \in [r_1, r_2, \dots, r_L]\}$ divides the histogram into two sections (i.e., unchanged and changed). Histogram fitting techniques can then be used to estimate the density function parameters and prior probability of the classes (Ban and Yousif 2012). From all possible threshold values, the Kittler-Illingworth algorithm chooses the one that minimizes the following criterion function:

$$J_{KL}(r_T) = - \sum_{i \in \{u, c\}} \left[P_i(\omega_i; r_T) \ln P_i(\omega_i; r_T) + \sum_r h(r) \ln p_i(r|\omega_i; r_T) \right] \quad (5.2)$$

The criterion function $J_{KL}(r_T)$ is related to the average classification error—the smaller $J_{KL}(r_T)$ the smaller the classification error will be. The algorithm performs an intensive search in the 1D feature space trying to find a threshold that minimizes

the criterion function. The algorithm was originally developed assuming the classes to be normally distributed. For change detection using SAR images, the statistics of the classes in the ratio image are known to be far from normal. Several probability density functions have been proposed to model the statistics of the classes (Bazi et al. 2005; Moser and Serpico 2006). Here, the log-normal model, which proved to be effective in urban change detection (Ban and Yousif 2012), will be used. For more information about how to estimate the unknown probability quantities, please refer to (Ban and Yousif 2012).

5.2.4.2 Otsu's Method

This is also a histogram-based thresholding technique. Unlike the Kittler-Illingworth algorithm, however, the Otsu method is nonparametric—that is, no assumptions are made about the probability distribution of the classes (Otsu 1975). The Otsu method is very popular among the digital image processing community. Its application in remote sensing change detection using SAR images is not as common as the Kittler-Illingworth algorithm. The Otsu algorithm searches for a threshold that maximizes the separation between the object and the background (e.g., the changed and unchanged classes). This criterion is satisfied searching for a threshold r_T that maximizes the between-class variance $\sigma_b^2(r_T)$ shown in (3).

$$J_O(r_T) = \sigma_b^2(r_T) = P_u(\omega_u; r_T) P_c(\omega_c; r_T) [\mu_u(r_T) - \mu_c(r_T)]^2 \quad (5.3)$$

where, μ_u and μ_c are the means of the unchanged and the changed classes, respectively. The optimum solution can also be obtained by searching for the threshold that minimizes the within-class variance. Between-class minimization is often used since it only requires the calculation of first-order moments.

Despite the apparent difference between the Kittler-Illingworth and the Otsu algorithms, Yan (1996) provided a unified mathematical formulation, where their criterion functions were conceived as a weighted sum of the histogram grey levels. It turns out that these algorithms are similar except for the form of the cost function (i.e., the weight) adopted by each. Insights about the similarities and differences between these algorithms can be found in (Kurita et al. 1992; Xue and Zhang 2012).

5.2.4.3 Outlier Detection Technique

An outlier is defined as “an observation that deviates so much from other observations so as to arouse suspicion that it was generated by a different mechanism (Ben-Gal 2005)”. Outlier detection can either be parametric or nonparametric. The former makes assumption about the probability distribution of the observations. From a parametric point of view, changed objects can be considered outliers that contaminate the probability distribution of the unchanged class. Accordingly, outlier detection boils down to the identification of region in the feature space in which

an observation will be rejected (Ben-Gal 2005). Given the form of the probability density function of the unchanged class $p_u(r|\omega_u)$, and a confidence level $1 - \alpha$, it is possible to estimate an optimum threshold $r_{1-\alpha}$ that separates outlying observations (i.e., changed objects) from non-outlying observation (i.e., unchanged objects) such that:

$$P(r < r_{1-\alpha}) = \int_{-\infty}^{r_{1-\alpha}} p_u(r|\omega_u) dr = 1 - \alpha \quad (5.4)$$

Solving (5.4) for the threshold $r_{1-\alpha}$ is equivalent to computing the inverse cumulative distribution function for a certain confidence level. The parameters characterizing the unchanged class probability density function $p_u(r|\omega_u)$ are estimated from the observations (e.g., the modified ratio image). Unfortunately, the existence of outliers (i.e., changed objects) will contaminate (bias) the estimates of unchanged class PDF parameters and, consequently, affect the accuracy of outlier identification, i.e., masking and swamping effects (Ben-Gal 2005). For this reason, an iterative trimming procedure is usually adopted (Desclée et al. 2006), where at each iteration a new estimate of PDF parameters and a threshold value are obtained followed by identification and removal of outlying observations. The iterative trimming continues until a certain convergence condition is met (e.g., when the unchanged class PDF parameters stabilize). For a successful application of this technique, the size of the changed class (i.e., the outliers) should be small fraction of the size of the unchanged class (Bontemps et al. 2008).

Most applications of parametric univariate outlier detection assume the target distribution to be Gaussian. For the same reason discussed in the Kittler-Illingworth algorithm case, the unchanged class is assumed to be lognormally distributed. In this work, the confidence level $(1 - \alpha)$ is set equal to 0.995.

5.3 Datasets Description

To evaluate the object-based change detection using three unsupervised thresholding techniques, two multitemporal TerraSAR-X datasets, each has 4000×4000 pixels in size with a pixel spacing of 1.25 m, are used. The first dataset covers a portion of Shanghai, and consists of two TerraSAR-X scenes from August 20, 2008 (Fig. 5.2a), and September 16, 2011 (Fig. 5.2b). The second dataset covers part of Beijing, and consists of a pair of TerraSAR-X images acquired on May 9, 2008 (Fig. 5.3a) and May 9, 2013 (Fig. 5.3b). The SAR images in each dataset were acquired on near anniversary dates to eliminate seasonal effects. A substantial amount of change occurred in Shanghai and Beijing within the time frame. The changes vary in nature (i.e., type of change) and, subsequently, the intensity in the modified ratio image. To quantitatively assess the performance of the thresholding algorithms, 735 changed and 781 unchanged validation pixels for Shanghai, and 672 changed and 677



Fig. 5.2 Shanghai dataset (a) date I image, and (b) date II image

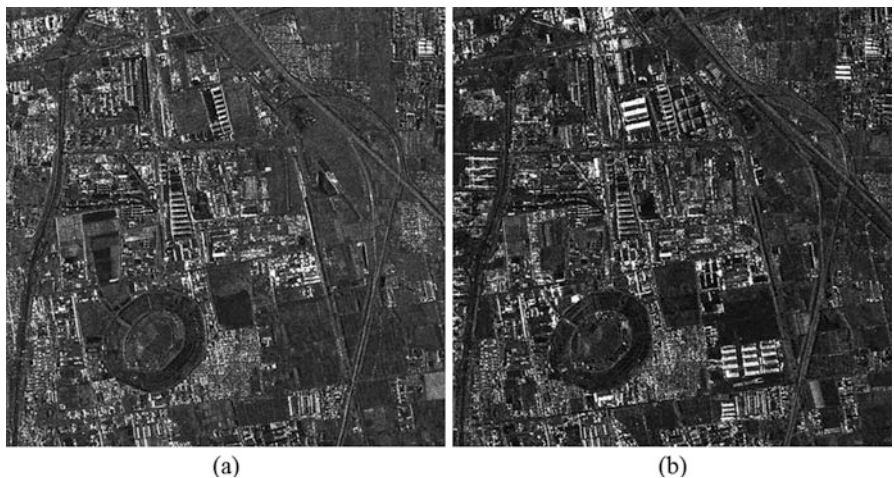


Fig. 5.3 Beijing dataset (a) date I image, and (b) date II image

unchanged validation pixels for Beijing, are used. The ground truth samples were collected using stratified random sampling strategy. Unchanged/changed labels were assigned to samples on a pixel-by-pixel basis with the help of Google Earth™ images acquired at approximately the same time as the experimental SAR images.

5.4 Results and Discussion

To carry out a successful segmentation, the multitemporal SAR images were first filtered using an enhanced Lee filter with a 7×7 pixels window size. The segmentation was then carried out using the eCognition *Multiresolution* segmentation module. For both datasets, the scale (i.e., heterogeneity), shape, and compactness (parameters required by the *Multiresolution* segmentation module) were set equal to 70, 0.5, and 0.5, respectively. These values give satisfactory results in the current experimentation setup.

Figure 5.4a–c show segmentation results of Shanghai date I and date II images, and the corresponding modified ratio image, respectively. In Fig. 5.4c the brighter the object, the higher the probability of being a change object. The change maps generated by thresholding the change image (i.e., the modified ratio image) using Kittler-Illingworth, Otsu, and outlier detection are shown in Fig. 5.4d–f, respectively. In these change maps, blue and gray colors indicate changed and unchanged areas, respectively.

From the figure, one can observe the great similarity between the change maps produced using the three techniques. This is also confirmed by the accuracy assessment report shown in Table 5.1, i.e., the three algorithms achieved comparable false alarm rates, detection accuracies, and kappa coefficients of agreement. This is surprising given the fact that these algorithms are developed based on different assumptions. Kittler-Illingworth and outlier detection are parametric techniques that employ the lognormal distribution. The Otsu method tries to maximize the separation between the classes, with no assumptions about their statistical distribution. This algorithm, therefore, does not consider the special characteristics of SAR images.

The comparison of these change maps with Google EarthTM optical images acquired at approximately the same time reveals that many false alarms are due to small objects of nonpermanent nature (e.g., cars) that happened to exist in the scene during the acquisition of one of the images. Furthermore, one can observe that some changes did not create sufficiently strong intensity in the change image to be detected. A representative example is indicated by the red ellipse in Fig. 5.4, where bare (smooth) soil changed to a new building with a smooth extended roof (see Date I and Date II Google EarthTM images shown in Fig. 5.4g and h, respectively). Both ground cover types interact similarly with the incident radar energy (i.e., a low intensity of change in the modified ratio image), thus the change that has occurred is not easily detectable. Note that with outlier detection this change can be detected reducing the confidence level to 0.99 for example. This action, however, will increase the false alarm rate from 8.07 % to 15.49 %.

Figure 5.5 shows the same information as in Fig. 5.4 but for the Beijing dataset. This figure shows important aspects of urban change detection using SAR images, in addition to what we have observed in the Shanghai case. The red arrow in Fig. 5.5 shows an agricultural field. From an urban point of view, no change of interest has occurred (see Date I and Date II Google EarthTM optical images shown in Fig 5.5g and h). However, from the perspective of the multitemporal SAR images, the field

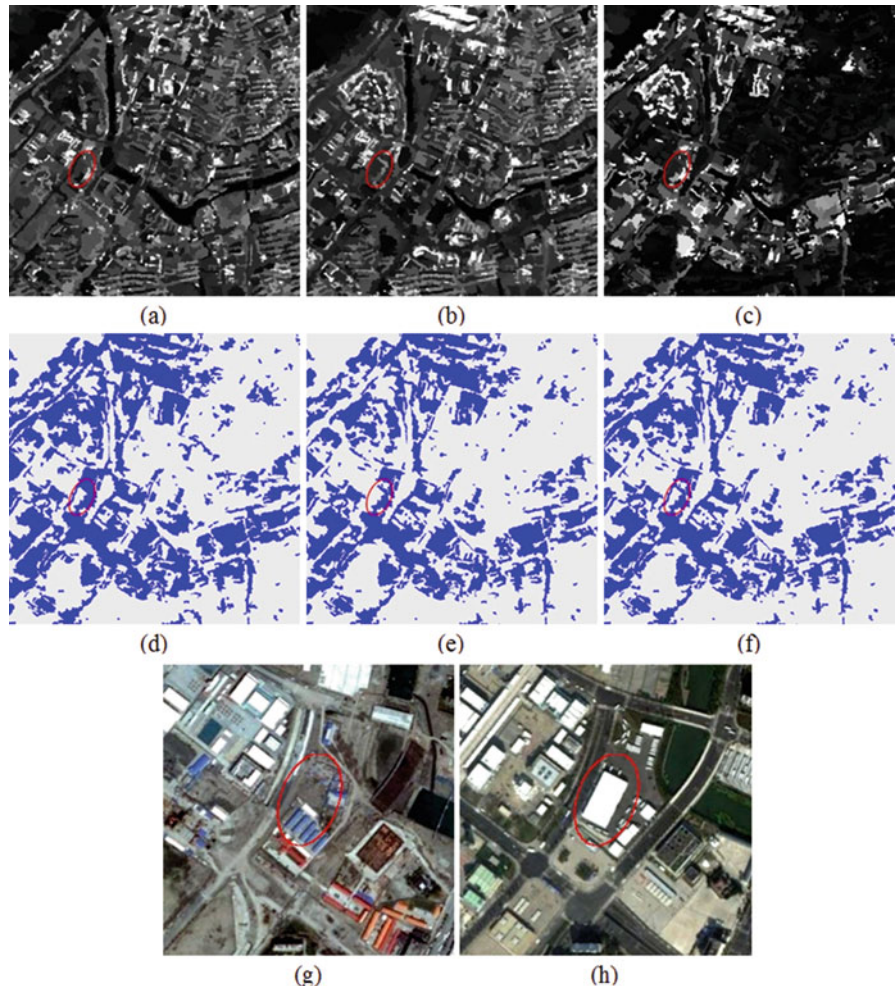


Fig. 5.4 Shanghai object-based (a) date I image, (b) date II image, (c) modified ratio image, and change maps produced using (d) Kittler-Illingworth algorithm, (e) Otsu method, (f) Outlier detection technique, (g) Date I image—Google EarthTM, (h) Date II image—Google EarthTM

Table 5.1 Shanghai results accuracy assessment

	False alarm	Detection accuracy	Overall accuracy	Kappa
K&I	11.14	85.58	87.27	0.74
Otsu	7.17	82.04	87.60	0.75
Outlier	8.07	82.72	87.47	0.75

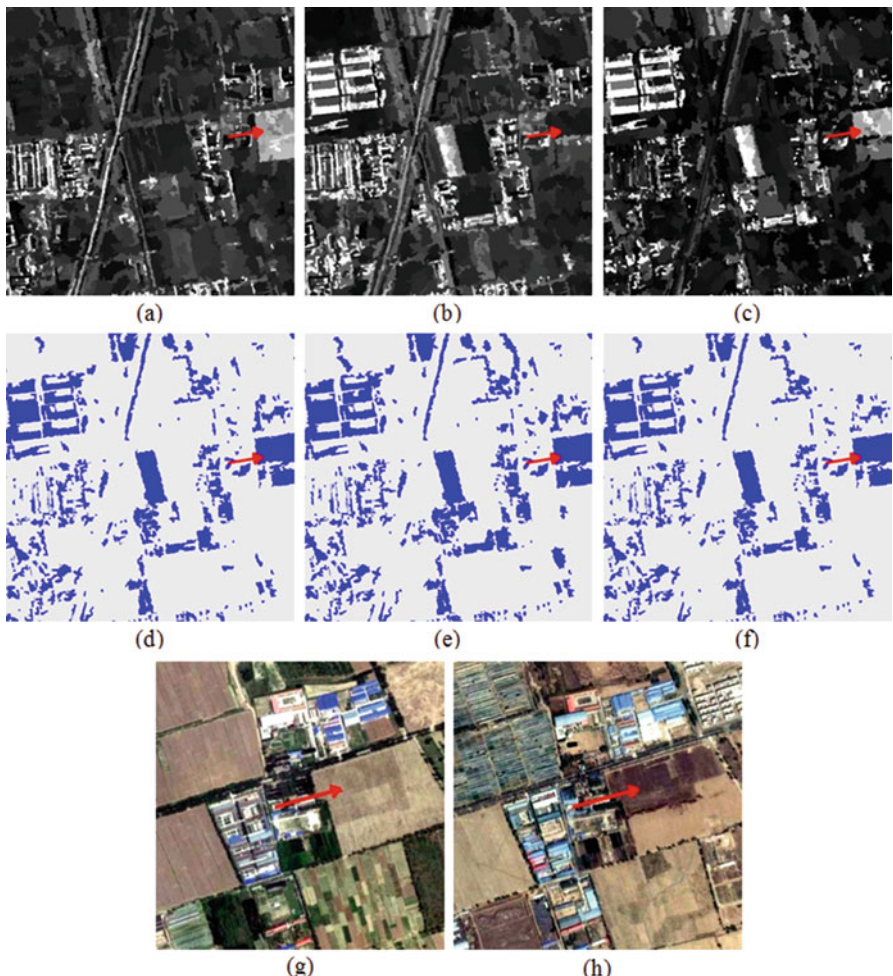


Fig. 5.5 Beijing object-based (a) date I image, (b) date II image, (c) modified ratio image, and change maps produced using (d) Kittler-Illingworth algorithm, (e) Otsu method, (f) Outlier detection technique, (g) Date I image—Google EarthTM, (h) Date II image—Google EarthTM

appears different. This can be attributed, for example, to different moisture content due to heavy rain before the acquisition of the first image. Note that the images in the Beijing dataset were acquired at the anniversary date (i.e., May 9th) and, consequently, one does not expect significant differences in the growth cycle. The difference in environmental condition was strongly reflected in the modified ratio image (the field appeared bright), and the field was identified as changed by all three thresholding algorithms. The accuracy assessment report for the Beijing results is shown in Table 5.2, which indicates that the three algorithms achieved similar kappa coefficients, and comparable false alarm rates.

Table 5.2 Beijing results accuracy assessment

	False alarm	Detection accuracy	Overall accuracy	Kappa
K&I	13.74	73.81	80.06	0.60
Otsu	18.32	79.32	80.50	0.61
Outlier	13.74	72.32	79.32	0.59

Tables 5.1 and 5.2 also show that the result obtained for the Beijing dataset is rather poor compared with that obtained for Shanghai dataset. This could be attributed to the fact that a substantial amount of the change that has occurred in the Beijing study area is due to the replacement of informal settlements with new modern buildings. This is another example of when the occurred ground change does not induce strong enough intensity in the change image to be successfully detected.

Although all three algorithms achieved equivalent results for both datasets, a few points need to be carefully considered. Kittler-Illingworth and outlier detection allow the inclusion of prior knowledge about the classes in the thresholding process. If the parametric form of the two classes probability density function is known, then capturing this knowledge in the thresholding process is an advantage, and Kittler-Illingworth could be the right choice. The distribution of the unchanged class in the ratio can often be inferred from empirical (e.g. log normal and Weibull) or theoretical (e.g., Gamma and square root Gamma) models used to describe the statistical behavior of the intensity/amplitude (Moser and Serpico 2006). The changed class in urban environments often consists of several types of changes. In this case, one would be less confident about which model to use to model the change class, and the use of Kittler-Illingworth could lead to the estimation of a biased threshold. In this case outlier detection could be the right choice. This technique is flexible in the sense that it only requires assumptions about the distribution of the unchanged class, and the false alarm rate (or for that matter the detection accuracy) can easily be controlled by varying the confidence level. As for the Otsu method, it is not possible to include any prior knowledge we might have about the statistics of the classes. The algorithm depends exclusively on the information conveyed by the histogram of the modified ratio image. The success of the algorithm depends on how the input image meets the assumptions on the background—for example, a biased threshold will be obtained if the assumption of equal class variances is violated (Kurita et al. 1992).

At this point it is pertinent to ask the question: is it possible to achieve a better detection accuracy using any other thresholding method? To answer the question, Fig. 5.6 shows variations in kappa coefficient of agreement as a function of the threshold value, for (a) Shanghai and (b) Beijing datasets. One hundred threshold values were used to construct the graphs. For each threshold value, a change map is generated and the kappa coefficient of agreement is calculated. The figure shows that the maximum attainable kappa coefficients for Shanghai and Beijing dataset are 0.75 and 0.62, respectively. The corresponding false alarm rates are 7.2 % and 18.8 %,

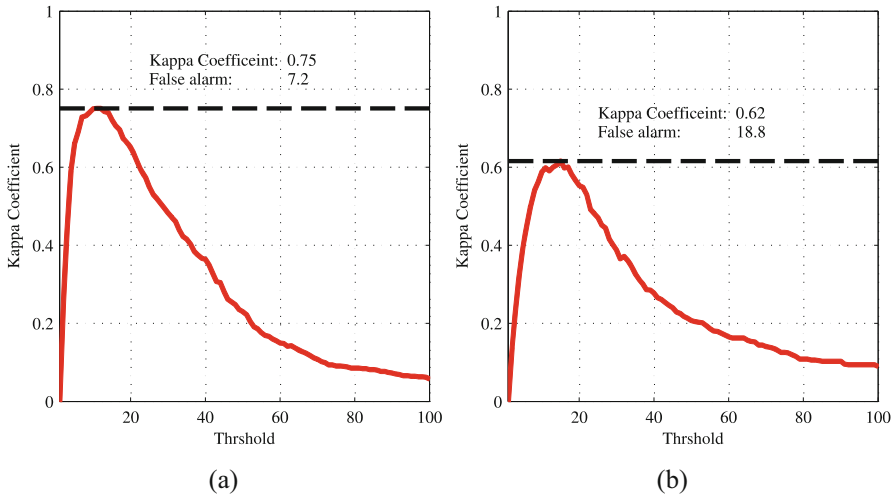


Fig. 5.6 Variations in kappa coefficient of variation as a function of the threshold value, (a) Shanghai, and (b) Beijing dataset

respectively. The graphs in Fig. 5.6 together with Tables 5.1 and 5.2 indicate that the three thresholding algorithms achieved results very close to the maximum possible given the modified ratio images as change indicator. The maximum achievable accuracies, however, are not very high especially for the Beijing dataset. This shortcoming could be attributed to the fact that multitemporal SAR images are not capable of reflecting/expressing all types of change that might have occurred in the urban environment. Some changes do not produce intensity in the change image strong enough to be correctly classified by any thresholding/classification algorithm without causing extremely high false alarm rates in the background. This finding emphasizes the need to include more information to characterize all types of urban changes. This could be achieved by (1) considering multichannel SAR images (e.g., polarimetric SAR images) with their richer information content as opposed to single-frequency single-polarization SAR images (Moser and Serpico 2009); (2) using more than one SAR image per date with different acquisition geometries (e.g., viewing angles) or different seasons; (3) resorting to SAR and optical data fusion for enhanced change detection analysis.

The abovementioned accuracy limitations can also be accredited to the way we construct our change image—that is, the mathematical comparison operator used. The ratio operator is suitable for SAR images because it suits SAR speckle statistics better. Some studies have pointed out that this comparison operator has certain limitations in accentuating the difference between the changed and the unchanged class (Gong et al. 2012). This fact necessitates the development of more sophisticated change image generation mechanisms capable of extracting more change information from the multitemporal high resolution SAR images.

5.5 Conclusion

In this study the unsupervised generation of a binary change map using multitemporal high resolution imagery was investigated using the object-based approach, because of the strong intensity variation in high resolution imagery and the SAR speckle. For image segmentation, multiday segmentation was used. Image comparison was carried out using a modified version of the ratio operator that groups both positive and negative changes together, and consequently allows for the separation of changed and unchanged classes using a single threshold. Three automatic thresholding algorithms, i.e., Kittler-Illingworth, Otsu, and outlier detection, were investigated for the generation of a binary change map. Qualitative and quantitative analyses of the results indicate that the three algorithms achieved similar accuracies. This finding is quite unexpected given the different assumptions upon which each algorithm is based. The analysis also reveals that compared with Shanghai, lower detection accuracies were achieved for the Beijing dataset. This is mainly due to the complicated nature of the changes that have occurred in this dataset.

Given the modified ratio change image, the analysis also reveals that the accuracies achieved by the three algorithms are very close to the maximum possible. Improvements are possible using multichannel multitemporal SAR images; using more than one SAR image per date with different acquisition geometries; or through the fusion of optical and SAR data since SAR has limited ability in reflecting all types of ground changes. Improvement could also be achieved by the development of more sophisticated images comparison techniques capable of extracting more change information from the multitemporal SAR images.

Acknowledgments The research was funded by the Swedish National Space Board through project ‘Change Detection in Urban Areas Using Multitemporal Spaceborne SAR and Fusion of SAR and Optical Data (Dnr 159/11, PI: Yifang Ban)’. This project is also part of the Urbanization project within the ESA/China MOST Dragon 3 program. The authors would like to thank DLR for providing the TerraSAR-X data.

References

- Adam O, Ban Y (2009) Multitemporal spaceborne SAR data for change detection in urban areas: a case study in Shanghai. Proceedings, ISPRS VCGVA, pp 1–5
- Baatz M, Schäpe A (2000) Multiresolution segmentation: an optimization approach for high quality multi-scale image segmentation. In: Proceedings of the Angewandte Geographische Informationsverarbeitung XII. Beiträge zum AGIT-Symposium Salzburg, pp 12–23
- Ban Y, Yousif OA (2012) Multitemporal spaceborne SAR data for urban change detection in China. IEEE J Sel Top Appl Earth Obs Remote Sens 5:1087–1094. doi:[10.1109/JSTARS.2012.2201135](https://doi.org/10.1109/JSTARS.2012.2201135)
- Ban Y, Hu H, Rangel IM (2010) Fusion of Quickbird MS and RADARSAT SAR data for urban land-cover mapping: object-based and knowledge-based approach. Int J Remote Sens 31:1391–1410. doi:[10.1080/01431160903475415](https://doi.org/10.1080/01431160903475415)

- Bazi Y, Bruzzone L, Melgani F (2005) An unsupervised approach based on the generalized Gaussian model to automatic change detection in multitemporal SAR images. *IEEE Trans Geosci Remote Sens* 43:874–887. doi:[10.1109/TGRS.2004.842441](https://doi.org/10.1109/TGRS.2004.842441)
- Ben-Gal I (2005) Outlier detection. In: Maimon O, Rokach L (eds) *Data mining and knowledge discovery handbook*. Springer, New York, pp 131–146
- Benz UC, Hofmann P, Willhauck G, Lingenfelder I, Heynen M (2004) Multi-resolution, object-oriented fuzzy analysis of remote sensing data for GIS-ready information. *ISPRS J Photogramm Remote Sens, Integ Geodata Image Automat Refine Update Spat Database* 58:239–258. doi:[10.1016/j.isprsjprs.2003.10.002](https://doi.org/10.1016/j.isprsjprs.2003.10.002)
- Bontemps S, Bogaert P, Titeux N, Defourny P (2008) An object-based change detection method accounting for temporal dependences in time series with medium to coarse spatial resolution. *Remote Sens Environ* 112:3181–3191. doi:[10.1016/j.rse.2008.03.013](https://doi.org/10.1016/j.rse.2008.03.013)
- Bovolo F, Bruzzone L (2007) A split-based approach to unsupervised change detection in large-size multitemporal images: application to tsunami-damage assessment. *IEEE Trans Geosci Remote Sens* 45:1658–1670. doi:[10.1109/TGRS.2007.895835](https://doi.org/10.1109/TGRS.2007.895835)
- Chen G, Zhao K, Powers R (2014) Assessment of the image misregistration effects on object-based change detection. *ISPRS J Photogramm Remote Sens* 87:19–27. doi:[10.1016/j.isprsjprs.2013.10.007](https://doi.org/10.1016/j.isprsjprs.2013.10.007)
- Chen G, Hay GJ, Carvalho LMT, Wulder MA (2012) Object-based change detection. *Int J Remote Sens* 33:4434–4457. doi:[10.1080/01431161.2011.648285](https://doi.org/10.1080/01431161.2011.648285)
- Dekker RJ (1998) Speckle filtering in satellite SAR change detection imagery. *Int J Remote Sens* 19:1133–1146
- Desclée B, Bogaert P, Defourny P (2006) Forest change detection by statistical object-based method. *Remote Sens Environ* 102:1–11. doi:[10.1016/j.rse.2006.01.013](https://doi.org/10.1016/j.rse.2006.01.013)
- Gong M, Zhou Z, Ma J (2012) Change detection in synthetic aperture radar images based on image fusion and fuzzy clustering. *IEEE Trans Image Process* 21:2141–2151. doi:[10.1109/TIP.2011.2170702](https://doi.org/10.1109/TIP.2011.2170702)
- Hu H, Ban Y (2014) Unsupervised change detection in multitemporal SAR images over large urban areas. *IEEE J Select Top Appl Earth Observ Remote Sens* 7:3248–3261. doi:[10.1109/JSTARS.2014.2344017](https://doi.org/10.1109/JSTARS.2014.2344017)
- Huang L-K, Wang M-JJ (1995) Image thresholding by minimizing the measures of fuzziness. *Pattern Recognit* 28:41–51. doi:[10.1016/0031-3203\(94\)E0043-K](https://doi.org/10.1016/0031-3203(94)E0043-K)
- Im J, Jensen JR, Tullis JA (2008) Object-based change detection using correlation image analysis and image segmentation. *Int J Remote Sens* 29:399–423. doi:[10.1080/01431160601075582](https://doi.org/10.1080/01431160601075582)
- Kittler J, Illingworth J (1986) Minimum error thresholding. *Pattern Recognit* 19:41–47
- Kurita T, Otsu N, Abdelmalek N (1992) Maximum likelihood thresholding based on population mixture models. *Pattern Recognit* 25:1231–1240. doi:[10.1016/0031-3203\(92\)90024-D](https://doi.org/10.1016/0031-3203(92)90024-D)
- Melgani F, Moser G, Serpico SB (2002) Unsupervised change-detection methods for remote-sensing images. *Opt Eng* 41:3288–3297
- Moser G, Serpico SB (2006) Generalized minimum-error thresholding for unsupervised change detection from SAR amplitude imagery. *IEEE Trans Geosci Remote Sens* 44:2972–2982. doi:[10.1109/TGRS.2006.876288](https://doi.org/10.1109/TGRS.2006.876288)
- Moser G, Serpico SB (2009) Unsupervised change detection from multichannel SAR data by Markovian data fusion. *IEEE Trans Geosci Remote Sens* 47:2114–2128. doi:[10.1109/TGRS.2009.2012407](https://doi.org/10.1109/TGRS.2009.2012407)
- Nielsen EM, Prince SD, Koehn GT (2008) Wetland change mapping for the U.S. mid-Atlantic region using an outlier detection technique. *Remote Sens Environ* 112:4061–4074. doi:[10.1016/j.rse.2008.04.017](https://doi.org/10.1016/j.rse.2008.04.017)
- Niemeyer I, Marpu PR, Nussbaum S (2008) Change detection using object features. In: Blaschke T, Lang S, Hay GJ (eds) *Object-based image analysis, Lecture Notes in Geoinformation and Cartography*. Springer, Berlin/Heidelberg, pp 185–201
- Otsu N (1975) A threshold selection method from gray-level histograms. *Automatica* 11:23–27
- Qin Y, Niu Z, Chen F, Li B, Ban Y (2013) Object-based land cover change detection for cross-sensor images. *Int J Remote Sens* 34:6723–6737. doi:[10.1080/01431161.2013.805282](https://doi.org/10.1080/01431161.2013.805282)

- Rignot EJ, van Zyl JJ (1993) Change detection techniques for ERS-1 SAR data. *IEEE Trans Geosci Remote Sens* 31:896–906
- Roth A, Huber M, Kosmann D (2004) Geocoding of TerraSAR-X data. In: Proceedings of 20th International Congress of the ISPRS. Istanbul, Turkey, pp 840–844
- Walter V (2004) Object-based classification of remote sensing data for change detection. *ISPRS J Photogramm Remote Sens* 58:225–238. doi:[10.1016/j.isprsjprs.2003.09.007](https://doi.org/10.1016/j.isprsjprs.2003.09.007)
- Xiaoxia S, Jixian Z, Qin Y, Liang Z (2013) Object-oriented change detection of multi-polarization SAR images based on unitemporal image segmentation. In: Urban remote sensing event (JURSE), 2013 Joint. Presented at the Urban Remote Sensing Event (JURSE), 2013 Joint, pp 171–173. doi:[10.1109/JURSE#.2013.6550693](https://doi.org/10.1109/JURSE#.2013.6550693)
- Xue J-H, Zhang Y-J (2012) Ridler and Calvard's, Kittler and Illingworth's and Otsu's methods for image thresholding. *Pattern Recognit Lett* 33:793–797. doi:[10.1016/j.patrec.2012.01.002](https://doi.org/10.1016/j.patrec.2012.01.002)
- Yan H (1996) Unified formulation of a class of image thresholding techniques. *Pattern Recognit* 29:2025–2032. doi:[10.1016/S0031-3203\(96\)00050-7](https://doi.org/10.1016/S0031-3203(96)00050-7)
- Ye X, Zhang H, Wang C, Zhang B, Wu F, Tang Y (2013) SAR image change detection based on object-based method. In: Geoscience and Remote Sensing Symposium (IGARSS), 2013 IEEE International. Presented at the Geoscience and Remote Sensing Symposium (IGARSS), 2013 IEEE International, pp 2083–2086. doi:[10.1109/IGARSS.2013.6723222](https://doi.org/10.1109/IGARSS.2013.6723222)
- Yousif O, Ban Y (2014) Improving SAR-based urban change detection by combining MAP-MRF classifier and nonlocal means similarity weights. *IEEE J Sel Top Appl Earth Obs Remote Sens* 7:4288–4300. doi:[10.1109/JSTARS.205.2347171](https://doi.org/10.1109/JSTARS.205.2347171)
- Yousif O, Ban Y (2013) Improving urban change detection from multitemporal SAR images using PCA-NLM. *IEEE Trans Geosci Remote Sens* 51:2032–2041. doi:[10.1109/TGRS.2013.2245900](https://doi.org/10.1109/TGRS.2013.2245900)
- Zhou W, Troy A, Grove M (2008) A comparison of object-based with pixel-based land cover change detection in the Baltimore Metropolitan Area using multitemporal high resolution remote sensing data. In: IEEE international geoscience and remote sensing symposium. Presented at the IGARSS 2008, pp IV – 683–IV – 686. doi:[10.1109/IGARSS.2008.4779814](https://doi.org/10.1109/IGARSS.2008.4779814)

Chapter 6

Fusion of Multitemporal Spaceborne SAR and Optical Data for Urban Mapping and Urbanization Monitoring

Yifang Ban and Alexander Jacob

Abstract The overall objective of this research is to evaluate multitemporal spaceborne SAR and optical data for urban land cover mapping and urbanization monitoring. Multitemporal Sentinel-1A SAR and historical ERS SAR and ENVISAT ASAR data as well as HJ-1B multispectral data were acquired in Beijing, Chengdu and Nanchang, China where rapid urbanization has taken place. KTH-SEG, a novel object-based classification method is adopted for urban land cover mapping while KTH-Pavia Urban Extractor, a robust algorithm is improved for urban extent extraction and urbanization monitoring. The research demonstrates that, for urban land cover classification, the fusion of multitemporal SAR and optical data is superior to SAR or optical data alone. The second best classification result is achieved using fusion of 4-date SAR and one HJ-1B image. The results indicate that carefully selected multitemporal SAR dataset and its fusion with optical data could produce nearly as good classification accuracy as the whole multitemporal dataset. The results also show that KTH-SEG, the edge-aware region growing and merging segmentation algorithm, is effective for classification of SAR, optical and their fusion. KTH-SEG outperforms eCognition, the commonly used commercial software, for image segmentation and classification of linear features. For Urban extent extraction, single-date and multitemporal SAR data including ERS SAR, ENVISAT ASAR and Sentinel-1A SAR achieved very promising results in all study areas using the improved KTH-Pavia Urban Extractor. The results showed that urban areas as well as small towns and villages could be well extracted using multitemporal Sentinel-1A SAR data while major urban areas could be well extracted using a single-date single-polarization SAR image. The results clearly demonstrate that multitemporal SAR data are cost- and time-effective way for monitoring spatiotemporal patterns of urbanization.

Y. Ban (✉) • A. Jacob

Division of Geoinformatics, KTH Royal Institute of Technology, Stockholm, Sweden
e-mail: yifang@kth.se

6.1 Introduction

For the first time in history, more than half of the people on the planet live in cities. By 2050, the world is expected to add an additional 2.5 billion urban dwellers, with nearly 90 % of the increase concentrated in Asia and Africa. Just three countries—China, India and Nigeria—together are expected to account for 37 % of the projected growth of the world's urban population between 2014 and 2050 (United Nations 2014). China, the most populous country on earth, has been in transition from a largely rural society to a predominantly urban one since 1980s (Fig. 6.1). With the urbanization rate at 50 %, now China has 89 cities with a population of a million or more while the United States has 37 and India 32. As a result, huge areas of arable land, forest, and grassland, as well as numerous bodies of water, have been used in new ways to meet strong demand stemming from urbanization and industrial development. Although only a small percentage of global land cover, urban areas significantly alter climate, biogeochemistry, and hydrology at local, regional, and global scales (Seto et al. 2011). Cities are hot spots of production, consumption, and waste generation. According to the United Nations, cities are responsible for 75 % of global energy consumption and 80 % of greenhouse gas emissions (Ash et al. 2008). Thus, accurate and timely information on the current state of urban land cover as well as the rate and distribution of urbanization is of critical importance to support sustainable urban development.

Despite the growing importance of urban land in local, regional to global scale environmental studies, it remains extremely difficult to map urban areas at multi-scales due to the heterogeneous mix of land cover types in urban environments. At present, the information urban planners and decision makers needed to support planning activities are either dated or collected through time-consuming field survey or visual interpretation of images. With its synoptic view and the repeatability, remote sensing can reveal spatio-temporal growth trajectories of cities, thus allow a thorough understanding of the impacts of urbanization on ecosystems and

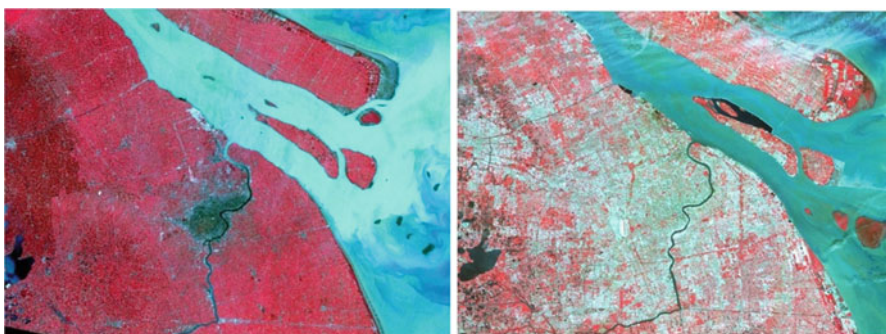


Fig. 6.1 Urbanization in Shanghai, *Left:* 1979 Landsat image; *Right:* 2010 HJ-1B image (Shanghai: dark grey in the center of 1979 image; light grey in 2010 image; Agriculture: red)

ecosystem services. Since the launch of Landsat-1 in 1972, a large number of earth observation (EO) satellites have been launched. With the recent launches of ESA Sentinel-1A/-B and Sentinel-2A, SAR and optical data with global coverage and operational reliability will become routinely available. They provide excellent opportunity to develop novel methods and algorithms for urban mapping and urbanization monitoring at local, regional and global scales.

Various studies have investigated the magnitude, patterns, and types of changes in urban regions with remote sensing images and spatially explicit data. However, the interpretation and analysis of urban land cover change using satellite imagery still presents many challenges because of the spatial and spectral heterogeneity of urban environment. Although urban areas could be extracted from time-series global land cover (GLC) databases, each of the datasets that have emerged during the last decade (e.g., GLC2000, GlobCover) suffers from limitations related to scale and definitional issues. Moreover, the maps differ by an order of magnitude in how they depict urban areas. The extreme variability in these estimates calls into question the accuracy of each map's depiction of urban and built-up land (Schneider et al. 2009). Using Landsat TM/ETM+ and HJ-1 data, China recently produced the first 30 m GLC maps, GlobeLand30 for 2000 and 2010 with a self-reported overall accuracy at 83 % (Chen et al. 2014, 2015). The artificial surface class was well extracted using a pixel-, object- and knowledge-based approach. These maps, however, took 4 years to produce at a very high cost. Using a fully automated approach, FROM GLC was also produced by China with a promising overall accuracy of 65 %. Several classes including impervious areas, however, were poorly classified. Some of the accuracies for impervious lands fall below 20 %, with a barely 10.5 % producer's accuracy and 30.8 % user's accuracy. In addition, for the 2010 classification, 74 % of all Landsat data were from 2006 to 2011 and majority of the data were from non-summer season (Gong et al. 2013). Therefore, there is an urgent need to development effective method for extracting and monitoring urban areas from satellite data in a timely, accurate and consistent manner.

Single-date and multitemporal SAR data have been increasingly used in urban applications for mapping urban extent (e.g., Ban et al. 2015; Esch et al. 2011, 2013; Gamba and Lisini 2013), urban land-cover classification (e.g., Hu and Ban 2012; Niu et al. 2015), and change detection (e.g., Ban and Yousif 2012; Yousif and Ban 2013). In terms of SAR data used, various multitemporal spaceborne SAR data in single polarization (e.g., Hu and Ban 2012), dual polarization (e.g., Ban and Jacob 2013), and full polarimetry (e.g., Niu and Ban 2012) have been evaluated for urban applications. In terms of SAR processing and feature extraction methods, texture measures (e.g., Dekker 2003; Pellizzeri et al. 2003), contextual information (e.g., Niu and Ban 2012, 2014), and classification algorithms such as statistical (e.g., Lombardo et al. 2003) neural network (e.g., Bruzzone et al. 2004), support vector machine (SVM) (Niu and Ban 2013a; Waske and Benediktsson 2008), knowledge-based, and rule-based approaches (e.g., Niu and Ban 2013b), have been investigated for urban mapping with varying degree of success.

Pixel-based methods have been commonly employed for image classification and information extraction. However, for high resolution optical and SAR data,

pixel-based approach often results in “pepper-salt” effects due to the high variance of the pixel values. Object-based methods, on the other hand, have been increasingly adopted in urban and land cover using high-resolution optical data (Blaschke 2010), SAR data (e.g. Hu and Ban 2012; Niu and Ban 2013a) and fusion of SAR and optical data (e.g. Ban et al. 2010) since more information such as object features and spatial relationships could be explored in the analysis thus improved classification accuracy. The existing automatic image segmentation techniques can be classified into four approaches, namely, (1) thresholding techniques, (2) boundary-based methods, (3) region-based methods, and (4) hybrid techniques. The pros and cons of the techniques are discussed in Blaschke (2010) and Fan et al. (2001). The most commonly used segmentation methods is region growing and merging in eCognition (Blaschke 2010). Such method often results in segments growing across region boundaries. Boundary-based methods using edge detection such as Canny edge detector are also explored for image segmentation (Senthilkumaran and Rajesh 2009). Several studies found that integrating edge and region detection can produce better segmentation of images (Yu and Clausi 2008; Yu et al. 2012) than region-based and boundary-based method. However, these studies used relatively simple images such as photographs of faces, flowers and buildings, not the complex Spaceborne SAR and optical data in challenging urban, land cover and coastal water environments. Therefore, further research is needed to develop robust methods for segmentation of SAR and optical data that integrates edge detection and region growing and merging. An initial study showed promising results using KTH-SEG, an edge-aware region growing and merging algorithm (Ban and Jacob 2013). Further development of this method are needed to make it more robust, automatic and with multi-resolution segmentation capability.

Very high resolution optical and/or SAR imagery and object-based approaches dominate urban remote sensing at the local level (e.g., Gong et al. 1992; Jacquin et al. 2008; Ban et al. 2010; Moran 2010; Gamba et al. 2011; Hu and Ban 2012; Haas and Ban 2016) while Landsat, ENVISAT ASAR, MERIS as well as MODIS or nighttime light data and pixel-based techniques are mostly used for regional and global analysis (e.g., Elvidge et al. 2010; Esch et al. 2010; Schneider et al. 2010; Wang et al. 2010; Zhang and Seto 2011; Taubenböck et al. 2012; Gamba and Lisini 2013; Haas and Ban 2014). One of the recent developments are moving towards global urban extraction using optical data at very high spatial resolution. For examples, Pesaresi et al. (2011) developed a texture-based algorithm to extract urban extent of over 40 cities around the globe using Ikonos and QuickBird panchromatic data resampled to a nominal resolution at 10 m. The technique is promising, but true global mapping with such data remains a challenge due to the huge amount of data and computations involved as well as data availability issue due to cloud cover. Compared to optical data, SAR data have not been equally explored in urban applications due to the complexity of their interactions with diverse urban features. With its all-weather/illumination capability and its unique information content, however, SAR data have been increasingly investigated for

global urban extent extraction at various spatial resolutions with promising results. For examples, Gamba et al. (2011) developed a method to extract global urban area extent from SAR images. The method has been tested in different set of SAR images produced using different sensors with different spatial resolutions that cover different cities around the world with promising results. Esch et al. (2012 and 2013), on the other hand, developed a method to extract global urban settlement from TanDEM-X images at 12 m spatial resolution. The proposed methodology was evaluated using images from several cities with an overall accuracy up to 94.8 % achieved. The Global Urban Footprints (GUF) produced by DLR showed promising results, but the final products are yet to be publically available. Recently, Ban et al. (2015) developed a robust processing chain, the KTH-Pavia Urban Extractor, using ENVISAT ASAR data and very good results were achieved in ten global cities. It is desirable to improve the Urban Extractor for effective urban mapping and urbanization monitoring using Sentinel data.

Furthermore, the fusion of SAR and optical data has been proven advantageous by making use of the complementary nature of the data acquired by different sensors. Both SAR and optical data have their own merits and limitations, thus the fusion of SAR and optical data can overcome the deficiencies associated with a single sensor. Various studies have been conducted for urban land-cover mapping and change detection using fusion of SAR and optical data (e.g., Amarsaikhan and Douglas 2004; Ban et al. 2010; Ban and Jacob 2013; Ban et al. 2014; Gamba and Houshmand 2001; Gamba and Aldrighi 2012; Griffiths et al. 2010; Waske and Linden 2008; Zhu et al. 2012). It was demonstrated that feature- and decision-level fusion of multi-source data could achieve higher accuracy for classification and object recognition than the use of single source data. Therefore, the objective of this research to investigate the fusion of multitemporal spaceborne SAR and optical data for urban mapping and urbanization monitoring.

6.2 Study Areas and Data Description

6.2.1 Study Areas

The study areas include Beijing, Chengdu and Nanchang where rapid urbanization has taken place in the past three decades. Beijing, the capital of China, is currently China's second largest and the world's eighth largest city with a population of 19.5 million in 2014 and the city is expected to grow further up to 25.7 million citizens until 2030, making it the world's fifth largest city (United Nations 2014). Chengdu, the capital of Sichuan province, is the fifth-most populous agglomeration in China. Nanchang, the capital of Jiangxi province, has 5 million inhabitants. The major land cover classes include high-density builtup areas, low-density builtup areas urban green spaces, golf courses, agricultural fields, forest and water bodies.

6.2.2 Data Description

For urban extent extraction and urbanization monitoring, multitemporal multi-resolution Sentinel-1A SAR acquired in Interferometric Wide swath mode (IW) at 20 m resolution were acquired in Beijing in 2015 during the vegetation season to maximize the difference between urban and rural areas. One date Sentinel-1A SAR Multi-date, dual-polarization SAR data from both ascending and descending orbit were selected to evaluate the potential of SAR data for improved urban extraction and urban change detection. Historical ENVISAT ASAR and ERS-1/2 SAR data were also collected in Beijing for urbanization monitoring. The Sentinel-1A SAR and historical SAR images used in Beijing are listed in Table 6.1. For urban extent extraction and urbanization monitoring, multitemporal ERS-1/2 SAR and ENVISAT ASAR acquired in 1998, 2003, 2008 and 2011 were selected Chengdu while one Sentinel-1A C-HH SAR image acquired on May 12, 2014 and one ENVISAT ASAR C-HH image acquired on April 19, 2006 were used in Nanchang (Fig. 6.2).

For urban land cover mapping, six-date ENVISAT ASAR images with multiple incidence angle, alternating polarization (HH/VV), and single polarization (VV) at 12.5 m pixel spacing (30 m resolution) were acquired from May to September, 2009. All SAR images were in ascending orbit except one. The data set contains four ASAR beam modes with incidence angles ranging from 20° to 45°. Table 6.2 shows the characteristics of the ASAR images used in this research. One scene of HJ-1B charge-coupled device (CCD) image acquired on May 12, 2009, was selected for this research since no images were acquired during the peak vegetation season when confusion between urban classes and bare fields can be reduced. The early season image also presents an opportunity for research into the role of SAR in improving land-cover classification of optical data acquired in non-optimal season as this is

Table 6.1 Multitemporal SAR images acquired in Beijing

Satellite	Sensor	Polarization	Beam mode	Orbit	Acquisition date
Sentinel-1A	SAR	VV/VH	IW	D	2015-05-24
Sentinel-1A	SAR	VV/VH	IW	D	2015-06-05
Sentinel-1A	SAR	VV/VH	IW	D	2015-06-17
Sentinel-1A	SAR	VV/VH	IW	D	2015-07-23
Sentinel-1A	SAR	VV/VH	IW	A	2015-07-30
Sentinel-1A	SAR	VV/VH	IW	A	2015-08-23
Sentinel-1A	SAR	VV/VH	IW	D	2015-09-09
Sentinel-1A	SAR	VV/VH	IW	D	2015-09-16
Sentinel-1A	SAR	VV/VH	IW	A	2015-10-03
Sentinel-1A	SAR	VV/VH	IW	A	2015-10-10
ENVISAT	ASAR	VV	IS2	D	2008
ERS-2	SAR	VV	IM	D	1998

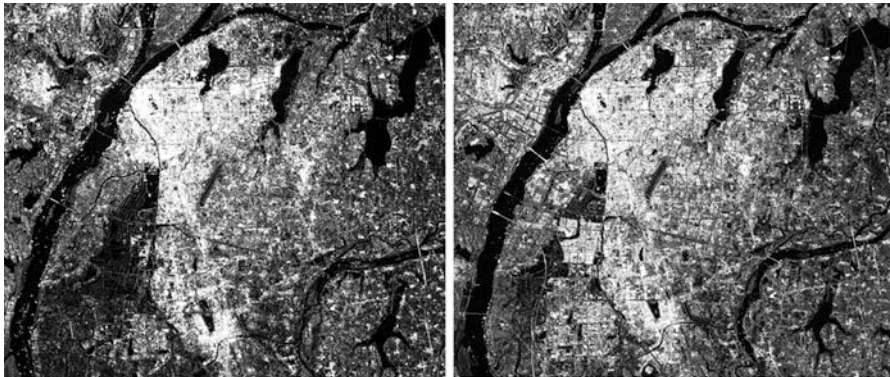


Fig. 6.2 Multitemporal Nanchang images: *Left*: 2006 ENVISAT ASAR; *Right*: 2014 Sentinel-1A SAR

Table 6.2 Multitemporal ENVISAT ASAR images acquired in Beijing

Satellite	Sensor	Polarization	Beam mode	Orbit	Acquisition date
ENVISAT	ASAR	HH/VV	IS2	A	2009-05-17
ENVISAT	ASAR	HH/VV	IS2	D	2009-05-27
ENVISAT	ASAR	HH/VV	IS4	A	2009-06-08
ENVISAT	ASAR	HH/VV	IS6	A	2009-06-11
ENVISAT	ASAR	VV	IS7	A	2009-08-04
ENVISAT	ASAR	VV	IS7	A	2009-09-08

often the case in many parts of the world due to cloud cover. HJ-1B stands for Disaster and Environment Monitoring and Forecast Small Satellite Constellation B, which is one of the small Chinese Earth observation satellites. Launched on September 6, 2008, HJ-1B payloads include a CCD camera that acquires images in blue, green, red, and near-infrared parts of the spectrum at 30-m resolution and an infrared camera (CEOS 2011). The ENVISAT ASAR multitemporal composite and HJ-1B images are shown in Fig. 6.3.

Field data, existing land cover maps as well as high resolution Google images were used for calibration and validation.

6.3 Methodology

The methodology in this research involves multitemporal analysis of spaceborne SAR and optical data as well as historical SAR data including image preprocessing, object-based image classification, urban extent extraction, change detection and validation/accuracy assessment.



Fig. 6.3 Multitemporal Beijing images, *Left*: ENVISAT ASAR; *Right*: HJ-1B Multispectral

6.3.1 *Image Preprocessing*

In order to evaluate and compare satellite data from different sensors and different dates, each image must be georeferenced to a common database by orthorectification using satellite orbital models and the 30 m Shuttle Radar Topographic Mission (SRTM) digital elevation model (DEM).

Multitemporal speckle filtering was then performed on all SAR data to remove speckle. After that, the SAR data were linearly scaled to 8 bits to enhance the contrast between urban and non-urban areas for urban extraction and to reduce computation cost.

6.3.2 *Urban Land Cover Classification with KTH-SEG*

KTH-SEG algorithm is selected for urban land cover classification for its edge-aware feature in region growing and merging and its ability to effectively segment both SAR and multispectral data (Ban and Jacob 2013). KTHSEG is based on an edge-aware region growing and merging algorithm. For edge detection a canny edge detector is applied on every image and a majority voting is used to derive the final edge. This layer is then used to enhance the region growing and merging stage of the segmentation procedure. Therefore region growing is performed along edges and offside the edges. As different ground features have different object size, multi-resolution segmentation is being investigated. To handle large volume of data, parallel computing is also implemented making use of an advanced tiling scheme that avoids edge effects between the borders of two different adjacent tiles. The growing phase can hence easily be parallelized and every tile is segmented by

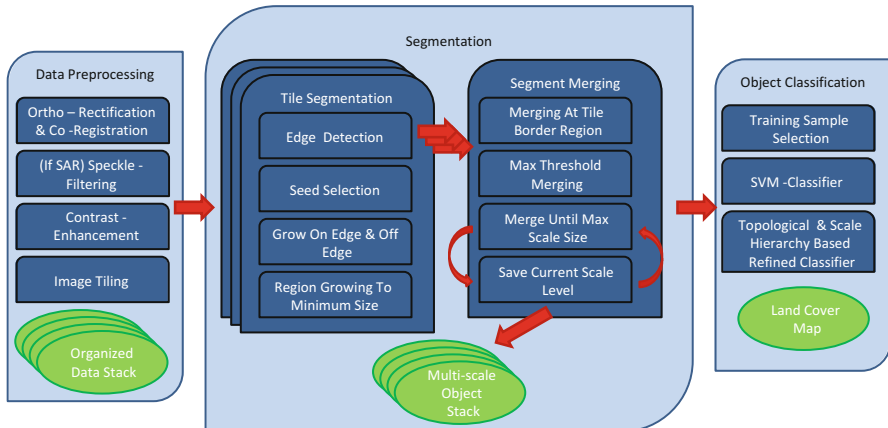


Fig. 6.4 KTH-SEG: multi-resolution edge-aware region growing and merging algorithm

itself first before merging into a bigger context of the adjacent tiles and regions. Support Vector Machines (SVM) is selected for post-segmentation classification as it has been proven superior to other classifiers in classification of multisensor, high-dimensional data. For benchmarking, the eCognition is used for assessing the quality of the segmentation from KTH-SEG. The methodology workflow of KTH-SEG is presented in Fig. 6.4.

6.3.3 *Urban Extent Extraction*

The KTH-Pavia Urban Extractor, the processing chain for urban extent extraction includes urban extraction based on spatial indices and Grey Level Co-occurrence Matrix (GLCM) textures, and SAR and optical data preprocessing, enhancement, and post-processing. The method is based on Local Indicators of Spatial Association (L.I.S.A.), including the Moran index, the Geary index and the Getis-Ord index, and Grey Level Co-occurrence Matrices (GLCM) variance and correlation textures. For Sentinel-1A SAR data, the dissimilarity texture is used instead of correlation. Preprocessing includes orthorectification, speckle filtering and scaling. Post-processing include mountain removal using the 30 m SRTM DEM and fusion of various urban extraction results using logical operators or majority voting (MV). The detailed methodology can be found in Fig. 6.5 below. The method has been tested on ENVISAT ASAR data, and the results showed urban areas can be automatically extracted in good accuracy with only 1–2 ASAR images (Ban et al. 2015). The method workflow of the KTH-Pavia Urban Extractor is presented in Fig. 6.5.



Fig. 6.5 Overview of the KTH-Pavia urban extractor for urban extent extraction

6.3.4 Accuracy Assessment

The urban land cover classifications, urban extent maps and urban changes are preliminarily validated using random sampling based on high resolution Google images and field survey. Rigorous validation are planned using more validation samples and in comparison with existing reliable land cover maps.

6.4 Results and Discussion

6.4.1 Fusion of Multitemporal SAR and Optical Data for Urban Land Cover Classification

The classification results for various combinations of multitemporal ENVISAT ASAR data and their fusion with HJ-1B multispectral data are presented in Table 6.3. The results show that the more multitemporal images are used, the better the SAR classification. The best classification accuracy (overall: 65.1 %, kappa: 0.61) is achieved using the whole multitemporal ASAR dataset while the second best accuracy (overall: 59 %, kappa: 0.54) is using 4-date SAR in both ascending and descending orbits. The best fusion result is achieved using all multitemporal

Table 6.3 Urban land cover classification accuracies in Beijing: a comparison

May 17	May 27	Jun. 8	Jun. 11	Aug. 04	Sept. 8	May 12	Overall accuracy	Kappa	Name
IS2 A	IS2 D	IS4 A	IS6 A	IS7 A	IS7 A	HJ-1B			
x	x						47.3	0.41	
	x		x				48.3	0.42	
x				x	x		50.6	0.44	
		x		x	x		53.4	0.48	
		x	x				53.9	0.48	
x	x		x	x			54.5	0.49	
			x	x	x		53.1	0.47	
	x	x					54.6	0.49	
x		x	x	x	x		54.4	0.49	ASC only
	x	x	x	x	x		56.9	0.52	ASC + DSC
x	x	x	x	x	x		56.9	0.52	
x			x	x	x		56.5	0.51	
x	x	x		x	x		59.0	0.54	4-Date SAR
x	x	x	x	x	x		65.1	0.61	All SAR
						x	70.6	0.67	Hj-1B only
x	x			x	x	x	74.1	0.71	Fusion red
x	x	x	x	x	x	x	75.5	0.72	Fusion all

SAR data and HJ-1B optical data at 75.5 % (kappa: 0.72), much better than the optical (overall: 70.6 %, kappa: 0.67) or SAR classification alone. Similar to the multitemporal SAR classification, the second best fusion result is achieved using the 4-date SAR data and HJ-1B data. These results clearly demonstrated that multitemporal SAR data could complement the optical data and improve urban land cover classification. Figure 6.6 presents the comparisons of the various results in Beijing International Airport. For examples, the new terminal on Beijing International Airport is shown in the encircled area on the right. This could easily be identified as a building using SAR data (B) but was classified as bare soil when using optical data (E). In lower-left corner of the encircled area shows the confusion among low backscatter classes such as airport runways, water, golf courses and roads, a problem of the SAR classification (B). These were much better separated in the optical result (E). When looking at these areas in the fusion result (C) it is evident that both confusions are mostly resolved, demonstrating a good synergy of the SAR and optical data. In (F) the best classification result based on the segments from eCognition is shown. The accuracy of the eCognition result is around 5 % lower than the best result from KTH-SEG. A possible reason for this could be that, attributed to edge detection, the segments of KTH-SEG find better boundaries especially for small linear features such as roads and rivers (see the river and the golf course in the left encircled area in C and F in Fig. 6.6).

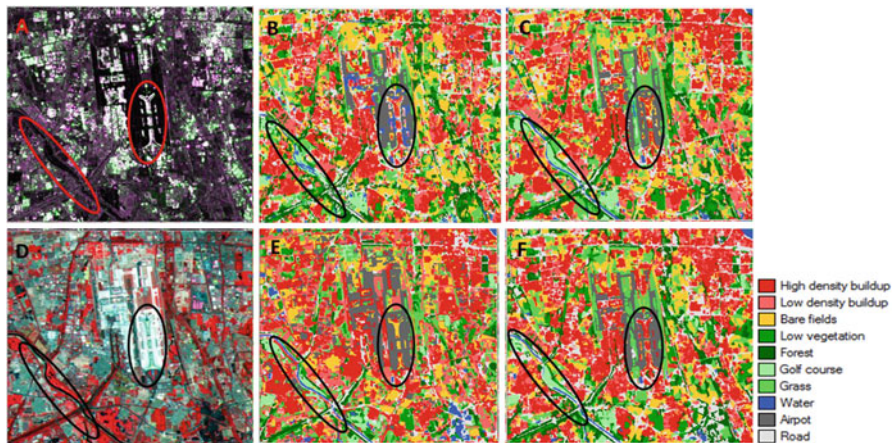


Fig. 6.6 Classification comparison in Beijing International Airport, (a): SAR image; (b): All SAR; (c): Fusion; (d): Optical Image; (e): Optical Alone; (f): eCognition

6.4.2 Multitemporal SAR Data for Urban Extent Mapping and Urbanization Monitoring

Figure 6.7 presents the urban extent extractions in Beijing using a single-date Sentinel-1A IW C-VV SAR acquired on May 24, 2015 as well as the multitemporal average Sentinel-1A SAR in both ascending and descending orbits during May to October, 2015. The results demonstrate that urban areas could be well extracted using a single-date single-polarization Sentinel-1A SAR data. However, the small towns and villages outside Beijing are under-estimated. Using the multitemporal average of Sentinel-1A SAR data in dual polarization from both ascending and descending orbits, urban areas as well as small towns and villages are well extracted. Visual comparison with 2010 GlobeLand30's artificial surface layer showed very good match except the new buildup areas during 2010 and 2015. Rigorous validation are being conducted using 10 000 random sampled pixels for urban/non-urban respectively and accuracy assessment are expected to be reported in the near future.

Urban extent extractions were also performed using historic ERS-2 SAR and ENVISAT ASAR SAR images with very good results. Figure 6.8 shows the urbanization patterns in Beijing during 1998 to 2015. It is observed that urban areas expended rapidly in Beijing during 1998 and 2003 as shown in A and B in Fig. 6.8. Urban expansions continue in the urban-rural fringe during 2003–2015, but they are outside the subset shown in Fig. 6.8. In the Olympic Park area, some buildings were built during 1998–2003, but then removed to built the Olympic Park during 2003–2008. Figure 6.9 shows the successful extraction of urban areas and the changes detected using 2014 Sentinel-1A SAR and 2006 ENVISAT ASAR data. Both new buildup areas, marked by the black oval, and smaller changes such as new bridges, the linear features inside the blue ovals are well extracted.

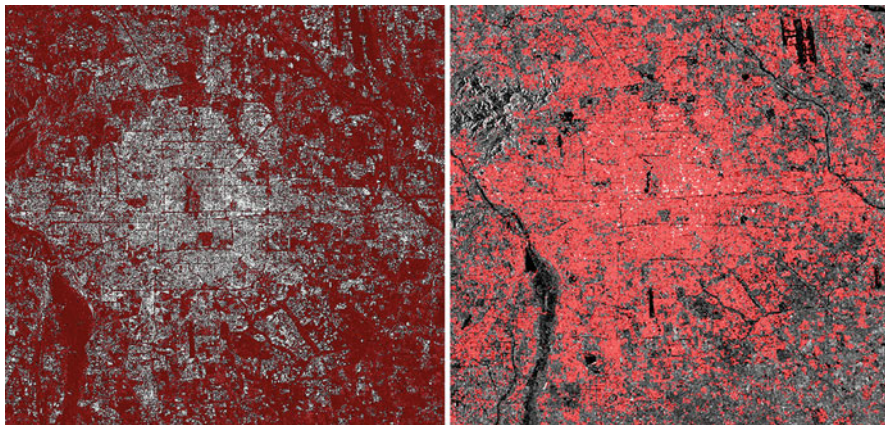


Fig. 6.7 Urban extent extraction in Beijing: *Left*: Extraction from a Single Date SAR (2015-05-24, C-VV); *Right*: Extraction from 2015 Multitemporal Average SAR

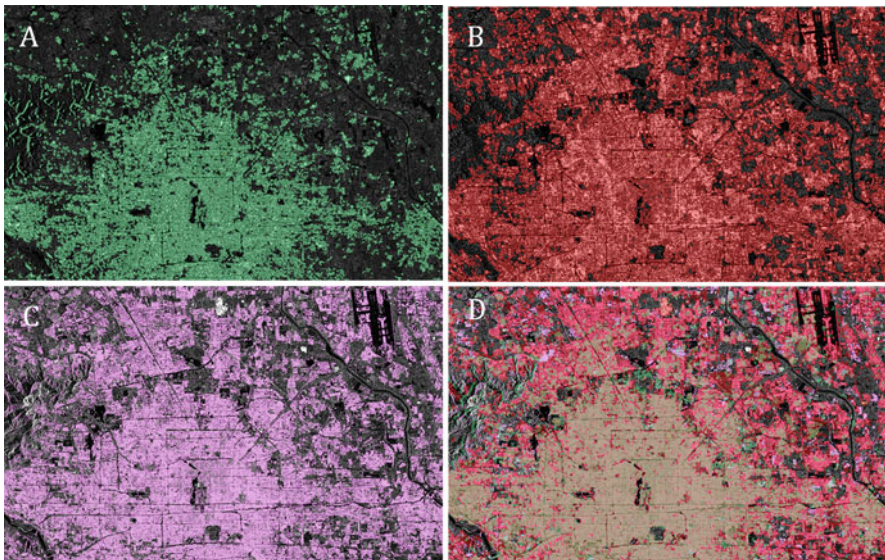


Fig. 6.8 Urban extraction in Beijing from SAR Data. (a): 1998 ERS-2; (b): 2008 ENVISAT ASAR; (c): 2015 Sentinel-1A SAR. (d): Change analysis result. ■ Buildings removed after 1998; ■ Buildings removed after 2008; ■ Buildings added between 1998 and 2008; ■ Buildings added between 2008 and 2015; ■ Agreement 1998–2015

Figure 6.10 presents the urbanization trend in Chengdu During 1998 to 2011, extracted from multitemporal SAR images. The time series clearly show that Chengdu expanded rapidly during the past two decades, connecting isolated satellite towns into a continuous urban area.

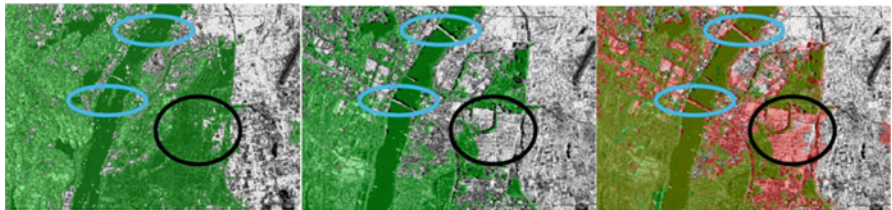


Fig. 6.9 Urban extraction and change detection in Nanchang. *Left:* 2006; *Center:* 2014, *Right:* Change with differences in Red)

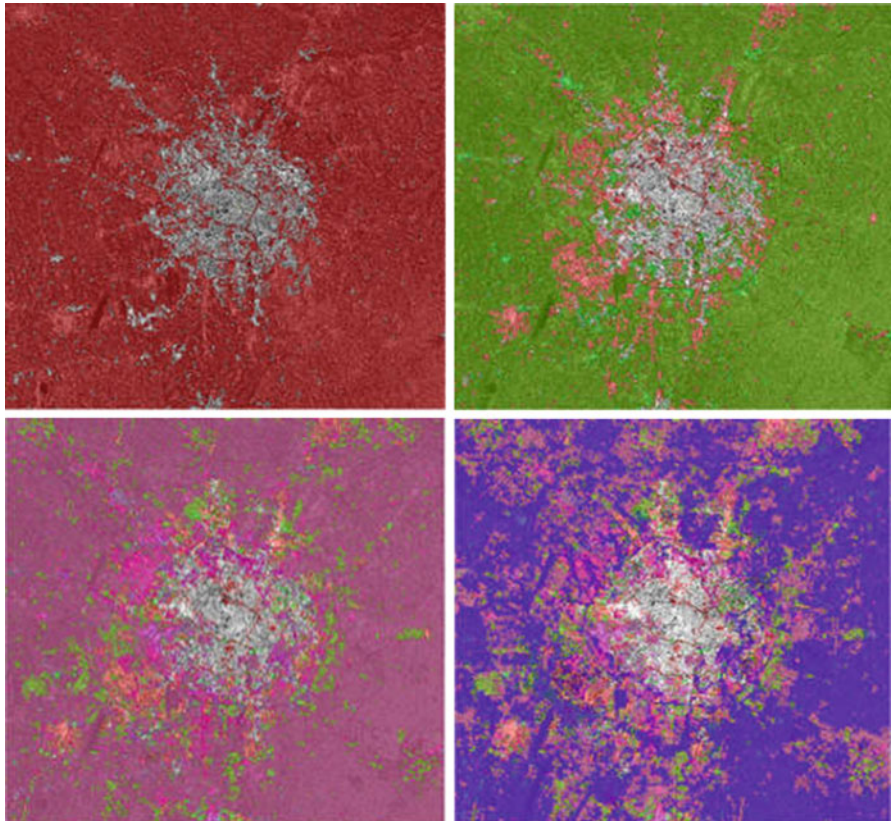


Fig. 6.10 Urbanization seen from SAR. *Upper Left:* Chengdu in 1998; *Upper Right:* Urban expansion from 1998 to 2003 in Red; *Lower Left:* 1998 to 2003 to 2008; *Lower Right:* 1998 to 2003 to 2008 to 2011, the cumulative changes between the years

6.5 Conclusions

The research demonstrates that the fusion of multitemporal SAR and optical data is superior to SAR or optical data alone for urban land cover classification. Fusion of 4-date SAR and one HJ-1B image could achieve almost as good classification accuracy as the whole multitemporal dataset. The results also show that the edge-aware region growing and merging segmentation algorithm, KTH-SEG, performs very well on SAR, optical and their fusion. KTH-SEG outperforms eCognition, the commonly used commercial software, for image segmentation and classification of linear features. For Urban extent extraction, single-date and multitemporal spaceborne SAR data including ERS SAR, ENVISAT ASAR and Sentinel-1A SAR achieved very promising results in Beijing, Chengdu and Nanchang using the improved KTH-Pavia Urban Extractor. The results clearly show that the SAR time series data are cost- and time-effective way for monitoring urbanization patterns and detecting urban changes.

Acknowledgement This research is part of the EO4Urban project funded by the ESA DUE INNOVATOR III program. It is also part of the ‘Urbanization and Environment/Climate’ project within the ESA/MOST, China’s joint Dragon III program. The authors thank Osama Yousif and Marvin Mc Cutchan for their assistance in this research

References

- Amarsaikhan D, Douglas T (2004) Data fusion and multisource image classification. *Int J Remote Sens* 25(17):3529–3539
- Ash C, Jasny BR, Roberts L, Stone R, Sugden AM (2008) Reimagining cities. *Science* 319:739
- Ban Y, Yousif O, Hu H (2014) Fusion of SAR and optical data for urban land cover mapping and change detection. In: Weng Q (ed) Global urban monitoring and assessment through earth observation. Taylor & Francis Group, LLC
- Ban Y, Jacob A (2013) Object-based fusion of multitemporal multiangle ENVISAT ASAR and HJ-1B multispectral data for urban land-cover mapping. *IEEE Trans Geosci Remote Sens* 51(4):1998–2006
- Ban Y, Yousif OA (2012) Multitemporal spaceborne SAR data for urban change detection in China. *IEEE J Select Topics Appl Earth Observ Remote Sens (JSARS)* 5(4):1087–1094
- Ban Y, Hu H, Rangel I (2010) Fusion of QuickBird MS and RADARSAT-1 SAR data for land-cover mapping: object-based and knowledge-based approach. *Int J Remote Sens* 31(6):1391–1410
- Ban Y, Jacob A, Gamba P (2015) Spaceborne SAR data for global urban mapping at 30 m resolution using a robust urban extractor. *ISPRS J Photogramm Remote Sens Spec Issue Glob Land Cov Map* 103:28–37
- Blaschke T (2010) Object based image analysis for remote sensing. *ISPRS J Photogramm Remote Sens* 65(1):2–16
- Bruzzone L, Marconcini M, Wegmüller U, Wiesmann A (2004) An advanced system for the automatic classification of multitemporal SAR images. *IEEE Trans Geosci Remote Sens* 42(6):1321–1334
- CEOS (2011) CEOS EO handbook—mission summary—HJ-1B. CEOS, Washington, DC. [Online]. Available: <http://database.eohandbook.com/database/missionsummary.aspx?missionID=464>

- Chen J, Ban Y, Li S (2014) China: open access to earth land-cover map. *Nature* 514(7523):434–434
- Chen J, Jin Chen, Liao A, Xin Cao, Lijun Chen, Xuehong Chen, Chaoying He, Gang Han, Shu Peng, Miao Lu, Weiwei Zhang, Xiaohua Tong, Jon Mills (2015) Global land cover mapping at 30 m resolution: a POK-based operational approach. *ISPRS J Photogramm Remote Sens* 103:7–27, ISSN 0924–2716
- Dekker RJ (2003) Texture analysis and classification of ERS SAR images for map updating of urban areas in The Netherlands. *IEEE Trans Geosci Remote Sens* 41(9):1950–1958
- Elvidge CD, Sutton PC, Tuttle BT, Ghosh T, Baugh KE (2010) Global urban mapping based on nighttime lights. In: *Global mapping of human settlements*. Taylor and Francis, London, pp 129–144
- Esch T, Thiel M, Schenk A, Roth A, Muller A, Dech S (2010) Delineation of urban footprints from TerraSAR-X data by analyzing speckle characteristics and intensity information. *IEEE Trans Geosci Remote Sens* 48(2):905–916
- Esch T, Schenk A, Ullmann T, Thiel M, Roth A, Dech S (2011) Characterization of land cover types in TerraSAR-X images by combined analysis of speckle statistics and intensity information. *IEEE Trans Geosci Remote Sens* 49(6):1911–1925
- Esch T, Taubenböck H, Roth A, Heldens W, Felbier A, Thiel M, Schmidt M, Müller A, Dech S (2012) TanDEM-X mission—new perspectives for the inventory and monitoring of global settlement patterns. *J Appl Remote Sens* 6(1):061702–1–061702–21
- Esch T, Marconcini M, Felbier A, Roth A, Heldens W, Huber M, Dech S (2013) Urban footprint processor—fully automated processing chain generating settlement masks from global data of the TanDEM-X mission. *IEEE Geosci Remote Sens Lett* 10(6):1617–1621
- Fan J, Yau DY, Elmagarmid AK, Aref WG (2001) Automatic image segmentation by integrating color-edge extraction and seeded region growing. *IEEE Trans Image Process* 10(10):1454–66. doi:[10.1109/83.951532](https://doi.org/10.1109/83.951532)
- Gamba P, Aldrighi M (2012) SAR data classification of urban areas by means of segmentation techniques and ancillary optical data. *IEEE J SelectTopics Appl Earth Observ Remote Sens* 5(4):1140–1148
- Gamba P, Houshmand B (2001) An efficient neural classification chain of SAR and optical urban images. *Int J Remote Sens* 22(8):1535–1553
- Gamba P, Lisini G (2013) Fast and efficient urban extent extraction using ASAR wide swath mode data. *IEEE J SelectTopics Appl Earth Observ Remote Sens* 6(5):2184–2195
- Gamba P, Aldrighi M, Stasolla M (2011) Robust extraction of urban area extents in HR and VHR SAR images. *IEEE JSTARS* 4(1):27–34
- Gong P, Marceau DJ, Howarth PJ (1992) A comparison of spatial feature extraction algorithms for land-use classification with SPOT HRV data. *Remote Sens Environ* 40(2):137–151
- Gong P, Wang J, Yu L, Zhao Y, Zhao Y, Liang L, Chen J (2013) Finer resolution observation and monitoring of global land cover: first mapping results with Landsat TM and ETM+ data. *Int J Remote Sens* 34(7):2607–2654
- Griffiths P, Hostert P, Gruebner O, van der Linden S (2010) Mapping megacity growth with multi-sensor data. *Remote Sens Environ* 114(2):426–439
- Haas J, Ban Y (2014) Urban growth and environmental impacts in Jing-Jin-Ji, the Yangtze River Delta and the Pearl River Delta. *Int J Appl Earth Obs Geoinf* 30:42–55
- Haas J, Ban Y (2016) Mapping and monitoring urban ecosystem services using multitemporal high-resolution satellite data. *IEEE J Select Topics Appl Earth Observ Remote Sens* PP(99):1–13. doi:[10.1109/JSTARS.2016.2586582](https://doi.org/10.1109/JSTARS.2016.2586582). <http://ieeexplore.ieee.org/document/7536135/>
- Hu H, Ban Y (2012) Multitemporal RADARSAT-2 Ultra-Fine-Beam SAR data for urban land cover classification. *Can J Remote Sens* 38(01):1–11
- Jacquin A, Misakova L, Gay M (2008) A hybrid object based classification approach for mapping urban sprawl in periurban environment. *Landscape Urban Plan* 84:152–165
- Lombardo P, Sciotti M, Pellizzeri TM, Meloni M (2003) Optimum model-based segmentation techniques for multifrequency polarimetric SAR images of urban areas. *IEEE Trans Geosci Remote Sens* 41(9):1959–1975

- Moran EF (2010) Land cover classification in a complex urban-rural landscape with Quickbird imagery. *Photogramm Eng Remote Sens* 76(10):1159–1168
- Niu X, Ban Y (2012) An adaptive contextual SEM algorithm for urban land cover mapping using multitemporal high-resolution polarimetric SAR data. *IEEE J Sel Topics Appl Earth Observ Remote Sens* 5(4):1129–1139
- Niu X, Ban Y (2013a) Multi-temporal RADARSAT-2 polarimetric SAR data for urban land-cover classification using an object-based support vector machine and a rule-based approach. *Int J Remote Sens* 34(1):1–26
- Niu X, Ban Y (2013b) Multitemporal polarimetric RADARSAT-2 SAR data for urban land cover mapping through a dictionary-based and a rule-based model selection in a contextual SEM algorithm. *Can J Remote Sens* 39(02):138–151
- Niu X, Ban Y (2014) A novel contextual classification algorithm for multitemporal polarimetric SAR data. *IEEE Transac GeoSci Remote Sens Lett* 11(3):681–685
- Niu X, Ban Y, Dou Y (2015) RADARSAT-2 fine-beam polarimetric and ultra-fine-beam SAR data for urban mapping: comparison and synergy. *Int J Remote Sens* 37(12):2810–2830. doi:[10.1080/01431161.2015.1054050](https://doi.org/10.1080/01431161.2015.1054050)
- Pellizzetti TM, Gamba P, Lombardo P, Dell'Acqua F (2003) Multitemporal/multiband SAR classification of urban areas using spatial analysis: statistical versus neural kernel-based approach. *IEEE Trans Geosci Remote Sens* 41(10):2338–2353
- Pesaresi M, Ehrlich D, Caravaggi I, Kauffmann M, Louvrier C (2011) Toward global automatic built-up area recognition using optical VHR imagery. *IEEE JSTARS* 4(4):923–934
- Schneider A, Friedl MA, Potere D (2009) A new map of global urban extent from MODIS satellite data. *Environ Res Lett* 4(4):044003-1–044003-11
- Schneider A, Friedl MA, Potere D (2010) Mapping global urban areas using MODIS 500-m data: new methods and datasets based on ‘urban ecoregions’. *Remote Sens Environ* 114(8): 1733–1746
- Senthilkumar N, Rajesh R (2009) Edge detection techniques for image segmentation—a survey of soft computing approaches. *Int J Recent Trends Eng* 1(2):250–254
- Seto KC, Fragkias M, Güneralp B, Reilly MK (2011) A meta-analysis of global urban land expansion. *PLoS One* 6(8), e23777
- Taubenböck H, Esch T, Felbier A, Wiesner M, Roth A, Dech S (2012) Monitoring urbanization in mega cities from space. *Remote Sens Environ* 117:162–176
- United Nations (2014) World urbanization prospects the 2014 revision. United Nations, Department of Economic and Social Affairs (DESA), Population Division, Population Estimates and Projections Section, New York
- Wang L, Gong P, Ying Q, Yang Z, Cheng X, Ran Q (2010) Settlement extraction over north china plain with landsat and Beijing-1 data using an improved watershed segmentation algorithm. *Int J Remote Sens* 31(6):1411–1426
- Waske B, Benediktsson JA (2008) Fusion of support vector machines for classification of multisensor data. *IEEE Trans Geosci Remote Sens* 45(12):3858–3866
- Waske B, Linden VDS (2008) Classifying multilevel imagery from SAR and optical sensors by decision fusion. *IEEE Trans Geosci Remote Sens* 46(5):1457–1466
- Yousif OA, Ban Y (2013) Improving urban change detection from multitemporal SAR images using PCA-NLM. *IEEE Transac Geosci Remote Sens* 51(4):2032–2041
- Yu Q, Clausi DA (2008) IRGS: image segmentation using edge penalties and region growing. *IEEE Trans Pattern Anal Mach Intell* 30(12):2126–2139
- Yu P, Qin AK, Clausi DA (2012) Unsupervised polarimetric SAR image segmentation and classification using region growing with edge penalty. *IEEE Trans Geosci Remote Sens* 50(4):1302–1317
- Zhang Q, Seto KC (2011) Mapping urbanization dynamics at regional and global scales using multi-temporal DMSP/OLS nighttime light data. *Remote Sens Environ* 115(9):2320–2329
- Zhu CE, Woodcock JR, Kellndorfer J (2012) Assessment of spectral, polarimetric, temporal, and spatial dimensions for urban and peri-urban land cover classification using landsat and SAR data. *Remote Sens Urban Environ* 117:72–82

Chapter 7

Post-classification Change Detection in Arctic Glaciers by Multi-polarization SAR

Vahid Akbari, Anthony P. Doulgeris, and Torbjørn Eltoft

Abstract This chapter presents a method for post-classification change detection in Arctic glaciers from multi-polarization synthetic aperture radar images. We produce terrain corrected multilook complex (MLC) covariance data by including the effects of topography on both geolocation and SAR radiometry, as well as azimuth slope variations on polarization signature. An unsupervised contextual non-Gaussian clustering algorithm is employed for segmentation of each terrain corrected polarimetric SAR image and subsequently labeled with the aid of ground truth data into glacier facies. We demonstrate the consistency of the segmentation algorithm by characterizing the expected random error level for different SAR acquisition conditions. This allows us to determine whether an observed variation is statistically significant and therefore can be used for post-classification change detection of Arctic glaciers. Subsequently, the average classified images of succeeding years are compared, and changes are identified as the detected differences in the location of boundaries between glacier facies. In the current analysis, a series of dual polarization C-band ENVISAT ASAR images over the Kongsvegen glacier, Svalbard, is used for demonstration.

7.1 Introduction

Identifying and monitoring fluctuations in glacier facies provide a visible manifestation of climate change (Solomon et al. 2007). The only feasible method to obtain good spatial and temporal coverage of the Arctic glaciers is through the use of satellites. Space-borne synthetic aperture radar (SAR) instruments, operating independently of weather and daylight, are a particularly valuable tool in Arctic areas. SAR has an added advantage over higher frequency instruments (visible and laser) because the signal penetrates some distance into the glacier such that the return signal is influenced not only by the surface, but also by the shallow

V. Akbari (✉) • A.P. Doulgeris • T. Eltoft
Earth Observation Laboratory, Department of Physics and Technology,
University of Tromsø – The Arctic University of Norway, 9037 Tromsø, Norway
e-mail: vahid.akbari@uit.no

subsurface. Another advantage of SAR in glacier monitoring is its sensitivity to moisture content and surface roughness, which enables it to detect different glacial zones. Multi-polarization SAR may provide additional information, and thus is a better tool for glacier monitoring than single-channel SAR sensors.

A difference in radar backscattering between multi-temporal multi-polarization SAR data may be caused by several factors such as actual land cover change, differences in viewing geometry (satellite orbit and sensor look angle), terrain topography (surface slopes), differences in polarization configuration, and differences in meteorological conditions. These considerations motivate us to develop a processing chain for post-classification change detection in Arctic glaciers. Models accounting for temporal variation in multi-temporal multi-polarization SAR images should separate useful temporal variation, i.e., land cover or seasonal changes from variation arising due to other factors mentioned above.

Satellite-borne SAR instruments have proven to be very useful tools for multi-temporal image analysis. However, terrain topography has a significant impact on the geometric and radiometric quality of SAR images. For the geometric correction of topographic effect, precise terrain geocoding of SAR data is required. This can be accomplished by using a digital elevation model (DEM) and precise satellite state vectors. In addition to geometric distortions, surface slopes modulate SAR backscatter and can be split into two main effects. The first effect is changes in radar cross sections (RCS) per unit image area (Ulander 1996; Small 2011) and the second effect is that polarization states are also affected since the terrain slopes, especially azimuthal slopes, induce polarization orientation changes (Schuler et al. 1999; Lee et al. 2000). Hence, before analyzing the data, terrain correction is a prerequisite for comparison of multi-temporal SAR images. This study first addresses the precise geocoding and geometric terrain correction (GTC) of SAR data and then radiometric terrain correction (RTC) of multi-polarization SAR data that utilizes the pixel size normalization on each element of the sample covariance matrix (Atwood et al. 2012). Moreover, orientation angle compensation (OAC) is included immediately following RTC (Lee et al. 2002). Accurate backscatter estimates enable more robust use of the retrieved values for our task of change detection.

Polarimetric SAR (PolSAR) data distributions are generally derived from the product model, which describes that the backscattered signal results from the product between a Gaussian speckle noise component and the textured terrain backscatter (Lee et al. 1994; Oliver and Quegan 2004). Several statistical models have been proposed in the literature to describe the texture term. For *textured* areas, the K_d (or K-Wishart) model is commonly used (e.g., Lee et al. 1994; Doulgeris et al. 2008). However, the analysis shows that this model does not always represent the data well. The G_d^0 -distribution is another multivariate distribution (Freitas et al. 2005) to model *extremely heterogeneous* data. The two-parameter Kummer- U distribution has been introduced by Bombrun et al. (2011) to model polarimetric vector data. We use its multilook extension, named the matrix-variate U_d -distribution, for multilook covariance matrix data. The U_d -distribution is applicable to describe both single-channel and PolSAR data. The flexibility of this model, with an extra texture parameter with respect to K_d and G_d^0 , encourages the authors to use this model for

multi-temporal multi-polarization SAR data. It is expected to yield improved results because of its flexibility to model more varied textures.

In this study, we use an unsupervised contextual non-Gaussian clustering algorithm, named *U*-MRF in (Doulgeris et al. 2012; Doulgeris 2015), to segment each terrain corrected SAR scene. This contextual non-Gaussian clustering algorithm uses a Markov random field (MRF) model that integrates the U_d -distribution for the multi-polarization SAR data statistics conditioned to each image cluster, and a Potts model for the spatial context. The parameters of the *U*-MRF model are estimated by the iterative expectation-maximization (EM) algorithm (Dempster et al. 1977) and Besag's algorithm (Besag 1977) in the segmentation process. Contextual information can improve the accuracy and robustness of the image segmentation and hence leads to improved change detection results. The theoretical approach proposed in this paper is general for multipolarization SAR data and applicable not only to full-polarization data, but also to dual polarization and single-channel SAR data, although with some reduction in distinguishing power. The analysis utilizes several ENVISAT ASAR, dual polarization scenes over Kongsvegen glacier, Svalbard from spring 2004, 2005 and 2006, together with some ground based field observations. Ground truth data are used to label segmented images and to investigate the accuracy of classifications. We demonstrate consistency by comparing classified scenes taken on the same day and from different acquisition parameters (e.g., look angle). The surface of a glacier can be roughly divided into accumulation and ablation areas, separated by the equilibrium line (the dividing line between the accumulation and ablation areas) (König et al. 2004). Monitoring the firn line position over time is of interest, because there are indications that this line is correlated with the equilibrium line. Hence, we demonstrate the consistency of the classification results as firn area total variation between chosen no change pairs to obtain the expected variation of firn area boundary with superimposed ice (SI) zone. Subsequent yearly classifications are discussed in terms of post-classification change detection and changes are identified as the detected difference in the location of boundaries between glacier facies.

This chapter is organized as follows: in Sect. 7.2, we define the backscatter quantities measured by a PolSAR, namely the scattering vector, radar backscatter, and the area normalized scattering vector. Section 7.3 describes the processing chain of time series analysis including multilook processing, terrain correction, unsupervised segmentation and post-classification change detection. Sect. 7.4 introduces the study area and describes the example data. Sect. 7.5 presents the results. Finally, conclusions from the presented research are given in Sect. 7.6.

7.2 Measurements from SAR Sensors

Fully-polarimetric imaging radar measures the amplitude and phase of backscattered signals in the four combinations of the linear receive and transmit polarizations: HH, HV, VH, and VV. Assuming that the target reciprocity condition is

satisfied, the backscattering of a monostatic polarimetric SAR system is characterized by the complex scattering vector, $\underline{\Omega}$, with dimension $d = 3$

$$\underline{\Omega} = [S_{hh} \ \sqrt{2}S_{hv} \ S_{vv}]^T \in \mathbb{C}^3 \quad (7.1)$$

where the elements represent the complex backscattering coefficients in the three polarimetric channels, the superscript T denotes the matrix transpose, and $\sqrt{2}$ arises from the requirement to conserve the total scattered power. The vector $\underline{\Omega}$ is the single-look complex (SLC) format representation of polarimetric SAR data. Single and dual-channel polarimetric data can be treated in a similar way as subsets of lesser dimension and, most likely, proportionally less information.

The radar backscatter (β) of a given target measured in the range-azimuth coordinates for linear polarizations $r, t \in \{H, V\}$ can be obtained from the elements of scattering vector in (1) as follows (Freeman 1992):

$$\beta_{rt} = 4\pi|S_{rt}|^2. \quad (7.2)$$

Both S_{rt} and β_{rt} are functions wave frequency, viewing geometry, wave polarization, geometrical structure and dielectric properties of the object (Lee and Pottier 2009). Eqs. 7.1 and 7.2 above represent the quantities which are directly measurable by a SAR sensor. The area normalized scattering vector in the slant range plane (subscript β) is defined as:

$$\underline{\Omega}_{\beta^0} = \frac{\underline{\Omega}_\beta}{\sqrt{A_\beta}}. \quad (7.3)$$

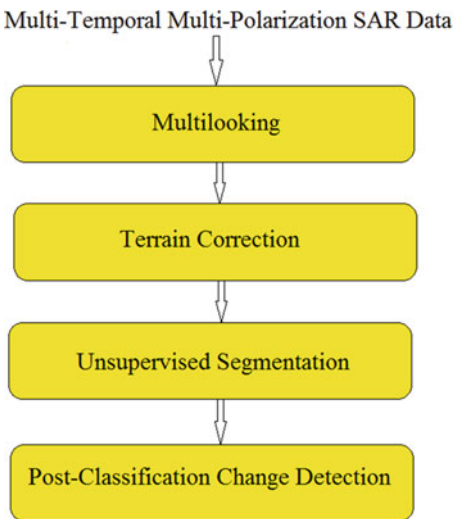
where A_β represents the reference area of the β^0 backscatter coefficient that contributes to the recorded signal.

Fully-polarimetric data is not always available because the wider coverage of dual polarization or single polarization modes are often preferred for monitoring purposes such as change detection. The different possible configurations of the dual polarization mode systems are: HH/HV, VV/VH, or HH/VV. Therefore, only a reduced version of $\underline{\Omega}$ is available. Single channels are also possible, generally in HH or VV.

7.3 Processing Chain for Post-classification Change Detection

The time series analysis of multi-temporal multi-polarization SAR data for post-classification change detection in this study consists of a processing chain with four stages, as depicted in Fig. 7.1, and can be used for both single and multi-channel SAR data. These stages are explained in detail below. The inputs are multi-temporal multi-polarization SAR images with different configurations.

Fig. 7.1 Processing chain for post-classification change detection



7.3.1 Stage 1: Multilooking

The scattering vectors are first transformed into the form of multilooked sample covariance matrices in order to reduce speckle noise at the expense of spatial resolution (Lee and Pottier 2009), i.e.,

$$\mathbf{C} = \sum_{l=1}^L \mathbf{\Omega}_l \mathbf{\Omega}_l^H \quad (7.4)$$

where L is the nominal number of looks used for averaging and $(\bullet)^H$ means the Hermitian transposition operator. Hence, after multilooking, each pixel in the image is a realization of the $d \times d$ stochastic matrix variable denoted \mathbf{C} , and the image is referred to as the multilook complex (MLC) covariance image. We assume that the MLC data is generated by a simple box-car multilook averaging of single-look scattering vectors. The box-car is used so that we can assume a global number of looks (degree of smoothing) and “simpler” statistical models, as opposed to advanced dynamic speckle filters that produce a variable number of looks that complicate the modelling.

7.3.2 Stage 2: Terrain Correction

Terrain topography influences both the placement of each observed point on the Earth’s surface and the brightness of the radar return in radar geometry (Wivell et al. 1992; Loew and Mauser 2007). In this stage, we implement a three-step method to

generate terrain corrected polarimetric SAR images for time series analysis. The procedure consists of the following steps:

1. Geometric terrain correction (GTC);
 2. Radiometric terrain correction (RTC);
 3. Orientation angle compensation (OAC);
- (1) **GTC:** The objective of SAR geocoding is to find the corresponding position on the Earth for each image pixel, thereby transforming from the SAR coordinate image into an Earth-based coordinate image. Since the satellite state vector is known from the orbit information, the position of each SAR pixel is estimated for a given earth model by solving the so-called *range-Doppler* equations (Curlander and McDonough 1991). Due to geometrical distortions caused by the side-looking geometry and rugged terrain, a one-to-one relation does not always exist between the radar and the geographic map coordinates (Small 2011). The pixels that are located in layover and radar shadow regions have to be masked out in this step. The importance of accurate geocoding of multi-temporal imagery is obvious because largely spurious results of change detection will be produced if there is misregistration. In cases of misregistration, a number of false alarms occur, especially in the region of rapid intensity change such as edges. This necessitates the use of precise terrain geocoding of SAR data that not only transforms the images to a standard map projection, but also accounts for topography with a high resolution DEM and precise orbital information.
- (2) **RTC:** The normalization of SAR imagery for systematic terrain variations is required for meaningful single sensor multi-track intercomparisons and post-classification change detection. Although the position of the backscatter estimate has been corrected by the GTC, the radiometry of the geocoded image remains in the slant range plane. Therefore, RTC is applied to correct distortions due to the side-looking geometry of SAR systems and hill-slope modulations. In this study, we first normalize the scattering coefficients with respect to the β^0 reference area (A_β) according to Eq. 7.3, and then apply the radiometric slope correction factor $\cos(\Psi)$, proposed in (Ulander 1996), on the covariance matrices. Provided that the data are already calibrated with respect to the elevation antenna pattern, range spreading loss, and channel to channel calibration, all elements of covariance matrix in Eq. 7.4 can be simultaneously radiometrically corrected to the ground range area by

$$\mathbf{C}_{RTC} = \frac{\cos(\Psi)}{L} \sum_{l=1}^L (\boldsymbol{\Omega}_{\beta^0})_l (\boldsymbol{\Omega}_{\beta^0})_l^H = \cos(\Psi) \cdot \mathbf{C}_{\beta^0} \quad (7.5)$$

where Ψ is the projection angle between the surface normal and the image plane normal, which is assumed to vary between 0° and 90° and exclude layover areas (Ulander 1996). All covariance matrix values now correspond to the σ^0 backscatter coefficient, which is equivalent to $\sigma^0 = \beta^0 \cdot \cos(\Psi)$. The

conventional radiometric normalization method, which relies on the ellipsoidal incidence angle only, is adequate for flatlands or for pixels with zero slope. The expected results are radiometrically “flattened” SAR images. The required parameters for performing the RTC are estimated in the geocoding step using an available DEM and satellite state vector. In cases where a DEM is not available, ellipsoidal-based radiometric correction is achieved over an earth model such as WGS-84.

- (3) **OAC:** Since different scattering mechanisms (double bounce, surface scattering, and volume scattering) have different sensitivity to terrain topography, RTC is not sufficient for polarimetric applications to produce reliable results for scattering characteristics (Atwood et al. 2012). The last step of terrain correction is to compensate the polarization signature which is due to topography effects, specifically azimuth slope variations. Polarization orientation angle (POA) shifts are introduced by terrain topography slopes in the azimuth direction. These shifts make the covariance matrix reflection asymmetric and can be compensated based on the DEM-derived POA in (Lee et al. 2000). After deriving the POA, the compensation can be done on the covariance matrices by

$$\mathbf{C}_{OAC} = R(\theta) \mathbf{C}_{RTC} R^T(\theta) \quad (7.6)$$

where θ is the shift in the POA determined from the DEM, $R(\theta)$ denotes the rotation matrix (Lee et al. 2002), and \mathbf{C}_{RTC} and \mathbf{C}_{OAC} are the covariance matrix before (after the RTC) and after rotation, respectively.

Reflection symmetry holds for most natural backscatter media, meaning that the co- and cross-polarized channels are uncorrelated. However, azimuth slope variations may induce correlation between these channels. Subsequently, OAC over natural images usually leads to reflection symmetric covariance matrix data. When a DEM is not available, target decomposition-based methods are an alternative to estimate the azimuth slope induced POAs directly from polarimetric SAR data, by essentially enforcing reflection symmetry. The data are now ready for quantitative image analysis, such as surface cover change detection.

7.3.3 Stage 3: Unsupervised Segmentation

An unsupervised, non-Gaussian, contextual segmentation method is used that combines an advanced statistical distribution with spatial contextual information for MLC data. The U_d -distribution is used for the data statistics because it is one of the most flexible distributions to model more varied SAR textures and includes the previously used models, the W_d , K_d and G_d^0 , as special cases. The Markov Random Field (MRF) model is used to introduce spatial contextual smoothing in a rigorous manner and produces more solid, contiguous clusters and reduces the effect of speckle noise. The fully automatic algorithm was chosen for its consistency and invariance to initial conditions to make the whole process more robust.

The textural-contextual model integrates the highly flexible U_d -distribution for the polarimetric SAR data statistics conditioned to each data cluster and a Potts model for the spatial context (Doulgeris et al. 2012; Akbari et al. 2013). The proposed algorithm is based upon the iterative expectation maximization (EM) algorithm (Dempster et al. 1977) for data clustering, with the mean-field approach of (Celeux et al. 2003) and the pseudo-likelihood algorithm of (Besag 1977) for optimizing the MRF. In addition, it adds a goodness-of-fit test stage to assess the fit of the estimated model to the actual data histogram and uses this to split poor fitting, and presumed mixed, clusters, or merge equal and competing clusters. This allows for a consistent initial condition as one single class that overcomes the well-known influence of random initial conditions, and also finally determines the statistically appropriate number of clusters. More details about the clustering algorithm can be found in (Doulgeris et al. 2012).

Although the method may be used fully automatically, including finding the number of clusters, the present work restricted it to three clusters for the expected glacier facies only. Even though the automatic number of clusters is not used, the algorithm benefits from the consistent initial condition and obtains a repeatable cluster result.

The U_d -distribution parameter estimation is achieved with the method of matrix log-cumulants (MoMLC) because closed form maximum likelihood estimates do not exist for the U_d -distribution model. MoMLC has been clearly shown to be fast, accurate and a suitable alternative for clustering when large sample sizes are routine.

We obtain unlabeled segmentation results that then need additional knowledge to align classes for comparison. The mean class backscatter (intensity) can be used for glacier facies labelling, as the three zones have distinctly different brightness. The majority ground truth data classes are used to obtain overall classification accuracies. Note that this stage applies for every scene of the multi-temporal multi-polarization SAR data.

7.3.4 Stage 4: Post-classification Change Detection

This approach for change detection requires very high accuracy of the classification results of each image scene from Stage 4. We believe that by using the unsupervised contextual non-Gaussian segmentation method on terrain corrected SAR scenes results in a robust segmentation that improves also the reliability of change detection. Since the class labels match on all images (due to the mean-backscatter relation and only 3 simple classes), we investigate changes for consistency and post-classification comparison change detection. The consistency of the segmentation method is characterized by comparing segmentation results of scenes taken on the same day (assumed ‘no change’) with different acquisition parameters. This ‘no-change’ variability gives a baseline and allows us to determine whether an observed variation is statistically significant. Subsequently, the differences between classified image pairs of succeeding years are compared to this baseline, to identify whether significant change has occurred.

7.4 Study Area and Data Set Description

The glacier Kongsvegen, situated at approximately $78^{\circ}50' N$ and $13^{\circ} E$ in the northwest of Spitsbergen, Svalbard, close to the meteorological station Ny-Ålesund, is selected for the workflow presented in Sect. 7.3. Kongsvegen is a surge-type glacier about 25 km long, covers an area of approximately 100 km^2 , and is oriented in a northwest-southeast direction extending from an elevation of 800 m above sea level to sea level. The glacier has a flow velocity of $< 4 \text{ m a}^{-1}$ and is thus a very slow moving glacier.

The satellite data set consists of a time series of acquired SAR images for the period 2004–2006 over the glacier. The images are generally collected under different acquisition configurations. The series consists of dual polarization C-band ENVISAT-advanced-synthetic-aperture-radar (ASAR) images in alternating polarization (AP) mode from both ascending and descending orbits; in both HH/HV and VV/VH polarizations; and over a large range of look angles, from 14° to 43° (swath angles IS1 to IS7). For a descending orbit, as seen in Fig. 7.2, the SAR looks down glacier and the satellite flight path is across glacier. In ascending orbits, the SAR look direction is across glacier and the satellite track is approximately parallel

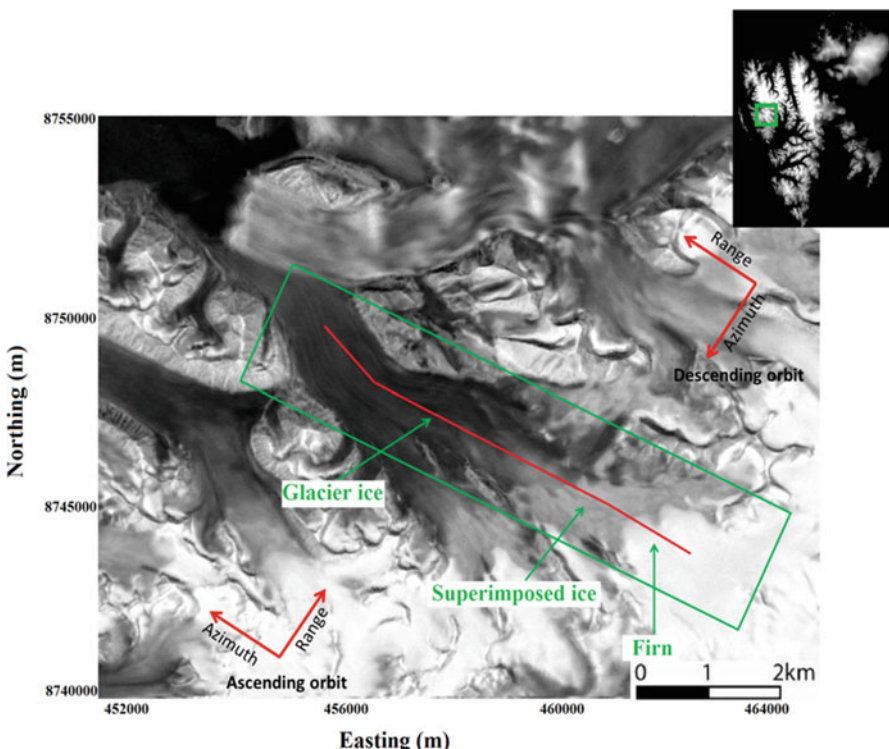


Fig. 7.2 Suitable ENVISAT C-band SAR scenes with different acquisition configurations for time series analysis

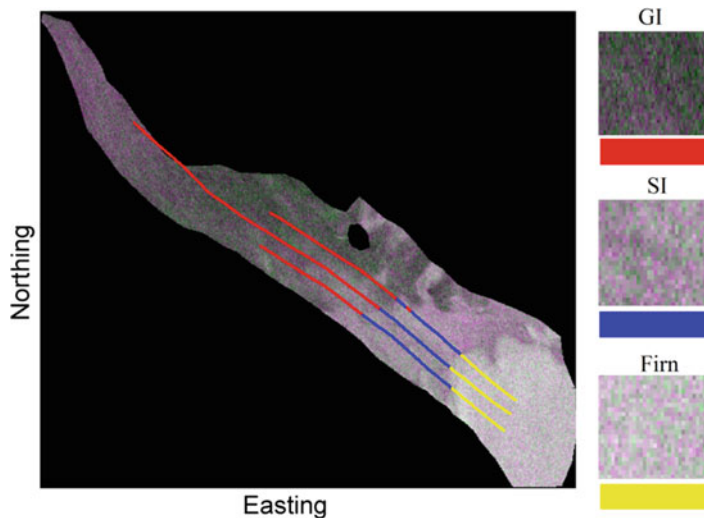


Fig. 7.3 Example of quasi-Pauli red, green, blue (RGB) images of Kongsvegen glacier from 2005 with GPR-derived ground truth overlaid. Legend on the right shows homogeneous samples of different glacier zones along with class label colors: red = GI, blue = SI, and yellow = firn

to the glacier center line. The initial resolution of the raw SAR SLC images is 7.8 m in the slant range and 3.2 m in the azimuth direction. The SAR intensity image in Fig. 7.3 shows the spatial variability of the three different distinct zones across the glacier. Each zone has specific backscatter characteristics. In the upper parts of the glacier, where firn accumulation occurs, layers dominated by large firn grains and ice layers cause considerable volume scattering on the ENVISAT SAR wavelength leading to high backscatter (Engeset et al. 2002). The SAR signature in the ablation area is dominated by backscatter from the previous summer surface only, with few bubbles and very little volume scattering. In the SI area, varying fractional volumes of bubbles cause more variability and medium backscatter values. Although the previous summer surface still contributes, the increase in total backscatter, which distinguishes SI from glacier ice (GI), is caused by the air bubbles (König et al. 2004). The smoothness of GI does not reflect much of the incoming SAR signal back to the sensor, resulting in low backscatter values.

A DEM of 20 m pixel resolution covering all of Svalbard was also available, which was produced by the Mapping Section of the Norwegian Polar Institute (NPI). Ground truth data are derived from a network of C-band ground penetrating radar (GPR) profiles oriented parallel to the glacier center line collected by the NPI in 2005 under the same spring conditions as the ASAR images. GPR is commonly used in glaciology for mapping layers within the glacier such as internal accumulation layers and the previous summer surface, as well as bedrock topography (Evans and Smith 1969). A differential GPS (DGPS) was used to determine the position of the GPR profiles with a horizontal accuracy within 10 cm. The C-band GPR is

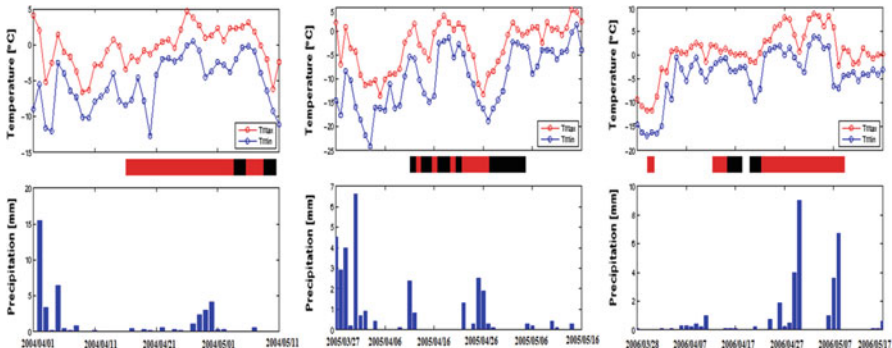


Fig. 7.4 Daily air temperature and precipitation observed in Ny-Ålesund between 2004 and 2006. Data are from the Norwegian Meteorological Institute. The black/red bars between the temperature and precipitation represents times of SAR acquisition. The black bars indicate the chosen SAR images based on the temperature and precipitation constraints, listed in Table 7.1, for time series analysis

a step-frequency continuous-wave (SFCW) radar operating at 4.8–5.8 GHz. The center frequency of 5.3 GHz is the same as the ASAR instrument onboard ENVISAT (Langley et al. 2008). Details of the GPR data are given in (Langley et al. 2008; Langley 2007). The along glacier profiles have been manually classified into three zones of interest, i.e., GI, SI, and firn.

Meteorological conditions also affect the backscatter in addition to the SAR imaging geometry and surface topography effects as discussed in Sect. 7.3.2. Therefore, from temperature and precipitation observations of Ny-Ålesund station, located at sea level about 15 km west of the terminus of Kongsvegen, we select only SAR images collected in spring under cold and dry conditions on the glacier surface (see Fig. 7.4). When just a small amount of liquid water is present in the upper layer of snow and firn, the radar backscatter properties change significantly and the underlying structure has no influence on the measurements (Engeset et al. 2002). However, in early spring the snow pack on the glacier surface is mostly dry and the previous summer surface at the base of the winter snow pack gives the strongest return. Thus, cold spring conditions give the most consistent annual measure for long time trend analysis and is recommended for monitoring of glaciers (Langley 2007). We refer readers to (Akbari et al. 2010) to show the influence of wet conditions on radar response. The authors demonstrated a good example image coinciding with the onset of rain in the meteorological records and an image taken after the onset of rain clearly showed significant change compared to the day before. The suitable SAR images are chosen based on the temperature and precipitation constraints. The remaining images for the time series analysis are listed in Table 7.1.

Table 7.1 Suitable ENVISAT C-band SAR scenes with different acquisition configurations for time series analysis

Image no	Date	Look angle	Path	Polarization
I ₁	04 May 2004	IS3	Des	VV/VH
I ₂	05 May 2004	IS5	Des	HH/HV
I ₃	05 May 2004	IS7	Asc	VV/VH
I ₄	09 May 2004	IS5	Asc	VV/VH
I ₅	10 May 2004	IS3	Asc	VV/VH
I ₆	28 Dec 2004	IS2	Dec	VV/VH
I ₇	02 Feb 2005	IS2	Asc	VV/VH
I ₈	09 Mar 2005	IS2	Asc	VV/VH
I ₉	11 Apr 2005	IS7	Des	VV/VH
I ₁₀	13 Apr 2005	IS2	Asc	VV/VH
I ₁₁	14 Apr 2005	IS6	Asc	VV/VH
I ₁₂	15 Apr 2005	IS4	Asc	VV/VH
I ₁₃	17 Apr 2005	IS6	Des	VV/VH
I ₁₄	17 Apr 2005	IS7	Asc	VV/VH
I ₁₅	18 Apr 2005	IS4	Asc	HH/HV
I ₁₆	19 Apr 2005	IS3	Des	HH/HV
I ₁₇	21 Apr 2005	IS1	Des	HH/HV
I ₁₈	27 Apr 2005	IS7	Des	VV/VH
I ₁₉	28 Apr 2005	IS2	Des	VV/VH
I ₂₀	28 Apr 2005	IS3	Asc	VV/VH
I ₂₁	29 Apr 2005	IS1	Asc	VV/VH
I ₂₂	29 Apr 2005	IS4	Des	VV/VH
I ₂₃	30 Apr 2005	IS6	Asc	HH/HV
I ₂₄	01 May 2005	IS2	Des	VV/VH
I ₂₅	01 May 2005	IS4	Asc	VV/VH
I ₂₆	02 May 2005	IS2	Asc	VV/VH
I ₂₇	03 May 2005	IS6	Des	HH/HV
I ₂₈	05 May 2005	IS3	Des	VV/VH
I ₂₉	17 May 2005	IS2	Des	VV/VH
I ₃₀	21 Feb 2006	IS2	Des	VV/VH
I ₃₁	15 Apr 2006	IS6	Asc	HH/HV
I ₃₂	16 Apr 2006	IS2	Des	VV/VH
I ₃₃	17 Apr 2006	IS2	Asc	VV/VH
I ₃₄	19 Apr 2006	IS4	Asc	VV/VH
I ₃₅	20 Apr 2006	IS2	Asc	VV/VH
I ₃₆	20 Apr 2006	IS3	Des	VV/VH

7.5 Experimental Results

We now use the proposed workflow in Sect. 7.3 to analyze multi-temporal dual polarization SAR data for glacier change detection. The calibrated SLC data are geocoded and multilooked simultaneously to a final geocoded resolution of approximately 30×30 m. The SLC image pixels were multilook averaged with

2 looks in the range direction and 12 looks in the azimuth, 24-looks in total. We have chosen 24-looks for the multilooking because it is a moderately large degree of multilooking and would achieve a high degree of speckle reduction. The 30 m ground resolution is good enough for monitoring purposes in glacier areas.

The reconstruction of radar geometry with the help of a DEM, the known orbit data vector, and image-line timing is done for each ASAR image. This stage not only derives the geocoding look-up tables, but also derives various geometrical parameters for each ground point that are required for terrain corrections, such as local incidence angle, and the layover-shadows mask. The pixels affected by the geometrical distortions are mainly located at slopes larger than 40° . Kongsvegen glacier has a gentle surface slope of $0.5^\circ - 5^\circ$ and therefore, such geometric corrections will be minimal over the glacier region.

The radiometric normalization of the covariance matrix data was then applied for each scene. Although the glacier slopes are generally small, if left uncorrected they may manifest as misclassification of the glacier class boundaries. The projection factor is shown in Fig. 7.5c as an example. The backscatter coefficient is reduced when using the projection factor to radiometrically correct the covariance matrix

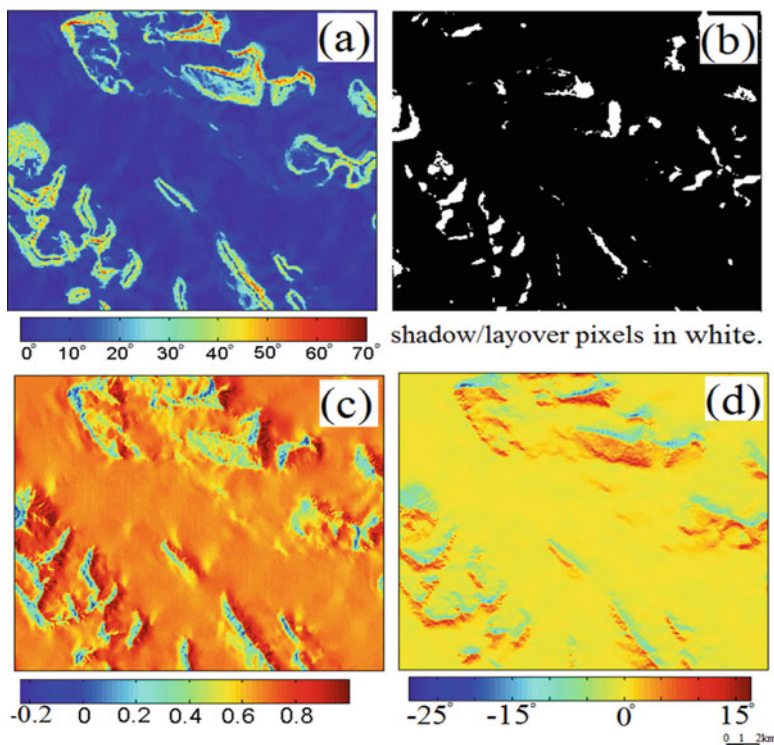


Fig. 7.5 Terrain correction parameters of the covered area in the map geometry. (a) slope angle map in degrees (b) shadow/layover mask produced from the geocoding step (c) projection factor (d) the DEM-derived POA in degrees

data. The negative projection factors (the projection angles larger than 90° .), correspond to the dark blue areas in Fig. 7.5c and red areas in the slope map. These areas are mostly affected by layover and in the geocoding step have to be masked out, as seen in Fig. 7.5b. The DEM-derived POAs are used to correct for the azimuth slope effect on the polarization signature. By estimating the POA for the data [see Fig. 7.5d], we observe that for the rugged-terrain areas surrounding the glacier, the polarization shifts are more significant. Subsequently, the OAC over images leads to reflection symmetric covariance matrix data sets.

To demonstrate the effect of both RTC and OAC on the covariance matrix data, the profile along the glacier center line was plotted for the four images with different geometries. It should be mentioned that the middle of the three GPR ground truth lines in Fig. 7.3 follows the glacier center line extending from the firn area into the GI zone. The original backscatter coefficient, RTC and OAC values are shown with red, green and blue lines respectively. The reduction of backscatter coefficient is geometry-dependent and shows the suppression of the SAR geometry effects on the data such that the images are comparable for monitoring purposes. For example, the offset between original backscatter and RTC backscatter for the look angle IS1 is larger than look angle IS7 (see Fig. 7.6). The total backscatter power

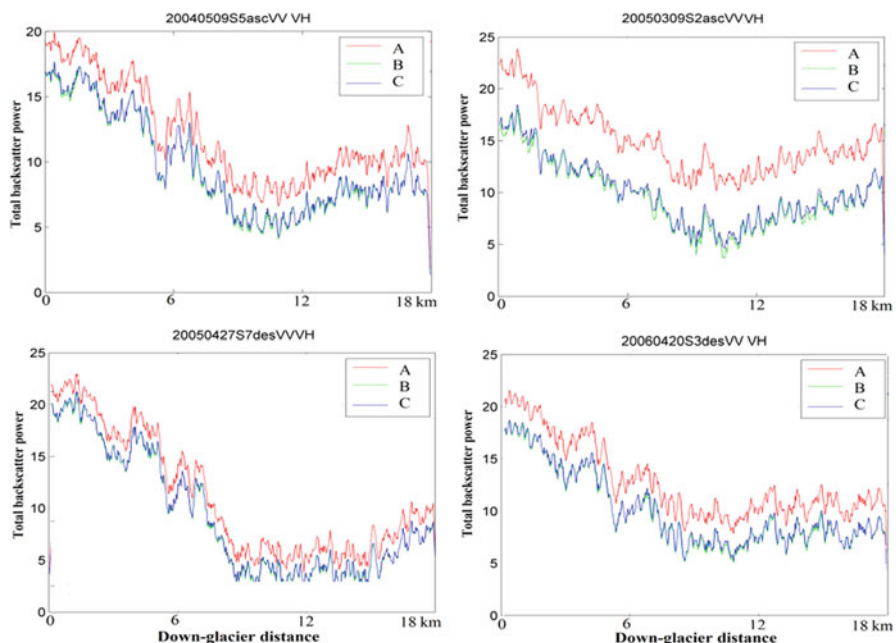


Fig. 7.6 The effect of terrain correction on dual polarization ASAR data for the four candidate images with different geometries: before radiometric normalization (a); after radiometric normalization (b); and after the OAC with DEM (c) along the glacier center line extending from the the firn area into GI zone

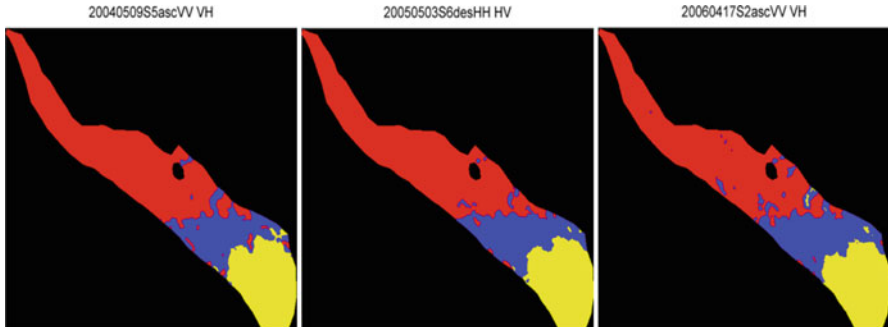


Fig. 7.7 Unsupervised segmentation of the candidate images for each year (2004, 2005, and 2006)

($\text{Span} = C_{11} + C_{22}$) in Fig. 7.6 does not change significantly after OAC except some small changes for the pixels located at the higher azimuth slopes. For those pixels, the total power increased after the OAC.

A mask is applied to mask out mountains and isolate the glacier pixels for classification. The segmentation algorithm was working with 2×2 covariance matrix data. Unsupervised contextual non-Gaussian segmentation was then performed using the *U-MRF* classifier on the terrain corrected dual polarization data set. We fix the number of clusters to 3 for the segmentation. Figure 7.7 shows the segmentation results for three SAR images as candidates from each year of the study period. Since the three surface types (GI, SI, and firn) have distinct backscatter characteristics, they can be reliably discriminated in the segmented images. The firm line, i.e., the boundary between SI and firn, is detected in all segmentations. The boundary between SI and GI is also detected. The segmentation results are now validated using in-situ observations. The three GPR ground truth lines acquired in 2005, shown in Fig. 7.7, are used to label the segmented images into glacier facies and to validate the classification results. The validation is only performed on scenes acquired in spring 2005 that are within a few weeks of the GPR data. Table 7.2 reports the overall classification accuracies and omission errors of the glacier zones for the 2005 images. The classification accuracies for the scenes indicate overall accuracies higher than 80 % for all cases. We did not find any obvious preference among different configurations because the geometric and radiometric terrain corrections should suppress the effects of both SAR geometry and surface topography on the covariance matrix data sets.

Next, the images that have been taken on the same day with different geometries are chosen as pairs for the consistency investigation of the classification results. Table 7.3 is a list of the total variation of firm line for given pairs and is an indicator of variability of this boundary in terms of percentage of the glacier mask error (PGME), the total change area error (TCAE), and equivalent linear displacement error (ELDE) along the glacier. PGME is defined as the percentage of the change area between the firm and SI boundaries with respect to the whole glacier. TCAE is

Table 7.2 Classification accuracies for the classification results for the 2005 images, including overall accuracy (OA) and omission error (OE) for the three glacier zones

Image	OA%	OE%		
		GI	SI	Firn
20050202IS2ascVV/VH	88.3	18.4	1.5	8.0
20050309IS2ascVV/VH	87.1	19.3	1.8	11.0
20050411IS7desVV/VH	81.1	18.9	4.3	37.7
20050413IS2ascVV/VH	88.3	17.5	1.3	10.3
20050414IS6ascVV/VH	94.7	1.3	4.8	16.0
20050415IS4ascVV/VH	95.3	1.6	5.9	11.3
20050417IS6desVV/VH	88.0	19.6	0.8	7.3
20050417IS7ascVV/VH	87.4	20.8	1.0	6.7
20050418IS4ascHH/HV	87.9	18.5	0.8	10.30
20050419IS3desHH/HV	86.4	23.5	0.0	6.0
20050421IS1desHH/HV	85.9	24.0	0.0	7.3
20050427IS7desVV/VH	85.7	24.3	0.0	7.7
20050428IS2desVV/VH	86.7	21.3	0.5	9.7
20050428IS3ascVV/VH	87.8	17.8	4.1	8.7
20050429IS1ascVV/VH	87.2	18.1	1.0	14.7
20050429IS4desVV/VH	84.8	26.1	0.0	7.3
20050430IS6aschHH/HV	86.3	23.5	0.0	6.7
20050501IS2desVV/VH	86.4	22.5	0.0	8.7
20050501IS4ascVV/VH	96.2	1.3	4.1	9.7
20050502IS2ascVV/VH	81.9	1.4	6.7	11.0
20050503IS6desHH/HV	95.5	4.2	3.3	6.7
20050505IS3desVV/VH	84.6	25.8	0.0	9.0
20050517IS2desVV/VH	86.5	21.7	0.0	10.3

Table 7.3 Consistency characterization: the variation of firn/SI boundary in terms of percentage of the glacier mask error (PGME), total change area error (TCAE), and equivalent linear displacement error (ELDE) for some pairs. Image identities are given in Table 7.1

Image 1	Image 2	PGME	TCAE (m^2)	ELDE(m)
I ₂	I ₃	1.36 %	763,200	120.74
I ₁₃	I ₁₄	0.63 %	354,600	57.70
I ₂₁	I ₂₂	1.81 %	1,017,000	179.52
I ₂₄	I ₂₅	1.55 %	869,400	153.20

measured as the areal variation between the firm and SI zones. ELDE is determined by dividing the TCAE by the total length of the firn/SI boundary. Among these three indicators, the ELD may be a very robust indicator, because the other two depend on the size of the glacier and the accuracy of its mask. An average ELDE error of 128 m is obtained between the pairs and represents the worst case “no-change” variation between different configurations. To produce an average classification result over each year, we take the majority count of the class label for each pixel from the stack of several yearly-classified images. The differences between average yearly-classified images can only be considered significant when compared to that

of the classification total variation. By taking the average classification result over each year, the expected variation of 128 m (between scene pairs with differing configurations) will decrease by \sqrt{N} for the mean, where N is the number of scenes used in the averaging. This variation may include the effect of different collection geometries, the segmentation algorithm, and other processing errors. Using similar geometries and the segmentation itself should have much reduced variability. Basically, if we have a collection of a time series using data acquired from similar geometries (i.e., interferometric pairs), then we could anticipate reduced variation and better change detection ability. In such cases, we may not need to perform radiometric terrain correction for change detection, since all would have the same geometric properties.

After consistency characterization, the classified images are compared and analyzed on a pixel-by-pixel basis to form a change matrix which describes the mapping of classes between the images. From this matrix we can extract a simple map of change versus no change, but also more detailed information on the nature of the change. Figure 7.8 shows the glacier change images within the periods of study (2004–2005, 2005–2006, and 2004–2006). It illustrates changes in the locations of boundaries between glacier facies.

Firn line monitoring is important for glaciologists, thus we concentrate only on the variation of firn area boundary with SI zone in the quantitative analysis. Total variation of the firn line in terms of both PGME and TCAE (firn to SI) and ELDE for change detection pairs are estimated to verify whether significant changes occur for the periods. Table 7.4 indicates these measures of variation of the firn/SI boundary for those periods. After averaging scenes within each year, we obtain the reduced

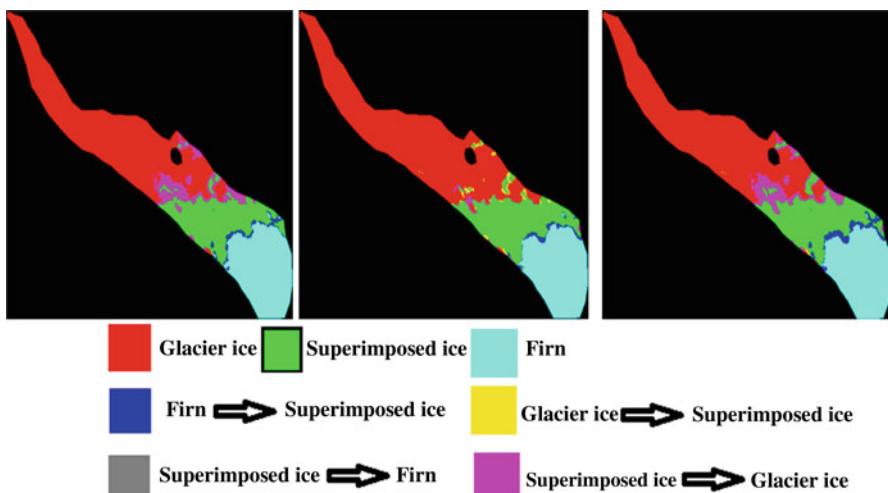


Fig. 7.8 Change images of Kongsvegen glacier within the periods of 2004–2005 (left), 2005–2006 (middle), and 2004–2006 (right). The changes of firn line for these periods are shown by blue color (movement toward top of the glacier which is bottom right)

Table 7.4 Change detection analysis: total change of firn line in terms of PGME, TCAE, and ELDE for three periods

Period	PGME	TCAE (m ²)	ELDE (m)
2004–2005	1.36 %	764,100	127.06
2005–2006	0.69 %	358,200	107.16
2004–2006	1.78 %	980,900	203.32

variation in the mean of 52.24 m, 26.72 m, and 47.58 m for the years 2004, 2005, and 2006 respectively, to be used when testing significance. The total variation of this boundary found between 2004 and 2005 exceeds the expected classification variation, which indicates significant change for this period. The same is found for the periods 2005–2006 and 2004–2006. A total movement of the approximately 200 m toward the top of the glacier is obtained for the whole period.

7.6 Conclusions and Discussion

This chapter addressed glacier change detection from multi-temporal multi-polarization SAR images. A robust algorithm for firn line monitoring was developed. This suggests that we have a tool for glacier change detection and monitoring that is applicable over the Arctic region on a timescale of a few years. The recent findings may form the basis for more operational monitoring of Arctic areas.

It is noted that when a difference in radar backscattering between multi-temporal data is taken as a change indicator, the difference may be due to several factors such as actual land cover change, viewing geometry, surface topography and other external factors (such as meteorological conditions, that are minimized by using radar frequencies and choosing the scenes wisely). These considerations were the main reason for developing a complete workflow for post-classification change detection from time series of polarimetric SAR images, and where we also choose our SAR images to avoid the wet weather conditions.

The algorithm has been tested on dual polarization ENVISAT ASAR images for the period 2004–2006 over the Arctic glacier, Kongsvegen, Svalbard. The images are first corrected for terrain effects by thoroughly reducing topographic effects on geolocation, radiometry and polarization signature, and subsequently stacked into proper time series for further analysis. This is an important step for a meaningful time series analysis.

We showed in (Akbari et al. 2013) that the K_d distribution can be used to model SAR image texture. However, the analysis shows that this model does not always represent the data well. We now chose a more flexible model, the matrix-variate U_d -distribution, for multilook covariance matrix data. It tends to yield improved results because of its flexibility to model more varied textures.

We then applied an unsupervised contextual non-Gaussian clustering method, named U -MRF, over terrain corrected SAR scenes. The unsupervised segmentation algorithm together with the DEM-based terrain correction are reliable and robust

enough to give consistent change detection results. It should be mentioned that the example glacier was only a very slow moving glacier and the annual change is small. More drastic change examples like deforestation, would likely work much better. Ground truth data are used to label segmented images into the three major classes of glacier facies, i.e., firn, glacier ice (GI), and superimposed ice (SI) and to investigate the classification accuracies.

We then characterized the consistency of the classification as the total variation of firn/SI boundary between two no-change images to obtain the expected variation due to processing errors in the processing chain. Finally, we did post-classification change detection analysis based on the classified images on a pixel-by-pixel basis. The variations of the boundaries between glacier facies were clearly detected within the period of study. The total variations of the firn/SI boundary for the 1-year periods, 2004–2005 and 2005–2006, exceed the measured classification variation, and thus show significant change (with respect to the ELDE) for both periods and also over the 2 years, i.e., 2004–2006.

References

- Akbari V, Eltoft T, Doulgeris AP (2010) Non-Gaussian clustering of SAR images for glacier change detection. *Proc ESA Living Planet Symp* 2:1–8
- Akbari V, Doulgeris AP, Moser G, Eltoft T, Anfinsen SN, Serpico SB (2013) A textural–contextual model for unsupervised segmentation of multipolarization synthetic aperture radar images. *IEEE Trans Geosci Remote Sens* 51(4):2442–2453
- Atwood DK, Small D, Gens R (2012) Improving PolSAR land cover classification with radiometric correction of the coherency matrix. *IEEE J Select Top Appl Earth Obs Remote Sens* 5(3): 848–856
- Besag J (1977) Efficiency of pseudo-likelihood estimation for simple Gaussian fields. *Biometrika* 64(3):616–618
- Bombrun L, Vasile G, Gay M, Totir M (2011) Hierarchical segmentation of polarimetric SAR images using heterogeneous clutter models. *IEEE Trans Geosci Remote Sens* 49(2):726–737
- Celeux G, Forbes F, Peyrard N (2003) EM procedures using mean fieldlike approximations for Markov model-based image segmentation. *Pattern Recogn* 36(1):131–144
- Curlander J, McDonough R (1991) Synthetic aperture radar-systems and signal processing. Wiley, New York
- Dempster AP, Laird NM, Rubin DB (1977) Maximum likelihood from incomplete data via EM algorithm. *J R Stat Soc Ser B* 39(1):1–38
- Doulgeris AP (2015) An automatic U-distribution and Markov random field segmentation algorithm for PolSAR images. *IEEE Trans Geosci Remote Sens* 53(4):1819–1827
- Doulgeris AP, Anfinsen SN, Eltoft T (2008) Classification with a non-Gaussian model for PolSAR data. *IEEE Trans Geosci Remote Sens* 46(10):2999–3009
- Doulgeris AP, Akbari V, Eltoft T (2012) Automatic PolSAR segmentation with the U-distribution and Markov random fields. Proceeding of 9th European Conference on Synthetic Aperture Radar (EUSAR), Nuremberg, p 183–186
- Engeset R, Kohler J, Melvold K, Lundén B (2002) Change detection and monitoring of glacier mass balance and facies using ERS SAR winter images over Svalbard. *Int J Remote Sens* 23(10):2023–2050
- Evans S, Smith B (1969) A radio echo equipment for depth sounding in polar ice sheets. *J Phys E Sci Instrum* 2(2):131–136

- Freeman A (1992) SAR calibration: an overview. *IEEE Trans Geosci Remote Sens* 30(6):1107–1121
- Freitas CC, Frey AC, Correia AH (2005) The polarimetric G distribution for SAR data analysis. *Environmetrics* 16(1):13–31
- König M, Winther JG, Kohler J, König F (2004) Two methods for firn area and mass-balance monitoring of Svalbard glaciers with SAR satellite images. *J Glaciol* 50(168):116–128
- Langley K (2007) Glacier subsurface interpretation combining ground penetrating radar and satellite synthetic aperture radar. Ph.D. dissertation, Faculty of Mathematics and Natural Sciences, University Oslo, Oslo, Norway
- Langley K, Hamran SE, Hogda KA, Storvold R, Brandt O, Kohler J, Hagen JO (2008) From glacier facies to SAR backscatter zones via GPR. *IEEE Trans Geosci Remote Sens* 46(9):2506–2516
- Lee JS, Pottier E (2009) Polarimetric radar imaging: from basics to applications, 2nd edn. CRC Press, Boca Raton
- Lee JS, Schuler DL, Lang RH, Ranson KJ (1994) K-distribution for multi-look processed polarimetric SAR imagery. *Proc IEEE Int Geosci Remote Sens Symp* 4:2179–2181
- Lee JS, Schuler D, Ainsworth T (2000) Polarimetric SAR data compensation for terrain azimuth slope variation. *IEEE Trans Geosci Remote Sens* 38(5):2153–2163
- Lee JS, Schuler DL, Ainsworth TL, Krogager E, Kasilingam D, Boerner WM (2002) On the estimation of radar polarization orientation shifts induced by terrain slopes. *IEEE Trans Geosci Remote Sens* 40(1):30–41
- Loew A, Mauser W (2007) Generation of geometrically and radiometrically terrain corrected SAR image products. *Remote Sens Environ* 106(3):337–349
- Oliver C, Quegan S (2004) Understanding synthetic aperture radar images. SciTech Publishing, Raleigh
- Schuler D, Lee JS, Ainsworth T (1999) Compensation of terrain azimuthal slope effects in geophysical parameter studies using polarimetric SAR data. *Remote Sens Environ* 69(2):139–155
- Small D (2011) Flattening gamma: radiometric terrain correction for SAR imagery. *IEEE Trans Geosci Remote Sens* 49(8):3081–3093
- Solomon S, Qin D, Manning M, Chen Z, Marquis M, Averyt K, Tignor M, Miller H (2007) IPCC, 2007: climate Change 2007: the physical science basis. Contribution of working group I to the fourth assessment report of the intergovernmental panel on climate change. Cambridge University Press, Cambridge
- Ulander L (1996) Radiometric slope correction of synthetic aperture radar images. *IEEE Trans Geosci Remote Sens* 34(5):1115–1122
- Wivell C, Steinwand D, Kelly G, Meyer D (1992) Evaluation of terrain models for the geocoding and terrain correction of synthetic aperture radar SAR images. *IEEE Trans Geosci Remote Sens* 30(6):1137–1144

Chapter 8

Interferometric SAR Multitemporal Processing: Techniques and Applications

Daniele Perissin

Abstract SAR Interferometry (InSAR) is a technology that makes it possible to extract ground deformation measurements from spaceborne radar sensors with a centimeter level precision. By processing long series of SAR images, InSAR techniques can be pushed forward up to reaching the millimeter sensitivity. In this way, data acquired by SAR satellites can be effectively used for monitoring not only ground movements but also tiny displacement of structures, dams, buildings, bridges and more. In this chapter, written at the beginning of year 2014, we give a brief overview of the concepts behind InSAR and Multi-Temporal InSAR techniques. Examples of results and processing steps implemented by Sarproz (www.sarproz.com) are shown and the interested reader can deepen his understanding of the topic by carrying out exercises on his own.

8.1 Introduction

Active radar imaging is a coherent technology that allows the generation of interferograms. An interferogram is the product of one image by the complex conjugate of another image. Whenever a correlation exists between corresponding pixels in the two images, the interferometric phase reveals very precise readings of the sensor-target distance. The phase is in fact a precise measurement of the alignment between two radar signals (as shown in Fig. 8.1) which is a fraction of the wavelength. Since microwave signals have wavelength in the order of centimeters, the interferometric phase has the potential to read changes of distance with sub-millimeter precision.

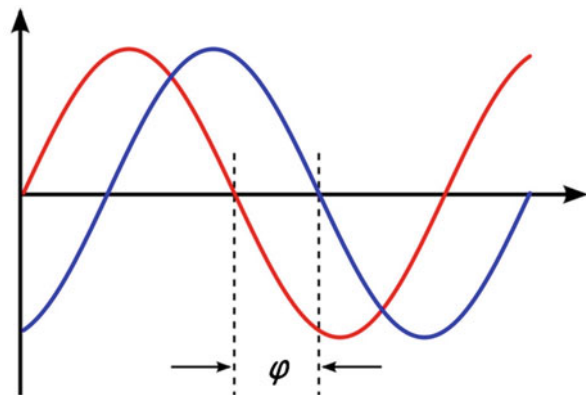
The first Synthetic Aperture Radar Interferometry (InSAR) experiment was carried out by Graham in 1974 (Graham 1974), using two receiving antennas mounted on an aircraft. In 1988 Goldstein published the first single-antenna repeat-pass InSAR Digital Elevation Map retrieved through interferometric processing of two images acquired by the Shuttle Imaging Radar (SIR-B) (Goldstein et al. 1988).

D. Perissin (✉)

Lyle School of Civil Engineering, Purdue University, West Lafayette, IN, USA

e-mail: perissin@purdue.edu

Fig. 8.1 The phase difference φ quantifies the delay or misalignment between two ElectroMagnetic signals. Since microwaves are characterized by centimetric wavelengths, the phase can reveal millimeter changes



Even though the potential of InSAR was clear since the beginning, many were the limitations and difficulties related to the technology. Changes in the terrain reflectivity cause radar decorrelation, which makes the InSAR phase unreadable (Zebker and Villasenor 1992). Moreover, atmospheric water vapor delays radar signals, turning phase readings into precise but inaccurate measurements (Hanssen 2001). It took a bit more than a decade before the availability of multi-temporal archives brought to the discovery of techniques for overcoming the InSAR limitations. Pioneer in multi-temporal InSAR processing is the Polytechnic of Milan, which published and patented the Permanent Scatterers technique (PSInSAR) in early 2000 (Ferretti et al. 2001). Since then, many groups worldwide worked on different Multi-temporal InSAR approaches (also called PSI, Persistent Scatterer Interferometry). Picking up a few representatives, it is worth to quote the Small Baseline Subset (SBAS) InSAR (Berardino et al. 2002), the Stanford Method for PSs (StaMPS) (Hooper et al. 2004) up to the most recent SqueeSAR (Ferretti et al. 2011). For a more complete list of references, the interested reader can refer to two recent reviews sketching the state of the art of SAR and multi-temporal InSAR (Moreira et al. 2013; Zhong and Lei 2014).

Applications of multi-temporal InSAR are mainly ground movements detection and DEM estimation. Examples of terrain movements are landslides (Colesanti and Wasowski 2006), subsidence (natural or due to underground operations as mines, excavations, water/oil extraction) (Herrera et al. 2010), soil compaction, seismic activity (Massonnet et al. 1993), volcanoes activity (Wadge 2003). However, with appropriate techniques and with higher spatial resolution, multi-temporal InSAR can also be successfully exploited to monitor buildings and infrastructures. Many examples of InSAR DEM generation are available from the literature (Ferretti et al. 1999), and the most recent mission dedicated to this aim is the Tandem-X bistatic configuration (Martone et al. 2013). Nevertheless, repeat-pass interferometry has been shown providing useful information also for terrain mapping and classification (Engdahl and Hyppa 2003).

Several books have been published on Synthetic Aperture Radar, SAR Interferometry and related processing techniques. Among them, we wish to quote here

Curlander for SAR (Curlander and McDonough 1991), the European Space Agency (ESA) manual for InSAR (Ferretti et al. 2007) and Kampes for PSI (Kampes 2006). It is not aim of this chapter to present a complete review of all works carried out in this field, neither to cover all possible multi-temporal techniques. Rather, the attempt is to provide the reader with a set of concepts for understanding the basics of InSAR and to conduct him through a series of experiments to keep the discussion as applied as possible.

The author of this Chapter received his education at the Polytechnic of Milan, where he started researching on PSI. After a few years as a postdoc in the same institution, he moved to Hong Kong as research assistant professor at the Chinese University and he is currently with the Civil Engineering School at Purdue University as assistant professor. The examples reported in this chapter have been processed with the software Sarproz (Perissin, www.sarproz.com; Perissin et al. 2011) developed by the author in his 12 years research career. The interested reader may replicate the examples by requesting the author for a Sarproz license.

The present Chapter is divided into two sections. In the first section, the basic of SAR interferometry are introduced, starting from the definition of the geometry of the problem and ending up with phase unwrapping. The second section presents the main PSI concepts, together with a few more recent extensions of the original Permanent Scatterers ideas, like multi-master and weighted approaches and non-linear time series estimation.

8.2 SAR Interferometry

For tackling InSAR concepts and processing techniques, we assume in this Chapter to deal with a set of co-registered SAR images. SAR images may be delivered by data providers either in L0 format (raw data) or in L1 format (also called SLC, Single Look Complex). Raw data need firstly to be focused before co-registration. The process of co-registration refers to the alignment of two SAR images, so that corresponding pixels in the two images contain the same portion of imaged terrain. To perform interferometry, images acquired with the same nominal geometry (orbit and incidence angle) are required. Even when the nominal geometry is the same, the satellite position may be slightly different from one acquisition to the other, and this is at the origin of the images misalignment. Usually, a single image is taken as reference (the Master image) and all other images (called Slaves) are resampled on the same sampling grid. We call pixel coordinates in range “samples” and pixels coordinates in azimuth “lines”. We will not consider hereafter possible oversampling factors and we assume to deal with zero-doppler geometry¹ (even if both aspects could be modified without affecting significantly the treatment).

¹In zero-doppler geometry, a target is focused at the location where it's closer to the satellite (as if the satellite would be looking down orthogonally to its path).

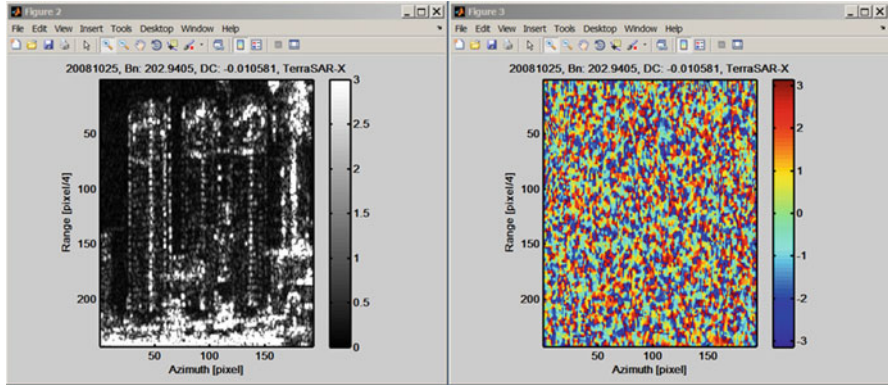


Fig. 8.2 Intensity (left) and phase (right) of a complex SAR image taken in Hong Kong by TerraSAR-X on 25th of October 2008. Three buildings are visible

We call $Img_i(s, l)$ the complex value of image i at coordinates s, l . An example of intensity and phase of a SAR image is shown in Fig. 8.2. Like all pictures presented in this Chapter, samples are the vertical coordinate (range) and lines the horizontal one (azimuth). The SAR image intensity in Fig. 8.2 reveals three buildings (the image has been taken in Hong Kong on the 25th of October 2008 by TerraSAR-X). The picture of the phase looks simply noisy. This is due to the independency of the phase of nearby resolution cells. In fact, each resolution cell (corresponding to about 3 m by 3 m on the ground for TerraSAR-X) is plotted with a color showing the corresponding phase value ϕ . Assuming a single target is present in a resolution cell, the phase can be expressed as a function of its distance R_i from the sensor in the following way:

$$\phi_i = \frac{4\pi}{\lambda} R_i \quad (8.1)$$

The phase quantity in Eq. 8.1 is ambiguous and it is measured in radians, thus

$$\phi_i = \phi_i \pm 2n\pi \quad (8.2)$$

where n is an arbitrary integer number. For TerraSAR-X $\lambda = 3.1 \text{ cm}$. Considering that the target may be located anywhere in the resolution cell (3 m by 3 m), it becomes evident how the phase of two nearby resolution cells is totally independent. In case more targets would be present in the resolution cell, the discussion would be slightly more complex, but the outcome would not change.

The interference between two radar images removes the independent component of the phase, leaving just phase variations among nearby resolution cells, which may be correlated, as visible in Fig. 8.3. The interferogram between images i and k can be expressed as

$$Int_{i,k}(s, l) = Img_i(s, l) \cdot Img_k^*(s, l) \quad (8.3)$$

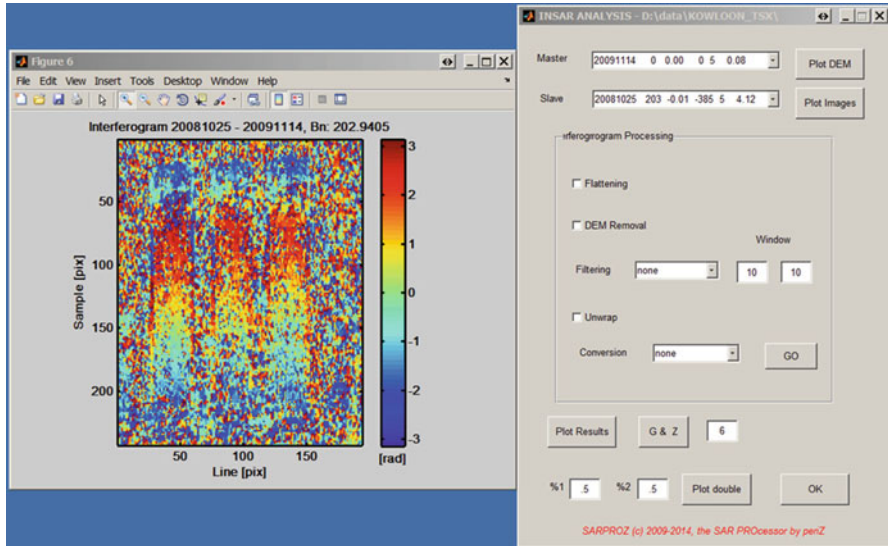


Fig. 8.3 Example of interferogram generated between the image shown in the previous picture and the Master image (taken on the 14th of November 2009). On the *right* the Sarproz window used for interferogram generation is shown

In Eq. 8.3 the product is applied pixel by pixel and the star sign * indicates the complex conjugate. The interferometric phase between images i and k can be expressed as

$$\phi_{i,k}(s, l) = \phi_i(s, l) - \phi_k(s, l) \quad (8.4)$$

and by exploiting Eq. 8.1 we obtain:

$$\phi_{i,k}(s, l) = \frac{4\pi}{\lambda} [R_i(s, l) - R_k(s, l)] \quad (8.5)$$

Figure 8.3 shows an example of interferogram generated between the image in Fig. 8.2 and the Master image acquired in November 2009. While the phase of the image in Fig. 8.2 was totally uncorrelated, the interferogram shows correlation on the facades of the three imaged buildings.

8.2.1 The InSAR Geometry

In order to better understand the interferometric phase in Eq. 8.5, we refer to the geometry depicted in Fig. 8.4. We abandon for a moment the pixel notation s, l and we concentrate on the targets coordinates on the ground. We want to derive the

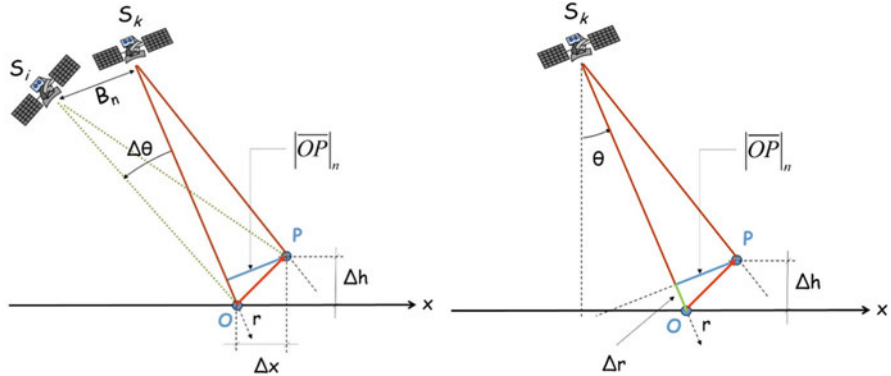


Fig. 8.4 Acquisition geometry for interferogram generation. S is the satellite at positions i and k . O is the reference point and P the target under examination. P is located at distance Δx w.r.t. O and at height Δh . The Master slant range is indicated as r . On the right the projections of OP along slant range and cross-range (normal to slant range) are highlighted in green and blue respectively

interferometric phase at point P with respect to a reference point O . Point P lies at a distance Δx from O and at a height Δh . The satellite reference location (Master) is S_k , while the Slave position is S_i . The relative position between Master and Slave is measured in terms of distance along the direction normal to the reference slant range (indicated with r in Fig. 8.4) and it is called Normal Baseline B_n . The relative incidence angle $\Delta\theta$ is thus

$$\Delta\theta = \frac{B_n}{R_k} \quad (8.6)$$

where $R_k = \overline{S_k O}$ is the Master range of reference point O . The relative interferometric phase is thus

$$\Delta\phi_{i,k} = \phi_{i,k}(P) - \phi_{i,k}(O) = \frac{4\pi}{\lambda} [R_{i,k}(P) - R_{i,k}(O)] \quad (8.7)$$

where $R_{i,k}(P) = \overline{S_i P} - \overline{S_k P}$ and $R_{i,k}(O) = \overline{S_i O} - \overline{S_k O}$. The double difference operation can be solved via trigonometry, leading to the following expression:

$$\Delta\phi_{i,k} = \frac{4\pi}{\lambda} \frac{B_n}{R_k} |\overline{OP}|_n \quad (8.8)$$

where $|\overline{OP}|_n$ (the blue arrow in Fig. 8.4) is the projection of \overline{OP} onto the direction normal to r . The term can be further decomposed into slant range and height components

$$|\overline{OP}|_n = \frac{\Delta r}{\tan \theta} + \frac{\Delta h}{\sin \theta} \quad (8.9)$$

as easily derived by looking at Fig. 8.4 on the right.

By combining Eqs. 8.8 and 8.9 the relative interferometric phase becomes

$$\Delta\phi_{i,k} = \Delta\phi_{i,k}^{flat} + \Delta\phi_{i,k}^{height} \quad (8.10)$$

where

$$\Delta\phi_{i,k}^{flat} = \frac{4\pi}{\lambda} \frac{B_n}{R_k} \frac{\Delta r}{\tan \theta} \quad \text{and} \quad \Delta\phi_{i,k}^{height} = \frac{4\pi}{\lambda} \frac{B_n}{R_k} \frac{\Delta h}{\sin \theta} \quad (8.11)$$

are called respectively flat terrain and topographic (height) phase terms.

8.2.2 Interferogram Flattening

Equations 8.10 and 8.11 highlight the first two main components of the interferometric phase. The first of them, the flat terrain phase term, is depending on the slant range coordinate of target P (and not on its height). In a generic interferogram $Int_{i,k}(s, l)$ we can thus expect a phase ramp in range direction, function of the coordinate s , with a rate proportional to the interferometric baseline B_n . An example of flat terrain phase component is shown in Fig. 8.5, where a Tandem-X interferogram is reported. The Interferometric baseline B_n is equal to 214 m. A longer baseline would generate a higher frequency of fringes.

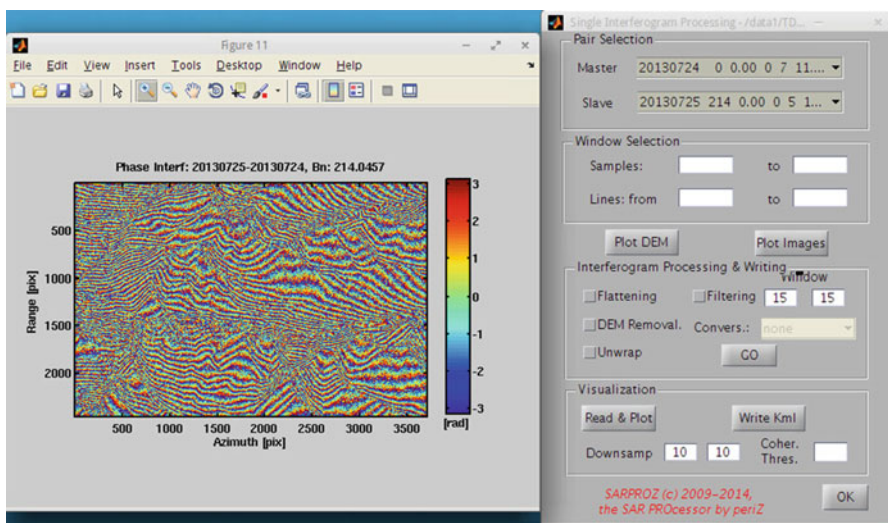


Fig. 8.5 Example of Tandem-X interferogram (Normal Baseline = 214 m). Fringes in the range direction (vertical in the image) show the flat terrain phase component

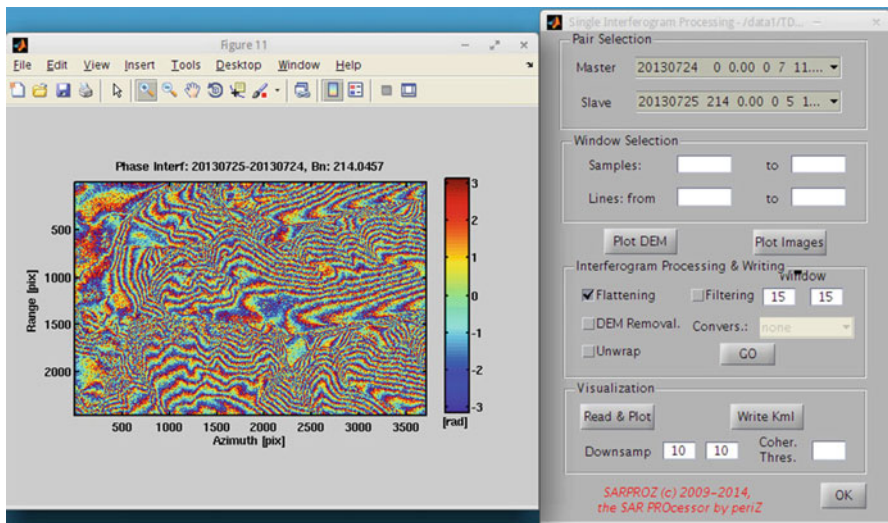


Fig. 8.6 Example of Tandem-X interferogram (Normal Baseline = 214 m), after estimation and removal of the flat terrain. Fringes are proportional to the topography of the imaged terrain

The flat terrain phase term is not carrying information useful for any kind of applications and it is usually simply removed. However, in case orbital data are not available, the flat terrain phase ramp can be used to estimate the interferometric normal baseline. The aim can be easily reached via a Fourier transform in the two-dimensional space range/azimuth. Conversely, if orbital data are available, the flat terrain phase term can be estimated by simulating the interferometric phase generated by a surface in ground coordinates with constant ellipsoidal height.

Figure 8.6 shows an example of flattened interferogram (that is, after removing the flat terrain phase term). The area reported in Fig. 8.6 is the same as the one in Fig. 8.5, the difference between the two images is the flat terrain removal.

8.2.3 The Topographic Term

The second phase term in Eqs. 8.10 and 8.11 is proportional to the height of point P with respect to the reference point O . This phase component reveals that interferograms are sensitive to the topography of the observed area. This is the reason why the production of Digital Elevation Maps (DEM's) was the first application developed for SAR interferometry over land.

From Eq. 8.11 we can derive an important quantification of the sensitivity of the interferometric phase towards topography: the ambiguity height. The ambiguity height Δh_a is the height that generates a phase rotation equal to 2π .

$$\Delta h_a = \frac{\lambda R_k \sin \theta}{2B_n} \quad (8.12)$$

In other words, while looking at a flattened interferogram like the one shown in Fig. 8.6, each phase fringe corresponds to a height range Δh_a . It is easy to understand then that the integration of all phase fringes in a flattened interferogram would lead to the estimation of the topography of the observed area. The operation of integration of phase fringes, when possible, is called phase unwrapping, and it will be discussed later in this Section.

Equation 8.11 shows the role played by the interferometric baseline B_n in the height estimation. A large normal baseline reduces the ambiguity height, increasing the frequency of topographic fringes of a given area. While this could be desirable for achieving a higher sensitivity of the interferometric phase towards the terrain height, its drawback is to cause decorrelation of the interferometric phase. Also decorrelation will be addressed further in this Section.

Other geometrical InSAR phase components may arise as a consequence of variation of other acquisition parameters (like central frequency and Doppler Centroid). Moreover, a precise treatment should consider the possible presence of single strong scatterers in the resolution cell and their sub-cell location. For both topics, the interested reader can refer to (Perissin and Rocca 2006; Perissin et al. 2006) for a detailed analysis.

8.2.4 Differential Interferometry and Displacement Detection

Repeat pass SAR interferometry is possible thanks to the characteristics of the orbits along which SAR satellites fly. Satellites carrying SAR sensors for Earth Observation are usually placed along sun-synchronous Polar orbits, which allow scanning the Earth surface regularly with a given (usually fixed) revisit time. In particular, every time a satellite flies over a given point on the ground at each revisit time, the UTC time of the day is the same, allowing keeping environmental parameters with daily variations constant. Moreover, the orbital tubes are designed in order to guarantee a distribution of normal baseline values compatible with interferometry.

As a consequence, besides the geometric component discussed in the previous sections, the interferometric phase may be influenced by the terrain displacement occurred between the two acquisition times. A movement of point P in a generic direction can be expressed in the x, h plane as

$$\vec{d} = \delta \vec{x} + \delta \vec{h} \quad (8.13)$$

where the arrow indicates a vector. The range displacement detected by the radar would therefore be

$$\Delta\phi_{i,k}^{disp} = \frac{4\pi}{\lambda} |\vec{d}|_r = |\delta \vec{x}| \sin \theta + |\delta \vec{h}| \cos \theta \quad (8.14)$$

The interferometric phase is thus very sensitive to displacement (half a wavelength movement causes a 2π phase rotation). However, the sensitivity is only along the slant range r . Given a single acquisition geometry, it is not possible to reconstruct the direction of the displacement. Moreover, a movement in the direction orthogonal to the slant range would not be detected at all. For an incidence angle $\theta = 30$ deg, almost 90 % of the vertical component of the displacement would be detected by the sensor, against only 50 % of the horizontal component.

The high sensitivity to displacement is what makes InSAR a very powerful tool for detecting ground movements. Whenever displacement estimation is the aim of the interferometric analysis (rather than topographic reconstruction), it is therefore helpful to remove the geometric phase component to facilitate the identification of phase temporal changes. The interferometric phase after removal of flat terrain and topographic phase components is called Differential Interferometric phase (DInSAR):

$$\Delta\phi_{i,k}^{DInSAR} = \Delta\phi_{i,k} - \Delta\phi_{i,k}^{flat} - \Delta\phi_{i,k}^{height} \quad (8.15)$$

An example of Differential interferogram is shown in Fig. 8.7. The interferogram in Fig. 8.7 has been generated using a pair of Envisat images over L'Aquila acquired one before and one after the Earthquake happened in 2009. To remove the topographic phase component SRTM data was used.

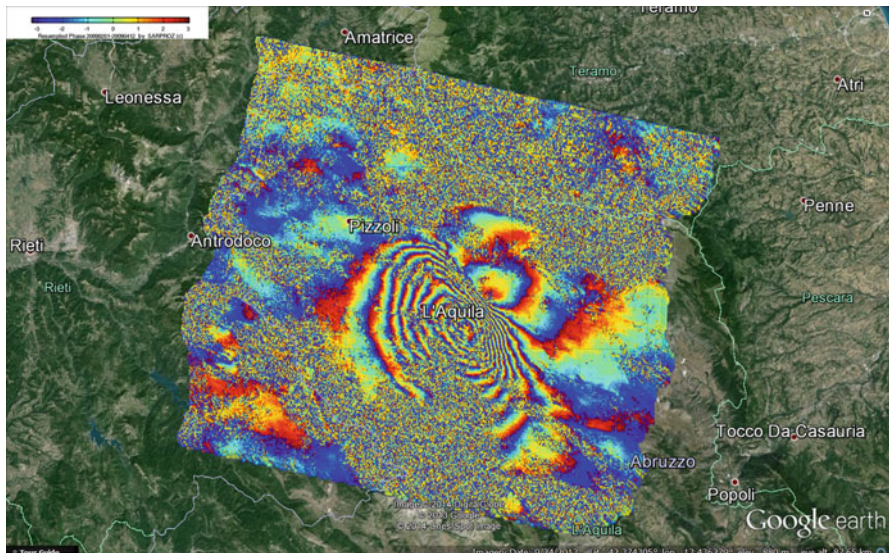


Fig. 8.7 Example of geocoded Differential Interferogram produced by Sarproz using Envisat images (20090201–20090412) showing the displacement caused by L'Aquila Earthquake. SRTM data has been used to remove the topographic phase component (Processing by A. Rocca)

8.2.5 Phase Decorrelation and the Interferometric Coherence

InSAR is potentially an extremely powerful technique for DEM generation and displacement monitoring. However, whenever changes occur in the terrain reflectivity, the two images involved in the interferogram generation may lose correlation and the phase may become unreadable. An example of this can be observed in Fig. 8.7, where the fringes become noisy. Changes could occur in time: some terrain characteristic (like shape, material, orientation) is modified. This happens often e.g. in case of vegetation/forests/fields, but also in case of human activities. We talk therefore of temporal decorrelation. However, changes could occur also because of geometric modification of the terrain reflectivity: due to the short wavelength of the radar signal, even slight changes of the looking angle may determine very different reflections (Perissin et al. 2006). This phenomenon takes the name of geometric decorrelation.

Regardless the source of decorrelation, it is useful to quantify its impact. To this aim, the normalized complex cross-correlation coefficient of images i,k is used:

$$\gamma_{i,k} = \frac{E[Img_i Img_k^*]}{\sqrt{E[|Img_i|^2]}\sqrt{E[|Img_k|^2]}} \quad (8.16)$$

In Eq. 8.16 $E[\cdot]$ denotes the expected value. The absolute value of $\gamma_{i,k}$ is called interferometric coherence. Values of the coherence close to 1 indicate high correlation between the two images, and thus readable interferometric phase. Conversely, low coherence identifies decorrelation and thus noisy and unreliable phase.

In order to estimate the quantity in Eq. 8.16 two main aspects have to be addressed. The first one is the substitution of the expected value with a spatial average of nearby pixels. Key role is played in this regard by size and shape of the window chosen for the average calculation. In the following we will simply adopt a general rectangular window, however, optimum performances are reached by an adaptive window. The second matter is phase ramps correction before the estimation of the expected value. Should the interferogram at the numerator of Eq. 8.16 be taken raw, phase ramps caused e.g. by the flat terrain would strongly reduce the estimated coherence. The estimator of $\gamma_{i,k}$ can then be expressed as

$$\gamma_{i,k}(s,l) \cong \frac{\sum_{u,v \in Win(s,l)} Img_i(u,v) Img_k^*(u,v) e^{-j\Delta\phi_{i,k}^{mod el}(u,v)}}{\sqrt{\sum_{u,v \in Win(s,l)} |Img_i(u,v)|^2} \sqrt{\sum_{u,v \in Win(s,l)} |Img_k(u,v)|^2}} \quad (8.17)$$

The quantity $\gamma_{i,k}$ is calculated for each pixel s,l over a given window $Win(s,l)$. The term $\Delta\phi_{i,k}^{mod el}$ indicates the phase ramps to be removed and it may include one or more geometrical phase terms described in the previous paragraphs.

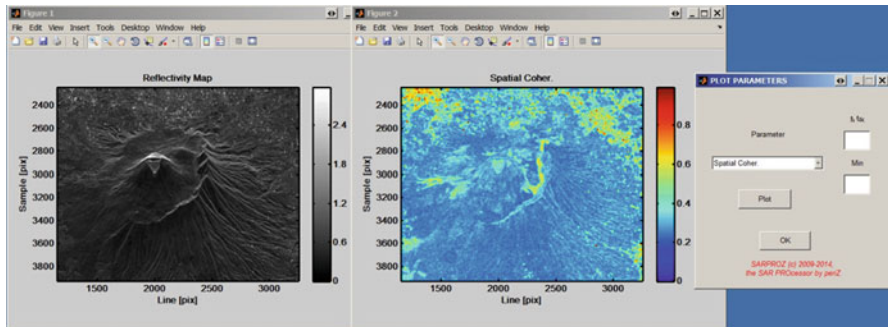


Fig. 8.8 Mount Vesuvius, Italy. *Left*: reflectivity map. *Right*: spatial interferometric coherence (taken from the average of 40 interferograms). The coherence maps reveals lava flows on the *right* and on the *left* of the caldera. Lava flows are more coherent than the surrounding terrain because of the lack of vegetation

The interferometric coherence $|\gamma_{i,k}|$ is not only a useful indicator of the reliability of the interferometric phase. The coherence can be used also for change detection or classification purposes. An example is shown in Fig. 8.8, where a case study in Italy, Mt Vesuvius is reported. The image on the left shows the reflectivity map of the volcano. The image on the right is the interferometric coherence (in particular, the map displayed in Fig. 8.8 has been generated from the average of 30 interferograms). It is very nice to notice the lava flows on the right and on the left of the caldera: they are pretty well visible from the coherence map, but not from the reflectivity map. The reason for the higher coherence is the lack of vegetation over the lava flows. The coherence can thus be used for mapping purposes, together with other SAR/InSAR products as well as with other data (as optical, multispectral, and more).

8.2.6 Interferogram Filtering

The absolute value of $\gamma_{i,k}$ tells us the correlation of nearby pixels. Its phase, on the other side, is an estimator of the expected value of the interferometric phase. The averaging operation of nearby pixels has the effect of smoothing noisy phase variations, enhancing the signal to noise ratio. This effect corresponds to the one of filtering for noise reduction.

Many typologies of filters have been introduced in the literature, addressing different aspects of decorrelation and of the possibility to recover information from noisy interferograms. Some of them are discussed in the ESA manual (Ferretti et al. 2007). It is worth to mention here the most widely used InSAR filter, proposed firstly by Goldstein (Goldstein and Werner 1998) and then later modified by other authors (Baran et al. 2003).

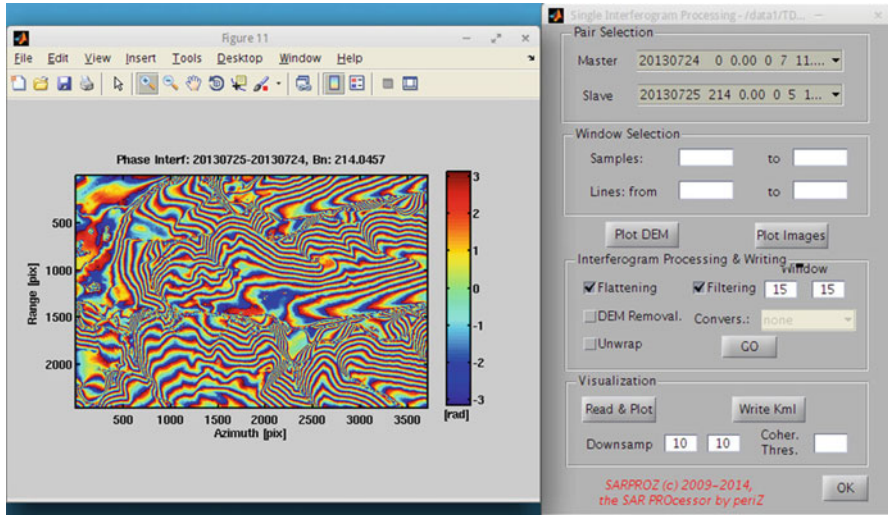


Fig. 8.9 Filtered Tandem-X interferogram (the same area as in Fig. 8.6). After filtering, fringes became much clearer, even if some spots of decorrelation can still be observed (in particular at the top of slopes)

An example of interferogram filtered by the modified Goldstein filter is shown in Fig. 8.9. The interferogram reported there is the same of Fig. 8.6, and data have been taken by Tandem-X in bistatic configuration. After filtering, fringes are much cleaner, even if one can observe a few spots of decorrelation, in particular on the top of slopes.

8.2.7 Interferogram Unwrapping

The integration of fringes of an interferogram for solving phase ambiguities is called phase unwrapping. More specifically, phase unwrapping refers to solving the following equation for the integer number n

$$\phi_{i,k}^{UW}(s,l) = \phi_{i,k}(s,l) \pm 2n\pi \quad (8.18)$$

The unwrapped phase (left in Eq. 8.18) is equal to the wrapped phase plus an integer multiple of 2π 's. Usually, if an interferogram is highly coherent, phase unwrapping is not a big issue. However, in case of poor coherence it may even be impossible to solve Eq. 8.18. Or at least, it may be impossible to solve it using a single interferogram. We will see in the next Section how multi-temporal InSAR is actually a much more robust solution to phase unwrapping.

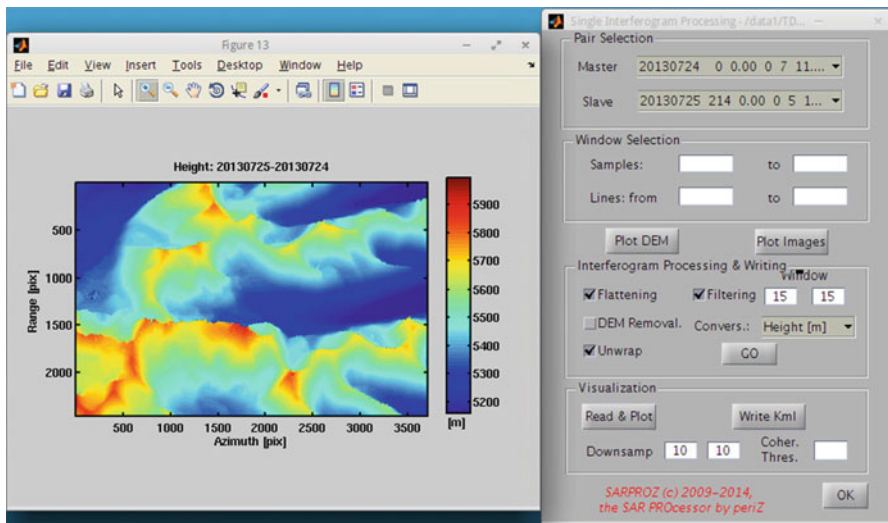


Fig. 8.10 Unwrapped and converted interferogram. The Tandem-X interferogram previously shown has been here unwrapped and converted into meters. The high coherence allowed a very precise unwrapping. Some flickering noise is still present in low coherence spots

Several solutions have been proposed in the literature for the phase unwrapping problem. Also in this case, the ESA manual can furnish an overview of some of them, providing a good starting point for a deeper investigation of the topic (Ferretti et al. 2007).

An example of interferogram unwrapped by Sarproz is shown in Fig. 8.10. The phase of the interferogram of Fig. 8.9 has been unwrapped and converted into height. The final result is pretty nice and smooth, thanks to the high coherence of the Tandem-X interferogram. However, the low coherence spots are still visible in the unwrapped phase.

8.2.8 The Atmospheric Delay

Despite the high potential of SAR interferometry, even when high coherence is found and fringes unwrapped correctly, an attentive analysis trying to interpret the result in terms of topography or of terrain displacement may end up showing poor accuracy. The reason for the possible frustrating outcome is that repeat-pass SAR interferometry is affected by different atmospheric conditions at the acquisition time. Water vapor is in fact delaying radar signals and its spatially

varying distribution biases the InSAR phase. Therefore, the expected millimeter precision of displacement measurements turns into centimeters accuracy, while the metric precision in height estimation can quickly become tens of meters.

In recent years many research group have worked on the atmospheric delay correction in InSAR (Li et al. 1978). Spectrometers, numerical weather models, GPS networks can in fact provide water vapor maps and partly mitigate atmospheric effects in InSAR, however, only at very low resolution and for very long spatial wavelengths. As a matter of fact, classical InSAR is strongly impaired by atmospheric disturbances. Research-based large scale applications (as earthquake modeling) are still possible, but, with a level of details far away from the claimed millimeter accuracy.

Figure 8.11 brings an example of the Atmospheric Phase Screen estimated from TerraSAR-X data over Los Angeles. The dataset used in the analysis is composed by 64 TerraSAR-X images over Los Angeles. The footprint is 30 km by 60 km. From Fig. 8.11 one can appreciate how important the impact of atmospheric delay is in X-band.

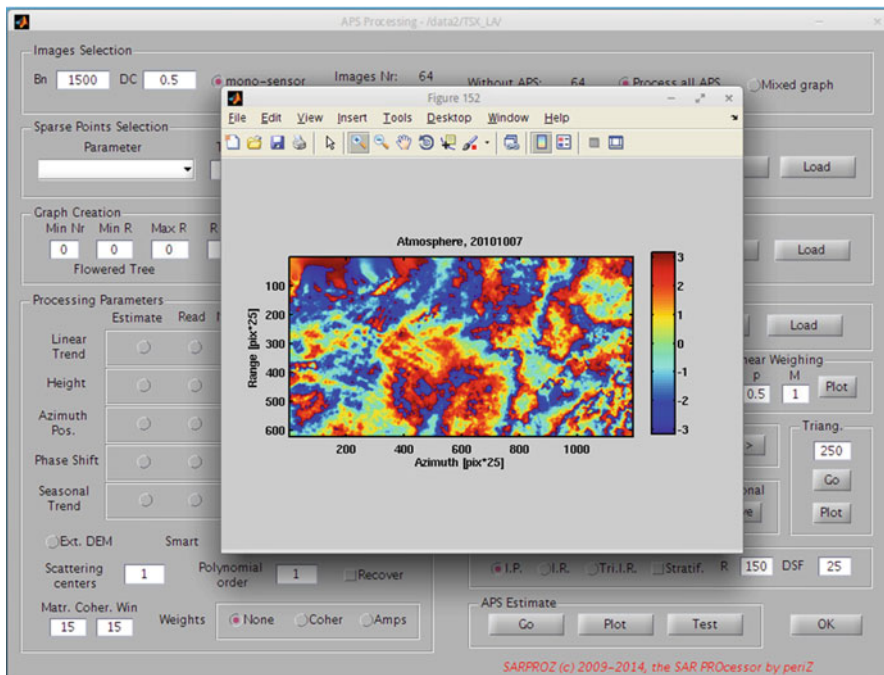


Fig. 8.11 Example of atmospheric delay estimated from TerraSAR data over Los Angeles. The image is 30 km by 60 km wide, and the high atmospheric variability is revealed by the X-band short wavelength. In the background the Sarproz module for atmospheric delay estimation

8.3 Multi-temporal InSAR

In the previous Section we have introduced the basics of classic InSAR. SAR interferometry is a very promising technology, however, it is affected by a series of important problems. First of all, interferograms suffer decorrelation (temporal and/or geometrical). In second instance, the interferometric phase is wrapped, and it may be quite difficult (if possible at all) to unwrap it correctly using a single interferogram. Moreover, if the topography of the area of interest is not known with enough precision, it may be very hard to distinguish between residual topography and terrain displacement. Finally, even by solving all previous problems, atmospheric artefacts can vanish all efforts, strongly biasing the detected signals. In this section, we introduce a possible solution to the mentioned problems: Multi-Temporal InSAR.

8.3.1 *Introduction*

The first satellite carrying a SAR sensor for Earth Observation was the NASA Seasat in 1978. Even though its life time was quite limited, the mission was very useful to demonstrate the SAR capabilities. However, only with the launch of ERS-1 in 1991, archives of repeated SAR images became available. As soon as multiple images of the same area were collected, researchers started working at problems like DEM estimation via Multi-Temporal InSAR, trying to solve limitations as decorrelation, phase unwrapping, atmospheric delay. In early 2000, the Polytechnic of Milan firstly proposed the Permanent Scatterers (PS) technique (Ferretti et al. 2001). The PS technique is based on the idea that, exploiting long series of SAR images, it is possible to identify targets that do not change their electromagnetic signature throughout the dataset. Such targets are not affected by temporal or geometrical decorrelation and their InSAR phase can thus be studied as a function of the acquisition parameters (normal and temporal baseline). It is possible then to observe that height, displacement and atmospheric delay show different spectral characteristics as a function of normal and temporal baseline and as a function of space. Based on such observation, their separation and estimation become then possible.

In this Section we will firstly introduce the basics of Persistent Scatterers Interferometry (PSI). Afterwards, we will discuss a series of extensions of the original ideas (like seasonal and non-linear signals estimation). We will then conclude the treatment with multi-master and weighted approaches. All examples brought here were processed by Sarproz ([Perissin, www.sarproz.com](http://www.sarproz.com); Perissin et al. 2011).

8.3.2 The PSI Approach

To introduce here the main concepts of the PSI technology, we take our steps from a real processing example. The interested reader can replicate the experiment on its own using a licensed copy of Sarproz (Perissin, www.sarproz.com; Perissin et al. 2011). The dataset under study is composed by $N_I = 51$ TerraSAR-X images acquired over Hong Kong in the period October 2008–May 2011. A sketch of the acquisition parameters of the dataset is reported in Fig. 8.12. From the upper left corner of Fig. 8.12 on the left, in clockwise order, we have the histogram of the Normal Baselines, the histogram of the Doppler Centroids, the temperature at the acquisition time, and the sensors that acquired the data (TerraSAR and Tandem). On the right of Fig. 8.12 we can see the interferometric configuration of the analysis: each image is connected to form an interferogram with the Master image, chosen at the barycenter of the distribution of normal and temporal baselines. From Fig. 8.12 on the right it is possible to observe eight images with a lower barycenter of normal baselines: they are the eight Tandem images of the dataset. The analyzed area is the same of the SAR image example reported in Fig. 8.2, and it covers three buildings in the Hong Kong harbor.

Figure 8.13 shows the starting point of the PSI analysis: the Reflectivity Map of the area of interest. The Reflectivity Map has been estimated as the average of all images of the dataset. It is interesting to compare it with the intensity of one single SAR image (as the one shown in Fig. 8.2). The averaging operation has strongly suppressed the noise, enhancing all targets which kept stable reflectivity throughout the dataset.

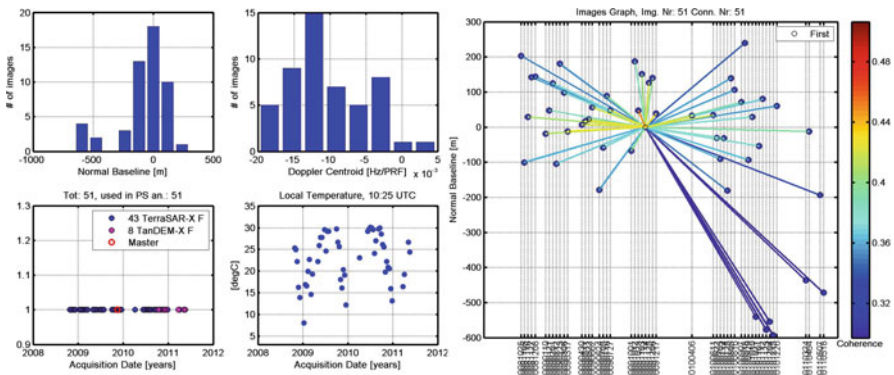


Fig. 8.12 Dataset used in the PSI experiment. 51 images taken by TerraSAR-X in Hong Kong. On the left, upper plots: Histograms of Normal Baseline and Doppler Centroid. Lower part, acquisition dates and temperature at the acquisition time. The image on the right shows the interferometric combination: one image is taken as reference and interferograms are generated with respect to it

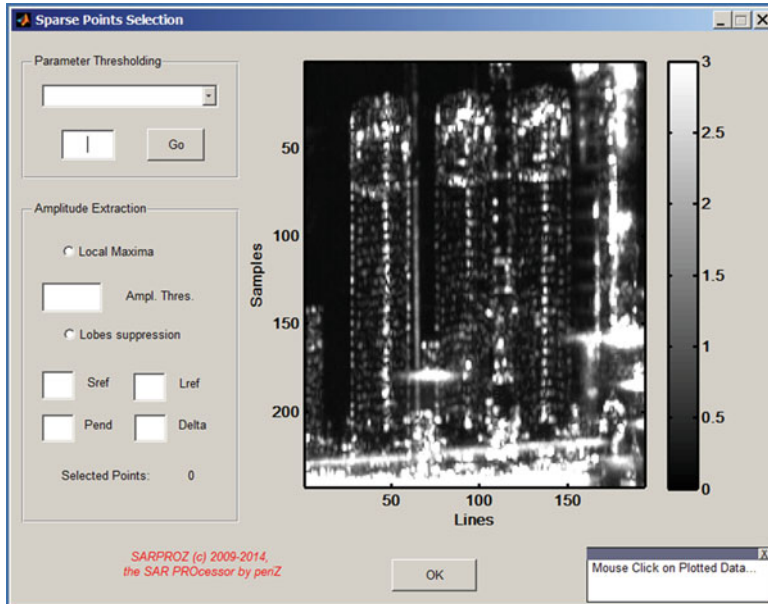


Fig. 8.13 Reflectivity map (average intensity) of the area of interest. Three buildings are visible in the area of interest

We decide then to analyze all targets that present a visible peak in the image, and we select them posing a threshold on the Reflectivity equal to 0.5. Figure 8.14 shows $N_p = 1472$ points selected for the analysis.

As previously mentioned, the aim of the analysis is solving the InSAR limitations, estimating height and displacement of targets. We take a reference point o among the selected targets (e.g. the one with highest Reflectivity) and we analyze the interferometric phase of all selected points p (we omit from now on the reference index o to lighten the notation)

$$\Delta\phi_{i,k}(p) = \Delta\phi_{i,k}^{flat}(p) + \Delta\phi_{i,k}^{height}(p) + \Delta\phi_{i,k}^{disp}(p) + \Delta\phi_{i,k}^{atmo}(p) + \Delta\eta_{i,k}(p) \quad (8.19)$$

Indexes i, k denote again the interferometric couple, with k master image and i a generic image of the dataset.

The interferometric phase in Eq. 8.19 is made of the following components: flat terrain, height, possible displacement, atmospheric delay and noise. As stated in the previous Section, more factors should be considered for a complete analysis (Perissin and Rocca 2006; Perissin et al. 2006), but we will keep the complexity limited in this discussion.

The first term in Eq. 8.19, the flat terrain, can be estimated from orbital data and removed. We will not consider here possible orbital inaccuracies for the sake of simplicity. The second term, the topographic phase, is given by Eq. 8.11, and it is

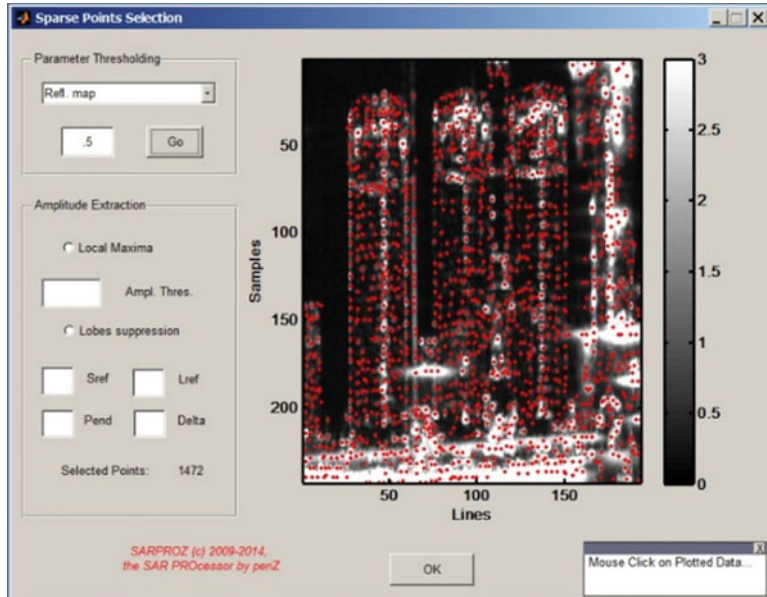


Fig. 8.14 Targets selected for the PSI processing: 1472 points with Reflectivity higher than 0.5

linear with the normal baseline and with the target height. We can rewrite it here, making explicit the dependency of the height $\Delta h(p)$ on the target of interest p and the dependency of the normal baseline $B_{n,i}$ on the i -th image of the dataset:

$$\Delta\phi_{i,k}^{height}(p) = \frac{4\pi}{\lambda} \frac{B_{n,i}}{R_k} \frac{\Delta h(p)}{\sin \theta} \quad (8.20)$$

The third term is the displacement. A common way to model the displacement is that of assuming it linear in time. We will see later on in this Section that such assumption is not always working, but we take it as a starting point. Defining thus $\Delta v(p)$ the relative velocity of point p with respect to the reference and $B_{t,i}$ the temporal baseline

$$\Delta\phi_{i,k}^{disp}(p) = \frac{4\pi}{\lambda} \Delta v(p) B_{t,i} \quad (8.21)$$

The fourth term is the atmospheric delay. It has been shown in the literature that the atmospheric delay has a decorrelation length of several hundreds of meters (Hanssen 2001). We can thus assume its impact small in our area of interest, and neglect it. We will not consider here how to extend the analysis at bigger areas and estimate the Atmospheric Phase Screen. For that purpose, the interested reader can refer to (Kampes 2006).

The last term in Eq. 8.19 is $\Delta\eta_{i,k}(p)$, with which we have indicated noise. The noise will be estimated from the model residuals, and it will tell us the stability and reliability of the target at hand.

As a conclusion, in our small area of interest, we can see our problem as a set of N_p equations with N_I samples each, where the unknowns are height $\Delta h(p)$ and velocity $\Delta v(p)$ of each point to be estimated in the space $B_{t,i}B_{n,i}$. The system looks linear, but, considering that the phase is wrapped, it is not. In (Ferretti et al. 2001) the proposed solution to solve the system comes from the maximization of the periodogram in which height and velocity represent the 2-dimensional frequencies to be scanned. In formulas, the periodogram $\xi[\Delta v(p), \Delta h(p)]$ is

$$\xi[\Delta v(p), \Delta h(p)] = \frac{1}{N_I} \sum_{i=1}^{N_I} e^{j[\Delta\phi_{i,k}(p) - \kappa_v \Delta v(p) B_{t,i} - \kappa_h \Delta h(p) B_{n,i}]} \quad (8.22)$$

In Eq. 8.22, $\kappa_v = \frac{4\pi}{\lambda}$ and $\kappa_h = \frac{4\pi}{\lambda R \sin \theta}$ group the factors linking velocity to time and height to normal baseline. For the sake of simplicity, we did not include here the flat terrain term: we assume it was already removed. The solution is given by the pair $\Delta\tilde{h}(p)$, $\Delta\tilde{v}(p)$ which maximizes the absolute value of the periodogram

$$\Delta\tilde{v}(p), \Delta\tilde{h}(p) = \arg \max \left\{ \left| \xi[\Delta v(p), \Delta h(p)] \right| \right\} \quad (8.23)$$

The maximum of the absolute value of the periodogram is called temporal coherence

$$\tilde{\xi}(p) = \left| \xi[\Delta\tilde{v}(p), \Delta\tilde{h}(p)] \right| \quad (8.24)$$

When the model driven by $\Delta\tilde{h}(p)$, $\Delta\tilde{v}(p)$ matches the observed interferometric phase, the argument of the periodogram in Eq. 8.22 is close to zero, and the temporal coherence tends to 1. Conversely, if the model does not match the observed phase, the argument of the periodogram will be random-like and the temporal coherence will get low values. Very important in this discussion is the number of images N_I used in the estimate. A low number of images will bias the temporal coherence to higher values, making it difficult to distinguish between stable and noisy points.

We are now ready to run the estimation in our test area. Figure 8.15 shows the PSI module for time series processing. In the left frame we can choose the parameters we want to estimate, and we select height and velocity. The search range of the height is $-50 \text{ m} \div 150 \text{ m}$, while for the velocity $-50 \text{ mm/year} \div 50 \text{ mm/year}$. The result of the analysis is shown in Fig. 8.16. The two upper plots in Fig. 8.16 are the estimated velocity and height, while the lower plot contains the temporal coherence. From Fig. 8.16 we can see that the bottom of the three buildings has been processed well, with the model matching the observed phase. In fact, the temporal coherence has values close to 1 and the estimated parameters look reasonable. However, the

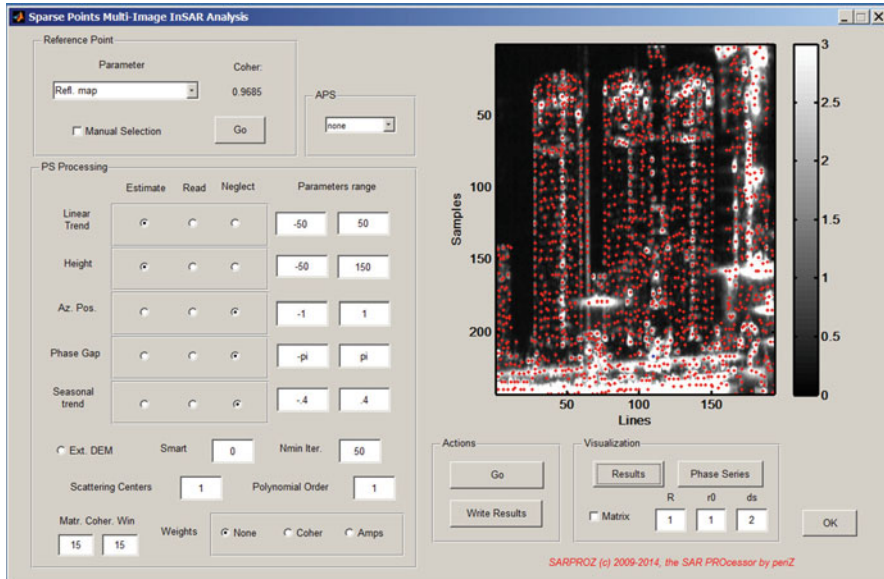


Fig. 8.15 PSI processing module. The settings show that the targets were processed estimating velocity (linear trend) and height. Velocity range: $-50 \div 50$ mm/year. Height: $-50 \div 150$ m

tops of the buildings have low coherence (around 0.3), and the estimated parameters show unreasonable jumps. To conclude, the analysis was only partly successful. The model we are using to process the InSAR time series of the top of the building is not matching the observations. In the next paragraph, we introduce a model modification to solve the situation.

8.3.3 Seasonal Signals

The reason for the failure of the time series processing described in the previous paragraph is that high buildings suffer thermal expansion (Perissin and Rocca 2006). As a consequence, by taking a reference point on the ground, targets at high elevation have a displacement which is not well modeled by a linear trend. The solution has then to be found by introducing a new model which can account for seasonal expansion. In particular, we can expect higher elongations with higher temperature. A possible model is thus the following

$$\Delta\phi_{i,k}^{therm}(p) = \frac{4\pi}{\lambda} \Delta\alpha(p) T_i \quad (8.25)$$

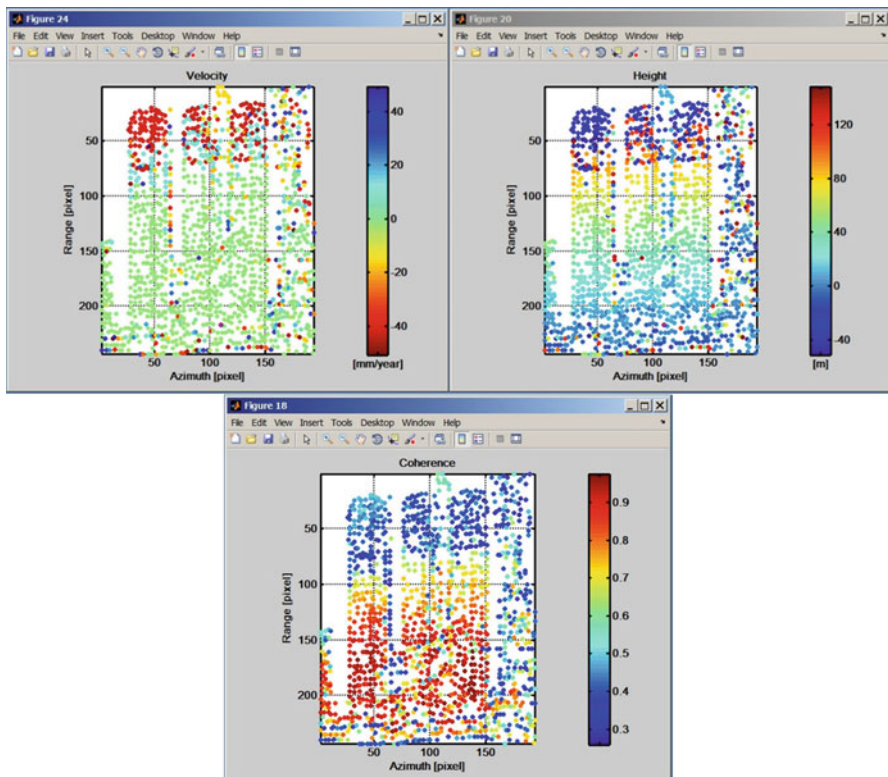


Fig. 8.16 PSI processing results. *Upper left corner*: estimated velocity. *Upper right corner*: estimated height. *Lower image*: estimated coherence. Where the temporal coherence is high (.7÷.9) the estimated parameters are reasonable. For lower coherence values (less than .5) both velocity and height show unreasonable jumps. The model is not matching the data

In Eq. 8.25 T_i is the temperature at the acquisition time² and $\Delta\alpha(p)$ is the thermal expansion coefficient of point p with respect to the reference point, measured in mm/degC. Equation 8.25 can be added to the model and the periodogram solved for three unknowns: height, velocity and thermal expansion coefficient.

Figure 8.17 shows the PSI module with the new added option for including in the estimation also the thermal expansion. Thermal expansion coefficient search values range from -.2 to .6 mm/degC. Figure 8.18 summarizes the result of the estimation. The first two plots report estimated height and velocity. The lower plots show coherence and thermal expansion coefficient. This time, targets on the buildings are coherent, the estimated velocity shows that no important movement is affecting

²Sarproz automatically downloads Temperature data from historic weather records, however, also independent Temperature data can be imported in the system.

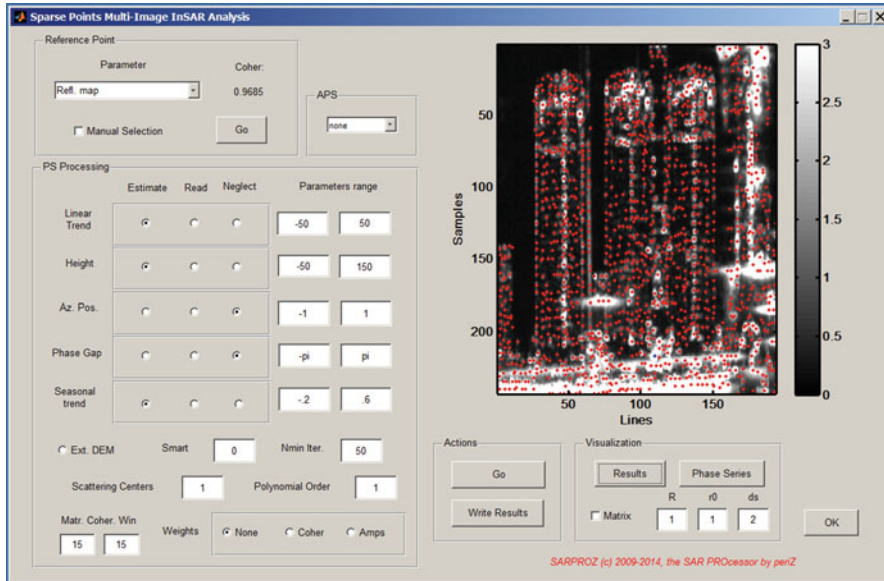


Fig. 8.17 PSI processing module. The settings show that, beside velocity and height, also a seasonal trend is going to be estimated. Range of the thermal expansion coefficient: $-.2 \div .6 \text{ mm}/\text{degC}$

the buildings, the estimated height is proportional to the buildings profile, and the thermal expansion coefficient is well correlated with the building height. The result demonstrates that the main reason for the low coherence detected on the building was due to the un-modeled thermal expansion.

Several points in Fig. 8.18 still show low coherence values. Such points are not well modeled neither by linear nor by seasonal displacement. In this particular example, the reason for low coherence resides in temporal random changes. The strip of low coherence targets on the right of the first building (starting from the left) is a harbor docking line, where boats stop for short periods of time. The strip of land on the right of the image is an area under construction, with excavators, cranes and other mechanical objects in motion. Thus both areas cannot be analyzed with Multi-Temporal InSAR. In the next paragraphs we will see other possible model extensions to fit different scenarios.

Before moving to other extensions of the PSI technique, we take a look of the geocoded results we've just processed. Figure 8.19 shows the results of the PSI processing in geographic coordinates over an optical layer as background. Figure 8.20 displays the same module, but the PSI results are plotted in 3 dimensions, with a color proportional to the estimated thermal expansion coefficient. The list of values beside the picture is relative to a selected point. Values show the target temporal coherence (.72), its height (113 m), displacement velocity (0 mm/year), thermal

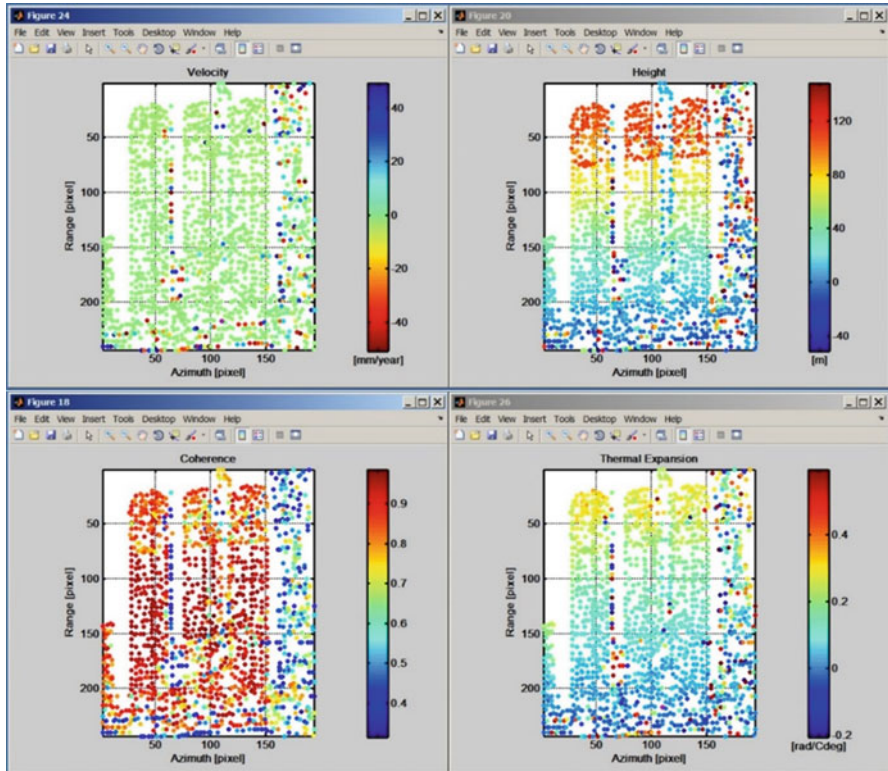


Fig. 8.18 PSI processing results. *Upper left corner*: estimated velocity. *Upper right corner*: estimated height. *Lower left*: temporal coherence. *Lower right*: thermal expansion. Now the temporal coherence has been increased also for high targets, and all parameters are correctly estimated. The thermal expansion is increasing proportionally to the targets height. Low coherence points are still present on the *right* of the *left* building and on the *right* of the image

expansion coefficient (.35 rad/degC). Finally, Fig. 8.21 displays an example of time series. Figure 8.21 is divided into two parts: in the upper one, the SAR intensity of the target at hand is plotted versus time; in the second one, the displacement in millimeters is plotted as a function of the acquisition time. In the second plot, 5 replicas of the time series are displayed. Replicas correspond to the phase ambiguity of the system: each vertical sample is equivalent. In particular when data are missing, one should consider the possibility that phase jumps occurred from one replica to another without being detected. In this example, the phase stability is quite high and phase jumps are not likely to have taken place. The trend in time is not smooth because the recorded temperature is not smooth in time. The blue line shows how well the model fits the data.

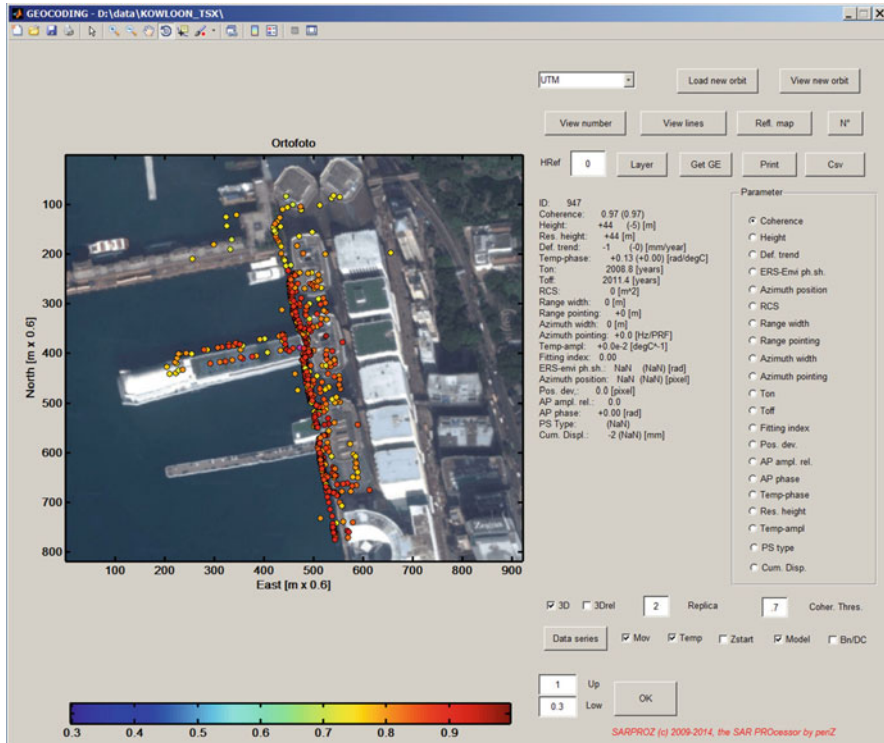


Fig. 8.19 PSI results geocoded on an optical layer. Here the color is proportional to the estimated coherence. One target is selected and a list of estimated parameters is visible on the right of the image

8.3.4 Non-linear Signals

Low temporal coherence can be caused also by displacement trends which are not linear and not correlated with temperature either. Movements may present acceleration: in this case a good model to use is the polynomial approximation

$$\Delta\phi_{i,k}^{disp}(p) = \frac{4\pi}{\lambda} \Delta v(p) B_{t,i} + \Delta a(p) B_{t,i}^2 \quad (8.26)$$

In Eq. 8.26, $\Delta a(p)$ is the acceleration of point p with respect to the reference. Other possible temporal behaviors are multiple linear segments, sudden jumps (like in the case of landslides activation or earthquakes), seasonal patterns (but not related to temperature, like dam oscillations related to the water level) or a combination of more of them. Even if still keeping the model-approach for comparison and for

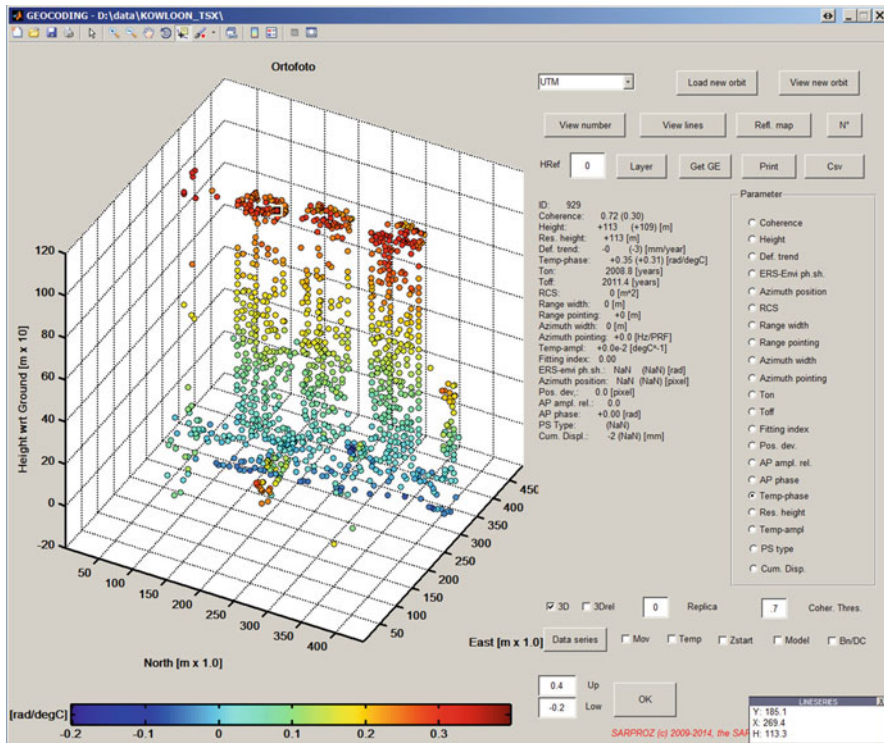


Fig. 8.20 3D visualization of the geocoded targets. The color is proportional to the thermal expansion coefficient. The three analyzed buildings are well resolved and the targets on the facades are geocoded vertically

educational purposes, Sarproz is now including alternative ways to process time series, without the need of models. An example is reported in Fig. 8.22. A dam in Hong Kong has been analyzed without displacement models, and a time series is reported on the left. The time series is displaying the interferometric phase after removal of the geometric terms (no smoothing is applied). The blue line, conversely, is derived by smoothing the phase to follow the displacement trend avoiding possible noisy oscillations. In the example in Fig. 8.23 the noise level is very low and smoothed line and phase values match pretty well.

When non-linear displacement trends are analyzed, velocity maps are not meaningful anymore. Cumulative displacement maps should be considered instead. A cumulative displacement map shows the total amount of millimeters a given area on the ground moved from the beginning to the end of the analyzed period. An example is shown in Fig. 8.23. A dataset of 64 TerraSAR-X images has been processed in Los Angeles. Red areas show a cumulative displacement of -50 mm in the period 2010–2014. Red spots in the picture identifies oil extraction areas. One

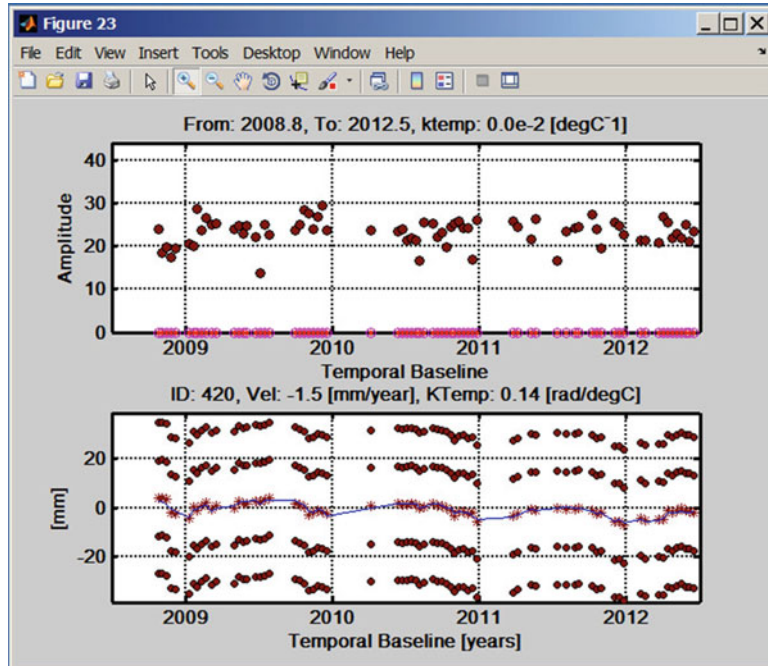


Fig. 8.21 Example of displacement time series. The time trend is not very smooth and not very sinusoidal, because summer in Hong Kong is longer than winter

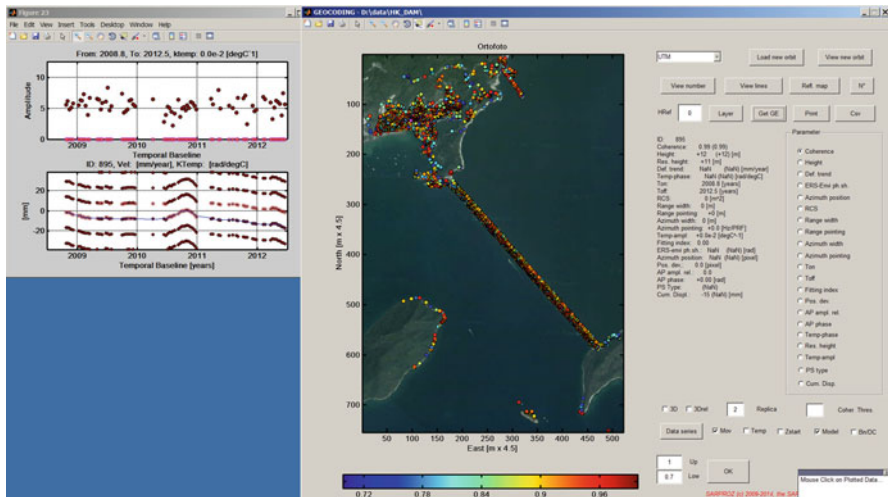


Fig. 8.22 A dam in Hong Kong. On the *right*: targets detected on the Dam structure. On the *left*: non-linear time series detected by Sarproz. Notice that the software does not apply any smoothing operation: the phase displayed there is the original interferometric phase after removing the topographic term

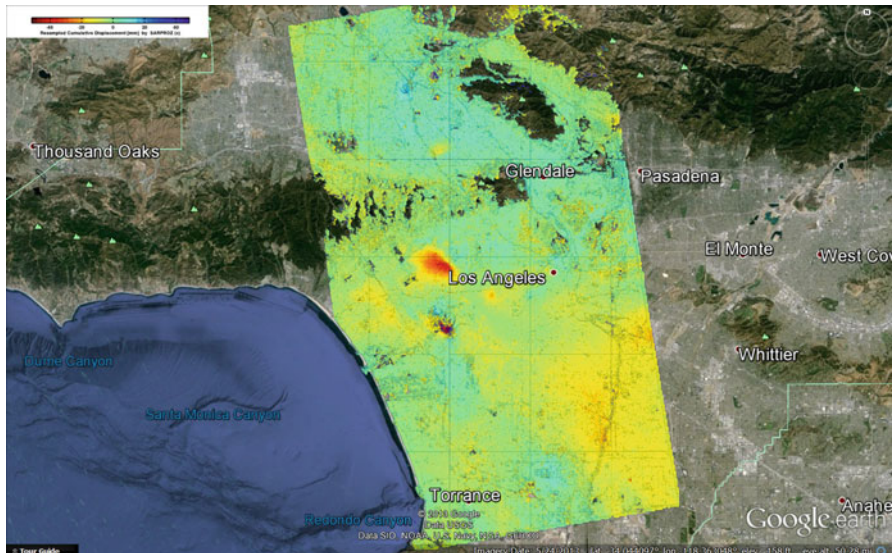


Fig. 8.23 Cumulative displacement map detected by Sarproz in Los Angeles using 64 TerraSAR-X images. Red corresponds to about -50 mm, in the period 2010–2014. The two spots of subsidence are over Oil extraction fields

of them has also blue features, meaning that water or gas is pumped underground to stabilize the subsidence. The Los Angeles basin is known to be characterized by seasonal movements. A linear analysis here would never work.

8.3.5 The Multi-master Approach

PSI techniques solved the main InSAR issues and made it possible to retrieve reliable time series from archived SAR data. However, the original PSI concept as published in (Ferretti et al. 2001) is very restrictive. In fact, according to the primordial algorithm, a target is required to be coherent in all interferograms generated with a single Master image. Such a strong condition is met only by manmade isolated targets whose dimensions are much smaller than the resolution cell. Whilst urban areas usually are characterized by such features, it is very difficult to find them in other scenarios (as rural/deserted/mountainous areas). The need thus for increasing the density of coherent targets also in extra-urban areas brought to a series of improvements/generalizations of the original PSI algorithm. We already mentioned in the introduction a couple of them (SBAS, StamPS and Squeesar), we briefly describe here the algorithm implemented by Sarproz: the Quasi-PS technique (Perissin and Wang 2012).

The main idea of multi-master approaches is to relax the strict conditions imposed by PSI techniques. Thus, instead of analyzing the InSAR phase generated

with respect to a single Master image, more options can be considered. If the computational power is not an issue, all possible interferograms should be evaluated, searching for the coherent ones. Otherwise, subset of interferograms can be selected (as small normal baseline subsets or pairs that can guarantee the connectivity of the images graph (Perissin and Wang 2012)). In any case, in a multi-master framework, in Eq. 8.19 and following, index k does not refer any more to a single image. Moreover, in the single-master approach, the number of samples per equation in the periodogram (Eq. 8.22) was indicated as N_l (equal to the number of images and also to the number of interferograms³). In a multi-master approach, the number of samples of Eq. 8.22 is equal to the number of interferograms N_{Int} , which is usually higher than N_l . By taking into account these points, we can modify Eq. 8.22 in the following way:

$$\xi [\Delta v(p), \Delta h(p)] = \frac{1}{N_{Int}} \sum_{i,k}^{N_{Int}} e^{j[\Delta\phi_{i,k}(p) - \kappa_v \Delta v(p) B_{t,i,k} - \kappa_h \Delta h(p) B_{n,i,k}]} \quad (8.27)$$

In Eq. 8.27, the sum is carried out on N_{Int} i,k pairs. Similarly to the single-master case, we can solve the system by searching for the model parameters (velocity and height in Eq. 8.27) which maximize the absolute value of the periodogram.

Figure 8.24 shows an example of DEM estimation by means of a Quasi-PS analysis of ALOS data. The image on the left of Fig. 8.24 is the interferometric combination used in the analysis: 34 interferograms were generated out of 9 images. The image on the right shows the estimated height in Google Earth. No initial

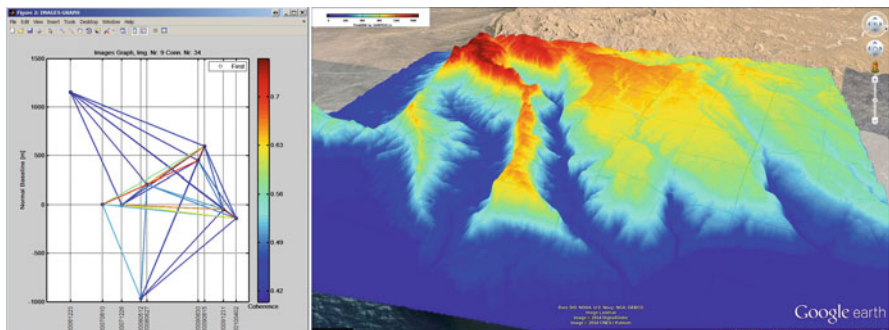


Fig. 8.24 Example of DEM generated via Quasi-PS analysis. On the left, interferometric configuration: 34 interferograms were generated out of 9 ALOS images. On the right, estimated height. Notice that no DEM was removed from the interferograms for this purpose. Multi-Temporal InSAR performs a reliable phase unwrapping

³Here for the sake of simplicity we assume that an all-zeros interferogram (Master-Master) is included in the dataset.

DEM was removed from the interferometric phase and no initial phase unwrapping was applied. This analysis shows that Multi-Temporal InSAR can provide a more reliable phase unwrapping than working with single interferograms.

8.3.6 Weighted Approaches

Together with the multi-master idea, a big improvement with respect to the original PSI algorithm is the introduction of weights in the parameters estimation. Weights act as flags that tell us in which interferograms a given target is coherent. Thus, not only highly coherent targets (Persistent Scatterers) can be successfully processed, but also decorrelating targets, thanks to the adaptive choice of interferograms subsets. For instance, seasonal targets (as mountain tops periodically covered by snow or trees loosing leaves) may be coherent only in summer (or only in winter) months. Extended geometrically decorrelating targets (as fields, low density vegetation) may be coherent only in very short normal baselines. Temporally decorrelating targets (as growing vegetation, areas under construction), may be coherent only in short temporal baselines. By knowing in which interferograms each of those target typologies is coherent, we can mask uncoherent interferograms out and keep only the informative ones.

The utilization of weights can be implemented with just a small modification in Eq 8.27. In order to keep an InSAR phase sample in the height/velocity estimation (or in order to disregard it) we can insert the weight $w_{i,k}$ (a number between 0 and 1) as it follows:

$$\xi [\Delta v(p), \Delta h(p)] = \frac{1}{\sum w_{i,k}} \sum_{i,k}^{N_{Int}} w_{i,k} e^{j[\Delta \phi_{i,k}(p) - \kappa_v \Delta v(p) B_{t,i,k} - \kappa_h \Delta h(p) B_{n,i,k}]} \quad (8.28)$$

The process for estimating the model parameters is still the same, but only InSAR pairs with high weight $w_{i,k}$ will be used. Notice that the same modification could be applied in a single-master framework with the same effect.

The Quasi-PS algorithm uses the absolute value of the interferometric coherence $\gamma_{i,k}(p)$ in Eq. 8.17 as weight. Sarproz gives different options for the choice of weights. Besides the coherence, another option is using intensity values or models estimated by processing intensity values. This is particularly useful when dealing with areas under construction, where targets remain coherent for short periods of time.

An example of a temporary target is reported in Fig. 8.25. The upper plot on the left in Fig. 8.25 displays the radar signal intensity, showing that the target disappeared in 2010. The plot below shows the displacement time series. Without masking the data-series for the life-time of the target, it would not be possible to successfully process it.

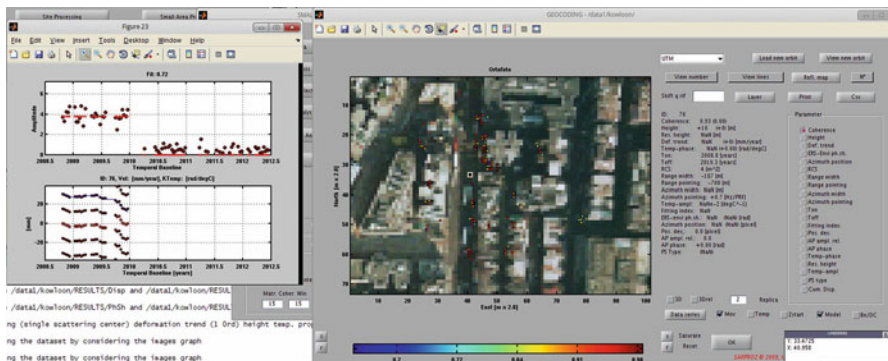


Fig. 8.25 Example of temporary target in Hong Kong. The plot on the *left, upper position* shows the intensity as a function of time. It is easy to observe that the target at hand was visible for a short period of time. The plot below shows the displacement time series during the target life time

8.4 Conclusions

In this Chapter we have discussed the basic theory behind SAR interferometry and Multi-Temporal InSAR. In particular, we have seen that InSAR is potentially a very powerful technology to estimate DEMs and ground movement, but also that InSAR is affected by important limitations (as decorrelation, phase ambiguity and atmospheric biases). Multi-Temporal InSAR techniques offer a series of tools for attenuating InSAR limitations, making it possible to process and analyze displacement time series, and also to precisely estimate ground elevation.

References

- Baran I, Stewart MP, Kampes BM, Perski Z, Lilly P (2003) A modification to the Goldstein radar interferogram filter. *IEEE Trans Geosci Remote Sens* 41(9):2114–2118
- Berardino P, Fornaro G, Lanari R, Sansosti E (2002) A new algorithm for surface deformation monitoring based on small baseline differential SAR interferograms. *IEEE Trans Geosci Remote Sens* 40(11):2375–2383
- Colesanti C, Wasowski J (2006) Investigating landslides with space-borne synthetic aperture radar (SAR) interferometry. *Eng Geol* 88(3–4):173–199
- Curlander JC, McDonough RN (1991) Synthetic aperture radar: systems and signal processing. Wiley, New York
- Engdahl ME, Hyypia JM (2003) Land-cover classification using multitemporal ERS-1/2 InSAR data. *IEEE Trans Geosci Remote Sens* 08/2003.
- Ferretti A, Prati C, Rocca F (1999) Multibaseline InSAR DEM reconstruction: the wavelet approach. *IEEE Trans Geosci Remote Sens* 37 I
- Ferretti A, Prati C, Rocca F (2001) Permanent scatterers in SAR interferometry. *IEEE Trans Geosci Remote Sens* 39(1):8–20
- Ferretti A, Monti-Guarnieri A, Prati C, Rocca F (2007) InSAR Principles: guidelines for SAR interferometry processing and interpretation (TM-19, February 2007)

- Ferretti A, Fumagalli A, Novali F, Prati C, Rocca F, Rucci A (2011) A new algorithm for processing interferometric data – stacks: SqueeSAR. *IEEE TGRS* 49(9):3460
- Goldstein RM, Werner CL (1998) Radar interferogram filtering for geophysical applications. *Geophys Res Lett* 25(21):4035–4038
- Goldstein RM, Zebker HA, Werner CL (1988) Satellite radar interferometry: two-Dimensional phase unwrapping. *Radio Sci* 23(4):713–720
- Graham LC (1974) Synthetic interferometer radar for topographic mapping. *Proc IEEE* 62(2): 763–768
- Hanssen RF (2001) Radar interferometry: data interpretation and error analysis. Kluwer, Dordrecht. ISBN 9780792369455
- Herrera G, Tomás R, Vicente F, Lopez-Sánchez JM, Mallorquí JJ, Mulas J (2010) Mapping ground movements in open pit mining areas using differential SAR interferometry. *Int J Rock Mech Min Sci* 47(7):1114–1125
- Hooper A, Zebker H, Segall P, Kampes B (2004) A new method for measuring deformation on volcanoes and other natural terrains using InSAR persistent scatterers. *Geophys Res Lett* 31:L23 611
- Kampes BM (2006) Radar interferometry: persistent scatterer technique, vol 12. Springer, Dordrecht
- Li Z, Muller JP, Cross P, Fielding EJ (1978–2012) Interferometric synthetic aperture radar (InSAR) atmospheric correction: GPS, Moderate Resolution Imaging Spectroradiometer (MODIS), and InSAR integration. *J Geophys Res Solid Earth* 110 (B3)
- Martone M, Rizzoli P, Bräutigam B, Krieger G (2013) First 2 years of TanDEM-X mission: interferometric performance overview. *Radio Sci* 48(5):617–627
- Massonnet D, Rossi M, Carmona C, Adragna F, Peltzer G, Feigl K, Rabaute T (1993) The displacement field of the landers earthquake mapped by radar interferometry. *Nature* 364(6433):138–142
- Moreira A, Prats-Iraola P, Younis M, Krieger G, Hajnsek I, Papathanassiou KP (2013) A tutorial on synthetic aperture radar. *IEEE Geosci Remote Sens Magaz* 1(1):6
- Perissin D, Sarproz. Webpage www.sarproz.com
- Perissin D, Rocca F (2006) High accuracy urban DEM using permanent scatterers. *IEEE Trans Geosci Remote Sens* 44(11):3338–3347
- Perissin D, Wang T (2012) Repeat-Pass SAR interferometry with partially coherent targets. *IEEE Trans Geosci Remote Sens* 50:271–280
- Perissin D, Prati C, Engdahl M, Desnos YL (2006) Validating the SAR wavenumber shift principle with the ERS–Envisat PS coherent combination. *IEEE Trans Geosci Remote Sens* 44(9): 2343–2351
- Perissin D, Wang Z, Wang T (2011) The SARPROZ InSAR tool for urban subsidence/manmade structure stability monitoring in China. In: Proceedings of the 34th International Symposium on Remote Sensing of Environment (ISRSE), Syndey, Australia, Jan. 2011
- Wadge G (2003) A strategy for the observation of volcanism on earth from space. *Philos Trans R Soc London* 361:145–156
- Zebker HA, Villasenor J (1992) Decorrelation in interferometric radar echoes. *IEEE Trans Geosci Remote Sens* 30(5):950–959
- Zhong L, Lei Z (2014) Frontiers of radar remote sensing. *PE&RS* 80:5

Chapter 9

TIMESAT for Processing Time-Series Data from Satellite Sensors for Land Surface Monitoring

Lars Eklundh and Per Jönsson

Abstract The TIMESAT software package has been developed to enable monitoring of dynamic land surface processes using remotely sensed data. The monitoring capability is based on processing of time-series for each image pixel using either of three smoothing methods included in TIMESAT: asymmetric Gaussian fits, double-logistic fits, and Savitzky-Golay filtering. The methods have different properties and are suitable for a wide range of data with different character and noise properties. The fitting methods can be upper-envelope weighted and can take quality data into account. Based on the fitted functions, growing season parameters are then extracted (beginning, end, amplitude, slope, integral, etc.), and can be merged into images. TIMESAT has been used in a number of application fields: mapping of phenology and phenological variations; ecological disturbances; vegetation classification and characterization; agriculture applications; climate applications; and for improving remote sensing signal quality. Future developments of TIMESAT will include new methods to better handle long gaps in time-series, handling of irregular time sampling, improved smoothing methods, and incorporation of the spatial domain. These modifications will enable use of TIMESAT also for high-resolution data, e.g. data from the planned ESA Sentinel-2 satellite.

9.1 Introduction

Time-series of Earth observation (EO) data can aid the understanding of land ecosystem dynamics, biogeochemical processes and exchanges, and ecosystem responses to climate and human-induced activities (Townshend and Justice 1986; Malingreau 1986; Hickler et al. 2005). With more than 30 years of data from the

L. Eklundh (✉)

Department of Physical Geography and Ecosystem Science, Lund University, Lund, Sweden
e-mail: lars.eklundh@nateko.lu.se

P. Jönsson

Group for Materials Science and Applied Mathematics, Malmö University, Malmö, Sweden

National Oceanic and Atmospheric Administration Advanced Very High Resolution Radiometer (NOAA AVHRR), close to 15 years of data from the Moderate Resolution Imaging Spectroradiometer (MODIS), and many new time-series products being developed, there is a need for efficient and practical methods for handling these data. In this chapter we describe the ideas behind the TIMESAT¹ software for meeting this need.

TIMESAT was developed from ideas based on the early uses of meteorological satellite data for studies of global land vegetation dynamics (Justice et al. 1985; Townshend and Justice 1986), as well as the use of time-series data for characterizing land cover classes (Defries and Townshend 1994; Running et al. 1994). The science field developed in tandem with the emergence of high temporal resolution data sets of vegetation index data from NOAA AVHRR, particularly the normalized difference vegetation index (NDVI) (Rouse et al. 1973; Tucker 1979; Tucker et al. 1983). A series of investigations of the properties of these data led to the development of biophysical vegetation models (Running 1990; Prince 1991; Ruimy et al. 1994; Prince and Goward 1995; Goetz et al. 1999), opening up for new applications in vegetation productivity mapping and estimation of land surface parameters. Implementing models based on physical understanding of the remotely sensed signals has led to improved capability to monitor biogeochemical and ecological land processes (Rautiainen et al. 2010). The ability to map the spatial and temporal variability of these factors using MODIS satellite data has enabled estimation of gross primary productivity (GPP) and net ecosystem exchange (NEE) (Sims et al. 2006; Potter et al. 2007; Olofsson et al. 2008; Schubert et al. 2010; Sjöström et al. 2011). Furthermore, analyses of the now relatively long time-series of EO records have demonstrated their value for monitoring changes in vegetation cover for large areas of the globe, helping to elucidate mechanisms and agents of change (Myneni et al. 1997; Zhou et al. 2001; Nemani et al. 2003; Eklundh and Olsson 2003; Olsson et al. 2005; Hickler et al. 2005). These and other studies have firmly established the role of time-series remote sensing in global change science.

However, given the large influence of noise on the satellite-derived measurements, the direct use of the data is often difficult. Cloud conditions and hazy atmosphere are the primary causes of noise in optical satellite sensor data, although other factors, e.g. directional effects, geometric inaccuracies, and sensor disturbances also contribute to the noise in the final products (Goward et al. 1991). While several highly processed data sets exist, they are usually far from noise-free. This noise severely affects the possibility to estimate accurate land surface parameters, particularly during the rainy parts of the season – which is year-round in many humid tropical areas. Tackling the noise problem was one of the reasons for developing TIMESAT.

¹TIMESAT (Jönsson and Eklundh 2004) is a freely available software package, accessible from <http://www.nateko.lu.se/TIMESAT/>

Early methods for handling noise were based on relatively simple methods, for example the use of maximum-value compositing (Holben 1986). This method relies on the ability of the normalized difference vegetation index (NDVI) to minimize noise, by selecting the highest value during a specific time-period. The principle of selecting the highest value is also the basis for the Best Index Slope Extraction (BISE) (Viovy et al. 1992), an early time-series processing method. Though simple and generally effective in removing many disturbances, these methods ignore the fact that also positively biased noise may be present in the NDVI series, and they are limited to NDVI and similar vegetation indices in which noise is negatively biased. For more general noise reduction, various smoothing filters have also been tested (van Dijk et al. 1987; Reed et al. 1994). Another line of development for extracting seasonality information from remotely sensed imagery is the use of Fourier series, whereby the periodic annual fluctuations in data is utilized (van Dijk et al. 1987; Menenti et al. 1993; Olsson and Eklundh 1994; Roerink et al. 2000). Though the parameters of these harmonic functions contain information about the timing of the seasons, the method is generally too inflexible for remotely sensed time-series data, in which the timing of seasons can vary considerably between different years.

Recent methods are generally based on fitting mathematical functions to the time-series data, e.g. asymmetric Gaussian functions (Jönsson and Eklundh 2002), logistic functions (Zhang et al. 2003; Jönsson and Eklundh 2004; Fisher et al. 2006), and spline functions (Bradley et al. 2007; Hermance et al. 2007; Atzberger and Eilers 2011). Also wavelet transforms have shown to be useful (Sakamoto et al. 2005; Lu et al. 2007; Campos and Di Bella 2012). Choices for data smoothing in TIMESAT are described in the sections below.

A further motivation for developing TIMESAT was the realization that satellite-observed changes in vegetation phenology may act as useful indicators of climate change (cf. Schwartz 2013). Phenology is the study of recurring seasonal phenomena such as leaf emergence, flowering, and leaf fall. Considerable changes in these phenological variables have been noted across extensive global regions during the last 20–30 years (Menzel et al. 2006; IPCC 2014), and future climate trends towards increasing temperatures will most likely affect forest phenology strongly (Schröter et al. 2005). Changes in tree phenology will have consequences on carbon allocation and biomass production (Bergh et al. 1998; Lucht et al. 2002); on tree vulnerability to frost damage (Jönsson et al. 2004); and on risks of increased problems with insects and pathogens (Ayres and Lombardero 2000; Jönsson et al. 2007). Phenological variations affect the physiological and biochemical state of the forest canopy, influencing albedo, heat flux, momentum flux, CO₂ flux, and net radiation (Menzel 2002). Visually, phenology is most apparent as variations in leaf area index (LAI), and is thereby directly observable by remote sensing. Consequently, extracting parameters that describe phenology and phenology variations from remotely sensed time-series data is another important aim of TIMESAT.

In the remainder of the chapter we describe the main concepts and technical solutions behind the algorithms in TIMESAT.

9.2 Processing Principles in TIMESAT

TIMESAT was developed over a series of years (Jönsson and Eklundh 2002, 2004; Eklundh and Jönsson 2012). It operates on stacks of images, where each image represents a certain time or time period. Typically, TIMESAT has been used for estimating vegetation seasonality, and is normally applied to NDVI, EVI, or some biophysical vegetation parameters like LAI or fAPAR (fractional absorbed photosynthetically active radiation). However, in principle, any signal with a clear seasonal trajectory can be used (e.g. albedo, spectral reflectance, soil moisture, or land surface temperature). Ideally several years of data should be used.

9.2.1 Extraction and Processing of Time-Series for a Pixel

Given a stack of images, time-series are extracted for each image pixel. The processing for each of these time-series is then carried out in a series of steps (further processing details are given in Eklundh and Jönsson 2012):

- (1) Temporal trend estimation. This was in the first TIMESAT versions done using second-order polynomials. To better adapt to non-linear trends, it is currently done using the STL (Seasonal Trend decomposition by Loess) algorithm (Cleveland et al. 1990). This is an efficient method for separating the data into trend, seasonal component and residual variation; it is used in TIMESAT for de-trending the data before further processing, and for identifying noise.
- (2) Pre-filtering of data. It is a step for weeding out extreme outliers. It can be either be done using median-filtered data and a user-defined threshold, or based on the residual of the STL filtering.
- (3) Determining the number of growing seasons. This is done using sinusoidal harmonics, and a user-defined amplitude threshold. The model function is defined as:

$$f(t) = c_1 + c_2 \sin(\omega t) + c_3 \cos(\omega t) + c_4 \cos(2\omega t) + c_5 \cos(2\omega t), \quad (9.1)$$

where t is time, $\omega = 2\pi/N$, where N is the number of observations per year. The model provides minima and maxima giving the approximate location of the seasons. Though in principle several seasons per year could be determined, the maximum number of annual seasons in TIMESAT is limited to two. The reason for this is that noise in the remotely sensed data makes determination of several annual seasons highly uncertain.

- (4) Data smoothing. This can be done using either of three methods: asymmetric Gaussian functions, double logistic functions, and Savitzky-Golay filtering. Gaussian and logistic functions are very smooth, enforce a bell-shaped pattern on the data, and are useful when data are very noisy. The Savitzky-Golay

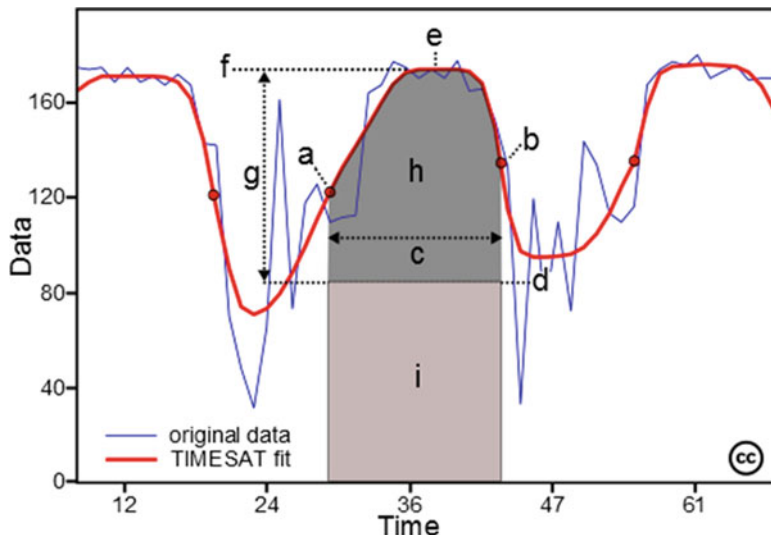


Fig. 9.1 Some of the seasonality parameters in TIMESAT: (a) beginning of season, (b) end of season, (c) length of season, (d) base value, (e) time of middle of season, (f) maximum value, (g) amplitude, (h) small integrated value, (h + i) large integrated value (Source: <http://www.nateko.lu.se/TIMESAT/>. Published under Creative Commons license)

method, on the other hand, follows local variations in the seasonal curve more closely. Descriptions of the three methods follow below.

- (5) Computing seasonal parameters for the extracted seasons. This is done based on user-defined thresholds for defining the start and end of seasons, using either absolute values or fractions of the amplitude. When these values are defined, TIMESAT computes eleven parameters for each season: times of start and end of season; length of the season; base level value; time of season midpoint; maximum seasonal value; seasonal amplitude; rates of increase and decrease; and large and small seasonal integrals (Fig. 9.1). As a final step, output data in the form of single-pixel data or images are generated.

9.2.2 Asymmetric Gaussian and Double Logistic Functions

These methods fit local model functions to data in intervals around maxima and minima of the approximate growing seasons defined in (1). The local model functions have the general form:

$$f(t) \equiv f(t, \mathbf{c}, \mathbf{x}) = c_1 + c_2 g(t; \mathbf{x}), \quad (9.2)$$

where the linear parameters $\mathbf{c} = (c_1, c_2)$ determine the base level and the amplitude. The non-linear parameters $\mathbf{x} = (x_1, x_2, \dots, x_p)$ determine the shape of the basis function $g(t; \mathbf{x})$.

The asymmetric Gaussian function is defined as:

$$g(t; x_1, x_2, \dots, x_5) = \begin{cases} \exp\left[-\left(\frac{t-x_1}{x_2}\right)^{x_3}\right] & \text{if } t > x_1 \\ \exp\left[-\left(\frac{x_1-t}{x_4}\right)^{x_5}\right] & \text{if } t < x_1 \end{cases} \quad (9.3)$$

where x_1 determines the position of the maximum or minimum, x_2 and x_3 determine the width and flatness of the right function half; x_4 and x_5 determine the width and flatness of the left half.

The double logistic function is defined as:

$$g(t; x_1, x_2, \dots, x_4) = \frac{1}{1 + \exp\left(\frac{x_1-t}{x_2}\right)} - \frac{1}{1 + \exp\left(\frac{x_3-t}{x_4}\right)} \quad (9.4)$$

where x_1 and x_3 determine the positions of the left and right inflection points, and x_2 and x_4 determine the rates of change at these points. To ensure smooth shapes of the model functions, all parameters are restricted in range. The parameters \mathbf{c} and \mathbf{x} are obtained by minimizing a merit function using the Levenberg-Marquardt method. Initial values of the non-linear parameters are obtained by searching a number of pre-defined model functions.

In order to create a flexible fit to the full time-series the local functions are finally merged to a global function.

9.2.3 Adaptive Savitzky-Golay Filtering

The Savitzky-Golay filtering suppresses noise by filtering the data by means of a least-squares fit to a quadratic polynomial. For each data point a polynomial is fitted to the data in a window:

$$f(t) = c_1 + c_2t + c_3t^2 \quad (9.5)$$

where c_1 , c_2 , and c_3 are determined by weighted least-squares fitting, and the degree of smoothing is controlled by the width of the window. The estimated value in the data point then replaces the original value. In TIMESAT, the window size is tightened in case of large increases or decreases around data points, thereby adapting to rapid changes in the data. This makes the method very flexible and useful for describing fast seasonal changes.

Examples of Savitzky-Golay smoothing and asymmetric Gaussian fits are shown in Fig. 9.2a, b.

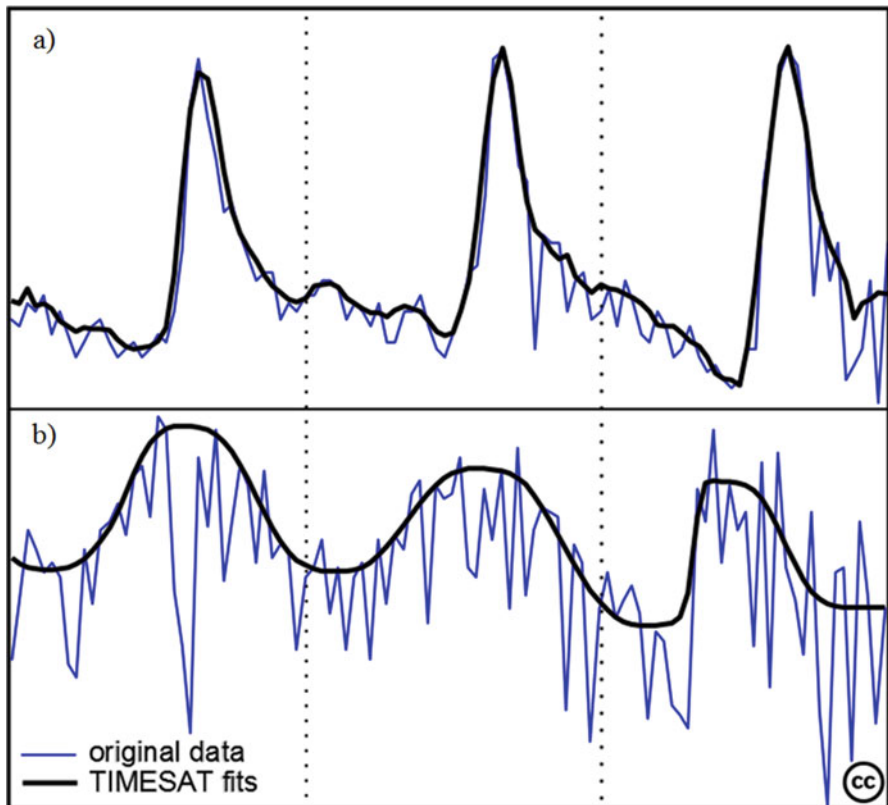


Fig. 9.2 TIMESAT fits to 3 years of 10-day AVHRR data for two pixels in the Sahel: (a) Savitzky-Golay fit to pixel in northern Sahel, (b) asymmetric Gaussian fit to pixel in S. Sahel. Both fits are upper envelope weighted and without use of ancillary quality data (Source: <http://www.nateko.lu.se/TIMESAT/>. Published under Creative Commons license)

9.2.4 Handling Measurement Error and Noise Bias in TIMESAT

By the use of weighted least squares, each data point can in TIMESAT be weighted by its data quality. Normally, the quality of remotely sensed data is described using qualitative flags, denoting missing data, cloudiness, or other conditions. With e.g. MODIS data, a complex combination of data quality flags (QA flags) is provided for each image pixel. These flags need to be converted to weights that express the relative contribution of the pixel to the final fit. For example, pixels denoted as “cloudy” can be given a weight of 0.01, “confident clear” a weight of 1.0, and “probably clear” a weight of 0.5. No objective system for assigning the weights exists, and judicious testing of various weights and combinations of flags to obtain

the best fit to the data is necessary. Nevertheless, the possibility to include not only perfect but also somewhat lower-quality data in the processing is an advantage.

NDVI and some other vegetation indices have the property of being negatively biased in the presence of e.g. clouds, snow and atmospheric disturbances. In TIMESAT, this property can be utilized by fitting to the upper envelope of the data cluster, rather than to its centre. This is done by iterative fitting and a user-defined value that regulates the degree of upper-envelope adjustment. This method for avoiding noise has proven very effective, and as TIMESAT uses least-squares fitting the final curves will not be forced to pass through extreme high values that may be caused by positive noise (e.g. due to bi-directional effects at high solar zenith angles).

9.2.5 Processing Considerations

Selection of smoothing algorithm and processing parameters is far from straight forward, and no objective method for doing this with unknown data points currently exists. The Gaussian and logistic methods are very similar, although the Gaussian functions sometimes adapt better than the logistic functions to flat growing season peak periods. The Savitzky-Golay implementation in TIMESAT is very adaptive to local variations in that it iteratively tightens the search window and may capture very rapid increase or decrease in the data. On the other hand, smoothing very noisy data requires an increased search window, which in turn can produce some artefacts. Therefore, Savitzky-Golay filtering should not be used with extremely noisy data.

Since the distributions of the noise and the true signal are unknown, it is generally not possible to apply objective statistical test parameters for choosing the best smoothing method or parameter settings. However, if possible the user should utilize data from ground-based measurements for known reference areas to gain experience about the accuracy of different methods and parameter settings (e.g., Baret et al. 2006; Eklundh et al. 2011). It might also be possible to use some indicators, e.g. to estimate inter-class variability of the output data, correlations with ancillary data (cloudiness, elevation etc.) or the temporal persistence of variations (Atzberger and Eilers 2011). Use of synthetic data sets for testing filter methods has also been proposed (Hird and McDermid 2009), but this relies on accurate statistical representation of the image noise. In TIMESAT, the results of different settings can be viewed in a graphical user interface, and it is advisable to do this for a number of areas across the image. If different land cover classes are to be processed, the TIMESAT user can define different smoothing methods and parameters for each land cover class.

When parameters have been selected, processing is carried out in a separate executable which has been compiled in FORTRAN for fast performance. This can be executed in parallel mode to exploit as many processing cores as possible. The method currently being tested in TIMESAT has nearly linear scaling with the number of CPUs.

9.2.6 *TIMESAT Outputs*

The outputs of TIMESAT consist of smoothed data and seasonality parameters for each growing season, which can be presented as ASCII data or graphs for single pixels, or as full images for each time step (smoothed data) or season (seasonality parameters). Examples are shown in Fig. 9.3, which, in addition to elevation, shows estimated values of start and length of the 2009 growing season, derived from MODIS 8-day values of EVI-2 for a mountain area in N. Sweden. The images clearly show the dependence of vegetation seasonality on topography; the length

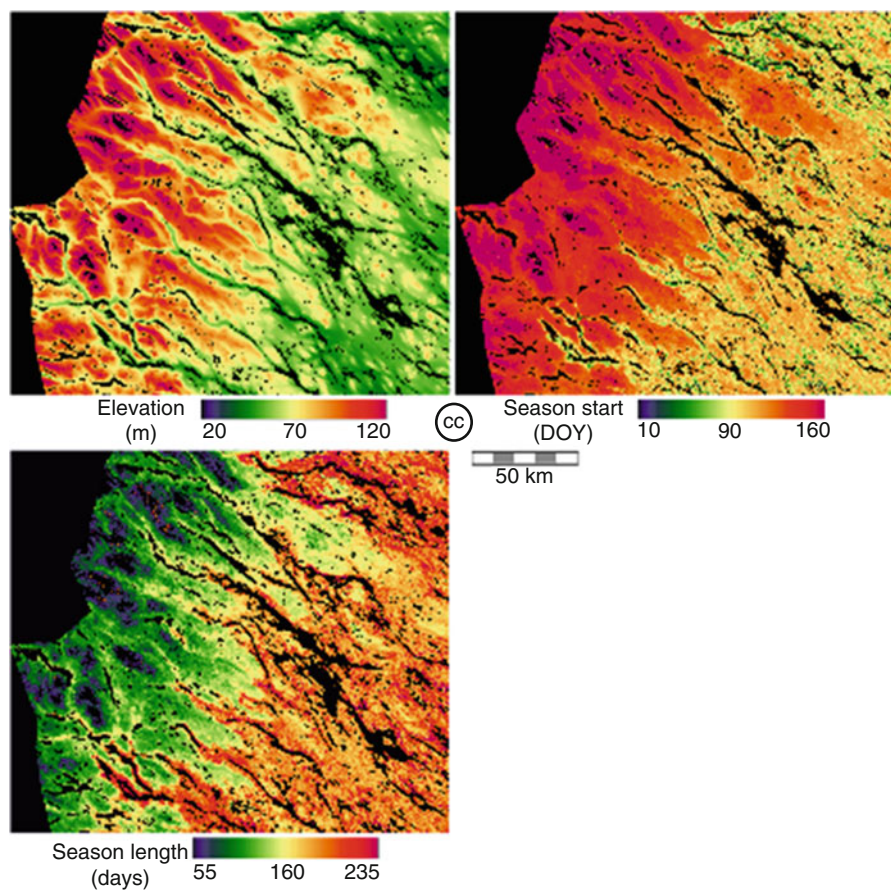


Fig. 9.3 Land elevation and TIMESAT estimated seasonal parameters for Ammarnäs mountain area, Sweden (lat. 65.3–67.0, long. 15.0–18.7) Seasonality parameters are computed from 250-m MODIS EVI-2 using double logistic and asymmetric Gaussian fits depending on land cover type (Source: <http://www.nateko.lu.se/TIMESAT>. Published under Creative Commons license)

of season has the strongest (negative) correlation with elevation ($R^2 = 0.7$), while the start of season date is somewhat weaker (positively) correlated with elevation ($R^2 = 0.54$).

9.2.7 *Uses of TIMESAT*

TIMESAT has since its first publication (Jönsson and Eklundh 2002) been used within several different application fields:

- Phenology, and phenological variations, e.g. for the Sahel by Heumann et al. (2007), for Fennoscandia and the Kola Peninsula by Beck et al. (2007), for Ireland by O'Connor et al. (2012), and for S. England by Boyd et al. (2011). TIMESAT was also used when investigating the difficulty in extracting phenological parameters over boreal coniferous forests by Jönsson et al. (2010). Some recent case studies have been conducted in different parts of the world, e.g. the US (Cong et al. 2013), Europe (Han et al. 2013), South America (van Leeuwen et al. 2013), and in Arctic areas (Zeng et al. 2013).
- Ecological disturbances, e.g. insect infestations (Eklundh et al. 2009; Olsson et al. 2012; Buma et al. 2013), and fire and fire risk modeling (Verbesselt et al. 2006; Veraverbeke et al. 2010; Le Page et al. 2010).
- Vegetation classification and phenological ecosystem characterization (Tottrup et al. 2007; Clark et al. 2010; van Leeuwen et al. 2010; Wessels et al. 2011; Zhang et al. 2013; Leinenkugel et al. 2013), and for investigating the impact of vegetation variability on the coupled land-atmosphere system (Weiss et al. 2012).
- Agricultural applications, e.g. for estimation of sow dates (Lobell et al. 2013) and for mapping of abandoned cropping fields (Alcantara et al. 2012).
- Climate applications, e.g. for estimating diurnal air temperature from MSG SEVIRI data (Stisen et al. 2007), to study change of the thermal growing season and biospheric carbon uptake (Barichivich et al. 2012), and to study the impact of extreme precipitation (Tang et al. 2013).
- Data smoothing to improve signal quality in satellite sensor data, e.g. in a number of studies pertaining to drought and dryland conditions in the African Sahel (Eklundh and Olsson 2003; Hickler et al. 2005; Olsson et al. 2005; Seaquist et al. 2009), and to improve estimation of carbon fluxes (Olofsson and Eklundh 2007; Olofsson et al. 2007, 2008; Sjöström et al. 2009, 2011; Schubert et al. 2010, 2012; Barichivich et al. 2013). It has been used for data quality improvement with MODIS and AVHRR satellite products (Fensholt and Proud 2012), and for smoothing of GIMMS NDVI(3G) data for high northern latitudes (Zhao et al. 2013). Data quality improvement is also the reason for using TIMESAT in an improved reprocessed version of the global MODIS LAI data set for land surface and climate modeling (Yuan et al. 2011).

The large number of applications of TIMESAT has proven its robustness and versatility, and contributed to its continued improvement.

9.3 Discussion

Although TIMESAT is today a widely used tool and has shown its versatility in analyzing different temporal data sets, there are several difficulties associated with processing of remotely sensed time-series data. Primarily, choosing optimal smoothing methods and parameters is by no means objective, and depends on data and noise properties of the area under study (Garcia 2010). Several alternative time-series methods exist in the literature, and in order to bring clarity into this, some comparisons of different smoothing methods have been made (Eilers 2003; Hird and McDermid 2009; White et al. 2009; Kandasamy et al. 2013). However, in general, these studies have not been able to identify any ultimate method that fits in all situations. A clear weakness with many methods, including TIMESAT, is the sensitivity to large numbers of missing data (Kandasamy et al. 2013). This was addressed by Verger et al. (2013), who utilized the average long-term seasonal curve to obtain robust estimates. Although their method may not be general enough to handle all data situations, the suggested approach to handling missing data is promising.

The Savitzky-Golay method in TIMESAT has become popular, since it can fit curves to very rapidly varying data. However, due to some artefacts there may be reason to look into also other local methods, such as smoothing splines (Eilers 2003; Atzberger and Eilers 2011). These are very flexible and have, in a modified version extendable to several dimensions (Garcia 2010), been tested with good results in TIMESAT (Eklundh and Jönsson 2013).

Beginnings and ends of seasons are in TIMESAT estimated based on fractions of amplitude or on absolute values. The former method is practical with images where different pixels have widely differing base levels; however, in situations with interannual variations caused by e.g. soil color variations, the use of amplitude fractions can lead to fluctuating seasonal parameters. Using absolute values to define the seasons is preferable when expressing their limits in terms of biophysical properties, e.g. when a certain LAI limit is exceeded. Some authors have used derivatives of the seasonal curve to define growing season limits (e.g. Zhang et al. 2003; Tan et al. 2008; Rodrigues et al. 2013). This is in practice not much different from defining a small threshold value of the amplitude, but has the disadvantage of being more sensitive to noise, in particular when using higher-order derivatives (e.g. Tan et al. 2008). Therefore, derivatives should not be used with local methods like Savitzky-Golay filtering, or the seasonally merged Gaussian or logistic functions in TIMESAT.

In light of increased use of time-series techniques for handling high-resolution data, e.g. from Landsat (e.g. Huang et al. 2010; Zhu et al. 2012), and from the

planned ESA Sentinel-2 satellite, there are good reasons to adapt TIMESAT to high-resolution data, and to utilize also the spatial domain when processing time-series data. This holds promise for reducing spatially uncorrelated noise (Eklundh and Jönsson 2013), although more developments and tests of these spatio-temporal methods are necessary.

A further consideration when dealing with time-series data is the physical meaning of the remotely sensed data sets. Without doubt, popular vegetation indices like the NDVI have simplified data analysis and made remote sensing more accessible and operational. However, the somewhat unclear physical meaning of most vegetation indices makes interpretation of the signals sometimes difficult. For example, apart from being responsive to vegetation development, both NDVI and EVI are strongly affected by snow (Huete et al. 2002; Jönsson et al. 2010; Schubert et al. 2012). This may be the reason for the use of the ambiguous term “land surface phenology”, a term adopted by the CEOS-LPV phenology Focus Group (LPVS 2014). The term addresses the visible dynamic phenomenon as observed by remote sensing instruments rather than the physical or biological phenological processes underlying these variations. To enable unambiguous interpretation of satellite-derived phenological parameters, biophysical variables like LAI or fAPAR are preferable. There is also a need for developing new accurate vegetation indices and products that more directly refer to identifiable biophysical processes (e.g. Jin and Eklundh 2014).

9.4 Conclusions and Future Developments

TIMESAT has been developed to enable monitoring of dynamic land surface processes using remotely sensed data, and has been used in a wide array of applications. It provides different smoothing algorithms, which gives the user the freedom to choose the most appropriate method depending on the characteristics of the data and noise. Although TIMESAT has proven its versatility for several years, there is a demand for continued development of new and efficient time-series processing methods, e.g. to handle high-resolution data from the planned ESA Sentinel-2 satellites.

To meet this demand, several improvements to TIMESAT are underway. These planned changes include the ability to handle irregular time-steps in data; new fast and efficient smoothing methods; methods for handling long data gaps; and inclusion of the spatial domain in the time-series analysis. Improved validation will be necessary to better understand the implementation of the methods and their effects on parameter estimation. Hence, the new methods will be tested against ground data sets, e.g. time-series of spectral measurements (Eklundh et al. 2011) and eddy-covariance flux measurements, to estimate their performance within the fields of phenology, vegetation productivity, and carbon modelling. It is our aim to make TIMESAT a useful and versatile tool that aids analyses and data integration for addressing a range of urgent environmental issues.

Acknowledgements The authors want to thank the many TIMESAT users, colleagues, and students who have contributed with constructive suggestions and ideas for improvement. We also thank the Swedish National Space Board, the Crafoord foundation, and the Kräpparup foundation for financial support.

References

- Alcantara C, Kuemmerle T, Prishchepov AV, Radeloff VC (2012) Mapping abandoned agriculture with multi-temporal MODIS satellite data. *Remote Sens Environ* 124:334–347
- Atzberger C, Eilers PHC (2011) Evaluating the effectiveness of smoothing algorithms in the absence of ground reference measurements. *Int J Remote Sens* 32:3689–3709
- Ayres MP, Lombardero MJ (2000) Assessing the consequences of global change for forest disturbance from herbivores and pathogens. *Sci Total Environ* 262:263–286
- Baret F, Morissette J, Fernandes R, Champeaux J-L, Myneni R, Chen J, Plummer S, Weiss M, Bacour C, Garrigues S, Nickeson J (2006) Evaluation of the representativeness of networks of sites for the global validation and intercomparison of land biophysical products: proposition of the CEOS-BELMANIP. *IEEE Trans Geosci Remote Sens* 44:1794–1803
- Barichivich J, Briffa KR, Osborn TJ, Melvin TM, Caesar J (2012) Thermal growing season and timing of biospheric carbon uptake across the Northern Hemisphere. *Glob Biogeochem Cycles* 26:GB4015
- Barichivich J, Briffa KR, Myneni RB, Osborn TJ, Melvin TM, Ciais P, Piao S, Tucker C (2013) Large-scale variations in the vegetation growing season and annual cycle of atmospheric CO₂ at high northern latitudes from 1950 to 2011. *Glob Chang Biol* 19:3167–3183
- Beck PSA, Jönsson P, Hogda K-A, Karlsen SR, Eklundh L, Skidmore AK (2007) A ground-validated NDVI dataset for monitoring vegetation dynamics and mapping phenology in Fennoscandia and the Kola peninsula. *Int J Remote Sens* 28:4311–4330
- Bergh J, McMurtrie RE, Linder S (1998) Climatic factors controlling the productivity of Norway spruce: a model-based analysis. *For Ecol Manag* 110:127–139
- Boyd DS, Almond S, Dash J, Curran PJ, Hill RA (2011) Phenology of vegetation in Southern England from Envisat MERIS terrestrial chlorophyll index (MTCI) data. *Int J Remote Sens* 32:8421–8447
- Bradley BA, Jacob RW, Hermance JF, Mustard JF (2007) A curve fitting procedure to derive inter-annual phenologies from time series of noisy satellite NDVI data. *Remote Sens Environ* 106:137–145
- Buma B, Pugh ET, Wessman CA (2013) Effect of the current major insect outbreaks on decadal phenological and LAI trends in southern Rocky Mountain forests. *Int J Remote Sens* 34:7249–7274
- Campos AN, Di Bella CM (2012) Multi-temporal analysis of remotely sensed information using wavelets. *J Geogr Inf Syst* 4:383–391
- Clark ML, Aide TM, Grau HR, Riner G (2010) A scalable approach to mapping annual land cover at 250 m using MODIS time series data: a case study in the dry Chaco ecoregion of South America. *Remote Sens Environ* 114:2816–2832
- Cleveland RB, Cleveland WS, McRae JE, Terpenning I (1990) STL: a seasonal-trend decomposition procedure based on loess. *J Off Stat* 6:3–73
- Cong N, Wang T, Nan H, Ma Y, Wang X, Myneni RB, Piao S (2013) Changes in satellite-derived spring vegetation green-up date and its linkage to climate in China from 1982 to 2010: a multimethod analysis. *Glob Chang Biol* 19:881–891
- Defries RS, Townshend JRG (1994) NDVI-derived land cover classifications at a global scale. *Int J Remote Sens* 15:3567–3586
- Eilers PHC (2003) A perfect smoother. *Anal Chem* 75:3631–3636
- Eklundh L, Jönsson P (2012) TIMESAT 3.1 software manual. Lund University, Lund

- Eklundh L, Jönsson P (2013) A new spatio-temporal smoother for extracting vegetation seasonality with TIMESAT, The 35th international symposium on remote sensing of environment, 22–26 April 2013, Beijing, China
- Eklundh L, Olsson L (2003) Vegetation index trends for the African Sahel 1982–1999. *Geophys Res Lett* 30:1430–1433
- Eklundh L, Johansson T, Solberg S (2009) Mapping insect defoliation in Scots pine with MODIS time-series data. *Remote Sens Environ* 113:1566–1573
- Eklundh L, Jin H, Schubert P, Guzinski R, Heliasz M (2011) An optical sensor network for vegetation phenology monitoring and satellite data calibration. *Sensors* 11:7678–7709
- Fensholt R, Proud SR (2012) Evaluation of Earth Observation based global long term vegetation trends—Comparing GIMMS and MODIS global NDVI time series. *Remote Sens Environ* 119:131–147
- Fisher JI, Mustard JF, Vadeboncoeur MA (2006) Green leaf phenology at Landsat resolution: scaling from the field to the satellite. *Remote Sens Environ* 100:265–279
- Garcia D (2010) Robust smoothing of gridded data in one and higher dimensions with missing values. *Comput Stat Data Anal* 54:1167–1178
- Goetz SJ, Prince SD, Goward SN, Thawley MM, Small J (1999) Satellite remote sensing of primary production: an improved production efficiency modeling approach. *Ecol Model* 122:239–255
- Goward SN, Markham Dye DG, Dulaney W, Yang J (1991) Normalized difference vegetation index measurements from the advanced very high resolution radiometer. *Remote Sens Environ* 35:257–277
- Han Q, Luo G, Li C (2013) Remote sensing-based quantification of spatial variation in canopy phenology of four dominant tree species in Europe. *J Appl Remote Sens* 7:073485
- Hermance JF, Jacob RW, Bradley BA, Mustard JF (2007) Extracting phenological signals from multiyear AVHRR NDVI time series: framework for applying high-order annual splines with roughness damping. *IEEE Trans Geosci Remote Sens* 45:3264–3276
- Heumann BW, Seaquist JW, Eklundh L, Jönsson P (2007) AVHRR derived phenological change in the Sahel and Soudan, Africa, 1982–2005. *Remote Sens Environ* 108:385–392
- Hickler T, Eklundh L, Seaquist J, Smith B, Ardö J, Olsson L, Sykes M, Sjöström M (2005) Precipitation controls Sahel greening trend. *Geophys Res Lett* 32:L21415
- Hird JN, McDermid GJ (2009) Noise reduction of NDVI time series: an empirical comparison of selected techniques. *Remote Sens Environ* 113:248–258
- Holben BN (1986) Characteristics of maximum-value composite images from temporal AVHRR data. *Int J Remote Sens* 7:1417–1443
- Huang C, Goward SN, Masek JG, Thomas N, Zhu Z, Vogelmann JE (2010) An automated approach for reconstructing recent forest disturbance history using dense Landsat time series stacks. *Remote Sens Environ* 114:183–198
- Huete A, Didan K, Miura T, Rodrigues EP, Gao X, Ferreira LG (2002) Overview of the radiometric and biophysical performance of the MODIS vegetation indices. *Remote Sens Environ* 83:195–213
- IPCC (2014) Climate Change 2014: impacts, adaptation, and vulnerability. IPCC Working Group II contribution to the Fifth Assessment Report. IPCC, Yokohama
- Jin H, Eklundh L (2014) A physically based vegetation index for improved monitoring of plant phenology. *Remote Sens Environ* 152:512–525
- Jönsson P, Eklundh L (2002) Seasonality extraction by function fitting to time-series of satellite sensor data. *IEEE Trans Geosci Remote Sens* 40:1824–1832
- Jönsson P, Eklundh L (2004) TIMESAT – a program for analysing time-series of satellite sensor data. *Comput Geosci* 30:833–845
- Jönsson AM, Linderson M-L, Stjernqvist I, Schlyter P, Bärring L (2004) Climate change and the effect of temperature backlashes causing frost damage in *Picea abies*. *Glob Planet Chang* 44:195–207
- Jönsson AM, Harding S, Bärring L, Ravn HP (2007) Impact of climate change on the population dynamics of *Ips typographus* in southern Sweden. *Agric For Meteorol* 146:70–781

- Jönsson AM, Eklundh L, Hellström M, Bärring L, Jönsson P (2010) Annual changes in MODIS vegetation indices of Swedish coniferous forests in relation to snow dynamics and tree phenology. *Remote Sens Environ* 114:2719–2730
- Justice CO, Townshend JRG, Holben BN, Tucker CJ (1985) Analysis of the phenology of global vegetation using meteorological satellite data. *Int J Remote Sens* 6:1271–1318
- Kandasamy S, Baret F, Verger A, Neveux P, Weiss M (2013) A comparison of methods for smoothing and gap filling time series of remote sensing observations – application to MODIS LAI products. *Biogeosciences* 10:4055–4071
- Le Page Y, Oom D, Silva JMN, Jönsson P, Pereira JMC (2010) Seasonality of vegetation fires as modified by human action: observing the deviation from eco-climatic fire regimes. *Glob Ecol Biogeogr* 19:575–588
- Leinenkugel P, Kuenzer C, Oppelt N, Dech S (2013) Characterisation of land surface phenology and land cover based on moderate resolution satellite data in cloud prone areas—A novel product for the Mekong Basin. *Remote Sens Environ* 136:180–198
- Lobell DB, Ortiz-Monasterio JI, Sibley AM, Sohu VS (2013) Satellite detection of earlier wheat sowing in India and implications for yield trends. *Agric Syst* 115:137–143
- LPVS (2014) Phenology focus area overview. http://lpvs.gsfc.nasa.gov/pheno_background.html. Accessed 24 June 2014
- Lu X, Liu R, Liu J, Liang S (2007) Removal of noise by Wavelet method to generate high quality temporal data of terrestrial MODIS products. *Photogramm Eng Remote Sens* 73:1129–1139
- Lucht W, Prentice C, Myneni RB, Sitch S, Friedlingstein P, Cramer W, Bousquet P, Buermann W, Smith B (2002) Climatic control of the high-latitude vegetation greening trend and pinatubo effect. *Science* 296:1687–1689
- Malingreau J-P (1986) Global vegetation dynamics: satellite observations over Asia. *Int J Remote Sens* 7:1121–1146
- Menenti M, Azzali S, Verhoef W, van Swol R (1993) Mapping agroecological zones and time lag in vegetation growth by means of Fourier analysis of time series of NDVI images. *Adv Space Res* 13:233–237
- Menzel A (2002) Phenology: its importance to the global change community. *Clim Chang* 54:379–385
- Menzel A, Sparks TH, Estrella N, Koch E, Aasa A, Ahas R, Alm-Kübler K, Bissolo P, Braslavská O, Briede A, Chmielewski FM, Crepinsek Z, Curnel Y, Dalh Å, Defila C, Donnelly A, Filella Y, Jateczak K, Måge F, Mestre A, Nordli O, Peñuelas J, Pirinen P, Remišov V, Scheifinger H, Striz M, Susnik A, VanVliet A, Wielgolaski F-E, Zach S, Zust A (2006) European phenological response to climate change matches the warming pattern. *Glob Change Biol* 12:1969–1976
- Myneni RB, Keeling CD, Tucker CJ, Asrar G, Nemani RR (1997) Increased plant growth in the northern high latitudes from 1981 to 1991. *Nature* 386:698–702
- Nemani RR, Keeling CD, Hashimoto H, Jolly WM, Piper SC, Tucker CJ, Myneni RJ, Running SW (2003) Climate-driven increases in global terrestrial net primary production from 1982 to 1999. *Science* 300:1560–1563
- O'Connor B, Dwyer E, Cawkwell F, Eklundh L (2012) Spatio-temporal patterns in vegetation start of season across the island of Ireland using the MERIS Global Vegetation Index. *ISPRS J Photogramm Remote Sens* 68:79–94
- Olofsson P, Eklundh L (2007) Estimation of absorbed PAR across Scandinavia from satellite measurements. Part II: modeling and evaluating the fractional absorption. *Remote Sens Environ* 110:240–251
- Olofsson P, Eklundh L, Lagergren F, Jönsson P, Lindroth A (2007) Estimating net primary production for Scandinavian forests using data from Terra/MODIS. *Adv Space Res* 39:125–130
- Olofsson P, Lagergren F, Lindroth A, Lindström J, Klemedtsson L, Kutsch W, Eklundh L (2008) Towards operational remote sensing of forest carbon balance across Northern Europe. *Biogeosciences* 5:817–832
- Olsson L, Eklundh L (1994) Fourier transformation for analysis of temporal sequences of satellite imagery. *Int J Remote Sens* 15:3735–3741

- Olsson L, Eklundh L, Ardö J (2005) A recent greening of the Sahel_97trends, patterns and potential causes. *J Arid Environ* 63:556–566
- Olsson P-O, Jönsson AM, Eklundh L (2012) A new invasive insect in Sweden -Physokermes inopinatus – tracing forest damage with satellite based remote sensing. *For Ecol Manag* 285:29–37
- Potter C, Gross P, Genovese V, Smith ML (2007) Net primary productivity of forest stands in New Hampshire estimated from Landsat and MODIS satellite data. *Carbon Balance Manage* 2:9
- Prince SD (1991) A model of regional primary production for use with coarse resolution satellite data. *Int J Remote Sens* 12:1313–1330
- Prince SD, Goward SN (1995) Global primary production: a remote sensing approach. *J Biogeogr* 22:815–835
- Rautiainen M, Heiskanen J, Eklundh L, Möttus M, Lukes P, Stenberg P (2010) Ecological applications of physically-based remote sensing methods. *Scand J For Res* 25:325–339
- Reed BC, Brown JF, VanderZee D, Loveland TR, Merchant JW, Ohlen DO (1994) Measuring phenological variability from satellite imagery. *J Veg Sci* 5:703–714
- Rodrigues A, Marcal A, Cunha M (2013) Monitoring vegetation dynamics inferred by satellite data using the PhenoSat tool. *IEEE Trans Geosci Remote Sens* 51:2096–2104
- Roerink GJ, Menenti M, Verhoef W (2000) Reconstructing cloudfree NDVI composites using Fourier analysis of time series. *Int J Remote Sens* 21:1911–1917
- Rouse JWJ, Haas RH, Schell JA, Deering DW (1973) Monitoring vegetation systems in the Great Plains with ERTS, Third ERTS Symposium, NASA SP-351, Washington DC, December 10–14 1973, 309–317
- Ruimy A, Saugier B, Dedieu G (1994) Methodology for the estimation of terrestrial net primary production from remotely sensed data. *J Geophys Res* 99:5263–5283
- Running SW (1990) Estimating terrestrial primary productivity by combining remote sensing and ecosystem simulation. In: Hobbs RJ, Mooney HA (eds) *Remote sensing of biosphere functioning*. Springer, New York, pp 65–86
- Running SW, Loveland TR, Pierce LL (1994) A vegetation classification logic based on remote sensing for use in global biogeochemical models. *Ambio* 23:77–81
- Sakamoto T, Yokozawa M, Toritani H, Shibayama M, Ishitsuka N, Ohno H (2005) A crop phenology detection method using time-series MODIS data. *Remote Sens Environ* 96:366–374
- Schröter D, Cramer W, Leemans R, Prentice IC, Araújo MB, Arnell NW, Bondeau A, Bugmann H, Carter TR, Gracia CA, de la Vega-Leinert AC, Erhard M, Ewert F, Glendining M, House JI, Kankaanpää S, Klein RJT, Lavorel S, Lindner M, Metzger MJ, Meyer J, Mitchell TD, Reginster I, Rounsevell M, Sabaté S, Sitch S, Smith B, Smith J, Smith P, Sykes MT, Thonicke K, Thuiller W, Tuck G, Zaeble S, Zierl B (2005) Ecosystem service supply and vulnerability to global change in Europe. *Science* 310:1333–1337
- Schubert P, Eklundh L, Lund M, Nilsson M (2010) Estimating northern peatland CO₂ exchange from MODIS time series data. *Remote Sens Environ* 114:1178–1189
- Schubert P, Lagergren F, Aurela M, Christensen T, Grelle A, Heliasz M, Klemedtsson L, Lindroth A, Pilegaard K, Vesala T, Eklundh L (2012) Modeling GPP in the Nordic forest landscape with MODIS time series data – comparison with the MODIS GPP product. *Remote Sens Environ* 126:136–147
- Schwartz MD (2013) *Phenology: an integrative environmental science*. Springer, Dordrecht
- Seaquist JW, Hickler T, Eklundh L, Ardö J, Heumann B (2009) Disentangling the effects of climate and people on sahel vegetation dynamics. *Biogeosciences* 6:469–477
- Sims DA, Rahman AF, Cordova VD, El-Masri BZ, Baldocchi DD, Flanagan LB, Goldstein AH, Hollinger DY, Misson L, Monson RK, Oechel WC, Schmid HP, Wofsy SC, Xu L (2006) On the use of MODIS EVI to assess gross primary productivity of North American ecosystems. *J Geophys Res* 111:G04015
- Sjöström M, Ardö J, Eklundh L, El-Tahir BA, El-Khidir HAM, Hellström M, Pilesjö P, Seaquist J (2009) Evaluation of satellite based indices for gross primary production estimates in a sparse savanna in the Sudan. *Biogeosciences* 6:129–138

- Sjöström M, Ardö J, Arneth A, Cappelaere B, Eklundh L, de Grandcourt A, Kutsch WL, Merbold L, Nouvellon Y, Scholes B, Seaquist J, Veenendaal EM (2011) Exploring the potential of MODIS EVI for modeling gross primary production across African ecosystems. *Remote Sens Environ* 115:1081–1089
- Stisen S, Sandholt I, Norgaard A, Fensholt R, Eklundh L (2007) Estimation of diurnal air temperature using MSG SEVIRI data in West Africa. *Remote Sens Environ* 110:262–274
- Tan B, Morisette J, Wolfe R, Gao F, Ederer G, Nightingale J, Pedelty J (2008) Vegetation Phenology metrics derived from temporally smoothed and Gap-filled MODIS data, Geoscience and Remote Sensing Symposium, 2008. IGARSS 2008. IEEE International
- Tang XG, Wang X, Wang ZM, Liu DW, Jia MM, Dong ZY, Xie J, Ding Z, Wang HR, Liu XP (2013) Influence of vegetation phenology on modelling carbon fluxes in temperate deciduous forest by exclusive use of MODIS time-series data. *Int J Remote Sens* 34:8373–8392
- Tottrup C, Schultz Rasmussen M, Eklundh L, Jönsson P (2007) Mapping fractional forest cover across the highlands of mainland Southeast Asia using MODIS data and regression tree modelling. *Int J Remote Sens* 28:23–46
- Townshend JRG, Justice CO (1986) Analysis of the dynamics of African vegetation using the normalized difference vegetation index. *Int J Remote Sens* 7:1435–1445
- Tucker CJ (1979) Red and photographic infrared linear combinations for monitoring vegetation. *Remote Sens Environ* 8:127–150
- Tucker CJ, Vanpraet C, Boerwinkel E, Gaston A (1983) Satellite remote sensing of total dry matter production in the Senegalese Sahel. *Remote Sens Environ* 13:461–474
- van Dijk A, Callis SL, Sakamoto CM, Decker WL (1987) Smoothing vegetation index profiles: an alternative method for reducing radiometric disturbance in NOAA/AVHRR data. *Photogramm Eng Remote Sens* 53:1059–1067
- van Leeuwen WJD, Davison JE, Casady GM, Marsh SE (2010) Phenological characterization of desert sky island vegetation communities with remotely sensed and climate time series data. *Remote Sens* 2:388–415
- van Leeuwen WJD, Hartfield K, Miranda M, Meza FJ (2013) Trends and ENSO/AAO driven variability in NDVI derived productivity and Phenology alongside the Andes mountains. *Remote Sens* 5:1177–1203
- Veraverbeke S, Lhermitte S, Verstraeten WW, Goossens R (2010) The temporal dimension of differenced Normalized Burn Ratio (dNBR) fire/burn severity studies: the case of the large 2007 Peloponnese wildfires in Greece. *Remote Sens Environ* 114:2548–2563
- Verbesselt J, Jönsson P, Lhermitte S, van Aardt J, Coppin P (2006) Evaluating satellite and climate data-derived indices as fire risk indicators in Savannah ecosystems. *IEEE Trans Geosci Remote Sens* 44:1622–1632
- Verger A, Baret F, Weiss M, Kandasamy S, Vermote E (2013) The CACAO method for smoothing, gap filling, and characterizing seasonal anomalies in satellite time series. *IEEE Trans Geosci Remote Sens* 51:1963–1972
- Viovy N, Arino O, Belward AS (1992) The Best Index Slope Extraction (BISE): a method for reducing noise in NDVI time-series. *Int J Remote Sens* 13:1585–1590
- Weiss M, Hurk B, Haarsma R, Hazeleger W (2012) Impact of vegetation variability on potential predictability and skill of EC-Earth simulations. *Clim Dyn* 39:2733–2746
- Wessels K, Steenkamp K, von Maltitz G, Archibald S (2011) Remotely sensed vegetation phenology for describing and predicting the biomes of South Africa. *Appl Veg Sci* 14:49–66
- White MA, De Beurs KM, Didan K, Inouye DW, Richardson AD, Jensen OP, O'keefe J, Zhang G, Nemani RR, Van Leeuwen WJD, Brown JF, De Wit A, Schaepman M, Lin X, Dettinger M, Bailey AS, Kimball J, Schwartz MD, Baldocchi DD, Lee JT, Lauenroth WK (2009) Intercomparison, interpretation, and assessment of spring phenology in North America estimated from remote sensing for 1982–2006. *Glob Chang Biol* 15:2335–2359
- Yuan H, Dai Y, Xiao Z, Ji D, Shangguan W (2011) Reprocessing the MODIS leaf area index products for land surface and climate modelling. *Remote Sens Environ* 115:1171–1187
- Zeng H, Jia G, Forbes BC (2013) Shifts in Arctic phenology in response to climate and anthropogenic factors as detected from multiple satellite time series. *Environ Res Lett* 8:035036

- Zhang X, Friedl MA, Schaaf CB, Strahler AH, Hodges JCF, Gao F, Reed BC, Huete A (2003) Monitoring vegetation phenology using MODIS. *Remote Sens Environ* 84:471–475
- Zhang M-Q, Guo H-Q, Xie X, Zhang T-T, Ouyang Z-T, Zhao B (2013) Identification of land-cover characteristics using MODIS time series data: an application in the Yangtze River Estuary. *PLoS ONE* 8:e70079
- Zhao J, Wang Y, Hashimoto H, Melton FS, Hiatt SH, Zhang H, Nemani RR (2013) The variation of land surface Phenology from 1982 to 2006 along the Appalachian Trail. *IEEE Trans Geosci Remote Sens* 51:2087–2095
- Zhou L, Tucker CJ, Kauffman RK, Slayback D, Shabanov N, Myneni RB (2001) Variations in northern vegetation activity inferred from satellite data of vegetation index during 1981 to 1999. *J Geophys Res* 106:20069–20083
- Zhu Z, Woodcock CE, Olofsson P (2012) Continuous monitoring of forest disturbance using all available Landsat imagery. *Remote Sens Environ* 122:75–91

Chapter 10

PhenoSat – A Tool for Remote Sensing Based Analysis of Vegetation Dynamics

Arlete Rodrigues, André R. S. Marcal, and Mário Cunha

Abstract PhenoSat is a software tool that extracts phenological information from satellite based vegetation index time-series. This chapter presents PhenoSat and tests its main characteristics and functionalities using a multi-year experiment and different vegetation types – vineyard and semi-natural meadows. Three important features were analyzed: (1) the extraction of phenological information for the main growing season, (2) detection and estimation of double growth season parameters, and (3) the advantages of selecting a sub-temporal region of interest. Temporal NDVI satellite data from SPOT VEGETATION and NOAA AVHRR were used. Six fitting methods were applied to filter the satellite noise data: cubic splines, piecewise-logistic, Gaussian models, Fourier series, polynomial curve-fitting and Savitzky-Golay. PhenoSat showed to be capable to extract phenological information consistent with reference measurements, presenting in some cases correlations above 70 % ($n = 10$; $p \leq 0.012$). The start of in-season regrowth in semi-natural meadows was detected with a precision lower than 10-days. The selection of a temporal region of interest, improve the fitting process (R-square increased from 0.596 to 0.997). This improvement detected more accurately the maximum vegetation development and provided more reliable results. PhenoSat showed to be capable to adapt to different vegetation types, and different satellite data sources, proving to be a useful tool to extract metrics related with vegetation dynamics.

A. Rodrigues (✉) • M. Cunha

Faculdade de Ciências da Universidade do Porto, Department of GAOT & Centro de Investigação em Ciências Geo-Espaciais, Universidade do Porto, Porto, Portugal
e-mail: dr.arlete@gmail.com; mcunha@mail.icav.iup.pt

A.R.S. Marcal

Faculdade de Ciências da Universidade do Porto, Department of Matemática & INESC TEC, Universidade do Porto, Porto, Portugal
e-mail: andre.marcal@fc.up.pt

10.1 Introduction

Temporal vegetation profiles based on remotely sensed data provide valuable information for understanding land cover dynamics, generally interpreted by vegetation phenological events. Sensors such as the Advanced Very High Resolution Radiometer (AVHRR), SPOT VEGETATION (Satellite Pour l' Observation de la Terre – Vegetation), MODIS (Moderate-Resolution Imaging Spectroradiometer), MERIS (Medium Resolution Imaging Spectrometer) and PROBA-V (Project for On-Board Autonomy – Vegetation) are able to provide a spatial overview of the land surface and spectral reflection information, which can be measured and used to monitor phenology, stage type and crops health (pionnering studies were made by Allen et al. 1969, 1973; Gausman et al. 1969, 1974; Wooley 1971; Gausman and Allen 1973; Gausman and Hart 1974). Furthermore, their ability to collect imagery at frequent time intervals (multitemporal images) permits to observe how the vegetation changes throughout the growing season and better monitor the changes naturally occurred or induced by humans.

Vegetation phenology based on remote sensing data refers to the spatio-temporal development of the vegetated land surface as revealed by satellite sensors (de Beurs and Henebry 2004). The main assumption behind all methods for phenological determination from satellite sensor data is that the signal is related to measures of vegetation. A time-series of a given vegetation index (VI) follows annual cycles of growth and decline. Thus, deriving phenological metrics from remotely sensed data consists on the analysis of the seasonal VI trajectory, and identifying critical points such as the start-of-season or the end-of-season (Bradley and Mustard 2008).

Although the access to Earth Observation Satellite VI time-series is currently widespread, with low or without costs, there is still a gap between the data itself and the meaningful information that can be extracted. Phenological metrics exploit the seasonal growth cycle information, which could be influenced by non-climatic factors, biogenic and anthropogenic disturbances (fires, land degradation, insect attacks), or temperature and rainfall variations (Julien and Sobrino 2009; Potter et al. 2003). The large amounts of data and the presence of noise can make the analysis and extraction of relevant vegetation information a difficult and time consuming process.

The Maximum Value Composites (MVC) process is generally used to minimize the noise influence by analyzing the VI values on a pixel-by-pixel basis, in a predefined time-period, retaining the highest value for each pixel location (Holben 2007). A MVC image is obtained when all pixels have been evaluated. The MVC imagery is highly related to the green vegetation dynamics, and common problems encountered in single-date remote sensing studies, as cloud contamination, atmospheric attenuation and observation geometry are minimized using MVC (Tucker et al. 1985). However, generally the MVC process is not sufficient to eliminate all unrealistic variability from VI time-series (Jonsson and Eklundh 2004; Rodrigues et al. 2013). Furthermore, additional noise may be also introduced by the process of overlaying several images (for example due to image

Table 10.1 Filtering methods proposed for smoothing remotely sensed time-series of vegetation indices

Filtering method	Some prominent applications
Running medians	Velleman (1980)
Best index slope extraction	Viovy et al. (1992) and Lovell and Graetz (2001)
Weighted least squares windowed regression	Sweets et al. (1999)
Harmonic series and higher order splines	Roerink et al. (2000), McCloy and Lucht (2004) and Bradley et al. (2007)
Wavelets	Li and Kafatos (2000) and Sakamoto et al. (2005)
Asymmetric Gaussian	Jonsson and Eklundh (2002)
Double logistic	Zhang et al. (2003) and Beck et al. (2006)
Savitzky-Golay	Chen et al. (2004)
Mean value iteration	Ma and Veroustraete (2006)
Whittaker smoother	Atzberger and Rembold (2009) and Atzberger and Eilers (2010)
Breaks for additive seasonal and trend	Verbesselt et al. (2010)
Frequency analysis	Lhermitte et al. (2011)
Adaptive local iterative logistic fitting	Cao et al. (2015)

misregistration). Thus, it is necessary to fit a model to the observed data before the extraction of vegetation dynamics information. An appropriate model should be capable of smoothing the data without introducing artifacts or suppressing natural variations of the vegetation (Fontana et al. 2008). During the last years, different filtering techniques have been proposed (summarized in Table 10.1). In general, data smoothing facilitates the satellite time-series analyses, by eliminating the unrealistic abrupt peaks and aberrant values that appears in the VI profile (Fontana et al. 2008). Moreover, it permits a better observation of the vegetation changes over time and the identification of the main and double growing seasons, which is not always clearly possible using the VI original data. This is illustrated in the example presented in Fig. 10.1.

Developing algorithms to automatically remove the time-series noise and retrieve land surface phenology metrics from satellite data has been an active research topic for the last decade. TIMESAT (Jonsson and Eklundh 2004) is the most known software for time-series phenology analysis, being used in several research studies (e.g. Gao et al. 2008; Verbesselt et al. 2012; Zeng et al. 2013). It is an open source software and provides three different smoothing functions to fit the time-series data: asymmetric Gaussian, double logistic and adaptive Savitzky-Golay filter. TIMESAT uses a simple method, based on thresholds, to determine a set of phenological metrics, including the start-of-season, mid-season and end-of-season.

Besides TIMESAT, there are other software packages allowing the analysis of the satellite time-series, reduction of noise components and/or extraction of phenological metrics from satellite time-series data. HANTS (Roerink et al. 2000),

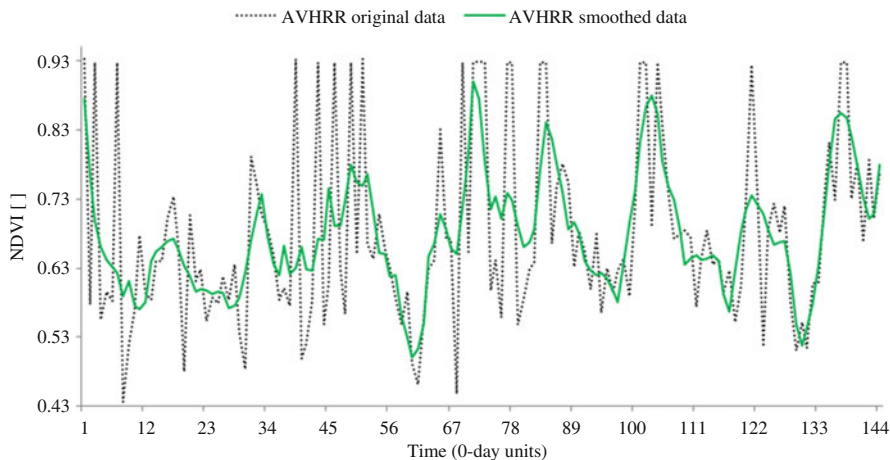


Fig. 10.1 Example of a temporal series of NDVI acquired from NOAA AVHRR for a semi-natural meadows region in Montalegre (Portugal) between 2001 and 2004. The *dotted black line* corresponds to the original NDVI data and the *solid green line* the smoothed data produced using the Savitzky-Golay method

TiSeG (Colditz et al. 2008), TSPT (Prados et al. 2006; McKellip et al. 2008), PPET (McKellip et al. 2010), TIMESTATS (Udelhoven 2011), the software developed by USGS Earth Resources Observation and Science Center (Ross et al. 2009), Enhanced TIMESAT (Tan et al. 2011) and the SPIRITS (Eerens et al. 2014) are some examples. Although these software products have important functionalities for the extraction of phenological information, they present two great limitations: (i) none of them allows the selection of an in-season window of interest, which is fundamental for analyzing vegetation types and crop systems with more than one growth cycle through the year; and (ii) except for TIMESAT, none of them has a specific option to characterize a double growth season phenology. Moreover, they work well in ecosystems with predictable minimum and maximum VI values, however they cannot adapt so well to different vegetation dynamics over the years, caused by uncontrollable conditions (drought year, unseasonal snow, fire, plagues and diseases), and crops with partial ground cover or period of dormancy.

To address the aforementioned limitations, PhenoSat was developed to detect the number of growth seasons in each year and has the option to define an in-season window of interest. The ability to model more than one growing season makes PhenoSat an useful tool for study different crops, able to deal with adverse weather and soil conditions. The main characteristics and functionalities of PhenoSat were tested using a multi-year experiment and different vegetation types, as well as data from two different sensors.

10.2 PhenoSat Description

PhenoSat is a software tool developed to extract phenological information from satellite VI time-series. This tool was implemented in Matlab (Higham and Higham 2000) using a simple interface to provide an easy-to-use soft-ware. PhenoSat can receive two standard input text files: containing the orig-inal satellite VI images, or containing a temporal VI dataset. For the VI im-ages, a pixel-by-pixel approach is conducted, and a specific region can be selected instead of using all image size. For a temporal dataset, the numerical values (VI) are already standardized in a text file.

A number of satellite based metrics related with main growing season phe-nological parameters (e.g. start-of-season, maximum vegetation develop-ment, end-of-season) can be determined by PhenoSat. Some vegetation types and crops systems present more than one growth cycle through the year manly related with crop rotation or vegetation regrowth. The timing and magnitude of these in-season cycles present high intra-annual variability due to some factors such as climate, animal grazing and human land use decisions. Information about the timing of start and maximum of these seasonal cycles can be obtained using PhenoSat. It is important to note that some extreme conditions (e.g. fire, unseasonal snow) could result in a false report of a double growing season. For this reason, a new feature was developed in PhenoSat that allows the selection of a sub-temporal region of interest, based on vegetation dynamics knowledge. The annual VI time-series subinterval, defined manually or automatically, improves the fitting process, providing more realistic results of the vegetation dynamics.

PhenoSat outputs two files containing the phenological information (es-timated date and respective VI value) and the processed data at each of the fitting steps. When the VI images are used as input, three additional output images will be created. These images present, for each pixel analyzed, the phenological estimated dates for three main stages: start-of-season, maximum vegetation development and end-of-season.

10.2.1 *PhenoSat Fitting Methods*

Some VI datasets available online from different sensors (e.g. AVHRR, SPOT VEGETATION (SPOT_VGT), MODIS) are already preprocessed in order to reduce the noise caused by a variety of biophysical factors (Carreiras et al. 2003; Gutman 1991; Li and Strahler 1992). Although this preprocessing is generally effective, the VI datasets still retain some problems (punctual outliers or abrupt changes) that require additional processing. Noise reduction filters can be applied to remove the undesirable artifacts, improving the subsequent analysis, and leading to more reliable vegetation dynamics information.

PhenoSat analyses year-by-year and considers as outliers the VI values that present a VI difference above 0.2 from the median (Mw), and from its left and right spatial neighbors. A VI profile variation of more than 0.2 is considered a high variation (abrupt increase or decrease) which is unexpected between consecutive observations in any vegetative crop cycle. The values of these outliers are replaced by the Mw value. To modify the bias of the fit, an upper envelope (Beck et al. 2006) can be applied. The upper envelope compares the smoothed and original data, and the data points below the model function are considered to be less important. This method enhances the spring and summer periods, allowing a better discrimination of the maximum vegetation development. Although these actions can remove the VI time-series outliers, some noise might still remain. For this reason, PhenoSat provides six methods that can be used to obtain improvements in the noise reduction process. The methods are: cubic smoothing splines (CSS), piecewise-logistic (PL), Gaussian models (GM), Fourier series (FS), polynomial curve-fitting (PCF) and Savitzky-Golay (SG). The CSS algorithm (Reinsch 1967) fits a cubic smoothing spline to the VI time-series data. The adherence of the smoothing spline method to the given data depends on the algorithm parameter selected.

Beck et al. (2006) and Fontana et al. (2008) proved that vegetation dynamics tends to follow a well-defined growth temporal pattern and the vegetation cycle can be represented by a double-logistic function. PhenoSat uses a particular case of a double-logistic function (PL) defined by Eq. 16.1, where t represents the time, VI_t the VI value at time t , c and d are the slopes at the ‘left’ and the ‘right’, and p and e are the inflection points dates. VI_w and VI_{w1} are the VI values before the bud break and after the leaf fall, respectively. The k parameter is related with the asymptotical value and assures the continuity between vegetation growth and senescence parts, even when they differ in shape (Cunha et al. 2010). The PL seven parameters are estimated using the Levenberg-Marquardt algorithm (Montgomery et al. 2006), which requires reasonable initial values.

$$VI_t = VI_w + \frac{k}{1 + \exp[-c(t - p)]} - \frac{k + VI_w - VI_{w1}}{1 + \exp[-d(t - e)]} \quad (10.1)$$

Figure 10.2 presents a representation of the PL parameters, using two consecutive years of NDVI (Normalized Difference Vegetation Index) SPOT_VGT data. The continuity between the 2 years is assured by the VI_w and VI_{w1} , being the VI_w for the second year (beginning of the time-series) the same as the VI_{w1} for the first year (final of the time-series).

The GM adjustment to data is given by the Eq. 16.2 (Goshtasby and O'Neill 1994):

$$y = \sum_{i=1}^n a_i e^{-\left(\frac{x - b_i}{c_i}\right)^2} \quad (10.2)$$

where a is the amplitude, b the centroid (location), c is related to the peak width and n is the number of peaks to fit ($1 \leq n \leq 8$).

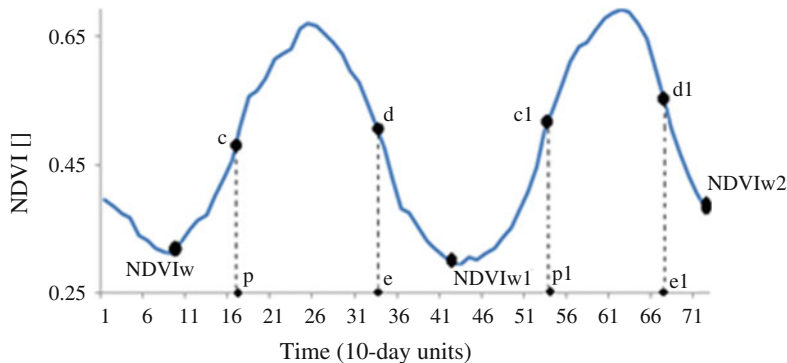


Fig. 10.2 Representation of the piecewise-logistic function parameters, using NDVI SPOT VEG-ETATION data from two consecutive years

The FS is a sum of sine and cosine functions of different period that describes a periodic signal (Mitra 2010). In the trigonometric form, it is represented as:

$$y = a_0 + \sum_{i=1}^n [a_i \cos(nwx) + b_i \sin(nwx)] \quad (10.3)$$

where a_0 models a constant (intercept) term in the data and is associated with the $i = 0$ cosine term, w is the fundamental frequency of the signal, and n is the number of terms (harmonics) in the series ($1 \leq n \leq 8$).

The PCF (Verschelde 2007) finds the coefficients of a polynomial, of a given degree, that fits the data. The higher the degree, the closer the fitting curve will be to the data, although this should be done only up to a certain (reasonable) degree.

The SG filter (Press et al. 2007) defined by

$$g_i = \sum_{nL}^{nR} c_n f_i + n \quad (10.4)$$

is a particular type of low-pass filter, that replaces each data value f_i , $i = 1, \dots, N$, by a linear combination g_i of nearby values in a window defined by the number of points ‘to the left’ (nL) and ‘to the right’ (nR) of a data point i . In PhenoSat, the SG filter uses $nL = nR$ and is always applied to smooth the original VI data. For the subsequent analysis, it can be used alone or combined with one of the other methods.

Figure 10.3 presents a comparison of the six fitting methods described, using a NDVI SPOT_VGT annual time-series obtained from a Closed Deciduous Forest. The PCF and GM methods present the most distinct fitting results for the main and double growing seasons. The biggest differences are on the double growth season, where these two methods present low sensitivity to detect the regrowth peak, over smoothing this occurrence. It is important to note that PCF, GM, FS and CSS require a smoothing parameter to fit the da-ta. The results presented were obtained using an

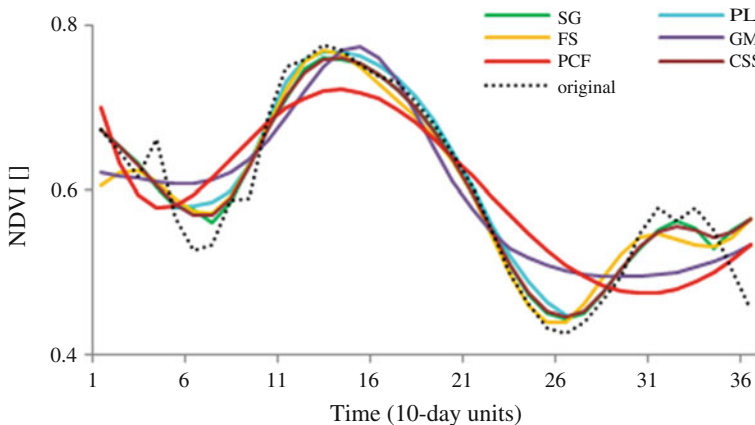


Fig. 10.3 Comparison of PhenoSat fitting methods using a NDVI SPOT VEGETATION annual time-series obtained from a Closed Deciduous Forest

intermediate value for each method in order to provide a more coherent comparison (a parameter of 5 was used in FS, GM and PCF methods, and a value of 0.5 for CSS).

10.2.2 Phenological Metrics

PhenoSat is able to determine the VI value and time of occurrence of the following seven phenological events in the main growing season: start-of-season (SOS), maturity (MAT- beginning of the ripening stage/full canopy), maximum vegetation development (MVD), senescence (SEN), end-of-season (EOS), and the maximum growth and maximum senescence rates (namely left (LIP) and right (RIP) inflection points, respectively).

The phenological information is obtained using the derivatives of the fitting VI time-series, as illustrated in Fig. 10.4. The LIP (and RIP) corresponds to the maximum (and minimum) of the fitted first derivative. The MVD is determined as the maximum VI fitted value in the interval defined by LIP and RIP. The maxima of the fitted VI time-series second derivative, at the left/right of the MVD, identify the SOS/EOS. Similarly, the MAT/SEN can be found using the minima of the fitted data second derivative, at the left/right of the MVD.

Some factors, such as adverse weather conditions (snow, ice or extreme heat), water availability, pasture management and/or herbaceous vegetation growth in the winter season, can interrupt the first growth vegetation cycle and induce an annual regrowth in some crops (e.g. crop systems with more than one growth cycle a year, shrublands or semi-natural meadows). This phenological information can also be extracted by PhenoSat if required. This option allows recording the VI value and

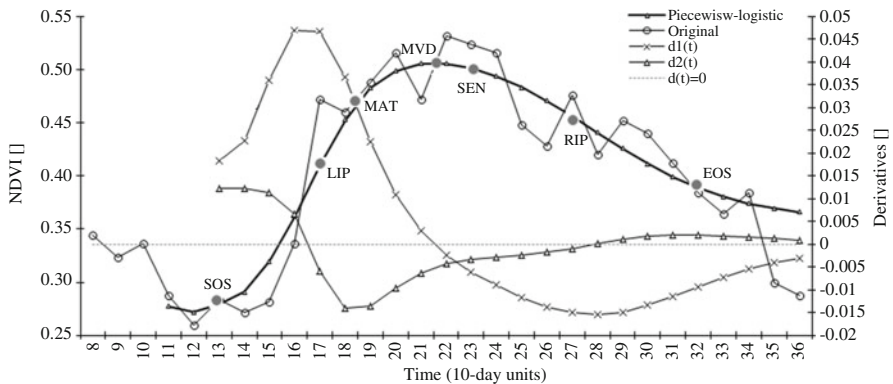


Fig. 10.4 Representation of PhenoSat derived phenological stages using the maxima and minima of the first and second derivatives of the NDVI fitted data

date of occurrence for the start and maximum of this in-season period. PhenoSat calculates the regrowth parameters using the pre-smoothed time-series (removed outliers and SG filter application) after the EOS time occurrence.

The regrowth start is defined as the point where an increase of three or more points occurs after the EOS stage. After this starting point, a decreasing period of two or more points determines the maximum of the regrowth. In some cases, the regrowth reported can be a “false regrowth”. For example in vineyards, as many other discontinuous canopies, during the winter season the inter-row vegetation growth appears as a regrowth in the vineyard annual profile. The unseasonal snow could also result in a false report of a double growth season in many environments. Only with the knowledge/analysis of the ground conditions it is possible to infer about the truth of the regrowth.

The selection of an in-season temporal region of interest, based on known vegetation dynamics, can help dealing with a false regrowth, particularly for natural land cover types. PhenoSat has the possibility to select, automatically or manually, the in-season temporal region of interest. The manual selection can be done by inputting the initial and final time positions, based on known behavior of the vegetation in the field at normal growth conditions. This type of selection presents some limitations when adapting to different dynamics over the years. PhenoSat tries to solve this problem with an optional approach that automatically detects the region of interest. This option, based on the VI time-series profiles, is more flexible and can adapt to the dynamics variations over the years. To determine the annual time-series subinterval, PhenoSat firstly calculates the maximum value of the VI unfitted data. Then, searches for the initial position, which corresponds to the point where a significant increase (or abrupt decrease) is verified to the left of the maximum. Afterwards, to determine the final position, the algorithm proceeds in a similar way but evaluating the data to the right of the maximum.

10.3 PhenoSat Application

10.3.1 Study Area and Satellite Data

The PhenoSat software was tested for different vegetation types and geographical locations in continental Portugal. The NDVI time-series from AVHRR (10-days composite and 1-km resolution) and SPOT_VGT (10-days composite and 1-km resolution) covering Portugal, were downloaded from The Joint Research Centre Community Image Data portal (JRC-CID 2013).

The performances of PhenoSat were tested in two land use types that present, mainly, a different annual growth pattern (Table 10.2): vineyard (VIN) in Douro wine region (Northeast Portugal); and semi-natural meadows (SNM) in Montalegre (Northeast Portugal). In Douro region the predominant land cover is the vineyard with extensive contiguous areas. The vineyard has a long dormancy period with intense understory vegetation growth and a discontinuous canopy (Cunha et al. 2010). The SNM are an essential element of the mountain landscapes in Northern Portugal, and represent the main fodder resource for livestock production. This type of crop is characterized by a regrowth around the month of August, whose intensity and date of occurrence are mainly dependent of climatic conditions (Pocas et al. 2012).

The different vegetation profiles provided by these crops (Fig. 10.5) permit to evaluate the adaptability and performance of PhenoSat to distinct situations. For each crop, a training area was defined carefully to avoid pixel boundaries with other crops, hence the reduced number of pixels (Table 10.2) used in these experiments. Entire training areas were considered as units, instead of using a pixel-by-pixel approach. The median of the NDVI values of the pixels assigned to each crop

Table 10.2 Description of training areas and satellite datasets used to test PhenoSat

Land cover	Acronym	Coordinates (Long/Lat WGS84)	Satellite products	Time-series period	Size (pixels)
Vineyard ^a	VIN	UL: 7d45'17.7W, 41d09'51.6N	SPOT_VGT AVHRR	2001–2010	6
		BR: 7d43'41.8W, 41d08'48.4N			
Semi-natural meadows	SNM	UL: 7d57'36.9W, 41d38'15.2N	SPOT_VGT AVHRR	2001–2010	4
		BR: 7d56'33.4W, 41d37'11.6N			

^aphenological field measures available

UL upper left corner, BR bottom right corner

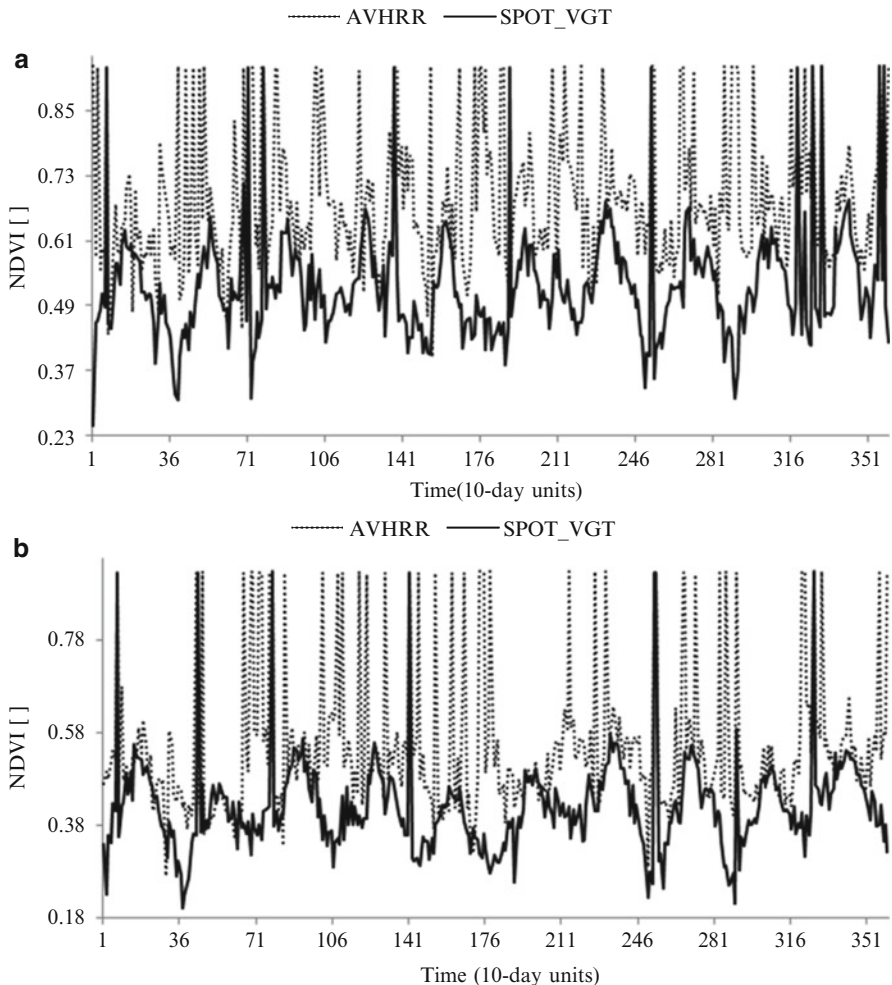


Fig. 10.5 Original NDVI temporal profiles obtained from SPOT VEGETATION and AVHRR data, for the semi-natural meadows (a) and vineyard (b) land use types, for the period 2001–2010

were computed. The yearly NDVI time-series were created using the median values obtained for each of the images available in a year.

10.3.2 Extraction of Phenological Information

The ability of PhenoSat to estimate phenological metrics from satellite VI data was evaluated by a comparison between PhenoSat derived phenology and reference

Table 10.3 Statistics of reference phenological measures obtained for vineyard (VIN) and semi-natural meadows (SNM) vegetation types

Phenological stage	Statistics	VIN	SNM
Start-of-Season	Mean (DOY)	82.16	98.00
	Maximum (DOY)	92.00	150.00
	Minimum (DOY)	78.00	70.00
	Standard deviation (days)	4.73	23.15
Flowering	Mean (DOY)	145.76	n.a.
	Maximum (DOY)	153.00	n.a.
	Minimum (DOY)	125.30	n.a.
	Standard deviation (days)	7.18	n.a.
Veraison/Maximum Vegetation Development	Mean (DOY)	204.20	169.00
	Maximum (DOY)	213.50	180.00
	Minimum (DOY)	199.70	150.00
	Standard deviation (days)	4.07	10.44
End-of-season	Mean (DOY)	n.a.	237.00
	Maximum (DOY)	n.a.	250.00
	Minimum (DOY)	n.a.	210.00
	Standard deviation (days)	n.a.	12.69

n.a. means that no reference phenological measurements were available. Flowering for SNM and End of Season for VIN are two stages extremely difficult to obtain through reference observations. For this reason they were not considered in this study

measures. Table 10.3 presents the statistics of reference phenological measures obtained for each study area. For the VIN test site, the reference phenological measures were obtained by field collection, according to the Baggolini scale (Baggolini 1952). The bud break (BUB), flowering (FLO) and veraison (VER, define as the ‘change of color grapes’ stage) reference measurements were compared with the SOS, MAT and SEN derived by PhenoSat. As no ground measures of phenology were available for SNM, the PhenoSat results for SNM were compared with the observed measures (named reference measures from this point) derived by visual inspection of the original VI time-series, taking into account the knowledge of the vegetation behavior in the field at normal conditions. As an example, Fig. 10.6 presents the reference measures determined from the SNM for 1 year. The SOS was determined as the first point where a significant (four or more points) NDVI growth was occurred (March/April). The MVD was identified as the maximum NDVI value in the annual time-series, which generally occurs in June or early July. The abrupt decrease verified after this point is due to the grass cutting process. The remaining ground vegetation (about 5 cm height) begins a senescence period until the maximum senescence (EOS), occurring mostly around August. In general the SNM EOS stage is followed by a regrowth (RG), representing the first significant (three or more points) vegetation growth after the EOS occurrence.

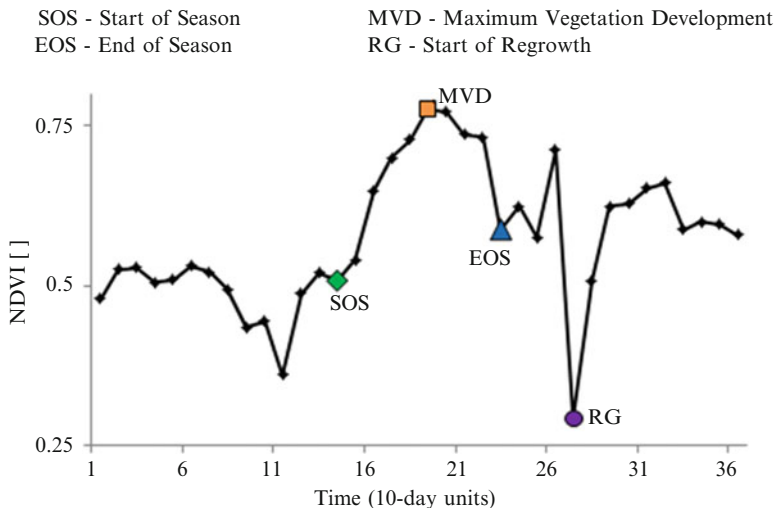


Fig. 10.6 Example of phenological “reference measures” derived from the analysis of a 1-year series (from NDVI SPOT VEGETATION for the semi-natural meadows)

Table 10.4 Correlations between reference and PhenoSat estimated vineyard phenology, using NDVI data from SPOT_VGT and AVHRR sensors

Fitting methods	SPOT_VGT (n = 10)			AVHRR (n = 10)		
	Start	Maturity	Mid-season	Start	Maturity	Mid-season
CSS	-0.27	-0.78	-0.40	0.49	-0.28	0.07
FS	-0.17	-0.76	-0.58	0.56	-0.32	-0.27
GM	0.77	-0.69	0.67	0.45	0.47	0.36
PCF	-0.33	-0.71	-0.38	-0.30	0.41	0.21
PL	0.63	-0.66	-0.55	-0.06	0.30	0.18
SG	0.30	-0.77	-0.25	0.30	-0.21	-0.08

The start, maturity and mid-season represent the comparison between SOSvsBUB, MATvsFLO and SENvsVER, respectively. The SOS, MAT and SEN are the derived PhenoSat phenology, and BUB, FLO and VER are the phenological measures obtained in the vineyard

Fitting methods: *CSS* Cubic Smoothing Splines, *FS* Fourier Series, *GM* Gaussian Models, *PCF* Polynomial Curve Fitting, *PL* Piecewise-Logistic, *SG* Savitzky-Golay

10.4 Results and Discussion

10.4.1 PhenoSat-Derived Phenology

The VIN phenological parameters estimated by PhenoSat were compared with those obtained from reference measurements. The results are presented in Table 10.4.

Using the SPOT_VGT data, the correlations obtained for the start-of-season were no higher than 33 %, except for GM and PL which obtained, respectively, values

of 0.77 ($n = 10$; $p = 0.004$) and 0.63 ($n = 10$; $p = 0.025$). The inter-row vegetation growth during the winter, and the difficulty in discriminating the first grapevine leaves from the satellite data, makes it difficult to estimate with high precision the SOS VIN stage. For maturity and mid-season stages, representing the period around VIN full canopy, PhenoSat obtained, in general, higher correlations than for the SOS stage.

The NDVI values for AVHRR were always greater than SPOT_VGT values (Fig. 10.5b), being the higher differences at the end of the years. Comparing with reference measurements (Table 10.4), the AVHRR data achieved better correlations for the SOS, for most of the fitting methods. For the remaining phenological stages, the SPOT_VGT data were better, providing correlations above 70 % ($n = 10$; $p \leq 0.012$), in some cases.

The overall results proved that PhenoSat is capable to extract phenological information from VI data provided by different satellite sensors, with a slightly better performance for the SPOT_VGT. The AVHRR sensor was not originally designed for vegetation studies (Cracknell 1997), having some limitations as water vapor sensitivity and lacks on quality and atmospheric corrections. These limitations are partially solved by the SPOT_VGT sensor that was specifically designed to capture the main characteristics of the vegetation development in the land surface, presenting better navigation, atmospheric correction and improved radiometric sensitivity system (Gobron et al. 2000).

The flexibility of PhenoSat to extract phenology data from different land use types was tested using the SNM. A comparison between the estimations and reference measures is presented in Table 10.5. The phenological dates for SOS, MVD and EOS stages were extracted with a reasonable precision with correlations higher than 0.50 in most cases. All the fitting methods produced similar results, being PCF the method with best performance for the SOS stage ($n = 10$; $r = 0.86$; $p = 0.001$).

Table 10.6 shows the standard error (SE) of PhenoSat estimations obtained using NDVI SPOT_VGT data, for VIN and SNM crops. For VIN, the SE was not

Table 10.5 Comparison between reference and PhenoSat estimated phenology for the semi-natural meadows crop, using SPOT_VGT data

Correlation Reference vs PhenoSat			
Fitting methods	Start of season	Maximum vegetation development	End of season
CSS	0.58	0.54	0.51
FS	0.50	0.45	0.66
GM	0.43	0.56	0.63
PCF	0.86	0.44	0.63
PL	0.38	0.51	0.65
SG	0.53	0.53	0.54

Fitting methods: *CSS* Cubic Smoothing Splines, *FS* Fourier Series, *GM* Gaussian Models, *PCF* Polynomial Curve Fitting, *PL* Piecewise-Logistic, *SG* Savitzky-Golay

Table 10.6 Standard error of PhenoSat estimations using SPOT_VGT data for the two crops studied

Fitting methods	Vineyard			Semi-natural meadows		
	SOS	Maturity	Mid-season	SOS	Maximum vegetation development	EOS
CSS	6.76	4.08	2.22	16.5	14.4	10.2
FS	7.95	4.35	3.21	11.2	14.1	12.3
GM	8.03	5.65	2.44	7.2	14.1	10.7
PCF	9.94	4.08	4.21	13.1	14.3	10.3
PL	5.08	2.47	1.76	11.7	4.4	5.4
SG	8.83	4.08	4.12	15.3	14.9	10.4

SOS Start of season, *EOS* End of season

Fitting methods: *CSS* Cubic Smoothing Splines, *FS* Fourier Series, *GM* Gaussian Models, *PCF* Polynomial Curve Fitting, *PL* Piecewise-Logistic, *SG* Savitzky-Golay

higher than 10 days. The higher values were obtained for VIN SOS stage, being in accordance with the low correlations showed in Table 10.4. For both VIN and SNM crops, the PL was, in general, the best method with a minimum SE for the VIN mid-season of 1.76 days, and a maximum of 11.7 days for SNM start of season.

The capability of PhenoSat in determining multiple growths in a same year was also tested using the SNM data. This crop is characterized by an annual regrowth around the month of August. However, the start of the regrowth can suffer changes due to some factors such as the climatic conditions and human intervention.

Figure 10.7 presents the original and smoothed NDVI SPOT_VGT profiles for the SNM land use type, for the three final years (2008, 2009 and 2010). The smoothed data were obtained using a SG filter with a first degree polynomial and frame size 5. These parameters removed the outliers/spikes without suppressing the natural variations of the SNM VI original data. From the analysis of the smoothed profiles it is possible to see that 2010 is the only year that presents a double growth season, with start (3 or more consecutive points increasing) around the DOY 270. Table 10.7 shows the timing of regrowth derived from the original data and determined using PhenoSat. All six fitting methods were capable to detect the start of the regrowth, obtaining similar results. The similar, and in some cases equal, results can be explained by the fact that the regrowth estimations are obtained using the pre-smoothed data (removed outliers and SG application). These pre-smoothed data present high correlation (around 88 %) with the original data, thus allowing a more realistic analysis and leading to more reliable results. In the years 2001, 2003, 2007, 2008 and 2009 there was no regrowth, which was correctly verified by PhenoSat. For the remaining years, PhenoSat accurately detected the beginning of the double growth season, being the differences between original and estimated parameters of 10-days (except for PCF in the year 2004). Similar conclusions were observed for the maximum of the regrowth.

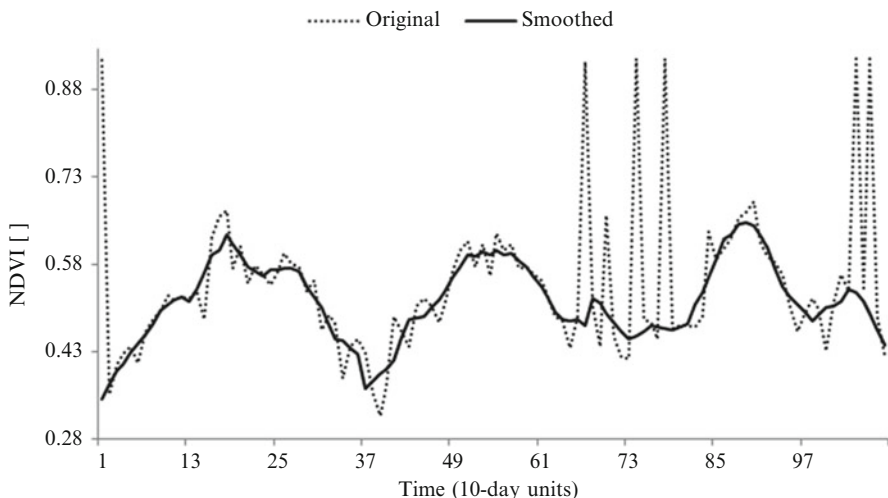


Fig. 10.7 Original and smoothed NDVI SPOT VEGETATION time-series for the semi-natural meadows crop, for years 2008, 2009 and 2010

Table 10.7 Start of double growth season estimations using original and fitted data, for semi-natural meadows

	Start of double growth (day of the year)									
Method	2001	2002	2003	2004	2005	2006	2007	2008	2009	2010
CSS	n.a.	260	n.a.	230	260	250	n.a.	n.a.	n.a.	260
FS	n.a.	270	n.a.	230	260	260	n.a.	n.a.	n.a.	260
GM	n.a.	260	n.a.	230	260	260	n.a.	n.a.	n.a.	270
PCF	n.a.	260	n.a.	250	270	260	n.a.	n.a.	n.a.	270
PL	n.a.	260	n.a.	230	260	250	n.a.	n.a.	n.a.	260
SG	n.a.	260	n.a.	230	260	250	n.a.	n.a.	n.a.	280
Original	n.a.	260	n.a.	230	260	250	n.a.	n.a.	n.a.	270

n.a. signifies that no regrowth is verified on this year

Fitting methods: *CSS* Cubic Smoothing Splines, *FS* Fourier Series, *GM* Gaussian Models, *PCF* Polynomial Curve Fitting, *PL* Piecewise-Logistic, *SG* Savitzky-Golay

10.4.2 Advantages of Selecting an In-season Region of Interest

PhenoSat has the option to select a region of interest, instead of using all range of observations in a year. The reduction of the VI time-series improves the fitting process, capturing more efficiently the maximum vegetation development, thus producing more realistic results. To evaluate the utility of this feature on phenological studies, PhenoSat was tested using the VIN. The interest region must be selected according to the behavior of the studied vegetation in the field, under normal conditions. The grape-growth cycle in Douro (Portugal) starts with the bud break stage, which occurs around March. The harvest period typically occurs

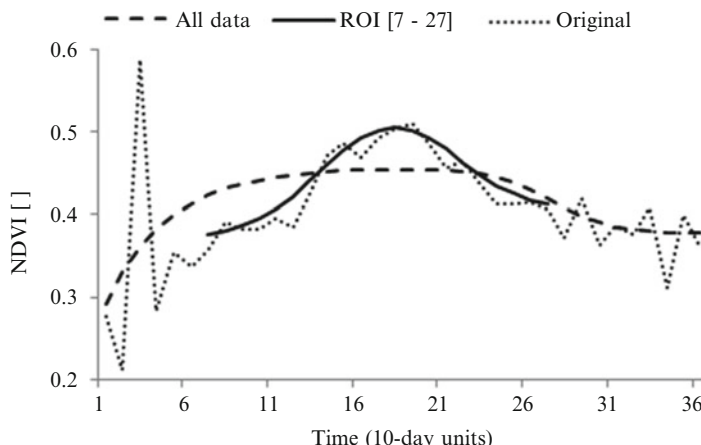


Fig. 10.8 NDVI SPOT VEGETATION original time-series (*dot line*) and the piecewise-logistic fitted results using all range of observations (*dash line*) and the in-season region of interest (*solid line*), for the vineyard in 2009

between August and September/October, however it is deeply dependent on the winemakers according to the style and quality of the wine they wish to produce. Considering these facts, the main phenological cycle of the studied VIN crop is assumed to be ranged from March (DOY 70) to September (DOY 270).

Figure 10.8 presents the VIN NDVI SPOT_VGT data for the year 2009, and the PL fitting results using all range of observations (dash line) and the in-season region of interest. Using all range of observations, the maximum peak of the VIN (around the DOY 180/190) cannot be detected due to the initial peak around the DOY 30 that could be related with winter vegetation growth in the vineyard inter-row. The inclusion of this early pick of NDVI profile led to an over smoothed of the main growing cycle. On the other hand, the use of the region of interest allowed a more accurate adaptation of the fitting method to the variations of the original data during the main growth cycle. The full canopy and senescence stages were captured with high precision and more realistic results were produced. The PL fitted data, produced using region of interest (from 7 to 27 10 days NDVI; 21 observations) instead the all 36 observations, improves the R-square from 0.596 to 0.997.

Another example of the importance of the use of the interest zone in vineyards is presented in Fig. 10.9. The PL fitted results, using all the 36 observations, captured the initial peak (DOY 70) as the maximum development of the VIN crop. This erroneous information led to non-accurate phenological estimations. Using the region of interest, the fitted results captured more precisely the VIN growing season, over smoothing the period related with the soil vegetation growth.

The selection of a region of interest proved to be useful not only in reducing the processing time, but also in obtaining better fitted results, and consequently more reliable phenological information.

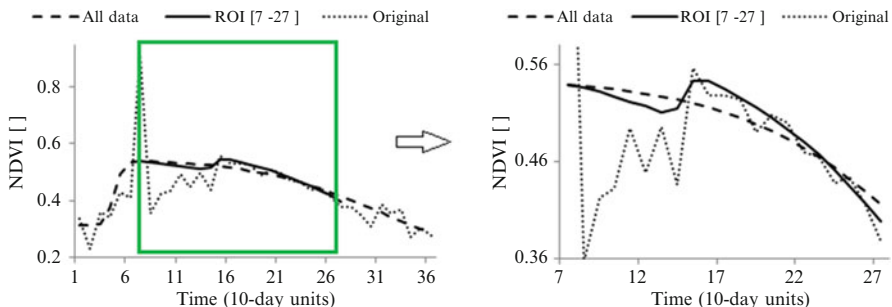


Fig. 10.9 NDVI SPOT VEGETATION original time-series (*dot line*) and the piecewise-logistic fitted results using all range of observations (*dash line*) and using an inseason region of interest (*solid line*), for the vineyard in 2001

10.5 Conclusions

PhenoSat is an easy-to-use software tool which enables phenological information to be extracted from satellite VI data. The experiments carried out indicate that PhenoSat is capable of estimating phenological metrics with significant precision, obtaining, in some cases, correlations with reference measurements above 70 % ($n = 10$; $p \leq 0.012$).

PhenoSat permits the detection of an annual regrowth and the possibility to define an in-season region of interest, which are limitations of other software packages used to extract phenology.

The option to select an in-season region of interest results on an improvement of the fitting process, leading to more reliable results. This PhenoSat feature proved to be a valuable tool for vineyard monitoring and can extend the PhenoSat application to crops with discontinuous canopy, like forestry and deciduous fruit trees. PhenoSat proved to be capable to detect efficiently the regrowth occurrence. The independency of the fitted results leads to a more realistic time-series profile over the year and, thus, more accurate regrowth-derived results.

Comparing PhenoSat with other tools available for phenological studies (e.g. TIMESAT, HANTS, Enhanced TIMESAT, PPET), PhenoSat appears as an intuitive, easy-to-use software with two new important features: the possibility to select an in-season region of interest, and the capability of identifying multiple regrowth within a single year. Moreover, the extraction of phenological parameters using an algorithm based on changes of growth rates allows PhenoSat to avoid thresholds or empirical constants, providing a flexible tool that can be applied to different crops and VI data provided from different data sources.

PhenoSat is freely available at <http://www.fc.up.pt/PhenoSat> website.

Acknowledgments The authors would like to thank JOINT RESEARCH CENTRE (Community Image Data portal) for providing access to the SPOT_VGT and AVHRR images.

Arlete Rodrigues would like to thank to Fundação para a Ciência e a Tecnologia (FCT) for the Doctoral Grant (SFRH/BD/62189/2009).

Part of this project was supported by European Regional Development Fund (ERDF), programme COMPETE and National funds by FCT – Fundação para a Ciência e a Tecnologia, project PTDC/AGR-AAM/67182/2006, LAMESAT_XXI.

References

- Allen WA, Gausman HW, Richardson AJ, Thomas JR (1969) Interaction of isotropic light with a compact plant leaf. *J Opt Soc Am* 59:1376–1379
- Allen WA, Gausman HW, Richardson AJ (1973) Willstater-stoll theory of leaf reflectance evaluated by ray tracing. *Appl Opt* 12:2448–2453
- Atzberger C, Eilers PHC (2010) A smoothed 1-km resolution NDVI time series (1998–2008) for vegetation studies in South America. *Int J Digital Earth* 4:365–386
- Atzberger C, Rembold F (2009) Estimation of inter-annual winter crop area variation and spatial distribution with low resolution NDVI data by using neural networks trained on high resolution images. *Proc SPIE Remote Sens Agric Ecosyst Hydrol XI*: 7472
- Bagliolini M (1952) Les stades repères dans le développement annuel de la vigne et leur utilisation pratique. *Revroman de Agric Vitic Arboric* 8:4–6
- Beck PSA, Atzberger C, Hogda KA, Johansen B, Skidmore AK (2006) Improved monitoring of vegetation dynamics at very high latitudes: a new method using MODIS NDVI. *Remote Sens Environ* 100(3):321–334
- Bradley BA, Mustard JF (2008) Comparison of phenology trends by land cover class: a case study in the Great Basin, USA. *Glob Chang Biol* 14:334–346
- Bradley B, Jacob R, Hermance J, Mustard J (2007) A curve fitting procedure to derive inter-annual phenologies from time-series of noisy satellite NDVI data. *Remote Sens Environ* 106:137–145
- Cao R, Chen J, Shen M, Tang Y (2015) An improved logistic method for detecting spring vegetation phenology in grasslands from MODIS EVI time-series data. *Agric For Meteorol* 200:9–20
- Carreiras JMB, Pereira JMC, Shimabukuro YE, Stroppiana D (2003) Evaluation of compositing algorithms over the Brazilian Amazon using SPOT-4 Vegetation data. *Int J Remote Sens* 24(17):3427–3440
- Chen J, Jonsson P, Tamura M, Gu Z, Matsushita B, Eklundh L (2004) A simple method for reconstructing a high-quality NDVI time-series data set based on the Savitzky-Golay filter. *Remote Sens Environ* 91:332–334
- Colditz RR, Conrad C, Wehrmann T, Schmidt M, Dech S (2008) TiSeG: a flexible software tool for time-series generation of MODIS data utilizing the quality assessment science data set. *IEEE Trans Geosci Remote Sens* 46:3296–3308
- Cracknell AP (1997) The advanced very high resolution radiometer. Taylors & Francis Publisher, London, ISBN 0-7484-0209-8
- Cunha M, Marcal ARS, Rodrigues A (2010) A comparative study of satellite and ground-based vineyard phenology. In: Proceedings of the 29th symposium on EARSeL, Chania, Greece, pp 68–77
- de Beurs KM, Henebry GM (2004) Land surface phenology, climatic variation, and institutional change: analyzing agricultural land cover change in Kazakhstan. *Remote Sens Environ* 89: 497–509

- Eerens H, Haesen D, Rembold F, Urbano F, Tote C, Bydekerke L (2014) Image time series processing for agriculture monitoring. *Environ Model Softw* 53:154–162
- Fontana F, Rixen C, Jonas T, Aberegg G, Wunderle S (2008) Alpine grassland phenology as seen in AVHRR, VEGETATION and MODIS NDVI time series – a comparison with in situ measurements. *Sensors* 8(4):2833–2853
- Gao F, Morisette JT, Wolfe RE, Ederer G, Pedelty J, Masuoka E, Myneni R, Tan B, Nightingale J (2008) An algorithm to produce temporally and spatially continuous MODIS-LAI time series. *IEEE Geosci Remote Sens Lett* 5:60–64
- Gausman HW, Allen WA (1973) Optical parameters of leaves of 30 plant species. *Plant Physiol* 52:57–62
- Gausman HW, Hart WG (1974) Reflectance of sooty mold fungus on citrus leaves over the 2.5 to 40-micrometer wavelength interval. *J Econ Entomol* 67:479–480
- Gausman HW, Allen WA, Myers VI, Cardenas R (1969) Reflectance and internal structure of cotton leaves *Gossypium hirsutum* L. *Agron J* 61:374–376
- Gausman HW, Allen WA, Escobar DE (1974) Refractive index of plant cell walls. *Appl Opt* 13:109–111
- Gobron N, Pinty B, Verstraete M, Widlowski J (2000) Development of spectral indices optimized for the VEGETATION instrument. *Proc VEGETATION 2000*:275–280
- Goshtasby A, O'Neill WD (1994) Curve-fitting by a sum of Gaussians. *CVGIP – Graph Models Image Process* 56(4):281–288
- Gutman GG (1991) Vegetation indexes from AVHRR – an update and future-prospects. *Remote Sens Environ* 35(2/3):121–136
- Higham DJ, Higham NJ (2000) Matlab guide. SIAM, Philadelphia
- Holben BN (2007) Characteristics of maximum-value composite images from temporal AVHRR data. *Int J Remote Sens* 7(11):1417–1434
- Jonsson P, Eklundh L (2002) Seasonality extraction by function fitting to time-series of satellite sensor data. *IEEE Trans Geosci Remote Sens* 40(8):1824–1832
- Jonsson P, Eklundh L (2004) TIMESAT – a program for analyzing time-series of satellite sensor data. *Comput Geosci* 30(8):833–845
- JRC-CID: Joint Research Centre Community Image Data portal (2013) Available at <http://cidportal.jrc.ec.europa.eu/home/>. Accessed 13 July 2013
- Julien Y, Sobrino JA (2009) Global land surface phenology trends from GIMMS database. *Int J Remote Sens* 30:3495–3513
- Lhermitte S, Verbesselt J, Verstraeten WW, Coppin P (2011) A comparison of time series similarity measures for classification and change detection of ecosystem dynamics. *Remote Sens Environ* 115:3129–3152
- Li Z, Kafatos M (2000) Interannual variability of vegetation in United States and its relation to El Niño/Southern Oscillation. *Remote Sens Environ* 71:239–247
- Li XW, Strahler AH (1992) Geometric-optical bidirectional reflectance modeling of the discrete crown vegetation canopy-Effect of crown shape and mutual shadowing. *IEEE Trans Geosci Remote Sens* 30(2):276–292
- Lovell JL, Graetz RD (2001) Filtering pathfinder AVHRR land NDVI data for Australia. *Int J Remote Sens* 22:2649–2654
- Ma M, Veroustraete F (2006) Reconstructing pathfinder AVHRR land NDVI time-series data for the Northwest of China. *Adv Space Res* 37:835–840
- McCloy KR, Lucht W (2004) Comparative evaluation of seasonal patterns in long time series of satellite image data and simulations of global vegetation model. *IEEE Trans Geosci Remote Sens* 42:140–153
- McKellip R, Prados D, Ryan R, Ross K, Spruce J, Gasser G, Greer R (2008) Remote-sensing time series analysis, a vegetation monitoring tool. *NASA Tech Briefs* 32:63–64
- McKellip RD, Ross KW, Spruce JP, Smoot JC, Ryan RE, Gasser GE, Prados DL, Vaughan RD (2010) Phenological parameters estimation tool. *NASA Tech Briefs*, September 30. New York

- Mitra SK (2010) Digital signal processing: a computer-based approach, 4th edn. McGraw-Hill Science/Engineering/Math, Boston. ISBN 978-0077366766
- Montgomery D, Peck E, Vining G (2006) Introduction to linear regression analysis, 4th edn. Wiley, Hoboken
- Pocas I, Cunha M, Pereira LS (2012) Dynamics of mountain semi-natural grassland meadows inferred from SPOT-VEGETATION and field spectroradiometer data. *Int J Remote Sens* 33(14):4334–4355
- Potter C, Tan PN, Steinbach M, Klooster S, Kumar V, Myneni R, Genovese V (2003) Major disturbance events in terrestrial ecosystems detected using global satellite data sets. *Glob Chang Biol* 9:1005–1021
- Prados D, Ryan RE, Ross KW (2006) Remote sensing time series product tool. AGU Fall Meeting 2006
- Press WH, Teukolsky SA, Vetterling WT, Flannery BP (2007) Numerical recipes: the art of scientific computing, 3rd edn. Cambridge University Press, Cambridge, pp 766–768. ISBN 10:0521880688
- Reinsch CH (1967) Smoothing by spline functions. *Numer Math* 10:177–183
- Rodrigues A, Marcal ARS, Cunha M (2013) Monitoring vegetation dynamics inferred by satellite data using the PhenoSat tool. *IEEE Trans Geosci Remote Sens* 51(4):2096–2104
- Roerink GJ, Menenti M, Verhoef W (2000) Reconstructing cloud free NDVI composites using Fourier analysis of time series. *Int J Remote Sens* 21(9):1911–1917
- Ross KW, Spiering BA, Kalcic MT (2009) Monitoring phenology as indicator for timing of nutrients inputs in northern gulf watersheds. *Oceans'09 MTS/IEEE Conference*, October 26–29, United States
- Sakamoto T, Yokozawa M, Toritani H, Shibayama M, Ishitsuka N, Ohno H (2005) A crop phenology detection method using time-series MODIS data. *Remote Sens Environ* 96:366–374
- Sweets D, Reed B, Rowland J, Marko S (1999) A weighted least-squares approach to temporal smoothing of NDVI. *Proc Am Soc Photog Remote Sens Conf* 526–536
- Tan B, Morisette JT, Wolfe RE, Gao F, Ederer GA, Nightingale J, Pedelty JA (2011) An enhanced TIMESAT algorithm for estimation vegetation phenology metrics from MODIS data. *IEEE J Select Top Appl Earth Obs Remote Sens* 4(2):361–371
- Tucker CJ, Hielkema JU, Roffey J (1985) The potential of satellite remote sensing of ecological conditions for survey and forecasting desert-locust activity. *Int J Remote Sens* 6(1):127–138
- Udelhoven T (2011) TimeStats: a software tool for the retrieval of temporal patterns from global satellite archives. *IEEE J Select Top Appl Earth Obs Remote Sens* 4(2):310–317
- Velleman P (1980) Definition and comparison of robust nonlinear data smoothing algorithms. *J Am Stat Assoc* 75:609–615
- Verbesselt J, Hyndman R, Zeileis A, Culvenor D (2010) Phenological change detection while accounting for abrupt and gradual trends in satellite image time series. *Remote Sens Environ* 114:2970–2980
- Verbesselt J, Jonsson P, Lhermitte S, Jonckheere I, van Aardt J, Coppin P (2012) Relating time-series of meteorological and remote sensing indices to monitor vegetation moisture dynamics. In: Chen CH (ed) Signal and image processing for remote sensing. CRC Press, Boca Raton, pp 129–146
- Verschelde J (2007) Introduction to symbolic computation: MCS320. UIC, Dept of Math, Stat & CS, Springer
- Viovy N, Arino O, Belward A (1992) The Best Index Slope Extraction (BISE): a method for reducing noise in NDVI time-series. *Int J Remote Sens* 13:1585–1590
- Woolley JT (1971) Reflectance and transmittance of light by leaves. *Plant Physiol* 47:656–662
- Zeng H, Jia G, Forbes BC (2013) Shifts in Arctic phenology in response to climate and anthropogenic factors as detected from multiple satellite time series. *Environ Res Lett* 8:1–12
- Zhang X, Friedl M, Schaaf C, Strahler A, Hodges J, Gao F, Reed F, Huete A (2003) Monitoring vegetation phenology using MODIS. *Remote Sens Environ* 84:471–475

Chapter 11

Temporal Techniques in Remote Sensing of Global Vegetation

Alexandre Verger, Sivasathivel Kandasamy, and Frédéric Baret

Abstract Time series processing is an important ingredient of a biophysical algorithm in order to get the expected continuous and smooth dynamics required by many applications. Several temporal techniques have been proposed to reduce noise and fill gaps in the time series of satellite data. The choice of the compositing method may have a large impact on the accuracy of the phenology extracted from the reconstructed time series. This chapter presents a comparison of six methods to improve the temporal coherence and continuity of leaf area index (LAI) time series. The temporal smoothing gap filling (TSGF) method which is based on an adaptive Savitzky-Golay filter combined with a linear interpolation approach for filling gaps over a limited temporal window showed the best performance when applied to time series with less than 60 % of gaps. A climatology based approach outperformed other approaches for filling gaps in time series with more than 60 % of missing data or when the period of missing data is longer than 100 days. Based on these findings, a dedicated approach combining the local TSGF filter with a climatology gap filling technique was developed. It constitutes the basis of the algorithm for the operational production of continuous and smooth time series of biophysical variables from VEGETATION data within the European Copernicus Global Land Service.

11.1 Introduction

Continuous and consistent time series of satellite biophysical variables raised an increasing interest in the context of the global change studies. A set of Essential Climate Variables was identified as being both accessible from remote sensing

A. Verger (✉)
CREAF, Cerdanyola del Vallès, 08193 Catalonia, Spain
e-mail: verger@creaf.uab.cat

S. Kandasamy
CCRS, Ottawa, ON K1S1Z9, Canada

F. Baret
EMMAH-UMR 1114 – INRA UAPV, Avignon 84914, France

observations and intervening within key processes (GCOS 2010) including Leaf Area Index (LAI). LAI is defined as half the total developed area of leaf elements per unit horizontal ground area (Chen and Black 1992). It controls the exchanges of energy, water and greenhouse gases between the land surface and the atmosphere. Satellite observations in the reflective solar domain have been used intensively for more than a decade to monitor LAI dynamics over the globe using medium resolution sensors such as MODIS (Knyazikhin et al. 1998), VEGETATION (Baret et al. 2007, 2013; Deng et al. 2006), MERIS (Bacour et al. 2006a) or AVHRR (Ganguly et al. 2008; Zhu et al. 2013; Verger et al. 2012). However, these satellite derived biophysical products show a significant fraction of missing observations as well as sometimes unexpected high frequency temporal variations mainly caused by cloud contamination, residual atmospheric or directional effects, and snow cover in addition to the possible instrumental and algorithmic effects (Garrigues et al. 2008; Weiss et al. 2007; Verger et al. 2011).

Several mathematical filters which use either temporal or spatial techniques have been proposed to fill gaps in remotely sensed data and produce temporally smoothed and spatially continuous products. Spatial filters using pixel-level or regional ecosystem statistical data include geostatistical and regression methods (Goovaerts 1997; Berterretche et al. 2005; Wang et al. 2012). Nevertheless, spatial filters may fail for LAI products derived from coarse resolution satellites to represent the complexity of real landscapes mainly over mixed pixels where LAI could vary widely within a short distance. To overcome this limitation, some studies tried to combine both temporal and spatial methods by using historical high-quality data and temporal curves from neighbor pixels. Fang et al. (2008) proposed a temporal spatial filtering algorithm for MODIS LAI data applying an improved ecosystem curve fitting method based on the MODIS vegetation continuous fields product which imposes regional dependant phenological behaviour onto each target pixel's temporal data in order to maintain pixel-level spatial and temporal integrity. Gao et al. (2008) proposed using preferentially a seasonal-variation curve within a small window around the pixel of the MODIS LAI product and an ancillary seasonal curve within the tile when no high-quality data is available within the defined maximum distance.

Temporal filters include a broad variety of strategies such as the well-known MVC (maximum value compositing) (Holben 1986), best index slope extraction (BISE) (Viovy et al. 1992), Fourier-based fitting methods (Roerink et al. 2000), wavelet decomposition (Martínez and Gilabert 2009), asymmetric Gaussian filtering (Jönsson and Eklundh 2002), Savitzky-Golay filtering (Savitzky and Golay 1964), logistic function fitting (Zhang et al. 2003) or curve-fitting procedure (Bradley et al. 2007). The choice of the smoothing gap filling or compositing method may have a large impact on the accuracy of the phenology extracted from the reconstructed time series (Hird and McDermid 2009; Atkinson et al. 2012). However, quantitative comparisons of alternative temporal filters are relatively rare. Chen et al. (2004) showed the effectiveness of a modified Savitzky–Golay filter in comparison to the BISE algorithm and fast Fourier transform technique for reconstructing SPOT VEGETATION high-quality NDVI time-series. Later, Hird and McDermid (2009) revealed the general superiority of the Beck et al. (2006)

double logistic and Jönsson and Eklundh (2002) asymmetric Gaussian function-fitting methods over more simple local filtering methods: Chen et al. (2004) Savitzky–Golay, Velleman (1980) 4253H Twice filter, Ma and Veroustraete (2006) mean-value iteration, and Filipova-Racheva and Hall-Beyer (2000) autoregressive combination ARMD3-ARMA5 filters for noise reduction of MODIS NDVI time series. It is however still difficult to identify the potentials and limitations associated with different methods since most of these studies focus on a small sample of global conditions and they have been applied to NDVI rather than on a true biophysical variable such as LAI with few exceptions (Gao et al. 2008; Fang et al. 2008; Jiang et al. 2010; Kandasamy et al. 2013).

This chapter focuses on the temporal techniques used operationally to provide continuous estimates of biophysical variables from global satellite observations. The chapter is divided into two parts. We first evaluate the capacity of several methods to provide faithful reconstructions of LAI time series in the presence of a significant amount of missing observations and noise. The gap filling capacity and the fidelity of reconstructed values with the actual ones is evaluated with due attention given to the missing data structure: length of gaps and fraction of missing data in the time series. Based on the findings of this first comparison, the principles of the temporal compositing techniques which are proposed for the generation of LAI time series from VEGETATION data within the European Copernicus Global Land Service are justified in the second part of the chapter.

11.2 A Comparison of Methods for Smoothing and Gap-Filling Satellite LAI Time Series

A selection of six methods is systematically evaluated for the ability to provide continuous and smooth reconstructions of the noisy and discontinuous MODIS LAI time series estimates. To exclude implementation bias in this comparison, the methods were implemented as close as possible to their original source with similar parameterization as suggested by their authors. If the parameterizations were not provided, their values are obtained by trial and error. The various methods are presented first. Then the evaluation approach is detailed. Finally the performances of the six compared methods are analyzed.

11.2.1 *Temporal Smoothing and Gap Filling Techniques*

Six methods were selected based either on local curve-fitting techniques, or decomposition techniques working on the time series as a whole:

Empirical Mode Decomposition Method (EMD) This method was proposed by Huang et al. (1998) as a precursor to the Hilbert-Spectrum Analysis for nonlinear and non-stationary time series data. The method decomposes a given time series data

into a series of Intrinsic Mode Frequencies (IMFs) through a data-driven adaptive iterative process. The method includes two parameters: a threshold of convergence to identify an IMF which was set to 0.3 and the maximum number of IMFs which was fixed to 10. The first IMF containing the highest frequency component, mostly affected by noise, was smoothed using a uniform mean kernel (Demir and Erturk 2008). The EMD method requires the time series to be continuous. The missing data within 128 days were filled by linear interpolation as proposed by Verger et al. (2011). However, EMD was not applied to time series containing gaps longer than 128 days and, in this case, EMD was considered unsuccessful to reconstruct the time series.

Low Pass Filtering (LPF) This method, originally proposed by Thoning et al. (1989) for analyzing CO₂ data from Mauna Lao observatory, was later adapted by Bacour et al. (2006b) for processing AVHRR satellite time series. This method involves fitting a time-dependent function with 2 polynomial and 8 harmonic terms. The residuals of this fitting are then filtered using 2 Low Pass Filters to separate inter- and intra-annual variations. The final reconstructions result from the sum of the time-dependent function and the filtered residuals. This method requires the data to be continuous. Similarly to EMD method, the gaps within 128 days were first filled by linear interpolation (Verger et al. 2011). For time series containing longer gaps than 128 days, the LPF reconstructions are missing.

Whittaker Smoother (Whit) This method is based on a penalized regression method proposed by Whittaker (1922) as an alternative form of b-spline with the number of knots equal to the number of data points. The method involves the minimization of a cost function having two terms – a term for fidelity expressed as a quadratic difference between the estimates and actual observations, and a term for roughness expressed as a quadratic difference between two successive estimates. The balance between these two terms is achieved by a smoothing parameter (λ). The higher the λ , the smoother is the estimated series but at the expense of fidelity. Analytical estimation of this value is difficult as the value is dependent on the time series being smoothed. Hence, by trial and error this value was set to 100. The smoothness is also controlled by the order of differentiation, which is fixed to 3 in this study as proposed by Eilers (2003).

Asymmetric Gaussian Fitting (AGF) This method was proposed by Jönsson and Eklundh (2002) within the TIMESAT toolbox. An asymmetric Gaussian function is locally fitted to the data over the growing and senescent parts of each season. Then the fitted functions are merged to get a smooth transition between seasons. This method can handle small gaps (up to 72 days). The original TIMESAT implementation requires a minimum seasonality in the data and a maximum fraction of missing data of 25 %. However, in this study these two conditions were removed to allow a more rigorous comparison between the different time series methods.

Temporal Smoothing and Gap Filling (TSGF) This method proposed by Verger et al. (2011) is an adaptation of the Savitzky-Golay filter (Savitzky and Golay 1964) where the order of the polynomial is fixed to 2 but an asymmetric and variable in

length temporal window is considered. The temporal window is defined to include 3 observations on each side of the date being smoothed within a maximum 64 day period. If less than 6 observations are available in the compositing period, the polynomial fitting is not applied. Gaps shorter than 128 days are reconstructed with a 2-iteration linear interpolation. Gaps longer than 128 days will result in missing data. The possible flattening of the seasonal peaks due to smoothing is further corrected by scaling the smoothed series to the actual series (Verger et al. 2011).

Climatology (Clim) The climatology describes the average yearly time pattern. It may provide smooth and continuous time series with, however, no changes from 1 year to another. The climatology was computed at 8-day time steps as the inter-annual average of the values available in a ± 12 -day window across all the years in the time series (Baret and Weiss 2010). The climatology was then corrected to provide a more continuous and smoother time course. A Savitzky-Golay filter (Savitzky and Golay 1964) was first applied. Linear interpolation was applied to fill gaps shorter than 128 days (Verger et al. 2011). Gaps longer than 128 days will result in missing data. The corrected climatology was then replicated across all years to provide the reconstructed time series.

11.2.2 Evaluation Approach

The several methods were evaluated using time series corresponding to actual MODIS LAI products over the 420 BELMANIP2 sites identified by Baret et al. (2006) to represent the variability of vegetation types and conditions around the world. The considered methodology to evaluate the methods is based on a two-step process as proposed by Kandasamy et al. (2013):

1. In a first step, reference LAI time series were first generated. MODIS LAI time series (LAI_{ori}) over a sample of 25 sites of different biome types were selected to be both representative of the diversity of seasonal patterns and with a low fraction of missing observations. The different evaluated methods were applied to each of the 25 sites and the median value across all reconstructions was kept as the reference time course for the evaluation (LAI_{ref}).
2. In the second step, emphasis was put on the occurrence of missing data (% gap) and noise to provide realistic LAI values. The original time series (LAI_{ori}) were first completed at the location of missing data by LAI_{ref} values contaminated by a noise that was randomly drawn within the distribution of residuals ($LAI_{ref} - LAI_{ori}$) for each site. This results in realistic but continuous temporal profiles with no gaps (LAI_{comp}). Then, the gap structure observed over each one of the 420 sites belonging to the same vegetation class was applied to the 25 sites with completed time series (LAI_{comp}). This results in 1920 simulated time series (LAI_{sim}). This approach was expected to improve the realism of the analysis that accounts for the implicit links between the vegetation type and the distribution of missing observations. The various methods were applied over

the simulated time series (LAI_{sim}) and the resulting reconstructions (LAI_{rec}) compared to the reference data (LAI_{ref}) were used to quantify the accuracy of each of the 6 methods as a function of the fraction of missing observations.

The fidelity of reconstruction, i.e. how similar the LAI_{rec} reconstructed values are to the LAI_{ref} reference values, is evaluated based on the root mean square evaluation over all the simulation cases over dates with missing data in LAI_{sim} :

$$RMSE = \sqrt{\frac{\sum_{j=1}^N \sum_{t=1}^{n_j} (LAI_{\text{rec}}^j(t) - LAI_{\text{ref}}^j(t))^2}{\sum_{j=1}^N n_j}} \quad (11.1)$$

where $LAI_{\text{rec}}^j(t)$ and $LAI_{\text{ref}}^j(t)$ are the reconstructed and reference values for date t and case j , respectively. n_j is the number of dates with observations for case j and N is the number of cases considered.

In many cases, the methods may fail to reconstruct the time series due to the long periods of gaps or due to the large amount of gaps. These are respectively quantified by the success fraction (%success), i.e. the fraction of gaps that were able to be filled, and the reconstruction fraction (%reconstructions), i.e. the fraction of dates with reconstructed LAI values.

11.2.3 Performances for Time Series Reconstruction

The capacity of the considered methods to reconstruct the time series under varying conditions of length of gaps (LoG) and amount of gaps (%Gap) is first evaluated. The fidelity of the reconstructions is then evaluated.

11.2.3.1 Gap-Filling Performances

Among the evaluated methods, only Whit method was able to fill all the gaps even if they are very long (Fig. 11.1a). Conversely, EMD, AGF and LPF methods show a rapid decrease in the %success with the increase in the LoG. AGF was unable to provide any reconstructions for $\text{LoG} > 88$ days, while the EMD and LPF fail for $\text{LoG} > 128$ days. Even for small gaps, only 50 % of them were filled. The TSGF was able to successfully fill the gaps up to a gap length of 128 days as expected by its definition. The Clim also shows a decrease of %success as a function LoG but was able to fill gaps in more than 80 % of cases for $\text{LoG} < 128$ days because of the accumulation of observations over the 9 year period.

LPF, AGF and EMD fail in about 50 % of the cases when the fraction of missing observations (%gap) was larger than 20 % (Fig. 11.1b), which represents about 60 %

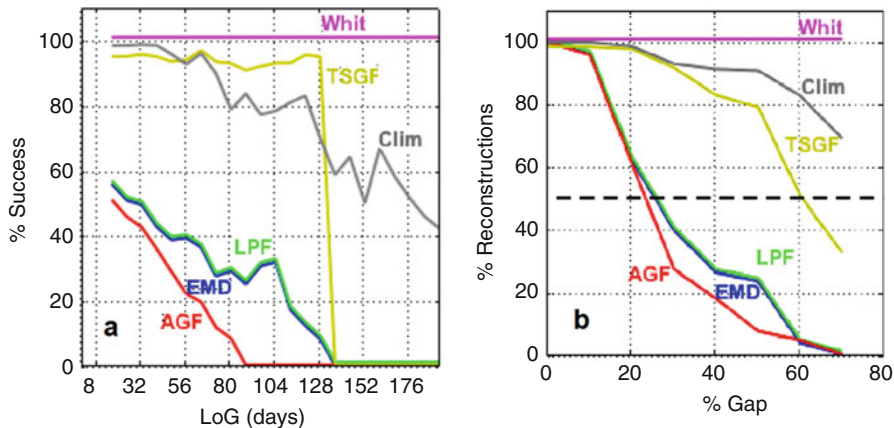


Fig. 11.1 (a) Fraction of gaps reconstructed (%success) as a function of length of gaps (LoG). (b) Fraction of dates reconstructed (%reconstruction) as a function of %gap. The horizontal dashed line represents the 50 % threshold of %reconstructions. The different methods are indicated by the different colors. Some values were slightly shifted vertically for better readability (Adapted from Kandasamy et al. 2013)

of the simulation cases investigated in this study. This is partly attributed to their principles and partly to their implementation. Hence, great care should be taken during the implementation of such methods to improve their rate of applicability in cases with significant periods of gaps. Conversely, Whit and Clim methods were applicable in almost all situations while TSGF shows an intermediate behavior (Fig. 11.1b).

11.2.3.2 Fidelity of Reconstructions

The fidelity of the methods degrades rapidly as a function of the length of gaps (Fig. 11.2a), particularly, for Whit method. Clim shows similar performance independently of the LoG. For LoG < 100 days, LPF and TSGF are found to provide the best performances. For gaps exceeding 100 days, Clim appears to be more robust and performs the best.

The fidelity of reconstructions in gaps as a function of the fraction of missing observations in the time series (Fig. 11.2b) shows relatively low RMSE values (around 0.1) up to %gap < 20 % for all methods except for Clim which performs the worst in this condition since it is not able to capture the inter-annual variability in LAI seasonality. Then Whit shows a rapid increase of the RMSE with %gap with poorer performance as compared to Clim for %gap > 30 %. TSGF was found to perform the best up to 60 % gap.

To summarize the first part of this chapter, TSGF provides more accurate reconstructions of MODIS LAI time series up to a %gap < 60 %. Most methods performed worse than Clim for gap durations longer than about 100 days or when

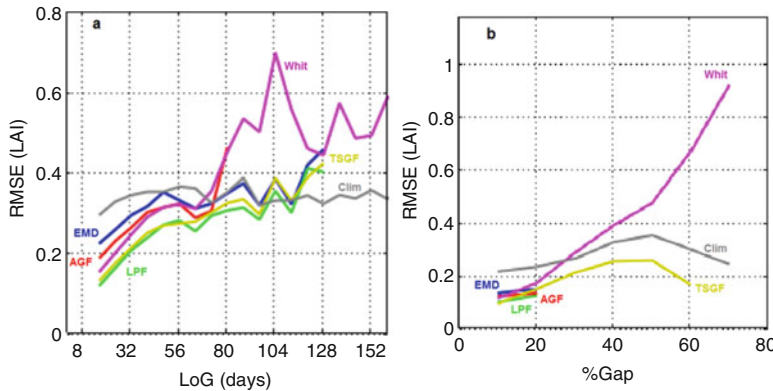


Fig. 11.2 RMSE as a function of LoG (a) and %Gap (b). The RMSE is computed between LAI_{ref} and LAI_{rec} over dates with missing observations in LAI_{sim} (Adapted from Kandasamy et al. 2013)

the fraction of gaps in the time series is greater than 60 %. The combination of the local TSGF fitting with the climatology gap-filling approach appears to be optimal for improving the consistency and continuity of LAI time series from moderate resolution satellite sensors. This combined approach is further explored in the second part of this chapter.

11.3 Temporal Techniques in Remote Sensing of Global Vegetation

The temporal compositing techniques for ensuring consistency and continuity of GEOV2/VGT LAI products derived from VEGETATION (VGT) data within the Copernicus Global Land Service are here presented as well as the derived products. The principles of the temporal composition are presented first. Then the GEOV2/VGT products are evaluated as compared to the first version GEOV1/VGT products (Baret et al. 2013) with emphasis on the improvements in terms of temporal continuity and smoothness.

11.3.1 Principles of the Temporal Compositing Approach

The GEOV2/VGT algorithm for the estimation of global LAI from VEGETATION satellite data at 1 km spatial resolution and 10-day steps in near real time as well as in offline mode (time series from 1999 to 2013) consists of three main steps: (1) neural networks to provide instantaneous estimates from daily VGT-P reflectances,

(2) a multi-step filtering approach based on an iterative upper envelope process to eliminate data mainly affected by atmospheric effects and snow cover, and (3) a temporal composition to ensure consistency and continuity of the LAI time course every 10 days. Here we focus on this third step, i.e. the temporal composition, and the historic LAI time series generated in offline mode. We refer the interested reader to Verger et al. (2014, 2016) for further details about the GEOV2/VGT algorithm.

The GEOV2/VGT temporal composition combines the TSGF (Verger et al. 2011) and the climatology-based CACAO (Verger et al. 2013) techniques. TSGF fits a second-degree polynomial over an asymmetric temporal window as described in Sect. 11.2.1. The compositing period is made of past and future semi-windows of adaptive length varying between 30 and 60 days. The length of the semi-window is determined by the availability of 6 valid observations the closest to the date of the dekad at which the product is estimated (Verger et al. 2011). If less than 6 observations exist in a 60 day semi-window, CACAO values evenly distributed every 10-days are used to fill gaps before the application of TSGF.

CACAO (Consistent Adjustment of Climatology to Actual Observations) consists of fitting the climatology to actual observations for each growth season by scaling the magnitude and shifting the phenology. CACAO copes better with missing and noise contaminated data as compared to standard methods as found in Verger et al. (2013). The climatology is computed as the inter-annual average of GEOV1/VGT time series over the 1999–2010 period (Verger et al. 2015). If it is available for a given pixel, the CACAO method allows filling all the gaps in the time series, even for missing data during long periods. Indeed, CACAO is closer to the actual data than the original climatology (Clim) because it allows inter-annual variations of the time course (Fig. 11.4). However, the main limitation of CACAO reconstruction method is its inability to capture underlying atypical modes of seasonality including rapid natural and human induced disturbances in the time series that strongly differ from the average climatology (e.g. flood or fire events, changes in the land cover) (Verger et al. 2013). To avoid this drawback, priority is given to TSGF smoothing since it is closer than CACAO to the actual observations, while CACAO is only used to fill large gaps in the time series before the application of TSGF.

11.3.2 Assessment of the Temporal Continuity and Consistency

11.3.2.1 Inspection of a Sample of Sites

Few BELMANIP2 sites showing typical features have been selected to illustrate the performances of GEOV2/VGT LAI time series per large biome types (Fig. 11.3).

For the evergreen broad leaf forest (site #445), the effect of residual clouds is very pronounced, creating strongly negatively biased estimates of daily products. These are efficiently filtered thanks to the frequency criterion used. This results in

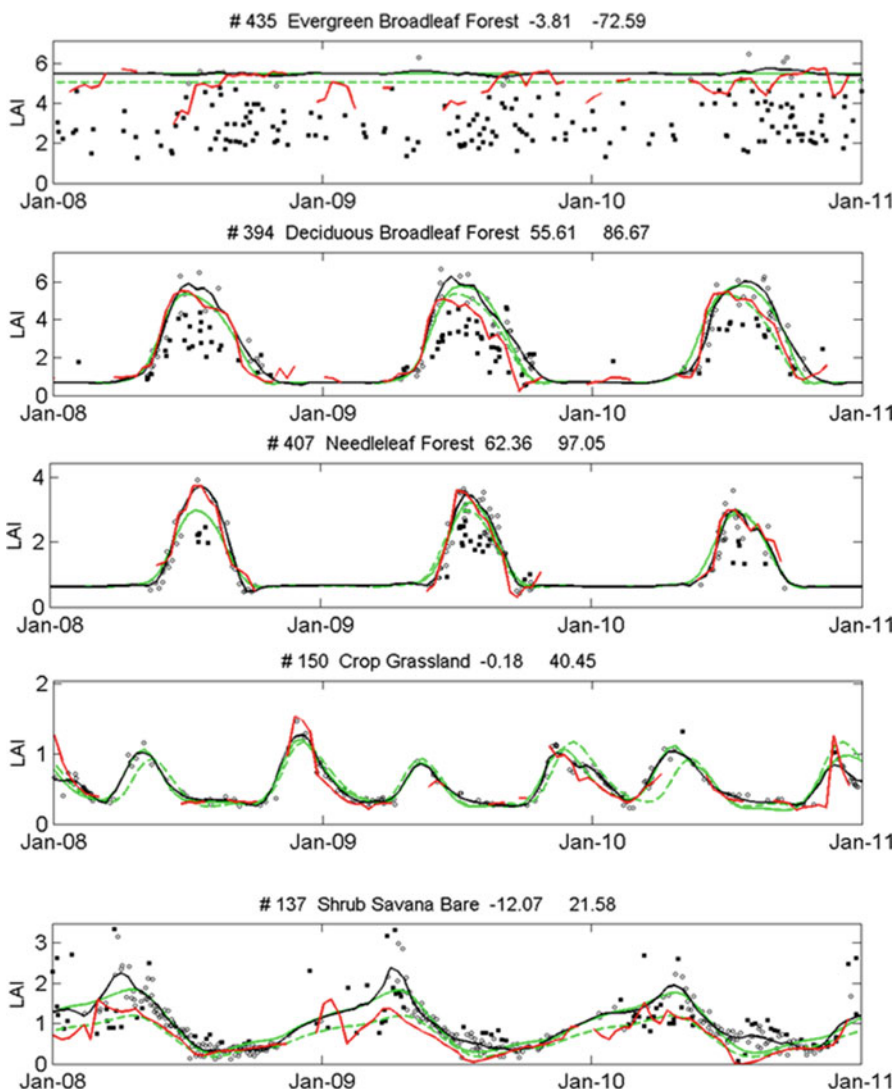


Fig. 11.3 Temporal profile of GEOV2/VGT (black solid line) over typical sites of different biome types. Daily estimates derived from VGT-P products are indicated by the dots: black squares correspond to outliers. Empty circles to the valid LAI estimates used to compute the GEOV2/VGT product. The dashed green line corresponds to the GEOV1/VGT climatology. The solid green line to the CACAO estimates. The red line corresponds to GEOV1/VGT product

a very flat temporal profile with a high level of LAI as expected. As compared to GEOV2, GEOV1 shows generally lower LAI values, discontinuous and shaky temporal profiles.

For deciduous broadleaf forest (site #394), similarly, the negative bias due to cloud contamination is efficiently filtered by the GEOV2 algorithm. For this high latitude site, the winter period is continuously and consistently gap filled although very few observations are available in GEOV2 while some discontinuities are observed in GEOV1.

For very high latitude needle leaf forests (site #407), the GEOV2 temporal profile is very consistent with that of GEOV1 during the vegetation season, with however no interruption during the winter period conversely to GEOV1.

The temporal profiles over the cropland site with double seasonality (site #150) show also a high consistency between GEOV1 and GEOV2. However, some artifacts noticed for GEOV1 (site #150, end of 2010) have disappeared in GEOV2 due to the use of the CACAO fitted climatology as a background information to provide dekad estimates in absence of observations. For this particular site near the Equator (site #150), GEOV2 shows significant improvements in terms of continuity as compared to GEOV1.

The temporal profiles of shrub-savana-bare soils are also very well captured by GEOV2, with large improvements as compared to GEOV1 regarding continuity and smoothness of estimates. However, site #137 shows large scattering of daily estimates, particularly during the winter season probably largely contaminated by clouds.

To summarize, as compared to the GEOV1/VGT products, GEOV2/VGT displays more continuous and smooth temporal profiles (Fig. 11.3). This will be better quantified in the following.

11.3.2.2 Temporal Continuity

The continuity of time series is evaluated by the fraction of missing data based on the BELMANIP2 sites during the 2003–2010 period. Only 1 % of the potential dekads are missing globally, i.e. much less than for GEOV1/VGT showing about 20 % of missing data. GEOV1/VGT products are missing if less than 2 observations exist in the 30-day compositing window. GEOV2/VGT benefits from the use of the TSGF and the CACAO climatology based techniques for filling, respectively, the small gaps within 120 days or the larger gaps: data are missing only if the climatology is not available due to too large discontinuities in the data.

The climatology values are used to fill large gaps in 10–55 % of the cases depending on the biome type as displayed in Fig. 11.4. The fraction of dekads that were not filled but with available observations are slightly higher than those observed for GEOV1/VGT due to the use of daily estimates and a larger compositing window. Identical patterns per biome are observed with lower fraction of high quality observations for evergreen broadleaf forests mostly located in areas with continuous cloud cover around the Equator. In this particular case, the fraction of non filled data is higher for GEOV1/VGT because in GEOV2/VGT a high fraction of data is filtered out in the outlier rejection process.

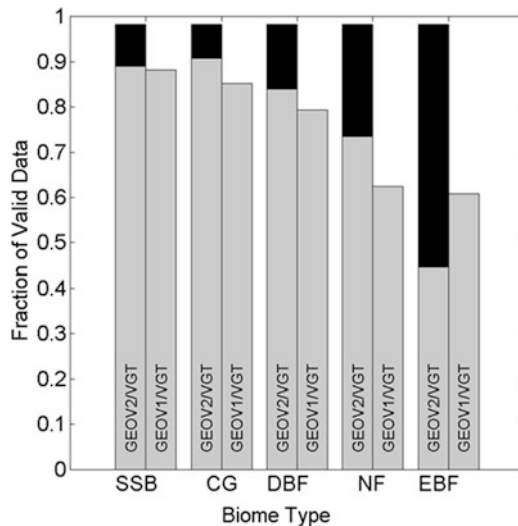
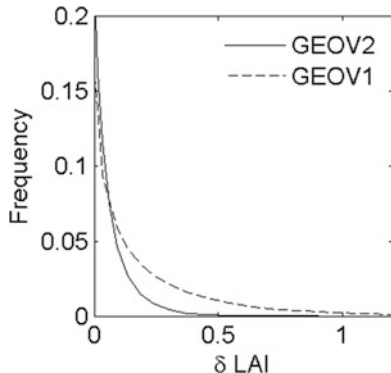


Fig. 11.4 Average fraction of valid GEOV1/VGT and GEOV2/VGT products per biome. The biome classes are derived from the GLOBCOVER (Defourny et al. 2009) global landcover: *SSB* Shrubs/Savana/Bare soil, *CG* Crops and Grassland, *DBF* Deciduous Broadleaf Forests, *NF* Needleleaf Forest, *EBF* Evergreen Broadleaf Forest. For GEOV2/VGT, high quality data (grey) and gap filled data (black) are distinguished. Evaluation over the BELMANIP2 sites for the 2003–2010 period

11.3.2.3 Temporal Smoothness

LAI variable results from incremental bio-physical processes. It is therefore expected to show relatively smooth temporal variations except in extreme situations such as flooding, fire or changes in the land-use. High variability in the temporal profiles would indicate a lack of reliability of the derived products. The smoothness of the LAI temporal series was evaluated based on the absolute value of the difference, δLAI , between $LAI(t)$ product value at date t and the mean value between the two closest bracketing dates in a maximum Δt period of 60 days: $\delta LAI = |1/2(LAI(t + \Delta t) + LAI(t - \Delta t)) - LAI(t)|$ (Verger et al. 2011). The smoother the temporal evolution, the smaller the δ difference should be. The histogram of δ over the whole dataset of BELMANIP2 sites in the 2003–2010 period (Fig. 11.5) shows that both GEOV1/VGT and GEOV2/VGT products are very smooth with differences lower than 0.25 for most of cases. However, GEOV2/VGT shows generally smoother temporal profiles as attested in Fig. 11.3.

Fig. 11.5 Histogram of the δ LAI absolute difference representing temporal smoothness for GEOV2/VGT and GEOV1/VGT LAI products. Evaluation over the BELMANIP2 sites for the 2003–2010 period



11.4 Conclusions

Time series processing is an important ingredient of a biophysical algorithm in order to get the expected continuous and smooth dynamics required by many applications. A comparison of six widely used smoothing and gap filled techniques shows that the structure of missing data in the time series (length of gaps and fraction of missing data) appears as a major limitation of the accuracy of the reconstructed temporal profiles. A local asymmetric Savitzky-Golay filter using linear interpolation for gap filling over a limited temporal window of 120 days provides the best performances in terms of the fidelity of reconstructions to actual LAI observations for time series with a gap fraction up to 60 %. Most methods were performing poorer than the climatology to fill gaps longer than about 100 days or fraction of gaps greater than 60 %. This suggest the interest of developing dedicated methods where the features derived from the exploitation of the several years available in the time series including the climatology, could be injected more explicitly as a background information for improving the reliability of methods working over a limited time window, such as a season or part of it. This constitutes the basis of the proposed temporal techniques for the generation of continuous and consistent time series of LAI from global VEGETATION observations. A climatology is fitted to the data for each sub-season and used to fill data before the application of a Savitzky-Golay filter. This method is being implemented within the Copernicus Global Land service and GEOV2/VGT continuous (less than 1 % of missing data) biophysical products over the whole globe will be freely delivered through the Copernicus portal (land.copernicus.eu/global) at 1/112° spatial resolution every 10 days in near real time as well as in offline mode (time series from 1999 to 2013). The GEOV2 algorithm will be further adapted to other sensors including AVHRR, PROBA-V, Sentinel-3 for the extension of the time series after 2014.

Acknowledgments This research was partially supported by the European Copernicus Global Land Service, GIOBIO (32–566) project, the Spanish Government grant CGL2013-48074-P, the Catalan Government grant SGR 2014-274, and the European Research Council Synergy grant ERC-2013-SyG-610028 IMBALANCE-P. Aleixandre Verger was the recipient of a *Juan de la Cierva* postdoctoral fellowship from the Spanish Ministry of Science and Innovation.

References

- Atkinson PM, Jeganathan C, Dash J, Atzberger C (2012) Inter-comparison of four models for smoothing satellite sensor time-series data to estimate vegetation phenology. *Remote Sens Environ* 123:400–417
- Bacour C, Baret F, Béal D, Weiss M, Pavageau K (2006a) Neural network estimation of LAI, fAPAR, fCover and LAIxCab, from top of canopy MERIS reflectance data: principles and validation. *Remote Sens Environ* 105:313–325
- Bacour C, Bréon F-M, Maignan F (2006b) Normalization of the directional effects in NOAA–AVHRR reflectance measurements for an improved monitoring of vegetation cycles. *Remote Sens Environ* 102(3–4):402–413
- Baret F, Weiss M (2010) Climatology of LAI, FAPAR and FCover products (V1). INRA-EMMAH, Avignon
- Baret F, Morissette JT, Fernandes RA, Champeaux JL, Myneni RB, Chen J, Plummer S, Weiss M, Bacour C, Garrigues S, Nickeson JE (2006) Evaluation of the representativeness of networks of sites for the global validation and intercomparison of land biophysical products: proposition of the CEOS-BELMANIP. *Geosci Remote Sens IEEE Trans* 44(7):1794–1803
- Baret F, Hagolle O, Geiger B, Bicheron P, Miras B, Huc M, Berthelot B, Weiss M, Samain O, Roujean JL, Leroy M (2007) LAI, fAPAR and fCover CYCLOPES global products derived from VEGETATION. Part 1: principles of the algorithm. *Remote Sens Environ* 110:275–286
- Baret F, Weiss M, Lacaze R, Camacho F, Makhmara H, Pacholczyk P, Smets B (2013) GEOV1: LAI, FAPAR essential climate variables and FCover global time series capitalizing over existing products. Part1: principles of development and production. *Remote Sens Environ* 137:299–309
- Beck PSA, Atzberger C, Hogda KA, Johansen B, Skidmore AK (2006) Improved monitoring of vegetation dynamics at very high latitudes: a new method using MODIS NDVI. *Remote Sens Environ* 100(3):321
- Berterretche M, Hudak AT, Cohen WB, Maiersperger TK, Gower ST, Dungan J (2005) Comparison of regression and geostatistical methods for mapping Leaf Area Index (LAI) with Landsat ETM+ data over a boreal forest. *Remote Sens Environ* 96(1):49–61
- Bradley BA, Jacob RW, Hermance JF, Mustard JF (2007) A curve fitting procedure to derive inter-annual phenologies from time series of noisy satellite NDVI data. *Remote Sens Environ* 106:137–145
- Chen JM, Black TA (1992) Defining leaf area index for non-flat leaves. *Plant Cell Environ* 15:421–429
- Chen J, Jönsson P, Tamura M, Gu Z, Matsushita B, Eklundh L (2004) A simple method for reconstructing a high quality NDVI time series data set based on the Savitzky-Golay filter. *Remote Sens Environ* 91:332–344
- Defourny P, Bicheron P, Brockmann C, Bontemps S, Van Bogaert E, Vancutsem C, Pekel JF, Huc M, Henry C, Ranera F, Achard F, di Gregorio A, Herold M, Leroy M, Arino O (2009) The first 300 m global land cover map for 2005 using ENVISAT MERIS time series: a product of the GlobCover system. In: Proceedings of the 33rd international symposium on remote sensing of environment, Stresa (Italy), May 2009
- Demir B, Erturk S (2008) Empirical mode decomposition pre-process for higher accuracy hyperspectral image classification. In: Geoscience and remote sensing symposium, 2008. IGARSS 2008. IEEE International, 7–11 July 2008. pp II-939–II-941

- Deng F, Chen JM, Chen M, Pisek J (2006) Algorithm for global leaf area index retrieval using satellite imagery. *IEEE Trans Geosci Remote Sens* 44(8):2219–2229
- Eilers PHC (2003) A perfect smoother. *Anal Chem* 75(14):3631–3636
- Fang H, Liang S, Townshend JR, Dickinson RE (2008) Spatially and temporally continuous LAI data sets based on an integrated filtering method: examples from North America. *Remote Sens Environ* 112(1):75
- Filipova-Racheva D, Hall-Beyer M (2000) Smoothing of NDVI time series curves for monitoring of vegetation changes in time. In: Ecological monitoring and assessment network national science meeting 2000, Toronto, Ontario, Canada, January 17–22, 2000. Available online at: http://www.eman-rese.ca/eman/reports/meetings/national2000/toc_posters.html
- Ganguly S, Schull MA, Samanta A, Shabanov NV, Milesi C, Nemani RR, Knyazikhin Y, Myneni RB (2008) Generating vegetation leaf area index earth system data record from multiple sensors. Part 1: theory. *Remote Sens Environ* 112(12):4333
- Gao F, Morisette JT, Wolfe RE, Ederer G, Pedelty J, Masuoka E, Myneni R, Tan B, Nightingale J (2008) An algorithm to produce temporally and spatially continuous MODIS LAI time series. *IEEE Geosci Remote Sens Lett* 5:60–64
- Garrigues S, Lacaze R, Baret F, Morisette J, Weiss M, Nickeson J, Fernandes R, Plummer S, Shabanov NV, Myneni R, Yang W (2008) Validation and intercomparison of global leaf area index products derived from remote sensing data. *J Geophys Res* 113(G02028)
- GCOS (2010) GCOS-13.: Implementation plan for the global observing system for climate in support of the UNFCCC (2010 update). GCOS-138. WMO
- Goovaerts P (1997) Geostatistics for natural ressources evaluation, Applied geostatistics series. Oxford University Press, Oxford
- Hird JN, McDermid GJ (2009) Noise reduction of NDVI time series: an empirical comparison of selected techniques. *Remote Sens Environ* 113:248–258
- Holben BN (1986) Characteristics of maximum-value composite images from temporal AVHRR data. *Int J Remote Sens* 7:1417–1434
- Huang NE, Shen Z, Long SR, Wu MC, Shih HH, Zheng Q, Yen N-C, Tung CC, Liu HH (1998) The empirical mode decomposition and the Hilbert spectrum for nonlinear and non-stationary time series analysis. *Proc R Soc London Ser A Math Phys Eng Sci* 454(1971):903–995
- Jiang B, Liang S, Wang J, Xiao Z (2010) Modeling MODIS LAI time series using three statistical methods. *Remote Sens Environ* 114(7):1432–1444
- Jönsson P, Eklundh L (2002) Seasonality extraction by function fitting to timeseries of satellite sensor data. *IEEE Trans Geosci Remote Sens* 40(8):1824–1832
- Kandasamy S, Baret F, Verger A, Neveux P, Weiss M (2013) A comparison of methods for smoothing and gap filling time series of remote sensing observations: application to MODIS LAI products. *Biogeosciences* 10(6):4055–4071
- Knyazikhin Y, Martonchik JV, Myneni RB, Diner DJ, Running SW (1998) Synergistic algorithm for estimating vegetation canopy leaf area index and fraction of absorbed photosynthetically active radiation from MODIS and MISR data. *J Geophys Res* 103(D24):32257–32275
- Ma M, Veroustraete F (2006) Reconstructing pathfinder AVHRR land NDVI timeseries data for the Northwest of China. *Adv Space Res* 37:835–840
- Martínez B, Gilabert MA (2009) Vegetation dynamics from NDVI time series analysis using the wavelet transform. *Remote Sens Environ* 113(9):1823–1842
- Roerink GJ, Menenti M, Verhoef W (2000) Reconstructing cloud free NDVI composites using Fourier analysis of time series. *Int J Remote Sens* 21(9):1911–1917
- Savitzky A, Golay MJE (1964) Smoothing and differentiation of data by simplified least square procedures. *Anal Chem* 36(8):1627–1639
- Thoning KW, Tans PP, Komhyr WD (1989) Atmospheric carbon dioxide at Mauna Loa Observatory: 2. Analysis of the NOAA GMCC data, 1974–1985. *J Geophys Res Atmos* 94(D6):8549–8565
- Velleman P (1980) Definition and comparison of robust nonlinear data smoothing algorithms. *J Am Stat Assoc* 75:609–615
- Verger A, Baret F, Weiss M (2011) A multisensor fusion approach to improve LAI time series. *Remote Sens Environ* 115:2460–2470

- Verger A, Baret F, Weiss M, Lacaze R, Makhmara H, Vermote E (2012) Long term consistent global GEOV1 AVHRR biophysical products. In: Proceedings of 1st EARSeL workshop on temporal analysis of satellite images, 2012, pp 28–33
- Verger A, Baret F, Weiss M, Kandasamy S, Vermote E (2013) The CACAO method for smoothing, gap filling and characterizing seasonal anomalies in satellite time series. *IEEE Trans Geosci Remote Sens* 51(4):1963–1972
- Verger A, Baret F, Weiss M (2014) Near real time vegetation monitoring at global scale. *IEEE J Select Topics App Earth Observ Remote Sen* 7:3473–3481
- Verger A, Baret F, Weiss M, Filella I, Peñuelas J (2015) GEOCLIM: a global climatology of LAI, FAPAR, and FCover from VEGETATION observations for 1999–2010. *Remote Sensing of Environment* 166:126–137
- Verger A, Baret F, Weiss M (2016) GIO global land component – algorithm theoretical basis document – Leaf Area Index (LAI), Fraction of Absorbed Photosynthetically Active Radiation (FAPAR) and Fraction of green Vegetation Cover (FCover) Version 2.0 (GEOV2), Issue I1.31, p 78, CREAF, Barcelona
- Viovy N, Arino O, Belward A (1992) The Best INdex Slope Extraction (BISE): a method for reducing noise in NDVI timeseries. *Int J Remote Sens* 13(8):1585–1590
- Wang G, Garcia D, Liu Y, de Jeu R, Johannes Dolman A (2012) A three-dimensional gap filling method for large geophysical datasets: application to global satellite soil moisture observations. *Environ Modell Softw* 30(0):139–142
- Weiss M, Baret F, Garrigues S, Lacaze R, Bicheron P (2007) LAI, fPAR and fCover CYCLOPES global products derived from VEGETATION. Part 2: validation and comparison with MODIS collection 4 products. *Remote Sens Environ* 110:317–331
- Whittaker ET (1922) On a new method of graduation. *Proc Edinb Math Soc* 41(–1):63–75
- Zhang X, Friedl MA, Schaaf CB, Strahler AH, Hodges JCF, Gao F, Reed BC, Huete A (2003) Monitoring vegetation phenology using MODIS. *Remote Sens Environ* 84(3):471–475
- Zhu Z, Bi J, Pan Y, Ganguly S, Anav A, Xu L, Samanta A, Piao S, Nemani R, Myneni R (2013) Global data sets of vegetation Leaf Area Index (LAI)3 g and Fraction of Photosynthetically Active Radiation (FPAR)3 g derived from Global Inventory Modeling and Mapping Studies (GIMMS) Normalized Difference Vegetation Index (NDVI3g) for the period 1981 to 2011. *Remote Sens* 5(2):927–948

Chapter 12

Soil Moisture Dynamics Estimated from MODIS Time Series Images

Thomas Gumbrecht

Abstract The annual cyclic phenomena of soil surface wetness influences for instance vegetation growth, drought, flooding, and soil properties. This study presents an attempt to define metrics relevant for capturing the soil moisture dynamics from an annual series of wetness estimates derived from global Moderate-resolution imaging spectroradiometer (MODIS) images. Different algorithms for both smoothing and gap-filling the time series are tested with the results compared to in-situ data. Neither the smoothing nor the gap-filling improve the capturing of the surface wetness phenology compared to using unsmoothed time series data. The smoothing, however removes the effects of erratic rainfall events and noise, and the smoothed time series was considered more robust for identification of wetness phenology. Metrics capturing the global surface wetness phenology for 2011, extracted after smoothing using a simplified locally weighted scatterplot smoothing (LOWESS) model, are presented at a spatial resolution of 500 m for the calendar year 2011.

12.1 Introduction

Soil moisture content and its annual variation are of key interest for understanding e.g. vegetation production, rainfall to runoff response and flooding, drought and fire risk, and soil formation including the occurrence of wetlands. Hitherto, time-series of continental to global scale soil surface wetness have been restricted to coarse scale ($\sim 25\text{--}50$ km) estimates derived from passive microwave sensors and global hydrological models (Haddeland et al. 2011; Ochsner et al. 2013; Papa et al. 2013; Reichle et al. 2004; Wagner et al. 2003). The successful launch of the Soil Moisture Active Passive (SMAP, smap.jpl.nasa.gov) mission in January 2015 now produces refined estimates, even though one the radar instruments stopped operating in July 2015. But also the SMAP data is at a too coarse scale for satisfying the needs in many applications. Elsewhere (Gumbrecht 2015) I introduce an attempt to develop a quantitative estimation of soil wetness retrieved from optical image data,

T. Gumbrecht
Karttur AB, Stockholm, Sweden

the Transformed Wetness Index (TWI). TWI is a non-linear normalized difference (ND) index that uses biophysical feature vectors representing the soil line and wetness as input. TWI can in principle be derived from any multi-spectral image data source, but soil moisture content is better captured with Short-Wave Infra-Red (SWIR, 1100–2500 nm) compared to visible and near-infrared (VNIR, 400–1100 nm) wavelengths. Adopting Bidirectional Reflection Distribution Function (BRDF) corrected Moderate-resolution Image Spectroradiometer (MODIS) data for calculating TWI has several advantages for soil moisture mapping; the product includes three SWIR bands, the data are reflectance corrected and easily accessible for the whole earth, atmospheric attenuations including cloud contaminations are negligible, and the annual cycle of wetness can be captured from discrete images over an annual cycle, each representing a 16-day period. A disadvantage is that the exact date for each observation is not known, only the 16-day interval within which it falls is.

This study briefly describes TWI, and focuses on techniques for retrieving metrics for capturing the global annual soil moisture dynamics. While several studies validate the temporal performance of microwave derived soil-moisture estimates compared to in-situ probes measuring soil moisture (Draper et al. 2009; Jackson et al. 2010; Reichle et al. 2007), relatively few studies have explored the metrics of seasonal and annual variations in soil-moisture (Cheema et al. 2011). To remove noise and outliers, and fill in data-gaps, different smoothing algorithms are tested, and model results compared to in-situ probed wetness. The study presents phenological metrics depicting the global soil moisture dynamics for the calendar year 2011.

12.1.1 Phenological Characterization

Characterization of cyclic annual or seasonal natural phenomena (phenology) has been widely adopted for studying vegetation dynamics extracted from time-series of satellite images (Heumann et al. 2007; Jones et al. 2011; Tan et al. 2011). Phenological characterization includes both value based and temporal metrics. The most common value metrics include mean (MEAN), minimum (MIN), maximum (MAX), and seasonal integration (INT) (e.g. accumulated vegetation growth). The most widely used temporal metrics include time of start of (growing) season (SS), end of season (ES), length of season (LS) and timing of peak season (PS). Some vegetation phenological studies also explore the derivative of the vegetation cycle during green-up and brown-down to identify both timing and rate of change representing the periods of maximum growth and maximum senescence.

Most vegetation phenology studies use a per-pixel definition of seasons, either by analyzing derivates or by threshold(s). Seasonal separation is usually dynamic, derived from the statistical moments of an annual cycle, or by using multi-year

statistical moments. The latter requires that the data show some persistency, and the more advanced models used in e.g. the widely adopted TIMESAT software (Jönsson and Eklundh 2004) for instance require a minimum of 3 years of data. Studies capturing the phenology of for instance snow cover or ice formation (Kang et al. 2012), instead rely on absolute thresholds.

The soil moisture regimes in many landscapes vary more erratically and less predictable than vegetation growth and density (or snow/ice phenology). While vegetation growth is dependent on soil moisture, the biological processes driving vegetation growth and senescence moderate the variability and change rates of the vegetation density compared to soil moisture. Further, the surface wetness cycle can vary on short distances, dependent on e.g. topography, hydrology and, not least, human management. Hydrological recharge (“uphill”) and discharge (“downhill”) areas usually have different wetness conditions, with e.g. ridges next to floodplains able to show extreme differences both in moisture content and timing. These differences between the phenology of vegetation and surface wetness prompt different approaches for both time-series smoothing and definition of relevant metrics for characterization of phenology.

12.1.1.1 Smoothing

Reducing bias and smoothing noise is commonly regarded as a prerequisite when retrieving phenology from satellite derived time-series data (Atkinson et al. 2012; de Beurs and Henebry 2010; Hird and McDermid 2009; Jönsson and Eklundh 2004). Noise reduction and gap-filling techniques are either based on model fitting or smoothing algorithms. The best technique depends both on the satellite derived index, as well as the objective of the study and the phenology metrics explored. For indexes with a known bias (e.g. the Normalized Difference Vegetation Index, NDVI), methods adjusting the smoothing considering this bias perform better; Hird and McDermid (2009), for instance, found that asymmetric Gaussian (Jönsson and Eklundh 2004) and double logistic (Beck et al. 2006) model fitting outperformed smoothing algorithms when cleaning time series derived from NDVI. These models, however, performed less well in a comparative study using the (unbiased) Medium Resolution Imaging Spectrometer (MERIS) Terrestrial Chlorophyll Index (MTCI) (Atkinson et al. 2012).

More advanced models for smoothing vegetation indexes implicitly rely on rates and restrictions in biological processes, and are also criticized for being over-parameterized (de Beurs and Henebry 2010). Advanced models are further less suited for studies covering different ecological or climatic regions or landscapes, and most can not be adopted without a-priori assumptions on the annual seasonality. Also, other routine algorithms used for smoothing time-series, including Fourier-analysis and harmonics, can not be adopted for smoothing irregular and asymmetrical time-series with an unknown number of annual cycles.

Assuming that the TWI soil moisture estimates are unbiased, the smoothing should aim at identifying the local mean. The most widely approach for identifying the local mean is moving average. Seeking a more flexible approach, this study adopted a modified variant of the robust locally weighted scatterplot smoothing (LOWESS) (Cleveland 1979; Cleveland and Devlin 1988) for smoothing time-series of soil moisture. LOWESS is flexible both through allowing weighting, and the selection of polynomial functions for fitting local regressions to an arbitrary sized filter window. LOWESS can be applied without any a-priori assumptions on seasonality (smoothness) and at the same time adapts well to data variations. Outlier removal in LOWESS most commonly uses an iterative process and the statistical moments of the time-series itself to decide whether any single observation should be omitted or not. As discussed above, changes in soil surface moisture can be fast, but are not per se linked to the statistical moments of the time-series at large. An alternative LOWESS approach was thus developed in this study, using absolute thresholds for discarding outliers. For regular interval time-series data, the filter size in effect determines the length of the period influencing any observation, and in this study also the LOWESS filter size was set to absolute values.

12.1.1.2 Metrics

For vegetation, the local variations in production can be directly captured from a vegetation index and used for setting both dynamic and local thresholds for e.g. growing seasons. Relevant thresholds for soil wetness instead relate to biophysical characteristics, including e.g. wilting point, field capacity and water content at fully saturated soils. These thresholds vary both locally and with soil type (Brady and Weil 2007), and ideally soil wetness phenology should relate to local thresholds. There is, however at present no technique available for directly capturing these thresholds from remote sensing data. The TWI soil moisture estimates used in this study are given as volume water over total volume, and converted to percent. Assuming a soil pore volume of 50 %, a soil moisture estimate of 50 thus represent a fully water saturated soil.

In this study, the phenological extraction was done for four arbitrarily fixed soil moisture thresholds: Flooding Seasons (FS) (soil moisture >50 %), Soaking Season (SS) (soil moisture >37.5 %), Wet Season (WS) (soil moisture >25 %), and non-Dry Season (DS) (soil moisture >12.5 %). The thresholds are loosely set to represent: FS, fully water saturated soil conditions, SS: soil conditions favoring rapid rainfall to runoff conditions; WS: soil wetness at field capacity (threshold for drainage of soil water), and DS: representing soil moisture at the wilting point. The labeling should be regarded as one of convenience. Both the length of the season with soil moisture exceeding each threshold, as well as the annual integrated soil moisture above each of these thresholds are calculated as phenological metrics (Table 12.1). Additionally, the start and end dates of up to three seasons of each threshold are also calculated.

Table 12.1 Definition of metrics for capturing the annual soil surface moisture phenology

Abb.	Full label	Definition
Value metrics		
MEAN	Mean soil wetness	Mean annual soil wetness (%)
SD	Standard deviation of soil wetness	Variation in annual soil wetness (%)
MIN	Minimum soil wetness	Lowest recorded wetness (%)
MAX	Maximum soil wetness	Highest recorded wetness (%)
IFS	Integration of flood season wetness	Integration of soil moisture >50 %
ISS	Integration of soaking season wetness	Integration of soil moisture >37.5 %
IWS	Integration of wet season wetness	Integration of soil moisture >25 %
IDS	Integration of non-dry season wetness	Integration of soil moisture >12.5 %
Temporal metrics		
LFS	Length of flooding season	Length of season with soil moisture >50 %
LSS	Length of soaking season	Length of season with soil moisture >37.5 %
LWS	Length of wet season	Length of season with soil moisture >25 %
LDS	Length of non-dry season	Length of season with soil moisture >12.5 %
PWS	Peak wet season	Day of year with highest recorded wetness
PDS	Peak dry season	Day of year with lowest recorded wetness

12.2 Objective

The primary aim of the study was to create global maps of annual soil moisture dynamics at moderate spatial resolution, to be used as support for other mapping efforts, including mapping of tree cover, soil organic carbon and wetlands (Gumbricht 2015). The main objective was to define metrics for capturing the surface wetness phenology, and to identify a smoothing algorithm that both removes/reduces outliers and smoothes soil moisture time-series noise.

12.3 Data

This study was based on a global annual time-series of 16-day composited MODIS BRDF data (MCD43A4) for the calendar year 2011. To allow Inverse Distance Weighting (IDW) of data gaps, and smoothing at the beginning and end of the calendar year 2011, the two last MODIS tile-dates for 2010 and the two first for 2012 were also included. If data for IDW were lacking, the 2011 MODIS TWI time-series was filled by extrapolation (all data used for model development could be filled by IDW, but the production of the global maps required extrapolation over some densely clouded regions). For the equatorial tropics (MODIS vertical tiles 8 and 9) the complete time series for 2010, 2011 and 2012 were combined to fill in data gaps over heavily clouded regions.

Ground probed soil moisture data were taken from all networks and stations available from the International Soil Moisture Network (ISMN) (Dorigo et al. 2011; Ochsner et al. 2013). For each station only the top most recording (usually within 5 cm from the soil surface) was used. In total 745 stations were used in this study. 451 stations with data covering at least 6 months in 2011 were used for testing the time series smoothing and divided into two random sub-sets, for model calibration (281 stations) and model validation (170 stations). The land cover for each ISMN station was extracted from the MODIS land cover product (MCD12Q1 version 051) for 2011 using the International Geosphere-Biosphere Program (IGBP) classification scheme.

The performance validation of TWI compared to in-situ data was done solely using the 2011 MODIS data, and all ISMN stations with available data for 2011 (disregarding the number of observations coinciding with the MODIS imagery).

12.4 Definition of the Transformed Wetness Index (TWI)

At its core, TWI is a normalized difference (ND) index, but rather than using original satellite image bands as inputs, the ND algorithm in TWI uses data obtained after a linear transformation of the image bands. The transformation is achieved by a fixed orthogonal matrix optimized to separate wet and dry pixels. The first transformation component aligns from dark soil reflectance to light soil reflectance, representing the soil-line (Baret et al. 1993) brightness (Eq. 12.1). The second and third components represent photosynthetic and non-photosynthetic vegetation, while the fourth represents open water (Eq. 12.2). Omitting the vegetation components and using the soil line and wetness components in an ND approach has two distinct advantages; the vegetation influence is reduced, and the index can be adjusted for local soil conditions. The calculations of MODIS TWI used in here retain the reflectance value factors (reflectance * 10⁵) of the MODIS MCD43A4 product, and the soil line (*sl*) and wetness (*w*) components are calculated as:

$$\begin{aligned} sl = & 0.3148(RL - 563) + 0.3209(NIR - 1008) + 0.3595(BL - 147) \\ & + 0.3364(GL - 507) + 0.2498(SWIRa - 1531) \\ & + 0.6573(SWIRb - 1836) + 0.2471(SWIRc - 1699) \end{aligned} \quad (12.1)$$

$$\begin{aligned} w = & 0.1882(RL - 563) + 0.0384(NIR - 1008) + 0.4940(BL - 147) \\ & + 0.3501(GL - 507) - 0.3581(SWIRa - 1531) \\ & - 0.1731(SWIRb - 1836) - 0.6621(SWIRc - 1699) \end{aligned} \quad (12.2)$$

with band order given as in the MODIS reflectance products (RL = red, NIR = near infrared, BL = blue, GL = green, SWIR = short wave IR).

The TWI ND algorithm is defined by a reference line of iso-wetness and applied using a trigonometric, scale preserving, rotation combined with a re-scaling factor (R) and a calibration factor (C) allowing for non-linear reflectance mixing between soil and water:

$$TWI = R * \frac{\sin(\beta + 45)(sl + w + a) + \cos(\beta + 45)(-sl + w + a)}{\sin(\beta + 45)(sl - w - a) + \cos(\beta + 45)(sl + w + a) + C} \quad (12.3)$$

where a is the reference iso-wetness line intercept with the soil-line and β the reference iso-wetness line slope. The global values for the reference iso-wetness line and the calibration factor were determined from reference sites sampled by the author in Botswana, Uganda, Kenya and Indonesia: a (2080), β (-57°) and C (7000). Setting the re-scaling factor R to 5942 scales the TWI range to approximately -4300 for dry soil, 2000 for water saturated dark soil and 3500 for deep open water. MODIS TWI is converted to actual soil moisture, Θ_{TWI} (volume/volume) by a linear-power function:

$$\Theta_{TWI} = (TWI + 4300)/430 + 1.067^{(TWI+4300)*0.0086} \quad (12.4)$$

TWI performance was evaluated directly comparing Θ_{TWI} to in-situ data and after assimilation of Θ_{TWI} to fit the statistical moments (mean and variance) of each local in-situ time-series (Reichle et al. 2004, 2007). The assimilation was done against the in-situ data representing the same 16-day period as each Θ_{TWI} estimate. Each 24 h cycle of in-situ data, adjusted for the local noon where first calculated separately, and then averaged. The smoothing algorithms and parameterizations were evaluated by aggregating all local results, and comparing model results to in-situ data by the coefficient of determination (r^2), the Random Mean Square Error (RMSE), and model efficiency (E) (Nash and Sutcliffe 1970):

$$E = 1 - \frac{\sum (\Theta_o - \Theta_m)^2}{\sum (\Theta_o - \bar{\Theta}_o)^2} \quad (12.5)$$

where $\bar{\Theta}_o$ is the mean of observed soil moisture, and Θ_m is modeled and Θ_o observed soil moisture for matching data pairs.

12.5 Estimating Soil Moisture Dynamics from TWI

To retrieve metrics of the global annual soil moisture dynamics, the TWI estimates (Θ_{TWI}) derived for each 16-day cycle in 2011 were used. Soil moisture metrics for the annual phenology were extracted from the original TWI time-series, and after applying different smoothing procedures. Adopted smoothing models include a weighted moving average (WMA) model, and a modified LOWESS model assigning lower weights to gap-filled data points. In the latter, the weighting (w_i) combines the standard LOWESS tri-cube weight function with lower weights for gap-filled points:

$$w_i = \left(1 - \left| \frac{x - x_i}{d(x)} \right|^3 \right)^3 * wf_i \quad (12.6)$$

where x is the point to be estimated, wf_i is the weight assigned for each data value i falling within the filter span of x , and $d(x)$ the maximum distance (i.e. number of days) between x and the predictors x_i . The weights for gap-filled points (wf) were varied between 0.25 and unity (step = 0.25), whereas original points were assigned a wf of unity. The maximum filter span ($d(x)$) was set to predefined values of 24 days (3 data points), 40 days (5 data points), and 56 days (7 data points). The LOWESS local polynomial fitting was done using linear regression (first degree polynomial). The weighting for the WMA used wf directly, and the same filter spans.

Different approaches were validated for (1) general smoothing, (2) reducing or removing outliers, and (3) gap-filling. The influence of outliers was tested by an iterative approach, identifying outliers after an initial smoothing by comparing the original and smoothed time-series and assigning points varying more than between 1 to 10 % units of soil moisture (step = 1 % unit) as outliers. The smoothing algorithm was then iterated but with the outlier values altered (set either to the smoothed value, or replaced by IDW gap-filling) or removed. Gap-filling was tested by first filling all data time-series using IDW and then applying the smoothing algorithm. In the combined tests of outlier smoothing and gap-filling, the IDW for gap-filling was iterated after the outlier replacement to reflect the initially smoothed outliers. Trials were made using varying weights also for outliers, and by using separate weights for outliers and gap-filled points. None of these more complex models, however improved model performances, and hence they are not presented. Tested smoothing approaches and models are summarized in Table 12.2.

All smoothing models operate on the original Θ_{TWI} time-series, and assimilation to fit in-situ data (see Sect. 12.4) was done as a post-processing step. The results of the smoothing models were then evaluated compared to the original Θ_{TWI} estimate, with all Θ_{TWI} time-series assimilated to the in-situ data. The effects of smoothing outliers and gap-filling was also separately examined using r^2 and RMSE compared to coinciding observations in the in-situ data.

Table 12.2 Summary of smoothing algorithms tested for extracting annual phenology from soil moisture time-series data

Model code	Gap-filling	Outliers	Smoothing algorithm	Smoothed data
GF	IDW	No action	None (original model)	None
GF_{WMA}	IDW	WMA smoothed	WMA	All
GF_{LOWESS}	IDW	LOWESS smoothed	LOWESS	All
GFO_{LOWESS}	IDW	LOWESS smoothed	LOWESS	Outliers only
$GFRO_{LOWESS}$	IDW	Replaced by IDW	LOWESS	All
T	None	No action	None (original model)	None
T_{LOWESS}	None	LOWESS smoothed	LOWESS	All
TO_{LOWESS}	None	LOWESS smoothed	LOWESS	Outliers only

For in-situ sites with data covering at least 10 months, the phenological performance was evaluated modified after Hird and McDermid (2009). Phenology was calculated for both assimilated Θ_{TWI} and in-situ data representing; value metrics: MIN, MAX and INT (integration of soil moisture during wet season); and temporal metrics: LS, PWS and PDS. To allow all local time-series to be evaluated in the model development, the threshold between wet and dry seasons was set to the mean wetness of each local time-series (with Θ_{TWI} assimilated to fit the in-situ data, the mean is always the same for both time-series). The score for each phenological metric (PS_m) was calculated as:

$$PS_m = 1 - \frac{|P_m^M - P_i^M|}{P_{max}} \quad (12.7)$$

where P^M is the derived phenological metric of the in-situ (i) and modeled (m) time-series of soil moisture, and P_{max} is the maximum range for each metric, simply pre-defined to a soil moisture value of 50 %, and a maximum temporal value of 365 days. To convert INT to a maximum range of 50, INT was divided by LWS. Phenological metrics for in-situ data was calculated using the full in-situ time series. The phenological performance was evaluated for each local (pixel-wise) time-series individually, and using the overall mean of all local performances for model evaluation.

Model performances were evaluated using all the criteria presented above, but primarily ranked from the smoothing model abilities to capture the soil-moisture phenology compared to the in-situ data. Model performances for the best phenological parameter settings for each smoothing model were tested against the validation data set using the same smoothing and rescaling approach as in the calibration. Exploring the results of the smoothing algorithms, the global phenology for 2011 was calculated using a LOWESS smoothing without any gap-filling (and thus no weighting) or outlier adjustment, and a filter size of 5 data points (or less if gaps occur within the filter) with a maximum distance span ($d(x)$) set to 35 days.

Figure 12.1 illustrates some of the smoothing algorithms and the effects of varying filter sizes and how the adjustment of outliers affect the smoothing results. The figure also shows the simplified LOWESS weighing algorithms selected for generating the global surface wetness phenology for 2011.

12.6 Results and Discussions

12.6.1 Transformed Wetness Index

Compared to 745 in-situ ground sites Θ_{TWI} has a bias of 2.5 % and a global RMSE of 14.0 %, which reduces to 8.5 % when assimilating the mean and variance to fit local in-situ data. The assimilated RMSE for cosmic-ray soil moisture probes (Zreda

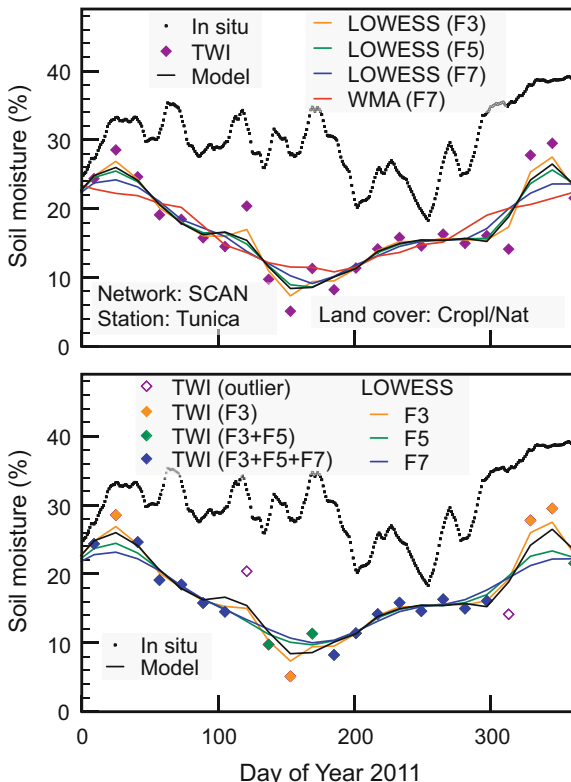


Fig. 12.1 Illustration of the effects of different smoothing parameterizations. The *upper panel* shows the results for LOWESS smoothing with filter sizes (F) of 3, 5 and 7 elements, and the results from a WMA smoothing using 7 elements. The *lower panel* shows how the smoothing is affected by identified outliers, using LOWES smoothing with filter sizes of 3, 5 and 7 elements. The identified outliers are replaced by the initial smoothing value, and the smoothing algorithm applied in a second iteration which generated the finally smoothed time-series. Both panels also show the simplified LOWESS model selected for calculating the global phenology for 2011 (see text). The example represent a real time-series without any data gaps (see Fig. 12.2)

et al. 2008), with a foot-print comparable to the resolution of MODIS images, is 5.3 % (with a bias of 3.7 %). The assimilated model efficiency for the cosmic-ray probes is 0.79, compared to an overall global model efficiency of 0.42.

Θ_{TWI} overestimates surface wetness for regions with dark surfaces, including basaltic outcrops and vertisols. Dense stands of e.g. reeds and papyrus leads to underestimations of soil moisture content over wetlands, whereas the soil moisture is overestimated in dense and moist forests (in particular over evergreen needleleaf forests). The model performance for non forested areas is hence better, with an estimated bias of -0.4% and a global RMSE of 11.6 % (574 stations), reduced to 8.0 % for assimilated time-series. Θ_{TWI} in general underestimates the variations in soil moisture, which is probably related both to the inability of optical sensors to

capture surface conditions under clouds (i.e. during precipitation events and rainy seasons), and to differences in soil moisture variations at point scale compared to the 500 m foot-print of the MODIS images.

12.6.2 Phenological Characterization

The differences in overall smoothing model performance, whether using statistical measures or scores relating to phenological metrics, are small (Tables 12.3 and 12.4). No particular model can be identified as performing better than the others. Indeed, the unsmoothed time-series performs equally well, or better, compared to the smoothing algorithms. Further, the results of the calibration tests for each individual model only show minimal variances in performance between different parameter settings (not explicitly shown, but indicated from the results in Table 12.3). The parameters presented in Table 12.3 represent the parameterizations that best captures the phenological performances compared to in-situ data. Using other criteria (e.g. model RMSE, model efficiency E , or outlier RMSE) for selecting the optimal model lead to different parameterizations.

The largest variations between different models relate to the smoothing of outliers. Models smoothing the complete time-series (GF_{WMA} , GF_{LOWESS} and T_{LOWESS}) all indicate that a thresholds of 6 % soil moisture is optimal for identifying outliers (i.e. peaks and troughs in soil moisture larger than 6 % units over a period of approximately one to two months are likely to be erroneous). But only very few such peaks and troughs are identified (Tables 12.3 and 12.4), and the RMSE of the identified outliers themselves increase in the smoothing except for in the T_{LOWESS} model. Applying smoothing to only outliers (models GFO_{LOWESS} and TO_{LOWESS}), instead identifies a very large number of outliers as optimal. Non-outliers are not smoothed in these models, and the outlier smoothing hence replaces the general smoothing, reducing both the overall RMSE and the RMSE of the outliers themselves. The model replacing the outliers with IDW filled value ($GFRO_{LOWESS}$) is the worst performing. These results indicate that in general the Θ -TWI time-series data have no problems related to outliers. Visual inspection of the data (Fig. 12.2), reveals that most peaks and troughs are no artifacts, but discernible also in the in-situ data. MODIS TWI rather tends to miss peaks with short duration. For any 16-day interval the MODIS data always represent cloud free conditions, more likely to represent drier ground conditions compared to cloudy conditions.

The RMSE and r^2 of the gap-filled data points show a low fit to the in-situ data (Table 12.3), and gap-filled models do not perform better compared to those with no gap-filling. With rainfall events linked to cloud cover, it is more likely that peaks in surface wetness are missed by the MODIS optical sensors, indicated in Fig. 12.2. As the gap-filling interpolates adjacent observations, gaps due to cloudy conditions with associated precipitation can not be properly estimated. The LOWESS models used in this study utilize the trends adjacent to gaps for the gap-filling, but the LOWESS filling of gaps only performs slightly better than the filling by IDW.

Table 12.3 Smoothing model calibration results, showing the performances of different smoothing algorithms compared to in-situ data. The overall results compare the fully smoothed and then assimilated time-series with the in-situ data, with performance reported as the random mean square error (RMSE), coefficient of determination (r^2), model efficiency (E), and the mean score for phenological metrics agreement ($\overline{PS_m}$). Results for the gap-filling are reported as the RMSE and r^2 compared to in-situ data coinciding with the gap-filled data points. Outlier smoothing results are reported in the same manner as for gap-filling, but also comparing the unsmoothed RMSE and r^2 for the smoothed outliers. For both gap-filling and outlier smoothing the number of validated points (and in the parenthesis, the total number of affected points) are given (n). The model results shown represent the best performing parameterization for $\overline{PS_m}$ for each model. For the parameter settings; F = filter size, T = threshold for identifying outliers (%) and wf = weight for gap filled data points

Model	Overall results			Gap-filling			Outlier smoothing			Parameters			
	RMSE	r^2	E	$\overline{PS_m}$	RMSE	r^2	n	RMSE	r^2	n	F	T	wf
<i>GF</i>	7.84	0.53	0.46	0.85	8.34	0.29	320(1429)	—	—	—	—	—	—
<i>GF_{WMA}</i>	7.89	0.53	0.45	0.86	8.56	0.26	320(1429)	6.64	0.71	6.26	0.74	21(99)	3 6 0.25
<i>GF_{LOWESS}</i>	7.89	0.53	0.45	0.86	8.47	0.27	320(1429)	5.87	0.80	6.92	0.72	15(63)	5 6 0.25
<i>GFO_{LOWESS}</i>	7.87	0.53	0.45	0.86	8.41	0.28	320(1429)	8.14	0.46	8.01	0.47	1093(3299)	5 1 0.75
<i>GFRO_{LOWESS}</i>	7.90	0.52	0.45	0.86	8.75	0.22	320(1429)	8.28	0.44	8.78	0.36	616(1837)	3 1 0.75
<i>T</i>	7.82	0.53	0.46	0.85	—	—	—	—	—	—	—	—	—
<i>T_{LOWESS}</i>	7.88	0.53	0.45	0.86	—	—	—	5.93	0.77	3.23	0.93	13(60)	5 6 —
<i>TO_{LOWESS}</i>	7.85	0.53	0.46	0.86	—	—	—	8.06	0.48	7.91	0.50	1029(3069)	5 1 —

Table 12.4 Smoothing model validation results. See Table 12.3 for explanations

Model	Overall results				Gap-filling				Outlier smoothing				Parameters		
	RMSE	r^2	E	\overline{PS}_m	RMSE	r^2	n	RMSE	r^2	RMSE	r^2	n	F	T	wf
<i>GF</i>	7.90	0.49	0.40	0.85	8.56	0.28	256(1260)	—	—	—	—	—	—	—	—
<i>GF_{WMA}</i>	8.00	0.48	0.38	0.85	8.75	0.25	256(1260)	7.49	0.42	7.07	0.49	44(144)	3	6	0.25
<i>GF_{LOWESS}</i>	8.00	0.48	0.40	0.85	8.75	0.25	256(1260)	7.80	0.36	7.57	0.40	30(96)	5	6	0.25
<i>GFO_{LOWESS}</i>	7.98	0.48	0.38	0.85	8.68	0.26	256(1260)	7.98	0.48	7.83	0.50	942(3015)	5	1	0.75
<i>GFR_{LOWESS}</i>	8.06	0.47	0.37	0.85	8.71	0.26	256(1260)	8.12	0.47	7.62	0.47	499(1704)	3	1	0.75
<i>T</i>	7.90	0.49	0.40	0.85	—	—	—	—	—	—	—	—	—	—	—
<i>T_{LOWESS}</i>	8.0	0.48	0.38	0.85	—	—	—	7.80	0.36	7.50	0.41	30(94)	5	6	—
<i>TO_{LOWESS}</i>	7.96	0.48	0.39	0.85	—	—	—	7.93	0.49	7.74	0.52	895(2817)	5	1	—

Table 12.5 Production model results (including both the calibration and validation data sets), reported for both the original (not rescaled) MODIS TWI model (with wet season set to the average wetness of the in-situ data for each local site) and with each MODIS TWI local time-series assimilated to fit the mean and standard deviation of the in-situ data. Results are reported for the global dataset, and separately for cosmic-ray probes, and for forests and non-forest (as identified from the MODIS land cover product MCD12Q1.v005). See Table 12.3 for explanations. Phenological scores (Eq. 12.7) for applicable metrics are separately reported

Regionalization	Overall results				Phenological scores (\bar{PS}_m)						
	RMSE	r^2	E	\bar{PS}_m	MIN	PDS	MAX	PWS	LWS	IWS	MEAN
Orginal time-series											
Global	11.1	0.02	-0.50	0.74	0.80	0.74	0.80	0.61	0.57	0.86	0.84
Cosmic-ray probes	11.3	0.06	-0.51	0.79	0.84	0.85	0.86	0.69	0.51	0.90	0.82
Non-forested sites	10.9	0.06	-0.07	0.75	0.84	0.75	0.81	0.63	0.56	0.87	0.86
Forested sites	11.3	0.0	-2.1	0.69	0.65	0.70	0.71	0.56	0.61	0.81	0.75
Assimilated time-series											
Global	7.9	0.51	0.42	0.85	0.94	0.74	0.93	0.61	0.88	0.92	-
Cosmic-ray probes	5.0	0.82	0.80	0.89	0.96	0.85	0.95	0.69	0.89	0.95	-
Non-forested sites	7.4	0.56	0.50	0.86	0.94	0.75	0.94	0.63	0.89	0.92	-
Forested sites	9.4	0.32	0.13	0.82	0.93	0.70	0.91	0.56	0.84	0.91	-

Accepting that neither outlier reduction nor gap-filling improve the phenological extraction, but that smoothing in general removes small temporal variations (noise), a simpler LOWESS model was used for calculating global wetness phenology. The selected model smoothing filter size was set to five elements, with a maximum date span of 35 days. The advantage of five elements is primarily that, compared to a filter with only three elements, it bridges single data gaps. Reducing the maximum date span from 40 to 35 days, however reduces the weight of the more distant dates. With the identification of outliers omitted and no gap-filling (i.e. no weighting), the LOWESS weighting algorithm (Eq. 12.6) can be replaced by a simple weighting vector (w) applied to each element of the original time-series:

$$w = [0.08 \ 0.74 \ 1.0 \ 0.74 \ 0.08] \quad (12.8)$$

The results using w for weighting, and a first degree polynomial for estimating the smoothed values are summarized in Table 12.5. In general the smoothing reduces the variance, but otherwise does not affect model performance. The global phenology value metrics (% soil moisture) for mean (MEAN) and standard deviation (SD) are shown in Fig. 12.3, with additional global maps shown as Figs. 12.5 and 12.6 in the Appendix.

The smoothing algorithm adopted for calculating wetness phenology reduces the variance compared to the original time-series data. The Θ_{TWI} original model underestimates the variance compared to point scale in-situ data, and this underestimation is further accentuated by the smoothing. Comparing the smoothing results

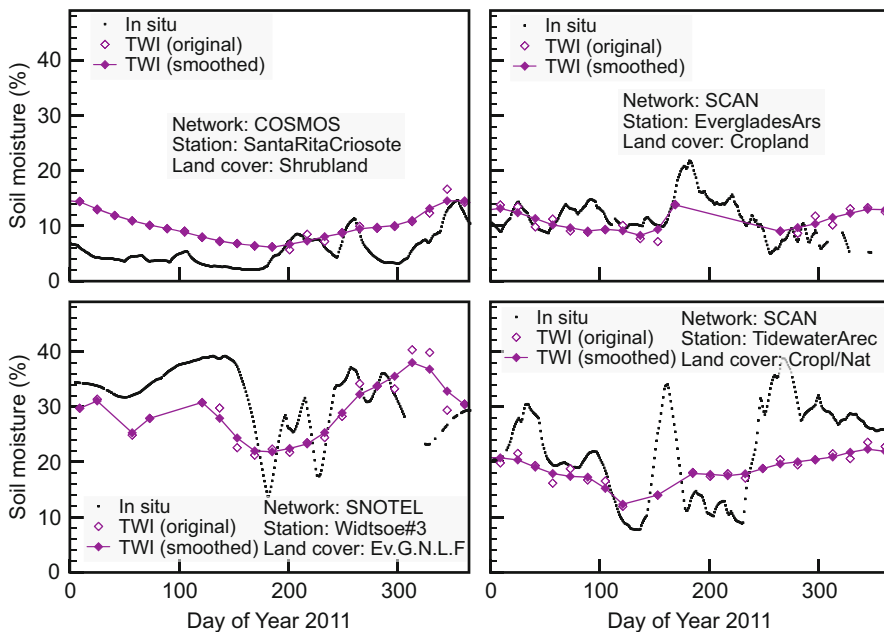


Fig. 12.2 Comparison of soil moisture observations from in-situ station data and soil moisture estimated by the MODIS Transformed Wetness Index (TWI) (expressed as volumetric soil moisture – Θ_{TWI}). Each panel shows the MODIS TWI original (not rescaled) time-series, and the same time-series smoothed using the simplified LOWESS weighting algorithm selected for calculating the global phenology for 2011 (see text). The four panels represent different networks and land cover (from the MODIS land cover product MCD12Q1.v051) as indicated in each graph (Ev.G.N.L.F. = evergreen needleleaf forest; Cropl/Nat = cropland/natural vegetation mosaic). Details about each station are available in the ISMN dataset

with cosmic-ray probes (measuring soil moisture at a spatial scale equalling that of the MODIS pixel size) the variances of the Θ_{TWI} time-series are adjusted to closer matching the variances captured by the cosmic-ray probes. Arguably, the results for the cosmic-ray probes more correctly represent the ability of Θ_{TWI} to capture the spatially integrated soil moisture regime.

For non-forested sites the Θ_{TWI} estimated soil moisture bias is negligible (-0.4%) and does only marginally affect extraction of the wetness phenology. The phenology is also better captured for non-forested sites compared to forested sites (Table 12.5). Large positive bias over primarily evergreen needleleaf forests (16.2%), but also other forests (10%), cause over-estimation of both temporal metrics and value metrics when retrieving soil moisture. The Okavango Swamps in Botswana (Fig. 12.4 and Appendix Fig. 12.7) are less affected. The maps over the Okavango Swamps clearly capture both the wetter sites, but also separates the more permanent (central swamps) from the distal floodplains.

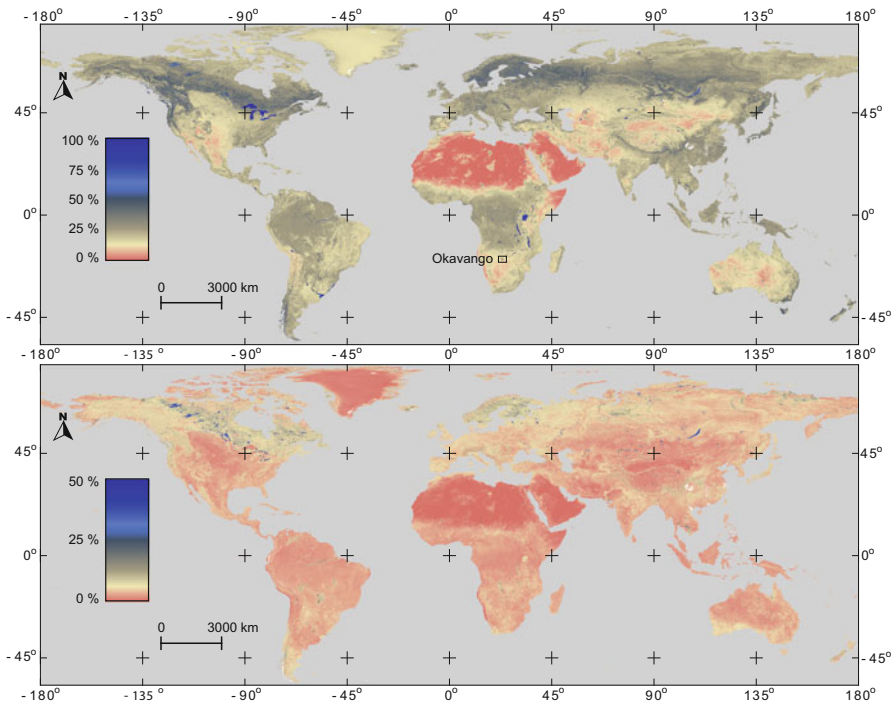


Fig. 12.3 Mean (MEAN) (top panel) and standard deviation (SD) (bottom panel) soil surface wetness (%) metrics for 2011 estimated from the Moderate-resolution imaging spectroradiometer (MODIS) Transformed Wetness Index (TWI). The wetness phenology metrics is calculated after applying a locally weighted scatterplot smoothing (LOWESS) to the original MODIS TWI time-series (expressed as volumetric soil moisture – Θ_{TWI}). For the tropical region (between 20 degrees latitudes) the map represents the average conditions for 2010, 2011 and 2012, whereas for other regions it represents the calendar year 2011. Note that the scaling is different for MEAN and SD. White areas have too few recordings for extracting phenological metrics

12.7 Conclusions

This study has attempted to define metrics and identify smoothing algorithms for capturing the annual soil moisture phenology from Θ_{TWI} , a soil wetness index derived from MODIS data. While most approaches for retrieving time-series of e.g. vegetation, snow or ice cover are based on the assumption that proximity in time or space is the key for cleaning and smoothing, this assumption is challenged when mapping variable properties with unknown or unpredictable scales of spatial and temporal variation.

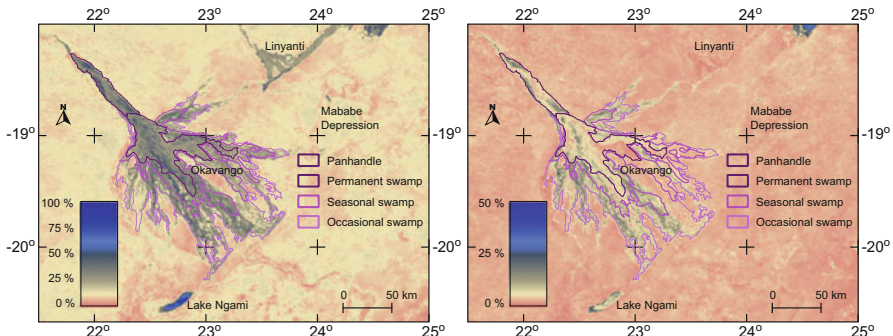


Fig. 12.4 Mean (MEAN) (left panel) and standard deviation (SD) (right panel) phenological soil moisture metrics for the Okavango Swamps, Botswana for 2011 (see Fig. 12.3). The wetland mask is modified after McCarthy et al. (2003) and divided into four regions: (1) the Panhandle tectonically bound entry channel, (2) the central permanent wetlands, (3) the seasonally inundated wetlands, and (4) the most distal areas only temporally flooded. Okavango is situated on a tectonically active region and the swamp naturally oscillates across the underlying alluvial fan. Compared to the estimated area of wetlands between 1972 and 2000, the maps indicate that the north-eastern parts of the swamps are drying out and the south-western parts receive more water. Further, the maps reveal that Lake Ngami was filled during 2011, whereas it contained no or little water from 1972 to 2000

Metrics for the global surface wetness phenology have been developed at a spatial scale of 500 m. A large bias and high RMSE for ecosystems dominated by dense forests causes overestimated wetness conditions in particular for higher latitude evergreen needleleaf forests. The phenology metrics for non forested landscapes, and large (non forested) wetlands are better captured. Phenology is better captured when compared to in-situ data captured by cosmic-ray probes, integrating the soil moisture over a spatial scale closely matching the MODIS image resolution.

The LOWESS smoothing algorithm used in this study is a compromise, but does have several advantages. It is flexible by allowing selection of both filter size (i.e. defining the temporal range that influences the soil wetness conditions at any particular date), and customized weighting (and also by selecting different fitting functions, but this was not tested in this study). But primarily LOWESS can handle irregular time-series data, and thus removes the need for pre-defining e.g. rates of changes and seasonality commonly required by more advanced smoothing algorithms and model fitting routines. As the MODIS product used in this study is delivered with regular interval time-steps (16 days), the LOWESS weighing function could be replaced by a fixed vector, also decreasing the computational processing time manyfold.

Acknowledgements This work was supported by USAID (Grant No. EEM-G-00-04-00010-00) as part of the CGIAR research programme on Forests, Trees and Agroforestry.

Appendix

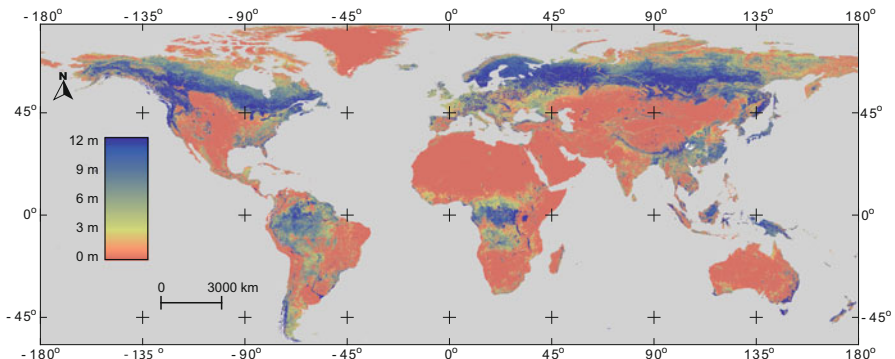


Fig. 12.5 Lengths of wet season (LWS) (months (m) with soil wetness >25 % in 2011). The overestimation of soil moisture content under forests, in particular evergreen needleleaf forests causes a large positive bias in temperate forests

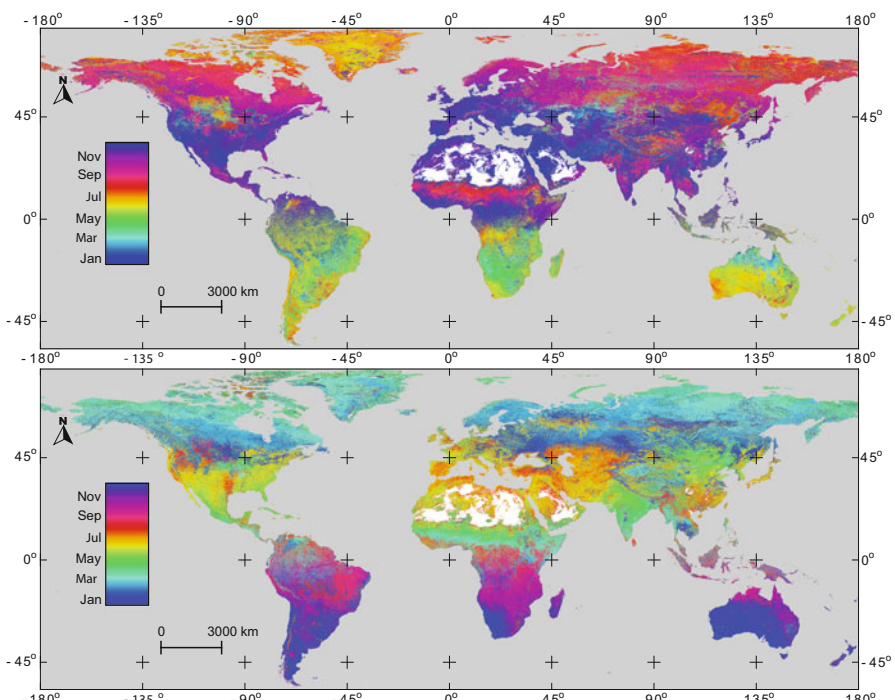


Fig. 12.6 Day of year with highest (PWS – top panel) and lowest (PDS – bottom panel) recorded wetness 2011. The map clearly shows the spatially mirrored wetness phenology across the equator. Large parts of the Sahara Desert have no discernible seasonality, and no dates for peak wet and dry seasons can be retrieved

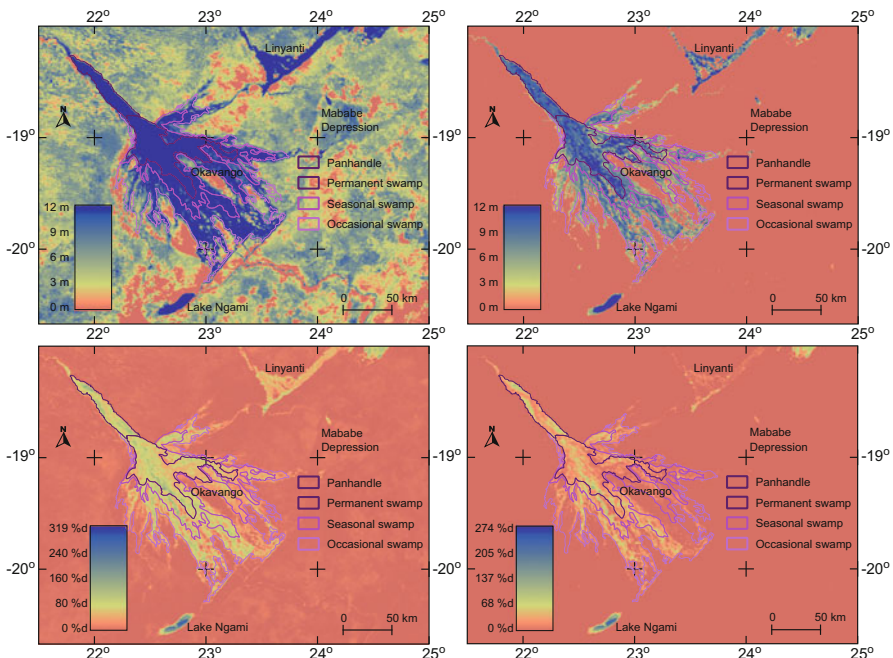


Fig. 12.7 Illustration of soil moisture phenological metrics for the Okavango Swamps in Botswana. The *upper panels* show the Lengths of non-dry season (LDS) and Wet season (LWS), while the *lower panels* show the integrated non-dry season (IDS) and integrated wet season (IWS). All panels represent the calendar year 2011. The location of the Okavango swamps is indicated in Fig. 12.3

References

- Atkinson PM, Jeganathan C, Dash J, Atzberger C (2012) Inter-comparison of four models for smoothing satellite sensor time-series data to estimate vegetation phenology. *Remote Sens Environ* 123:400–417. doi:[10.1016/j.rse.2012.04.001](https://doi.org/10.1016/j.rse.2012.04.001)
- Baret F, Jacquemoud S, Hanocq JF (1993) The soil line concept in remote sensing. *Remote Sens Rev* 7(1):65–82. doi:[10.1080/02757259309532166](https://doi.org/10.1080/02757259309532166)
- Beck PSA, Atzberger C, Hogda KA, Johansen B, Skidmore AK (2006) Improved monitoring of vegetation dynamics at very high latitudes: a new method using MODIS NDVI. *Remote Sens Environ* 10:321–334
- Brady NC, Weil RR (2007) The nature and properties of soils, 14th edn. Prentice Hall, Upper Saddle River
- Cheema M, Bastiaanssen W, Rutten M (2011) Validation of surface soil moisture from AMSR-E using auxiliary spatial data in the transboundary Indus Basin. *J Hydrol* 405(1–2):137–149. doi:[10.1016/j.jhydrol.2011.05.016](https://doi.org/10.1016/j.jhydrol.2011.05.016)
- Cleveland WS (1979) Robust locally weighted regression and smoothing scatterplots. *J Am Stat Assoc* 74:829–826
- Cleveland WS, Devlin SJ (1988) Locally weighted regression: an approach to regression analysis by local fitting. *J Am Stat Assoc* 83(403):596–610

- de Beurs KM, Henebry GM (2010) Spatio-temporal statistical methods for modeling land surface phenology, chap 9. In: Hudson IL, Keatley MR (eds) *Phenological research*. Springer Netherlands, Dordrecht, pp 177–208. doi:[10.1007/978-90-481-3335-2](https://doi.org/10.1007/978-90-481-3335-2)
- Dorigo WA, Wagner W, Hohensinn R, Hahn S, Paulik C, Xaver A, Gruber A, Drusch M, Mecklenburg S, van Oevelen P, Robock A, Jackson T (2011) The international soil moisture network: a data hosting facility for global in situ soil moisture measurements. *Hydrol Earth Syst Sci* 15(5):1675–1698. doi:[10.5194/hess-15-1675-2011](https://doi.org/10.5194/hess-15-1675-2011)
- Draper CS, Walker JP, Steinle PJ, de Jeu RAM, Holmes TRH (2009) An evaluation of AMSR-E derived soil moisture over Australia. *Remote Sens Environ* 113(4):703–710. doi:[10.1016/j.rse.2008.11.011](https://doi.org/10.1016/j.rse.2008.11.011)
- Gumbrecht T (2015) Hybrid mapping of pantropical wetlands from optical satellite images, hydrology, and geomorphology, chap 20. In: Tiner R, Lang MW, Klemas VV (eds) *Wetland classification and mapping*. CRC Press/Taylor and Francis, pp 435–455. doi:[10.1201/b18210-24](https://doi.org/10.1201/b18210-24)
- Haddeland I, Clark DB, Franssen W, Ludwig F, VoßF, Arnell NW, Bertrand N, Best M, Folwell S, Gerten D, Gomes S, Gosling SN, Hagemann S, Hanasaki N, Harding R, Heinke J, Kabat P, Koitala S, Oki T, Polcher J, Stacke T, Viterbo P, Weedon GP, Yeh P (2011) Multimodel estimate of the global terrestrial water balance: setup and first results. *J Hydrometeorol* 12(5):869–884. doi:[10.1175/2011JHM1324.1](https://doi.org/10.1175/2011JHM1324.1)
- Heumann B, Seaquist J, Eklundh L, Jönsson P (2007) AVHRR derived phenological change in the Sahel and Soudan, Africa 1982–2005. *Remote Sens Environ* 108(4):385–392. doi:[10.1016/j.rse.2006.11.025](https://doi.org/10.1016/j.rse.2006.11.025)
- Hird JN, McDermid GJ (2009) Noise reduction of NDVI time series: an empirical comparison of selected techniques. *Remote Sens Environ* 113(1):248–258. doi:[10.1016/j.rse.2008.09.003](https://doi.org/10.1016/j.rse.2008.09.003)
- Jackson TJ, Cosh MH, Bindlish R, Starks PJ, Bosch DD, Seyfried M, Goodrich DC, Moran MS, Du J (2010) Validation of advanced microwave scanning radiometer soil moisture products. *IEEE Trans Geosci Remote Sens* 48(12):4256–4272. doi:[10.1109/TGRS.2010.2051035](https://doi.org/10.1109/TGRS.2010.2051035)
- Jones MO, Jones LA, Kimball JS, McDonald KC (2011) Satellite passive microwave remote sensing for monitoring global land surface phenology. *Remote Sens Environ* 115(4):1102–1114. doi:[10.1016/j.rse.2010.12.015](https://doi.org/10.1016/j.rse.2010.12.015)
- Jönsson P, Eklundh L (2004) TIMESAT – a program for analyzing timeseries of satellite sensor data. *Comput Geosci* 30:833–845
- Kang K, Duguay CR, Howell SEL (2012) Estimating ice phenology on large northern lakes from AMSR-E: algorithm development and application to Great Bear Lake and Great Slave Lake, Canada. *The Cryosphere* 6:235–254. doi:[10.5194/tc-6-235-2012](https://doi.org/10.5194/tc-6-235-2012)
- McCarthy JM, Gumbrecht T, McCarthy T, Frost P, Wessels K, Seidel F (2003) Flooding patterns of the Okavango Wetland in Botswana between 1972 and 2000. *AMBIO* 32(7):453–457. doi:[10.1579/0044-7447-32.7.453](https://doi.org/10.1579/0044-7447-32.7.453)
- Nash JE, Sutcliffe JV (1970) River flow forecasting through conceptual models part I – a discussion of principles. *J Hydrol* 10(3):282–290. doi:[http://dx.doi.org/10.1016/0022-1694\(70\)90255-6](http://dx.doi.org/10.1016/0022-1694(70)90255-6)
- Ochsner TE, Cosh MH, Cuenca RH, Dorigo WA, Draper CS, Hagimoto Y, Kerr YH, Njoku EG, Small EE, Zreda M (2013) State of the art in large-scale soil moisture monitoring. *Soil Sci Soc Am J* 77(6):1888. doi:[10.2136/sssaj2013.03.0093](https://doi.org/10.2136/sssaj2013.03.0093)
- Papa F, Prigent C, Aires F, Jimenez C, Rossow WB, Matthews E (2010) Interannual variability of surface water extent at the global scale, 1993–2004. *J Geophys Res* 115(D12):D12111. doi:[10.1029/2009JD012674](https://doi.org/10.1029/2009JD012674)
- Reichle RH, Koster RD, Dong J, Berg AA (2004) Global soil moisture from satellite observations, land surface models, and ground data: implications for data assimilation. *J Hydrometeorol* 5(3):430–442
- Reichle RH, Koster RD, Liu P, Mahanama SPP, Njoku EG, Owe M (2007) Comparison and assimilation of global soil moisture retrievals from the advanced microwave scanning radiometer for the Earth observing system (AMSR-E) and the scanning multichannel microwave radiometer (SMMR). *J Geophys Res Atmos* 112(D9):D09,108. doi:[10.1029/2006JD008033](https://doi.org/10.1029/2006JD008033)

- Tan B, Morisette JT, Wolfe RE, Gao F, Ederer GA, Nightingale J, Pedelty JA (2011) An enhanced TIMESAT algorithm for estimating vegetation phenology metrics from MODIS data. *IEEE J Select Top Appl Earth Observ Remote Sens* 4(2):361–371. doi:[10.1109/JSTARS.2010.2075916](https://doi.org/10.1109/JSTARS.2010.2075916)
- Wagner W, Scipal K, Pathe C, Gerten D, Lucht W, Rudolf B (2003) Evaluation of the agreement between the first global remotely sensed soil moisture data with model and precipitation data. *J Geophys Res Atmos* 108(D19):4611. doi:[10.1029/2003JD003663](https://doi.org/10.1029/2003JD003663)
- Zreda M, Desilets D, Ferré TPA, Scott RL (2008) Measuring soil moisture content non-invasively at intermediate spatial scale using cosmic-ray neutrons. *Geophys Res Lett* 35(21):L21,402. doi:[10.1029/2008GL035655](https://doi.org/10.1029/2008GL035655)

Chapter 13

Temporal Analysis of Remotely Sensed Land Surface Shortwave Albedo

Tao He and Shunlin Liang

Abstract Satellite-derived surface albedo products have offered great opportunities in monitoring surface energy budget. However, existing satellite albedo products may have suffered from data gaps and/or inconsistency caused by cloud contamination, sensor difference, and retrieval algorithm failure, which will lead to the limitations in long-term time series land surface albedo analysis. This chapter presents some recently developed methods to detect sensor change, to reduce data gaps, and to improve data consistency and accuracy of existing satellite products, followed by a case study on the temporal analysis of regional long-term land surface albedo changes.

13.1 Introduction

Surface albedo, defined as the ratio of the outgoing to the incoming solar radiation at Earth's surface, is a critical variable that controls surface energy budget in the climate studies. Albedo is highly variable both spatially and temporally. Significant changes in surface albedo are accompanied by variations in surface conditions, such as snow cover (He et al. 2013), vegetation cover (Loarie et al. 2011; Lyons et al. 2008), soil moisture (Govaerts and Lattanzio 2008; Zhu et al. 2011), and urbanization (Offerle et al. 2005). Ghimire et al. (2013) reconstructed the global albedo change with land cover changes, and found the global albedo increase of 0.0012 had a net cooling effect of a top-of-atmosphere (TOA) radiative forcing of -0.23 W m^{-2} from 1700 to 2005. Aerosols like dust and soot may also contaminate snow and greatly reduce its albedo (Hansen and Nazarenko 2004; Xu et al. 2009).

T. He (✉)

Department of Geographical Sciences, University of Maryland, College Park, MD, USA
e-mail: taohers@gmail.com

S. Liang

Department of Geographical Sciences, University of Maryland, College Park, MD, USA
State Key Laboratory of Remote Sensing Science, School of Geography, Beijing Normal University, Beijing 100875, China

Accurate surface albedo data are needed to characterize climate system and to help improve the development and predictability of climate models.

Satellite data provide unique capabilities in monitoring surface albedo on the global basis (Liang et al. 2010, 2013b). Algorithms for albedo estimation from various remote sensing imagery have been developed, including those designed for different sensor characteristics, from geostationary to polar-orbiting, from multispectral to hyperspectral, from nadir-view to multi-angle, from coarse resolution to fine resolution, and from space-borne to air-borne (e.g., Csiszar and Gutman 1999; Govaerts et al. 2010; He et al. 2012, 2014b; Liang et al. 2005a; Maignan et al. 2004; Martonchik et al. 1998; Pinty et al. 2000; Roman et al. 2013; Schaaf et al. 2002; Shuai et al. 2011; Wang et al. 2013). During the past few decades, many albedo products have been generated from satellite observations (listed in Table 13.1).

Surface albedo products with an absolute accuracy of 0.02–0.03 are generally required for regional and global climate studies (Dozier et al. 1989; Sellers et al.

Table 13.1 List of some existing satellite land surface shortwave albedo products

Albedo data sets ^a	Resolution	Frequency	Temporal coverage	References
GLASS	1 km/0.05°	8-day	1981–present	Liang et al. (2013a), Liu et al. (2013), Qu et al. (2014)
GlobAlbedo	1 km/0.05°	8-day	1998–2011	Lewis et al. (2013), Muller et al. (2012)
MERIS	0.25°	Monthly	2002–2006	Popp et al. (2011)
MODIS	500 m/0.05°	daily/8-day	2000–present	Lucht et al. (2000), Schaaf et al. (2002)
CLARA-SAL	0.25°	10-day/monthly	1982–2009	Riihela et al. (2013), Xiong et al. (2002)
VIIRS	375 m	daily	2011–present	Liang et al. (2005b), Wang et al. (2013)
MISR	1100 m	16-day	2000–present	Martonchik et al. (1998)
POLDER	8 km	10-day	1996–1997	Maignan et al. (2004)
			2003	
			2005–present	
Geoland2	1 km	10-day	1999–present	Hagolle et al. (2005)
Meteosat	3 km	daily/10-day	1982–present	Carrer et al. (2010), Pinty et al. (2000)

^aGLASS global land surface satellites, MERIS medium resolution imaging spectrometer; MODIS moderate resolution imaging spectroradiometer, CLARA-SAL clouds, albedo and radiation–surface albedo, VIIRS visible infrared imaging radiometer suite, MISR multi-angle imaging spectroradiometer, POLDER polarization and directionality of the Earth’s reflectances

1995). Extensive validations have been made on the existing satellite albedo products using ground measurements and fine-resolution remote sensing data (Cescatti et al. 2012; He et al. 2012, 2013, 2014c; Liang et al. 2002; Liu et al. 2009; Stroeve et al. 2013; Wang et al. 2006, 2012b), showing that most of these products can satisfy the accuracy requirements and be used to validate and calibrate regional and global climate models (He et al. 2014a).

Surface albedo varies both spatially and temporally. For example, Gao et al. (2005) found that the inter-annual variation of the MODIS shortwave albedo is less than 0.01 over snow-free surfaces and the averaged values over 20° latitude vary little between consecutive years. Fang et al. (2007) observed that the albedo variation shows a strong seasonal character that it increases in winter and spring and decreases in the growing season. They also found the strong linkage between the largest variation in surface albedo and events such as winter snow and spring thaw. Zhang et al. (2010) analyzed MODIS albedo data from 2000 to 2008 and found that although there was no significant global annual mean surface albedo change, a decrease of ∼0.01 for the Northern Hemisphere and an increase of ∼0.01 for the Southern Hemisphere was identified during the time period.

Although extensive examinations on these satellite albedo products showed satisfactory accuracy for global scale research, in some cases the albedo accuracy was reported to be between 10 and 28 % (Chen et al. 2008; Liu et al. 2009; Pinty et al. 2011; Roman et al. 2009; Rutan et al. 2009; Stroeve et al. 2005), out of which 3–5 % error was reported as a result of the band differences in generating the broadband albedos (Govaerts et al. 2006). Sensor changes (degradation, orbital drift, and spectral response difference) may have also contributed to the systematic bias found in existing products (Gao et al. 2014; Kim et al. 2014; Loew and Govaerts 2010; Wang et al. 2012a). This accuracy can be translated into absolute values of around 0.03–0.09, which suggests that current albedo products may still need improvement to satisfy the requirement of climate modeling studies (Yang et al. 2008; Zhang et al. 2010). Moreover, there is a common problem of data gaps in current albedo products due to either cloud contamination or rapid changes in surface albedo. Take the MODIS albedo products for example: the global mean annual probability of obtaining a sufficient number of clear sky observations for a typical 16-day compositing period is 80 %; as the temporal window reduces to 10 days, the amount of data gaps increases to 40 % (Liu et al. 2013; Roy et al. 2006).

In this chapter, various methods from recent studies are briefly introduced for detecting and correcting changes in TOA reflectance/surface albedo resulted due to sensor degradation, orbital drift, and spectral response changes, gap-filling and smoothing to obtain continuous and complete surface albedo product, and fusing multiple albedo products to reduce data uncertainties (Sect. 13.2). Section 13.3 shows some examples of time series albedo analysis, followed by conclusions in Sect. 13.4.

13.2 Sensor Change Detection and Correction, Gap-Filling, and Data Fusion for Time Series Albedo Analysis

13.2.1 *Detection and Correction of Sensor Changes on Surface Broadband Albedo Estimation*

Long-term time series analysis usually relies on well-calibrated data and temporally consistent data from different satellite sensors. However, previous research has found that issues such as the sensor degradation and orbital drift could have undermined the long-term trend analysis for surface properties (Gao et al. 2013; Jiang et al. 2008; Wang et al. 2012a). Various approaches have then been developed to detect sensor changes and/or to adjust either the TOA observations or directly the surface albedo estimation (e.g., Cao et al. 2009; Gao et al. 2014; Kim et al. 2014; Loew and Govaerts 2010; Molling et al. 2010). Some examples are given below.

13.2.1.1 Sensor Degradation

Kim et al. (2014) developed a new approach to detect the radiometric degradation of satellite sensor. Two time series algorithms, seasonal trend decomposition procedures based on loess (STL) and discrete wavelet transform (DWT) have been developed in this study trying to remove the seasonal oscillation in the TOA signal that was caused by changes and variation in the atmosphere and surface, and then detect the trend of sensor degradation that has not been well calibrated. Details on the algorithm implementation can be found in (Kim et al. 2014). Both algorithms were found successful in detecting long-term trends in TOA reflectance without introducing the surface anisotropy model and radiative transfer (see an example in Fig. 13.1). In addition, the STL and DWT algorithms were found to have higher statistical significance than other approaches. Assuming the surface target (e.g., desert) is stable, the extracted trend would be able to improve the radiometric calibration coefficients, and eventually to correct the TOA reflectance.

13.2.1.2 Orbital Drift

Apart from the sensor degradation, orbital drift of satellite platforms could also result in significant variation of TOA reflectance on the scene-basis. Gao et al. (2013, 2014) evaluated the orbital drift effect on the historical Landsat-5 data from 1984 to 2010 and found the TOA reflectance may be biased as much as ~6 % if the nominal 10 am local time rather than the actual local acquisition time was not considered in surface anisotropy correction (Fig. 13.2). A database for bidirectional reflectance distribution function (BRDF) built from MODIS albedo/BRDF product was later used in their study as a priori information to compensate the orbital drift effects in surface albedo estimation.

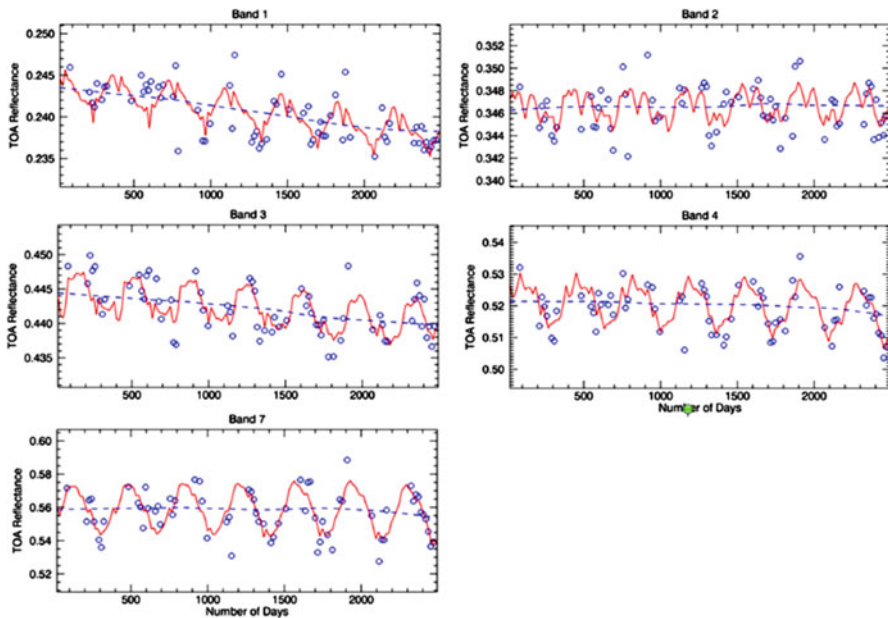


Fig. 13.1 STL decomposition of Landsat TOA reflectance on an area in Lydia desert (Kim et al. 2014). Blue dots: Landsat TOA spectral reflectance; red curve: STL fitted pattern; blue line: trend of sensor degradation

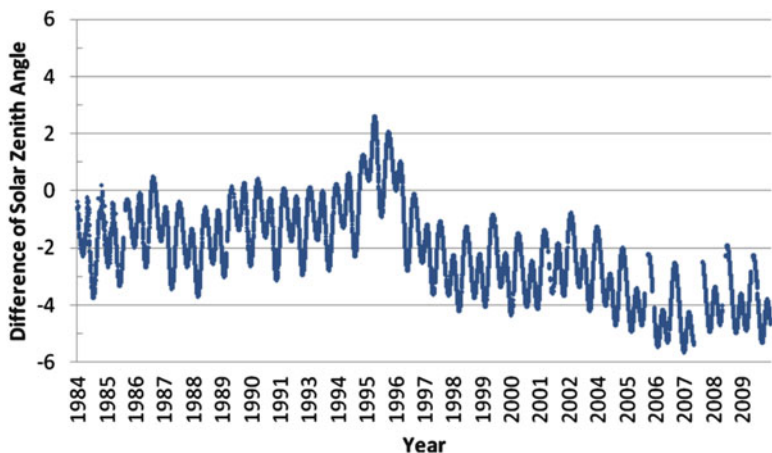


Fig. 13.2 Variation of solar zenith angle from Landsat 5 data (45°N) because of orbital drift (Gao et al. 2013)

13.2.1.3 Temporal Continuities Between Sensors

Systematic discontinuities identified in existing long-term surface albedo product would have been a critical issue in climate change related surface energy budget analysis. Besides the sensor degradation and orbital drift, difference in sensor spectral response also contributed in the discontinuities. Loew and Govaerts (2010) evaluated the surface albedo product derived from Meteosat First Generation (MFG) satellites from 1982 to 2006 and proposed a new set of coefficients to account for changes in sensor spectral response in albedo narrow-to broadband conversion in order to generate consistent broadband albedo from different satellite sensors. Figure 13.3 shows that the impacts of sensor changes have been significantly reduced in the albedo generated using the new coefficients.

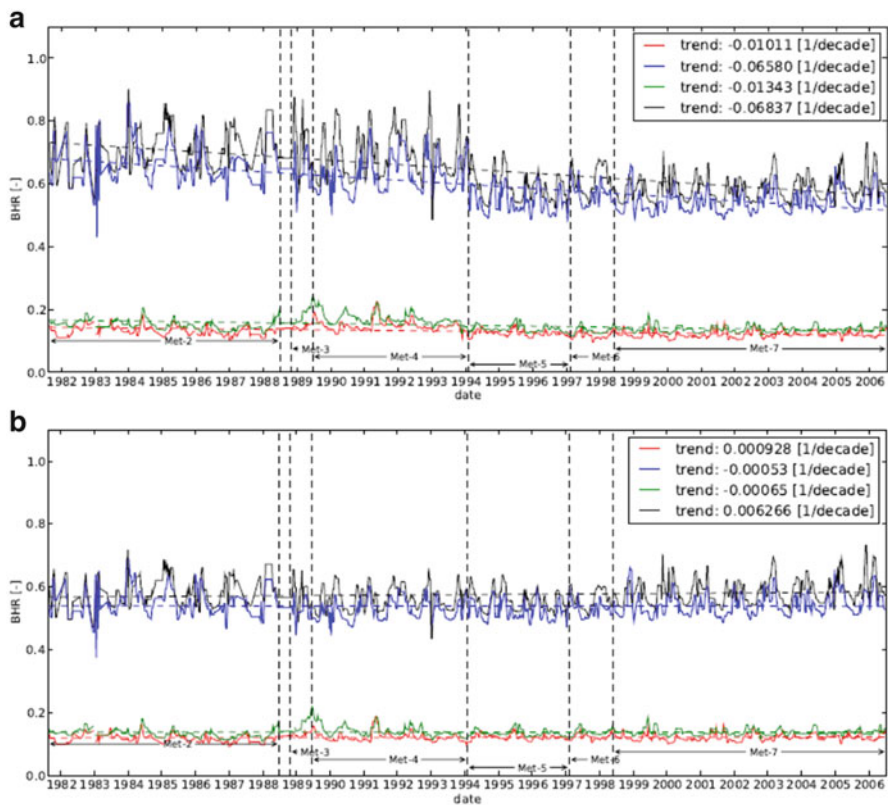


Fig. 13.3 Surface broadband albedo (BHR: bi-hemispheric reflectance) time series of different targets calculated using: (a) original band conversion coefficients, (b) new conversion coefficients considering the sensor differences (Loew and Govaerts 2010)

13.2.2 *Gap-Filling and Data Fusion*

To reduce the gaps and improve the albedo estimations, researchers have been working on two types of approaches. The first one is to improve the retrieving procedure by introducing some other sources of data, such as the prior information (He et al. 2012). The second is to improve the albedo datasets from existing satellite data, which can take advantage of the sensor characteristics, and/or retrieving algorithms from different satellites (Fang et al. 2007; He et al. 2008, 2014c; Jin et al. 2002; Ju et al. 2010; Moody et al. 2005; Roy et al. 2008; Shuai et al. 2011).

13.2.2.1 *Gap-Filling and Data Smoothing*

Many researchers have been focusing on reducing the data gaps and producing spatially and temporally continuous albedo maps based on currently available satellite products. There are two major methodologies used to generate this type of albedo dataset to satisfy the needs of land surface modeling studies. The first one is the physical method, which relies on the surface bidirectional reflectance distribution function (BRDF) information. Research has been done using BRDF information from datasets with better angular sampling to convert surface reflectance with reduced angular sampling to albedo (Jin et al. 2002; Ju et al. 2010; Roy et al. 2008; Shuai et al. 2011). Multiple other strategies using a priori knowledge have been developed to reduce gaps in existing albedo products. Based on the standard retrieval technique of MODIS nadir BRDF-adjusted reflectance products, an adapted method was employed to improve the integrity of reflectance/albedo time series (Ju et al. 2010; Shuai et al. 2011). These methods assume that there are some homogeneous pixels with coarser spatial resolution that correspond to the finer resolution data for each of the land cover types. Therefore, it is sometimes difficult to translate information across scales if pure pixels are hard to be found at the coarser resolution. To reduce the data gaps through the retrieval procedure, a Kalman filter was used to improve the completeness of BRDF coefficients series (Samain et al. 2008). In the retrieval algorithm of the GlobAbledo albedo product, a regularization method was utilized to generate daily kernel coefficients (Lewis et al. 2013). In addition, He et al. (2012) used the multiyear surface BRDF database as a priori knowledge and fewer instantaneous TOA observations to retrieve surface albedo with much less gaps.

The second methodology uses the data-driven models that are directly based on the albedo products and utilize the spatial and/or temporal information to fill the gaps (Fang et al. 2007; He et al. 2008; Liu et al. 2013; Moody et al. 2005). Albedo climatology is the basis of temporal filter in gap-filling product from a single sensor. Fang et al. (2007) designed a temporal-spatial filter (TSF) based on Liang's (2004) method to generate gap-free albedo product from multiyear MODIS albedo data. In the TSF method, the climatology of each pixel α_b is first determined from multiyear observations. Gap-filled surface albedo α_a was then calculated from weighted average of multiyear background and temporal neighbor observations using Eq. (13.1).

$$\alpha_a(r_i) = \alpha_b(r_i) + \frac{\sum_{j=1}^n w(r_i, r_j) [\alpha_o(r_i) - \alpha_b(r_i)]}{\sum_{j=1}^n w(r_i, r_j)} \quad (13.1)$$

Here, α_b denotes the multiyear average background albedo; $\alpha_a(r_i)$, $j = 1, 2, \dots, n$, denote a set of MODIS albedo product; n is the size of the influence window. $w(r_i, r_j)$ is the weighting function dependent on the temporal distance $d_{i,j}^2$ between r_i and r_j ,

$$w(r_i, r_j) = \max \left(0, \frac{R^2 - d_{i,j}^2}{R^2 + d_{i,j}^2} \right) \quad (13.2)$$

where R is the radius of the influence. This technique implicitly assumed that all the observed values are error-free and could represent the “true” values of the dynamic system.

As Fang's et al. (2007) method took no account of observational errors, Liu et al. (2013) developed a spatial-temporal filter (STF) method by considering both the temporal correlation and the observational errors of the albedos in neighboring days. The surface albedo estimates were calculated using the maximum likelihood approach. Albedo climatology (multiyear mean and standard deviation) was adopted to fill in data gaps when the available temporal observations were not enough. In addition, this method could generate mean and standard deviation of surface albedo estimates based on the posterior from the maximum likelihood approach.

This algorithm has been applied on the intermediate GLASS albedo product, in order to generate smooth land surface albedo in the final stage (Liang et al. 2013a). Figure 13.4 showed an example of applying the STF algorithm in the GLASS albedo retrieval procedure and it turned out that the algorithm improved the smoothness of surface albedo time series.

13.2.2.2 Data Fusion of Multiple Surface Albedo Products

Most of the existing algorithms mentioned before use only one dataset, which may introduce systematic bias in the final albedo maps, which possibly results from simplified atmospheric/surface condition and/or sensor calibration (Govaerts et al. 2006; Pinty et al. 2011). Utilizing data from multi-source satellite products may be a solution to simultaneously reduce data gaps and improve estimation accuracy of surface albedo.

Dou et al. (2013) proposed a method called multi-angular and multi-band inversion model to estimate surface albedo/BRDF from MODIS and AVHRR surface reflectances. They first established an empirical relationship between spectral bands of AVHRR and MODIS based on surface spectra libraries:

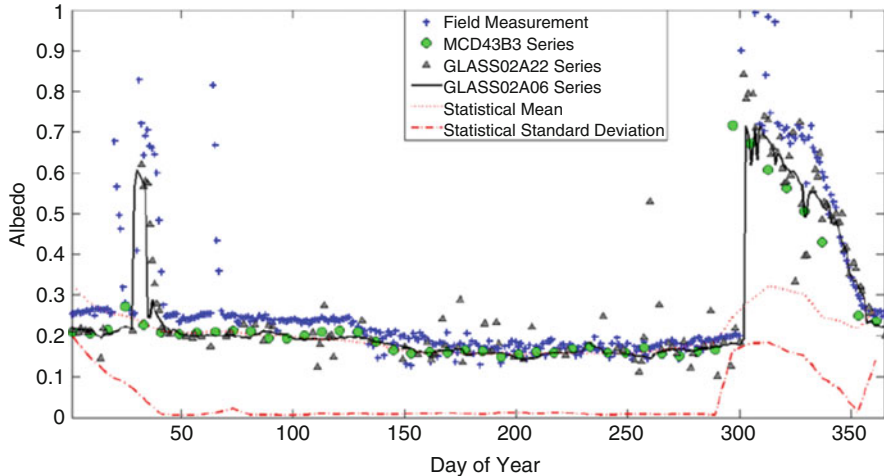


Fig. 13.4 Comparison of surface albedo derived from STF and other data sets at automatic weather station BJ (31.3687°N , 91.8987°E) (Liu et al. 2013). GLASS02A22 is the intermediate product estimated using algorithm mentioned in (Qu et al. 2014). GLASS02A06 is the final GLASS albedo product

$$\rho_{A,j} = \sum_{i=1}^n a_{i,j} \rho_{M,i} \quad (13.3)$$

where $\rho_{A,j}$ and $\rho_{M,i}$ are the directional reflectances for band j of AVHRR and band i of MODIS, respectively. $a_{i,j}$ is the regression coefficients.

Surface directional reflectance can then be modeled by the BRDF kernel models for MODIS bands (Eq. 13.4) and AVHRR bands (Eq. 13.5) assuming surface anisotropic properties do not change:

$$\rho_{M,i} = f_{iso,i} + f_{vol,i} K_{vol}(\theta_M^s, \theta_M^v, \varphi_M) + f_{geo,i} K_{geo}(\theta_M^s, \theta_M^v, \varphi_M) \quad (13.4)$$

$$\rho_{A,j} = \sum_{i=1}^n a_{i,j} [f_{iso,i} + f_{vol,i} K_{vol}(\theta_A^s, \theta_A^v, \varphi_A) + f_{geo,i} K_{geo}(\theta_A^s, \theta_A^v, \varphi_A)] \quad (13.5)$$

Here, $f_{iso,i}$, $f_{vol,i}$, $f_{geo,i}$ are the kernel coefficients to be estimated for band i. K_{vol} and K_{geo} are the volumetric and geometric kernels, which can be directly calculated from sensor-target-sun geometries (θ_M^s , θ_M^v , φ_M are solar zenith angle, sensor zenith angle, and relative azimuth angle for MODIS; θ_A^s , θ_A^v , φ_A are for AVHRR). In this way, the reflectance data from both sensors can be combined to estimate the kernel coefficients with a smaller temporal composite window. This research, however, did not take into account of errors in the surface reflectance in MODIS and AVHRR products.

An alternative way to fusing data from different satellite products is using statistical models to establish relationship among different products. The multi-resolution tree (MRT) method being developed in recent years offered a great opportunity to take advantage of data across different spatial resolutions by assuming a statistical model that is autoregressive in levels of resolution (Chou et al. 1994). The MRT method has been widely used on large datasets to overcome the computational difficulties that other existing methods (optimal interpolation, kriging, etc.) may have (Yue and Zhu 2006). Many researchers have been applying this method to interpolate and to smooth data over various satellite products (Huang et al. 2002; Wang and Liang 2010; Yue and Zhu 2006; Zhu and Yue 2005; Zhu et al. 2010).

He et al. (2014c) developed a prototype data fusion procedure based on MRT that combines three satellite albedo products from MISR, MODIS, and Landsat to generate consistent and gap-free albedo datasets at different spatial resolutions. The theoretical basis of the MRT is the assumption that data at different spatial resolutions are autoregressive and can be organized in a tree structure. The linear tree-structure model can be expressed using Eq. (13.6):

$$y_u = A_u y_{pa(u)} + w_u \quad (13.6)$$

where y_u is the variable used to estimate at the scale u and $y_{pa(u)}$ is the variable at the parent node. w_u is the spatial stochastic process that follows a Gaussian normal distribution with a variance of W_u . A_u is the state conversion matrix that estimates the variable at scale u from its parent node. There is a similar formulation that transfers the variable at scale u from its child node $ch(u)$. To determine the state conversion matrix, the “change-of-support” problem has been widely discussed (Huang et al. 2002; Plumejeaud et al. 2011; Wikle 2003). An observation model is also used in this method by linking the satellite products to the “truth” data:

$$z_u = C_u y_u + \varepsilon_u \quad (13.7)$$

Here, z_u is the satellite product with a white noise ε_u that follows a normal distribution $N(0, \Phi_u)$. C_u is the observation matrix that converts the variable of interest to the satellite data.

To apply the MRT algorithm and fuse multiple satellite albedo products, three steps were included.

First, the data uncertainties of different satellite products need to be evaluated and quantified based on ground measurements and product inter-comparison. Systematic biases of each product could be removed in this step.

Second is the leaves-to-root filtering (Eq. 13.8). The basic assumption of the tree model is that the tree-structure follows a Markov chain process, which implies that the state variable is only related to its instant child nodes and instant parent node(s). The step is a fine-to-coarse resolution filtering, which is used to estimate the state variable from higher resolution data. The major purpose of this step is to fill in the gaps at different resolutions using Kalman filter.

Third is the root-to-leaves smoothing step (Eq. 13.9). A coarse-to-fine resolution smoothing was used to update the state variable with the information at a coarser resolution. This step generally assumes that the process at the parent scale provides the foundation of the process at current scale. After the Kalman-smoothing step, the datasets at different spatial scales become smooth and consistent. Details of the Kalman filter derivations can be found in Huang et al. (2002).

$$\widehat{\mathbf{y}}_u = E(\mathbf{y}_u | \mathbf{Z}_u, \mathbf{Z}_{ch(u)}) \quad (13.8)$$

$$\widehat{\mathbf{y}}_u = E(\mathbf{y}_u | \mathbf{Z}_u, \mathbf{Z}_{pa(u)}) \quad (13.9)$$

Uncertainties of each satellite albedo products have been significantly reduced after applying the MRT algorithm (Fig. 13.5). A new set of gap-free albedo products were produced with improved data consistency across different spatial resolutions (Fig. 13.6).

13.3 Time Series Analysis of Surface Albedo: A Case Study at Greenland

Surface albedo may change with land cover dynamics caused by deforestation, afforestation, urbanization, snowfall, and snowmelt, etc. Previous studies have shown the surface albedo changes at different locations throughout the past three decades (He et al. 2013, 2014a; Shi and Liang 2013). With the help of various temporal/spatial filtering and data fusion techniques, a set of more accurate and continuous albedo products can be used for long-term albedo analysis. In this section, a case study of long-term surface albedo analysis using GLASS product over Greenland (He et al. 2013) is present.

13.3.1 Validation and Evaluation of Satellite Albedo Product

The GLASS albedo product is derived from the Advanced Very High Resolution Radiometer (AVHRR) and Moderate Resolution Imaging Spectroradiometer (MODIS) observations (Liang et al. 2013a). It records surface shortwave broadband albedo every 8 days at a spatial resolution of 0.05° from 1981 to 2012. The impacts of orbital drift have been considered and minimized in the albedo retrieval and post-processing algorithms (Liu et al. 2013; Qu et al. 2014). Evaluation and/or removal of the impacts of sensor degradation and sensor changes on GLASS surface albedo are needed before the time series analysis can be carried out.

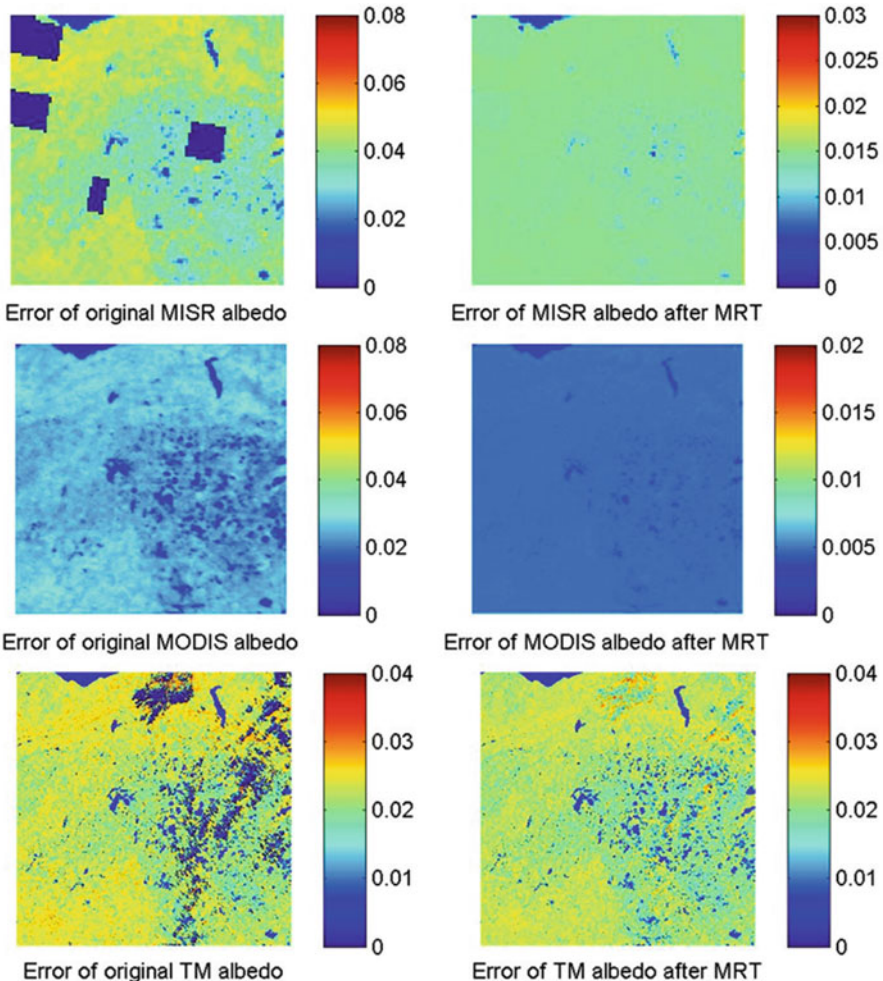


Fig. 13.5 Error comparisons between albedo maps before and after MRT for the three products on DOY 192, 2005 (zero means no data). The error of the original albedo datasets is calculated as the product of the relative error and absolute albedo value (He et al. 2014c)

Ground measurements of surface albedo are available at 19 Greenland Climate Network (GC-Net) sites from 1995 (Steffen and Box 2001). While the ground measurements of surface albedo were obtained from the pyranometers every 30 mins, satellite products provide local noon albedo values. Ground measurements within 1 h range of satellite overpass time were averaged to match the satellite albedo product. Validation of the monthly mean albedo with ground measurements (Fig. 13.7) showed consistent accuracy of GLASS albedo from 1995 to 2012. Inter-comparison of albedo derived from AVHRR and MODIS in the overlap time period

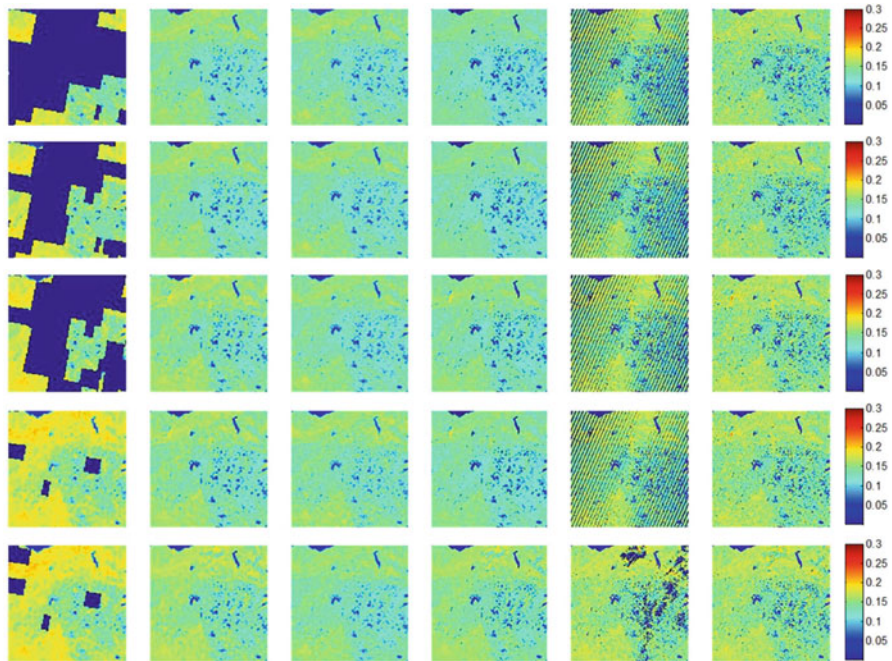


Fig. 13.6 Time-series comparison of albedo maps before and after MRT (left-to-right order: original MISR albedo, MISR albedo after MRT, original MODIS albedo, MODIS albedo after MRT, original Landsat albedo, and Landsat albedo after MRT); dark blue color (0 value) means no data. DOYs for the rows from the top to bottom are 160, 168, 176, 184, and 192 (He et al. 2014c)

(2000, 2003, and 2004) also showed consistent root-mean-square-error (0.041–0.045) and R2 (0.964–0.970). This indicates that sensor changes did not result in significant differences between albedo estimates derived from the two satellite platforms.

13.3.2 Time Series Changes in Surface Albedo at GC-Net Sites

To examine whether the changes in surface albedo detected from satellite data were artifacts or real signals, time series of surface albedo from satellite product and ground measurements were compared at GC-Net sites (Fig. 13.8). In the overlap time periods, albedo decreases were observed from both satellite observations and ground measurements at most sites with similar magnitude of trends (He et al. 2013). This demonstrates that the magnitude of albedo trend was much larger than artifacts caused possibly by sensor degradation, etc. In other words, sensor degradation would not have resulted in significant errors in the albedo trend detection over Greenland.

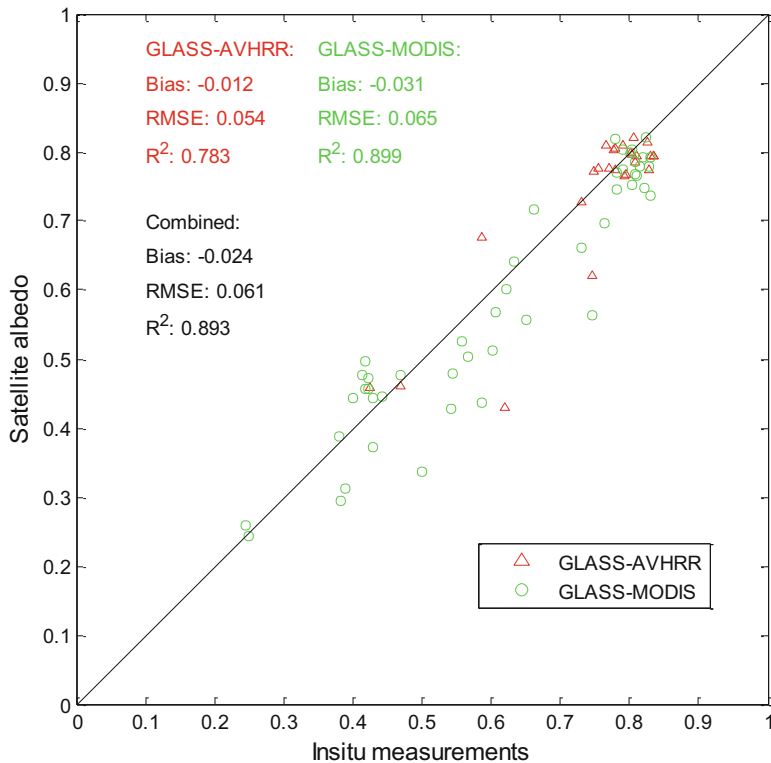


Fig. 13.7 Comparison of July GLASS albedo with ground measurements at all GC-Net sites (He et al. 2013)

The accompanied increase of near surface air temperature would explain a large portion of albedo decrease, particularly at the two sites of Swiss Camp and JAR1, where temperature was close to snow melting point. Accelerated albedo decrease was observed from both satellite data and ground measurements because of positive feedback of snow albedo to temperature.

13.3.3 Time Series Changes in Surface Albedo over the Entire Greenland

After removing/minimizing the possible impacts of sensor changes on GLASS surface albedo trend analysis using ground measurements and data inter-comparison, the satellite product could be used to assess albedo changes over the entire Greenland, which otherwise could not be possible with only ground measurements.

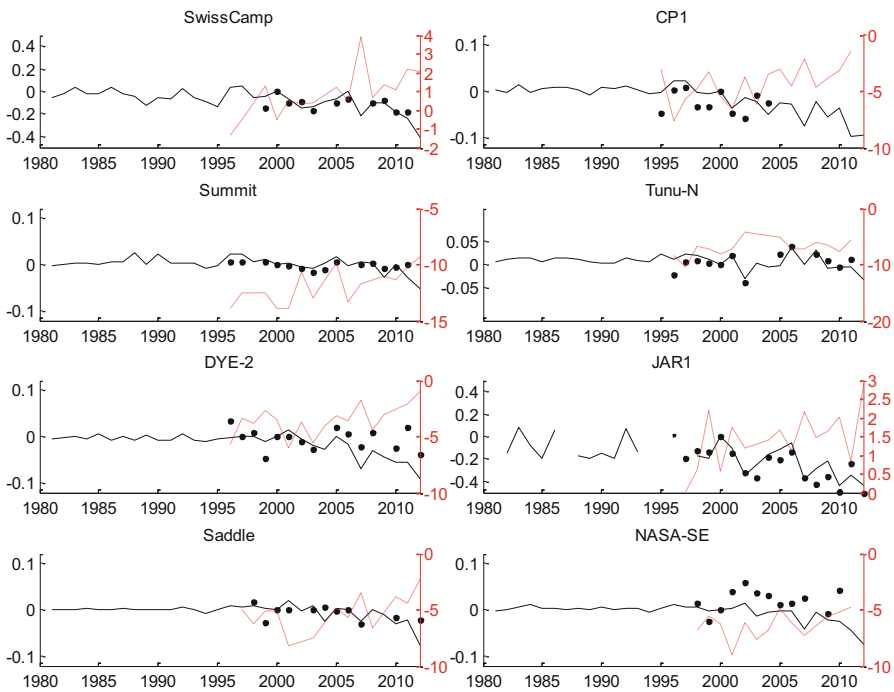


Fig. 13.8 Time series of albedo anomaly (left axis) and near surface air temperature ($^{\circ}\text{C}$) (right axis) at GC-Net sites in July (1981–2012). Black solid line: GLASS albedo products; black dots: ground albedo data; red dashed line: ground measured air temperature (He et al. 2013)

Albedo trends were found to vary both spatially and temporally (Fig. 13.9). He et al. (2013) found that over the entire study area, albedo decreased at a rate of $0.009 \pm 0.002 \text{ decade}^{-1}$ ($p < 0.01$). However, the decrease has been accelerating with a large decrease since 2000 ($-0.028 \pm 0.008 \text{ decade}^{-1}$, $p < 0.01$). Most significant decreases occurred at elevations between 1000 m and 1500 m ($-0.055 \text{ decade}^{-1}$, $p < 0.01$). The accelerated decrease in land surface albedo since 1980s may cause expansion of ablation area towards inner Greenland if temperature continues to increase.

13.4 Conclusions

Long-term time series analyses of satellite land surface albedo have been carried out in some recent studies thanks to the development of multiple long-term satellite products, which would greatly improve our understanding of climate change induced by human activities and benefit the climate modelling communities to improve the model predictions in the future. However, data gaps, systematic bias,

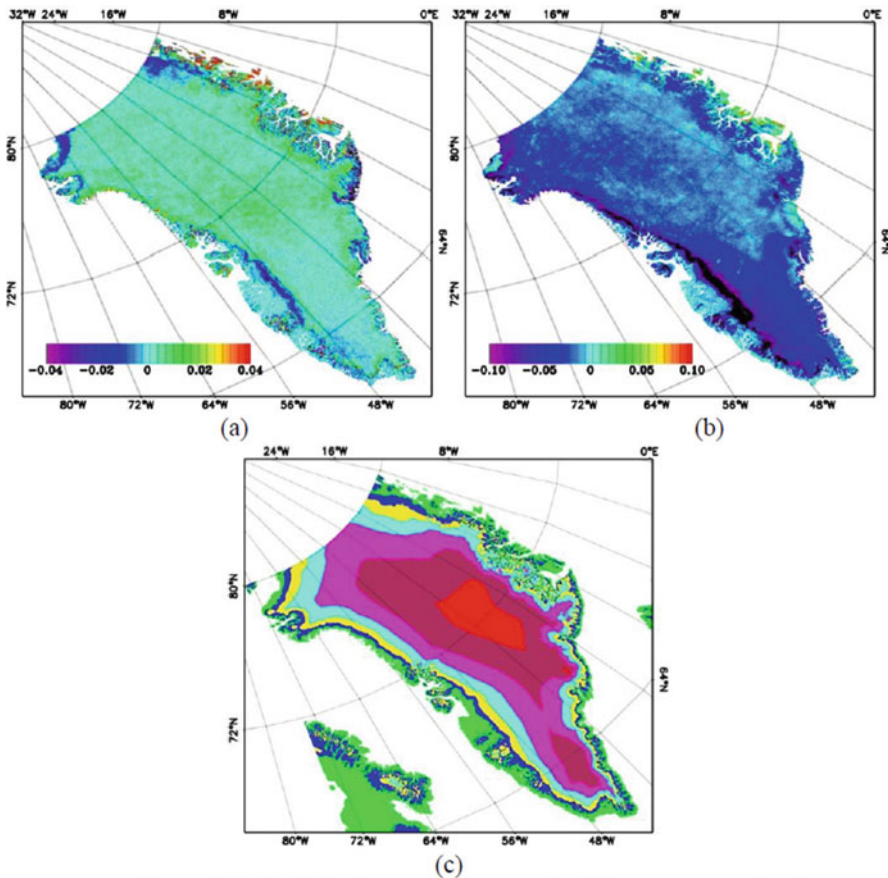


Fig. 13.9 (a) Decadal July albedo change rate over Greenland from GLASS products in 1981–2000; (b) Decadal July albedo change rate over Greenland from GLASS products in 2000–2012; (c) Digital elevation model of Greenland from USGS GMTED data divided into 8 levels: sea level and below (white), ≤ 500 m (green), 501–1000 m (blue), 1001–1500 m (yellow), 1501–2000 m (cyan), 2001–2500 m (magenta), 2501–3000 m (maroon), and above 3000 m (red) (He et al. 2013)

and artefacts from sensor degradation, orbital drift, and sensor inconsistency may have undermined such analyses. This chapter presents some recent research trying to detect and remove these problems. It would be very helpful if the user community can understand and mitigate these issues in long-term time series analyses in surface energy budget studies.

Acknowledgements This work was supported by NOAA grants of JPSS VIIRS and GOES-R land surface albedo products through the University of Maryland, College Park.

References

- Cao C, Vermote E, Xiong X (2009) Using AVHRR lunar observations for NDVI long-term climate change detection. *J Geophys Res* 114, D20105. doi:[10.1029/2009JD012179](https://doi.org/10.1029/2009JD012179)
- Carrer D, Roujean JL, Meurey C (2010) Comparing operational MSG/SEVIRI land surface Albedo products from land SAF with ground measurements and MODIS. *IEEE Trans Geosci Remote Sens* 48:1714–1728
- Cescatti A, Marcolla B, Vannan SKS, Pan JY, Roman MO, Yang XY, Ciais P, Cook RB, Law BE, Matteucci G, Migliavacca M, Moors E, Richardson AD, Seufert G, Schaaf CB (2012) Intercomparison of MODIS albedo retrievals and in situ measurements across the global FLUXNET network. *Remote Sens Environ* 121:323–334
- Chen YM, Liang S, Wang J, Kim HY, Martonchik JV (2008) Validation of MISR land surface broadband albedo. *Int J Remote Sens* 29:6971–6983
- Chou KC, Willsky AS, Nikoukhah R (1994) Multiscale systems, Kalman filters, and Riccati-equations. *IEEE Trans Autom Control* 39:479–492
- Csiszar I, Gutman G (1999) Mapping global land surface albedo from NOAA AVHRR. *J Geophys Res-Atmos* 104:6215–6228
- Dou B, Wen J, Liu Q, Sun C, Shi J, Tang Y, Liu N (2013) The multi-angular and multi-band model for BRDF and albedo retrieval. In: *Geoscience and remote sensing symposium (IGARSS), 2013 IEEE International*, pp 3044–3047
- Dozier J, Barry RJ, Jezek KM, Thomas RH, Veseycky J (1989) Prospects and concerns for satellite remote sensing of snow and ice. National Academy Press, Washington, DC
- Fang HL, Liang SL, Kim HY, Townshend JR, Schaaf CL, Strahler AH, Dickinson RE (2007) Developing a spatially continuous 1 km surface albedo data set over North America from Terra MODIS products. *J Geophys Res-Atmos* 112, D20206
- Gao F, Schaaf CB, Strahler AH, Roesch A, Lucht W, Dickinson R (2005) MODIS bidirectional reflectance distribution function and albedo Climate Modeling Grid products and the variability of albedo for major global vegetation types. *J Geophys Res* 110, D01104. doi:[10.1029/2004JD005190](https://doi.org/10.1029/2004JD005190)
- Gao F, He T, Masek JG, Shuai Y, Schaaf CB, Wang Z (2013) Influence of angular effects and adjustment on medium resolution sensors for crop monitoring. In: *Agro-geoinformatics (Agro-geoinformatics), 2013 second international conference on*, pp 296–301
- Gao F, He T, Masek JG, Shuai Y, Schaaf CB, Wang Z (2014) Angular effects and correction for medium resolution sensors to support crop monitoring. *IEEE J Spec Top Appl Earth Observations Remote Sens, revised* 7(11):4480–4489
- Ghimire B, Williams CA, Masek J, Gao F, Wang Z, Schaaf C, He T (2013) Global albedo change and radiative cooling from anthropogenic land-cover change, 1700 to 2005 based on MODIS, land-use harmonization and radiative kernels. *Geophys Res Lett* 41(24):9087–9096
- Govaerts Y, Lattanzio A (2008) Estimation of surface albedo increase during the eighties Sahel drought from Meteosat observations. *Glob Planet Chang* 64:139–145
- Govaerts YM, Pinty B, Taberner M, Lattanzio A (2006) Spectral conversion of surface albedo derived from meteosat first generation observations. *IEEE Geosci Remote Sens Lett* 3:23–27
- Govaerts YM, Wagner S, Lattanzio A, Watts P (2010) Joint retrieval of surface reflectance and aerosol optical depth from MSG/SEVIRI observations with an optimal estimation approach: 1. Theory. *J Geophys Res* 115, D02203. doi:[10.1029/2009JD011779](https://doi.org/10.1029/2009JD011779)
- Hagolle O, Lobo A, Maisongrande P, Cabot F, Duchemin B, De Pereyra A (2005) Quality assessment and improvement of temporally composited products of remotely sensed imagery by combination of VEGETATION 1 and 2 images. *Remote Sens Environ* 94:172–186
- Hansen J, Nazarenko L (2004) Soot climate forcing via snow and ice albedos. *Proc Natl Acad Sci U S A* 101:423–428
- He T, Xiao ZQ, Wang JD (2008) An improved algorithm to produce spatio-temporally continuous MODIS albedo product in China. In: *Geoscience and remote sensing symposium, 2008. IGARSS 2008. IEEE International*, pp III – 1095–III – 1098

- He T, Liang SL, Wang D, Wu H, Yu Y, Wang J (2012) Estimation of surface albedo and directional reflectance from Moderate Resolution Imaging Spectroradiometer (MODIS) observations. *Remote Sens Environ* 119:286–300
- He T, Liang SL, Yu Y, Wang D, Gao F, Liu Q (2013) Greenland surface albedo changes in July 1981–2012 from satellite observations. *Environ Res Lett* 8:044043
- He T, Liang SL, Song DX (2014a) Analysis of global land surface albedo climatology and spatial-temporal variation during 1981–2010 from multiple satellite products. *J Geophys Res* 119(17):10281–10298
- He T, Liang SL, Wang D, Shi Q, Tao X (2014b) Estimation of high-resolution land surface shortwave albedo from AVIRIS data. *IEEE J Select Top Appl Earth Observations Remote Sens* 7(12):4919–4928
- He T, Liang SL, Wang D, Shuai Y, Yu Y (2014c) Fusion of satellite land surface albedo products across scales using a multiresolution tree method in the north central United States. *IEEE Trans Geosci Remote Sens* 52(6):3428–3439
- Huang HC, Cressie N, Gabrosek J (2002) Fast, resolution-consistent spatial prediction of global processes from satellite data. *J Comput Graph Stat* 11:63–88
- Jiang L, Tarpley JD, Mitchell KE, Zhou S, Kogan FN, Guo W (2008) Adjusting for long-term anomalous trends in NOAA's global vegetation index data sets. *IEEE Trans Geosci Remote Sens* 46:409–422
- Jin YF, Gao F, Schaaf CB, Li XW, Strahler AH, Bruegge CJ, Martonchik JV (2002) Improving MODIS surface BRDF/Albedo retrieval with MISR multiangle observations. *IEEE Trans Geosci Remote Sens* 40:1593–1604
- Ju JC, Roy DP, Shuai YM, Schaaf C (2010) Development of an approach for generation of temporally complete daily nadir MODIS reflectance time series. *Remote Sens Environ* 114:1–20
- Kim W, He T, Wang D, Cao C, Liang SL (2014) Assessment of long-term sensor radiometric degradation using time series analysis. *IEEE Trans Geosci Remote Sens* 52(5):2960–2976
- Lewis P, Brockmann C, Danne O, Fischer J, Guanter L, Heckel A, Krueger O, Lopez G, Muller JP, North P, Potts D, Preusker P (2013) GlobAlbedo: algorithm theoretical basis document (V4.12)
- Liang SL (2004) Quantitative remote sensing of land surface. Wiley, Hoboken
- Liang SL, Fang HL, Chen MZ, Shuey CJ, Walthall C, Daughtry C, Morisette J, Schaaf C, Strahler A (2002) Validating MODIS land surface reflectance and albedo products: methods and preliminary results. *Remote Sens Environ* 83:149–162
- Liang SL, Stroeve J, Box JE (2005a) Mapping daily snow/ice shortwave broadband albedo from Moderate Resolution Imaging Spectroradiometer (MODIS): the improved direct retrieval algorithm and validation with Greenland in situ measurement. *J Geophys Res-Atmos* 110(D10), D10109
- Liang SL, Yu Y, Defelice TP (2005b) VIIRS narrowband to broadband land surface albedo conversion: formula and validation. *Int J Remote Sens* 26:1019–1025
- Liang SL, Wang KC, Zhang XT, Wild M (2010) Review on estimation of land surface radiation and energy budgets from ground measurement, remote sensing and model simulations. *IEEE J Select Top Appl Earth Observations Remote Sens* 3:225–240
- Liang SL, Zhang XT, He T, Cheng J, Wang D (2013a) Remote sensing of the land surface radiation budget. In: Remote sensing of energy fluxes and soil moisture content. CRC Press, Boca Raton, pp 121–162
- Liang SL, Xiao Z, Zhang XT, Liu Q, Cheng J, Zhao X (2013b) Global Land Surface Satellite (GLASS) products: algorithms, validation and analysis. Springer, Cham
- Liu JC, Schaaf C, Strahler A, Jiao ZT, Shuai YM, Zhang QL, Roman M, Augustine JA, Dutton EG (2009) Validation of Moderate Resolution Imaging Spectroradiometer (MODIS) albedo retrieval algorithm: dependence of albedo on solar zenith angle. *J Geophys Res-Atmos* 114, D01106
- Liu NF, Liu Q, Wang LZ, Liang SL, Wen JG, Qu Y, Liu SH (2013) A statistics-based temporal filter algorithm to map spatiotemporally continuous shortwave albedo from MODIS data. *Hydrol Earth Syst Sci* 17:2121–2129

- Loarie SR, Lobell DB, Asner GP, Mu QZ, Field CB (2011) Direct impacts on local climate of sugar-cane expansion in Brazil. *Nat Clim Chang* 1:105–109
- Loew A, Govaerts Y (2010) Towards multidecadal consistent Meteosat surface albedo time series. *Remote Sens* 2:957–967
- Lucht W, Schaaf CB, Strahler AH (2000) An algorithm for the retrieval of albedo from space using semiempirical BRDF models. *IEEE Trans Geosci Remote Sens* 38:977–998
- Lyons EA, Jin YF, Randerson JT (2008) Changes in surface albedo after fire in boreal forest ecosystems of interior Alaska assessed using MODIS satellite observations. *J Geophys Res Biogeosci* 113, G02012
- Maignan F, Breon FM, Lacaze R (2004) Bidirectional reflectance of earth targets: evaluation of analytical models using a large set of spaceborne measurements with emphasis on the Hot Spot. *Remote Sens Environ* 90:210–220
- Martonchik JV, Diner DJ, Pinty B, Verstraete MM, Myneni RB, Knyazikhin Y, Gordon HR (1998) Determination of land and ocean reflective, radiative, and biophysical properties using multiangle imaging. *IEEE Trans Geosci Remote Sens* 36:1266–1281
- Molling CC, Heidinger AK, Straka WC, Wu XQ (2010) Calibrations for AVHRR channels 1 and 2: review and path towards consensus. *Int J Remote Sens* 31:6519–6540
- Moody EG, King MD, Platnick S, Schaaf CB, Gao F (2005) Spatially complete global spectral surface albedos: value-added datasets derived from terra MODIS land products. *IEEE Trans Geosci Remote Sens* 43:144–158
- Muller JP, Lopez G, Watson G, Shane N, Kennedy T, Yuen P, Lewis P, Fischer J, Guanter L, Domenc C, Preusker R, North P, Heckel A, Danne O, Kramer U, Zuhlke M, Brockmann C, Pinnock S (2012) The ESA GlobAlbedo project for mapping the Earth's land surface albedo for 15 years from European sensors. In: *IEEE Geoscience and Remote Sensing Symposium (IGARSS) 2012*. IEEE, Munich
- Offerle B, Jonsson P, Eliasson I, Grimmond CSB (2005) Urban modification of the surface energy balance in the West African Sahel: Ouagadougou, Burkina Faso. *J Clim* 18:3983–3995
- Pinty B, Roveda F, Verstraete MM, Gobron N, Govaerts Y, Martonchik JV, Diner DJ, Kahn RA (2000) Surface albedo retrieval from Meteosat – 1. Theory. *J Geophys Res-Atmos* 105:18099–18112
- Pinty B, Taberner M, Haemmerle VR, Paradise SR, Vermote E, Verstraete MM, Gobron N, Widlowski JL (2011) Global-scale comparison of MISR and MODIS land surface Albedos. *J Clim* 24:732–749
- Plumejeaud C, Mathian H, Gensel J, Grasland C (2011) Spatio-temporal analysis of territorial changes from a multi-scale perspective. *Int J Geogr Inf Sci* 25:1597–1612
- Popp C, Wang P, Brunner D, Stammes P, Zhou Y, Grzegorski M (2011) MERIS albedo climatology for FRESCO+ O-2 A-band cloud retrieval. *Atmos Meas Techn* 4:463–483
- Qu Y, Liu Q, Liang S, Wang L, Liu N, Liu S (2014) Direct-estimation algorithm for mapping daily land-surface broadband albedo from MODIS data. *IEEE Trans Geosci Remote Sens* 52:907–919
- Riihela A, Manninen T, Laine V, Andersson K, Kaspar F (2013) CLARA-SAL: a global 28 yr timeseries of Earth's black-sky surface albedo. *Atmos Chem Phys* 13:3743–3762
- Roman MO, Schaaf CB, Woodcock CE, Strahler AH, Yang XY, Braswell RH, Curtis PS, Davis KJ, Dragoni D, Goulden ML, Gu LH, Hollinger DY, Kolb TE, Meyers TP, Munger JW, Privette JL, Richardson AD, Wilson TB, Wofsy SC (2009) The MODIS (Collection V005) BRDF/albedo product: assessment of spatial representativeness over forested landscapes. *Remote Sens Environ* 113:2476–2498
- Roman MO, Gatebe CK, Shuai Y, Wang Z, Gao F, Masek JG, He T, Liang S, Schaaf CB (2013) Use of in situ and airborne multiangle data to assess MODIS- and Landsat-based estimates of directional reflectance and albedo. *IEEE Trans Geosci Remote Sens* 51:1393–1404
- Roy DP, Lewis P, Schaaf CB, Devadiga S, Boschetti L (2006) The global impact of clouds on the production of MODIS bidirectional reflectance model-based composites for terrestrial monitoring. *IEEE Geosci Remote Sens Lett* 3:452–456

- Roy DP, Ju J, Lewis P, Schaaf C, Gao F, Hansen M, Lindquist E (2008) Multi-temporal MODIS-Landsat data fusion for relative radiometric normalization, gap filling, and prediction of Landsat data. *Remote Sens Environ* 112:3112–3130
- Rutan D, Rose F, Roman M, Manalo-Smith N, Schaaf C, Charlock T (2009) Development and assessment of broadband surface albedo from Clouds and the Earth's Radiant Energy System Clouds and Radiation Swath data product. *J Geophys Res-Atmos* 114, D08125
- Samain O, Roujean JL, Geiger B (2008) Use of a Kalman filter for the retrieval of surface BRDF coefficients with a time-evolving model based on the ECOCLIMAP land cover classification. *Remote Sens Environ* 112:1337–1346
- Schaaf CB, Gao F, Strahler AH, Lucht W, Li XW, Tsang T, Strugnell NC, Zhang XY, Jin YF, Muller JP, Lewis P, Barnsley M, Hobson P, Disney M, Roberts G, Dunderdale M, Doll C, d'Entremont RP, Hu BX, Liang SL, Privette JL, Roy D (2002) First operational BRDF, albedo nadir reflectance products from MODIS. *Remote Sens Environ* 83:135–148
- Sellers PJ, Meeson BW, Hall FG, Asrar G, Murphy RE, Schiffer RA, Bretherton FP, Dickinson RE, Ellingson RG, Field CB, Huemmrich KF, Justice CO, Melack JM, Roulet NT, Schimel DS, Try PD (1995) Remote sensing of the land surface for studies of global change – models, algorithms, experiments. *Remote Sens Environ* 51:3–26
- Shi Q, Liang S (2013) Characterizing the surface radiation budget over the Tibetan Plateau with ground-measured, reanalysis, and remote sensing datasets. Part 2: spatiotemporal analysis. *J Geophys Res-Atmos* 118:8921–8934
- Shuai YM, Masek JG, Gao F, Schaaf CB (2011) An algorithm for the retrieval of 30-m snow-free albedo from Landsat surface reflectance and MODIS BRDF. *Remote Sens Environ* 115:2204–2216
- Steffen K, Box J (2001) Surface climatology of the Greenland ice sheet: Greenland climate network 1995–1999. *J Geophys Res-Atmos* 106:33951–33964
- Stroeve J, Box JE, Gao F, Liang SL, Nolin A, Schaaf C (2005) Accuracy assessment of the MODIS 16-day albedo product for snow: comparisons with Greenland in situ measurements. *Remote Sens Environ* 94:46–60
- Stroeve J, Box JE, Wang Z, Schaaf C, Barrett A (2013) Re-evaluation of MODIS MCD43 Greenland albedo accuracy and trends. *Remote Sens Environ* 138:199–214
- Wang D, Liang S (2010) Using multiresolution tree to integrate MODIS and MISR-L3 LAI products. In: Geoscience and remote sensing symposium (IGARSS), 2010 IEEE International, pp 1027–1030
- Wang S, Trishchenko AP, Khlopenkov KV, Davidson A (2006) Comparison of International Panel on Climate Change Fourth Assessment Report climate model simulations of surface albedo with satellite products over northern latitudes. *J Geophys Res* 111, D21108. doi:[10.1029/2005JD006728](https://doi.org/10.1029/2005JD006728)
- Wang D, Morton D, Masek J, Wu A, Nagol J, Xiong X, Levy R, Vermote E, Wolfe R (2012a) Impact of sensor degradation on the MODIS NDVI time series. *Remote Sens Environ* 119:55–61
- Wang Z, Schaaf CB, Chopping MJ, Strahler AH, Wang J, Roman MO, Rocha AV, Woodcock CE, Shuai Y (2012b) Evaluation of Moderate-resolution Imaging Spectroradiometer (MODIS) snow albedo product (MCD43A) over tundra. *Remote Sens Environ* 117:264–280
- Wang D, Liang SL, He T, Yu Y (2013) Direct estimation of land surface albedo from VIIRS data: algorithm improvement and preliminary validation. *J Geophys Res-Atmos* 118:12,577–12,586
- Wikle CK (2003) Hierarchical models in environmental science. *Int Stat Rev* 71:181–199
- Xiong XZ, Stammes K, Lubin D (2002) Surface albedo over the Arctic Ocean derived from AVHRR and its validation with SHEBA data. *J Appl Meteorol* 41:413–425
- Xu BQ, Cao JJ, Hansen J, Yao TD, Joswia DR, Wang NL, Wu GJ, Wang M, Zhao HB, Yang W, Liu XQ, He JQ (2009) Black soot and the survival of Tibetan glaciers. *Proc Natl Acad Sci U S A* 106:22114–22118
- Yang FL, Mitchell K, Hou YT, Dai YJ, Zeng XB, Wang Z, Liang XZ (2008) Dependence of land surface albedo on solar zenith angle: observations and model parameterization. *J Appl Meteorol Climatol* 47:2963–2982

- Yue W, Zhu J (2006) On estimation and prediction for multivariate multiresolution tree-structured spatial linear models. *Stat Sin* 16:981–1020
- Zhang XT, Liang SL, Wang KC, Li L, Gui S (2010) Analysis of global land surface shortwave broadband albedo from multiple data sources. *IEEE J Select Top Appl Earth Observations Remote Sens* 3:296–305
- Zhu J, Yue W (2005) A multiresolution tree-structured spatial linear model. *J Comput Graph Stat* 14:168–184
- Zhu XL, Chen J, Gao F, Chen XH, Masek JG (2010) An enhanced spatial and temporal adaptive reflectance fusion model for complex heterogeneous regions. *Remote Sens Environ* 114:2610–2623
- Zhu XF, Liang SL, Pan YZ, Zhang XT (2011) Agricultural irrigation impacts on land surface characteristics detected from satellite data products in Jilin Province, China. *IEEE J Select Top Appl Earth Observations Remote Sens* 4:721–729

Chapter 14

Observing the Response of Terrestrial Vegetation to Climate Variability Across a Range of Time Scales by Time Series Analysis of Land Surface Temperature

Massimo Menenti, H. R. Ghafarian Malamiri, Haolu Shang, Silvia M. Alfieri, Carmine Maffei, and Li Jia

Abstract Satellite observations of the terrestrial biosphere cover a period of time sufficiently extended to allow the calculation of a reliable climatology. The latter is particularly relevant for studies of vegetation response to climate variability. Observations from space of the land surface are hampered by clouds at shorter wavelength and affected by water in the atmosphere in the microwave range. Both polar orbiting and geostationary satellites have a revisit frequency high enough to allow for some redundancy relative to the processes being observed, so that time

M. Menenti • H. Shang

Department of Geoscience and Remote Sensing, Faculty of Civil Engineering, Delft University of Technology, Delft, The Netherlands

Institute of Remote Sensing and Digital Earth (RADI, CAS), Beijing, China

e-mail: m.menenti@tudelft.nl; H.Shang@tudelft.nl

H.R.G. Malamiri

Department of Geoscience and Remote Sensing, Faculty of Civil Engineering, Delft University of Technology, Delft, The Netherlands

Yazd University, Yazd, Iran

e-mail: hrghafarian@yazd.ac.ir

S.M. Alfieri

Department of Geoscience and Remote Sensing, Faculty of Civil Engineering, Delft University of Technology, Delft, The Netherlands

Institute for Mediterranean Agricultural and Forest Systems (ISAFOM), Naples, Italy

e-mail: silvia_alfieri@tiscali.it

C. Maffei

Department of Geoscience and Remote Sensing, Faculty of Civil Engineering, Delft University of Technology, Delft, The Netherlands

e-mail: C.Maffei@tudelft.nl

L. Jia

Institute of Remote Sensing and Digital Earth (RADI, CAS), Beijing, China

e-mail: jiali@radi.ac.cn

series where a fraction of observations are removed and the resulting gaps filled are still very useful to monitor land surface processes. Two examples illustrate this concept in two different spectral regions: Thermal Infrared (TIR) and observations of land surface temperature to study the thermal behavior of the land surface in response to weather and climate and 37 GHz observations of the polarization difference in brightness temperature to retrieve the fractional abundance of water-saturated soil. Three applications of time series of land surface temperature are presented: (a) monitoring of spectral thermal admittance of the land surface; (b) estimation and mapping of air temperature and (c) monitoring of thermal load to assess the risk of forest fires.

Two methods were applied to identify and remove anomalous observations (outliers) and to fill the resulting gaps: Harmonic ANalysis of Time Series (HANTS) and the Multichannel Singular Spectrum Analysis (M-SSA). The HANTS algorithm has been widely used to reconstruct time series of Normalized Difference Vegetation Index (NDVI), Leaf Area Index (LAI), Land Surface Temperature (LST) as well as the polarization difference brightness temperature (PDBT) during the past 20 years to remove random noise or eliminate cloud/snow contamination. The M-SSA, an advanced methodology for time series analysis, was utilized to reconstruct gap-free LST time series using both the spatial and the temporal information content in the data set.

14.1 Introduction

The Earth's surface and atmosphere form a complex and dynamic system in which matter and energy are continuously exchanged at different time scales. Observations of the exchange of available energy between the land surface and the atmosphere (i.e. the latent and sensible heat flux) are important to understand land surface processes, to evaluate parameterization schemes in weather and climate models, water resource management, and for agricultural applications such as irrigation scheduling (Bowen 1926; Penman 1948; Monteith 1965; Priestley and Taylor 1972; Brutsaert 1982; Morton 1983; Menenti 1984; Famiglietti and Wood 1994; Su and Menenti 1999).

The Fast Fourier transform (FFT) and HANTS have been developed and applied to time series of satellite observations, e.g. NDVI and Land Surface Temperature, to study vegetation phenology and land surface climate (Menenti et al. 1993, 2010; Verhoef 1996; Roerink and Menenti 2000; Julien et al. 2006; Jia et al. 2011; Moody and Johnson 2001; Roerink et al. 2000, 2003; Alfieri et al. 2013). In contrast to the FFT which uses all observations regardless of quality, HANTS identifies and removes outliers in data samples.

A global study of the accuracy of HANTS in the reconstruction of NDVI time series has been completed by (Zhou et al. 2015). The overall reconstruction error was divided into gaps-related error and fitting method-related error.

A 3 year time series (2008–2010) of gap-free daily and hourly Land Surface Temperature (LST) and actual evaporation derived from geostationary data collected by the Fengyun-2C (FY-2C) satellite was reconstructed for a large area including the Qinghai – Tibet Plateau and the surrounding river basins (Faivre 2014; Ghafarian 2015). Hourly LST observations, estimated from radiometric data acquired by the Single channel Visible and Infrared Spin Scan Radiometer (S-VISSR) sensor onboard the FY-2C Chinese geostationary satellite have been used to construct a gap- and cloud-free data set which covers the whole Tibetan Plateau from 2008 through 2010 with a 5×5 km spatial resolution. Multi-channel Singular Spectrum Analysis (M-SSA), an advanced methodology for time series analysis, has been utilized to reconstruct LST time series.

Due to the revisit frequency and swath width of microwave radiometers on polar orbiting satellites, time series of passive microwave data will have gaps of 3–5 days. To make a consistent daily time series, we need some statistical methods, such as a moving window filter, to fill these observation gaps. In addition, the effects of rain drops on microwave ground surface observations at 37GHz are not negligible. Geo-location and resampling introduce random errors in the conversion from swath brightness temperature to the gridded data. Radiometric noise, such as the reference warm-up, also has an additional and unpredictable impact on observed BT. Erroneous observations need therefore to be identified and removed. In this case, we applied the Harmonic ANalysis of Time Series algorithm (HANTS) (Menenti et al. 1993; Roerink et al. 2000; Verhoef 1996) to fill gaps and remove noisy samples.

14.2 Material and Methods

14.2.1 Modeling and Reconstruction of Cloud-Free LST Time Series

14.2.1.1 HANTS Algorithm

HANTS algorithm was proposed by Verhoef (1996) to fill the missing or cloudy observations and eliminate the outliers in time series data with periodic behaviour. HANTS algorithm is based on the concept of discrete Fourier transform (Menenti et al. 1993; Verhoef 1996; Roerink and Menenti 2000; Verhoef et al. 1996) to model time series of satellite data.

A temporal sequence of N observations y_i , $i = 1$ to N can be described by a Fourier series as:

$$y_i = a_0 + \sum_{j=1}^M a_j \cos(\omega_j t_i - \varphi_j) \quad (14.1)$$

where ω_j is the frequency of j^{th} harmonic term in the Fourier series, t_i is the time at which the i^{th} sample was taken, M is the number of frequencies of the Fourier series ($M <= N$), a_j and φ_j are the amplitude and the phase of the j^{th} harmonic term respectively. Because the zero frequency has no phase, the amplitude related to the zero frequency, a_0 , is equal to the average of all N observations of y . The harmonic frequencies are a base frequency (i.e. $\omega_1 = 2\pi/N$) and all integer (i.e. $i = 1$ to N) multiples of the base frequency:

$$\omega_i = (2\pi/N) \times i, \text{ where } i = 1, 2, \dots, N$$

In the HANTS algorithm after selecting the number of frequencies (M) and the frequencies (ω_j), the unknown parameters of the Fourier series are the amplitudes a_j and the phase φ_j values, which are determined by fitting the time series of observations.

In order to create a reliable model of the signal with HANTS, there are multiple parameters that should be defined by users:

1. Valid data range: the acceptable range of observed values. The observations out of this range are removed at the first stage by assigning zero weight to them.
2. Period: number of time samples in each periodic component in the Fourier series.
3. Number Of Frequencies (NOF): the number of harmonic terms. NOF determines the amount of detail that can be captured in the reconstructed signal. Low NOF creates a smoother signal than a high NOF value. The number of frequencies is counted from the base period onwards (numbered one).
4. Direction of outliers: indicates the direction of outliers with reference to the current model of the signal. For example, cloud contamination causes lower LST values, therefore, the direction of outliers should be selected as low when applying the HANTS algorithm to LST data.
5. Fit Error Tolerance (FET): specifies which absolute deviation from the current curve in the selected direction is still acceptable. After each iteration, observations that have a deviation greater than FET are set as outliers and removed from the calculation by assigning a zero weight to them. Iterations stop when the deviation of all remaining observations becomes smaller than FET.
6. Degree of Over Determinedness (DOD): minimum number of extra data points which have to be used in curve fitting. The number of valid observations must always be greater than the number of parameters required to describe the signal ($2 \times \text{NOF}-1$). In order to get a reliable result more data points than the necessary minimum should be included which is indicated by DOD. The iteration is terminated if the number of remaining points becomes less than $\text{DOD} + 2 \times \text{NOF}-1$, if it was not already terminated because the FET criterion was met.

The HANTS algorithm was designed to execute two tasks: (i) identifying and removing outliers and cloudy observations, and (ii) gap-filling of the remaining valid observations by temporal interpolation. Besides that, HANTS can be used

to decompose a periodic time series into the significant periodic components that describe the time series. HANTS handles the Fourier analysis as a curve fitting problem using a weighted least squares solution. In the HANTS algorithm, each observation in the time series is assigned a weight of one or zero for good and bad (outliers) data, respectively. In order to find outliers and cloud contaminated observations, HANTS performs the curve fitting iteratively. In the first step, the least square curve fitting is performed using all data in the series. In the second step, observations are compared to the curve determined in the 1st iteration. Observations that deviate more than a pre-defined threshold are removed by assigning a zero weight to them. The remaining data are used to compute the least square curve fitting again, and the outliers are identified and removed again using the same threshold as in the first step. This iteration procedure is repeated until either all the remaining observations are within the pre-defined threshold or the number of remaining data becomes less than the number of parameters by which the curve is described (or < DOD).

14.2.1.2 Multi-channel Singular Spectrum Analysis (M-SSA)

The workflow of the SSA algorithm is illustrated as follows based on (Musial et al. 2011):

Step 1: A single scalar time series $F(t); t = 1, 2, \dots, n$ is embedded into a multidimensional trajectory matrix of lagged vectors $X = [f_1, \dots, f_k]$ where $k = n - m + 1$ and each lagged vector is defined as $X_j = (f_j, \dots, f_{j+m-1}); j = 1, \dots, k$. This trajectory matrix contains the complete record of patterns present within a time window of size $(m; m < n)$. Increasing the window size increases the spectral coverage of SSA and more information about the basic pattern of the time series will be captured, while decreasing the window size enhances the statistical confidence of the final results (Elsner and Tsonis 1996), since the structure of a time series will be captured repeatedly (Ghil et al. 2002). The final form of the trajectory matrix X is a rectangular matrix of the form:

$$X = \begin{pmatrix} f_1 & f_2 & f_3 & \dots & f_k \\ f_2 & f_3 & f_4 & \dots & f_{k+1} \\ f_3 & f_4 & f_5 & \dots & f_{k+2} \\ \dots & \dots & \dots & \dots & \dots \\ f_m & f_{m+1} & f_{m+2} & \dots & f_n \end{pmatrix} \quad (14.2)$$

Step 2: The next step is the decomposition of the trajectory matrix X of size $m \times k$ using the Singular Value Decomposition (SVD) method which yields:

$$X = DLE^T \quad (14.3)$$

where D and E are left and right singular vectors of X with $m \times m$ and $k \times k$ size respectively, and L is a rectangular diagonal matrix of size $m \times k$. The elements of L , called singular values, are the square roots of the eigenvalues of the lagged covariance matrix $S = XX^T$ of size $m \times m$. The lagged covariance matrix is a symmetric matrix (i.e. $S = S^T$), and the elements of S are proportional to the linear correlation between all pairs of snapshots (patterns appearing in the m -window). The columns of matrix D are the eigenvectors of S also known as Empirical Orthogonal Functions (EOFs). The rows of E^T are eigenvectors of matrix $X^T X$. If the time series is naturally periodic and corresponding eigenvalues have high covariance elements along the diagonal values of the lagged-covariance matrix, the eigenvectors will include the periodic components of the time series, but this is not the case for aperiodic time series. Since periodic patterns in the time series will result in some segments being in phase and others out of phase, high covariance elements aligned along the diagonals of the lagged covariance matrix S will indicate oscillations in the time series (Elsner and Tsonis 1996). If we plot the singular values in descending order, one can often distinguish between an initial steep slope, representing a signal, and a (more or less) flat floor, representing the noise level (Vautard et al. 1992). Then any subset of d eigenvectors (EOFs), $1 \leq d \leq m$, for which the related eigenvalues are positive provides the best representation of the matrix X as a sum of matrices X_i , $i = 1, 2, \dots, d$ (Golyandina et al. 2001).

Step 3: Partitioning d eigentriples into p distinct subsets and then summing all the components inside each subset so that

$$X = \sum_{n'=1}^p X_{I_{n'}} \text{ where, } X_{I_{n'}} = \sum_{i \in I_{n'}} X_i \quad (14.4)$$

The matrices $X_{I_{n'}}$ have the form of a Hankel matrix (a square matrix in which the positive diagonal elements are constant) in an ideal case and consequently fit the trajectory matrices.

Step 4: Since the ideal case described in step 3 is not usually the case, the $X_{I_{n'}}$ matrices should be transformed into the form of a Hankel matrix to fit the trajectory matrices. This step is known as diagonal averaging. In this sense, the original matrix can be reconstructed as the sum of these matrices.

$$x_t = \sum_{n'=1}^p x_t^{n'}, t = 0, 1, \dots, n-1 \quad (14.5)$$

where for each p , the series $x_t^{n'}$ is the result of the diagonal averaging of the matrix $X_{I_{n'}}$.

The multi-channel SSA (M-SSA) is an extension of SSA that is used when time series of maps exist (e.g. our time series of hourly LST maps) (Broomhead and King 1986b). In this context, M-SSA utilizes an L number of spatial time profiles ($L \leq m$, where m is the window size chosen in SSA) and uses the Spatial information

(i.e. a few leading S-PCA components of spatial time series) along with Temporal information (T-PCA) to reconstruct the time series more accurately especially where the gaps are long.

If we have more than one time series of given observations, X_{li} , where $i = 1, 2, \dots, N$ and $l = 1, 2, \dots, L$; the generalization of SSA to construct the multi-variable lagged covariance matrix (T) will be as follows:

$$T = \begin{bmatrix} T_{1,1} & T_{1,2} & \cdots & T_{1,L} \\ T_{2,1} & T_{2,2} & \cdots & \\ \vdots & \vdots & \ddots & \\ T_{L,1} & T_{L,2} & \cdots & T_{L,L} \end{bmatrix} \quad (14.6)$$

where $T_{l,l'}$ is the lagged-covariance matrix between channel l and l' . The $T_{l,l}$ is the same as S for single channel SSA with just one time series with $l=1$. By diagonalizing matrix T , $L \times m$ eigenvectors and eigenvalues of matrix T are calculated by M-SSA. Each eigenvector (E^k), which is called Space-Time Principal Components (ST-PCs), consists of L successive m -long segments. As with SSA, by selecting p ST-PCs, the original time series can be reconstructed.

The (M)-SSA software, manuals and help can be freely downloaded from the following website: <http://web.atmos.ucla.edu/tcd/ssa/guide/guide4.html> (Ghil et al. 2002).

14.2.2 Downscaling and Estimation of Air Temperature

The SINTESI approach (Alfieri et al. 2013) is a procedure developed to map air temperature at fine spatial resolution by combining the LST observed by satellite and Ta data at a reference location. SINTESI is structured in several steps including preprocessing of the LST time series image-data to identify missing data and outliers and to fill the resulting gaps (see Sect. 14.2.1). These steps include: the evaluation of the temporal stability of LST spatial patterns, determination of the relationships between near-surface Ta and LST and finally the combination of the model of the time series of normalized LST with the regression Ta vs LST to obtain $Ta(x,y,t)$ as a function of $LST(x_0,y_0,t)$.

Spatial variability is normalized to a reference location by the construction of the time series of the ratio of $LST(x,y,t)$ to the LST at the reference location $LST(x_0,y_0,t)$, with x and y as the East and North coordinates respectively and t the time. The result is the pixel-wise ratio r :

$$r(x,y,t) = \frac{LST(x,y,t)}{LST(x_0,y_0,t)} \quad (14.7)$$

The choice of the reference location is arbitrary provided $r(x,y,t)$ is stationary and can be modeled by maps of the Fourier coefficients. The choice of the reference location changes the value of the ratio $r(x,y,t)$ but does not change the value of $LST(x,y,t)$.

The temporal stability of the pixel-wise ratio is evaluated using harmonic analysis. Fourier analysis is used to decompose the ratio $r(x,y,t)$ in three periodic signals with periods respectively 365, 180 and 120 days by means of HANTS (see Sect. 14.2.1.1). The r time series are processed by Fourier analysis on a yearly basis. For each frequency the amplitude and phase of the sine and cosine functions are determined. The inter-annual stability of the spatial pattern is evaluated on the basis of the inter-annual variability of the Fourier coefficients (amplitudes).

Mapping of Ta at fine spatial resolution can be done by determining the relationship between LST and air temperature. The relationship between the Ta measured at the available stations within a study area and LST is established by linear regression analysis:

$$Ta = LST \times m_i + n_i \quad (14.8)$$

where subscript i refers to a ground (meteorological) station. A single regression equation with coefficients m and n for the entire study area, estimated by averaging m_i and n_i , may be used in some cases. When aiming at the estimation of Ta over a period of time when no satellite observations of LST are available, the inverse regression is required at the reference location:

$$LST(x_0, y_0, t) = \frac{1}{m_0} \times Ta(x_0, y_0, t) - n_0 \quad (14.9)$$

where subscript 0 indicates the reference location. The result of this analysis are the parameters m , n , $1/m_0$ and $-n_0$. The Ta at each pixel location is estimated by:

$$Ta(x, y, t) = \left[\left(T_a(x_0, y_0, t) \times \frac{1}{m_0} - n_0 \right) \times r(x, y, t) \right] \times m + n \quad (14.10)$$

with $T_a(x_0, y_0, t)$ the air temperature at the reference location. In Eq. 14.7 the ratio r is calculated as:

$$r(x, y, t) = a_0 + \sum_{i=1}^{i=3} a_i \cos(2\pi f_i t_y) + b_i \sin(2\pi f_i t_y) \quad (14.11)$$

where,

$$a_i = \bar{A}_i \times \cos\left(\bar{\psi}_i \times \frac{\pi}{180}\right); b_i = \bar{A}_i \times \sin\left(\bar{\psi}_i \times \frac{\pi}{180}\right) \quad (14.12)$$

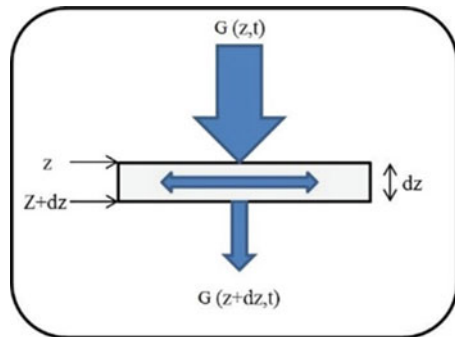
with \bar{A}_i and $\bar{\psi}_i$ being respectively the amplitude and phase of the i^{th} harmonic component averaged over the years spanning the analysed LST time series, once the inter-annual stability of the ratio r has been verified.

14.2.3 Time Series of LST Anomalies and Fourier Coefficients to Characterize Fire Occurrence and Size

The research focussed on the study area of Campania ($13,595 \text{ km}^2$), Italy and the results are presented later in this Chapter. The Italian Forest Corps (Corpo Forestale dello Stato) provided a dataset including more than 7700 fire records between 2000 and 2008. The data included date and time, coordinates, duration and extent of each event. A collection of daily Terra-MODIS LST data observed at approximately 10:30 am local time from 2000 to 2008 was used for this study. These data are publicly available at the Land Processes Distributed Active Archive Center (LP DAAC) hosted by the United States Geological Survey (USGS). Fourier series comprising three harmonics (365, 180 and 120 days) were fitted to the data with two different methods, to achieve two different purposes:

- HANTS (see Sect. 14.2.1.1) was executed on each yearly sequence of daily LST data separately, to reconstruct missing or cloudy data (Roerink and Menenti 2000; Roerink et al. 2000). The retrieved yearly images of Fourier coefficients (mean LST, amplitude and phase of the three harmonics) were masked on forest and natural areas and segmented into labelled classes. The number of fires and mean burnt area were then mapped using the fire records mentioned above, then the spatial patterns of both variables were compared with the probability given by a random null model (Bajocco and Ricotta 2007). This comparison indicates that fires are induced by external drivers.
- The algorithm was executed on the whole 2000–2008 dataset to construct daily maps of reference temperature (Azzali and Menenti 2000). Thermal anomalies (TA) were computed by subtracting the daily reference temperature from daily MODIS LST. Forest fires are expected to occur in areas where there has been a prolonged exposure to lack of rainfall and high air temperature. In these circumstances an LST anomaly is observed over a number of consecutive days. For this reason cumulated anomalies (CTA) were calculated as the sum of all the observed thermal anomalies from the day when the thermal anomaly was first recorded in the pixel up to the current day. Each fire in the database was then associated to the values of TA and CTA observed at each fire location on the day preceding the event.

Fig. 14.1 A soil slab at depth z



14.2.4 Monitoring of the Spectral Thermal Admittance of the Land Surface

Heat transfer takes place by three different processes, namely, conduction, convection and radiation. In a porous solid, conduction is the dominant process, while convection and radiation are usually negligible (Carslaw and Jaeger 1959). In this section, the general theory of heat conduction in the soil will be explained to define the spectral thermal admittance. As mentioned above, heat is mainly transported in soils by conduction. The analytical solution we applied to relate the amplitude of heat flux at the surface to the amplitude of surface temperature holds under the following assumptions:

1. Heat flow is one dimensional in the vertical direction.
2. No heat source or sink is present in the soil.

Under these conditions the heat flux density at depth z (Fig. 14.1) is directly proportional to the vertical temperature gradient at that depth:

$$G = -\lambda \left(\frac{\delta T}{\delta z} \right) \quad (14.13)$$

where G is the soil heat flux density (Wm^{-2}) (positive and downward if the temperature decreases with depth), λ is the thermal conductivity ($\text{Wm}^{-1}\text{K}^{-1}$) and $\delta T/\delta z$ is the temperature gradient (Km^{-1}). The amount of heat stored in the same slab per unit of time can be written as $\rho c(\delta T/\delta t)dz$. The ρc is the volumetric soil heat capacity and it is defined as the amount of heat required to increase by 1 K the temperature of a unit volume of soil and $\delta T/\delta t$ is the temperature change per unit time.

We assumed that no heat source or sink is present, so that the continuity equation reads:

$$\frac{\delta G}{\delta z} = -\rho c \frac{\delta T}{\delta t} \quad (14.14)$$

and by substitution of Eq. 14.13 in Eq. 14.14 we get:

$$\frac{\delta}{\delta z} \left(\lambda \frac{\delta T}{\delta z} \right) = \rho c \frac{\delta T}{\delta t} \quad (14.15)$$

Assuming constant λ and ρc in a soil slab, the vertical heat flow in the soil (Eq. 14.15) becomes:

$$\lambda \frac{\delta}{\delta z} \left(\frac{\delta T}{\delta z} \right) = \rho c \frac{\delta T}{\delta t} \quad (14.16)$$

$$\frac{\delta T}{\delta t} = \alpha \frac{\delta^2 T}{\delta z^2} \quad (14.17)$$

where $\alpha = \lambda/\rho c$ (m^2s^{-1}) is soil thermal diffusivity.

The Eq. 14.17 can be solved to obtain the soil temperature at any depth and time if the proper initial and boundary conditions are given (van Wijk and De Vries 1963; Carslaw and Jaeger 1959). In order to solve the Eq. 14.17 for a homogeneous semi-infinite soil, we need to define the boundary condition, i.e. if we assume a periodic surface temperature $T(0,t)$ at time t and depth $z = 0$:

$$T(0, t) = \bar{T} + A \sin(\omega t + \varphi) \quad (14.18)$$

where \bar{T} is the mean surface temperature, A is the amplitude of the surface temperature, φ is the phase and ω is the angular frequency ($2\pi/p$ and p is the period, i.e., $2\pi/86,400 = 7.27 \times 10^{-5} \text{ s}^{-1}$ for diurnal variation). The traveling wave solution of Eq. 14.17 can be sought with the boundary condition Eq. 14.18 (van Wijk and De Vries 1963; Horton and Wierenga 1983; Carslaw and Jaeger 1959) as:

$$T(z, t) = \bar{T} + A \exp(-z/d) \sin(\omega t + \varphi - z/d) \quad (14.19)$$

where d (m) is damping depth defined as:

$$d = \sqrt{\frac{2a}{\omega}} \quad (14.20)$$

When the soil heat flux passes through the soil surface, the change in LST and soil heat flux is not in phase and soil heat flux has a phase shift of $\pi/4$ relative to LST (i.e. G leads T by 3 h for diurnal cycle and 1.5 month for the annual cycle) (Carslaw and Jaeger 1959). The soil heat flux $G(z, t)$ for a sinusoidal variation of temperature can be obtained from Eqs. 14.13 and 14.19 as follows (Sellers 1965):

$$G(z, t) = A(\lambda\rho c\omega)^{1/2} \exp(-z/d) \sin\left(\omega t + \varphi - z/d + \frac{\pi}{4}\right) \quad (14.21)$$

The final relationship between soil heat flux and soil temperature is illustrated by (Menenti 1984) as follows:

$$G(z, t) = \lambda\gamma T(z, t) \quad (14.22)$$

The complex variable $\lambda\gamma$ can be written as:

$$\lambda\gamma = (\lambda\rho c\omega)^{1/2} \exp(i\pi/4) \quad (14.23)$$

$$\gamma = (1 + i) \left(\frac{\omega}{2\alpha} \right)^{1/2} \quad (14.24)$$

At the soil surface, the parameter $\lambda\gamma$ is defined as the thermal admittance y_0 ($\text{Wm}^{-2}\text{K}^{-1}$) at the frequency ω . The term $\exp(i\pi/4)$ accounts for the phase shift between flux and temperature waves of period P , while the modulus $(\lambda\rho c\omega)^{1/2}$ accounts for the ratio between surface amplitude of soil heat flux and LST (Eq. 14.25) (Menenti 1984).

The soil thermal admittance (y_0) can be determined as done by (Menenti 1984; Idso et al. 1976; Wang et al. 2010) as follows:

$$y_0 = \frac{\Delta G_0}{\Delta T_0} \quad (14.25)$$

where y_0 ($\text{Wm}^{-2}\text{K}^{-1}$) is the thermal admittance at the soil surface, ΔG_0 (Wm^{-2}) is the surface amplitude of soil heat flux and ΔT_0 (K) is the surface amplitude of land surface temperature. As defined above, the surface soil thermal admittance is the ratio between the amplitude of soil heat flux and soil surface temperature. The same relationship can be derived by Eqs. 14.19 and 14.21, now at any frequency ω and assuming again a semi – infinite homogenous soil, if we use just the amplitudes as follows:

$$y_0(\omega) = \frac{\Delta G_0}{\Delta T_0} = (\lambda\rho c\omega)^{1/2} \quad (14.26)$$

The spectral soil thermal admittance is defined as a set of observations of the apparent soil thermal admittance at multiple frequencies and conveys information about the soil thermal properties of different layers (Menenti 1984). We estimated the frequency dependent (spectral) soil thermal admittance of the entire Qinghai – Tibet Plateau using the 2008–2010 time series data on LST and G_0 . The Eqs. 14.19 and 14.21 assume a homogeneous semi-infinite soil whose surface is heated by a periodic (sinusoidal) heat flux that corresponds to the daily, annual or other significant periodic heating cycles. The soil surface temperature and soil heat flux variations are not a pure periodic function of time around a mean value (van Wijk and De Vries 1963), but yet the periodic model can be applied successfully to represent the time series by a series of harmonic functions at significant frequencies.

So if we have the amplitudes of soil heat flux and soil surface temperature at those frequencies, then we can obtain the thermal admittance at these frequencies.

It is necessary first to identify the most significant periodic components in a time series and then estimate the related amplitudes. As we deal with hourly LST time series to estimate the soil thermal admittance, we are interested in finding some harmonic components which may exist in the data over a rather wide spectral range.

In the Sect. 14.3.4, we will illustrate first the results of estimating the significant frequencies and then the amplitudes of G_0 and LST. Then we will estimate the Spectral Soil Thermal Admittance (SSTA) which is the variation of soil thermal admittance versus frequency.

14.2.5 Monitoring Flooded Area Using Time Series of the Polarization Difference Brightness Temperature (PDBT) at 37 GHz

The zero-order radiative transfer model (Kirdiashev et al. 1979; Wigneron et al. 1993) was simplified to retrieve the water saturated soil and standing water area from the PDBT data at 37GHz (Shang et al., 2012). The Vertical Brightness Temperature (VBT) data at 37GHz and NDVI data are the auxiliary data: the former is used to retrieve the land surface temperature (Holmes et al. 2009), and the latter one is used to retrieve the vegetation fractional area and vegetation transmission function (Shang et al. 2012). All these remote sensing data are full of observation gaps and contaminated by noisy samples and thus need to be preprocessed before they can be used in the simplified model.

14.2.5.1 Materials and Study Area

The PDBT and VBT observations at 37 GHz by the SSM/I, on board the Defense Meteorological Satellite Program (DMSP) F13 satellite, were used in this case. They have been calibrated and registered to the Equal-Area Scalable Earth Grid (EASE-Grid) with a spatial resolution of 25 km (Brodzik and Knowles 2002). The NDVI data were calculated from the MOD09A1 data product, which is the 8-day reflectance data with a spatial resolution of 500 m. The mean reflectance in the red and near-infrared bands was calculated for each 25 km EASE-Grid. The EASE-Grid NDVI is then calculated from these aggregated reflectance data.

The study area is the Poyang Lake, the largest lake in the Yangtze River Basin, which is located between 28.048° N to 29.384° N, and from 115.444° E to 117.007° E and includes 10 pixels area of EASE-Grid. There is a clear dry season from October to March and the flooding season is from April to September.

14.2.5.2 Time Series Analysis of the SSM/I and MODIS Data

The gaps are given a zero value, then the processing of the SSM/I data includes three steps:

1. Moving window filter: a moving window of 10 days, is applied to the original time series of PDBT and VBT, taking into account the 3–5 days gaps in the observations. The window size needs to be greater than the double of the maximum gap length. The maximum and minimum values within the window are eliminated and the valid observations are averaged to estimate the observation on the central day of each window, reducing the noise.
2. Fast Fourier Transform (FFT) algorithm: it calculates the Fourier Transform of the filtered time series. The power spectrum helps separate the surface signal at lower frequencies from the atmospheric signal, including precipitation, at higher frequencies.
3. Harmonic ANalysis of Time Series (HANTS) algorithm: it reconstructs the upper-envelop of the filtered time series and eliminates the remaining outliers.

The NDVI data are processed by applying the 3rd step only, with the significant components identified on the basis of vegetation phenology in the area observed.

14.2.5.3 Retrieve Flooded Area from PDBT Observations

To correct observations for the attenuation by vegetation, the zero-order radiative transfer model (Shang et al. 2012, 2015) was simplified by assuming that the single scatter albedo of vegetation canopy is the same for horizontal and vertical polarization and that the apparent sky brightness temperature is negligible compared with the surface brightness temperature. Then the PDBT at 37GHz (ΔT) can be expressed as:

$$\Delta T = T_s \times \Delta\epsilon \times [(1 - f_v) + f_v \times \delta] \quad (14.27)$$

$$\delta = \exp(-2\tau_0/\mu) \quad (14.28)$$

Where T_s is the surface brightness temperature; $\Delta\epsilon$ is the Polarized Effective Emissivity Difference (PEED); f_v is the fractional vegetation cover; δ is the vegetation transmission function; $\mu = \cos(\theta)$, θ is zenith view angle; τ_0 is the optical thickness of vegetation.

The PEED can be derived from Eq. 14.27, when the remaining variables, i.e. the land surface temperature, fractional vegetation cover and vegetation transmission function, are derived from auxiliary remote sensing data, as described in (Shang et al. 2012, 2015). The fractional Water Saturated Soil (WSS) and standing water area, f_{ss} , can be derived from the PEED, $\Delta\epsilon$, as:

$$f_{ss} = (\Delta\varepsilon - \Delta\varepsilon_{dry}) / (\Delta\varepsilon_{sat} - \Delta\varepsilon_{dry}) \quad (14.29)$$

where $\Delta\varepsilon_{dry}$ and $\Delta\varepsilon_{sat}$ are the PEED of a completely dry soil and water saturated soil respectively. Their derivation can be found in (Shang et al. 2012, 2015). $\Delta\varepsilon_{sat}$ has the same value as that of water, thus the fractional area in Eq. 14.29 represents the sum of the WSS and standing water.

14.3 Results

14.3.1 Modeling and Reconstruction of Cloud-Free LST Time Series

The SSA technique was applied to hourly observations by the FY – 2C S-VISSL to reconstruct the LST diurnal variation over a period of time. As described in Sect. 14.2.1.2, window size (m) and main SSA dominant modes (d) are the two main parameters of SSA. To select the optimum window size and the number of relevant periodic components we used ground measurements with a 10 min sampling time during January 2008 with a total 4464 measurements. This is because we need error- and gap-free data to evaluate the impact of different window sizes and of periodic components on the accuracy of the reconstructed time series. Cross-validation is then used to determine the optimum number of leading SSA dominant modes and the window size. We created some artificial gaps in the ground measurements and then applied SSA with different window sizes and number of components to the gappy data. The R-squared (R^2) metric was applied to determine the optimum SSA parameters.

Figure 14.2a shows that by increasing the Number of component (No.com) from 7 to 28, the R^2 increased from 89.43 to 91.26 %: given the limited improvement in accuracy at the price of a much higher computation time, we selected 7 as the number of components. A similar test led to selection of the optimum window size and as Fig. 14.2b shows, the optimum window size is 432 which is equal to 3 days or 72 h. These values (7 as No.com and 72 h as window size) were then used as main SSA parameters to reconstruct the hourly time series of FY – 2C LST observations.

14.3.1.1 Removal of Positive and Negative Outliers

The existence of outliers (negative and positive) besides gaps imposes additional challenges in the reconstruction of LST time series. Hourly LST time series observed from space appear as a combination of slow, periodic signal components, e.g. daily and yearly, and faster changes, which often appear as random, unpredictable events (noise), as due to random errors in the observations. By modeling the time series using the selected signal components, the outliers can be removed (see

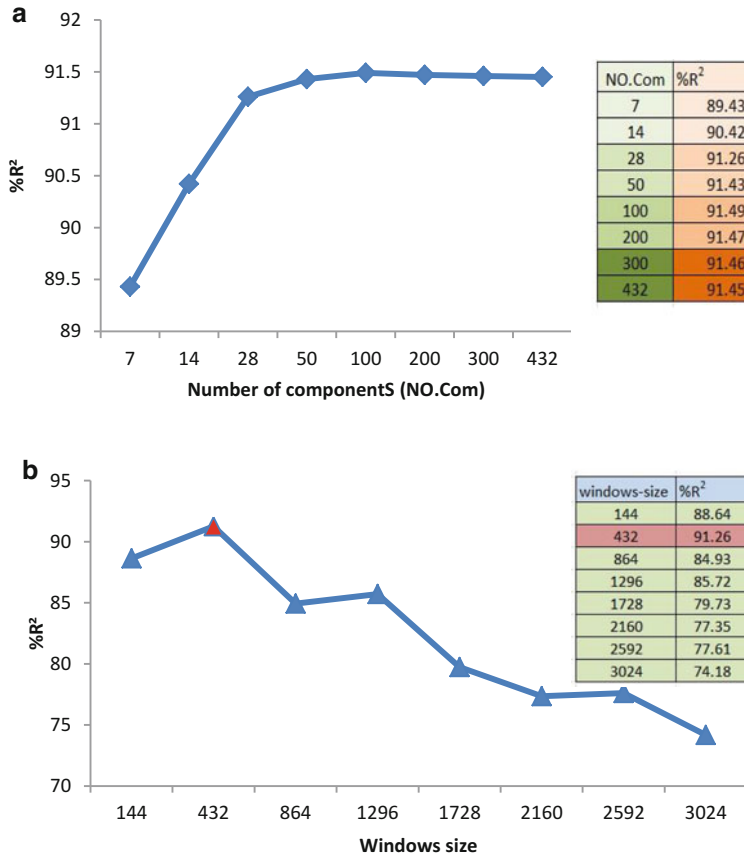


Fig. 14.2 (a) Correlation coefficient of estimated and observed LST as a function of the number of components, (b) Correlation coefficient of estimated and observed LST as a function of the windows size (right)

Fig. 14.3). Neither SSA nor M-SSA allow the direct identification and removal of outliers, so we adopted an alternate approach. We first applied M-SSA to the original LST time series and estimated the reconstructed time series (Fig. 14.4, green line) and determined the absolute differences between the original values and the ones given by the reconstructed time series.

Outliers in a LST time series appear as clearly lower values. The latter is most likely due to clouds: taking into account a lapse rate of about 10 K km^{-1} , we set 10 K as a threshold to identify outliers. By replacing cloud – contaminated observations with zero, these were excluded in the reconstructed time series. Then we applied again M-SSA on the new time series and the results show that the reconstructed time series gets much closer to the valid observations in the original data (Fig. 14.4, red line).

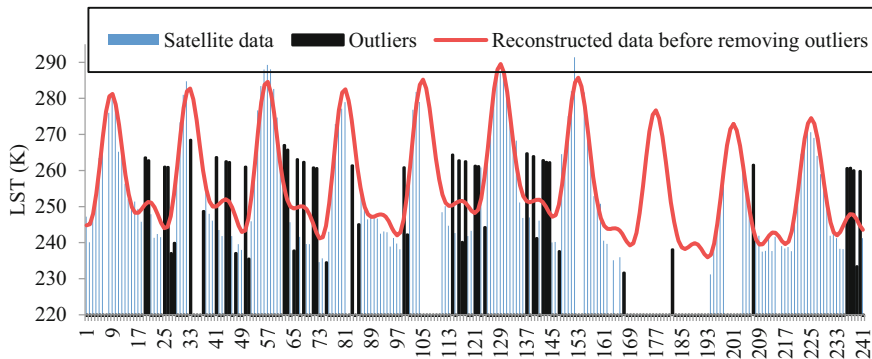


Fig. 14.3 Outliers removal and reconstruction using M-SSA

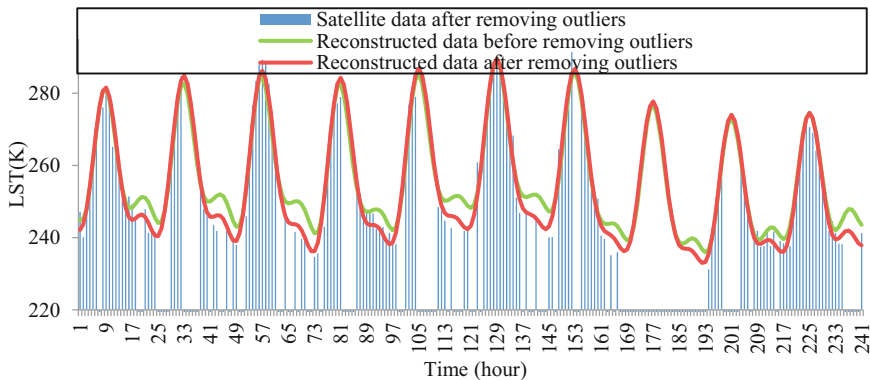


Fig. 14.4 Reconstruction of LST before and after outliers removal

14.3.1.2 Validation of SSA Using Ground Measurement of LST

We evaluated the performance of our reconstruction method by applying the cross-validation method, by creating some randomly distributed gaps in the time series and then comparing the reconstructed with the original observations. This was again done using a gap-free time series of LST ground measurements at the Nagqu station (165257.0112°N, -279574.1757°E) in January 2008.

We identified the outliers using HANTS (see Sect. 14.2.1.1), then imposed the same gaps on the time series of ground measurements. Then SSA was applied on the gapped ground measurements and the reconstructed time series was compared with the actual data. In Fig. 14.5, the red areas show the gaps while the blue areas belong to actual ground measurements. The black line shows the result of applying SSA to fill the gaps: even with 63 % of gaps, we obtained $R^2 = 0.83$ with Mean Absolute Error (MAE) = 2.25 Kelvin.

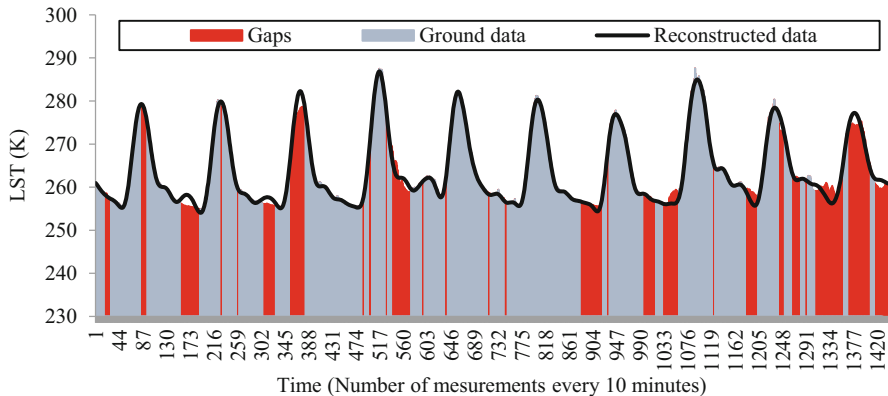


Fig. 14.5 Validation of SSA gap-filling using ground measurements with the same pattern of gaps as in the FY – 2C observations

14.3.2 Downscaling and Estimation of Air Temperature

The SINTESIS approach described in Sect. 14.2.2 has been applied to the Valle Telesina area (20,000 ha), a complex landscape located in Southern Italy using two sets of meteorological data: daily meteorological measurements at four ground stations (period 2000–2010); daily meteorological data available for the period from 1950 onwards gridded at $35\text{ km} \times 35\text{ km}$ resolution and derived by kriging with external drift method (Esposito 2010). The SINTESIS approach was used to downscale these gridded data on Ta to a finer $1\text{ km} \times 1\text{ km}$ grid using MODIS LST time series.

The spatial pattern of LST on any given day was characterized by the ratio r of LST image to the LST at the position of the node 1221 (San Salvatore Telesino), using reconstructed surface temperature values. Intra-annual variability cannot be neglected although its inter-annual trend seems to be stable. Here we only show the summer and winter patterns of a representative year (2007) compared with the anomalous year 2003 (Fig. 14.6). Summer and winter spatial fields of the ratio r calculated over the remaining years present similar patterns.

Harmonic analysis was applied to the LST time series for each year separately in order to obtain a quantitative estimation of the inter-annual variability of the yearly, half yearly and seasonal periodic components of the r signal. The inter-annual variability of the pixel-wise ratio r has been evaluated by statistics of the yearly mean value A_0 and of the amplitudes A_1, A_2, A_3 of components with periods of 365, 180 and 120 days obtained by Fourier analysis. We have then evaluated the contributions δr_i to the total error on r (x,y,t) due to assuming constant values of A_0, A_1, A_2 and A_3 (Table 14.1). We have taken $\delta r_0 = \sigma_{A0}/A_0$ and $\delta ri = \sigma_{Ai}/(A_0 + \bar{A}_i)$ (A_0 is the yearly average of r and A_i is the amplitude of the i^{th} component of the Fourier series with $i \neq 0$). This gives an estimation of the contribution to the total

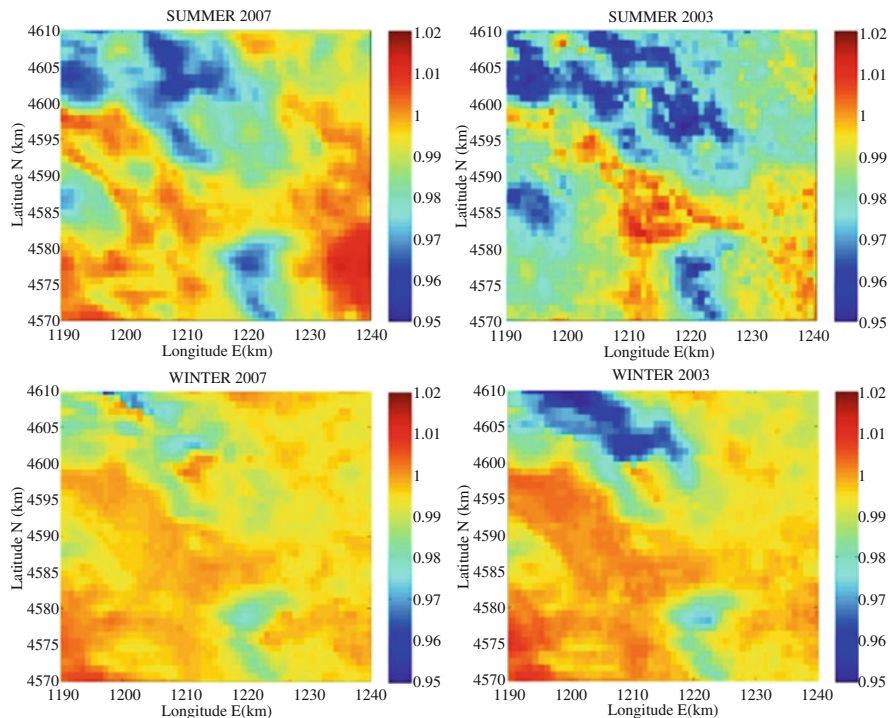


Fig. 14.6 Spatial pattern of the winter and summer average of the daily ratio r in 2003 and 2007

Table 14.1 Comparison of the statistics (mean (\bar{A}_i), standard deviation (σ) and coefficient of variation (δr_i) of the mean ratio r and harmonic amplitudes calculated over the period 2001–2010

	Statistics over 2001–2010				Statistics leaving out 2003			
	Period in days				Period in days			
	A_0	$365 (A_1)$	$180 (A_2)$	$120 (A_3)$	A_0	$365 (A_1)$	$180 (A_2)$	$120 (A_3)$
$A_i (\times 10^2)$	98.96	0.72	0.49	0.36	99.06	0.62	0.37	0.32
$\sigma (\times 10^2)$	0.31	0.32	0.35	0.14	0.09	0.10	0.07	0.09
$\delta r_i (\%)$	0.31	0.32	0.35	0.14	0.10	0.10	0.07	0.09

relative error we introduced when assuming inter-annual stability of the ratio r , i.e. assuming constant values of A_0 , A_1 , A_2 and A_3 .

The total relative error has been calculated as $\delta r = \sum_{i=0}^{i=3} \delta r_i$ using the statistics over the period 2001–2010 and then over the same period but leaving out 2003. In the former case we obtained $\delta r = 1.1\%$ and in the latter $\delta r = 0.3\%$. On the basis of these findings we considered negligible the inter-annual variability of the annual evolution of the ratio r . Then we can construct a yearly time series of the ratio r ,

describing the spatial and intra-annual variability in any period of time, using the mean values of r and of the harmonic components over the period from 2001 to 2010.

The relationship between Ta data at the stations within the Valle Telesina area and MODIS LST observations has been determined by linear regression analysis. Daily values of maximum Ta and daytime MODIS LST were correlated for each station and for each year from 2001 till 2010. The coefficients R^2 were always greater than 0.83 and do not vary significantly across the stations. The largest variation has been observed at Guardia Sanframondi that is located at a higher altitude than the other stations. Considering these results as well as the impossibility to define a detailed spatial pattern of regression coefficients (because of the scarce availability of ground stations) we used a single relationship valid for the whole area under study ($m = 0.81$; $n = 59.41$).

The inverse relationship (LST vs Ta) was evaluated at the reference location (node 1221) giving the regression coefficients $1/m_0 = 0.87$ and $-n_0 = 38.81$.

In order to validate the proposed approach we evaluated using Eq. 14.10:

1. the $Ta(x, y, t)$ estimates over 2007–2009 (using the mean Fourier coefficients from 2000 to 2006) against available observations in the same period.
2. a set of data collected during the pre-MODIS period of time at ground stations within the MODIS image frame. Some of these stations are located outside the Valle Telesina area, although in the same physiographic region. These data were rather sparse both in time and in space because of the irregular operation of the stations.

In each case we compared estimated maximum daily Ta with the one measured at the available ground stations. We calculated the following statistics: RMSE, AME, mean and standard deviation of the differences between estimated and measured Ta (MR and STDR) and R^2 .

In case 1 (Table 14.2) RMSE values range between 1.98 and 3.33 K. Higher values were found for the Castelvenere and Guardia Sanframondi stations, although the mean deviation for Guardia is rather small, i.e. -0.25 K. The RMSE values for all the stations are consistent with the scientific literature, e.g. (Yan et al. 2009; Shen and Leptoukh 2011).

In case 2 (Table 14.3) we overestimated Ta, particularly during the winter, but the available observations span a very short period of time. For all stations, observations

Table 14.2 Statistics of case 1 (values in K). Error statistics of Ta estimates over 2007–2009 using the mean of the Fourier coefficients from 2000 to 2006 against Ta observations

	RMSE	AME	MR	STDR	R^2
Castelvenere	3.33	2.81	2.25	2.45	0.94
Teles	2.41	1.88	0.80	2.27	0.95
Guardia Sanframondi	3.30	2.78	-0.25	3.29	0.90
Solopaca	1.98	1.55	-0.20	1.97	0.95

Table 14.3 Statistics of case 2 (values in K). Error statistics of Ta estimates in different periods of time using the mean of the Fourier coefficients from 2001 to 2011

	RMSE	AME	MR	STDR	R ²
Castelvenere (1999–2000)	2.86	2.27	1.48	2.45	0.94
Solopaca (1999)	2.74	2.13	0.09	2.74	0.90
Bucciano (1984)	3.11	2.57	2.31	2.09	0.95
Piedimonte Matese (1984–1985)	4.9	3.93	3.03	3.85	0.92
Piedimonte Matese M.(1984–1985)	4.64	3.72	2.84	3.67	0.95

are available for just about one year, even in different years. Larger errors were observed for stations located at higher altitude, i.e. 523 m at Piedimonte Matese and 865 m at Piedimonte Matese Muto. The RMSE values found when using the same linear regression relationship for the entire area were slightly larger than when using station specific relationships. We have observed that both slope and intercept depend on elevation but it was not possible to parameterize such dependence on elevation with sufficient accuracy given the limited number of stations at higher elevation and the short record of observations. To some extent the difference between estimated and observed daily Ta is due to the quality of ground observations of air temperature.

14.3.3 Time Series of LST Anomalies and Fourier Coefficients to Characterize Fire Occurrence and Size

The mean annual temperature and the amplitudes of the three harmonics used in the analysis have an evident role in determining spatial patterns of fire occurrence (Tables 14.4, 14.5, 14.6, and 14.7). Among the phase components, fire occurrence shows clear spatial selectivity only against the first (Table 14.8, other tables not shown). Mean fire size shows unambiguous spatial selectivity solely in the amplitude of the second harmonic (Table 14.6).

Temperature anomalies (TA) and cumulated temperature anomalies (CTA) were evaluated against fire size by first calculating the conditional mean fire size observed when the TA (CTA) was larger than the considered value, and then plotting the calculated means against the values of anomaly (cumulated anomaly) used in the calculation. In a similar manner, the conditional proportion of large fires (larger than 16 ha, which is the 90th percentile in the study area) was evaluated against anomaly and cumulated anomaly.

Fire size appears to be related to daily thermal anomalies: with increasing values of the thermal anomaly, the expected mean fire size in all areas with thermal anomaly larger than that value increases (Fig. 14.7a). A similar pattern is observed with the conditional fraction of large fires (Fig. 14.7b). A wider dynamic range in fire size and fraction of large fires is observed when the same analysis is performed against CTA (Fig. 14.8a, b).

Table 14.4 Selectivity of fires' number and mean size for mean temperature classes

Mean LST classes (K)				
Class	Number of fires		Mean fire size (ha)	
<288	34	----	15.74	+++
288–289	47	----	7.09	+++
289–290	121	--	5.39	+
290–291	264	+++	7.34	+
291–292	494	+++	4.4	-
292–293	782	+++	4.23	-
293–294	904	+++	4.85	-
294–295	751	+++	3.99	--
295–296	560	-	5.52	+
296–297	279	----	4.81	+
297–298	127	----	9.67	+++
>298	41	----	4.79	+

Symbol “+” means class preference, “-” class avoidance. One symbol: selectivity non-significant. Two symbols: significant $P<0.05$. Three symbols: significant $P<0.01$

Table 14.5 Selectivity of fires' number and mean size for classes of amplitude of the first harmonic

Amplitude of the first harmonic (K)				
Class	Number of fires		Mean fire size (ha)	
<8	59	-	7.79	+
8–9	203	+	4.97	+
9–10	453	+++	5.8	+
10–11	984	+++	4.55	-
11–12	1242	+++	4.94	+
12–13	872	----	4.71	-
13–14	411	----	4.39	-
14–15	158	----	6.02	+
>15	22	----	27.05	+++

Symbol “+” means class preference, “-” class avoidance. One symbol: selectivity non-significant. Two symbols: significant $P<0.05$. Three symbols: significant $P<0.01$

14.3.4 Monitoring of Spectral Thermal Admittance

14.3.4.1 Finding the Most Significant Periodic Components in LST Time Series

The power spectrum $P(f)$ at frequency f is $p(f) = A(f)^2$ and it can be applied to identify significant periodic components in a time series (Fig. 14.9).

Figure 14.9a shows the actual LST signal for a pixel (having very few gaps in the original time series data) in the study area from the 1st of January 2008 until the 31st of December 2010. The power spectrum is shown in Fig. 14.9b. Since

Table 14.6 Selectivity of fires' number and mean size for classes of amplitude of the second harmonic

Amplitude of the second harmonic (K)				
Class	Number of fires		Mean fire size (ha)	
0–1	2083	+++	3.52	---
1–2	1723	+	6.01	+++
2–3	570	---	7.24	+++
>3	28	---	12.85	++

Symbol “+” means class preference, “–” class avoidance. One symbol: selectivity non-significant. Two symbols: significant $P<0.05$. Three symbols: significant $P<0.01$

Table 14.7 Selectivity of fires' number and mean size for classes of amplitude of the third harmonic

Amplitude of the third harmonic (K)				
Class	Number of fires		Mean fire size (ha)	
0–1	1486	+++	5.06	+
1–2	2450	+++	4.99	–
2–3	447	---	5.2	+
>3	21	---	4.88	+

Symbol “+” means class preference, “–” class avoidance. One symbol: selectivity non-significant. Two symbols: significant $P<0.05$. Three symbols: significant $P<0.01$

Table 14.8 Selectivity of fires' number and mean size for classes of phase of the first harmonic

Phase of the first harmonic (°)				
Class	Number of fires		Mean fire size (ha)	
<180	21	---	10.15	++
180–185	126	---	3.12	---
185–190	645	---	3.21	---
190–195	1438	+++	4.29	–
195–200	1329	+++	6.63	+++
200–205	623	++	5.28	+
205–210	193	+++	5.27	+
>210	29	+	6.9	+

Symbol “+” means class preference, “–” class avoidance. One symbol: selectivity non-significant. Two symbols: significant $P<0.05$. Three symbols: significant $P<0.01$

some of the components have very high power and some very low, the variations are not completely visible. Since we are attempting to find the most significant periodic components that have relatively higher power values than others, we first sorted all power values in descending order, then we normalized power values to the integral of the power spectrum. The first few higher values are the significant periodic components as shown in Fig. 14.9c: the most significant periods are 365 and 1 day(s) respectively with a total relative power of 82.5 %. We selected the

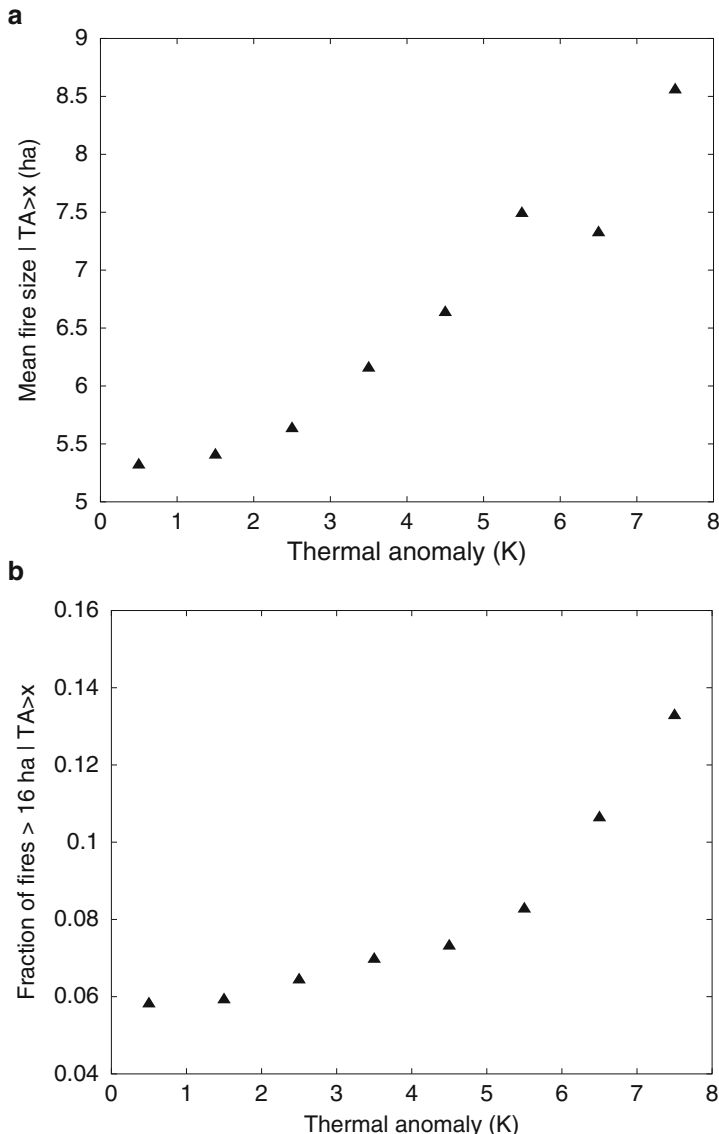


Fig. 14.7 (a) Relationship between conditional mean fire size and, (b) conditional fraction of large fires against values of thermal anomaly (TA) observed on the day preceding the event at the fires' locations

11 most important periods which account for 88.4 % relative power. They are the yearly, daily, 1252 h (1.74 months), 2190 h (~3 months), 2630 h (~3.65 months), 2920 h (~4 months), 3288 h (~4.5 months), 3757 h (~5 months), 4384 h (~6 months), 5260 h (~7 months) and 6576 h (~9 months).

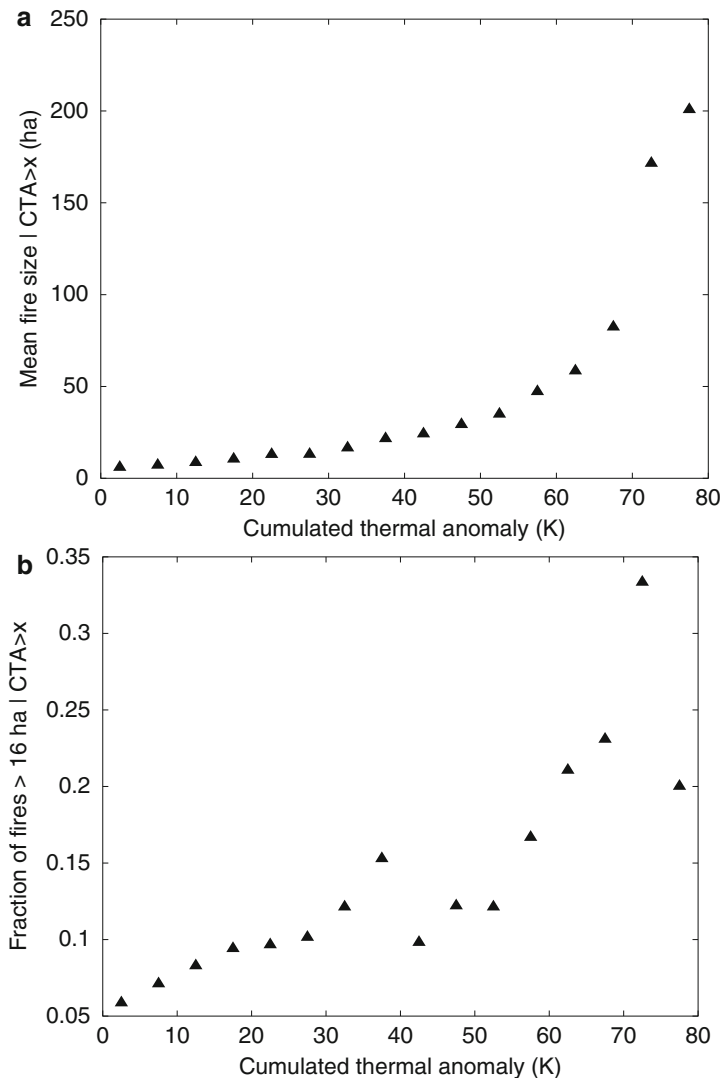


Fig. 14.8 (a) Relationship between conditional mean fire size and, (b) conditional fraction of large fires against values of cumulated thermal anomaly (CTA) observed in the day previous to the event at the fires' locations

14.3.4.2 Estimating the Amplitudes of LST and Soil Heat Flux Data at Significant Frequencies

We calculated the amplitude of the dominant components of LST and soil heat flux (G_0) for the entire study area. To do so, we used the procedures described in Sect. 14.2.1.1 and estimated the amplitude and phase of LST in each pixel in

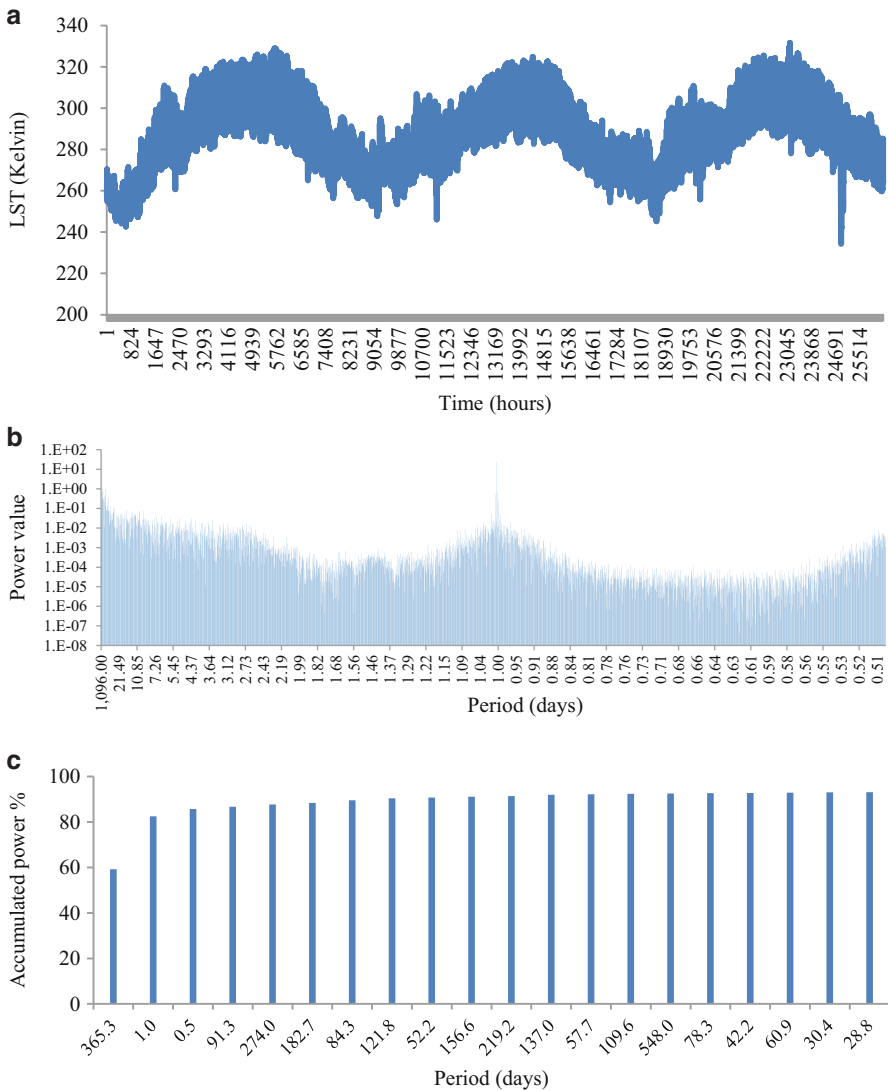


Fig. 14.9 (a) Actual three year hourly time series of LST for a pixel in the study area with lower gaps in the original data; (b) Power spectrum of LST time series against the period in days; (c) accumulated power in percentage against the related period

the study area. As we selected 11 frequencies as the dominant components (see Sect. 14.3.4.1), this gives 11 maps of LST amplitudes and 11 maps of soil heat flux amplitudes. The LST amplitude map of the 24 h component is shown in Fig. 14.10a. The daily LST amplitudes vary from 1.5 to 24 Kelvin and clearly show patterns related to land cover. The large amplitudes belong to the drier areas, i.e. lower soil

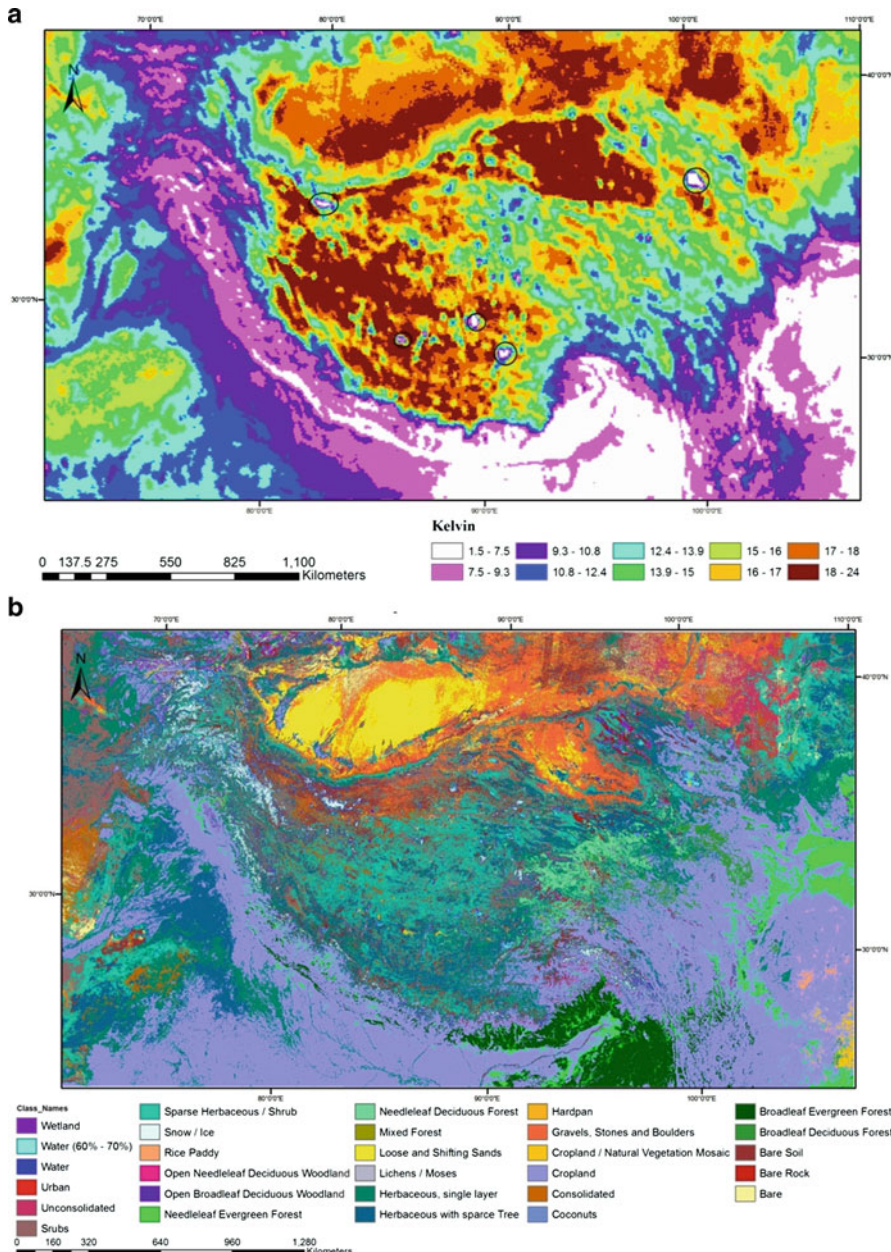


Fig. 14.10 (a) Amplitude map of LST for a period of 24 h, (b) Land cover map for the Tibetan Plateau for the year 2000

moisture in the top soil layer (i.e. desert area in the northern part of the study area with brown colours). The water bodies, shown as black circles in the amplitude map, have lower daily amplitudes, because of the high thermal capacity of water and also glaciers (some parts with pink and white colour in the southern and western part of the study area) have smaller daily amplitudes. The land cover map of the Tibetan Plateau is shown for reference in Fig. 14.10b.

14.3.4.3 Estimating the Spectral Soil Thermal Admittance (SSTA)

As we have already estimated the amplitudes of G_0 and LST at significant periods (see Sect. 14.3.4.2), we calculated the soil thermal admittance (Eqs. 14.25 and 14.26) for those periodic components in the study area. Figure 14.11 shows as an example the spatial variation of the soil thermal admittance for daily and annual periods covering the whole study area. They show the variability of thermal admittance in the study area as different patterns ($\sim 2\text{--}11 \text{ Wm}^{-2} \text{ K}^{-1}$ for the daily period and $0.14\text{--}6 \text{ Wm}^{-2} \text{ K}^{-1}$ for the yearly period). Assuming constant soil heat flux amplitude, the areas having higher thermal admittance values are areas which may have higher soil water content or vegetation area with lower LST fluctuations (low LST amplitude), while areas having lower values of soil thermal admittance have lower soil water content which cause higher LST fluctuations (high LST amplitude). This result is confirmed by the comparison between the daily LST amplitude (Fig. 14.10a) and daily soil thermal admittance (Fig. 14.11b). The Spectral Soil Thermal Admittance is given for some pixels in Fig. 14.12.

14.3.5 Monitoring Flooded Area Using Time Series of the Polarization Difference Brightness Temperature (PDBT) at 37 GHz

14.3.5.1 Noise-Free PDBT and NDVI Data

The original PDBT time series of an arbitrary EASE grid (Fig. 14.13) is full of observation gaps (zero values) adding up to about 42.7 % of the total. The low value observations always occur when there is precipitation in this area. This proves that the precipitation largely attenuates the PDBT at 37 GHz, however, the magnitude of the attenuation depends on the rain drop size. After applying the moving window filter, the overall trend of the original time series is captured by the filtered one (Fig. 14.14), but the fluctuation range of the whole time series is reduced from 5.3 to 44.7 K of the original time series to 19.7–40.8 K. The filter reduces the noise in adjacent pixels but also the dynamic range of the signal. It is interesting to note that there are large and frequent jumps in the whole time series. They are caused by the combination of observation gaps and persistent attenuation. For example, the short duration of precipitation events leads to continuous and sharp jumps from the end

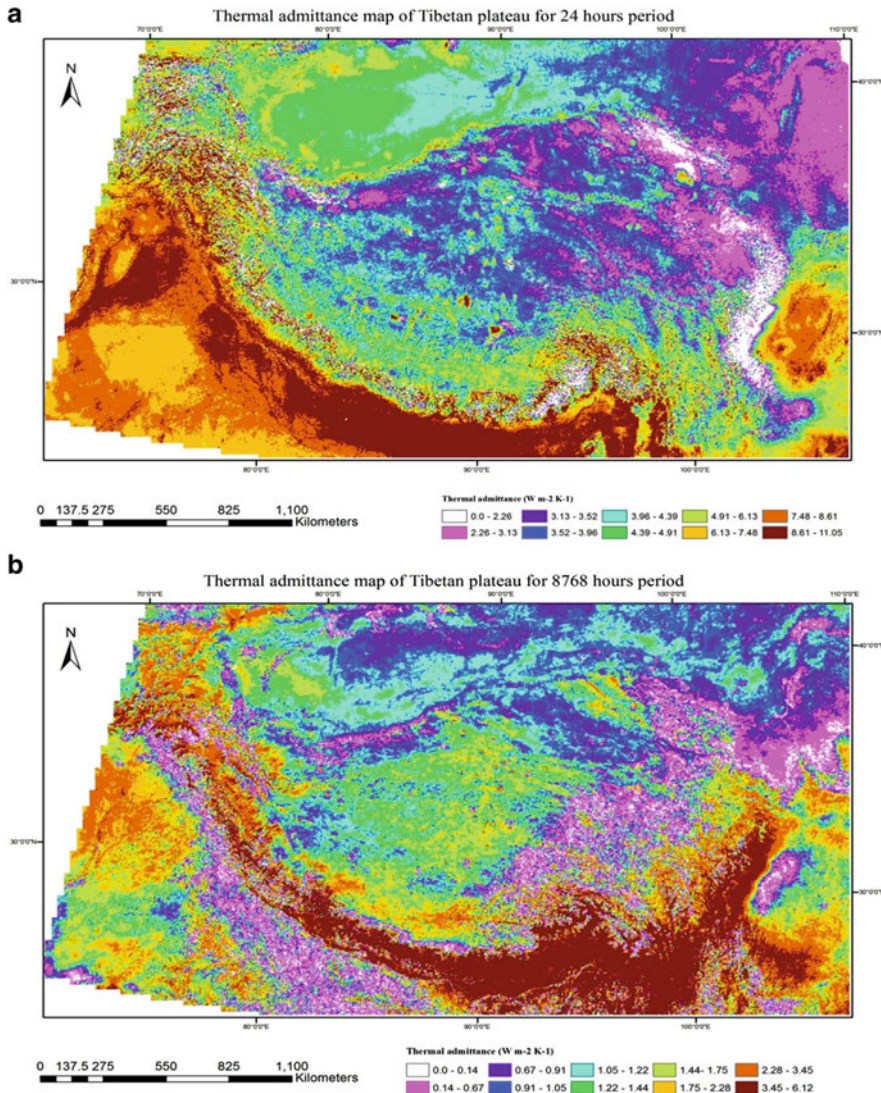


Fig. 14.11 (a) Soil thermal admittance maps for daily and, (b) yearly periods

of February to the middle of April 1998 (Fig. 14.14) while the relatively longer duration of precipitation events from June to July causes persistent attenuation during the same period.

To filter out these jumps in the filtered time series by HANTS, the amplitude of each frequency component needs to be analyzed in detail on the basis of the FFT results. We found that the component with period 73 days separates the real seasonal

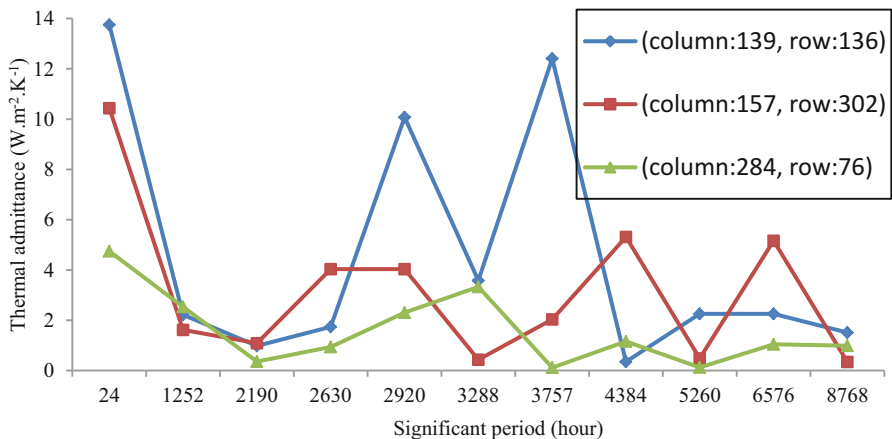


Fig. 14.12 Soil spectral thermal admittance of some pixels in the study area

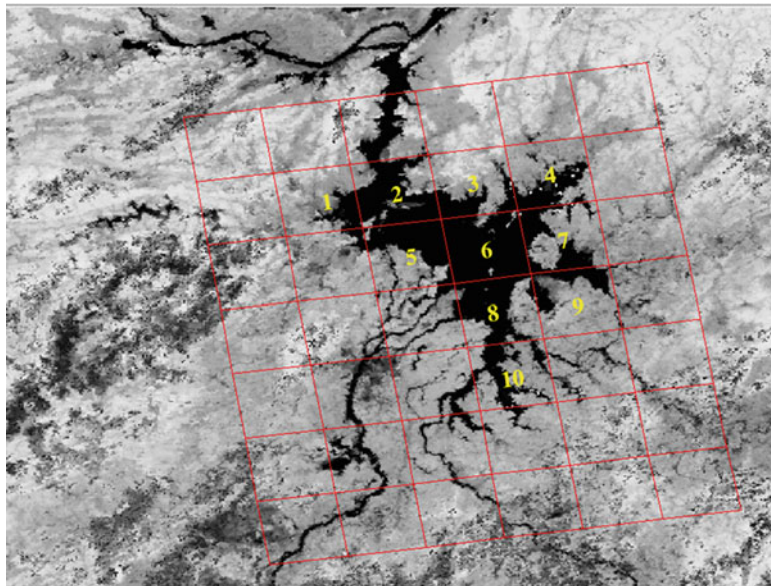


Fig. 14.13 The study area of the Poyang Lake within white numbered EASE-Grid pixels

surface changes from the (atmosphere) contaminated changes in the filtered time series. As shown in Fig. 14.15, the components with periods greater than 73 days contribute to the major seasonal surface changes, although the amplitude of the 73 days component has relatively low values in the amplitude map (Fig. 14.16). This is because this component and those with periods shorter than 73 days are contaminated by large jumps (Fig. 14.14). To remove the influence of jumps on the

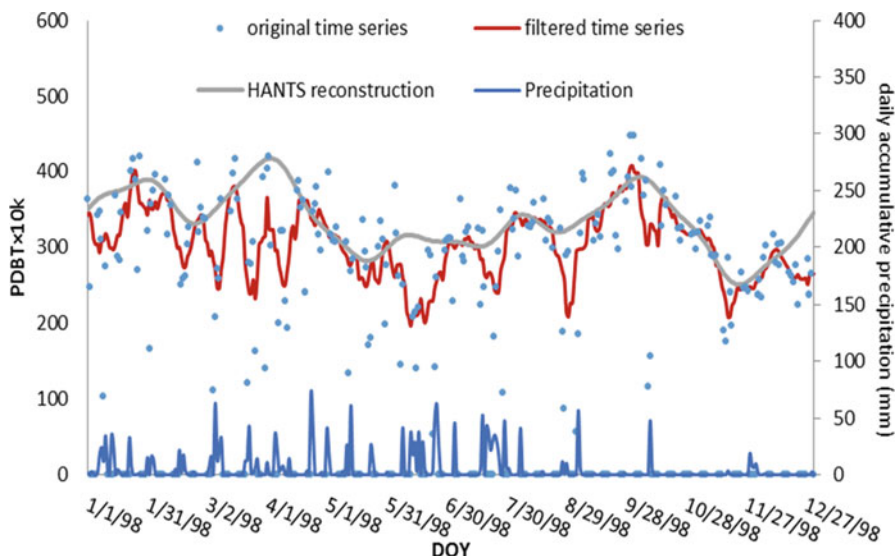


Fig. 14.14 The original, moving filtered, and reconstructed time series of the 6th numbered open water area in Poyang Lake, 1998, with the daily cumulated precipitation data

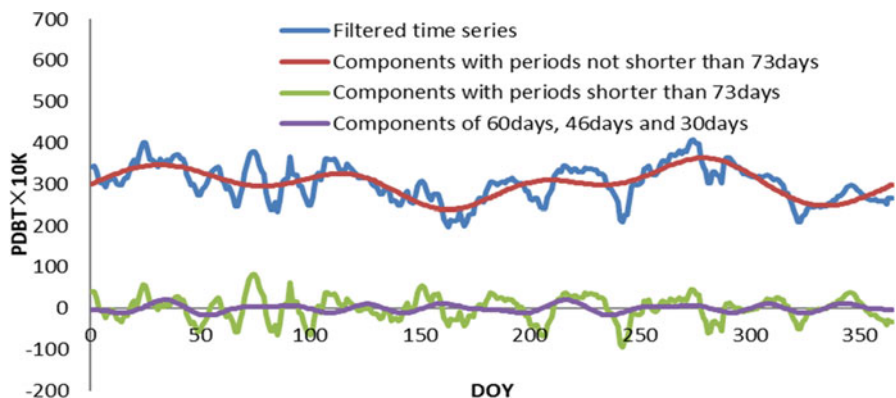


Fig. 14.15 The filtered time series, and oscillations of components with periods not shorter than 73 days, periods shorter than 73 days, and periods of 60 days, 46 days and 30 days, for the 6th numbered open water area of Poyang Lake in 1998

amplitudes of the periodic components, the ones with relatively small amplitudes, i.e. at 60 days, 46 days and 30 days, are selected. Finally, the components with periods of 365 days, 183 days, 122 days, 91 days, 73 days, 61 days, 46 days and 30 days are taken as the noise-free components and used in the Harmonic ANalysis of Time Series. The Vertically polarized Brightness Temperature, VBT, time series has exactly the same frequency components. The parameter settings of the HANTS algorithm for the PDBT, VBT and NDVI time series are shown in Table 14.9.

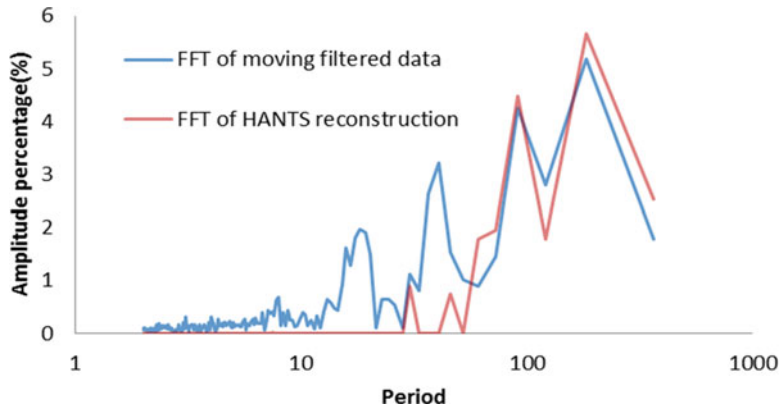


Fig. 14.16 The FFT of moving filtered data and HANTS reconstruction data for the 6th numbered open water area; x-axis is the period of frequencies used in FFT, y-axis is the percentage of each amplitude to the annual average

Table 14.9 The parameter settings of the HANTS algorithm for the PDBT, VBT and NDVI time series

Data set	SSM/I 37GHz vertical brightness temperature	SSM/I 37GHz polarized difference brightness temperature	MODIS NDVI
Number of frequencies	8	8	6
Corresponding periods (unit of days)	365, 183, 122, 91, 73, 61, 46, 30	365, 183, 122, 91, 73, 61, 46, 30	360, 184, 123, 91, 74, 61
Data range	0–100 k	0–400 K	0–1
Direction of outlier	low	low	low
Number of over-determine	80	80	10
Delta	0.5	0.5	0.5
Fit of tolerance	1.5 K	1.5 K	0.05 K

The reconstructed time series of PDBT follows the upper-envelope of the filtered time series, and also the overall trend of the original time series. It is interesting to see that the amplitude maps of the filtered and reconstructed time series are rather similar (Fig. 14.16).

The reconstructed one is not simply the combination of the same frequency components in Fig. 14.15. This is the major advantage of HANTS, which filters out the outliers, and the reconstructed signal captures the upper envelop of the observed time series.

14.3.5.2 Water Saturated Soil and Standing Water Retrieved from PDBT Time Series

Using the noise-free reconstructed time series, we can retrieve the WSS and standing water area of the Poyang Lake from 2001 to 2003. Our results have a similar trend as the lake area monitored by MODIS (with the spatial resolution of 250 m) and Advanced Synthetic Aperture Radar (ASAR with the spatial resolution of 30 m) data, as shown in Fig. 14.17. The RMSE of the retrieved WSS and standing water area is 361.22 km² or 17.74 % of the mean area during the same period of time. A comparison of microwave data and MODIS observations (spatial resolution of 1 km) for the area centered at 29.0485° N and 116.0954°E is shown in Fig. 14.18. On July 4th, 2002, the fractional area of WSS and standing water, which is calculated from SSM/I (65.28 %), is close to the fractional area of open water (58.81 %) observed from MODIS. However, On October 24th, 2002, the fractional area of WSS and standing water area (46.24 %) was much larger than that estimated from NDVI (21.85 %). That is because, while the lake area is now smaller, a large wetland occupied by aquatic vegetation, mainly Phragmites, has appeared. An optical sensor, like MODIS, cannot observe the standing water beneath the vegetation canopy, while a microwave radiometer can penetrate it. Thus the WSS and standing water area is close to the total area of open water and the wetland vegetation in Fig. 14.18.

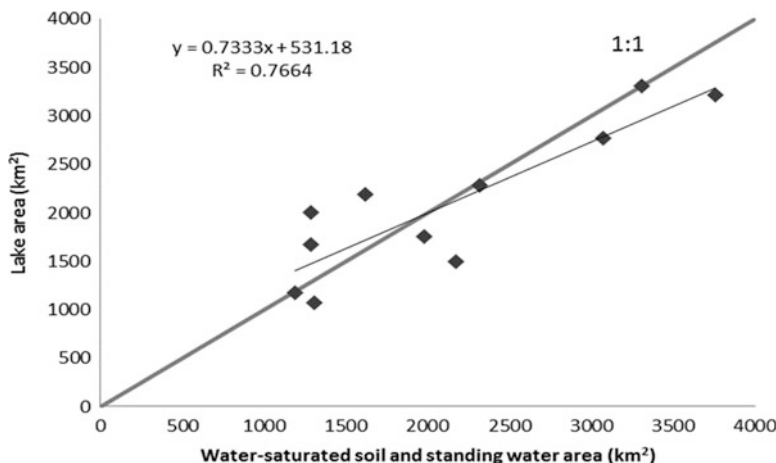
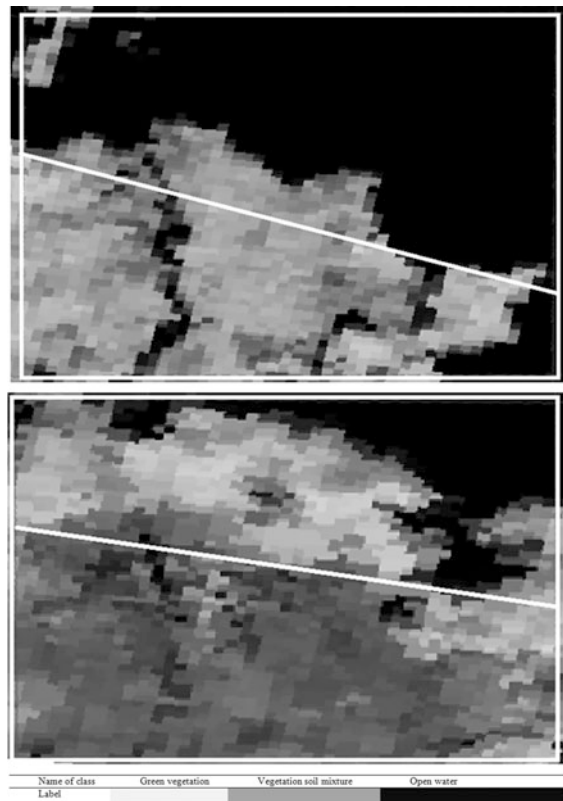


Fig. 14.17 Scatter plot of lake area estimated with MODIS and ASAR data by Yesou et al. (2011) and water-saturated soil and standing water area calculated from SSMI 37GHz (Yésou and Coauthors 2011)

Fig. 14.18 The wet and dry case of the 5 numbered pixel at the Poyang Lake with corresponding NDVI image



14.4 Summary and Discussion

General The materials summarized above show that observations from space of surface emittance in both the thermal infrared and the microwave spectral range are affected by gaps in the data records and by atmospheric effects, namely clouds in the thermal infrared and precipitation at 37 GHz. This notwithstanding, such observations are still useful, as demonstrated by the applications described in this Chapter. The combination of gaps and outliers in the data record requires additional processing to generate consistent time series of at-surface observations and two aspects need to be mentioned here. First, the data record must be somewhat redundant with respect to the process to be observed, i.e. the sampling interval must be shorter than the inherent temporal scale of variability of observed variables and processes. If this is the case, methods like HANTS can be applied to model the observed time series with fewer and irregularly spaced observations. We have demonstrated that HANTS, a method based on Fourier series developed to model NDVI time series, can successfully be applied to very diverse time series: hourly (FY-2C) and daily LST (MODIS) and daily PDBT (SSM/I). Second, a systematic

evaluation should be carried out, e.g. by applying an approach similar to the one proposed by Zhou et al. (2015), of the accuracy of the time series reconstructed with few and irregular observations.

Downscaling air temperature We presented a new approach to map air temperature at high resolution. The innovation is in the use of time series of land surface temperature (LST) observed by a spaceborne imaging radiometer to construct a stable model of the spatial and annual pattern of LST and, subsequently, to estimate time series of air temperature Ta maps using such a model. The spatial and annual pattern of LST is constructed by normalizing the $LST(x,y,t)$ at any location to the $LST(x_0,y_0,t)$ at a reference location (x_0,y_0) . In our study the latter is a node where gridded climate data are available for both past and future climate. Once the model $r(x,y,t)$ has been constructed we estimate $Ta(x,y,t)$ using only the $Ta(x_0,y_0,t)$ at the reference location. The relationship between Ta and LST has been constructed using a limited number of meteorological stations (just four in this study). This is inherently different from approaches reported in literature where air temperature is estimated from concurrent observations of LST or LST and NDVI. The advantage of our method is that it can be applied to periods of time, including predicted future climate, when no LST observations are available. The accuracy of our estimated daily Ta is comparable, e.g. RMSE = 3 K, with other studies, which are based on use of concurrent satellite data. We have also shown that the spatial annual pattern of LST has a rather limited inter-annual variability, i.e. the pattern is mainly determined by the combination of the yearly evolution of solar irradiance with rather stable landscape properties such as terrain, land cover (albedo, aerodynamic roughness) and soil thermal properties.

Thermal load and forest fires The HANTS algorithm plays an important role in both characterizing spatial patterns of fire occurrence and in predicting mean fire size. Fire occurrence shows clear selectivity against mean value, amplitude of the three harmonics and phase of the first harmonic of LST computed on a yearly basis. Mean fire size is selective only against the amplitude of the second harmonic. Here, an inverse relationship between number of fires and mean fire size is observed, with larger fires significantly preferring areas where the amplitude is larger (Table 14.6). The only phase component of the Fourier analysis related to fires occurrence is that of the first harmonic. The phase carries information on the timing of fire events: a larger number of fires is observed where the phase is higher, i.e. when a prolonged warm season occurs.

A relationship was found between conditional mean fire size and thermal anomalies (Fig. 14.7). With increasing values of the thermal anomaly, the conditional mean fire size increases. A similar trend is observed with the conditional fraction of fires larger than 16 ha. CTA is a measure of heat “accumulated” in a certain area, providing more direct information on the prolonged exposure of vegetation to stress conditions. This is reflected in the prediction of expected mean fire size over two orders of magnitude (Fig. 14.8), potentially allowing the production of more meaningful fire hazard maps as compared to TA.

Land surface thermal admittance We have shown that it is feasible to use time series of satellite observations of LST and soil heat flux to estimate the soil thermal admittance. The method developed here is simple, and it needs minimum input data compared to other methodologies. The data needed to estimate the soil thermal admittance are the amplitudes of LST and G_0 , which can be estimated assuming the periodicity of both time series by means of Fourier series and least square method. When the available time series is incomplete (i.e. time series of G_0) and consists of just the daily mean and instantaneous value in each day, it is still possible to derive the amplitude of time series components with good accuracy and estimate the soil thermal admittance. The soil thermal admittance values at different frequencies give us the Spectral Soil Thermal Admittance (SSTA) which contains valuable information about the soil thermal properties in different soil layers. The thermal properties of soil layers can be estimated indirectly using spectral soil thermal admittance (Ghafarian 2015).

Water saturated soil and flooded area We used a simplified radiative transfer model and linear model to retrieve the fractional area of water saturated soil (WSS) and standing water from the polarization difference brightness temperature (PDBT) at 37 GHz. The moving filter is first used to fill the observation gaps of the PDBT time series. Noise-free daily PDBT, vertical brightness temperature (BT), and NDVI are derived from the Harmonic ANalysis of Time Series (HANTS) algorithm of their raw data time series. The vegetation transmission function is obtained from the regression between NDVI and its dependent variable PDBT for flooded paddy fields, under the assumption that the land surface temperature and PEED of the flooded rice is constant during its growing season. The quasi-linear relationship between the PEED and fractional area of WSS and standing water exists no matter what the frequencies are. This indicates that the regional water-storage capacity can be derived from PDBT observations at other frequencies. The retrieved WSS and standing water area in the Poyang Lake region shows a good fit with the lake area from the MODIS and SAR data. Our method seems to provide satisfactory estimates of the water-storage capacity of the upper catchment of the Poyang Lake, and as such, it is a useful early indicator of flooding events in the lake area.

14.5 Conclusion

Time series of satellite observations of land surface temperature capture multiple aspects of the land surface response to radiative forcing. We have demonstrated that such response leads to a strong dependence of air temperature on the surface energy budget and specifically on land surface temperature, which is determined by the dynamic equilibrium of radiative and heat fluxes. Such dependence can be exploited to use land surface temperature as a predictor of air temperature and particularly of its spatial variability.

Reduced water availability forces the land surface temperature to increase to the point where both soil and foliage can dissipate the excess energy. Large positive anomalies in the foliage temperature appear to be a significant driver of forest fires, particularly of their size.

References

- Alfieri S, Lorenzi FD, Menenti M (2013) Mapping air temperature using time series analysis of LST: the SINTESI approach. *Nonlinear Process Geophys* 20(4):513–527
- Azzali S, Menenti M (2000) Mapping vegetation-soil-climate complexes in southern Africa using temporal Fourier analysis of NOAA-AVHRR NDVI data. *Int J Remote Sens* 21(5):973–996
- Bajocco S, Ricotta C (2007) Evidence of selective burning in Sardinia (Italy): which land-cover classes do wildfires prefer? *Landscape Ecol* 23:241–248
- Bowen IS (1926) The ratio of heat losses by conduction and by evaporation from any water surface. *Phys Rev* 27(6):779–787
- Brodzik M, Knowles K (2002) EASE-Grid: a versatile set of equal-area projections and grids. Paper presented at the national center for geographic information & analysis, Santa Barbara, California, USA
- Broomhead DS, King GP (1986) On the qualitative analysis of experimental dynamical systems. In: Sarkar S (ed) Nonlinear phenomena and chaos. Hilger, Boston, pp 113–144
- Brutsaert WH (1982) Evaporation into the atmosphere. Reidel, Dordrecht
- Carslaw HS, Jaeger JC (1959) Conduction of heat in solids, 2nd edn. Oxford University Press, Oxford
- Elsner JB, Tsonis AA (1996) Singular spectrum analysis: a new tool in time series analysis. Plenum Press, New York
- Esposito S (2010) Prime Caratterizzazioni agro-climatiche delle aree di studio di Agroscenari mediante i dati dei nodi di griglia, Technical Note. Agroscenari, CRA-CMA, Rome, Italy, 30 pp
- Faivre R (2014) Multi-sensor remote sensing parameterization of heat flux over heterogeneous land surface. Delft University of Technology, Delft
- Famiglietti JS, Wood EF (1994) Multiscale modeling of spatially variable water and energy balance processes. *Water Resour Res* 30:3061–3078
- Ghafarian HR (2015) Reconstruction of gap-free time series satellite observations of land surface temperature to model spectral soil thermal admittance. Delft University of Technology, Delft
- Ghil M, Allen MR, Dettinger MD, Ide K, Kondrashov D, Mann ME, Robertson AW, Saunders A, Tian Y, Varadi F, Yiou P (2002) Advanced spectral methods for climatic time series. *Rev Geophys* 40(1):3.1–3.41
- Golyandina N, Nekrutkin V, Zhigljavsky A (eds) (2001) Analysis of time series structure: SSA and related techniques. Chapman & Hall/CRC, Washington, DC
- Holmes TRH, De Jeu RAM, Owe M, Dolman AJ (2009) Land surface temperature from Ka band (37 GHz) passive microwave observations. *J Geophys Res-Atmos* 114. doi:[Artn D04113](https://doi.org/10.1029/2008jd010257) doi:[10.1029/2008jd010257](https://doi.org/10.1029/2008jd010257)
- Horton R, Wierenga PJ (1983) Estimating the soil heat flux from observations of soil temperature near the surface1. *Soil Sci Soc Am J* 47(1):14–20. doi:[10.2136/sssaj1983.03615995004700010003x](https://doi.org/10.2136/sssaj1983.03615995004700010003x)
- Idso SB, Jackson RD, Reginato RJ (1976) Compensating for environmental variability in the thermal inertia approach to remote sensing of soil moisture. *J Appl Meteorol* 15(8):811–817. doi:[10.1175/1520-0450\(1976\)015<0811:cfevit>2.0.co;2](https://doi.org/10.1175/1520-0450(1976)015<0811:cfevit>2.0.co;2)
- Jia L, Shang H, Hu G, Menenti M (2011) Phenological response of vegetation to upstream river flow in the Heihe River basin by time series analysis of MODIS data. *Hydrol Earth Syst Sci* 15:1047–1064

- Julien Y, Sobrino JA, Verhoef W (2006) Changes in land surface temperatures and NDVI values over Europe between 1982 and 1999. *Remote Sens Environ* 103(1):43–55. doi:[10.1016/j.rse.2006.03.011](https://doi.org/10.1016/j.rse.2006.03.011)
- Kirdiashev KP, Chucklantsev AA, Shutko A (1979) Microwave radiation of the earth's surface in the presence of vegetation cover. *Radiotekhnika* 24:256–264
- Menenti M (1984) Physical aspects of and determination of evaporation in deserts applying remote sensing techniques. Report 10 (special issue), Institute for Land and Water Management Research (ICW), The Netherlands
- Menenti M, Azzali S, Verhoef W, van Swol R (1993) Mapping agroecological zones and time lag in vegetation growth by means of fourier analysis of time series of NDVI images. *Adv Space Res* 13(5):233–237
- Menenti M, Jia L, Azzali S, Roerink G, Gonzalez-Loyarte M, Leguizamón S (2010) Analysis of vegetation response to climate variability using extended time series of multispectral satellite images. *Remote sensing Optical Observation of Vegetation Properties*, pp 131–165
- Monteith JL (1965) Evaporation and environment. *Symp Soc Exp Biol* 19:205–234
- Moody A, Johnson D (2001) Land surface ohenoogy from AVHRR using discrete Fourier transform. *Remote Sens Environ* 75:305–323
- Morton FL (1983) Operational estimates of areal evapotranspiration and their significance to the science and practice of hydrology. *J Hydrol* 66(1–4):1–76
- Musial JP, Verstraete MM, Gobron N (2011) Technical note: comparing the effectiveness of recent algorithms to fill and smooth incomplete and noisy time series. *Atmos Chem Phys* 11:7905–7923
- Penman H (1948) Natural evaporation from open water, bare soil and grass. *Proc R Soc Lond A Math Phys Sci* 193:120–146
- Priestley CHB, Taylor RJ (1972) On the assessment of surface heat flux and evaporation using large-scale parameters. *Mon Weather Rev* 100(2):81–92
- Roerink GJ, Menenti M (2000) Reconstructing cloudfree NDVI composites using Fourier analysis of time series. *Int J Remote Sens* 21(9):1911–1917
- Roerink GJ, Menenti M, Verhoef W (2000) Reconstructing cloudfree NDVI composites using Fourier analysis of time series. *Int J Remote Sens* 21(9):1911–1917
- Roerink GJ, Menenti M, Soepboer W, Su Z (2003) Assessment of climate impact on vegetation dynamics by using remote sensing. *Phys Chem Earth, Parts A/B/C* 28(1):103–109
- Sellers WD (1965) Physical climatology. University of Chicago Press, Chicago
- Shang H, Jia J, Menenti M (2012) Analyzing the inundation patterns in Asia floodplains by passive microwave. Paper presented at the SPIE Asia-Pacific, Kyoto, 21 November 2012
- Shang H, Jia J, Menenti M (2015) Analyzing the inundation pattern of the Poyang lake floodplain by passive microwave data. *J Hydrometeorol* 16(2):652–667
- Shen S, Leptoukh GG (2011) Estimation of surface air temperature over central and eastern Eurasia from MODIS land surface temperature. *Environ Res Lett* 6:045206
- Su Z, Menenti M (1999) Mesoscale climate hydrology: the contribution of the new observing systems. Report USP-2. Publications of the National Remote Sensing Board (BCRS), 141p
- van Wijk WR, De Vries DA (1963) Periodic temperature variations in a homogenous soil. In: van Wijk WR (ed) Physics of plant environment. North-Holland, Amsterdam, pp 102–143
- Vautard R, Yiou P, Ghil M (1992) Singular-spectrum analysis: a toolkit for short, noisy chaotic signals. *Physica D: Nonlinear Phenomena* 58(1–4):95–126. doi:[10.1016/0167-2789\(92\)90103-t](https://doi.org/10.1016/0167-2789(92)90103-t)
- Verhoef W (1996) Application of Harmonic Analysis of NDVI Time Series (HANTS). In: Fourier analusis of temporal NDVI in southern Africa and America continent. Dlo Winand Staring Center, Wageningen
- Verhoef W, Menenti M, Azzali S (1996) Cover A colour composite of NOAA-AVHRR-NDVI based on time series analysis (1981–1992). *Int J Remote Sens* 17(2):231–235
- Wang J, Bras RL, Sivandran G, Knox RG (2010) A simple method for the estimation of thermal inertia. *Geophys Res Lett* 37(5), L05404. doi:[10.1029/2009gl041851](https://doi.org/10.1029/2009gl041851)
- Wigneron JP, Kerr Y, Chanzy A, Jin YQ (1993) Inversion of surface parameters from passive microwave measurements over a soybean field. *Remote Sens Environ* 46(1):61–72

- Yan H, Zhang J, Hou J, Hea J (2009) Estimation of air temperature from MODIS data in east China. *Int J Remote Sens* 30:6261–6275
- Yésou H, Coauthors (2011) Nine years of water resources monitoring over the middle reaches of the Yangtze River, with ENVISAT, MODIS, Beijing-1 time series, Altimetric data and field measurements. *Lakes Reservoirs* 16:231–247
- Zhou J, Jia L, Menenti M (2015) Reconstruction of global MODIS NDVI time series: performance of Harmonic ANalysis of Time Series (HANTS). *Remote Sens Environ* 163:217–228

Chapter 15

A Review of Multitemporal Synthetic Aperture Radar (SAR) for Crop Monitoring

Heather McNairn and Jiali Shang

Abstract Synthetic Aperture Radars (SARs) transmit and receive energy at microwave frequencies. The response recorded by these sensors is largely a function of the structure and dielectric properties of the target. The structure of a canopy is different among crops, and changes as crops grow. SARs respond very well to these structural differences and thus these sensors are able to accurately identify crop type and have proven sensitive to several crop biophysical parameters (Leaf Area Index, biomass, canopy height). Although optical sensors have traditionally been used for crop monitoring, advances in SAR applications research coupled with availability of SAR data at different frequencies and polarizations has raised the profile of these sensors for agricultural monitoring. And the “all weather” capability of SARs makes their use in operational activities of particular interest. Advancements in SAR applications development, continued improved access to data, and a push to transfer SAR research methods to monitoring agencies will lead to an increased role of SAR in monitoring agricultural production. This chapter reviews SAR research as it relates to crop type and acreage estimation, as well as determination of crop condition and crop bio-physical properties.

15.1 Requirements for Crop Monitoring

Balancing the supply of food with the demands from a growing global population is an ongoing challenge. To meet changing global food requirements, the UN Food and Agriculture Organization (FAO) estimated that food production must double in the next 40 years (www.un.org/News/Press/docs/2009/gaef3242.doc.htm). Quantifying food supply can be difficult as national, regional and global crop production fluctuates due to local land management decisions (what and where to seed) and meteorological conditions (principally precipitation and temperature). Anticipating production is further exacerbated when unforeseen disasters hit. Thus forecasting food supply necessitates on-going and frequent updates on acres seeded, yields

H. McNairn (✉) • J. Shang
Agriculture and Agri-Food Canada, Ottawa, ON, Canada
e-mail: heather.mcnaire@agr.gc.ca; jiali.shang@agr.gc.ca

(bushels per acre) and meteorological parameters which impact crop growth. Crop production data can be gathered from a range of sources (for example, knowledge from extension workers, reports from farmers, climate data (Jayne and Rashid 2010)). Earth observing satellites also offer a source of data and as an example, will be used in initiatives such as the Group on Earth Observations Global Agricultural Monitoring (GEO-GLAM) to identify crop types and estimate acreages to monitor global food production (European Space Agency 2012).

Satellites suitable to map acreage and monitor crop growth condition are numerous. Sensors on these satellite platforms operate in both the electro-optical spectrum (400–2500 nm) and longer microwave wavelengths (1–100 cm). The configurations of these sensors also vary in terms of frequency of orbital repeat (and re-look), available swath and spatial resolution. At the global scale operational monitoring is for the most part, limited to coarser-resolution optical sensors such as the Moderate Resolution Imaging Spectroradiometer (MODIS) and the National Oceanic and Atmospheric Administration (NOAA) Advanced Very High Resolution Radiometer (AVHRR) (Becker-Reshef et al. 2010). These sensors are a source of daily data, yet their coarse spatial resolutions are less suitable for field-based production monitoring. When field-level monitoring is needed, higher resolution sensors are required.

15.2 Synthetic Aperture Radar (SAR) Responses to Crop Type and Condition

Optical sensors are well suited for mapping crop type and monitoring crop growth condition. At shorter wavelengths, the amount of solar energy absorbed, reflected and transmitted by vegetation is mainly driven by plant pigmentation as well as internal leaf structure and moisture. These chemical and physical properties (at the atom level) are crop type specific and are indicative of the growth stage and condition of the plant. At the other end of the electromagnetic spectrum, scattering of longer-wavelength microwaves is driven by larger scale structures (size, shape and orientation of leaves, stems and fruit) as well as the volume of water in the vegetation canopy (at the molecule level). Soil conditions (moisture and roughness) also effect microwave response. The significance of the effects of these soil conditions depends upon the crop type and growth stage, and the configuration of the microwave sensor. While optical wavelengths are more intuitively linked with crop condition, atmospheric conditions (for example presence of ozone, carbon dioxide, water, pollution) also cause absorption and scattering thus affecting spectral signals. As well, since these sensors rely on ambient energy imaging is limited to “daylight” hours.

Synthetic Aperture Radars (SARs), although currently not widely used for operational crop monitoring, provide a reliable source of data. These are active sensors generating their own source of energy, measuring the magnitude of transmitted energy scattered by the Earth back to the radar antenna. With their own source

of energy SARs can operate day or night and at these longer wavelengths are unaffected by the presence of cloud and haze. Using data from SARs for crop monitoring is not without challenge, primarily due to the confounding contributions of canopy moisture, crop structure and soil properties to the returned radar signal.

15.2.1 SAR Sensor Configurations

SAR sensors are defined by their operating frequency, incident angle and polarization. Incident angle can be defined by the angle (in degrees) between the radar beam and a line perpendicular to the Earth's surface. Each of these configurations affects the interaction of microwaves with the target in terms of backscatter intensity and scattering characteristics. Frequency (GHz or wavelength (cm)) and incident angle affect penetration depth of the transmitted microwave into the crop canopy. Depth of penetration increases with wavelength but decreases as angle increases. This depth affects which elements of the crop canopy interact with the microwave signal. Higher frequencies (i.e. X-Band with wavelengths of 2.4–3.75 cm) respond more to upper canopy structures while lower frequency (i.e. L-Band with wavelengths of 15–30 cm) microwaves penetrate further and generate more interaction with structures lower in the canopy. McNairn et al. (2009a) suggested that this differential penetration was the reason that crops were best identified when C-Band and L-Band data were integrated into a classifier; the higher frequency C-Band microwaves penetrated low biomass crops (wheat and hay-pasture) without significant interference from the soil, while L-Band waves penetrated further into larger biomass crops (corn and soybeans) allowing greater canopy interaction. Also important, to create scatter from a target element the target should be of equivalent size or larger than the wavelength of the transmitted wave. Otherwise attenuation of the radar signal will dominate.

Polarization is defined by the orientation of the electric field vector of the transmitted and received electromagnetic wave (Raney 1998). Polarization should be interpreted in the context of the structure of the target. The types of scattering from a target are identified as single bounce (surface), multiple (volume) or double-bounce. One source of scattering typically dominates, but depending on the complexity of the target secondary and tertiary sources of scattering can also be present. For well-developed crop canopies, vertical structures (stalks) can create double-bounce scattering, randomly oriented leaves, stems and fruit volume scattering, and large scatters (leaves, stems) oriented towards the sensor can result in single bounce scattering. Direct scattering from the soil, as well as double-bounce and multiple scattering events between the soil and canopy, may also contribute to the SAR response. The contribution from the soil will depend on penetration depth (determined by frequency, incident angle and canopy development).

Most SAR sensors transmit and receive microwaves in the horizontal (H) and/or vertical (V) linear polarizations. Early satellites transmitted and received microwaves in a single linear polarization (European Remote Sensing 1 and 2

(ERS-1/2) (VV), Japanese Earth Resources Satellite 1 (JERS-1) (HH) and RADARSAT-1 (HH)). Second-generation sensors (i.e. Advanced Synthetic Aperture Radar (ASAR)) were capable of transmitting and/or receiving in both linear polarizations, generating like (HH and/or VV) as well as cross (HV or VH) polarizations. A linear cross polarization response (HV or VH) results when the transmitted wave (i.e. H) is re-polarized to its orthogonal polarization (i.e. V). A strong HV or VH response is characteristic of targets where multiple scattering (at least two bounces) dominates (Raney 1998). Without multiple or double-bounce scattering events, HV or VH response will be low.

15.2.2 SAR Polarimetry

Polarimetric-capable satellites (i.e. the Advanced Land Observation Satellite (ALOS) Phased Array type L-band Synthetic Aperture Radar (PALSAR), RADARSAT-2 and TerraSAR-X) capture the complete characterization of the scattering field by recording all four mutually coherent channels (HH, VV, HV, VH), as well as retaining and processing the phase information between orthogonal polarizations. With phase retained, users can synthesize any wave orientation or ellipticity (providing linear, elliptical or circular polarizations) in addition to parameters that characterize target scattering. SARs can transmit completely polarized waves, but multiple scattering events will completely or partially de-polarize the wave. The degree of de-polarization (d) increases as multiple and volume scattering increases. With multiple scattering events phase becomes less predictable (more random) from point to point within the target. Degree of de-polarization varies by crop type and condition. Single bounce scattering (from smooth soil before crop emergence, for example) creates little de-polarization (Evans and Smith 1991), while thick vegetation canopies created diffuse scattering and almost completely un-polarized responses (d close to 0) (Groot et al. 1992). Pedestal height is one measure of degree of de-polarization with height increasing as multiple scattering increases. Hinds et al. (1993) discovered that the degree of polarization varied by crop type, growth stage and polarization. For the same crop type, degree of polarization varied through the growth cycle, decreasing as the crop canopy developed and increasing as the crop matured and dried out.

Cloude-Pottier (1997) and Freeman-Durden (1998) provided methods to decompose the polarimetric SAR signal within each resolution cell into characteristics of target scattering. Cloude-Pottier decomposes the signal into a set of eigenvectors (which characterize the scattering mechanism) and eigenvalues (which estimate the intensity of each mechanism) (Alberga et al. 2008). From the eigenvalues, entropy (H) and anisotropy (A) are calculated. H measures the degree of randomness of the scattering (from 0 to 1); values near zero are typical of single scatter targets while entropy increases in the presence of multiple scattering events as expected in a crop canopy. Anisotropy estimates the relative importance of the dominant scattering mechanism and the contribution from secondary and tertiary scattering mechanisms. Zero anisotropy indicates two mechanisms of approximately equal proportions; as

values approach 1 the second mechanism dominates the third (Lee and Pottier 2009). The average alpha ($\bar{\alpha}$) angle (0–90°) calculated by Claude-Pottier identifies the dominant scattering source (Alberga et al. 2008). Single bounce scatters have alpha angles close to 0°; for crop canopies angles close to 45° (volume scattering) and nearing 90° (double-bounce) will be observed.

Freeman-Durden (1998), a three-component decomposition method, separates the total power of each SAR resolution cell into contributions from three scattering mechanisms – single bounce (surface), volume (multiple) and double bounce. This decomposition provides the magnitude of the contribution from each scattering mechanism.

15.2.3 Crop Characteristics Affecting SAR Response

SARs measure the intensity of energy scattered from targets back towards the radar antenna (recorded as backscatter in decibels (dB)). Properties of the target affect not only the intensity of backscatter, but also the scattering behavior. Scattering caused by natural targets can only occur when the radar waves encounter a dielectric discontinuity. Typically discontinuity is due to the presence of water which has a high dielectric constant (~80) relative to air (~1) (Dobson and Ulaby 1998). Backscatter is positively correlated with the dielectric constant of a target and thus typically, backscatter increases as water content increases. This relationship has been demonstrated repeatedly for soils, with higher backscatter recorded as soil moisture increases. However the relationship between canopy water content and SAR backscatter is more complex due to the sensitivity of SAR response to canopy structure. Findings have been mixed depending on the crop type, growth stage and SAR configuration. Studies have reported negative correlations with canopy water content for cereals (Hinds et al. 1993 using Ku-VV) and potatoes (McNairn et al. 2002 using C-HH). For canola, positive correlations with volume of canopy water have been reported by some (Hinds et al. 1993) while others reported no correlation (McNairn et al. 2002).

It is precisely because microwave scattering is sensitive to canopy structure that SARs can provide information on crop type and condition. When targets are physically oriented to the polarization of the incident wave, greater microwave interaction occurs. This is most pronounced for crops with vertical structures which align well with vertical (V) transmitted waves. Secondly the structure (stems, leaves, fruit) within the crop volume create ample opportunity for multiple scattering events which re-polarize and de-polarize the incident wave. Re-polarization creates higher HV or VH backscatter while de-polarization increases the un-polarized component of the scattered wave. Considering the scattering in the context of crop canopy structures, the linear cross polarization (HV or VH) has repeatedly proven to be the single best polarization for classification (Paris 1983; Brisco et al. 1991; Foody et al. 1994; McNairn et al. 2000, 2009a, b). Increases in classification accuracy can be achieved by including a second polarization into the classification. Because of the coupling of V-polarized waves with the vertical crop structure, an integration of

VV and VH (or HV) is preferred (McNairn et al. 2009a, b; Deschamps et al. 2012; McNairn and Shang 2014). Smaller incremental improvements are also reported with the inclusion of a third polarization (typically HH) (McNairn et al. 2000, 2009a; Hoekman and Vissers 2003).

Planting density and row direction (relative to the SAR look direction) can also impact SAR response. The intensity of scattering is generally higher when crop row direction is perpendicular rather than parallel to SAR look direction (Paris 1983). The cross polarization has the advantage of being insensitive to planting row direction (McNairn and Brisco 2004) and this, along with its sensitivity to canopy structure, make HV (or VH) an important polarization for crop monitoring. Wiseman et al. (2014) observed differences in C-Band backscatter and scattering responses among soybean fields due to differences in planting densities, even though all fields were at the same phenology stage.

15.3 Crop Classification to Support Acreage Estimation

15.3.1 Requirement for Multi-temporal SAR Data

Regardless of the sensor used, accurate crop identification requires that the energy recorded be unique to each crop type. Different crops can look “spectrally similar” at a given point in their growth cycle. For SARs, this confusion is due primarily to similarities in the crop structures. However, as crops move from one growth stage to the next, the development of leaves and fruit and the accumulation of biomass change the canopy structure, helping to differentiate one crop from another. The number of images required depends upon the crops present and the complexity of the cropping system (for example number of crops, consistency of planting practices, presence of inter-cropping and number of cropping seasons per year).

A key to successful crop classification is to understand which growth stages are best for crop separation and to identify which SAR configurations are best suited for crop classification. McNairn et al. (2009b) found that SAR response was very sensitive to changes in canopy structure during seed and fruit development, stages which occur later in the growing season. This study and a second study by Deschamps et al. (2012) recommended including a SAR image acquired during seed and reproductive phenology stages, at the point of peak biomass, in order to maximize classification accuracies.

15.3.2 Combining Multiple Frequencies for Crop Classification

Researchers have disagreed on recommendations for the optimal SAR frequency for crop discrimination. Discrepancies are most likely due to differences in crops

(and thus canopy structure and total canopy biomass) among the various studies. Some studies have reported that shorter Ku-, X- and C-Band wavelengths were very sensitive to canopy architecture and were better at separating crops (Bouman and Hoekman 1993; Brown et al. 1992; Paris 1986). Longer wavelengths penetrate deeper into the canopy and for low biomass crops this could introduce scattering from the soil. Yet for larger biomass crops these lower frequencies offer more opportunity for waves to interact with deeper canopy structures. Jia et al. (2012) favoured longer wavelengths at C-Band (ASAR) over X-Band (TerraSAR-X) for separating winter wheat from cotton. McNairn et al. (2009a) found that longer L-Band data (from ALOS PALSAR) was needed to accurately identify higher biomass crops (corn, soybean), although C-Band data was most suitable for separating lower biomass crops (wheat, hay-pasture).

Regardless of conclusions regarding the single best frequency, researchers agree on the advantages of integrating SAR acquired at multiple frequencies. Wooding (1992) clearly stated that discrimination of crops was best achieved by integrating SAR data acquired at more than one frequency, rather than combining two polarizations or two incidence angles. Using airborne and satellite SAR platforms researchers have determined that relative to single frequency data, higher crop classification accuracies are achieved using X- and C-Band (Thomson et al. 1990; Jia et al. 2012), C- and L-Band (Bouman and Uenk 1992; Dobson et al. 1996; Skriver 2012) X-, C- and L-Band (Brisco and Protz 1980; Guindon et al. 1984; Baghdadi et al. 2009), and C- and L- and P-Band (Chen et al. 1996; Ferrazzoli et al. 1997, 1999; Hill et al. 2005; Hoekman et al. 2011).

Engineering advances have meant that current SAR sensors can now provide data at multiple polarizations (in some cases fully polarimetric) and multiple incident angles. Studies have also used multi-frequency airborne or scatterometer sensors, or combined data from satellites operating at different frequencies, to demonstrate the importance of multiple frequencies for crop separation. Yet even with these multi-polarization and multi-frequency data, the temporal domain remains critical to successfully separate crop types (Skriver et al. 2011). Thus when multi-temporal data are available at multiple SAR configurations, crop classification is successful. As an example, McNairn and Shang (2014) report that when a multi-temporal C-Band data set with all linear polarizations (HH, VV, HV/VH) is available, high overall accuracies are achievable. Depending on the crop mix, accuracies of 85.5 % (more complex cropping system) to 90 % (simple mix of corn, soybeans, wheat, and pasture) are reached.

15.3.3 Full and Compact Polarimetry for Crop Classification

As described in Sect. 15.2.2 when a SAR sensor operates in a full polarimetric mode, the intensities of all four mutually coherent channels (HH, VV, HV, VH) are recorded as well as the phase information between orthogonal polarizations (also referred to as quadrature polarization (QP) sensors). Some improvement

in accuracies has been reported when decomposition parameters generated from these polarimetric data are used in a classification. McNairn et al. (2009a) used polarimetric L-Band data from ALOS PALSAR to demonstrate that overall accuracies improved by 4–7 % when decomposition parameters (from Cloude-Pottier, Freeman-Durden or Krogager) were used instead of the four linear intensity channels (HH, VV, VH/HV). Although all crops fell within the same class of scatterers, differences in the relative contributions of scattering mechanisms among the crops was observed and the authors attributed this to the improved classification.

These results were repeated when McNairn and Shang (2014) examined decompositions (Cloude-Pottier and Freeman-Durden) applied to C-Band RADARSAT-2 data. However increases in overall accuracies were smaller at this frequency. This research found that when overall accuracy using all linear polarizations is high (90 %), gains are minor (1–2 % when using the Cloude-Pottier entropy, alpha and anisotropy; 1–3 % when using the Freeman-Durden surface, volume and double-bounce scattering). Nevertheless, decomposition parameters will improve accuracies when the linear polarizations are unable to reach accuracies above 90 %.

In order to acquire the full scattering matrix, polarimetric sensors must double their Pulse Repetition Frequency (PRF) which immediately reduces the swath coverage by half (Charbonneau et al. 2010). Consequently, polarimetric acquisitions can be problematic if the intent is to use this mode for regional or national mapping. With compact polarimetry (CP) only one polarization is transmitted, and two orthogonal polarizations are received with the relative phase between the two received polarizations retained (Raney 2006). A CP SAR accesses the 2×2 covariance matrix of the backscattered field and thus contains less information than full polarimetric (QP) data (Charbonneau et al. 2010). However the main advantage of CP is that this mode does not force a reduction in swath. The RADARSAT-Constellation will implement a CP mode in a hybrid-polarity (CL) configuration where H and V will be transmitted simultaneously and 90° out of phase (circular polarization) and dual linearly polarizations will be received (Charbonneau et al. 2010).

To prepare to exploit this CP-CL mode for crop classification, full polarimetric RADARSAT-2 data have been used to simulate CP data. Results from the decompositions of the full polarimetric data (QP) and the Stokes vector parameters from CP have been compared. McNairn and Shang (2014) assessed QP decompositions and the four Stokes vector parameters from CP against the four linear intensity channels (HH, VV, VH, HV) for classification accuracy. The comparisons were carried out for three cropping systems. When the linear polarizations produced accurate (85–90 %) end of season classifications, the QP decompositions provided only small gains (1–2 % increase using Cloude-Pottier; 1–3 % increase using Freeman-Durden). With inputs from the Freeman-Durden decomposition classifications reached accuracies of 87–91 %. The Stokes vectors from CP produced similar results to the QP classifications. This confirmed early results reported in Charbonneau et al. (2010) for a simple cropping mix where late season results using the Stokes vectors were similar to QP decomposition results. In this case, using the Stokes vector parameters synthesized from four C-Band RADARSAT-2 images, end of season classification reached 91 % with individual crop classification accuracies ranging from 81 to

96 %. Both studies (McNairn and Shang 2014; Charbonneau et al. 2010) reported improvement in mid-season classifications using the Stokes vector parameters or QP decompositions, relative to results using the four linear polarizations. By mid-July classification accuracies for canola were 70 % (QP), 80 % for small grains (QP), 80 % for corn (QP or CP), 93 % for wheat (QP or CP) and 80 % for soybeans (CP).

CP is a relatively new concept in land applications and these results are considered preliminary. Although more research is needed, results to date indicate that both QP and CP hold promise for early, mid- and end-of-season crop classification.

15.3.4 Case Studies – The Successful Application of SAR for Crop Classification

Monitoring Rice Acresages Rice is a staple food for many providing between 30 and 70 % of the daily calories for half the world's population (Chen and McNairn 2006). In China, rice accounts for about 42 % of the nation's food production (Pei et al. 2011). Consequently, disruptions in rice production can seriously impact global food security. For this important commodity forecasting supply is critical.

Many studies have documented success in mapping rice paddies and monitoring rice growth using SAR. Backscatter increases significantly during a short period of vegetation growth, although large spatial variations in rice crop growth occur due to shifts in the crop calendar. Many studies have demonstrated sensitivity of multi-temporal C-Band backscatter to the phenology of rice growth, including Le Toan et al. (1997) who used ERS-1 (C-VV), Ribbes (1999) as well as Shao et al. (2001) who used RADARSAT-1 (C-HH), Chen et al. (2007) who used ASAR (HH and HV), Yang et al. (2008) who used ASAR (VV and HH) and Zhang et al. (2009) who used ALOS PALSAR. Classification accuracies of rice paddies have typically been reported well above 90 % (Shao et al. 2001; Li et al. 2003). Choudhury and Chakraborty (2006) used multi-temporal RADARSAT-1 ScanSAR data and a knowledge-based decision rule classifier to achieve 98 % accuracy. Chen and McNairn (2006) used multi-temporal RADARSAT-1 fine mode data to identify hectares (ha) of rice paddies in a region of the Philippines. A minimum mapping accuracy of 96 % was achieved. The authors then used C-HH backscatter from RADARSAT-1 to predict rice yield (kg/ha) to an accuracy of 94 %. Timing of rice planting was also mapped.

The legacy of C-Band sensors has meant a focus on this frequency although more recent research has evaluated space-borne X-Band for rice monitoring. In a study in southern China TerraSAR-X dual-polarized (VV, VH) data were used to map rice acreage, as well as to estimate changes in rice acreage between two years (2008 and 2009) (Pei et al. 2011). Using each individual TerraSAR-X image for each year, rice paddies were classified to a 95.6 % accuracy. Combining these 2 years of data, the change in acreages of rice was estimated to an overall accuracy of 99.0 % (Fig. 15.1). The study reported that almost 15 000 ha of rice was under cultivation

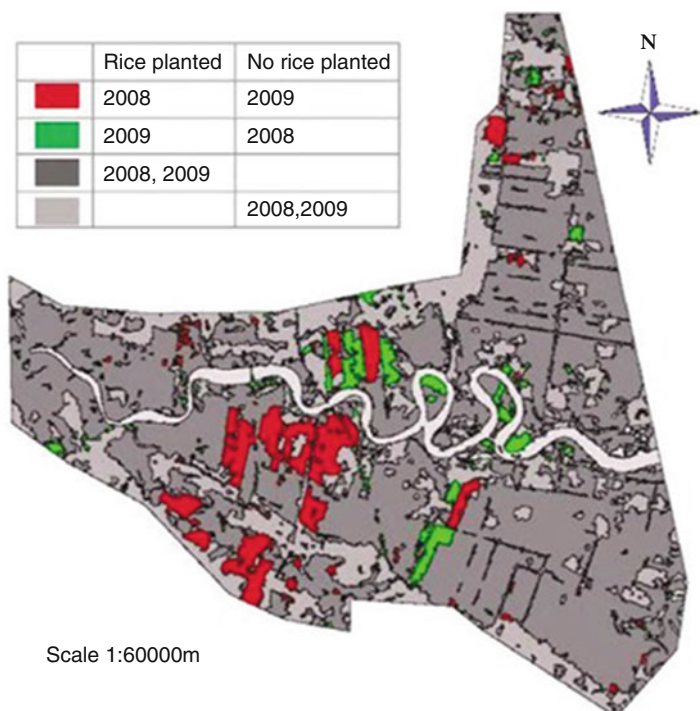


Fig. 15.1 Changes in acreages of late rice between the 2008 and 2009 seasons (Xuwen, China). Paddies planted in rice in 2008 but not 2009 are mapped in red; those planted in rice in 2009 but not 2008 are mapped in green. Land planted in rice both years appears in dark grey. Non-rice fields are identified in light grey (Taken from Pei et al. 2011)

in the Xuwen study site and that about 10 % of this land experienced change (rice to non-rice or non-rice to rice). Experts speculated that rice acreage change in this area was driven mainly by market demand as prices of other cash crops such as peanut and watermelon were high spurring some farmers to drain rice paddies to plant cash crops (Pei et al 2011). These annual fluctuations in rice production were deemed significant as they impact local and regional food security.

Operational End-of-Season Crop Mapping In one of the few examples of operational crop mapping with SAR data, Agriculture and Agri-Food Canada (AAFC) uses RADARSAT-2 and optical data to classify crops for all of Canada (Fig. 15.2) (Fisette et al. 2013). This inventory is delivered every year and supports policy and market development as well as program delivery. In 2011, Canadian Federal and Provincial governments paid out more than \$420 M (CDN) to offset the impacts of climate related disasters, much of which was due to excessive soil moisture preventing farmers from seeding their fields. The AAFC crop inventory mapped the location of unseeded fields and was used to calculate the number of hectares affected. Acreage estimates from this satellite-derived map fell within 3 % of independent Provincial estimates (Fisette et al. 2013).

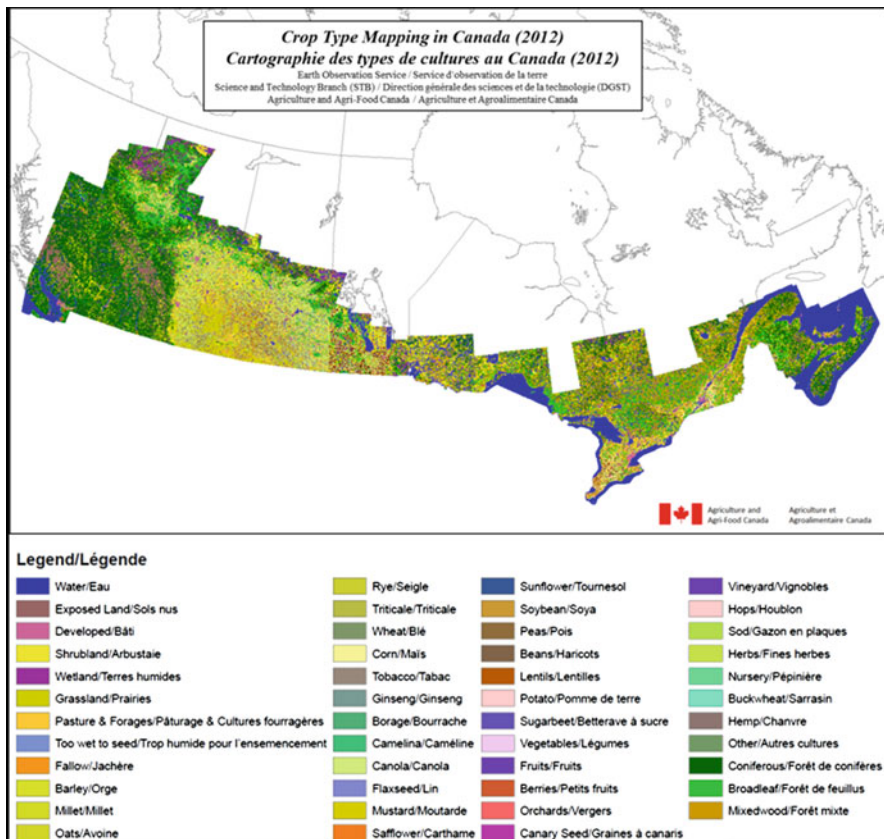


Fig. 15.2 The 2012 crop inventory for Canada. The map is created by classifying both optical and RADARSAT-2 satellite data. Image provided by Agriculture and Agri-Food Canada, Earth Observation Service

To produce this national crop map, data from optical satellites are integrated with C-Band data from RADARSAT-2. In 2013, the total number of scenes used included 1200 RADARSAT-2 scenes and 800 Landsat-8 images (Fisette et al. 2013). The project tasks dual-polarization (VV, VH) ScanSAR mode (300 km swath and 50 m resolution) over western Canada where fields are large and Wide mode (150 km swath and 30 m) over the rest of the country. Little is required to pre-process the SAR imagery other than ortho-rectification and speckle filtering. A Tasseled Cap transformation is applied to the Landsat data to reduce data processing. This is followed by semi-automated cloud and shadow masking.

Crops are classified using a supervised Decision Tree classifier, although a Random Forest classifier is being evaluated to improve processing time and accuracies (Fisette et al. 2013). Under agreements with crop insurance agencies AAFC accesses insurance data to train the classifier and validate the map product. For provinces where insurance data are unavailable, ground-truth information is collected by field crews. The inventory is able to consistently deliver a crop

inventory that meets the overall target accuracy of at least 85 % with a final product at a spatial resolution of 30 m (Fisette et al. 2013). Results from this operational project confirm the research leading to the implementation of the inventory (McNairn et al. 2009b); that integration of SAR can increase accuracies over the use of optical data alone. Here the addition of the RADARSAT-2 data has increased overall accuracies by up to 16 % (Fisette et al. 2013).

Early Season Crop Identification Forecasting in-season production means that crop acreage products must be delivered early in the season. Updates are required if multiple cropping occurs within a season or to improve the accuracy of early season acreage estimates. Considering the discussion in Sect. 15.3.1 where it was suggested that the highest accuracies are achieved when a classification uses SAR data collected at periods of peak biomass, delivery of early season products from this technology may be a challenge. Most studies in the literature have strived to maximize accuracies using all available data.

To evaluate the potential of SAR to deliver early season crop classification, McNairn et al. (2014a) used a supervised decision tree classifier with TerraSAR-X (VV, VH) and RADARSAT-2 (HH, VV, HV/VH). The cropping mix was relatively simple, with only three main crops present (corn, soybeans and hay-pasture). Either the C-Band or X-Band data were capable of delivering highly accurate maps of corn and soybeans at the end of the growing season. Accuracies far exceeded 90 % (Fig. 15.3). Of particular interest was the finding that with three early season TerraSAR-X images corn could be accurately identified by the end of June, a mere 6 weeks after planting and at a V6 vegetative growth stage (where the 6th leaf collar is visible). Identification this early in the season would assist in forecasting corn production. Soybeans required additional acquisitions given the variance in planting densities and planting dates in this region. In this case, accurate soybean classification required TerraSAR-X images until early August when seed development was beginning (R5 reproductive stage).

15.4 Monitoring Crop Condition with SAR

Production forecasting requires not only estimates of acreages planted (calculated from image classifications, for example) but also estimates of how productive crops appear to be. Different strategies have been adopted to estimate crop productivity from satellite data. A great deal of research has been undertaken to develop vegetation indices (primarily from optical sensors) and to use these as indicators of crop productivity (Becker-Reshef et al. 2010; Claverie et al. 2012; Gitelson 2004, 2011). Specifically, indices like the Normalized Difference Vegetation Index (NDVI) are tracked over the growing season and temporal changes in the index are compared to historical “normal” responses for the region. When indices are at or above “normals” crop production is expected to be on track. If these indices fall below historical norms, shortfalls in production might be expected. When coupled with knowledge of acreages, these provide estimates of total production.

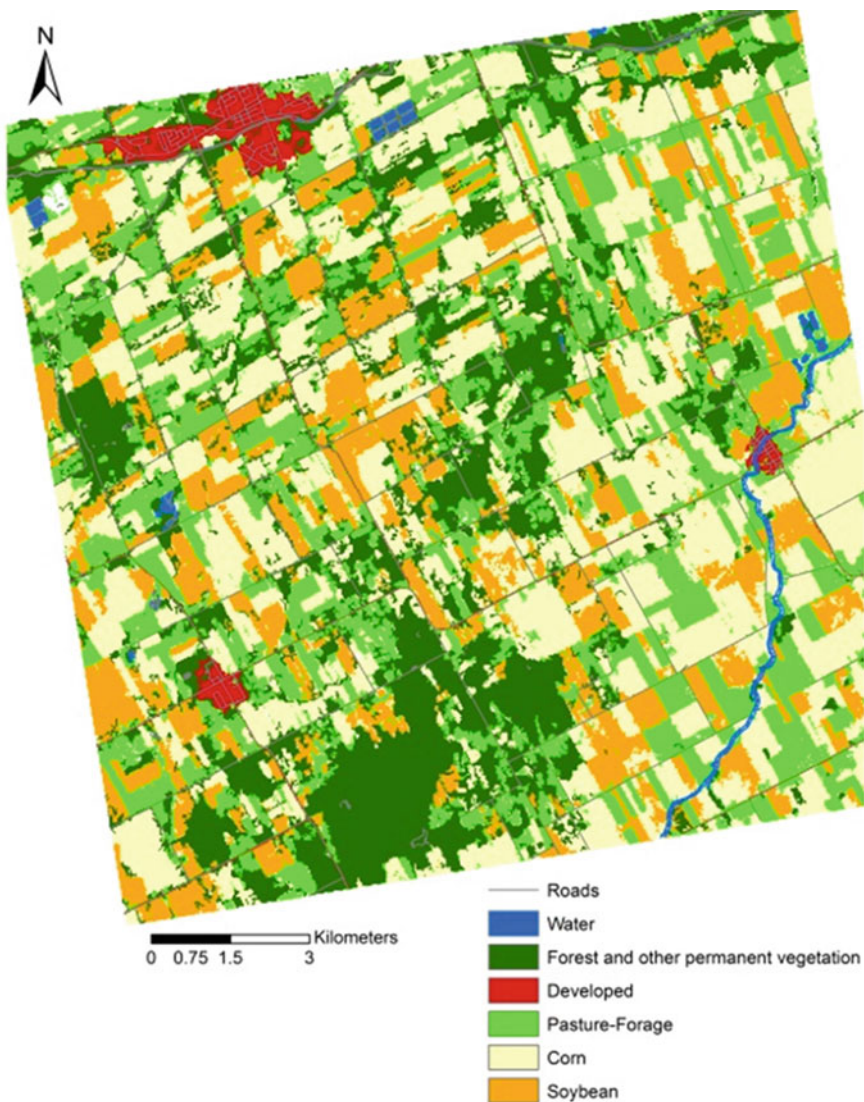


Fig. 15.3 An end-of-season classification map derived from TerraSAR-X (overall accuracy of 97.2 %) (Taken from McNairn et al. 2014a)

Alternatively, satellite response can be used to estimate crop properties which are chemically and biophysically related to crop yield. These properties include for example, biomass, height, leaf area, canopy water content, chlorophyll and nitrogen content. The leaf area index (LAI) is linked to crop productivity and is a critical variable in many crop growth models. Optical remote sensing data have been used to estimate LAI and to calibrate these models (Baret and Guyot 1991; Chen and Cihlar 1996; Brown et al. 2000). Jégo et al. (2012) demonstrated that LAI estimates

from optical data, when assimilated into the Simulateur multidisciplinaire pour les Cultures Standard (STICS) crop growth model, significantly improved yield and biomass prediction. However, knowledge of LAI variation during the entire crop cycle is essential for modelling crop growth and estimating crop yield (Clevers and van Leeuwen 1996). Interference by clouds often creates gaps in optical time series data. These gaps are problematic especially if they occur in the early season when biomass accumulation is greatest. With these challenges SAR data might be considered an option to fill these gaps, especially since microwaves respond to crop structure and thus the intensity and characteristics of scattering could be indicative of canopy biomass, height, LAI or water content.

Regardless of the approach taken, frequent multi-temporal acquisitions are needed to monitor crop condition and changes in these conditions through the entire cropping season. In addition to frequent temporal monitoring, estimates of these properties must be linked with both crop phenology and meteorological conditions, especially since vulnerability of crop growth detractants (disease, fungus) is dependent upon crop phenology (McNairn et al. 2014b).

15.4.1 Temporal Trends in SAR Response and Sensitivity of SAR to Crop Phenology

Although NDVI is perhaps the most widely recognized optically-based vegetation index, other indices can be linked with crop condition, and offer some advantages over NDVI. The Soil Adjusted Vegetation Index (SAVI) is of interest for multi-temporal monitoring of crop condition as this index is linked directly with LAI (Huete 1988 and Choudhury et al. 1994). SAVI has an advantage over other optical indices like NDVI since SAVI minimizes soil effects. When Freeman-Durden decomposition parameters (derived from RADARSAT-2) are compared with SAVI index values (derived from RapidEye), a similar temporal trend in response is observed (Fig. 15.4). Here volume (corn, canola and soybeans) and double-bounce (wheat) scattering derived from RADARSAT-2 increase after crop emergence during vegetative growth stages as crops accumulate leaf area and biomass. Peaks in scattering response are observed in mid-season, near coincident with when SAVI reaches its maximum. Both SAVI and scattering responses decline during the period of senescence, reaching a minimum at the point of harvest. This suggests that volume and double-bounce scattering are responsive to crop development over time, and that the use of these scattering parameters could be considered to temporally track crop condition in an approach similar to optical indices. Further research is needed, particularly since responses appear to be crop type specific.

A Radar Vegetation Index (RVI) was proposed by Kim and van Zyl (2009) for monitoring the vegetation growth using SAR. For natural targets RVI ranges

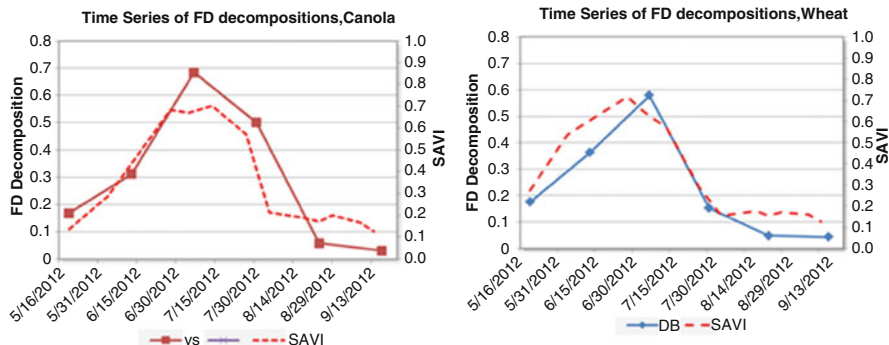


Fig. 15.4 Soil Adjusted Vegetation Index (SAVI) plotted with Freeman-Durden decompositions for canola (VS volume scattering) and wheat (DS double-bounce scattering) derived from C-Band RADARSAT-2. Responses are graphed from crop emergence (May) to senescence and harvest (August)

from 0 to 1 with values close to zero typical of smooth un-vegetated fields. As the vegetation canopy increases, scattering increases as does RVI. RVI is defined as:

$$RVI = \frac{8\sigma^{\circ}_{hv}}{\sigma^{\circ}_{hh} + 2\sigma^{\circ}_{hv} + \sigma^{\circ}_{vv}} \quad (15.1)$$

where σ° is SAR intensity for each transmit (h or v) and receive (h or v) polarization. RVI derived from RADARSAT-2 is statistically correlated with plant height and plant area index (PAI) (Shang et al. 2013, 2014) and biomass (Wiseman et al. 2014). However, other SAR parameters that respond to volume scattering provide higher correlations. The RVI incorporates the linear co-polarizations which are less sensitive to volume scattering. In the case of HH, backscatter responses are largely created by single scattering events as would occur from direct soil interaction early in the growing season. The inclusion of these “less vegetation sensitive” polarizations in the RVI may explain these lower correlations.

Moran et al. (2012) confirmed that HV intensity at C-Band (from RADARSAT-2) is effective for temporally monitoring crop conditions. As well, these authors suggested that this cross-polarized backscatter could be used to track growth stages for grain (jointing and heading) and corn (leaf development and reproduction). Liu et al. (2013) studied the feasibility of monitoring crop growth based on a trend analysis of three basic scattering mechanisms using multi-year (2008–2010) RADARSAT-2 polarimetric data. In this case surface, double-bounce and volume scattering were generated using the Pauli decomposition. The temporal evaluation of the intensity of the scattering mechanisms generally tracked the measured LAI as well as phenology growth stage for wheat, corn and soybeans. Inoue et al. (2002) found that higher frequency X-Band backscatter was sensitive enough to detect thin

rice seedlings just after transplanting. Finally, Wiseman et al. (2014) reported that for spring wheat HV backscatter, volume scattering and pedestal height were able to detect when wheat entered the milking stage which could prove useful as an indicator for the timing of spring wheat harvest.

McNairn et al. (2014b) looked specifically at X- and C-Band responses for identifying the growth stage of canola. Canola is susceptible to a range of diseases which can impact yields. This crop is most vulnerable to fungal infection at flowering and insect infestation at the pod stage. If soil moisture is high at flowering, risk of fungal infection increases and yields can be reduced by as much as 50 %. This study found that X- and C-Band cross-polarization ratios (VV/VH) are high in the weeks following crop emergence due to the dominance of surface scattering from the soil. As canola leaves develop, volume scattering increases as does this ratio. A significant drop in this ratio (below 5 at X-Band and below 4 at C-Band) was observed when the canola flowered – a change in phenology of interest in monitoring for fungal infection. After flowering as the crop transitions to seed development, thick volumes of canola pods create significant multiple scattering increasing VH backscatter, with a further decline in the ratio observed. The decrease in the ratio at seed development was more pronounced at X-Band than C-Band, likely due to the small pods structures which are more closely aligned (in dimension) with X-Band wavelengths. At C-Band, the volume to surface ratio appeared to be more sensitive to pod development than the VV/VH ratio. Alpha angle from RADARSAT-2 was also interesting as the angle increased as scattering transitioned from surface to volume scattering.

15.4.2 *Sensitivity of SAR to Crop Bio-physical Properties*

15.4.2.1 Leaf Area Index

As far back as 1984, Ulaby et al. reported strong correlations between the LAI of corn and Ku-VV backscatter (up to an LAI of two, an R^2 of 0.9 was reported). Paris (1986) reported equally strong correlations at this high frequency (K-VV and K-HH) when examining LAI of corn. In the Ulaby study, only weak correlations were reported for wheat. Using lower frequency C-HH and C-VV backscatter, Ferrazzoli et al. (1992) also reported increases in backscatter with LAI. However as Ulaby et al. (1984) found, eventually the signal saturated becoming insensitive to further increases in LAI above a leaf area of 2–3. In a more recent study by Jiao et al. (2011) and using C-Band RADARSAT-2, sensitivity was lost above an LAI of three. Ulaby et al. (1984) explained that during the early stages of crop growth when LAI is less than 0.5, backscatter is dominated by soil moisture contributions. Leaf contributions dominate during periods of peak crop growth, but in the later stages just prior to harvest ($LAI < 0.5$), backscatter is dominated by soil and stalk contributions for corn, and by soil and head contributions from wheat. Jiao concurred and using the Water Cloud Model (WCM) found that at early growth stages (LAI less than one) soil moisture still had a significant contribution to scattering from corn and soybean

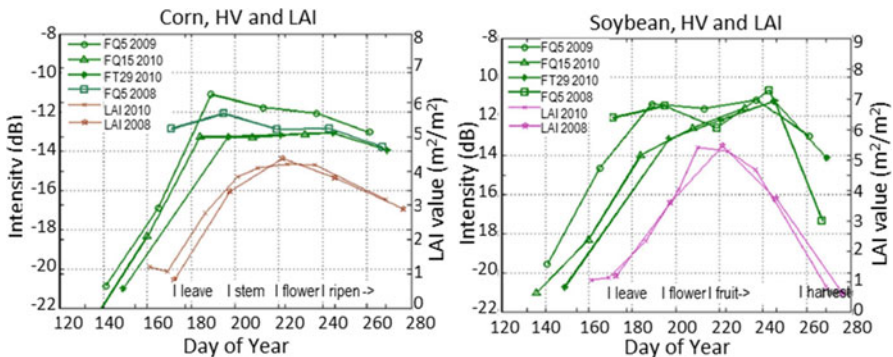


Fig. 15.5 Pauli volume scattering plotted with LAI for corn (left) and soybeans (right). Results are from 3 years of RADARSAT-2 data (2008, 2009 and 2010) collected in different fine quad (*FQ*) modes. Graphs taken from Liu et al. (2013)

fields. However, as the canopy developed and LAI increased to above one, scattering of C-Band microwaves was only minimally affected by soil moisture. After LAI reached three, 90 % of the scattering originated from the canopy.

Even though the evidence indicates that sensitivity is lost at higher LAI, SAR is sensitive to changes in LAI in the critical early growth stages. Additional studies have found strong correlations between SAR response and LAI for cotton (Maity et al. 2004 using C-Band), soybeans (Prasad 2011 using X-Band), corn and soybeans (Jiao et al. 2011 using C-Band) and wheat (McNairn et al. 2012 using C-Band). Liu et al. (2013) found that the RADARSAT-2 generated Pauli decomposition parameters generally tracked LAI development through the growing season (Fig. 15.5). Kim et al. (2013) monitored soybean growth over the season using data collected by an L-, C-, and X-band scatterometer. Although these results confirmed sensitivity to LAI, contrary to other studies, the authors reported that among the different frequencies and polarizations, L-band HH backscatter was most sensitive to growth changes and provided the highest correlation with LAI (as well as vegetation water content).

Jiao et al. (2011) and McNairn et al. (2012) correlated RADARSAT-2 SAR parameters to LAI for corn, soybeans and wheat. As previously observed, SAR parameters indicative of the intensity and characteristics of volume scattering (HV intensity, pedestal height, the Freeman-Durden volume scattering parameter and entropy) were strongly statistically correlated with LAI. Next, these authors parameterized with WCM using SAR responses, LAI and ancillary inputs of soil moisture. The WCM proved to adequately simulate SAR responses as the canopy developed and LAI increased, demonstrating the potential of polarimetric SAR data for monitoring indicators of crop productivity. The degree of model fit varied. For corn the fit (R^2) of LAI to these parameters ranged from 0.92 to 0.95 and for soybeans, 0.76–0.86. For wheat, entropy was selected with a goodness of fit statistic of 0.70. In McNairn et al. (2012) a Look Up Table was then used to invert the WCM and produce a map of LAI from RADARSAT-2 entropy.

15.4.2.2 Canopy Biomass

In addition to LAI, above ground dry biomass is a strong indicator of crop productivity (Liu et al. 2010) and thus monitoring dry biomass is of interest for yield forecasting. As might be expected, most researchers found HV intensity backscatter correlated with vegetation biomass (Paloscia 2002), although the sensitivity was crop type dependent. C-HV backscatter has proven correlated with dry biomass for corn, canola and soybeans (Ferrazzoli et al. 1999). However in an early study Ferrazzoli et al. (1997) reported strong correlations (R^2 of 0.75) between biomass and C-HV backscatter for smaller biomass crops like colza, wheat and alfalfa, but weak correlations (R^2 of 0.31) for corn, sunflower and sorghum, speculating that less weaker results were due to the signal saturation at C-Band. Mattia et al. (2003) used a simulated C-Band HH/VV channel to correlate response to wheat biomass, with an overall correlation of 0.87 reported.

Wiseman et al. (2014) closely examined correlations between C-Band response and dry biomass, and offered other explanations related to changes in crop phenology and thus canopy structure. In this 6 week study, responses of RADARSAT-2 to dry biomass were assessed for corn, canola, soybeans and wheat. SAR response increased more rapidly earlier in the season as biomass accumulation accelerated, leading to stronger correlations with non-linear (logarithmic) statistical models. For corn and canola, the strongest correlations with dry biomass were observed for entropy (R -values of 0.81 for corn and 0.84 for canola), suggesting that early in the season accumulations of biomass increased randomness in scattering within these canopies. For soybeans, the linear cross-polarized backscatter (HV) was most sensitive to increases in biomass (R -value of 0.81). For spring wheat, correlations were weak and these results were attributed to the late start of RADARSAT-2 acquisitions. Mid to late season, crop development was more focused on seed and fruit development and during these periods, a reduced rate of increase in SAR response was observed. It is at this point of crop development where SAR returns became more responsive to changes in growth stage rather than biomass (mostly leaf and stem) accumulation. This sensitivity to changes in structure due to phenology may partially explain reduced sensitivity of SAR to biomass from mid to late season. For canola C-HV backscatter reacted to flowering and ripening. For wheat HV backscatter, volume scattering and pedestal height changed as this crop entered its milking and dough stages.

15.4.2.3 Crop Height

Shang et al. (2013, 2014) illustrated that crop height for wheat is strongly correlated with both crop phenology and plant area index. Given this relationship, the authors explored sensitivity of RADARSAT-2 responses to wheat height and reported significant correlations (R^2) of 0.83 and 0.87 using both the HH and HV polarizations. The C-Band alpha angle gave even stronger correlations (R^2 of 0.93). This confirmed earlier results where McNairn et al. (2002) established that

crop height was significantly correlated with C-HH (RADARSAT-1) backscatter. In McNairn et al. (2002) height, biomass and LAI were used together to in a multi-variate statistical model to more fully characterize the crop canopy. With this multi-variate model as much as 85 % of the variance in C-HH backscatter was explained. Results were crop type dependent with the best RADARSAT-1 results from lower biomass wheat and potato crops. C-HH backscatter was insensitive to variations in corn growth. However using RADARSAT-2 C-HV backscatter, Shang et al. (2014) demonstrated good sensitivity to corn crop height and PAI, with R^2 values of 0.88 and 0.92 respectively. This sensitivity to crop height also explained variances in RADARSAT-2 responses among corn fields in a study completed by Wiseman et al. (2014).

15.5 Summary

A growing global population and a changing environment are placing increased pressure on the agriculture sector to continue to meet requirements of food supply. Early indications of imbalances in regional and global supplies can assist in managing these inequities to avoid crises in food security. Earth observing satellites provide one source of data to map acreages planted and crop growth, and to monitor changes in production over space and time. Although optical sensors have been used extensively for this purpose, poor atmospheric conditions can lead to gaps in data needed for ongoing monitoring. Synthetic Aperture Radar (SAR) sensors provide a reliable source of data, yet the interaction of active microwaves with crop canopies is complex.

Since the launch of the European Remote Sensing Satellite 1 (ERS-1) in 1991 and the Japanese Earth Resources Satellite 1 (JERS-1) in 1992 advances in SAR applications research have been significant. Today users have access to data from many more SAR satellites which operate at different frequencies (X-, C- and L-Band), varying incident angles and are either polarization-diverse or polarimetric-capable. SAR can accurately identifying crops, map crop acreages and identify acreage change. Yet as with optical sensors multi-temporal data is critical to successful classification. In addition higher accuracies are observed when multi-frequency SAR data are combined; research using quad-polarimetry or compact polarimetry SAR modes has proven that classification benefits from higher polarization diversity. Estimates of crop production also require data on crop growth. Here findings from scientists using different SAR sensors and cropping mixes have been consistent. Radar parameters which are responsive to canopy volume scattering (for example HV backscatter, entropy, volume scattering) are sensitive to canopy biophysical parameters including Leaf Area Index, biomass and height. These crop biophysical parameters can be used either directly or through assimilation into yield models to estimate crop productivity and when combined with crop maps, provide an estimate of total production.

The potential of SAR satellites to support national, regional and global crop monitoring is clear. Increased access to advanced SAR sensors, in conjunction with open data access, will foster wider use of this technology. This coming together of research and engineering sets the stage for a greater role for radar satellites in monitoring agricultural production and it is expected that as this technology accelerates, the contribution of SAR in creating knowledge on crop production will increase.

References

- Alberga V, Satalino G, Staykova DK (2008) Comparison of polarimetric SAR observables in terms of classification performance. *Int J Remote Sens* 29:4129–4150
- Baghdadi N, Boyer N, Todoroff P, El Hajj M, Begue A (2009) Potential of SAR sensors TerraSAR-X, ASAR/ENVISAT and PALSAR/ALOS for monitoring sugarcane crops on Reunion Island. *Remote Sens Environ* 113:1724–1738
- Baret F, Guyot G (1991) Potentials and limits of vegetation indices for LAI and APAR assessment. *Remote Sens Environ* 35:161–173
- Becker-Reshef I, Justice C, Sullivan M, Vermote E, Tucker C, Anyamba A, Small J, Pak E, Masuoka E, Schmaltz J, Hansen M, Pittman K, Birkett C, Williams D, Reynolds C, Doorn B (2010) Monitoring global croplands with coarse resolution Earth observations: the Global Agriculture Monitoring (GLAM) project. *Remote Sens* 2:1589–1609
- Bouman BAM, Hoekman D (1993) Multi-temporal, multi-frequency radar measurements of agricultural crops during the Agriscatt-88 campaign in The Netherlands. *Int J Remote Sens* 14:1595–1614
- Bouman BAM, Uenk D (1992) Crop classification possibilities with radar in ERS-1 and JER-1 configuration. *Remote Sens Environ* 40:1–13
- Brisco B, Protz R (1980) Corn field identification accuracy using airborne radar imagery. *Can J Remote Sens* 6:15–24
- Brisco B, Brown RJ, Gairns JG, Snider B (1991) Temporal radar observations of crops in western Canada. *Can J Remote Sens* 18:14–21
- Brown RJ, Manore MJ, Poirier S (1992) Correlations between X-, C and L-band imagery within an agricultural environment. *Int J Remote Sens* 13:1645–1661
- Brown L, Chen JM, Leblanc SG, Cihlar J (2000) A shortwave infrared modification to the simple ratio for LAI retrieval in boreal forests: an image and model analysis. *Remote Sens Environ* 71:16–25
- Charbonneau FJ, Brisco B, Raney RK, McNairn H, Liu C, Vachon PW, Shang J, DeAbreu R, Champagne C, Merzouki M, Geldsetzer T, Trudel M (2010) Compact polarimetry overview and applications assessment. *Can J Remote Sens* 36:298–315
- Chen JM, Cihlar J (1996) Retrieving leaf area index of boreal conifer forests using Landsat TM images. *Remote Sens Environ* 55:153–162
- Chen C, McNairn H (2006) A neural network integrated approach for rice crop monitoring. *Int J Remote Sens* 27:1367–1393
- Chen KS, Huang WP, Tsay DH, Amar F (1996) Classification of multifrequency polarimetric SAR imagery using a dynamic learning neural network. *IEEE Trans Geosci Remote Sens* 34: 814–820
- Chen J, Lin H, Pei Z (2007) Application of ENVISAT ASAR data in mapping rice crop growth in southern China. *IEEE Geosci Remote Sens Lett* 4:431–435
- Choudhury I, Chakraborty M (2006) SAR signature investigation of rice crop using RADARSAT data. *Int J Remote Sens* 27:519–534

- Choudhury BJ, Ahmed NU, Idso SB, Reginato RJ, Daughtry CST (1994) Relations between evaporation coefficients and vegetation indices studied by model simulations. *Remote Sens Environ* 50:1–17
- Claverie M, Demarez V, Duchemin B, Hagolle O, Ducrot D, Marais-Sicre C, Dejoux J-F, Huc M, Keravec P, Béziat P, Fieuza R, Ceschia E, Dedieu G (2012) Maize and sunflower biomass estimation in southwest France using high spatial and temporal resolution remote sensing data. *Remote Sens Environ* 124:844–857
- Clevers JGPW, van Leeuwen HJC (1996) Combined use of optical and microwave remote sensing data for crop growth monitoring. *Remote Sens Environ* 56:42–51
- Cloude SR, Pottier E (1997) An entropy based classification scheme for land applications of polarimetric SAR. *IEEE Trans Geosci Remote Sens* 35:68–78
- Deschamps B, McNairn H, Shang J, Jiao X (2012) Towards operational radar-only crop type classification: comparison of a traditional decision tree with a random forest classifier. *Can J Remote Sens* 38:60–68
- Dobson MC, Ulaby FT (1998) Mapping soil moisture distribution with imaging radar. In: Henderson FM, Lewis AJ (eds) *Principles and applications of imaging radar, manual of remote sensing*, vol 2, 3rd edn. Wiley, New York, pp 407–433
- Dobson MC, Pierce LE, Ulaby FT (1996) Knowledge-based land-cover classification using ERS-1/JERS-1 SAR composites. *IEEE Trans Geosci Remote Sens* 34:83–99
- European Space Agency (2012) *The Earth observation handbook: 2012 special edition for Rio + 20*. European Space Agency, Noordwijk
- Evans DL, Smith MO (1991) Separation of vegetation and rock signatures in thematic mapper and polarimetric SAR images. *Remote Sens Environ* 34:63–75
- Ferrazzoli P, Paloscia S, Pampaloni P, Schiavon G, Solimini D, Coppo P (1992) Sensitivity of microwave measurements to vegetation biomass and soil moisture content: a case study. *IEEE Trans Geosci Remote Sens* 30:750–756
- Ferrazzoli P, Paloscia S, Pampaloni P, Schiavon G, Sigismondi S, Solimini D (1997) The potential of multifrequency polarimetric SAR in assessing agricultural and arboreous biomass. *IEEE Trans Geosci Remote Sens* 35:5–17
- Ferrazzoli P, Guerriero L, Schiavon G (1999) Experimental and model investigation on radar classification capability. *IEEE Trans Geosci Remote Sens* 37:960–968
- Fiset T, Rollin P, Aly Z, Campbell L, Daneshfar B, Flyer P, Smith A, Davidson A, Shang J, Jarvis I (2013) AAFC annual crop inventory: status and challenges. The second international conference on agro-geoinformatics 2013, Fairfax, Virginia, 12–16 August 2013
- Foody GM, McCulloch MB, Yates WB (1994) Crop classification from C-Band polarimetric radar data. *Int J Remote Sens* 15:2871–2885
- Freeman A, Durden SL (1998) A three component scattering model for polarimetric SAR data. *IEEE Trans Geosci Remote Sens* 36:963–974
- Gitelson AA (2004) Wide dynamic range vegetation index for remote quantification of biophysical characteristics of vegetation. *J Plant Physiol* 161:165–173
- Gitelson AA (2011) Remote sensing estimation of crop biophysical characteristics at various scales. *Hyperspectral remote sensing of vegetation*. CRC Press, Boca Raton, pp 329–358
- Groot JS, van den Broek AC, Freeman A (1992) An investigation of the potential of polarimetric SAR data for discrimination between agricultural crops. In: Proceedings of the MAESTRO-1/AGRISCATT: radar techniques for forestry and agricultural applications, Final Workshop, ESTEC, Noordwijk, The Netherlands, 6–7 March 1992
- Guindon B, Teillet PM, Goodenough DG, Palimaka JJ, Sieber A (1984) Evaluation of the crop classification performance of X, L and C-band SAR imagery. *Can J Remote Sens* 10:4–16
- Hill MJ, Ticehurst CJ, Lee J-S, Grunes MR, Donald GE, Henry D (2005) Integration of optical and radar classifications for mapping pasture type in western Australia. *IEEE Trans Geosci Remote Sens* 43:1665–1681

- Hinds MR, Sofko GJ, Wacker AG, Koehler JA (1993) Ku-band polarization characteristics of crops and fallow, radar polarimetry. *Proc SPIE* 1748:47–58
- Hoekman DH, Vissers AM (2003) A new polarimetric classification approach evaluated for agricultural crops. *IEEE Trans Geosci Remote Sens* 41:2881–2889
- Hoekman DH, Vissers AM, Tran TN (2011) Unsupervised full-polarimetric SAR data segmentation as a tool for classification of agricultural areas. *IEEE J Select Top Appl Earth Observ Remote Sens* 4:402–411
- Huete AR (1988) A Soil-Adjusted Vegetation Index (SAVI). *Remote Sens Environ* 25:295–309
- Inoue Y, Kurosu T, Maeno H, Uratsuka S, Kozu T, Dabrowska-Zielinska K, Qi J (2002) Season-long daily measurements of multifrequency (Ka, Ku, X, C, and L) and full-polarization backscatter signatures over paddy rice field and their relationship with biological variables. *Remote Sens Environ* 2–3:194–204
- Jayne TS, Rashid S (2010) The value of accurate crop production forecasts. Fourth African Agricultural Markets Program (AAMP) policy symposium, Lilongwe, Malawi, 6–10 September 2010
- Jégo G, Pattey E, Liu J (2012) Using Leaf Area Index, retrieved from optical imagery, in the STICS crop model for predicting yield and biomass of field crops. *Field Crop Res* 131:63–74
- Jia K, Li Q, Tian Y, Wu B, Zhang F, Meng J (2012) Crop classification using multi-configuration SAR data in the North China Plain. *Int J Remote Sens* 33:170–183
- Jiao X, McNairn H, Shang J, Pattey E, Liu J, Champagne C (2011) The sensitivity of RADARSAT-2 polarimetric SAR data to corn and soybean leaf area index. *Can J Remote Sens* 37:69–81
- Kim Y, van Zyl JJ (2009) A time-series approach to estimate soil moisture using polarimetric radar data. *IEEE Trans Geosci Remote Sens* 47:2519–2527
- Kim Y, Jackson T, Bindlish R, Hoonyol L, Hong S (2013) Monitoring soybean growth using L-, C-, and X-band scatterometer data. *Int J Remote Sens* 34:4069–4082
- Le Toan T, Ribbes F, Li-Fang W, Flory N, Kung-Hau D, Jin Au K, Fujita M, Kurosu T (1997) Rice crop mapping and monitoring using ERS-1 data based on experiment and modeling results. *IEEE Trans Geosci Remote Sens* 35:41–56
- Lee JS, Pottier E (2009) Polarimetric radar imaging: from basics to applications. CRC Press, New York
- Li Y, Liao Q, Li X, Liao S, Chi G, Peng S (2003) Towards an operational system for regional-scale rice yield estimation using a time-series of Radarsat ScanSAR images. *Int J Remote Sens* 24:4207–4220
- Liu J, Pattey E, Miller JR, McNairn H, Smith A, Hu B (2010) Estimating crop stresses, aboveground dry biomass and yield of corn using multi-temporal optical data combined with a radiation use efficiency model. *Remote Sens Environ* 114:1167–1177
- Liu C, Shang J, Vachon PW, McNairn H (2013) Multiyear crop monitoring using polarimetric RADARSAT-2 data. *IEEE Trans Geosci Remote Sens* 51:2227–2240
- Maity S, Patnaik C, Panigraphy S (2004) Analysis of temporal backscattering of cotton crops using a semi-empirical model. *IEEE Trans Geosci Remote Sens* 42:577–587
- Mattia F, Toan TL, Picard G, Posa FI, D'Alessio A, Notarnicola C, Gatti AM, Rinaldi M, Satalino G, Pasquarello G (2003) Multitemporal C-band radar measurements on wheat fields. *IEEE Trans Geosci Remote Sens* 41:1551–1558
- McNairn H, Brisco B (2004) The application of C-band polarimetric SAR for agriculture: a review. *Can J Remote Sens* 30:525–542
- McNairn H, Shang J (2014) Evaluation of C-band polarimetric synthetic aperture radar for crop classification. In: Principles and applications of PolInSAR, European Space Agency (ESTEC), Noordwijk, The Netherlands, in press
- McNairn H, van der Sanden JJ, Brown RJ, Ellis J (2000) The potential of RADARSAT-2 for crop mapping and assessing crop condition. In: Proceedings of the 2nd international conference on geospatial information in agriculture and forestry, Lake Buena Vista, Florida, 10–12 January 2000
- McNairn H, Ellis J, van der Sanden JJ, Hirose T, Brown RJ (2002) Providing crop information using RADARSAT-1 and satellite optical imagery. *Int J Remote Sens* 23:851–870

- McNairn H, Shang J, Jiao X, Champagne C (2009a) The contribution of ALOS PALSAR multipolarization and polarimetric data to crop classification. *IEEE Trans Geosci Remote Sens* 47:3981–3992
- McNairn H, Champagne C, Shang J, Holmstrom D, Reichert G (2009b) Integration of optical and Synthetic Aperture Radar (SAR) imagery for delivering operational annual crop inventories. *ISPRS J Photogramm Remote Sens* 64:434–449
- McNairn H, Shang J, Jiao X, Deschamps B (2012) Establishing crop productivity using RADARSAT-2. International archives of the photogrammetry, remote sensing and spatial information sciences, Volume XXXIX-B8, 2012 XXII ISPRS Congress, Melbourne, Australia, 25 August–01 September 2012
- McNairn H, Kross A, Lapen D, Caves R, Shang J (2014a) Early season monitoring of corn and soybeans with TerraSAR-X and RADARSAT-2. *Int J Appl Earth Obs Geoinf* 28:252–259
- McNairn H, Wiseman G, Powers J, Merzouki A, Shang J (2014b) Assessment of disease risk in canola using multi-frequency SAR: preliminary results. In 10th European conference on synthetic aperture radar, Berlin, Germany, 2–6 June 2014
- Moran MS, Moreno JF, Mateo MPC, de la Cruz DF, Montoro A (2012) A RADARSAT-2 quad-polarized time series for monitoring crop and soil conditions in Barra. Spain *IEEE Trans Geosci Remote Sens* 50:1057–1070
- Paloscia S (2002) A summary of experimental results to assess the contribution of SAR for mapping vegetation biomass and soil moisture. *Can J Remote Sens* 28:246–261
- Paris JF (1983) Radar backscattering properties of corn and soybeans at frequencies of 1.6, 4.75, and 13.3 GHz. *IEEE Trans Geosci Remote Sens* 21:392–400
- Paris JF (1986) The effect of leaf size on the microwave backscattering by corn. *Remote Sens Environ* 19:81–95
- Pei Z, Zhang S, Guo L, McNairn H, Shang J, Jiao X (2011) Rice identification and change detection using TerraSAR-X data. *Can J Remote Sens* 37:151–156
- Prasad R (2011) Estimation of kidney bean crop variables using ground-based scatterometer data at 9.89 GHz. *Int J Remote Sens* 32:31–48
- Raney RK (1998) Radar fundamentals: technical perspective. In: Henderson FM, Lewis AJ (eds) Principles and applications of imaging radar, manual of remote sensing, vol 2, 3rd edn. Wiley, New York, pp 9–130
- Raney RK (2006) Dual-polarized SAR and Stokes parameters. *IEEE Geosci Remote Sens Lett* 3:317–319
- Ribbes F (1999) Rice field mapping and monitoring with RADARSAT data. *Int J Remote Sens* 20:745–765
- Shang J, Jiao X, McNairn H, Kovacs J, Waters D, Ma B, Geng X (2013). Tracking crop phenological development of spring wheat using Synthetic Aperture Radar (SAR) in northern Ontario, Canada. The second international conference on agro-geoinformatics 2013, Fairfax, Virginia, 12–16 August 2013
- Shang, J., Liu, J., Huffman, T., Ma, B., Zhao, T., McNairn, H., and Jiao, X. (2014). Using Earth observation to monitor corn growth in Ontario, Canada. In: Proceedings of the 68th Northeastern corn improvement conference, Ohio Agricultural Research and Development Centre, Wooster, Ohio, USA, 14–15 February, 2014
- Shao Y, Fan X, Liu H, Xiao J, Ross S, Brisco B, Brown R, Staples G (2001) Rice monitoring and production estimation using multitemporal RADARSAT. *Remote Sens Environ* 76:310–325
- Skriver H (2012) Crop classification by multitemporal C- and L-Band single- and dual-polarization and fully polarimetric SAR. *IEEE Trans Geosci Remote Sens* 50:2138–2149
- Skriver H, Mattia F, Satalino G, Balenzano A, Pauwels VRN, Verhoest NEC, Davidson M (2011) Crop classification using short-revisit multitemporal SAR data. *IEEE J Select Top Appl Earth Observ Remote Sens* 4:423–432
- Thomson KPB, Edwards G, Landry R, Jaton A, Cadieux SP, Gwyn QHJ (1990) SAR applications in agriculture: multiband correlation and segmentation. *Can J Remote Sens* 16:47–54
- Ulaby FT, Allen CT, Eger G III, Kanemasu E (1984) Relating the microwave backscattering coefficient to leaf area index. *Remote Sens Environ* 14:113–133

- Wiseman G, McNairn H, Homayouni S, Shang J (2014) RADARSAT-2 polarimetric SAR response to crop biomass for agricultural production monitoring. *J Select Top Appl Earth Observ Remote Sens* 7(11):4461–4471
- Wooding MG (1992) Radar system configurations for crop and forest discrimination using AGRISCATT 8 data of the Feltwell Test Site. In: Proceedings of MAESTRO-1/AGRISCATT: Radar techniques for forestry and agricultural applications: Final Workshop, ESTEC, Noordwijk, The Netherlands, 6–7 March 1992
- Yang S, Shuanghe S, Bingbai L, Le Toan T, Wei H (2008) Rice mapping and monitoring using ENVISAT ASAR data. *IEEE Geosci Remote Sens Lett* 5:108–112
- Zhang Y, Wang C, Wu J, Qi J, Salas WA (2009) Mapping paddy rice with multitemporal ALOS/PALSAR imagery in southeast China. *Int J Remote Sens* 30:6301–6315

Chapter 16

An Approach for Determining Relationships Between Disturbance and Habitat Selection Using Bi-weekly Synthetic Images and Telemetry Data

**Nicholas D. A. Brown, Trisalyn Nelson, Michael A. Wulder,
Nicholas C. Coops, Thomas Hilker, Christopher W. Bater, Rachel Gaulton,
and Gordon B. Stenhouse**

Abstract Ecological studies can be limited by the mismatch in spatial-temporal scales between wildlife GPS telemetry data, collected sub-hourly, and the large-area maps used to identify disturbances, generally updated annually. Recent advancements in remote sensing, data fusion modeling, mapping, and change detection approaches offer environmental data products representing every 16-day period through the growing season. Here we highlight opportunities and challenges for integrating wildlife location data with high spatial and temporal res-

N.D.A. Brown

Department of Geography and Environmental Studies, Carleton University, Ottawa, ON, Canada

T. Nelson (✉)

School of Geographical Sciences and Urban Planning, Arizona State University, Tempe, AZ, USA
e-mail: trisalynnelson@asu.edu

M.A. Wulder

Canadian Forest Service (Pacific Forestry Centre), Natural Resources Canada,
Victoria, BC, Canada

N.C. Coops

Integrated Remote Sensing Studio, Department of Forest Resources Management, University
of British Columbia, Vancouver, BC, Canada

T. Hilker (Deceased Sep 5, 2016)

Department of Geography and Environment, University of Southampton, Highfield Rd,
Southampton SO17 1BJ, UK

C.W. Bater

Forest Management Branch, Forestry Division, Alberta Agriculture and Forestry, Edmonton, AB,
Canada

R. Gaulton

School of Civil Engineering and Geosciences, Newcastle University, Newcastle upon Tyne, UK

G.B. Stenhouse

Foothills Research Institute, Hinton, AB, Canada

olution landscape disturbance data sets, available from remotely sensed imagery. We integrated 16-day outputs from the Spatial Temporal Adaptive Algorithm for mapping Reflectance Change (STAARCH) disturbance maps with grizzly bear (*Ursus arctos*) telemetry data. Our results indicate that males and females avoided same-year disturbances, while male bears were most likely to avoid recently disturbed areas in summer. When intra-year (disturbances mapped at a 16-day time-step) analysis of disturbance was compared to traditional annual time-step analysis, annual aggregation of disturbance data resulted in an increase in the observed selection of same-year disturbed habitat, although change was not statistically significant ($\alpha = 0.05$). We caution the use of low-temporal resolution disturbance data to evaluate short-term impacts on wildlife and highlight the need for further development of probabilistic- and model-based techniques for overcoming spatial-temporal differences between datasets.

16.1 Introduction

Capture of forest disturbance is a critical source of information for landscape management. Traditionally, forest disturbance inventories are completed through field work or by aerial surveys at 5- to 10-year time intervals and are operationally costly and time consuming to implement over large areas. Alternatively, disturbance records may be obtained from forest managers (Nielsen et al. 2004a) or government agencies (Koehler et al. 2007); however, spatial coverage can be limited and accuracy and consistency variable when data are collected by multiple agencies for different uses. Satellite data are often also used by forest managers to provide information regarding disturbance within an inventory cycle (Masek et al. 2008). These inventory and disturbance datasets have become valuable in understanding interactions between wildlife and their environment.

Availability of satellite imagery has allowed large-area mapping of landscape disturbance (Zhang et al. 2002; Healey et al. 2005; He et al. 2009; Asner 2013). For instance, the Landsat series, first launched in 1972, has emerged as one of the most useful satellite datasets for mapping large-area disturbance due to its long temporal record (Wulder et al. 2008, 2011), relevant spectral bands for vegetation mapping, and affordability (Cohen and Goward 2004; Wulder et al. 2004). Landsat has been used extensively by geographers, ecologists, and managers to map landscape disturbance and vegetation change (Cohen and Goward 2004; Gu and Wylie 2010; Huang et al. 2010). Traditionally, large-area maps of disturbance tended to be representative of annual, or longer, time-steps (Masek et al. 2008; Cohen et al. 2010). In contrast, wildlife data, which are increasingly collected using GPS-based telemetry systems, are commonly generated with much greater frequency; wildlife locations are often now recorded on an hourly basis (Johnson et al. 2002; Sunde et al. 2009; Boyce et al. 2010). The temporal discrepancy between environmental and wildlife data has been identified as a limitation when using global positioning system (GPS) technology in ecological studies (Hebblewhite and Haydon 2010).

The opening of the Landsat archive in 2008 to provide free access to analysis-ready imagery (Woodcock et al. 2008) has enabled implementation of applications

that would not have previously been practical due to image costs (Wulder et al. 2012). Notwithstanding the free and open access to all available Landsat imagery, there is a maximum possible revisit of 16 days for image acquisition. When combining the temporal revisit with the limited number of images that can be collected on any given day, for a given path/row location there is variability in the frequency of acquisition both within and between years.

The Spatial Temporal Adaptive Algorithm for mapping Reflectance Change (STAARCH) is a data fusion model that allows for the creation of high spatial and temporal resolution disturbance maps (Hilker et al. 2009). STAARCH integrates Landsat and Moderate Resolution Imaging Spectrometer (MODIS) imagery to enable mapping of disturbance at high spatial and temporal resolution. MODIS, with a repeat cycle of one (towards the poles) or two days (near the equator), is designed to provide near continuous monitoring of biophysical parameters (Justice et al. 1998; Huete et al. 2002) at spatial resolutions from 250 to 1000 m, depending on the spectral channel. A time series of MODIS images can be aggregated through compositing daily observations in order to reduce cloud contamination (Vermote et al. 1997; Hilker et al. 2009). The synthetic STAARCH product takes advantage of the high spatial resolution of Landsat and high temporal resolution of MODIS composite images to provide disturbance maps with a 16-day return interval and 30-m spatial resolution (Hilker et al. 2009; Gaulton et al. 2011).

In this chapter we examine the opportunities and challenges of integrating new high spatial and temporal resolution disturbances maps with detailed wildlife GPS data. As a case study, we integrated STAARCH disturbance maps with grizzly bear (*Ursus arctos*) telemetry data from Alberta, Canada. Using a 16-day time-step, we assessed the impact of disturbance presence and timing on spatial patterns of grizzly bear habitat selection by statistically comparing observed frequency of disturbance selection to a null hypothesis that, within available habitat, disturbances are selected randomly regardless of time since disturbance. Results from the analysis using the disturbance products with a 16-day time-step are compared with those obtained when using a single annual disturbance layer.

16.2 Study Area

The 14,000 km² study area is located in the foothills of the Rocky Mountains north of the town of Grand Cache, Alberta, Canada (Fig. 16.1). Terrain heights range from 600 m above sea level in the northeast to 2400 m in the Rocky Mountains towards the southwest of the study area. The landscape is characterized largely by forest cover, with forest disturbance and land use determined primarily by resource extraction industries, including forestry, mining and oil and gas (Schneider et al. 2003), with the exception of a small area in the southwest that intersects the Kakwa-Wilmore Interprovincial Park. Forests within our study area have been managed for resource extraction for over 50 years with a substantial increase since the 1980s (White et al. 2011). Given fire suppression, resource extraction and related activities are the dominant landscape disturbance, with most disturbances arising from the forest industry and oil and gas exploration (Schneider 2002). Approximately 76 %

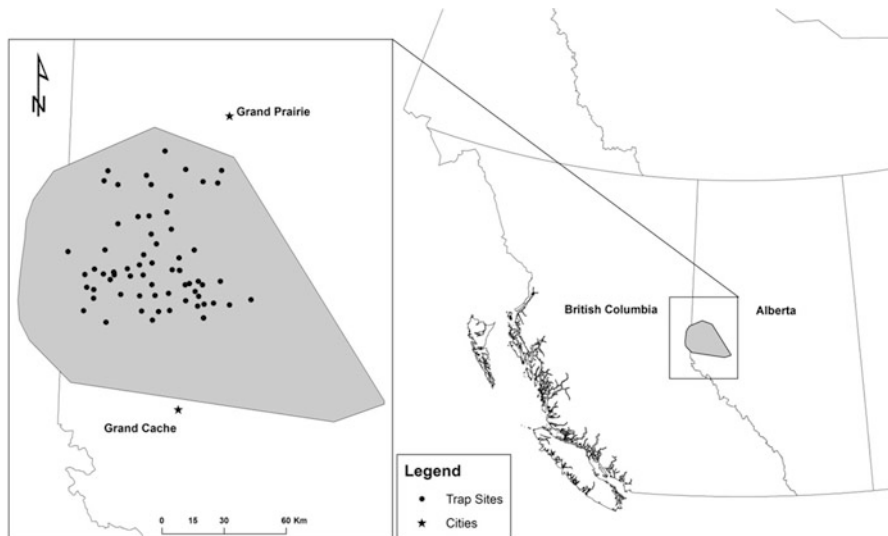


Fig. 16.1 Study area in west central Alberta, Canada

of the forested land base in the Kakwa Region is managed for timber harvesting. Forestry activities have created a patchwork of forest harvests as well as roads. The growing oil and gas industry has also led to new roads as well as pipelines and well sites. The longevity of the disturbances from resource extraction activities varies. Forest harvests will undergo vegetation succession and provide food resources for wildlife (Stewart et al. 2013). Roads that are not deactivated, pipelines, and active well sites are more permanent.

16.3 Data and Methods

16.3.1 STAARCH-Derived Disturbance

The STAARCH algorithm requires a minimum of two Landsat images to mark the beginning and end of the time period of interest (Hilker et al. 2009). The STAARCH algorithm captures disturbance using a Tasseled Cap transformation of the Landsat observations, yielding a disturbance index (DI) value (described in Healey et al. 2005). A change mask is generated by thresholding consecutive DI values of a given pixel. Changes detected in the Landsat imagery are then dated using marked deviations through a time series analysis of a modified disturbance index calculated from the MODIS imagery. The STAARCH process requires MODIS 8-day composite images to create a suite of high temporal resolution disturbance indices (Zhang et al. 2002) for the time period between the first and last Landsat images. Changes in DI values for the Landsat change mask are then matched to the dates of disturbance obtained from the MODIS imagery. Preliminary results indicate that 87 and 89 % disturbances are assigned correct dates (Hilker et al. 2009) when

validated against a manually verified, remotely sensed disturbance inventory (Linke et al. 2009). More recent work has reported overall accuracies of 62 %, with the lower value being attributed to a larger study area, smaller disturbance sizes, and an increased time period (Gaulton et al. 2011).

Previous research has demonstrated the Tasseled Cap Transformation (TCT) of spectral image data as a tool for effective mapping of land cover change and disturbance (Healey et al. 2005; Masek et al. 2008). The accuracy and applicability of STAARCH as a disturbance detection technique has been assessed in this study area. Using many of the same Landsat scenes as applied to this study, Hilker et al. (2009) found STAARCH had an accuracy rate for correctly identifying disturbances in the correct year of 87 %, 87 % and 89 % in 2002, 2003, and 2005 respectively, based on a disturbance mapping dataset derived independently from aerial photography. The spatial accuracy of the detection area itself was 93 % when compared to the validation dataset. Areas where the algorithm had poorer accuracy were wetter sites, and as a result, disturbances within flood plains and bogs, may be more poorly represented.

An example of STAARCH disturbance mapping is shown in Fig. 16.2. Disturbance is defined as any event that increases the disturbance index of a previously

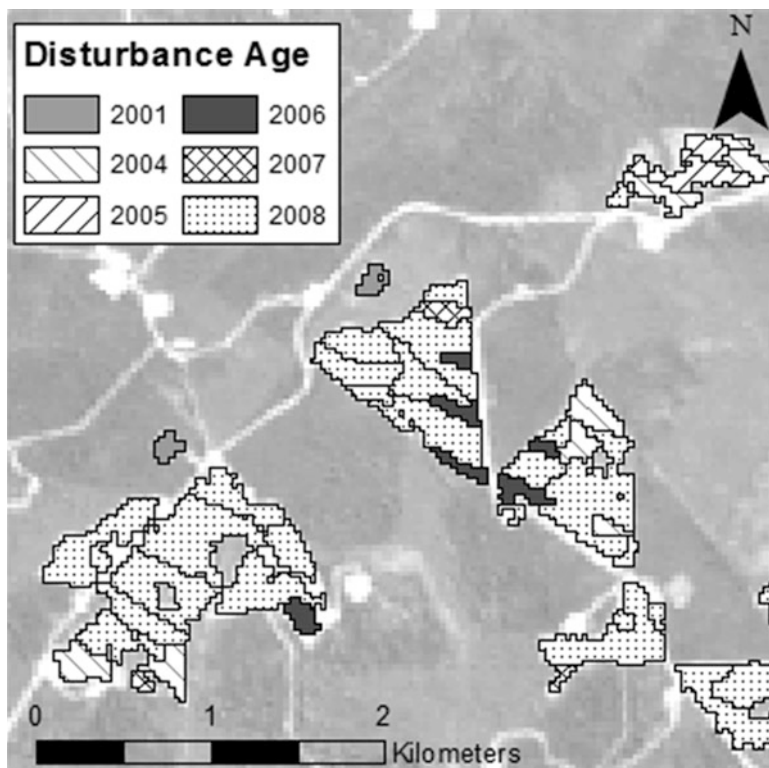


Fig. 16.2 Sample of map of disturbance created using the STAARCH algorithm. Also shown is a Tasseled-Cap-based disturbance index. Bright pixels indicate areas of greater disturbance

forested region as assessed by the STAARCH algorithm. Disturbances in this region are predominantly, if not exclusively, anthropogenic including forest harvests, wellsites, and roads. Disturbance mapping was conducted using a 16-day return interval and extended from September 2001 to June 2008. The modal disturbance patch size is 1.08 ha (Gaulton et al. 2011).

16.3.2 Telemetry Points

Grizzly bear telemetry data were collected using GPS radio collars attached to 40 adult (age 5+) bears. The locations of 23 male and 17 female bears were obtained between May 2005 and December 2009. The GPS collars were programmed to record a location each hour during the non-denning period (April–November), however actual recorded locations varied with individual collars. Individual bears were tracked for between one and three years. Only bears with high sampling frequencies (≥ 10 GPS fixes/day) and ≥ 500 telemetry point locations were included, resulting in 23 total bears, 12 females and 11 males. The spatial distribution of trap locations are shown in Fig. 16.1 and the number of traps varied annually between 10 and 22.

16.3.3 Data Integration

To integrate bear telemetry data with the 16-day temporal resolution STAARCH disturbance data, we evaluated the spatial-temporal overlap between the two data sets. First, telemetry data were aggregated to represent 16-day periods to correspond with the STAARCH time intervals. For each 16-day period, the number of grizzly bear collar locations intersecting disturbance polygons was quantified, and the total disturbed area recorded by STAARCH calculated.

16.4 Grizzly Bear Response to Disturbance

We compared the observed habitat selection, recorded in the telemetry data, to expected habitat selection, based on a model to randomize telemetry data within available habitat.

16.4.1 Observed Selection

Many aspects of grizzly bear biology, such as diet and behaviour, change seasonally (Nielsen et al. 2004a, c; Munro et al. 2006), which in turn affects the spatial pattern of habitat selection (Nielsen et al. 2004a). To account for seasonal variability,

disturbance and telemetry data were subdivided into: spring (den emergence to June 25), summer (June 26 to August 15) and autumn (August 16 to denning) (Nielsen et al. 2006; Smulders et al. 2012).

For each telemetry point, the nearest forest disturbance polygon was identified. Due to the availability of unique, high spatial and temporal resolution disturbance data it was possible to only consider disturbances that occurred prior to when a bear was observed when calculating nearest disturbance. Grizzly bear telemetry locations that were farther than 500 m from any disturbance were excluded from analysis. A 500 m threshold has been used previously in relating landscape disturbance to grizzly bear habitat selection (Berland et al. 2008). For each disturbance, by year, observed selection was quantified as the number of telemetry points nearest to a disturbance. Since the number of telemetry points and the sampling frequency associated with each bear was different, results were normalized by dividing the number of telemetry points associated with a particular disturbance age by the total number of telemetry points within that season.

16.4.2 Expected Selection

Observed patterns of disturbance selection were statistically compared to an expected pattern. The expected pattern or null model was that bears did not select for disturbances based on disturbance age (Smulders et al. 2010). We generated a frequency distribution of expected selection by randomizing the observed of telemetry locations within available habitat. Available habitat was defined using minimum convex polygons (MCP) that were created for each of the grizzly bears. The MCP is the smallest convex area that contains all data points (Mohr 1947) and represents the outer limit of observed habitat used by bears sampled through telemetry data collection. Ninety-nine randomizations were generated, and for each randomization the number of random telemetry points nearest to a disturbance was quantified, generating a null model for statistical comparison. Statistical results were grouped by disturbance age and presented using box plots. We defined disturbance age as the difference between the year a grizzly bear's location was recorded and the year a disturbance occurred. Disturbance age, or time since disturbance, indicates how much time has elapsed between initial disturbance and subsequent selection. The disturbance age is an indicator of forest successional stage and reflects food availability (Nielsen et al. 2004c).

16.4.3 Temporal Resolution of Disturbance Data

To assess the impact of the temporal resolution of disturbance data on research findings, we reprocessed the data for same-year disturbance with disturbance dates aggregated to an annual resolution. The effect of the temporal resolution of disturbance data on observed patterns of habitat selection was quantified by

comparing the resulting annual frequency-of-selection distributions to the 16-day resolution frequency-of-selection distributions using a Komologorov-Smirnov test.

16.5 Results

16.5.1 Data Integration

In Fig. 16.3 we show the total disturbed area and total number of telemetry points that fall within disturbance polygons for each 16-day time step. In this figure we are quantifying general correspondence between all the harvest areas and telemetry data. Generally, an increase in the total disturbed area corresponds to a larger number of telemetry points within the disturbances. The number of points within the

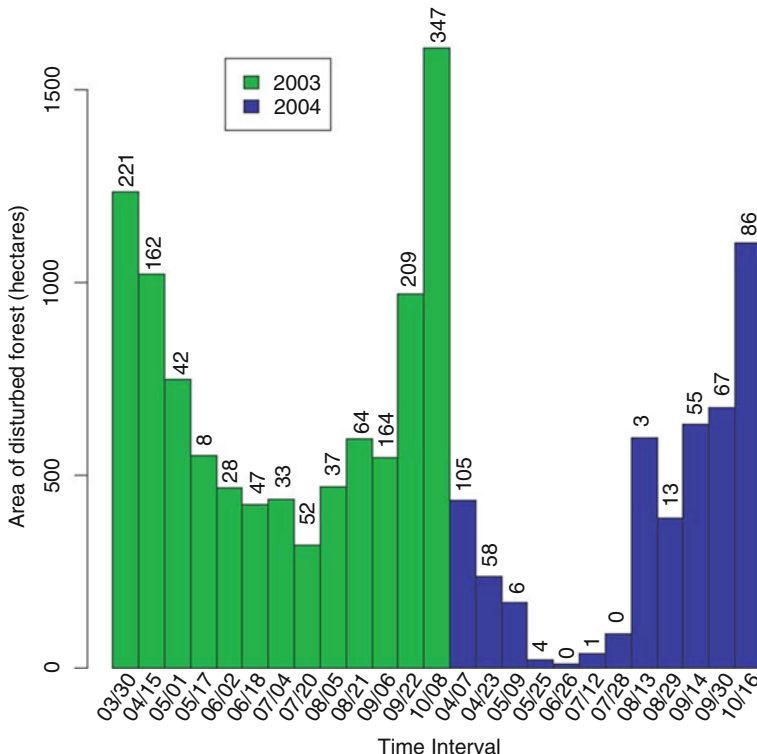


Fig. 16.3 Bar plot showing the variation in total disturbed area with time for 2 years. Numbers above bars indicate how many telemetry points fell within disturbance polygons for a given time interval ($n = 99,929$). All harvests are considered regardless of age, in order to show the general correspondence. As might be expected, as an area of disturbance increases there tends to be a larger number of telemetry points corresponding with disturbed locations

disturbance polygons is small relative to habitat usage; for any given time interval, the total number of points within a STAARCH forest disturbance polygon represents less than 0.005 % of the total number of points. Similarly, the total disturbed area for any one time interval is small (5.52 km^2) compared to the study area ($14,000 \text{ km}^2$).

16.5.2 Grizzly Bear Response to Disturbance

Figures 16.4 and 16.5 show the preferential selection of disturbed habitat through time for female and male bears, respectively. For most disturbance ages, selection was highly variable, as evidenced by the large interquartile ranges. Variability

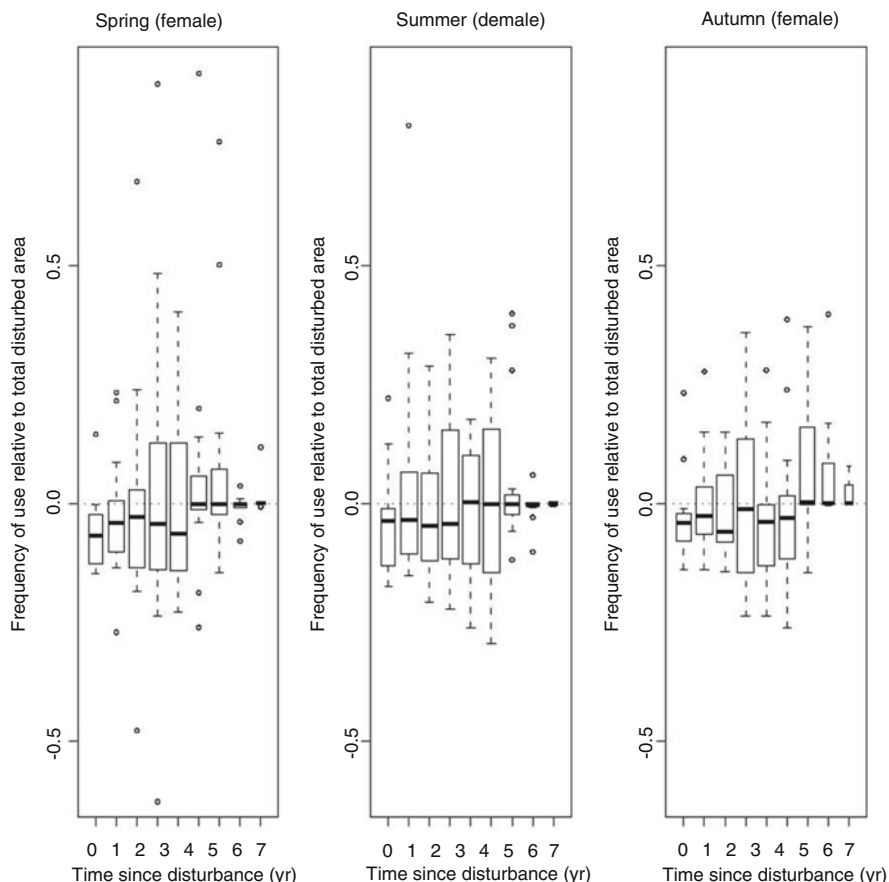


Fig. 16.4 Results for female bears grouped by season. Positive values represent selection of disturbed habitat. Negative values represent avoidance of disturbed habitat. Horizontal line at 0.0 signifies proportional selection of disturbance exactly equal to proportional disturbed area for a given year. Analysis includes 12 female bears and 53,139 telemetry locations

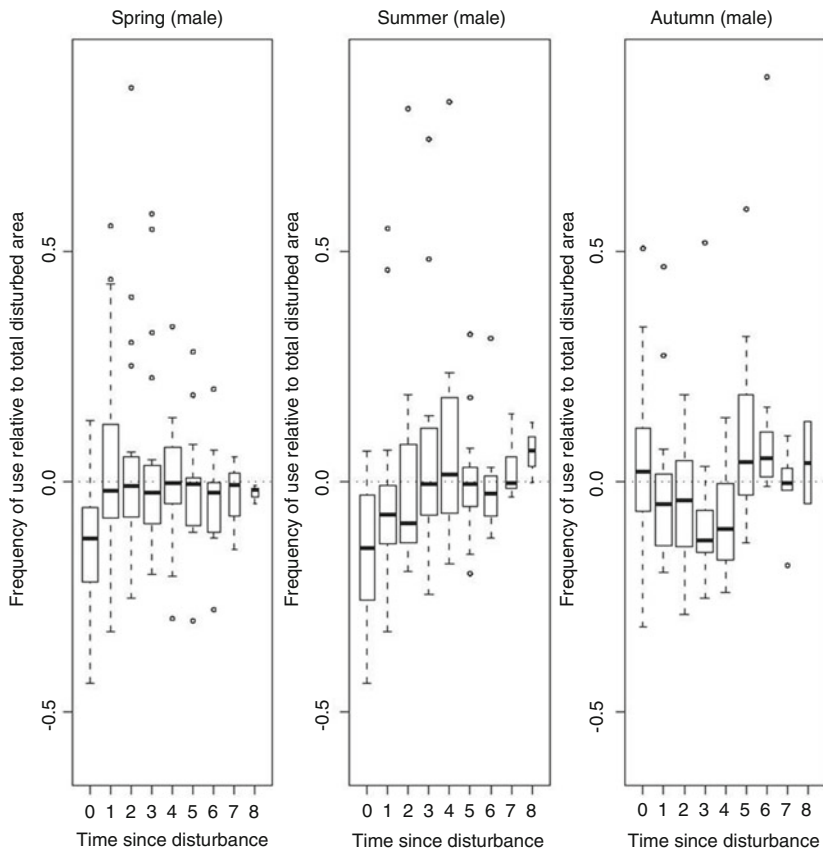


Fig. 16.5 Results for male bears grouped by season. Positive values represent selection of disturbed habitat. Negative values represent avoidance of disturbed habitat. Horizontal line at 0.0 signifies proportional selection of disturbance exactly equal to proportional disturbed area for a given year. Analysis includes 11 female bears and 46,732 telemetry locations

in selection of disturbance appeared to decline in the seventh and eighth years following disturbance, but this is likely a spurious finding resulting from smaller sample sizes (three bears as opposed to 12 or more bears).

In all seasons female bears exhibited avoidance of same-year disturbance and showed reduced selection of one- and two-year-old disturbances (Fig. 16.4). In spring, selection increased for older disturbances, with three- and four-year-old disturbances exhibiting mixed responses, and five- and six-year-old disturbances slight preferential selection. In summer, variability in selection generally increased with disturbance age up to five year old disturbances. In autumn, variability in selection increased for one-, two-, and three-year-old disturbances, and decreased for four- and five-year-old disturbances, which were generally avoided.

Table 16.1 Mean relative frequency of use for same-year disturbance. Negative values signify avoidance, whereas positive values signify preferential use. Data are presented here for 16-day STAARCH disturbance, as well as for down-sampled annual disturbance data. In every case, down-sampling of disturbance data to an annual resolution results in an increase in use

	Spring		Summer		Autumn	
	16-day	Annual	16-day	Annual	16-day	Annual
Female	-0.0625	-0.0196	-0.0409	-0.0332	-0.0276	-0.0212
Male	-0.127	-0.0403	-0.147	-0.134	0.0463	0.0573

In spring and summer, male bears exhibited slight avoidance of same-year disturbance (Fig. 16.5). During spring, selection of disturbed habitat increased slightly for one- to four-year-old disturbances, and decreased slightly for disturbances older than 5 years. For male bears in summer, older disturbances were selected more frequently than younger ones. Males in autumn were the only instance of male bears selecting for same-year disturbance. Selection of disturbance decreased for one- to four-year-old disturbance, with a minimum for 4-year-old disturbances, and then increased again for disturbances older than 5 years.

16.5.3 Temporal Resolution of Disturbance Data

In all cases, aggregating disturbance data to a yearly resolution resulted in an increase in the observed selection of same-year disturbed habitat. The difference in results was most pronounced for male bears in spring, though it was not statistically significant at the 5 % confidence interval for any of the categories (Table 16.1). Seasonal variation in the strength of trends could be due to the timing of den emergence. The sampling in spring may be less consistent as bears will emerge on different dates depending on snow pack and inter-annual variation. The summer signal may be slightly less biased by sampling.

16.6 Discussion

Our aim was to highlight opportunities and challenges of integrating high temporal resolution disturbance and telemetry data sets using a grizzly bear case study. One of the opportunities afforded by the availability of fine temporal resolution disturbance data is that the grizzly bear response to disturbance can be assessed intra-annually. Though remote sensing data have been used to investigate wildlife disturbances (e.g., Ndegwa and Murayama 2009), when disturbance data are represented annually it is not be possible to determine when within the year a given disturbance occurred on the landscape. The ability to determine when, to the

nearest 16-day interval, a given disturbance occurred is an important contribution of synthetic remote sensing products such as STAARCH in support of ecological and habitat studies.

A limitation when integrating fine temporal wildlife and disturbance data sets is the often insufficient spatial-temporal overlap between the animal GPS locations and mapped forest disturbance. In some cases, when there was little disturbance proximal to a bear's location, it was impossible to ascertain how selection of disturbance changed on a same-year basis because the bear would pass through the disturbed area only once in the entire year. Another difficulty associated with data integration is that, assuming negligible error, disturbance data represent all disturbed locations. However, as a consequence of the discrete sampling through time and the practical reality of collaring a sample of individuals, telemetry points necessarily represent a sample of selected wildlife locations (Wells et al. 2011). While the remote sensing-derived disturbance data represent the statistical population of events, the wildlife data represent a sample that is relatively sparse.

Artificially downgrading the temporal resolution of the disturbance data from 16 days to one year led to results that overrepresented the selection of disturbances. When disturbance is represented annually, the nearest disturbance that occurred at any time within the year would be selected. This may be problematic if the disturbance actually occurred after the grizzly bear utilized a specific location. Although the changes in selection results were not statistically significant, this may not always be the case, particularly in areas that are undergoing high levels of anthropogenic activity. Implications for wildlife management include misinterpretation of wildlife response to recently disturbed habitat. In cases where disturbance results in a loss of usable habitat and subsequent animal avoidance, selection of annually aggregated disturbance data could result in a failure to recognize the full impact of habitat loss.

Our results indicated that both male and female bears may be avoiding same-year disturbances, though the trend is stronger for females. Forest harvests are well documented to be attractors to bears due to the availability of food (Nielsen et al. 2004a). However, the establishment of berries will take at least a year. The noise and activity of humans during the year of harvesting may well be a deterrent to bears. The behavioural response of male bears to disturbance age is clearest in summer, where selection of disturbances increased markedly with age of disturbance. It is common to see differences in male and female patterns of habitat selection (Bourbonnais et al. 2013). The summer availability of bears likely explains the seasonal variation and related research has found that the spatial-temporal pattern of habitat selection, in female grizzly bears, has the strongest signal in summer (Smulders et al. 2012). Although sample size was insufficient to assess the impacts of offspring status on female patterns of habitat selection, we expect selection of disturbance to vary with presence and age of offspring and differences between summer and autumn responses to disturbance age may be partly associated with offspring (Smulders et al. 2012).

It is possible that recent disturbances have insufficient over- and mid-storey vegetation for visual cover and must mature before providing beneficial food resources (Ndegwa and Murayama 2009). During summer, a large part of the bears'

diet is comprised of forbs such as *Trifolium* and *Equisetum* spp. (Munro et al. 2006), both of which are more common in forest harvests than in mature forests (Nielsen et al. 2004b). However, immediately following forest disturbance, the abundance of forbs is likely reduced, and gradually increases for older disturbances before reaching a maximum abundance. In the case of locations subject to forest harvesting, subsequent successional developments mean that increasing age is positively correlated with increasing food availability (Nielsen et al. 2004c).

The consistently low selection of same-year disturbance, even when compared to one-year-old disturbance, suggests that the increased human activity associated with active forest disturbance may also discourage selection. Avoidance of human activity by grizzly bears is consistent with a recent study that found grizzly bears avoided habitat with active wellsites, but not habitat with inactive wellsites (Laberee et al. 2014). Given that 90% of recorded grizzly bear deaths are found within 500 m of a road or 200 m of a trail (Benn and Herrero 2002), avoiding areas with human activity may reduce mortality (Nielsen et al. 2004b). The avoidance of young disturbances by grizzly bears may be a mechanism for avoiding human interaction (Graham et al. 2010). Although the food resources near roads provide important food for bears, the increased interaction with people leads to increased risk of mortality (Nielsen et al. 2004c; Benn and Herrero 2002).

16.7 Outlook

The integration of remote sensing and telemetry data is in its infancy and there are many future developments both in terms of the methods that need to be developed and the biological research questions that can be addressed. At present, improved approaches to integrating the disparate space-time scales of remote sensing and wildlife telemetry data are required. While wildlife habitat selection research often focuses on relatively large areas, unique insights are anticipated through the integration of high spatial resolution remote sensing data, sub-meter optical imagery and/or lidar, with high resolution telemetry data sets (e.g., Loarie et al. 2013). Rather than characterizing the interaction over large areas, examination of patterns between movement and habitat use in smaller exemplar areas may reveal trends that can then be scaled up using appropriate remotely sensed data products that represent habitat over large areas. Long time series remotely sensed data, especially that from the Landsat program, can provide informative baseline data as well as capture trends over time (White et al. 2011) that, in turn, can be integrated with telemetry data sets. There is also much potential to integrate remotely sensed data into movement research by developing approaches to interpolate, condition, and inform movement based on habitat conditions (Long and Nelson 2013).

While here we highlight the integration of telemetry and remotely sensed there is additional potential for these data types over a wide range of hypothesis generating and confirming research topics. For example, we can assess impacts of new roads on wildlife habitat selection, quantify how long after large machines leave an area it

takes for wildlife to return, or to determine the influence of road closures on wildlife movement. Many of these research questions will benefit from data collection programs that have suitable overlap between telemetry data and landscape change.

16.8 Conclusions

An advantage when using disturbance products derived from remote sensing is the ability to synoptically and repeatedly map large areas. Using novel data processing to blend data with high temporal frequency with other imagery with fine spatial characterization provides for unique and otherwise unavailable data products. Through creating and applying data blending methods, such as offered by the STAARCH algorithm, high spatial and temporal resolution mapping of landscape change is afforded. These spatial tools may be most valuable for investigations covering large areas with needs for distance information within, as well as, between years. To act as an example of such an application, we demonstrated the use of high spatial and temporal resolution disturbance mapping products to provide a critical linkage disturbance and the GPS-based wildlife telemetry data. The new approaches and techniques presented here are useful in long-term monitoring efforts where it is important to determine species at risk population trends in conjunction with landscape change. However, probabilistic and model-based techniques must be developed and tested to enable differences in scale and limited overlap to be accounted for when investigating research questions. Research using low-temporal resolution disturbance data may generate results that misrepresent selection of disturbed habitat since same-year disturbances that occur before a GPS location is recorded are not differentiated from those occurring after the location is recorded. The preliminary findings of our case study suggest further investigation into the short term impacts of disturbance on habitat selection may be warranted. The complexity of interactions between bears, their habitat, and co-occurring disturbances is reiterated in our findings.

References

- Asner GP (2013) Biological diversity mapping comes of age. *Remote Sens* 5:374–376. doi:[10.3390/rs5010374](https://doi.org/10.3390/rs5010374)
- Benn B, Herrero S (2002) Grizzly bear mortality and human access in Banff and Yoho National Parks, 1971–98. *Ursus* 13:213–221
- Berland A, Nelson TA, Stenhouse G, Graham K, Cranston J (2008) The impact of landscape disturbance on grizzly bear habitat use in the Foothills Model Forest, Alberta, Canada. *For Ecol Manag* 256:1875–1883
- Bourbonnais ML, Nelson TA, Cattet MR, Darimont CT, Stenhouse GB (2013) Spatial analysis of factors influencing long-term stress in the grizzly bear (*Ursus arctos*) population of Alberta, Canada. *PLoS One* 8(12), e83768

- Boyce MS, Pitt J, Northrup JM, Morehouse AT, Knopff KH, Cristescu B, Stenhouse GB (2010) Temporal autocorrelation functions for movement rates from global positioning system radiotelemetry data. *Philos Trans R Soc B* 365:2213–2219
- Cohen WB, Goward SN (2004) Landsat's role in ecological applications of remote sensing. *Bioscience* 54:535–545
- Cohen WB, Yang Z, Kennedy R (2010) Detecting trends in forest disturbance and recovery using yearly Landsat time series: 2. TimeSync Tools for calibration and validation. *Remote Sens Environ* 114:2911–2924
- Gaulton R, Hilker T, Wulder MA, Coops NC, Stenhouse GB (2011) Characterizing stand replacing disturbance in western Alberta grizzly bear habitat, using a satellite-derived high temporal and spatial resolution change sequence. *For Ecol Manag* 261:865–877
- Graham K, Boulanger J, Duval J, Stenhouse G (2010) Spatial and temporal use of roads by grizzly bears in west-central Alberta. *Ursus* 21:43–56
- Gu Y, Wylie BK (2010) Detecting ecosystem performance anomalies for land management in the Upper Colorado River Basin using satellite observations, climate data, and ecosystem models. *Remote Sens* 2:1880–1891. doi:[10.3390/rs2081880](https://doi.org/10.3390/rs2081880)
- He Y, Franklin SE, Guo X, Stenhouse GB (2009) Narrow-linear and small-area forest disturbance detection and mapping from high spatial resolution imagery. *J Appl Remote Sens* 3:033570
- Healey SP, Cohen WB, Yang ZQ, Krankina ON (2005) Comparison of tasseled cap-based Landsat data structures for use in forest disturbance detection. *Remote Sens Environ* 97:301–310
- Hebblewhite M, Haydon DT (2010) Distinguishing technology from biology: a critical review of the use of GPS telemetry data in ecology. *Philos Trans R Soc B* 365:2303–2312
- Hilker T, Wulder MA, Coops NC, Linke J, McDermid G, Masek JG, Gao F, White JC (2009) A new data fusion model for high spatial- and temporal-resolution mapping of forest disturbance based on Landsat and MODIS. *Remote Sens Environ* 113:1613–1627
- Huang C, Goward SN, Masek JG, Thomas N, Zhu Z, Vogelmann JE (2010) An automated approach for reconstructing recent forest disturbance history using dense Landsat time series stacks. *Remote Sens Environ* 114:183–198
- Huete A, Didan K, Miura T, Rodriguez EP, Gao X, Ferreira LG (2002) Overview of the radiometric and biophysical performance of the MODIS vegetation indices. *Remote Sens Environ* 83: 195–213
- Johnson CJ, Heard DC, Parker KL (2002) Expectations and realities of GPS animal location collars: results of three years in the field. *Wildl Biol* 8:153–159
- Justice CO, Vermote E, Townshend JRG, Defries R, Roy DP, Hall DK, Salomonson VV, Privette JL, Riggs G, Strahler A, Lucht W, Myneni RB, Knyazikhin S, Running SW, Nemani RR, Wan Z, Huete AR, van Leeuwen W, Wolfe RE, Giglio L, Muller J, Lewis P, Barnsley MJ (1998) The Moderate Resolution Imaging Spectroradiometer (MODIS): land remote sensing for global change research. *IEEE Trans Geosci Remote Sens* 36:1228–1249
- Koehler GM, Maletzke BT, Von Kienast JA, Aubry KB, Wielgus RB, Naney RH (2007) Habitat fragmentation and the persistence of lynx populations in Washington State. *J Wildl Manag* 72:1518–1524
- Laberee K, Nelson TA, Stewart BP, McKay T, Stenhouse GB (2014) Oil and gas infrastructure and the spatial pattern of grizzly bear habitat selection in Alberta, Canada. *Can Geogr* 8(1):79–94
- Linke J, McDermid GJ, Laskin DN, McLane AJ, Pape A, Cranston J, Hall-Beyer M, Franklin SE (2009) A disturbance-inventory framework for flexible and reliable landscape monitoring. *Photogramm Eng Remote Sens* 75:981–996
- Loarie SR, Tambling CJ, Asner GP (2013) Lion hunting behaviour and vegetation structure in an African savanna. *Anim Behav* 85(5):899–906
- Long JA, Nelson TA (2013) A review of quantitative methods for movement data. *Int J Geogr Inf Sci* 27(2):292–318
- Masek JG, Huang C, Wolfe R, Cohen W, Hall F, Kutler J, Nelson P (2008) North American forest disturbance mapped from a decadal Landsat record. *Remote Sens Environ* 112:2914–2926
- Mohr CO (1947) Table of equivalent populations of North America. *Am Mid Nat* 37:223–249

- Munro RHM, Nielsen SE, Price MH, Stenhouse GB, Boyce MS (2006) Seasonal and diel patterns of grizzly bear diet and activity in west-central Alberta. *J Mammal* 87:1112–1121
- Ndegwa MC, Murayama Y (2009) Analysis of land use/cover changes and animal population dynamics in a wildlife sanctuary in East Africa. *Remote Sens* 1:952–970
- Nielsen SE, Boyce MS, Stenhouse GB (2004a) Grizzly bears and forestry I. Selection of clearcuts by grizzly bears in west-central Alberta, Canada. *For Ecol Manag* 199:51–65
- Nielsen SE, Herrero S, Boyce MS, Mace RD, Benn B, Gibeau ML, Jeavons S (2004b) Modelling the spatial distribution of human-caused grizzly bear mortalities in the Central Rockies Ecosystem of Canada. *Biol Conserv* 120:101–113
- Nielsen SE, Munro RHM, Bainbridge EL, Stenhouse GB, Boyce MS (2004c) Grizzly bears and forestry II. Distribution of grizzly bear foods in clearcuts of west-central Alberta, Canada. *For Ecol Manag* 199:67–82
- Nielsen SE, Stenhouse GB, Boyce MS (2006) A habitat-based framework for grizzly bear conservation in Alberta. *Biol Conserv* 130:217–229
- Schneider RR (2002) Alternative futures: Alberta's boreal forest at the crossroads. The Federation of Alberta naturalists. Edmonton, Alberta
- Schneider RR, Stelfox JB, Boutin S, Wasel S (2003) Managing the cumulative impacts of land uses in the Western Canadian Sedimentary Basin: a modeling approach. *Conserv Ecol* 7:8
- Smulders M, Nelson TA, Jelinski DE, Nielsen SE, Stenhouse GB (2010) A spatially explicit method for evaluating accuracy of species distribution models. *Divers Distrib* 16:996–1008
- Smulders M, Nelson TA, Jelinski DE, Nielsen SE, Stenhouse GB, Laberee K (2012) Quantifying spatial-temporal patterns in wildlife ranges using STAMP: a grizzly bear example. *Appl Geogr* 35:124–131
- Stewart BP, Nelson TA, Laberee K, Nielsen SE, Wulder MA, Stenhouse GB (2013) Quantifying grizzly bear selection of natural and anthropogenic edges. *J Wildlife Manag Wildlife Monographs* 77:957–964. doi: [10.1002/jwmg.535](https://doi.org/10.1002/jwmg.535)
- Sunde P, Olesen CR, Madsen TL, Haugaard L (2009) Behavioural responses of GPS-collared female red deer *Cervus elaphus* to driven hunts. *Wildl Biol* 15:454–460
- Vermote EF, Tanre D, Deuze JL, Herman M, Morcrette JJ (1997) Second simulation of the satellite signal in the solar spectrum, 6S: an overview. *IEEE Trans Geosci Remote Sens* 35:675–686
- Wells AG, Wallin DO, Rice CG, Chang WY (2011) GPS bias correction and habitat selection by mountain goats. *Remote Sens* 3:435–459
- White JC, Wulder MA, Gomez C, Stenhouse GB (2011) A history of habitat dynamics: characterizing 35 years of stand replacing disturbance. *Can J Remote Sens* 37:234–251
- Woodcock CE, Allen R, Andersson M, Belward A, Bindschadler R, Cohen W, Gao F, Goward SN, Helder D, Helmer E, Nemani R, Oreopoulos L, Schott J, Thenkabail PS, Vermote EF, Vogelmann J, Wulder MA, Wynne R (2008) Free access to Landsat imagery. *Science* 320:1011
- Wulder MA, Hall RJ, Coops NC, Franklin SE (2004) High spatial resolution remotely sensed data for ecosystem characterization. *Bioscience* 54:511–521
- Wulder MA, White JC, Goward SN, Masek JG, Irons JR, Herold M, Cohen WB, Loveland TR, Woodcock CE (2008) Landsat continuity: issues and opportunities for land cover monitoring. *Remote Sens Environ* 112:955–969
- Wulder MA, White JC, Masek JG, Dwyer J, Roy DP (2011) Continuity of Landsat observations: short term considerations. *Remote Sens Environ* 115:747–751
- Wulder MA, Masek JG, Cohen WB, Loveland TR, Woodcock CE (2012) Opening the archive: how free data has enabled the science and monitoring promise of Landsat. *Remote Sens Environ* 122:2–10
- Zhang X, Schaaf CB, Friedl MA, Strahler AH, Gao F, Hodges JCF (2002) MODIS tasseled cap transformation and its utility. In: Proceedings of the international geoscience remote sensing symposium 1063–1065 doi: [10.1109/IGARSS.2002.1025776](https://doi.org/10.1109/IGARSS.2002.1025776)

Chapter 17

Multitemporal Remote Sensing for Inland Water Bodies and Wetland Monitoring

Yeqiao Wang, Shuhua Qi, and Jian Xu

Abstract Remote sensing is critically important in monitoring inland water and wetlands for protecting the related environments and ecosystems. This chapter summarizes remote sensing applications in water and wetland monitoring, in particular in the subject areas of monitoring water quality, water surface areas and water fluctuation in wetland areas. The chapter then introduces two cases of monitoring studies in the Poyang Lake, the largest fresh water lake in China, in terms of monitoring of fluctuation and variation of water surface areas using MODIS data product, and monitoring of variation of natural wetlands corresponding to the changing water levels of Poyang Lake using Landsat data.

17.1 Introduction

Inland water bodies and wetlands are essential nature resources for human beings in terms of providing multiple ecosystem services (Costanza et al. 1998). However, inland lakes, rivers and wetlands are threatened by many environmental problems

Y. Wang (✉)

Department of Natural Resources Science, University of Rhode Island, 1 Greenhouse Road, Kingston, RI, USA

Ministry of Education's Key Laboratory of Poyang Lake Wetland and Watershed Research, School of Geography and Environmental Science, Jiangxi Normal University, Nanchang, Jiangxi, China

e-mail: yqwang@uri.edu

S. Qi

Ministry of Education's Key Laboratory of Poyang Lake Wetland and Watershed Research, School of Geography and Environmental Science, Jiangxi Normal University, Nanchang, Jiangxi, China

e-mail: qishuhua11@163.com

J. Xu

Ministry of Education's Key Laboratory of Poyang Lake Wetland and Watershed Research, School of Geography and Environmental Science, Jiangxi Normal University, Nanchang, Jiangxi, China

College of Chemistry and Chemical Engineering, Jiangxi Normal University, Nanchang, Jiangxi, China

e-mail: xujianjxnu@qq.com

caused by various natural and anthropogenic factors, such as eutrophication, other organic and inorganic pollution, acidification, spread of invasive species and climate change. Therefore, monitoring of inland water and wetland are critically important for the protection of related environments and ecosystems (Wang 2012). Remote sensing science and technologies, with the ability of covering large spatial areas at frequent temporal intervals, have been broadly applied in monitoring of inland and coastal waters and wetlands (Wang 2009). In particular, remote sensing is the most effective in monitoring of water and wetland environments with significant dynamic fluctuation and inundation hydrological patterns.

17.1.1 Monitoring of Water Quality

Water with different constituents has different spectral characteristics. Spectral reflectance of water body in visible spectrum provides effective information on optically significant materials present in water (Le et al. 2011), which makes it possible to use remote sensing techniques to monitor water quality.

With research development in understanding of inland water spectral characteristics, improvement of inversion algorithms and new sensor technology, the accuracy of remote sensing monitoring of inland water quality has been continuously improved (Palmer et al. 2015a; Ogashawara and Moreno-Madriñán 2014; Jaelani et al. 2015; Matthews and Odermatt 2015; Wu et al. 2014). In general, the techniques in retrieval of chlorophyll-a (Chl-a) and total suspended solids (TSS) are relatively mature in practical remote sensing applications of inland water bodies (Kutser et al. 1995; Le et al. 2011; Yu et al. 2012; Palmer et al. 2015a; Guo et al. 2015). Also, the retrieval of colored dissolved organic matter (CDOM) in inland water has gained attentions (Kutser et al. 2005; Kutser 2012; Jiang et al. 2014b). Other studies about indicators of remote sensing of water quality have been developed and reported, such as monitoring of dissolved organic carbon (DOC) (Kutser et al. 2015), particulate organic carbon (POC) (Duan et al. 2014), water surface temperature (Korosov et al. 2007), water transparency (Kutser et al. 1995), phycocyanin (PC) (Song et al. 2013), total nitrogen and total phosphorus (Kutser et al. 1995).

Applications of multitemporal remote sensing in monitoring of inland water quality have been reported. For example, a study of monitoring of a massive blue-green algae bloom in Taihu Lake of China presented an analysis with contrasting of Chl-a concentrations between the days before and after throughout the event (Wang and Shi 2008). Moderate Resolution Imaging Spectroradiometer (MODIS-Aqua) data were used to monitor seasonal and interannual variabilities and spatial distributions of water properties in Taihu Lake as well (Wang et al. 2011). Recently, 10 years (2002–2012) of Medium Resolution Imaging Spectrometer (MERIS) data over South Africa was employed to study the 50 largest standing water bodies in South Africa to obtain the time series of Chl-a, cyanobacteria and surface scum area coverage (Matthews 2014). Long-term distribution patterns of Chl-a concentration were also analyzed using MERIS full-resolution scenes of 10-year period for the Poyang Lake, the largest freshwater lake of China (Feng et al. 2014). Chl-a

concentration mapping using MERIS data has been used to evaluate spatiotemporal dynamics of bloom event for Lake Balaton (Palmer et al. 2015b). Study also reported temporal and spatial distributions of total suspended solids in the Poyang Lake using MODIS medium-resolution (250 m) data from 2000 to 2010 (Feng et al. 2012a). Shi et al. (2015) integrated MODIS-Aqua medium-resolution (250 m) data gathered from 2003 to 2013 and in situ data collected from a number of cruise surveys to estimate the concentrations of total suspended matter in Taihu Lake. Kutser (2012) evaluated suitability of Landsat archive for mapping CDOM changes in Swedish lakes over the last 30 years. Multitemporal remote sensing of inland water can provide immediate and accessible information in monitoring of concentrations of water constituents, which is critically important for establishing an early warning system for emergency management and governance of natural resources.

17.1.2 Monitoring of Water Area

Dramatic changes in the size and morphology of inland water, such as lakes and reservoirs, have occurred around the world in recent decades. For instance, lakes in arid regions have shrunk or vanished due to changes in precipitation/evaporation conditions (Awange et al. 2008). On the other hand, ice melting from mountain glaciers caused significant changes of lakes in the Tibet Plateau, Arctic coastal plain, and Western Siberia in recent decades (Kropácek et al. 2012; Yang and Lu 2014; Sheng and Li 2011; Wang et al. 2012; Smith et al. 2012). There are lakes, such as Poyang Lake in China, that have significant large and rapid water level variations controlled by monsoon climate and the hydrological conditions, which brings increasingly severe floods or droughts.

Remote sensing is extremely effective for monitoring of dynamics of areas of water surface. Landsat images have been used to monitor water environments (Plug et al. 2008; Ma et al. 2010). MODIS data have been used to study the short- and long-term characteristics of Poyang Lake inundation (Feng et al. 2012b) and the regional differences of water inundation duration in different geographic regions (Wu and Liu 2015). Meanwhile, satellite radar altimeter data have been used to monitor the water level and water area (e.g., Jarihani et al. 2013; Liao et al. 2014). Recently, new Sentinel-1 data were evaluated for monitoring of reservoirs (Amitrano et al. 2014). The monitoring results are valuable for hydrological safety and provide information for preparation and precautions against extreme harmful hydrological events.

17.1.3 Monitoring of Water Fluctuation in Wetland Areas

Wetland degradation has aroused widespread concerns. Monitor of water fluctuation in wetland areas is among important practices for conservation and management of wetland resources. Landsat and SPOT images are among major data sources that

have been used in monitoring of water fluctuations in wetland areas. Multi-temporal data are very effective in extraction of wetland information when combined with elevation and topography data (Ozesmi and Bauer 2002).

Early research employed Landsat and SPOT HRV multispectral data to evaluate aquatic macrophyte changes within the Florida Everglades (Jensen et al. 1995). Gong et al. (2010) identified changed areas in China's wetland between 1990 and 2000 and analyzed potential uncertainties in the wetland change mapping based on Landsat data acquired around 1990 and 2000. Landsat data have been used on Poyang Lake of China for monitoring of water inundation of wetland (Hui et al. 2008), and for monitoring of suitable habitat for Siberian cranes (Jiang et al. 2014a).

17.2 Multitemporal Remote Sensing of Poyang Lake, China

Poyang Lake is situated at the lower Yangtze River basin and it is the largest fresh water lake in China. Poyang Lake is fed by tributaries of five rivers of Gan, Fu, Xin, Rao and Xiu and it is connected and exchange water with Yangtze River through lake mouth in the north (Fig. 17.1). As controlled by water from the five tributary rivers as well as the Yangtze River, the Lake's highly dynamic and seasonal variations in water level present a unique landscape of fresh water lake-wetland ecosystem. The variation of the size of the lake is illustrated as an ocean when flooded during the wet season and as a line of river when withered during the dry season. The Poyang Lake wetland is a key habitat site for wintering migratory birds with global importance. The lake plays an irreplaceable role for flood control, river shipping, city water supply and conservation of biological diversity of middle and lower reaches of Yangtze River (Gao et al. 2014).

Poyang Lake is affected by subtropical monsoon climate with a mean annual precipitation of 1632 mm (Xu and Qin 1998), about 60 % of the annual rainfall happened in flood season during April to August within the Poyang Lake watershed. It was estimated that approximately 1.43×10^7 tons of sediments with nutritive materials were carried from the five tributary rivers and deposit in the floodplain each year. The sediment loaded by water discharge was deposit and formed fertile deltas. Lake sediment is important for a biologically productive lake-wetland system such as the Poyang Lake wetland. There are about 102 vegetation species of aquatic vascular plants and freshwater organisms presented in the fertile floodplain. Poyang Lake wetland was first selected as the protected area under the international Ramsar Convention in China because of its biological productivity, species richness and being a critical wintering habitat for rare and endangered migratory bird species such as the Siberian crane (*Grus leucogeranus*). The lake area has a long history of agricultural and fishery practices. The lake and associated wetlands support a high population densities of about 400–800 persons/km² (Shankman et al. 2006).

The area and shape of Poyang Lake were affected by natural deposition and erosion in the past decades. Increased human population and economic growth induced activities such as sand mining (Feng et al. 2011), reclamation for agriculture,

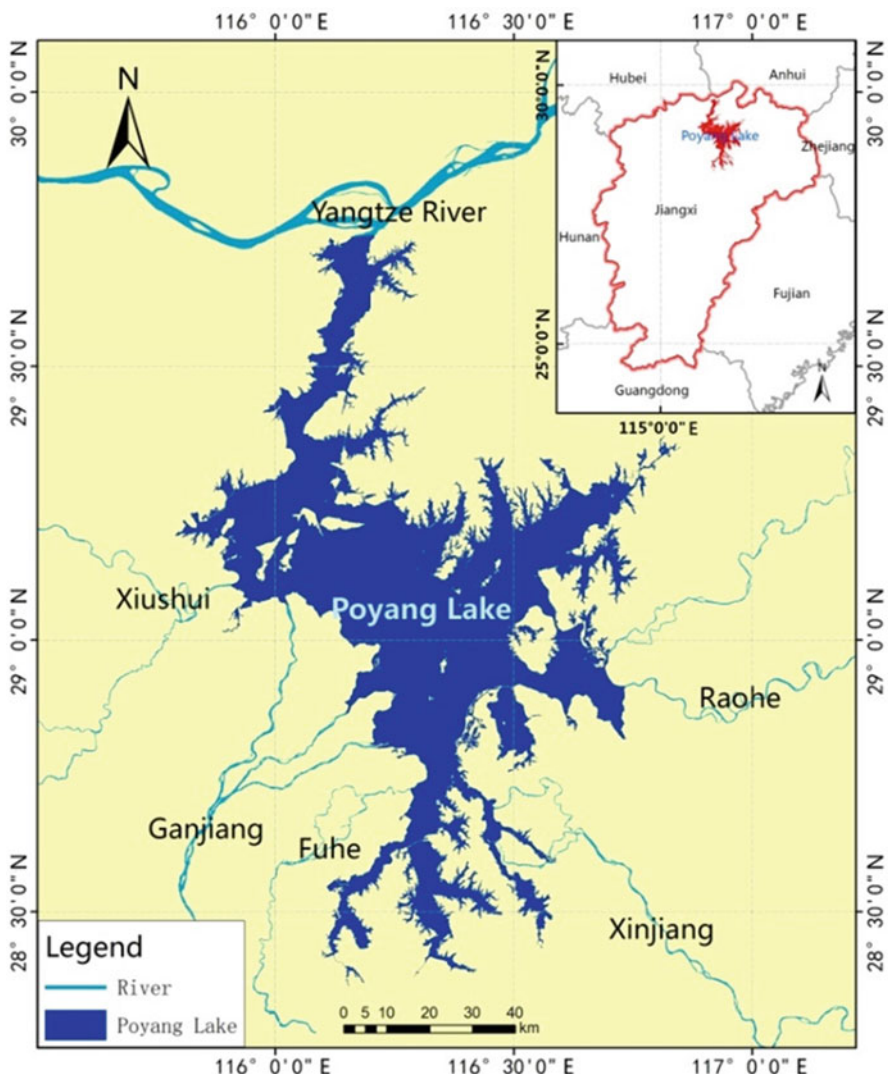


Fig. 17.1 Location of Poyang Lake

fishery, aquaculture and settlements (Qi et al. 2009; Min 1999), which also affected areas and surrounding landscape of the lake. It is estimated that area of Poyang Lake was reduced from 5160 km² in 1954 to 3860 km² in 1998 (Shankman and Liang 2003). Reclaiming farmland was the most significant activity changing the morphology of Poyang Lake dramatically before 1998. However sand dredging in the Poyang Lake water system was intensified since 2001 because of the demand of raw materials in the rapid urbanization in the lower Yangtze River valley, as well as that sand dredging was banned in the Yangtze River in 2000. Lured by

high profits, sand dredging business developed quickly with hundreds of large sand vessels assembled and operated in the Poyang Lake water system. Poyang Lake has attracted wide attention of the international and scientific communities (Jiao 2009; Yésou et al. 2011; Dronova et al. 2011; Zhang et al. 2014). We report two case studies in monitoring of water and wetland of Poyang Lake, respectively, in the follow sections.

17.2.1 Monitoring of Inundation Areas Using MODIS Data

The Poyang Lake experiences the most significant flood and drought rotation each year. The inundation with dynamics of water levels occurs in both short term on weekly and monthly basis and in long term with annual variations. In monitoring of inundation, time series MODIS data were employed.

17.2.1.1 Data Acquisition

The 8-day MODIS Surface Reflectance data (MOD09Q1) collected between 2000 and 2014 were obtained from an open source (<https://ladsweb.nascom.nasa.gov/data.html>). There are 46 scenes of MOD09Q1 images during every year, i.e., every 8 days to cover one image. Due to the missing of six scenes in 2000 and one scene in 2001, a total of 683 scenes of MOD09Q1 images were acquired between 2000 and 2014. MOD09Q1 contains 3 data layers, surface reflectance for band 1 (620–670 nm), surface reflectance for band 2 (841–876 nm) and surface reflectance quality control flags, all with 250 m spatial resolution.

17.2.1.2 Data Processing and Result

All the collected MODIS images were resampled using nearest neighbor method, and geometrically rectified to WGS84 datum with Universal Transverse Mercator (UTM) coordinate system. Then all the images were clipped by the boundary of the Poyang Lake using mask calculation. The water surface areas were extracted from other features using the normalized difference vegetation index (NDVI) threshold:

$$NDVI = \frac{(NIR - VIS)}{(NIR + VIS)} \quad (18.1)$$

Where, VIS and NIR stand for the spectral reflectance measurements acquired in the visible (red) and near-infrared regions, respectively. Normally, the value of NDVI for water is less than 0. However due to the existence of large amount of aquatic vegetation in Poyang Lake, which affects the absorption, reflection and transmission of visible and near-infrared spectrum on water surface. A modified NDVI threshold of less than 0.1 was applied to extract the water surface areas. For those MOD09Q1

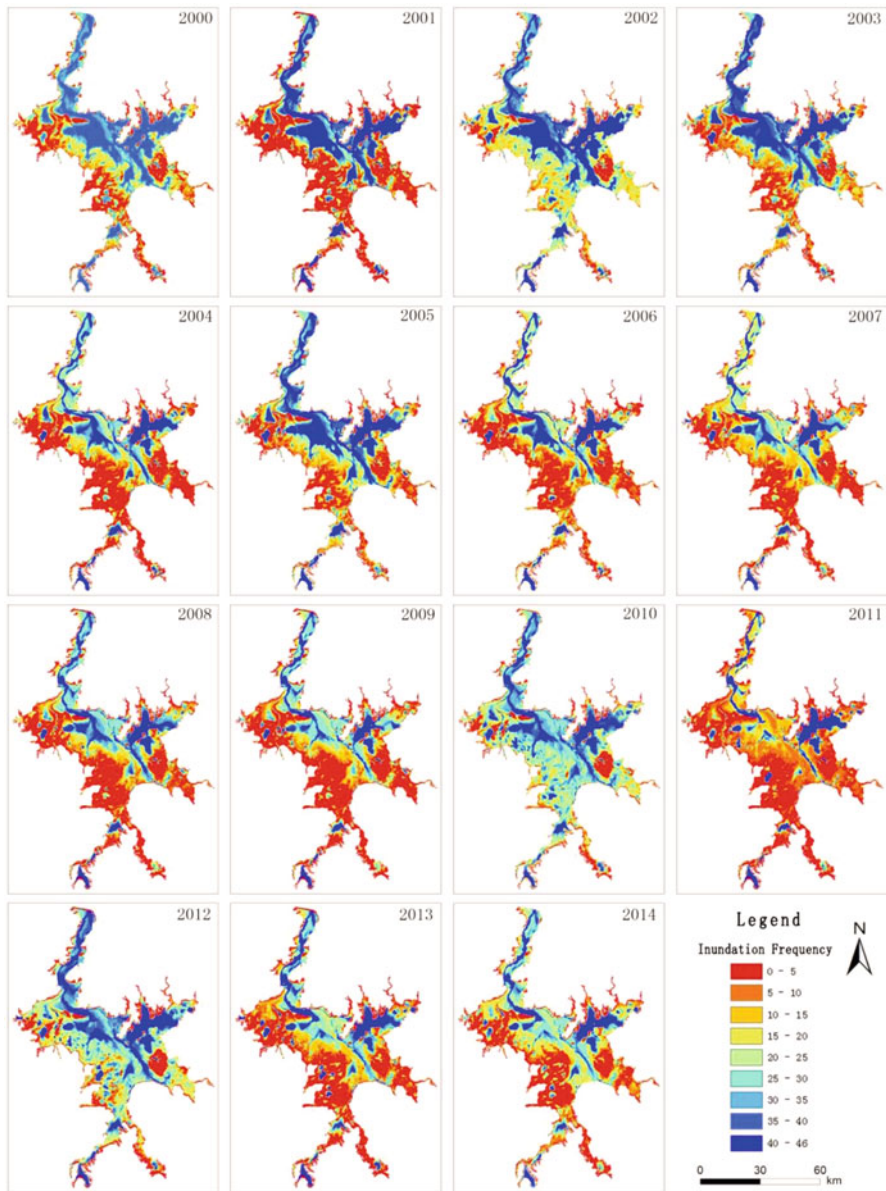


Fig. 17.2 Variation of inundation areas in Poyang Lake during each year between 2000 and 2014

images that have thick cloud covers, MODIS09Q1 images acquired in similar date were applied instead. At last, the extracted water surface images were added together for each year to obtain the inundation variation of water surface areas in Poyang Lake between 2000 and 2014 (Fig. 17.2). According to the extents of inundation areas, the maximum flooding time lake area was about 3400 km², while

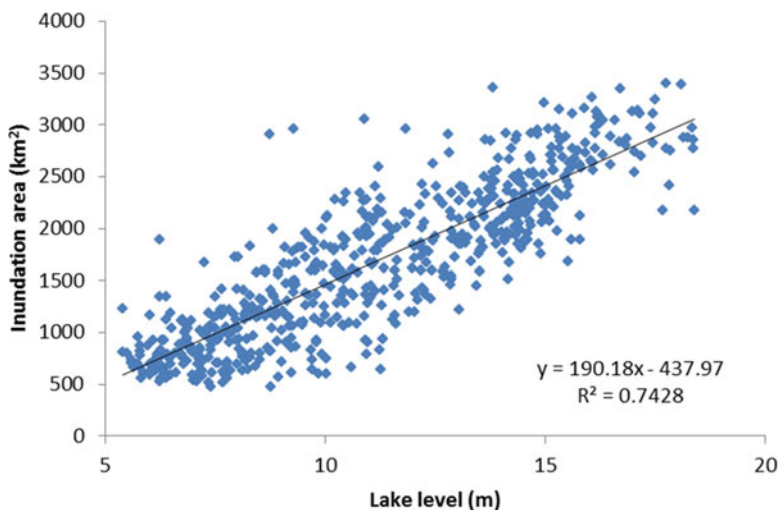


Fig. 17.3 The inundation area of Poyang Lake at different lake water level

Table 17.1 Annual maximum and minimum inundation area of Poyang Lake during 2000–2014

Year	Annual maximum inundation area (Km ²)	Annual minimum inundation area (Km ²)	Annual maximum Water level (m)	Annual minimum Water level (m)
2000	3363.44	1068.00	16.23	7.11
2001	2650.50	1183.38	15.14	7.67
2002	3396.88	941.94	18.36	6.51
2003	3241.31	799.38	17.49	6.07
2004	2526.44	614.75	15.53	5.23
2005	3104.50	1045.38	17.15	6.37
2006	2915.75	617.69	14.82	5.91
2007	3045.63	623.81	16.59	5.40
2008	2399.44	560.94	15.78	5.48
2009	2137.13	472.25	15.27	5.60
2010	2881.31	526.25	18.38	5.85
2011	2457.69	512.19	15.50	6.22
2012	2905.13	556.69	17.75	5.90
2013	2280.31	585	15.06	5.54
2014	3040.56	616.81	16.70	5.41

the minimum inundate area of the lake was only about 470 km^2 . The largest annual variability ratio between maximum and minimum water surface areas was 5.48 that occurred in year 2010. Together with water level records measured at a gauging station on the lake, a strong correlation existed between inundation areas and water levels (Fig. 17.3). A decreased trend is evident between maximum and minimum water levels since 2000 (Table 17.1).

17.2.2 Monitoring of Wetland Fluctuation Using Landsat Data

Poyang Lake wetlands provide wintering habitats for most of the estimated existing population of Siberian cranes. Hydrological regime of Poyang Lake is a dominant factor controlling the quality of the habitats. However the hydrological process in Poyang Lake wetland has been changing especially in recent decades due to human activities. Abnormal low water level in Poyang Lake occurred more frequently in autumns and winters in recent 10 years. In this case study, the fluctuation of Poyang Lake wetland areas in different water levels were extracted based on multitemporal Landsat images.

17.2.2.1 Data Selection

Twelve scenes of Landsat images (path 121/Row 40) with no or little cloud cover were selected (Table 17.2). Among those images, 10 scenes were acquired from October to March in different years, reflected different water levels with about 1 m interval. The images were select to evaluate habitat vulnerability to water levels with analysis on landscape configuration by land-cover types derived from imagery classification process. The image acquired in 5 July 2000 corresponded to the time that the lake water level was 15.6 m above a mean sea level. This image was selected as a surrogate of the water level controlled at 15.5 m as the proposed hydrologic engineering project of Poyang Lake Dam for analyzing the effects of water variation to wetland landscape. The image acquired in 8 July 1998 corresponded to the time that the lake water level was 19.6 m above a mean sea level. This image was used only for defining the boundary of the natural wetland areas of the Poyang Lake.

Table 17.2 Landsat TM/ETM+ images and water level in Xingzi gauging station

No.	Date of imagery acquisition (DD-MM-YYYY)	Satellite/Sensor	Water level (m)	Purpose of usage in this study
1	15 February 2004	Landsat 5/TM	5.3	a
2	6 January 2007	Landsat 5/TM	5.9	a
3	15 December 2004	Landsat 5/TM	7.1	a
4	27 January 2000	Landsat 7/ETM+	7.9	a
5	10 December 1999	Landsat 7/ETM+	8.8	a
6	5 March 2005	Landsat 5/TM	10.1	a
7	16 November 1999	Landsat 5/TM	11.1	a, b
8	2 November 1994	Landsat 5/TM	12.1	a
9	5 October 2007	Landsat 5/TM	13.0	a
10	9 October 2000	Landsat 7/ETM+	14.2	a
11	5 July 2000	Landsat 7/ETM+	15.6	a
12	8 July 1998	Landsat 5/TM	19.6	c

Note: a – land-cover classification, b – defining the boundary of inner-lakes of the Poyang Lake, c – defining the boundary of natural wetlands of the Poyang Lake

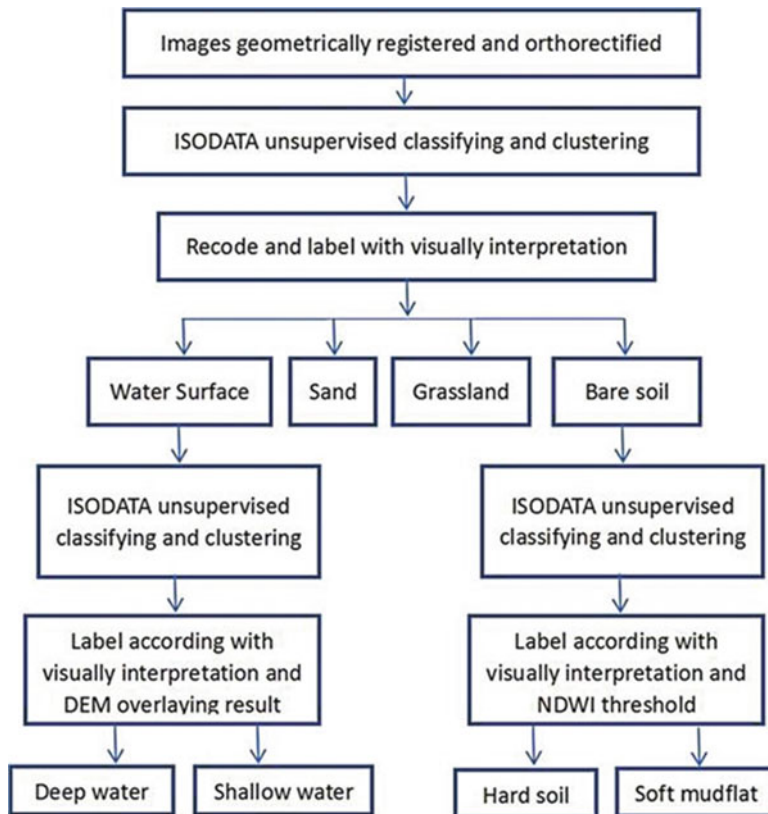


Fig. 17.4 The technological process of land-cover classification

17.2.2.2 Data Processing and Result

All Landsat images were geometrically rectified to WGS84 datum with UTM coordinate system and orthorectified using a digital elevation model (DEM). Eleven scenes of Landsat images were used to map six land-cover categories including deep water, shallow water, soft mudflat, hard soil, grassland and sand (Fig. 17.4).

Unsupervised classification by ISODATA algorithm was used to produce 10 clusters of pixels with corresponding spectral similarities. At first, the spectral clusters were recoded and labeled as four land-cover categories of water surface, sand, bare soil and grassland with visual interpretation. Unsupervised classification was applied again on pixels of water surface and bare soil categories, respectively. The water surface was then divided into deep and shallow water areas according to visual interpretation and estimation of water depth. Bare soil was divided into hard soil and soft mudflat by referencing to visual interpretation and NDWI threshold:

$$NDWI = \frac{(r2 - r5)}{(r2 + r5)} \quad (18.2)$$

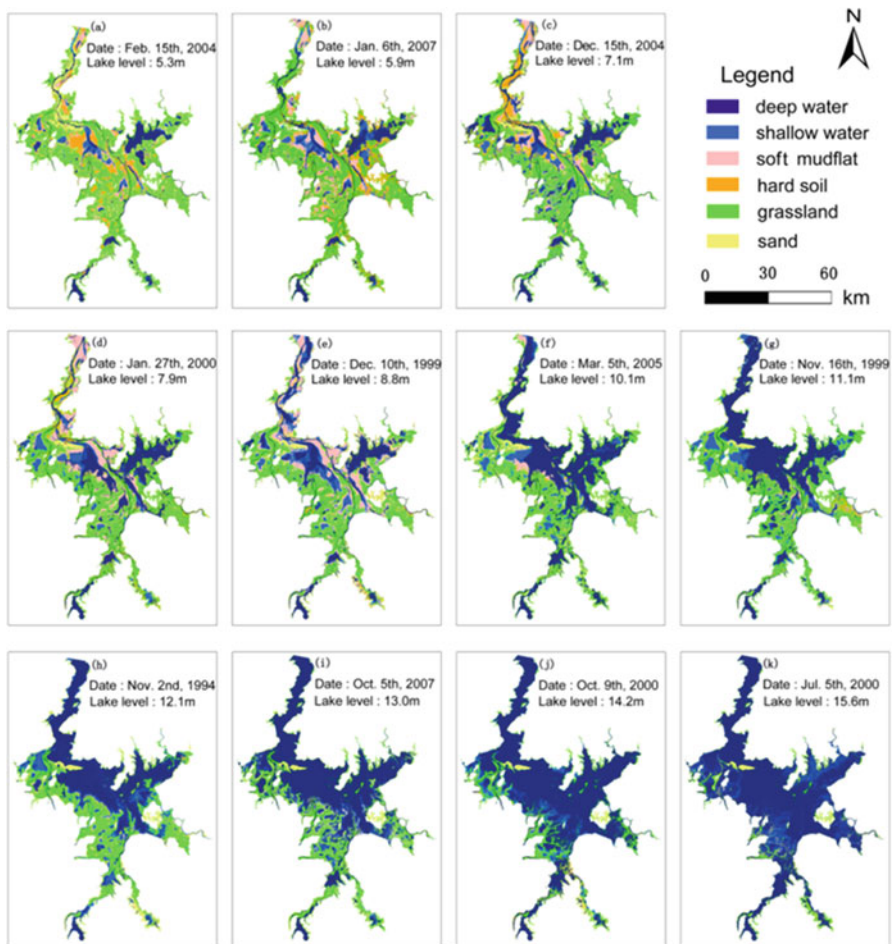


Fig. 17.5 Land-cover maps of Poyang Lake natural wetland in different water levels

where $r2$ and $r5$ refer to the at-sensor reflectance for Landsat TM/ETM+ band 2 and band 5, respectively. According to the GPS-guided field sampling, the NDWI threshold ($=0.65$) was applied to distinguish the categories of hard soil and soft mudflat. Additionally, the burned grassland area was also classified as hard soil because the post-fire grassland area was deprived of habitat function with drier soil for the year.

The land cover types of natural wetlands of the Poyang Lake were extracted from 11 Landsat scenes and illustrated as Fig. 17.5. Considering that the Landsat imagery acquired 15th December 2004 was coincident with lake water level of 7.1 m, which is very close to the water level of 7.06 m of our third field survey day, the land cover map derived from classification of 15th December 2004 image was assessed by 126 GPS-guided samplings sites during the field survey. According

Table 17.3 Error matrix and classification accuracy assessment

	G	S	HS	SM	SW	DW	Row total
G	35	0	0	0	0	0	35
S	0	12	0	0	0	0	12
HS	0	0	17	3	0	0	20
SM	0	0	2	12	1	0	15
SW	0	0	0	3	23	2	28
DW	0	0	0	0	0	16	16
Column total	35	12	19	18	24	18	126

Overall accuracy = $115/126 = 91\%$, kappa = 0.89

G Grassland, S Sand, HS Hard soil, SM Soft mudflat, SW Shallow water, DW Deep water

Table 17.4 Area of potential suitable habitat for Siberian cranes with different water level in Poyang Lake wetland (km^2)

WL	SW	SM	G	DW	HS	S
5.3 m	182.09	599.9	1510.62	414.72	451.35	147.34
5.9 m	229.39	547.81	1525.51	509.6	444.37	49.34
7.1 m	301.34	446.04	1262.75	735.72	392.33	167.84
7.9 m	230.52	658.38	1247.46	887.17	232.56	49.93
8.8 m	399.6	538.43	1068.4	779.38	340.23	179.98
10.1 m	291.03	246.24	1179.26	1400.1	85.04	104.35
11.1 m	397.93	257.37	1100.23	1341.56	152.63	56.3
12.1 m	404.35	186.7	908.11	1489.84	82.77	234.25
13 m	359.35	210.45	664.76	1866.13	25.71	179.62
14.2 m	246.76	87.05	418.24	2389.01	22.8	142.16
15.6 m	241.34	91.71	197.48	2660.32	18.4	96.77

WL Water level, SW Shallow water, SM Soft mudflat, G Grassland, DW Deep water, HS Hard soil, S Sand

to the error matrix (Table 17.3), all reference sites for grassland and sand types were classified correctly, but confusions existed between shallow and deep water, and soft mudflat and hard soil categories. Accuracy assessment results indicate of 91 % overall accuracy and 0.89 kappa coefficient for the land cover map of 2004. It was conclude that the total area of glassland, soft mudflat and shallow water areas that could be used as habitat for migrate birds in Poyang Lake was decreased with water level increasing (Table 17.4).

17.3 Conclusion Remarks

As the largest freshwater lake in China with the greatest variation in water level and inundation extent, multitemporal remote sensing plays a key role in monitoring of water quantity and quality, as well as the associate wetlands as critical habitats of a global significance in biodiversity conservation. Time-series MODIS data

products were very effective to capture the change of water surface areas due to the hydrologically sensitive nature of the Poyang Lake. MODIS data reveal that the largest annual variability ratio between 2000 and 2014 and between maximum and minimum water surface areas was 5.48 which occurred in year 2010. Together with water level records measured at a gauging station on the lake, a strong correlation existed between inundation areas and water levels. A decreased trend is evident between maximum and minimum water levels since 2000. On the other hand, finer spatial resolution multitemporal Landsat data are much appreciated for monitoring of the wetlands that are routinely affected by the dynamics of water levels of the Poyang Lake. Landsat data reveal that the total areas of suitable habitats for migrate birds in Poyang Lake, i.e., glassland, soft mudflat and shallow water areas, were decreased as water level increased. This may provide an important piece of information about the hydrological effects on key habitats conditions of the key migratory birds for planning and management actions in conservation of biodiversity of the Poyang Lake region. The data process and analysis approaches are applicable to most of the situations for monitoring of the changing environment, in particular, for the subjects of inland water and wetland monitoring.

References

- Amitrano D, Martino D, Iodice A, Mitidieri F, Papa M-N, Riccio D, Ruello G (2014) Sentinel-1 for monitoring reservoirs: a performance analysis. *Remote Sens* 6:10676–10693
- Awange JL, Sharifi MA, Ogonda G, Wickert J, Grafarend EW, Omulo MA (2008) The falling Lake Victoria water level: GRACE, TRIMM and CHAMP satellite analysis of the lake basin. *Water Resour Manag* 22(7):775–796
- Costanza R, d'Arge R, De Groot R, Farber S, Grasso M, Hannon B, Limburg K, Naeem S, O'Neill RV, Paruelo J (1998) The value of the world's ecosystem services and natural capital. *Ecol Econ* 1(25):3–15
- Dronova I, Gong P, Wang L (2011) Object-based analysis and change detection of major wet-land cover types and their classification uncertainty during the low water period at Poyang Lake, China. *Remote Sens Environ* 115(12):3220–3236
- Duan H, Feng L, Ma R, Zhang Y, Loiselle SA (2014) Variability of particulate organic carbon in inland waters observed from MODIS Aqua imagery. *Environ Res Lett* 9(8):084011
- Feng L, Hu C, Chen X, Li R, Tian L, Murch B (2011) MODIS observations of the bottom topography and its inter-annual variability of Poyang Lake. *Remote Sens Environ* 115(10):2729–2741
- Feng L, Hu C, Chen X, Tian L, Chen L (2012a) Human induced turbidity changes in Poyang Lake between 2000 and 2010: Observations from MODIS. *J Geophys Res* 117. doi: [10.1029/2011JC007864](https://doi.org/10.1029/2011JC007864)
- Feng L, Hu C, Chen X, Cai X, Tian L, Gan W (2012b) Assessment of inundation changes of Poyang Lake using MODIS observations between 2000 and 2010. *Remote Sens Environ* 121:80–92
- Feng L, Hu C, Han X, Chen X, Qi L (2014) Long-term distribution patterns of chlorophyll-a concentration in China's largest freshwater lake: MERIS full-resolution observations with a practical approach. *Remote Sens* 7(1):275–299
- Gao JH, Jia J, Kettner AJ, Xing F, Wang YP, Xu XN, Yang Y, Zou XQ, Gao S, Qi S, Liao F (2014) Changes in water and sediment exchange between the Changjiang River and Poyang Lake under natural and anthropogenic conditions, China. *Sci Total Environ* 481:542–553

- Gong P, Niu Z, Cheng X, Zhao K, Zhou D, Guo J, Liang L, Wang X, Li D, Huang H et al (2010) China's wetland change (1990–2000) determined by remote sensing. *Sci China Earth Sci* 53(7):1036–1042
- Guo Y, Li Y, Zhu L, Liu G, Wang S, Du C (2015) An improved unmixing-based fusion method: potential application to remote monitoring of inland waters. *Remote Sens* 7(2):1640–1666
- Hui F, Xu B, Huang H, Yu Q, Gong P (2008) Modelling spatial-temporal change of Poyang Lake using multitemporal Landsat imagery. *Int J Remote Sens* 29(20):5767–5784
- Jaelani LM, Matsushita B, Yang W, Fukushima T (2015) An improved atmospheric correction algorithm for applying MERIS data to very turbid inland waters. *Int J Appl Earth Obs Geoinf* 39:128–141
- Jarihani AA, Callow JN, Johansen K, Gouweleeuw B (2013) Evaluation of multiple satellite altimetry data for studying inland water bodies and river floods. *J Hydrol* 505:78–90
- Jensen JR, Rutchey K, Koch MS, Narumalani S (1995) Inland wetland change detection in the Everglades Water Conservation Area 2A using a time series of normalized remotely sensed data. *Photogramm Eng Rem Sens* 61(2):199–209
- Jiang F, Qi S, Liao F, Ding M, Wang Y (2014a) Vulnerability of Siberian crane habitat to water level in Poyang Lake wetland, China. *GISci Remote Sens* 51(6):662–676
- Jiang G, Ma R, Duan H, Loiselle SA, Xu J, Liu D (2014b) Remote determination of chromophoric dissolved organic matter in lakes, China. *Int J Digital Earth* 7(11):897–915
- Jiao L (2009) Scientists line up against dam that would alter protected wetlands. *Science* 326(5952):508–509
- Korosov A, Pozdnyakov D, Pettersson L, Grassl H (2007) Satellite-data-based study of seasonal and spatial variations of water temperature and water quality parameters in Lake Ladoga. *J Appl Remote Sens* 1(1):011508–011517
- Kropáček J, Braun A, Kang S, Feng C, Ye Q, Hochschild V (2012) Analysis of lake level changes in Nam Co in central Tibet utilizing synergistic satellite altimetry and optical imagery. *Int J Appl Earth Obs Geoinf* 17:3–11
- Kutser T (2012) The possibility of using the Landsat image archive for monitoring long time trends in coloured dissolved organic matter concentration in lake waters. *Remote Sens Environ* 123:334–338
- Kutser T, Arst H, Miller T, Käärmann L, Milius A (1995) Telespectrometrical estimation of water transparency, chlorophyll-a and total phosphorus concentration of Lake Peipsi. *Int J Remote Sens* 16(16):3069–3085
- Kutser T, Pierson DC, Kallio KY, Reinart A, Sobek S (2005) Mapping lake CDOM by satellite remote sensing. *Remote Sens Environ* 94(4):535–540
- Kutser T, Verpoorter C, Paavel B, Tranvik LJ (2015) Estimating lake carbon fractions from re-mote sensing data. *Remote Sens Environ* 157:138–146
- Le C, Li Y, Zha Y, Sun D, Huang C, Zhang H (2011) Remote estimation of chlorophyll a in optically complex waters based on optical classification. *Remote Sens Environ* 115(2):725–737
- Liao J, Gao L, Wang X (2014) Numerical simulation and forecasting of water level for Qinghai Lake using multi-altimeter data between 2002 and 2012. *IEEE J Sel Top Appl Earth Obs Remote Sens* 7(2):609–622
- Ma R, Duan H, Hu C, Feng X, Li A, Ju W, Jiang J, Yang G (2010) A half-century of changes in China's lakes: global warming or human influence? *Geophys Res Lett* 37(24):1–6
- Matthews MW (2014) Eutrophication and cyanobacterial blooms in South African inland waters: 10years of MERIS observations. *Remote Sens Environ* 155:161–177
- Matthews MW, Odermatt D (2015) Improved algorithm for routine monitoring of cyanobacteria and eutrophication in inland and near-coastal waters. *Remote Sens Environ* 156:374–382
- Min Q (1999) Evaluation of the effects of Poyang Lake reclamation on floods. *Yangtze River* 30(7):30–32
- Ogashawara I, Moreno-Madriñán MJ (2014) Improving inland water quality monitoring through remote sensing techniques. *ISPRS Int J Geo-Inf* 3(4):1234–1255
- Ozesmi SL, Bauer ME (2002) Satellite remote sensing of wetlands. *Wetl Ecol Manag* 10(5):381–402

- Palmer S, Kutser T, Hunter P (2015a) Remote sensing of inland waters: challenges, progress and future directions. *Remote Sens Environ* 157:1–8
- Palmer S, Odermatt D, Hunter P, Brockmann C, Presing M, Balzter H, Tóth V (2015b) Satellite remote sensing of phytoplankton phenology in Lake Balaton using 10years of MERIS observations. *Remote Sens Environ* 158:441–452
- Plug LJ, Walls C, Scott B (2008) Tundra lake changes from 1978 to 2001 on the Tuktoyaktuk Peninsula, western Canadian Arctic. *Geophys Res Lett* 35(3):1–5
- Qi S, Brown DG, Tian Q, Jiang L, Zhao T, Bergen KM (2009) Inundation extent and flood frequency mapping using LANDSAT imagery and digital elevation models. *GISci Remote Sens* 46(1):101–127
- Shankman D, Liang Q (2003) Landscape changes and increasing flood frequency in China's Poyang Lake region. *Prof Geogr* 55(4):434–445
- Shankman D, Keim BD, Song J (2006) Flood frequency in China's Poyang Lake region: trends and teleconnections. *Int J Climatol* 26(9):1255–1266
- Sheng Y, Li J (2011) Satellite-observed endorheic lake dynamics across the Tibetan Plateau between circa 1976 and 2000. In: Wang Y (ed) *Remote sensing of protected lands*. CRC, New York, pp 305–319
- Shi K, Zhang Y, Zhu G, Liu X, Zhou Y, Xu H, Qin B, Liu G, Li Y (2015) Long-term remote monitoring of total suspended matter concentration in Lake Taihu using 250m MODIS-Aqua data. *Remote Sens Environ* 164:43–56
- Smith LC, Beilman D, Kremenetski KV, Sheng Y, MacDonald GM, Lammers RB, Shiklomanov AI, Lapshina ED (2012) Influence of permafrost on water storage in West Siberian peatlands revealed from a new database of soil properties. *Permafro Periglac* 23(1):69–79
- Song K, Li L, Tedesco L, Clercin N, Hall B, Li S, Shi K, Liu D, Sun Y (2013) Remote estimation of phycocyanin (PC) for inland waters coupled with YSI PC fluorescence probe. *Environ Sci Pollut R* 20(8):5330–5340
- Wang Y (2009) *Remote sensing of coastal environments* (Editor). CRC Press, Boca Raton/London/New York, 457 p
- Wang Y (2012) *Remote sensing of protected lands* (Editor). CRC Press, Boca Raton/London/New York, 604 p
- Wang M, Shi W (2008) Satellite-observed algae blooms in China's Lake Taihu. *Eos, Trans Am Geophys Union* 89(22):201–202
- Wang M, Shi W, Tang J (2011) Water property monitoring and assessment for China's inland Lake Taihu from MODIS-Aqua measurements. *Remote Sens Environ* 115(3):841–854
- Wang J, Sheng Y, Hinkel KM, Lyons EA (2012) Drained thaw lake basin recovery on the western Arctic Coastal Plain of Alaska using high-resolution digital elevation models and remote sensing imagery. *Remote Sens Environ* 119:325–336
- Wu G, Liu Y (2015) Capturing variations in inundation with satellite remote sensing in a morphologically complex, large lake. *J Hydrol* 523:14–23
- Wu J-L, Ho C-R, Huang C-C, Srivastav AL, Tzeng J-H, Lin Y-T (2014) Hyperspectral sensing for turbid water quality monitoring in freshwater rivers: empirical relationship between reflectance and turbidity and total solids. *Sensors* 14(12):22670–22688
- Xu G, Qin Z (1998) Flood estimation methods for Poyang lake area. *J Lake Sci* 10(1):51–56
- Yang X, Lu X (2014) Drastic change in China's lakes and reservoirs over the past decades. *Sci Rep* 4. doi:[10.1038/srep06041](https://doi.org/10.1038/srep06041)
- Yésou H, Huber C, Lai X et al (2011) Nine years of water resources monitoring over the middle reaches of the Yangtze River, with ENVISAT, MODIS, Beijing-1 time series, Altimetric data and field measurements. *Lakes Reserv Res Manag* 16(3):231–247
- Yu Z, Chen X, Zhou B, Tian L, Yuan X, Feng L (2012) Assessment of total suspended sediment concentrations in Poyang Lake using HJ-1A/1B CCD imagery. *Chin J Oceanol Limnol* 30: 295–304
- Zhang Q, Ye X, Werner AD, Li Y, Yao J, Li X, Xu C (2014) An investigation of enhanced recessions in Poyang Lake: comparison of Yangtze River and local catchment impacts. *J Hydrol* 517:425–434

Chapter 18

Global Land Surface Water Mapping and Analysis at 30 m Spatial Resolution for Years 2000 and 2010

Xin Cao, Jun Chen, Anping Liao, Lijun Chen, and Jin Chen

Abstract Land surface water (LSW), one of the important components of land cover, is indispensable and important basic information for climate change studies, ecological environmental assessment, macro-control analysis, etc. In 2010 China launched a global land cover (GLC) mapping project, the aim of which was to produce a 30 m GLC data product (GlobeLand30) with 10 classes for years 2000 and 2010. This chapter describes an overall study on LSW in the project. Through collection and processing of Landsat TM/ETM+, China's HJ-1 satellite imagery and other remotely sensed data, the program achieves an effective overlay of global multi-spectral images at 30 m resolution for two base years, namely, 2000 and 2010. The water information was extracted in an elaborate way by combining a simple operation of pixel-based classification with a comprehensive utilization of various rules and knowledge through object-oriented classification, and finally the classification results were further optimized and improved by the human-computer interaction, thus realizing high-resolution remote sensing mapping of global water. The completed global LSW data results, including GlobeLand30-Water 2000 and GlobeLand30-Water 2010, are classification results featuring the highest resolution on a global scale, and the overall accuracy of self-assessment is 96 %. Based on the GlobeLand30-Water 2000/2010 products, this research analyzed the spatial distribution pattern and temporal fluctuation of land surface water at global scale. The GlobeLand30-Water products were corrected for the temporal inconsistency of the original remotely sensed data using MODIS time-series data, and then indices such as water area, water ration and coefficient of spatial variation were calculated for further analysis. Results show that the total water area of land surface is about 3.68 million km² (2010), and occupies 2.73 % of land area. The GlobeLand30-

X. Cao (✉) • J. Chen
State Key Laboratory of Earth Surface Processes and Resource Ecology,
Beijing Normal University, Beijing 100875, China
e-mail: caoxin@bnu.edu.cn

J. Chen • A. Liao • L. Chen
National Geomatics Center of China, Beijing 100830, China

Water products and their statistics provide fundamental information for analyzing the spatial distribution and temporal fluctuation of land surface water and diagnosing the global ecosystem and environment.

18.1 Introduction

Land surface water (LSW) is the aggregation of liquid water on land surfaces, existing as rivers, lakes, reservoirs, seasonal water, and so on. LSW is the main source of fresh water for production and life in many regions and one of most important resources for human subsistence and development, while accounting for only 0.3 % of all fresh water and less than 0.01 % of all global water. LSW is one of the main components of global water recycle. LSW's spatial distribution reflects the storage and usage status of water resources on land surface (Foley et al. 2005; Oki and Kanae 2006), while its fluctuation or change implies influence on water movement, chemical matter migration and ecosystem sustainability by climatic change, land surface processes, and human activity (Vörösmarty et al. 2000; Prigent et al. 2012). Overall understanding of the spatial distribution and fluctuation of global LSW by remote sensing is thus important for monitoring the global ecological environment.

Up to now, six sets of global land cover (GLC) data containing a land surface water class have been developed, including four sets of global 1 km land cover data developed by the U.S. Geological Survey (USGS) (Loveland et al. 2000), the University of Maryland (UMD) (Hansen et al. 2000), Boston University (BU) (Friedl et al. 2002), and the Joint Research Center (JRC) of the European Commission (Fritz et al. 2003). The European Space Agency (ESA) completed GLC data (GLOBCOVER) at 300 m resolution for 2005 and 2009 through global cooperation. In terms of global land surface water extraction, Boston University has extracted LSW mask raster data at 1 km resolution by using MODIS imagery, and river systems are in obviously discontinuous distribution (Friedl et al. 2002). The global lake wetland database (GLWD) generated by World Wildlife Fund (WWF) and University of Kassel through MGLD, DCW and other databases show the distribution of global water (Lehner and Doell 2004) roughly. In recent years, some international organizations and research institutions have begun to study and extract global LSW data with higher spatial resolution. For example, NASA-JPL generated global LSW vector data (SWBD2005) by use of SRTM data with 90 m grid interval in 2005, but the data cannot cover the global scale due to the limited scope of SRTM data; the University of Maryland, on the basis of SWBD2005 data, generated global 250 m LSW mask raster data (Carroll et al. 2009) using interpretation results of 250 m MODIS imagery in 2005.

At higher spatial resolutions, some researchers focus mainly on classification algorithms for water extraction (Xu 2006; Sheng et al. 2008; Michishita et al. 2012). Currently, the main classification algorithms for water extraction from 30 m spatial resolution remote sensing imagery include: (1) the single-band threshold

method, extracting water (Rundquist et al. 1987; Work and Gilmer 1976) by setting a threshold value based on the water's spectral feature of strong absorption in the near-infrared band (NIR); (2) the water index method, establishing water indexes mainly through the green band, NIR, middle-infrared band (MIR), and other characteristic bands, including the simple ratio index (Jordan 1969), NDWI index (McFeeters 1996), MNDWI index (Xu 2005, 2006), etc. and an extracting index by setting a threshold value; (3) a classification method based on statistics and machine learning, including non-ISODATA (Sivanpillai and Miller 2010) supervised classification, maximum likelihood method supervised classification (Sheng et al. 2008), etc.; (4) a prior information-based decision tree classification method, for instance, extracting various types of water (Cao et al. 2005; Xu and Chen 2008) by setting a discrimination function for a characteristic band, index or auxiliary information and removing shadow (Sun et al. 2012) based on the distribution of 99.2 % of water in the area (Niu et al. 2009) with slope less than 8°; and (5) an object-oriented method based on spatially continuous distribution of water objects (Blaschke 2010; Luo et al. 2009) or considering compactness, smoothness and connectivity of the targets (Frohn et al. 2005; Van der Werff and Van der Meer 2008).

Most of these water extraction methods can achieve a sound classification effect only in specific image conditions or some areas; however, it is difficult for mechanical application of any method to generate sound classification results on the global scale in case of global multi-source classification of basic imagery as well as complex and diverse spectral features and geometric shapes of water. With the support of the National High Technology Research and Development Program (the 863 Program) of China, the work of finer resolution mapping of GLC by remote sensing was the first to carry out (Chen et al. 2015), and produced LSW datasets (GlobeLand30-Water) at 30 m spatial resolution for the years 2000 and 2010 (GlobeLand30-Water 2000 and GlobeLand30-Water 2010). This paper introduces the mapping method for GlobeLand30-Water products, and the spatial distribution and fluctuation of LSW on a global scale.

18.2 Data and Pre-processing

1. Collection and processing of 30 m images

The remote sensing image data adopted for 30 m global water remote sensing mapping in 2000 and 2010 are mainly Landsat TM/ETM+ images, while China's HJ-1 satellite images are used as supplements for areas not covered by the 2010 Landsat images. All Landsat TM/ETM+ images are downloaded from EROS Data Center and are of L1T processing level. The error in registration of Landsat TM/ETM+ images of the two periods upon inspection and repeated rectification is less than 1 pixel, whereas that in registration between Landsat TM/ETM+ and HJ-1 remote sensing images is less than 1.5 pixels. For 2010 ETM+ SLC-off data, the interpolation methods proposed by Chen et al. (2011) were used to process the missing data.

Effective overlay of global 30 m classified images for the two periods is achieved through optimization and processing. In total, there were 10,270 Landsat TM and ETM+ images in 2000 and 9907 Landsat TM and ETM images and 2640 HJ-1 images in 2010.

2. Reference data

To improve water interpretation accuracy, many reference datasets were collected, such as a global 1:1,000,000 fundamental geographic base map database (rivers and lakes), 4 sets of global 1 km land cover products, 2 sets of global 300 m resolution land cover products, global 250 m LSW mask raster data, global 90 m SRTM and 30 m ASTER GDEM, and global lake wetland data. In addition, 30 m resolution land cover data were also collected in some areas, such as Europe's CLC (Corine Land Cover), NLCD (National Land Cover Dataset) of USGS, China's Land Use Data, etc. Other data used in this research include: (1) MODIS 8 day composite of surface reflectance product (MOD09A1) at 500 m spatial resolution, and (2) vector data of Köppen climate zone (13 one-level climate zones) for analyzing water area and water ratio of global and continental LSW.

18.3 Global 30 m LSW Mapping Methods

To improve water extraction accuracy and reduce workload, a detailed work process was developed with three aspects, namely, pixel extraction, object filtration, and human-computer interaction editing, so that the water extraction process benefits from integration of multiple classification methods and implementation of strict quality control over all links. Based on the analysis and comparison of different automatic classification algorithms for remote sensing extraction of water, three pixel-based automatic classification methods, namely, supervised classification, prior information-based decision tree extraction, and maximum likelihood mask extraction, are performed using spectral features (pure water, sediment-containing turbid water, and eutrophic water) and spatial-temporal features (geometric shapes and phase difference) of water in different areas worldwide, and the methods are used for classified water extraction in global water remote sensing mapping. As for the results of automatic classification, polygons are filtered by using segmented objects produced using eCognition software to remove finely-broken polygons, eliminate the salt and pepper effect, and obtain object-based water classification results. Meanwhile, knowledge rules are used to rapidly locate polygons that may have quality problems, to facilitate manual verification and processing. A convenient human-computer interaction environment is established to conduct inspection and editing for object-based water classification results image by image, including inspection of polygons one by one, coordination of polygons, classified edge matching, etc. to obtain high-accuracy water classification results. Refer to Fig. 18.1 for the process and method.

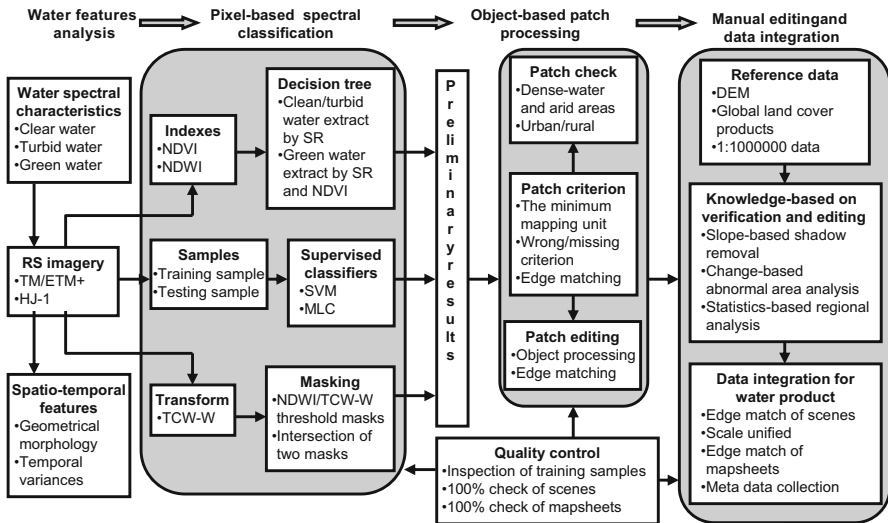


Fig. 18.1 Diagram of global water extraction methods

18.3.1 Pixel-Based Water Remote Sensing Extraction

Given spectral, scale and phase differences and other problems of global LSW extraction, and based on existing water remote sensing extraction algorithms, some integrated extraction methods such as prior information-based decision tree water extraction, maximum likelihood mask water extraction, and training sample-based supervised classification are formulated through the study and are recommended for automatic water extraction. Technicians can select and apply this method with maximum efficiency and the highest accuracy according to actual situations such as water distribution, water features, etc. on the classified image.

1. Prior information-based decision tree water extraction method

Various types of water are extracted (Sun et al. 2012) respectively through the decision tree method, e.g., using indexes, setting threshold values and slope filtration from the point of spectral difference and according to form features of a water reflectance curve. First, pure water can be extracted by setting band 2 to be greater than band 5 and less than a threshold value based on the feature that reflectance of pure water in TM/ETM+ images decreases with increase of wavelength. Secondly, eutrophic water can be extracted by setting the maximum reflectance to be in band 4 and less than a certain threshold value according to the feature that the maximum wave spectral reflectance of eutrophic water is in band 4 and much less than that of vegetation. NDVI can be used to further optimize the result to avoid being confused with rice paddy fields. Finally, sediment-containing turbid water can be extracted by setting the maximum reflectance to be in band 5 and less than a certain value

according to the feature that the maximum reflectance of the sediment-containing turbid water is in band 5 and much less than that of bare soil or settlement areas.

2. Maximum likelihood mask method based on spectrum relationship and tasseled cap transformation humidity component

In case of complex types of regional ground objects, the optimal space mask (Wu et al. 2008) of extracted water is established by use of the spectrum relationship ((band 2 + band 3) – (band 4 + band 5)) and the tasseled cap transformation humidity component TCW to compensate for the disadvantage that the information of tributaries of river systems and small water cannot be extracted accurately. The enhanced image threshold method of (band 2 + band 3) – (band 4 + band 5) > threshold value t_1 provides good water extraction in farmland, forest land and mountains, and the enhanced image threshold method of tasseled cap transformation humidity component TCW > threshold value t_2 provides good water extraction for building residents. The mask rule is used to acquire the optimal space mask to extract information about all water and some ground objects, and then the maximum likelihood method is used to extract water information exactly. The method reduces the ratio of extracting other ground objects mistakenly and thus ensures the information of tributaries and small water bodies can be extracted properly.

18.3.2 Object-Oriented Polygon Processing

Being subject to algorithm, sample, image, and many other factors, water classification results obtained through automatic pixel-based classification are of low accuracy generally, and there are problems such as polygon breaking, serious salt and pepper effect, etc. The second processing step of water remote sensing mapping is object-oriented processing of water classification results. Each basic image used for classification is segmented at three scales (15, 20, and 30) using the eCognition software, which generates segmented object results on the three scales. The scale segmentation result best matching water is selected from segmented objects of each image at multiple scales and will be used for automatic polygon filtration of pixel classification result, thus obtaining object-based water classification results of each image while reducing finely-broken polygons and eliminating the salt and pepper effect. The process is shown in Fig. 18.2.

After object-based water classification results of each image are obtained, a corresponding rule can be established by use of relevant knowledge to filter out water objects and search for polygons that may be mistakenly classified as water, which will be marked for manual verification. Main methods are as follows:

1. Using DEM data to search for mistakenly extracted polygons due to shadow. Based on global DEM data, calculate the area with slope greater than 8° , filter water classification objects of each period through slope information

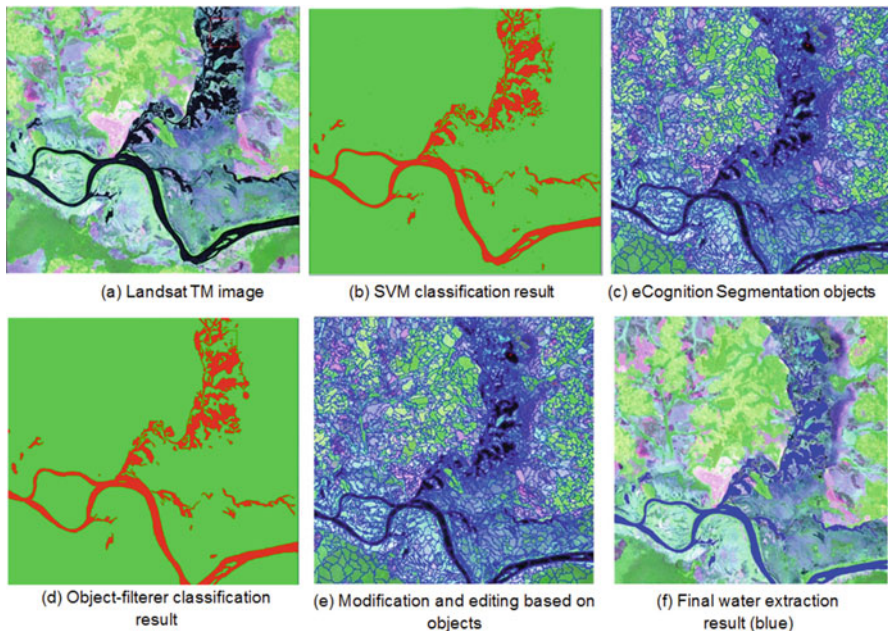


Fig. 18.2 Diagram of water extraction process based on segmented objects

aiming at mistaken extraction of water and shadow due to spectrum consistency, to identify areas with mountain shadows easily confused (Niu et al. 2009), and conduct verification and correction through human-computer interaction to reduce mistaken classification of water.

- Analysis of area with water data inconsistent in the two periods. Acquire the area with classification results inconsistent in the two periods through a spatial operation of water results of the two periods, mark the area with size greater than certain threshold value, and then develop a key manual examination on them in later period.
- Data statistics and analysis. Count dimensions in the two periods by county (region), compare them with each other or with official document data, and verify and analyze exceptional situations (if any).

18.3.3 Editing Based on Human-Computer Interaction

To ensure consistency of global water extraction in scales and spaces, editing and processing based on human-computer interaction are conducted for results of classified water extraction in accordance with unified mapping standards to address problems such as seasonal water, type confusion, distinction between inland

water and sea water, non-matching of edge of classified image, etc., to reduce omission and commission errors in classification of water information and maximize extraction accuracy. In addition to the check and modification of “defective” polygons one by one found through knowledge rules, classification results will also be processed according to the unified scale standard, while many quality control methods will be adopted for cross-checking to verify the correctness of water extraction.

18.4 Methods for Global LSW Analysis

This paper comprehensively analyzes the spatial distribution patterns and dynamic change characteristics of LSW by calculating indicators like water area, water ratio, and the spatial variability index.

18.4.1 Water Ratio and Spatial Variability Index

In order to better characterize the spatial distribution of LSW, this paper selects a 0.1×0.1 degree grid as the basic statistical unit and defines the water ratio (R) and the spatial variability index (V) as follows:

$$R = A_W/A_L \quad (18.1)$$

$$V = Std(R)/mean(R) \quad (18.2)$$

where A_W is the water area within the basic statistical unit, A_L is the corresponding land surface area, $Std(R)$ is the standard deviation of the water rate within the statistical unit, and $mean(R)$ is the average of water ratio. The greater the spatial variability index, the more uneven the water distribution in space; the lower the index, the more uniform the water distribution in space. Therefore, it can reflect or characterize the non-uniformity of LSW’s spatial distribution.

18.4.2 Temporal Correction for Water Area Counting

How to keep temporal consistency has long been regarded as a difficult task for mapping 30 m global land cover. The acquisition dates of most images used for the two GlobeLand30-Water products range from April to September, while a small number of imageries range from January to March and October to December.

Considering that each interpreted water result reflects the water distribution status at a specific time and cannot be directly used for spatio-temporal pattern analysis due to seasonal fluctuation of LSW, we proposed a method to correct temporal information for GlobeLand30-Water products on the basis of MODIS time series data. The Köppen climate zones were taken as the basic unit (Peel et al. 2007); within each unit we captured the seasonal characteristics of water area using MODIS images and then corrected the area of GlobeLand30-Water products according to the average annual water area. The water area at each date (A_D) and the average annual water area (A_m) based on MODIS images were counted for each climate zone. Thus the correction coefficient (k_D) at each date for each climate zone was calculated as the ratio of average annual water area (A_m) and water area at each date (A_D):

$$k_D = A_m / A_D \quad (18.3)$$

Then the corresponding correction coefficient can be determined to correct the water area to the average annual water area based on the acquiring date and location of each of the 30 m images:

$$A^{H'}_D = A^H_D \times k_D \quad (18.4)$$

Where D is the acquisition date of the 30 m imagery, A^H_D is the water area at date D based on the 30 m imagery, and $A^{H'}_D$ is the corrected water area to the average annual level.

We designed a Clustering by Eigen Space Transformation (CBEST) algorithm to extract water area using MODIS time series data rapidly and accurately. First, the multi-bands data were converted to the principal components space. The Eigen values derived from the principal component analysis were used to segment the whole space into spatial units. Then the original data were replaced with the number and mean value in each spatial unit. Finally a K-means cluster algorithm was employed based on spatial unit. Compared with the traditional K-means algorithm, the CBEST algorithm only traverses the feature space units, and thus greatly improves the clustering efficiency. A two-level CBEST clustering method was implemented to further improve the computational efficiency. The first level clusters each MODIS image by 100 classes. The second level clusters the centers of spectral clusters derived from the first level with the same number of classes. According to the mapping relationship between the two clusters, the pixel values of the imagery were assigned to spectral cluster terminals. Finally, the corresponding spectral cluster of water bodies was extracted from the spectral cluster terminals by interactive interpretation, and the time-series water results were thereby achieved.

To assess the accuracy of water results based on MODIS, 245 images covering water bodies from the years 2000 and 2010 were selected. The water area based on GlobeLand30-Water products was compared with that based on MODIS images from the same date. Figure 18.3 shows a high correlation relationship between these

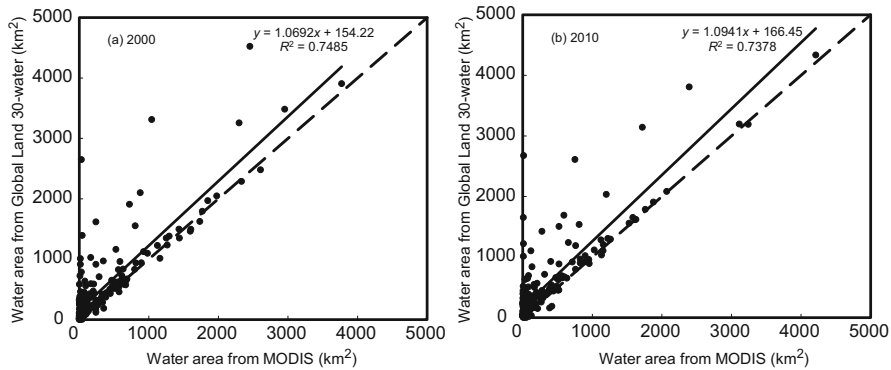


Fig. 18.3 Comparison between the water areas based on MODIS and GlobeLand30-Water

two results. The water areas based on MODIS were underestimated, which means some omissions exist for MODIS' results. However, the small omission errors have no influence on the relative relationship between different seasonal water areas. Therefore, it can be concluded that the water areas based on MODIS can be used to correct those based on GlobeLand30-Water products.

18.5 Global LSW Mapping Results and Validation

Figure 18.4 shows the global LSW mapping results for 2010, i.e. GlobeLand30-Water 2010 product. The accuracy assessment of the GlobeLand30-Water products was conducted by independent institutes. Samples for inspection comprise two parts: one consists of polygon samples selected from 30 m resolution images; the other consists of point samples acquired from the field survey. A method of stratified random sampling is adopted to acquire the spatial distribution of samples for inspection, and then specialists familiar with this area and with experience in visual interpretation will judge one by one based on the classified image, a high-resolution image (Google Earth, etc.), field observation data, etc., and finally establish datasets of samples for inspection for 2000 and 2010.

The accuracy assessment result of the global LSW product is obtained through calculation that provides accuracy self-assessment results for five global working areas. The numbers of global water samples for 2000 and 2010 are 10,237 and 9597 respectively, and the average overall accuracy is 96.51 % and 96.48 % respectively. Table 18.1 shows the numbers of validation samples and overall accuracy. There we can see that water remote sensing products in Europe, America, and Oceania have the highest accuracy, followed by Northeast Asia and Central Asia, and then by Africa, Southeast Asia and West Asia. Table 18.1 indicates that the lowest overall accuracy is higher than 92 % for Southeast Asia and West Asia.

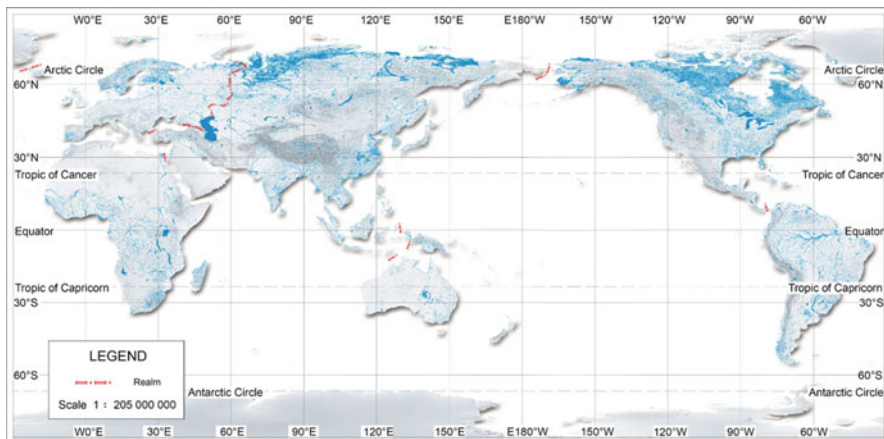


Fig. 18.4 Distribution map of global land surface water in the year 2010

Table 18.1 Global water accuracy self-assessment

Region	Water in 2000		Water in 2010	
	Number of samples	Overall accuracy (%)	Number of samples	Overall accuracy (%)
Northeast and Central Asia	2003	96.00	2040	97.00
Southeast and West Asia	725	93.20	697	92.70
Europe	1210	99.66	1200	98.75
Africa	2745	93.60	2745	93.70
America	1215	98.00	1215	98.00
Oceania	2339	98.60	1700	98.60
Global overall	10,237	96.51	9597	96.48

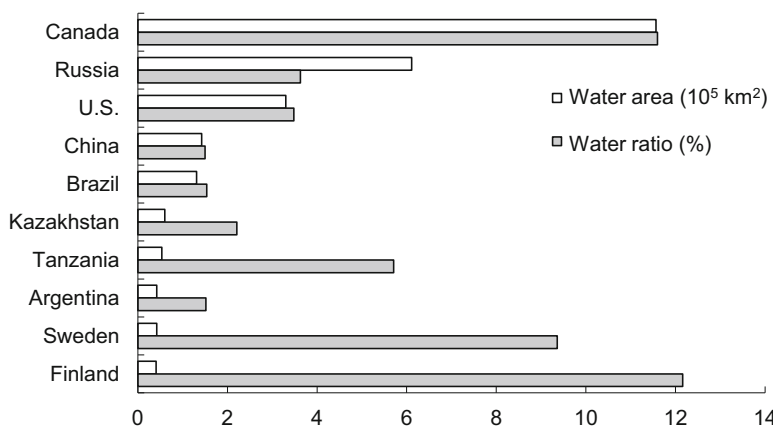
18.6 Global LSW Statistics and Analysis

18.6.1 Overall Statistics

Further statistics show that global LSW distributes unevenly. The proportions of LSW areas of all continents in 2010 are as follows: North America (41.62 %), Asia (33.80 %), Europe (8.59 %), Africa (7.40 %), South America (7.28 %), and Oceania (1.31 %). Sorted by water ratio, the descending order is North America, Europe, Asia, South America, Africa, and Oceania (Table 18.2). In terms of spatial variability index, the descending order is Africa, Oceania, South America, Asia, Europe, and North America (Table 18.2). It shows that the spatial distribution of LSW in North America is relatively uniform and that in Africa it is most concentrated with

Table 18.2 Land surface water area and water ratio statistics for continents in year 2010

	Water area ($\times 10^6 \text{ km}^2$)	Proportion to the global LSW area (%)	Water ratio (%)	Spatial variability index
Global	3.6767	100.00	2.73	3.42
Asia	1.2428	33.80	2.79	3.71
Europe	0.3159	8.59	3.22	2.90
Africa	0.2719	7.40	0.91	8.09
North America	1.5302	41.62	6.28	2.29
South America	0.2678	7.28	1.51	4.51
Oceania	0.0482	1.31	0.57	6.64

**Fig. 18.5** Top 10 countries with largest water areas and their water ratios in 2010

the greatest spatial discrepancy. The spatial distribution differences of LSW have some influence on water resources and the ecological environment.

According to national statistics, the top 10 countries with the largest LSW areas in 2010 are Canada, Russia, the United States, China, Brazil, Kazakhstan, Tanzania, Argentina, Sweden, and Finland. In these countries, the water ratio of Canada is the highest, and those of China and Argentina are the lowest (Fig. 18.5). The value of water ratio can partially reflect the situation of water deficit for a country.

18.6.2 Spatial Distribution Patterns of Land Surface Water

Figure 18.6 shows the global water ratio in 2010 and the curves of water area and water ratio along longitude and latitude. Latitudinally, the LSW area of the Northern Hemisphere accounts for 86.73 % of the world, and its water ratio is 3.18 %. LSW between the latitudes of 30°N and 75°N occupies 91.08 % of the Northern Hemisphere's water area. Many large water bodies, such as the Caspian

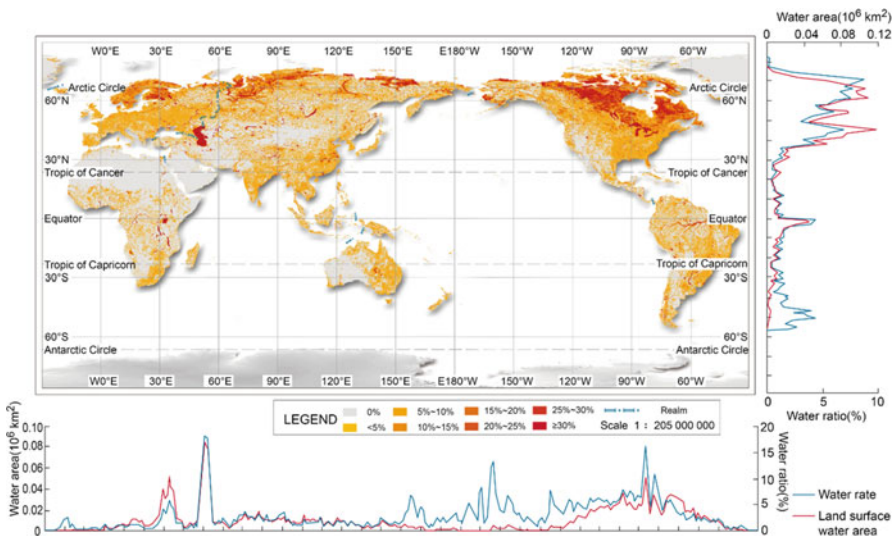


Fig. 18.6 Global water ratio map with water area and water ratio along latitude and longitude in 2010

Sea, the Aral Sea, and the Great Lakes, are distributed between 40°N and 50°N. The LSW area of the Southern Hemisphere is only 13.27 % of the world's total water area, and its water ratio is 1.41 %. The tropical region from the equator to 15°S occupies 59.91 % of the Southern Hemisphere's water area, and the water rate in this region is 1.97 %.

From the aspect of longitude, the water areas of the Eastern and Western Hemispheres are roughly equal, and LSW is distributed relatively uniformly in the Eastern Hemisphere. In the Western Hemisphere, LSW mainly gathers between 60°W and 140°W.

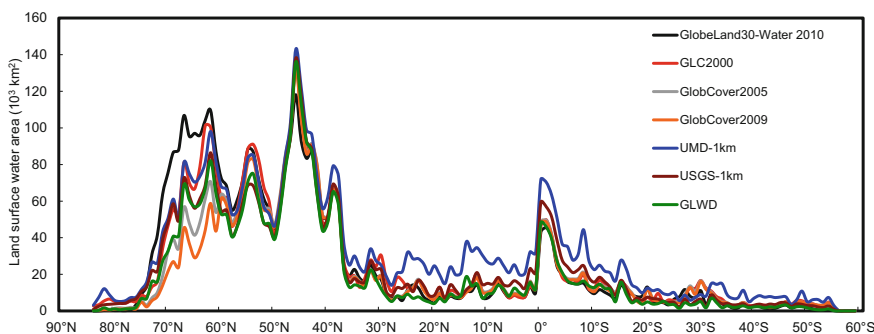
Compared with the water area results from some existing land cover or water products (Table 18.3), there are remarkable differences due to the use of different data sources, year/time, spatial resolution, classification systems, and classification methods. The results show that the global LSW areas range from 3.03 to 4.57 million km². Overall, GlobeLand30-Water products and other products have a high consistency (Fig. 18.7) from the distribution trend along latitude, and the advantage of its finer spatial resolution makes the result more accurate.

18.6.3 Land Surface Water Fluctuation Between 2000 and 2010

The total area of global LSW is 3,741,900 km² and the water ratio is 2.78 % in 2000, whereas in 2010 these are 3,676,700 km² and 2.73 %, respectively. The

Table 18.3 Water areas of existing global land cover or water products (unit: 10^6 km^2)

	GLC2000	GlobCover2005	GlobCover2009	UMD-1 km	USGS-1 km	GLWD
Global	3.64	3.26	3.05	4.57	3.49	3.03
Asia	1.14	1.09	1.02	1.66	1.18	0.99
Europe	0.28	0.26	0.23	0.44	0.35	0.23
Africa	0.31	0.31	0.30	0.48	0.36	0.31
North America	1.53	1.22	1.13	1.39	1.20	1.21
South America	0.27	0.27	0.26	0.36	0.34	0.26
Oceania	0.11	0.11	0.10	0.24	0.07	0.02

**Fig. 18.7** Water area distributions along latitude of existing global land cover products**Table 18.4** Land surface water area and water ratio for 2000 and 2010

	Water area in 2000 (10^6 km^2)	Water ratio in 2000 (%)	Water area in 2010 (10^6 km^2)	Water ratio in 2010 (%)	Difference (10^3 km^2)	Relative variation (%)
Global	3.74	2.78	3.68	2.73	-65.2	-1.77
Asia	1.25	2.81	1.24	2.79	-7.2	-0.58
Europe	0.33	3.32	0.32	3.22	-9.9	-3.12
Africa	0.29	0.96	0.27	0.91	-14.2	-5.22
North America	1.53	6.29	1.53	6.28	-2.1	-0.14
South America	0.29	1.62	0.27	1.51	-20.1	-7.49
Oceania	0.06	0.71	0.05	0.57	-11.6	-24.06

overall change of LSW between 2000 and 2010 is small, while the fluctuations for continents are significantly differentiated (Table 18.4). The LSW area fluctuation of Oceania is the largest one among all the continents, and the relative variation is -24.06% ; the relative variations of South America, Africa, and Europe are -7.49% , -5.22% , and -3.12% , respectively. The LSW areas in Asia and North America fluctuate least with variations of -0.58% and -0.14% . Figure 18.8 shows the spatial pattern of LSW fluctuation between 2000 and 2010.

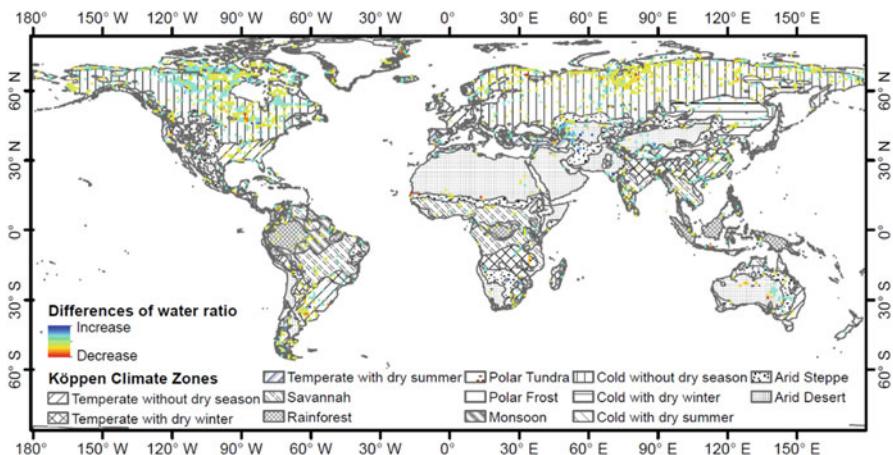


Fig. 18.8 The spatial pattern of land surface water fluctuation between 2000 and 2010

18.7 Conclusions and Discussion

Effective overlay of images for two periods is achieved through geometric and atmospheric rectification to image data, ETM+ band data interpolation and other processing with preference given to Landsat TM/ETM+, HJ-1 and other images with 30 m spatial resolution. Pixel-based integrated water extraction methods such as a prior information-based decision tree, maximum likelihood mask, etc. are used to acquire a water pixel classification result of each image rapidly. Segmented object results of different scales generated by eCognition software are used to filter pixel classification results and to form object-based water classification polygons for each image. Different knowledge rule sets are established to check classification polygons, and human-computer interaction is adopted for verification and editing, thus ensuring the correctness of water classification results and consistency of scales and standards. The completed global LSW datasets (GlobeLand30-Water 2000 and GlobeLand30-Water 2010) for the two periods have the highest available resolution on a global scale, and the average overall accuracy is 96 % based on accuracy self-assessment analysis. Based on 30 m resolution remote sensing image data and supplemented by 500 m resolution MODIS image data, two datasets of global land surface water (GlobeLand30-Water 2000/2010) were produced, and then statistics data of water area and water ratio were calculated. These data provide fundamental information for analyzing spatial distribution of global LSW, revealing the regional discrepancies, and its temporal fluctuation pattern.

Due to the dynamic nature of LSW, the water areas derived from remote sensing data only represent a specific temporal characterization of LSW, and cannot directly reflect the amount of water resources. The differences between LSW products of 2000 and 2010 can reflect only the variations of the climatic conditions and processes of the water cycle for these separate years. The trend analysis of LSW

change requires continuous and long time series data products. Therefore, further research should involve a sequence of measurements of LSW with high spatial resolution, and analyses of the effects and causes of LSW changes with regard to global warming, land use change and human activities in hotspot areas.

References

- Blaschke T (2010) Object based image analysis for remote sensing. *ISPRS J Photogramm Remote Sens* 65:2–16
- Cao K, Jiang N, Li X et al (2005) Based on the SPOT – 5 image of city water body automatic extraction model. *Remote Sens Land Resour* 4:24–27
- Carroll ML, Townshend JR, DiMiceli CM et al (2009) A new global raster water mask at 250 m resolution. *Int J Digital Earth* 2(4):291–308
- Chen J, Zhu X, Vogelmann JE et al (2011) A simple and effective method for filling gaps in Landsat ETM+ SLC-off images. *Remote Sens Environ* 115:1053–1064
- Chen J, Chen J, Liao A et al (2015) Global land cover mapping at 30 m resolution: a POK-based operational approach. *ISPRS J Photogramm Remote Sens* 103:7–27
- Foley JA, Gregory RD, Barford C et al (2005) Global consequences of land use. *Science* 309:570. doi:[10.1126/science.1111772](https://doi.org/10.1126/science.1111772)
- Friedl MA, McIver DK, Hodges JCF et al (2002) Global land cover mapping from MODIS: algorithms and early results. *Remote Sens Environ* 83:287–302
- Fritz S, Bartholomé E, Belward A et al. (2003) Harmonisation, mosaicing and production of the Global Land Cover 2000 database (Beta Version). Office for Official Publications of the European Communities, Luxembourg, EUR 20849 EN, 41 pp, ISBN 92-894-6332-5
- Frohn RC, Hinkel KM, Eisner WR (2005) Satellite remote sensing classification of thaw lakes and drained thaw lake basins on the North Slope of Alaska. *Remote Sens Environ* 97:116–126
- Hansen MC, DeFries RS, Townshend JRG et al (2000) Global land cover classification at 1 km spatial resolution using a classification tree approach. *Int J Remote Sens* 21:1331–1364
- Jordan CF (1969) Derivation of leaf area index from quality of light on the forest floor. *Ecology* 50:663–666
- Lehner B, Doell P (2004) Development and validation of a global database of lakes, reservoirs and wetlands. *J Hydrol* 296:1–22
- Loveland TR, Reed BC, Brown JF et al (2000) Development of a global land cover characteristics database and IGBP DISCover from 1 km AVHRR data. *Int J Remote Sens* 21:1303–1330
- Luo J, Sheng Y, Shen Z et al (2009) Step by step iteration of multispectral remote sensing information and high precision automatic water extraction. *J Remote Sens* 13(4):610–615
- McFeeters SK (1996) The use of the normalized difference water index (NDWI) in the delineation of open water features. *Int J Remote Sens* 17:1425–1432
- Michishita R, Gong P, Xu B (2012) Spectral mixture analysis for bi-sensor wetland mapping using Landsat TM and Terra MODIS data. *Int J Remote Sens* 33:3373–3401
- Niu Z, Gong P, Cheng X et al (2009) China's wetland preliminary analysis remote sensing mapping and relevant geographic features. *Sci China (D)* 39(2):188–203
- Oki T, Kanae S (2006) Global hydrological cycles and world water resources. *Science* 313:1068. doi:[10.1126/science.1128845](https://doi.org/10.1126/science.1128845)
- Peel MC, Finlayson BL, McMahon TA (2007) Updated world map of Köppen-Geiger climate classification. *Hydroclim Earth Syst Sci* 11:1633–1644
- Prigent C, Papa F, Aires F et al (2012) Changes in land surface water dynamics since the 1990s and relation to population pressure. *Geophys Res Lett* 39, L08403. doi:[10.1029/2012GL051276](https://doi.org/10.1029/2012GL051276)
- Rundquist DC, Lawson MP, Queen LP et al (1987) The relationship between summer-season rainfall events and lake-surface area. *Water Resour Bull* 23:493–508

- Sheng Y, Shah CA, Smith LC (2008) Automated image registration for hydrologic change detection in the lake-rich Arctic. *IEEE Geosci Remote Sens Lett* 5:414–418
- Sivanpillai R, Miller SN (2010) Improvements in mapping water bodies using ASTER data. *Ecol Inform* 5:73–78
- Sun F, Sun W, Chen J, Gong P (2012) Comparison and improvement of methods for identifying waterbodies in remotely sensed imagery. *Int J Remote Sens* 33(21):6854–6875
- Van der Werff HMA, Van der Meer FD (2008) Shape-based classification of spectrally identical objects. *ISPRS J Photogramm Remote Sens* 36:251–258
- Vörösmarty CJ, Green P, Salisbury J et al (2000) Global water resources: vulnerability from climate change and population growth. *Science* 289:284–288
- Work EA, Gilmer DS (1976) Utilization of satellite data for inventorying prairie ponds and lakes. *Photogramm Eng Remote Sens* 42:685–694
- Wu W, Shen X, Zou L et al (2008) Water body information extraction method based on Landsat ETM images. *Chin Sci Bull* 24:252–259
- Xu H (2005) Using the improved normalized difference water index (MNDWI) to extract water body information research. *J Remote Sens* 9(5):589–595
- Xu H (2006) Modification of normalised difference water index (NDWI) to enhance open water features in remotely sensed imagery. *Int J Remote Sens* 27:3025–3033
- Xu J, Chen S (2008) Based on the TM images of water body information extraction. *J Soil Water Conserv* 15(6):161–163

Chapter 19

Multitemporal Remote Sensing of Coastal Waters

**Susanne Kratzer, Krista Alikas, Therese Harvey,
José María Beltrán-Abaunza, Evgeny Morozov, Sélima Ben Mustapha, and
Samantha Lavender**

Abstract In this chapter we address some of the recent developments in marine coastal remote sensing with regards to the evaluation of water quality from space using multi-temporal data. Most chapters in this book are devoted to terrestrial applications, whereas aquatic remote sensing requires a completely different approach in terms of mission and sensor design as well as data analysis and processing. Therefore, the first section is a general introduction to marine remote sensing. Then we report recent results from remote sensing of the Baltic Sea, which is optically dominated by the absorption of light by coloured dissolved organic matter (CDOM), and during summer months, by high standing stocks of filamentous cyanobacteria. Results both from basin-wide as well as coastal applications in the north-western Baltic Sea are presented. In next section we report results from the Bay of Biscay in the north-eastern Atlantic Ocean west of France, which is an area highly influenced by river discharge and dinoflagellate blooms, and the subsequent section is about a coastal area in the eastern Beaufort Sea in the Arctic that's influenced by a pool

S. Kratzer (✉) • T. Harvey • J.M. Beltrán-Abaunza
Department of Ecology, Environment and Plant Sciences, Stockholm University,
10691 Stockholm, Sweden
e-mail: Susanne.Kratzer@su.se

K. Alikas
Department of Remote Sensing, Tartu Observatory, 61602 Tartumaa, Estonia

E. Morozov
Department of Ecology, Environment and Plant Sciences, Stockholm University,
10691 Stockholm, Sweden

NIERSC, 14th Line 7, Office 49, Vasilievsky Island, 199034 St. Petersburg, Russia

S.B. Mustapha
Department of Ecology, Environment and Plant Sciences, Stockholm University,
10691 Stockholm, Sweden

Institut Maurice-Lamontagne, Pêches et Océans Canada, C.P.1000, Mont-Joli, Québec,
G5H 3Z4, Canada

S. Lavender
Pixalytics Ltd, 1 Davy Road, Plymouth Science Park, Plymouth, Devon, PL6 8BX, UK

of CDOM. In all sections we discuss the relevance of regional remote sensing for ecological analysis and coastal management. The chapter concludes with a synthesis on merging of satellite data from different ocean colour missions and the limitations for coastal applications are discussed.

Abbreviations

Acronym	Explanation
AVHRR:	Advanced Very High Resolution Radiometer (NOAA)
Case-1 waters	Waters that are optically dominated by water itself and by Chl- <i>a</i> (and correlated CDOM)
Case-2 waters	Waters that are also optically significantly influenced by SPM and/or CDOM (besides water and Chl- <i>a</i>)
Chl- <i>a</i>	Chlorophyll-a
Chl- <i>b</i>	Chlorophyll-b
CDOM	Chromophoric or Coloured Dissolved Organic Matter
CZCS	Coastal Zone Colour Scanner (NASA)
DIN	Dissolved Inorganic Nitrogen
DIP	Dissolved Inorganic Phosphorus
EC	European Commission
ENVISAT	European ENVIronmental SATellite (ESA)
ESA	European Space Agency
EU	European Union
FR	Full resolution
FUB	Freie Universität Berlin
GMES	Global Monitoring of Environment and Security
GSM	Global System for Mobile communications
HELCOM	HELSinki COMmission
ICOL	Improved Contrast between Ocean and Land processor
IOPs	Inherent Optical Properties
MCI	Maximum Chlorophyll Index
MERIS	MEdium Resolution Imaging Spectrometer (ESA)
MLAC	Merged Local Area Coverage
MODIS	MODerate Imaging Spectroradiometer (NASA)
NASA	National Aeronautics and Space Administration
NIR	Near-InfraRed
NOAA	National Oceanic and Atmospheric Administration
NPP	Net Primary Production
NSIDC	National Snow and Ice Data Center
OC	Ocean Colour
OLCI	Ocean and Land Colour Instrument (ESA)
RGB	Red Green Blue
RR	Reduced resolution

SeaDAS	SeaWiFS Data Analysis Software
SeaWiFS	Sea-viewing Wide Field-of-view Sensor (NASA)
SPM	Suspended Particulate Matter
SST	Sea Surface Temperature
TOA	Top-of-Atmosphere
TSM	Total Suspended Matter
VIS	Visible
WFD	Water Framework Directive 2000/60/EC
MSFD	Marine Strategy Framework Directive 2008/56/EC

Optical coefficients

a	Absorption coefficient
b	Scattering coefficient
b_b	Backward scattering coefficient
b_f	Forward scattering coefficient
G_{440}	Absorption coefficient of CDOM
I	Radiance
E	Irradiance
E_d	Downwelling Irradiance
K_d	Diffuse attenuation coefficient of downwelling irradiance
Rrs	Remote Sensing Reflectance

19.1 Introduction

Before satellite ocean colour remote sensing techniques were available, measurements of water quality parameters derived from seawater optical properties were spatially isolated and infrequent, being available primarily from ships and moorings, with a few airborne campaigns. With the new space imagery the full dynamics of algal blooms and river plumes were suddenly revealed, and a new understanding of ocean currents and dynamics was fostered in an unprecedented way (Whitehouse and Hutt 2006). The first ocean colour (OC) sensor launched was the Coastal Zone Color Sensor (CZCS) developed by NASA. It was launched on the Nimbus-7 satellite and operational from 1978 to 1986 (McClain 2009). CZCS was very speculative and a proof-of-concept mission for studying phytoplankton from space, but worked well for open ocean applications and provided the first estimates of global ocean productivity (Behrenfeld and Falkowski 1997). However, it did not have the required spectral and spatial resolution to deal with the complexity of coastal waters, nor could it sufficiently correct for atmospheric effects. The main operational OC missions to date have been NASA's 'Sea-viewing Wide Field-of-view Sensor' SeaWiFS (1997–2010), and the 'MODerate Imaging Spectroradiometer' MODIS (since 1999) and ESA's 'Medium Resolution Imaging Spectrometer' MERIS (2002–2012). MERIS deserves a special mention as it was the first sensor especially designed for coastal applications (Doerffer et al. 1999). It

ceased working in March 2012 and has been replaced by the Ocean and Land Colour Instrument (OLCI) on Sentinel-3 on 16 February 2016 as part of the Copernicus mission (Donlon et al. 2012).

Difference Between Terrestrial and Ocean Colour Remote Sensing Before discussing the optical properties of marine waters, we will first have a closer look at the difference between terrestrial and OC remote sensing data in terms of spatial, spectral and temporal resolution. The main difference between the terrestrial and marine biota is that the sea is highly dynamic as marine algae are suspended in the water and so move with the currents (advection), whereas plants do not change location and so their growth and decay can be monitored by examining the temporal variability of each individual pixel. Vegetation growth and the change in tree and leaf cover happen generally over a span of weeks or months (10–100 d) rather than within a few days (IOCCG 2000). The life cycle of algal blooms is much shorter than that of typical terrestrial plants, and requires suitable hydrodynamic conditions to deliver the nutrients and solar radiation needed for phytoplankton growth. An algal bloom, can develop within a few days, and disappear again within a week (Sect. 19.2.4). This is important in terms of the required temporal resolution (frequency) of remote sensing data: in terrestrial remote sensing the development can focus on attaining the best possible spatial resolution. Nowadays, the spatial resolution of terrestrial remote sensing data is in the range of about 2–30 m, whereas in OC remote sensing one needs to focus on developing satellite systems with a good temporal resolution as phytoplankton dynamics in the coastal zone can change on a daily or even diurnal basis. Some dinoflagellates, for example, are known to migrate up and down the water column dependent on the light and food availability which may have a drastic effect on the chlorophyll-a (Chl-a) concentration in the upper water layers that are sensed by OC remote sensing. Phytoplankton are also known to exhibit a diurnal change in photosynthetic production, dependent on the change in solar radiation during the day which is at its maximum values during mid-day. In areas of high tidal influence, the physical dynamics in bays and estuaries can also change drastically within 4–6 h.

Trade-Off Between Spatial and Temporal Resolution In order to get a good spatial resolution, and hence retrieve pixels of a smaller size, higher resolution sensors have a narrower swath width, which means they can only cover a smaller area of the Earth when revolving around the Earth. It therefore requires the accumulation of many more orbits, over subsequent days, to build up a complete global picture, leading to revisit intervals of many days and thus to a lower temporal resolution. The revisit time of Landsat (30 m spatial resolution) is about 16 days for Landsat Thematic Mapper (TM) and Landsat Enhanced Thematic Mapper (ETM+), whereas OC sensors are designed and launched in such a way that they have a better temporal resolution i.e. the repeat time is optimised with a wider swath so that they cover a given location on the Earth over 1–3 days in order to capture the dynamics of phytoplankton production, coastal currents and river plumes, but this in turn increases the pixel size, leading to a lower spatial resolution. For OC missions the

standard pixel size is about 1000 m for open ocean applications (e.g. SeaWiFS and most MODIS channels), whereas in coastal water applications 250–300 m has been the highest spatial resolution. MODIS generally has 1 km resolution for its ocean colour bands and several terrestrial channels, plus a 250 m panchromatic channel, and it is also possible to retrieve 250 m resolution for the OC bands with a statistical method called ‘pan sharpening’. MERIS data has 300 m resolution, the so-called full resolution (FR), in all 15 programmable bands, but over the open ocean the full resolution was reduced in order to provide 1.2 km Reduced Resolution (RR) data. The Korean Geostationary Ocean Color Imager (GOCI), the first of its kind, has a spatial resolution of about 500 m over the Korean Sea.

Figure 19.1 shows RGB composites of a MERIS RR image (Fig. 19.1a) and a MERIS FR image (Fig. 19.1b) compared to a Landsat 5 TM image (Fig. 19.1c). One can clearly see that the 30 m resolution of Landsat is much more appropriate to resolve coastal morphology and to visualize coastal dynamics; the coastline is much clearer and the sediment plumes are much more detailed. However, the spectral

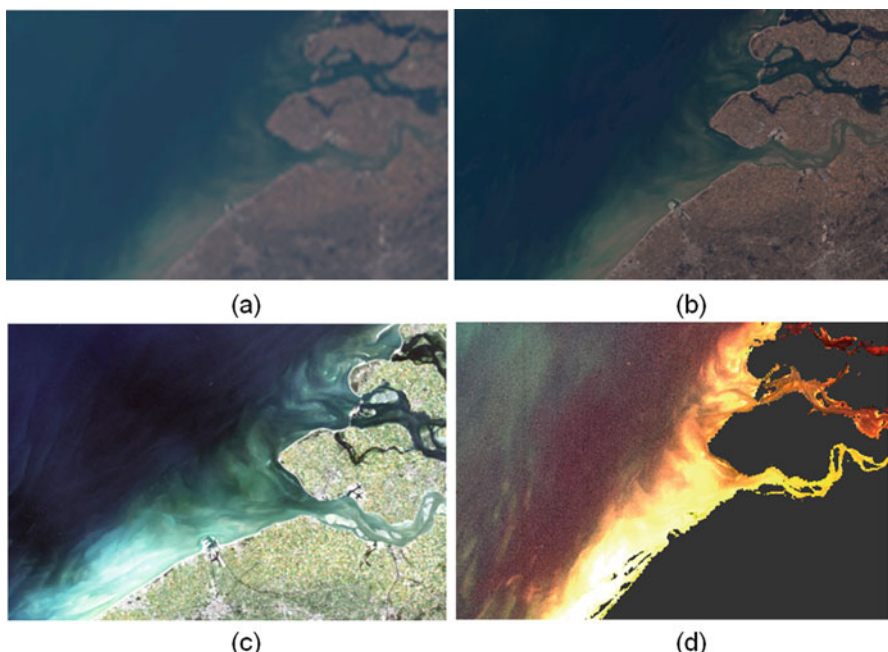


Fig. 19.1 Comparison of top-of-atmosphere (a) MERIS Reduced Resolution Image, (b) MERIS Full Resolution Image and (c) Landsat 5 TM image all acquired at the start of July 2006 over the Zeeland area of the Netherlands coast; images are in their provided projections, which is the satellite projection for the MERIS data and UTM for the Landsat data, with the geographical area shown being around 250 km in width. (d) is the MERIS Data corrected to bottom-of-atmosphere remote sensing reflectance using the NASA SeaDAS processor. Courtesy of ESA and the U.S. Geological Survey

bands for the Landsat missions were chosen with land rather than OC applications in mind, so above the sea it is primarily used to derive information on Suspended Particulate Matter (SPM) as it does not have the required spectral resolution of OC sensors (meaning that the bands in the visible are too broad and too few in numbers); however, Chl-*a* has been mapped with Landsat when present in high concentrations (e.g. Nazeer and Nichol 2015). Figure 19.1d shows atmospherically corrected MERIS FR data, which is the first step in deriving quantitative information as described later in this section.

In addition to Landsat, sensors such as the Compact High Resolution Imaging Spectrometer (CHRIS/PROBA) have also been used for coastal OC remote sensing (spatial resolution of approximately 18 m) although they were primarily designed for terrestrial applications. In summary, it may be stated that in terrestrial remote sensing it is possible to concentrate effort and technical development on achieving a better spatial resolution, whereas in OC remote sensing a good temporal resolution is mandatory.

Spectral Resolution Besides the difference in requirements for spatial and temporal resolution, there is also a difference in the requirements for spectral resolution and signal-to-noise ratio (SNR) within these bands. In terrestrial remote sensing the bands of multi-spectral sensors tend to be rather broad (30–70 nm), whereas the bands in OC remote sensing should not be broader than 10 nm and tend to be much greater in numbers to capture subtle spectral features (IOCCG 2000). The number of bands is important for the number of water quality parameters that can be retrieved from the reflectance signature e.g. when developing band ratio algorithms to derive various geophysical products. It must be stated, however, that there is a trend towards hyperspectral remote sensing (e.g. Hyperion and the underlying instrument for MERIS and CHRIS/PROBA), although capturing and downloading hyperspectral data is an operational constraint in terms of the mission cost-efficiency.

Difference in Data Analysis and Processing As well as differences in sensor and mission design, there is also a major difference in how the data is processed (Satyendranath 2000). In terrestrial remote sensing, clustering and classification are some of the methods used to derive information about different vegetation and land use types as well as soil cover. In OC remote sensing the main methods used to derive information about water quality are regression type empirical and semi-empirical algorithms plus inversion techniques such as neural networks (NN) that are more popular in coastal waters because of their optical complexity. These techniques are used to derive the main bio-geophysical products: Chl-*a*, SPM and CDOM that is sometimes also referred to as yellow substance (YS). This is possible because of the specific scattering and absorption properties of each optical constituent, with the reflectance of the sea (the colour of the sea) determined by a ratio between spectral absorption and backscatter.

In OC remote sensing, classification is mostly used to develop flags for those pixels that clearly differ from the spectral signature of a water pixel, so that

these pixels can be masked out (or flagged), and subsequently are not used in the processing of water pixels. Examples include the high reflectances from ice and clouds as well as land. It must be stated, however, that information about coastal soil and vegetation type is still interesting for coastal zone management and for coastal water optics, e.g. large expanses of bare soil lead to higher erosion, which may cause an increase in the run-off and therefore SPM. Wetlands, marshland and bog areas tend to be high in humic substance, and so the run-off may cause an increase in CDOM. Forests may act as a buffer area and reduce coastal run-off, and also have a lower impact on the land adjacency effect. ‘Adjacency effects’ can be described as blurring that occurs in pixels in close proximity to the coast. Land is usually more reflective than water, and an imager that measures above water close to the coastline may also receive scattered light that originated from the nearby land pixels.

Dynamic Range Another important requirement for OC sensors in coastal waters is that they must have a wide dynamic range to sense both the low reflectance from relatively dark water bodies as well as the high reflectance from waters that are laden with high concentrations of inorganic SPM. This means that they must achieve a high SNR even where the reflectance from water bodies is low i.e. 5–10 %, while not saturating at very high reflectances. Most of the top-of-the-atmosphere (TOA) signal over water surfaces originates from atmospheric processes such as gas and aerosol scattering. Atmospheric correction is therefore a critical step in the processing of OC data.

Optical in-Water Constituents As previously mentioned, the reason why we can sense optical water constituents is because of their specific absorption and scattering properties. Pure water absorbs at long wavelengths, in the red part of the electromagnetic spectrum, and the backscatter of water increases towards the blue wavelengths. Therefore, water with little or no other constituents appears blue. As the Chl-*a* concentration increases the water becomes greener and SPM often causes red/brown water. These constituents play a substantial role in the biogeochemistry of natural waters and are important for their optical properties. They all have specific spectral absorption properties, which have an effect on the reflectance signature, i.e. on the colour of the sea. The derived OC data products are called Level 2 (L2) products whereas the directly measured TOA signal is a Level 1 (L1) product. The key product for oceanographic studies and coastal management is Chl-*a* as it can give a good indication of changes in phytoplankton biomass and eutrophication (Sects. 19.2.4 and 19.3). Besides Chl-*a* one can also derive the Maximum Chlorophyll Index (MCI) (Sect. 19.2.1) the SPM concentration, which is a measure of the turbidity of the water, as well as the absorption coefficient of CDOM, g_{440} (Kirk 2011). Further important remote sensing products for management are Sea Surface Temperature (SST); (Sect. 19.2.1), the spectral diffuse attenuation coefficient, K_d490 (Sects. 19.2.2 and 19.2.4), Secchi depth (Sect. 19.2.4), and the distribution of harmful algal blooms (Sects. 19.2.3, 19.3, 19.4), all of which give important information about water quality.

Limitations Besides the limitation in spatial resolution there are several other restrictions for OC remote sensing. One is the above-mentioned blurring of pixels due to the adjacency effect. Adjacency has been quite a problem for coastal and inland water remote sensing, but in recent years significant progress has been made in correcting such effects. For example, the Improved Contrast between Ocean and Land (ICOL) processor (Santer and Schmechtig 2010) has been shown to correct for adjacency effects both in lake waters (Guanter et al. 2010) and the Baltic Sea (Kratzer and Vinterhav 2010). Another way to correct for adjacency is the SIMilarity Environment Correction (SIMEC), an algorithm first proposed by Sterckx et al. (2011, 2015) for the correction of high resolution airborne remote sensing data in the North Sea. SIMEC estimates the contribution of the background radiance in correspondence with the Near-InfraRed (NIR) similarity spectrum (Ruddick et al. 2006) and has also been shown to correct well for adjacency effects in coastal and in-land waters. Another limitation worth mentioning is the effect of cloud cover as visible and NIR light is not able to penetrate through clouds. Although operational OC imagers usually have a temporal resolution of about 1–3 days, about 50 % of the scenes in the Baltic Sea region will be covered by cloud during May–July (Isemer and Rozwadowska 1999), and in the Northern Atlantic it may even be up to 70 % during summer. Additionally, the registration of images at high latitudes is limited to March–October for the Baltic Sea, and only from April–September in the Arctic Ocean; in winter months the solar radiation at low sun angles is too low for passive remote sensing, and understandably the ice cover is also an obstacle to OC remote sensing. Despite the high cloud cover over the Baltic Sea, Harvey et al. (2015) could show that MERIS data still has a better temporal resolution than the data measured *in situ* by the coastal monitoring program in the Himmerfjärden area; one of the most monitored areas in the world. Combined with the good spatial resolution this makes MERIS data a very powerful and cost-effective tool for monitoring of algal blooms.

Sea Surface Temperature Very often analysis of spatial and temporal variations of OC variables/products is facilitated by availability of other oceanographic data. Algorithms for determination of such a key parameter as SST are worth mentioning. Satellite-derived SST products are based on measurements of the infrared radiance emitted from the sea surface which in turn depends on the water surface temperature and emissivity. To avoid the interference of the atmosphere, the NOAA and NASA SST retrieval algorithms (the so-called split-window algorithms) sense the brightness temperature at the two wavelengths with different sensitivity to water vapour: 11 μm (T11) and 12 μm (T12). This allows to retrieve SST accurately in different atmospheric conditions. The most general expression for such algorithm may be formulated as: $\text{SST} = f(T_{11}, T_{11}-T_{12})$; (Robinson 2004). In the following sections we show examples of how time series data derived from satellite can improve our understanding of phytoplankton bloom development and ecology in coastal waters. The areas of investigation are the Himmerfjärden bay in the Baltic Sea, the Bay of Biscay and the Beaufort Sea, all shown in Fig. 19.2.

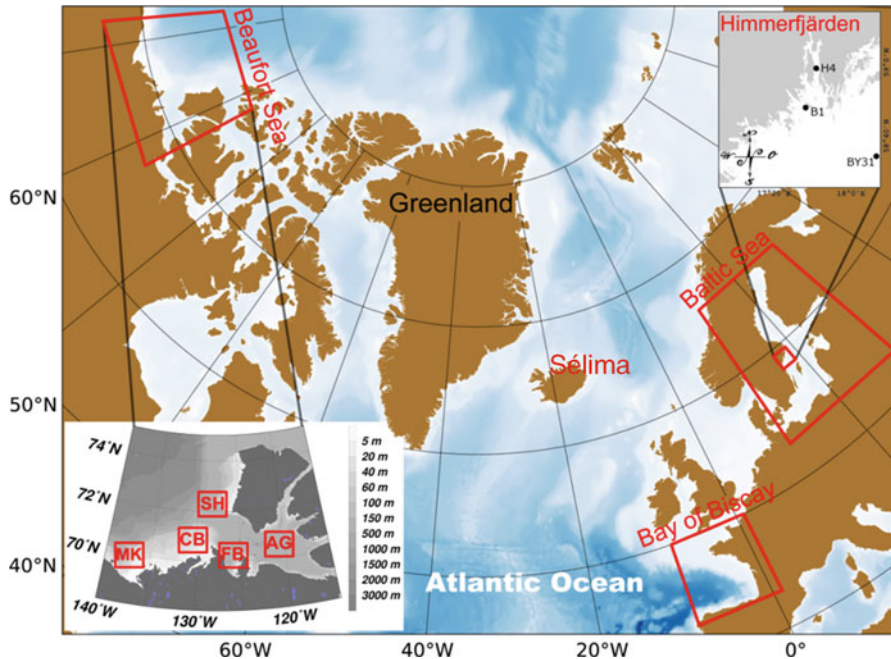


Fig. 19.2 Areas of investigation

19.2 Remote Sensing of the Baltic Sea

The Baltic Sea, a semi-enclosed brackish sea, is situated in the north-eastern part of Europe, and is surrounded by Scandinavia in the north, the Baltic countries in the east and by the Polish and German coast in the south (Fig. 19.2). The Baltic Sea has a salinity gradient ranging from 0 to 3 in the north to about 18–26 in the southwest, with a mean salinity of around 7. The low salinity is caused by: the topography with sills separating shallow basins and the narrow Danish Straits, which leads to a restricted water exchange with the North Sea and a low water turnover rate; and a high freshwater input from large rivers (Leppäranta and Myrberg 2009). The drainage basin is about four times larger than the Baltic Sea itself, and the catchment area covers 14 countries, nine of which border the sea. About 85 million people live in the drainage basin and 40 million of these inhabit the coastal areas and big cities along the coast, which leads to high anthropogenic stress for the marine ecosystem and environmental problems, like eutrophication (HELCOM 2007; Leppäranta and Myrberg 2009). The main optical constituent in the Baltic Sea is CDOM (Ferrari and Dowell 1998). The high CDOM content (like the salinity) is linked to the restricted water exchange, the freshwater input and land use with large forested and peat land areas.

19.2.1 Mapping Cyanobacteria Blooms in the Baltic Sea Using the Maximum Chlorophyll Index (MCI)

The main bloom-forming filamentous cyanobacteria are the toxic *Nodularia spumigena* and non-toxic *Aphanizomenon* sp in the open areas of Baltic Sea, and potentially toxic *Anabaena* spp in coastal areas. The development of blooms is favoured by Phosphorus (P)-rich water and, especially for *N. Spumigena*, by calm and warm weather. Filamentous cyanobacteria blooms can occur from July to September, and have a patchy spatial and temporal distribution.

Data and Methods Mapping extreme conditions, such as intense cyanobacteria surface blooms, by OC remote sensing data requires alternative approaches to the standard neural network approaches that have been used for atmospheric correction and bio-optical models. Especially towards the end of a surface accumulation, the cyanobacteria tend to break the water surface and therefore change the surface optical properties to appear more like those of vegetation on land, which can be identified using a red-edge ratio. During such events ($\text{Chl-}a > 30 \mu\text{g L}^{-1}$), the combination of Chl-*a* absorption and scatter can be clearly detected in the radiance spectrum (Gower et al. 2008) and algorithms can be applied to extract the parameters directly from L1 TOA data. The MCI has been developed by Gower et al. (2008), which considers a peak at 709 nm in the radiance spectrum that has been associated with high levels of Chl-*a* (above $30 \mu\text{g L}^{-1}$). It has been shown that parameters like Chl-*a*, phytoplankton biomass and cyanobacteria biomass could be extracted via MCI during cyanobacteria blooms (Binding et al. 2011, Alikas et al. 2010). As the MCI spectral index is applicable both to L1 and L2 data, atmospheric correction is not required.

Spatial Distributions of Phytoplankton Blooms in the Baltic Sea The MCI equation was applied to MERIS RR L1 images to estimate the intensity and frequency of surface accumulations in the Baltic Sea during the period 2002–2009 (Fig. 19.3). The monthly composites for July and August were calculated based on the maximum value of MCI for each pixel. MCI composites reveal high variability in surface accumulations between years. The most intense blooms usually develop in the central part of the Baltic Sea in July, and were most pronounced in 2003 and 2005 when high SST in July initiated intense, large surface accumulations in the central Baltic Sea. However, the locations and intensity of blooms can vary from year to year. For example, in 2006, July was the warmest month (similar to 2005) in the southern and western Baltic Sea (max values 23–25 °C, Fig. 19.4) where the most intense blooms developed. However in August, the most intense bloom was located in the Gulf of Bothnia where monthly mean SST reached the maximum values of that year. Note that cyanobacteria blooms are rather rare in the Gulf of Bothnia as these waters are P limited. The mean temperature in the central Baltic Sea for July 2006 was lower than the average for that month from 2002–2009 (Fig. 19.4). The patterns of SST (Siegel and Gerth 2013 and references therein) in 2006 correlate well with the bloom locations depicted by MCI; the

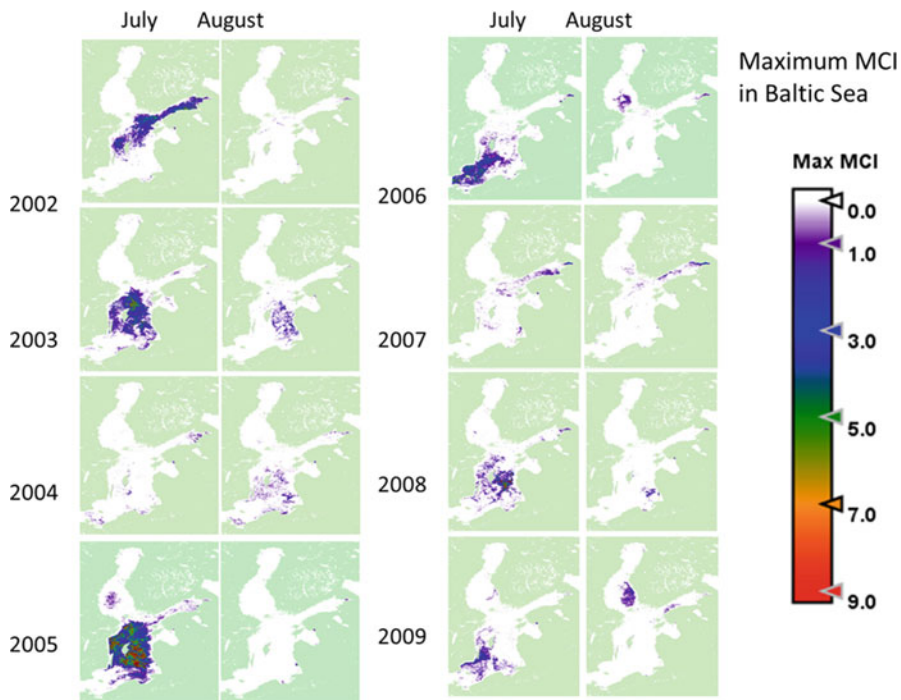


Fig. 19.3 Maximum Chlorophyll Index applied on the MERIS RR L1 data over the Baltic Sea

surface blooms were dominating in the central and southern part in July and in the northern part in August. SST was below the long-term mean in 2004 and 2007 and therefore the conditions were not suitable for intense bloom development. The surface accumulations of cyanobacteria blooms in the Baltic Sea, as derived by MCI, were compared with a method developed by Kahru et al. (2007) that was applied to MODIS L2 data by SMHI (Öberg 2013). Both methods give similar bloom patterns for the surface accumulations, demonstrating the capability of OC remote sensing methods to monitor the development and the spatial distribution of the blooms.

19.2.2 Mapping Changes in Water Transparency in the Central Baltic Sea

Remote sensing estimates of transparency plays an important role in describing the spatial and temporal variation of under-water light conditions that have a direct effect on water quality and on primary production. In optical oceanography the attenuation of light in the water column is commonly described by the diffuse

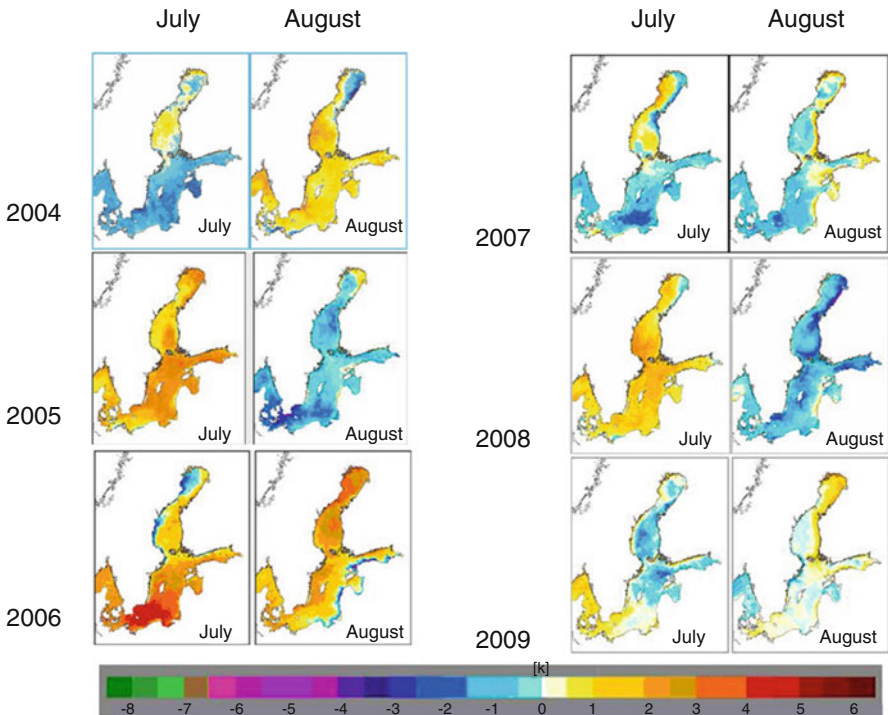


Fig. 19.4 Anomalies of the monthly mean SST temperature of the Baltic Sea (long term means 1990–2004). Adopted from Siegel and Gerth (2013) and references therein

attenuation coefficient of downwelling irradiance, $K_d(\lambda)$. Austin and Petzold (1981) first developed an empirical band ratio algorithm, which used the blue-to-green ratio of water-leaving radiances to derive $K_d(490)$ over optical Case-1 waters. Over optically-complex waters, a shift towards longer wavelengths is required since the ratio $R_{rs}(490)/R_{rs}(555)$ reaches an asymptotic value with increasing absorption and loses its sensitivity at high $K_d(490)$ values, resulting in an underestimation of $K_d(490)$ over turbid inland and coastal waters (Wang et al. 2009). It has been demonstrated (Alikas et al. 2015), that the combined algorithm based on $R_{rs}(490)/R_{rs}(709)$ and $R_{rs}(560)/R_{rs}(709)$ is very robust for retrieving $K_d(490)$ values over a wide range of all three main optical in-water constituents: Chl-*a*, Total Suspended Matter (TSM) and CDOM. The $K_d(490)$ algorithm was applied to the monthly means from May until September, and to MERIS FR data for 2005 (Fig. 19.5). The spatial distribution of $K_d(490)$ in the Baltic Sea was well described - indicating lowest transparency in the open Baltic Sea in July during the occurrence of cyanobacteria blooms, and also a decreased transparency in coastal areas, presumably due to an increase in both CDOM and TSM (Kratzer and Tett 2009). Therefore, this study demonstrates that $K_d(490)$ is a reliable measure of water transparency from space,

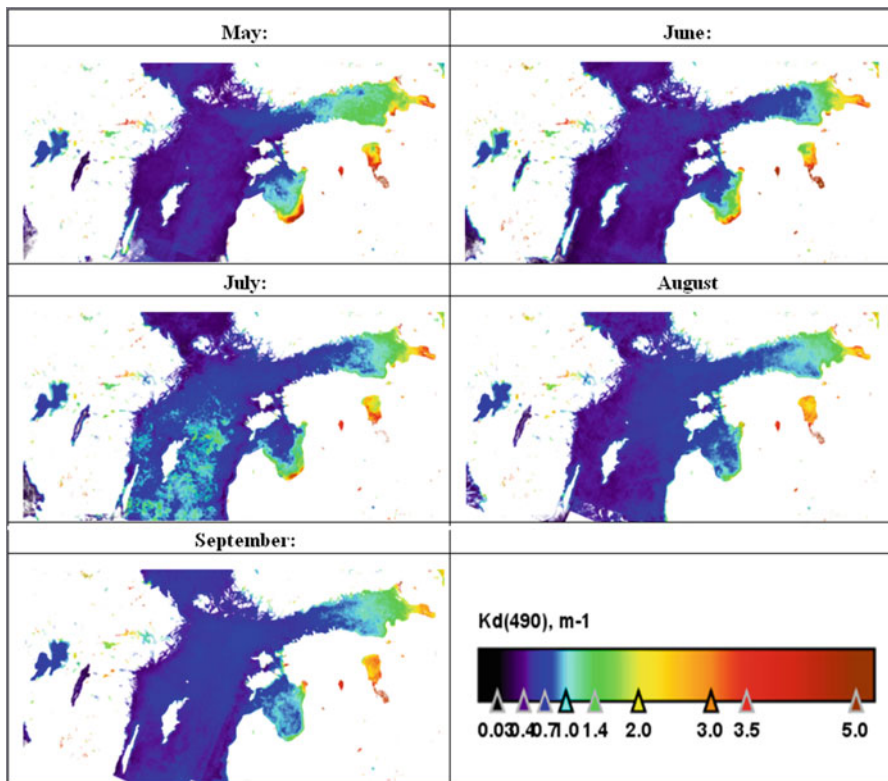


Fig. 19.5 MERIS-derived monthly means (from May to September) of $K_d(490)$ in Nordic lakes and the Baltic Sea in 2005

and using the combined algorithm it is possible to derive more reliable and basin-wide products from satellite data over coastal and open sea waters as well as inland waters.

19.2.3 *Remote Sensing of Algal Blooms in Himmerfjärden Bay, North-Western Baltic Proper, Sweden*

In this section we report results from a remote sensing study of Himmerfjärden bay which is situated about 60 km south of Stockholm at 58.42–59.20 N 16.22–8.70 E in the north-western part of the Baltic proper (Fig. 19.2). The bay and surrounding area have been investigated intensely since the 1970s; the ship-based monitoring program in this area is unique with an unusually high sampling frequency. A MERIS time series was used to visualize the natural spatial and temporal dynamics of

algal blooms, river outflows and seasonal variations in the region (Harvey et al. 2015). The Chl-*a* retrieval was based on a neural network (NN) approach adapted to coastal waters and developed by the Free University Berlin, FUB (Schroeder et al. 2007a, b). Before deriving the Chl-*a* concentrations, the data was corrected for adjacency using ICOL (Santer and Schmechtig 2010) and applied to the MERIS TOA radiances (Kratzer and Vinterhav 2010). The MERIS images were mostly cloud-free and had been geometrically corrected, and screened for low sun angle, failed atmospheric corrections as well as high sun glint (Harvey et al. 2015). The in situ Chl-*a* data were all sampled and analysed spectrophotometrically by the monitoring group at the Department of Ecology, Environment and Plant Sciences, Stockholm University. For the comparison between satellite retrieved and in situ measured Chl-*a* concentrations, an average of a 3×3 pixel-matrix around each in situ monitoring station in the MERIS scene was used for every station and date.

Figure 19.6 shows a time series of MERIS-derived Chl-*a* images from April to September 2010. The spatial patterns and terrestrial influence close to land can easily be followed on all images due to the observed changes in Chl-*a* concentration as a response to nutrient input, e.g. in the Nyköping coastal bay area marked as “Ny” on the image from 19 April 2010. Furthermore, the synoptic view makes it possible to follow the spring bloom that occurs during April and May, as well as the development and retreat of several summer blooms during July, August and September. The spatial patterns and the extent of the blooms are clearly visible. Figure 19.7 displays a synoptic view of the development of a cyanobacteria bloom with surface accumulations during July 2008. Remote sensing makes it possible to capture and study the change over time, the spatial coverage and the variable distribution of the Chl-*a* concentrations within the bloom (Kahru et al. 2007; Ruddick et al. 2008; Harvey et al. 2015). In Harvey et al. (2015) it was also demonstrated that OC time series data have a good agreement with in situ measurements and that both the temporal and spatial resolutions increase when adding satellite measurements; more data leads to an improved assessment of algal blooms i.e. both the timing of the blooms as well as extent (e.g. Kahru et al. 2007). Ship sampling is time consuming and expensive, thus restricting the possible number of stations and samples collected. In one example, the satellite data revealed blooms that the conventional monitoring obviously missed out (Harvey et al. 2015). Figure 19.8 shows a time series of MERIS and in situ Chl-*a* concentrations for the productive season (April–Sep) in 2010 from two monitoring stations in the Himmerfjärden bay. The spring bloom in April, typically for the area, is well described by both methods. Both the concentrations and the variability are higher at station H4. Harvey et al. (2015) also showed no difference between monthly means of Chl-*a* concentrations between the methods. The two sets of MERIS image time series data illustrate the increased information gained from remote sensing, thus demonstrating the effectiveness of using of OC data together with conventional methods when monitoring coastal zones; it is possible to follow the spatial and temporal changes in a more comprehensive way.

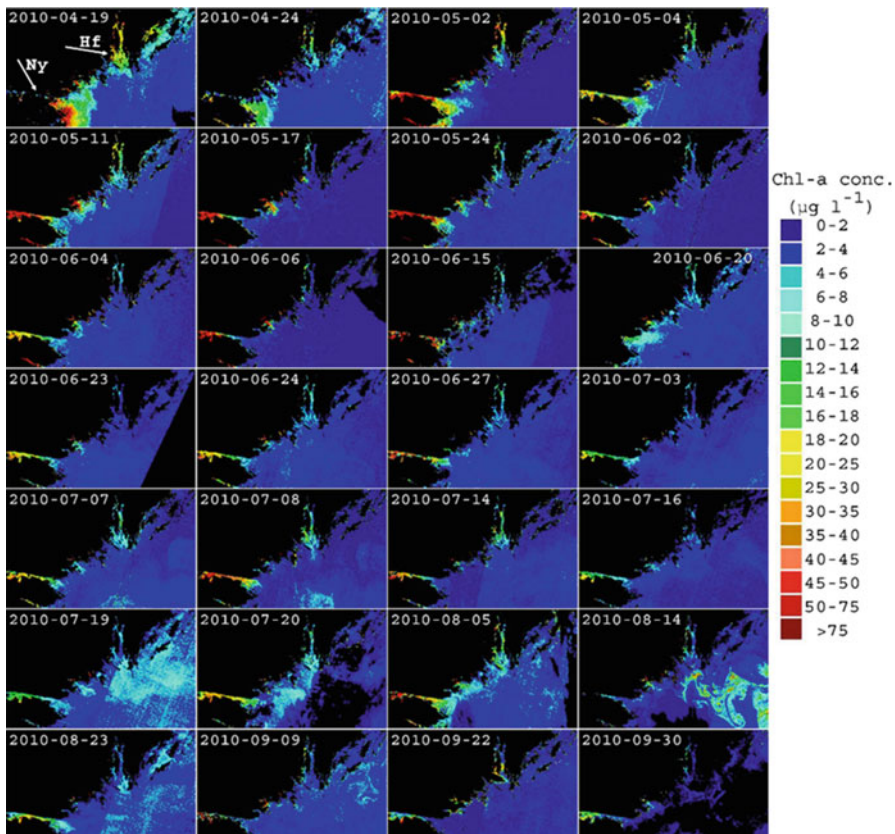


Fig. 19.6 MERIS images of chlorophyll-a concentrations for the productive season between April and September 2010 acquired from the archipelago south of Stockholm, Sweden. The Himmerfjärden bay (*Hf*) and Nyköping coastal area (*Ny*) are marked with arrows on the first image (2010-04-19). The river inflow and its effects on the chlorophyll-a during the both the spring bloom and summer blooms are clearly shown. MERIS data with courtesy from the European Space Agency (ESA) and Petra Philipson

The benefits of the improved amounts of data and spatial coverage as well as its cost effectiveness is important both for monitoring and management (e.g. Kahru et al. 2007; Kratzer et al. 2014). Satellite data can substantially increase the amount of data available for water quality classifications within the water quality directives and legislations, e.g. European Union's (EU) Water Framework Directive 2000/60/EC (WFD) and Marine Strategy Framework Directive 2008/56/EC (MSFD) from the European Commission (EC), the OSPAR Convention and the HELCOM's (HELSINKI COMmission) Baltic Sea Action Plan (CEC 2000, 2008; OSPAR Commission 1992; HELCOM 2007).

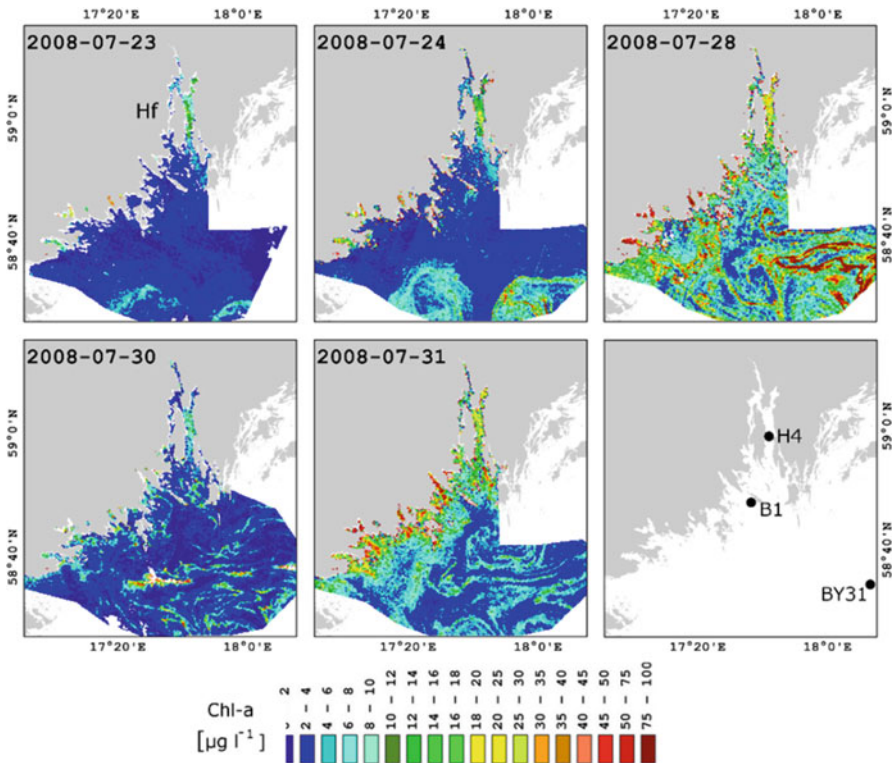


Fig. 19.7 Time series over Himmerfjärden bay (*Hf*) (Sweden) and adjacent areas derived from MERIS data (300 m resolution) during the summer of 2008. The images show the concentrations of chlorophyll-a ($\mu\text{g l}^{-1}$) on the 23rd, 24th, 28th, 30th and 31st of July 2008. This time series illustrates the dynamics and development of a cyanobacteria bloom, and how important it is to get a spatial coverage to capture the development and the spatial extent of the blooms. Map © Lantmäteriet, Gävle 2010, permission I 2010/0053. MERIS data with courtesy from the European Space Agency (ESA), Harvey et al. (2015)

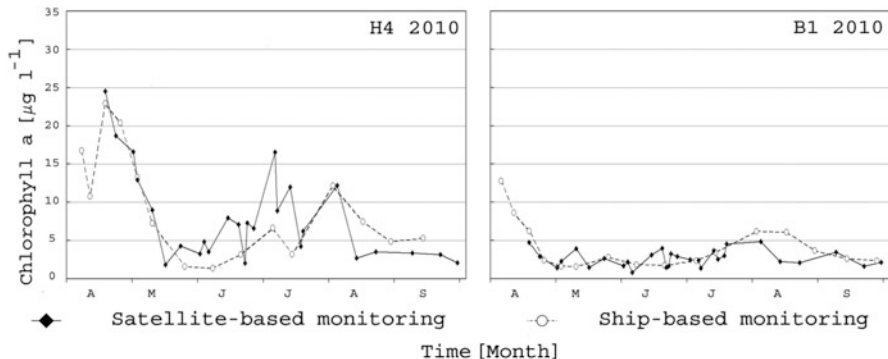


Fig. 19.8 Time series of chlorophyll-a ($\mu\text{g l}^{-1}$) from April to September 2010 for 2 monitoring stations, H4 (head of HF bay) and B1 (situated just outside the bay). The solid line is MERIS derived data and the dashed line represents *in situ* data. Adapted from Harvey et al. (2015)

19.2.4 Mapping the Spatial-Temporal Distribution of Secchi Depth and the Diffuse Attenuation Coefficient $K_d(PAR)$ in Himmerfjärden Bay

19.2.4.1 Background

The euphotic depth, Z_{eu} , is the upper, illuminated part of the water column. It is the layer in which photosynthesis can take place, and where photosynthesis exceeds heterotrophic consumption (Tett 1990). Physically, it is defined as the depth at which the irradiance has reached 1 % of its surface value. Assuming the diffuse attenuation of light, $K_d(z)$, to be approximately constant with depth, the euphotic zone can thus be derived by the following equation:

$$Z_{eu} = 4.6 * K_d(PAR)^{-1} \quad (19.1)$$

(Kirk 2011), where *PAR* stands for photosynthetically active radiation, which is the visible part of the spectrum that can be used for photosynthesis. An easy method to measure how light penetrates with depth in the water column is by using a Secchi disk. Usually, a white disk of 30 cm diameter is lowered into the water column. The depth at which the Secchi disk disappears from the viewer's vision, is known as Secchi depth. Although it is a rather common measurement of water clarity (transparency), Secchi depth is qualitative in nature rather than quantitative (Preisendorfer 1986). Secchi depth is inversely correlated to the diffuse attenuation coefficient of light, $K_d(PAR)$ depth (Kirk 2011). $K_d(PAR)$ can also be related to the spectral diffused attenuation coefficient, $K_d(490)$, e.g. via a regression analysis. Kratzer et al. (2003) found that the relationship between the two parameters in the NW Baltic Sea can be described as:

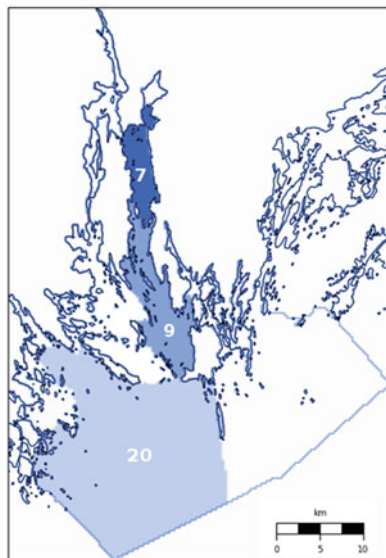
$$K_d(PAR) = K_d(490) * 1.48^{-1} \quad (19.2)$$

This relationship was based on a rather restricted number of data points ($n = 17$). Pierson et al 2008 showed that the relationship can also be described as a logarithmic function:

$$K_d(PAR) = 0.668 * K_d(490)^{0.676} \quad (19.3)$$

The regression model in Eq. 19.3 was based on a semi-empirical Baltic Sea model that simulated 500 matching data points for both variables. Kratzer et al. (2008), showed how to derive Secchi depth and the spectral diffuse attenuation coefficient, $K_d(490)$, from MERIS data using empirical regression models based on Secchi depth and $K_d(490)$ data, respectively, and the matching reflectance ratio of MERIS band 3 (490 nm) and band 6 (620 nm) derived from in-water radiometric measurements. For the present study we derived local algorithms for Secchi depth and for $K_d(PAR)$ from a much larger optical data base measured in

Fig. 19.9 Water bodies in Himmerfjärden bay according to the Swedish Hydrological and Meteorology Institute (SMHI). Selected water bodies showed an optical gradient from the inner bay (water body 7), outer bay (water body 9) to the open sea adjacent to the bay (water body 20)



the Himmerfjärden area during 2000–2012 ($n = 97$). These local algorithms were then applied to the whole MERIS archive (2002–2012), covering Himmerfjärden and adjacent areas (Fig. 19.9) in order to map the temporal and spatial variability in water quality.

19.2.4.2 Algorithm Development from Optical, in-Water Measurements

During the optical campaigns, Secchi depth, $K_d(490)$ and the main three optical components, Chl-*a*, SPM and CDOM were measured. The reflectance at different channels was derived from radiometric measurements (TACCS, Satlantic; Kratzer et al 2008; Zibordi et al 2012). Next, the optical data base from 2000 to 2012 was used to derive new local Secchi depth and $K_d(490)$ algorithms by regressing each parameter against various reflectance ratios measured by the TACCS. As in the previous study (Kratzer et al. 2008) it was found, that the MERIS reflectance band 3 (490 nm) and band 6 (620 nm) provided the best results for retrieving Secchi depth from in water reflectance data. The algorithms that explained most of the variance were:

$$\text{Secchi depth} = \exp \left(1.36 \times \ln \left(\frac{\rho_{490}}{\rho_{620}} \right) + 1.03 \right) \quad n = 97, r^2 = 0.75 \quad (19.4)$$

$$K_d(490) = \exp \left(-1.17 \times \ln \left(\frac{\rho_{490}}{\rho_{620}} \right) - 0.29 \right) \quad n = 97, r^2 = 0.80 \quad (19.5)$$

Where ρ_{490} and ρ_{620} are the MERIS band 3 and band 6, respectively. Equations 19.4 and 19.5 were then applied to MERIS data to derive Secchi depth and $K_d(490)$, respectively. $K_d(PAR)$ was then derived in a second step from MERIS $K_d(490)$ data using Eq. 19.3.

19.2.4.3 Satellite Data Processing

The MERIS dataset was provided by the CoastColour project (<http://www.coastcolour.org>). This dataset is an enhanced Level 1B (L1B) dataset, so-called Level 1P products (CCL1P, version 1.6.3). The main differences of CCL1P compared to the standard MERIS L1B products (v.3) includes: an accurate geolocation information for each pixel, radiometric correction providing similar quality as the standard L1B products from the 3rd reprocessing, plus smile correction and equalization of coherent noise. The CCL1P datasets also includes an additional pixel classification step, generating a precise coastline and additional quality flags (Ruescas et al. 2014). The CCL1P datasets were pre-processed for corrections of land adjacency effects using the Improved Contrast between Ocean and Land (ICOL, Santer and Schmechtig 2010). The L2 products were derived by using the WeW Water Processor developed by the Free University of Berlin (FUB, Schroeder et al. 2007a, b). Quality datasets were produced by masking out pixels based on CoastColour flags (i.e. flags indicating land and coastline, cloud and potential cloud pixels, snow and ice, and risk of sun glint) and FUB processor specific quality flags (i.e. general mask and flags indicating in the input and output products were within the training range); see Beltrán-Abaunza et al. (2016) for full details on processing and quality control. Weekly composites of averaged values of the L2 products, were spatially aggregated by using water bodies polygons defined by the Swedish Meteorological and Hydrological Institute (SMHI) (Fig. 19.9). A requirement for spatial aggregation was that a minimum of 25 quality pixels should be included per water body to describe their weekly statistics. Here, Hovmöller diagrams of MERIS-derived Secchi depth and the diffuse attenuation coefficient showed how the temporal and spatial distributions of water transparency can be aggregated to analyse an optical gradient from the inner bay (water body 7), the outer bay (water body 9), and towards the open sea (water body 20).

The spatial and temporal resolution of the MERIS archive can be used to complement *in situ* data, and so improve our understanding of light availability in the water column. The satellite data has an improved temporal and spatial resolution when compared to *in situ* monitoring data (Harvey et al. 2015; Beltrán-Abaunza et al. 2016). The coastal monitoring in Himmerfjärden is usually undertaken 2-weekly, and in weekly cycles during phytoplankton blooms. The results shown in Figs. 19.10 and 19.11 represent the full MERIS datasets available for Himmerfjärden. It is notable from these figures that it is possible to produce quality datasets as early

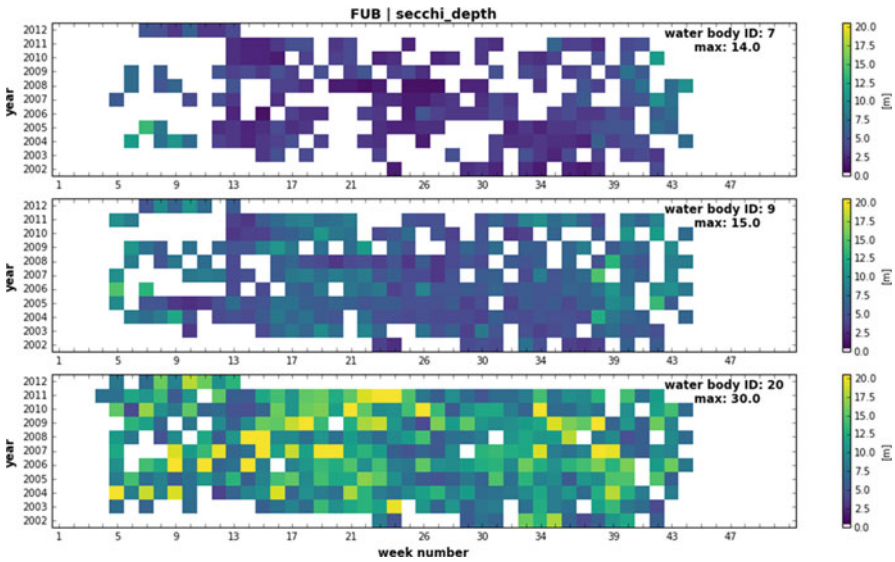


Fig. 19.10 Hovmöller diagram of MERIS-derived Secchi depth. The squares in the Hovmöller diagrams contain the weekly mean-aggregated value of all the valid pixels within a given water body. Selected water bodies showed an optical gradient from the inner bay (water body 7), outer bay (water body 9) to the open sea adjacent to the bay (water body 20) see Fig. 19.9

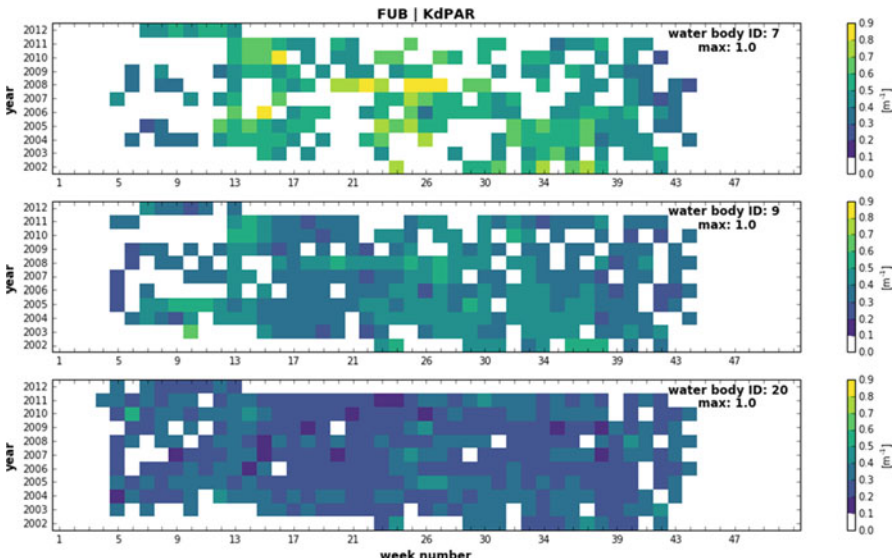


Fig. 19.11 Hovmöller diagrams of MERIS-derived $K_d(PAR)$. The squares in the Hovmöller diagrams contain the weekly mean-aggregated value of all the valid pixels within a given water body. Selected water bodies showed an optical gradient from the inner bay (water body 7), outer bay (water body 9) to the open sea adjacent to the bay (water body 20) see Fig. 19.9

as week 5 (i.e. the beginning of February) in the adjacent open sea. Beltrán-Abaunza et al. (2016) showed that through using Chl-*a* anomalies it is possible to detect early phytoplankton anomalies in Himmerfjärden during February; often related to the presence of *Mesodinium rubrum*, which occurs early in the year. The Hovmöller diagrams exemplify changes in coastal water transparency and show that light availability decreases towards the head of the bay; i.e. lower Secchi depths (Fig. 19.10) and higher diffuse attenuation coefficients (19.11) are found in the inner bay (water body 7). The increased light attenuation appears to trigger an increased frequency of quality flags for the radiometry over MERIS band 3 and 6, used to derive the algorithms, causing lower data quality when compared to the chlorophyll product (Beltrán-Abaunza et al. 2016). Quality flags are processor dependent, and the FUB processor used here has specialized flags for assessing the quality of reflectance products, and uses different flags for radiometry and water products (Schroeder et al. 2007a, b). However, the increased frequency of flagged radiometry products does not necessarily limit the successful retrieval of water quality-products, such as Chl-*a* or SPM. For example, in the study of Beltrán-Abaunza et al. (2016), where a similar methodology was applied using FUB-derived L2 water products, the retrieval of weekly Chl-*a* composites included enough information to complement *in situ* datasets from the Swedish national monitoring programme.

The higher $K_d(PAR)$ values in the inner bay, are directly correlated with the phytoplankton dynamics in the bay. With increased $K_d(PAR)$ values and low Secchi depths indicate also temporal changes during the spring and summer phytoplankton blooms. As more intensive blooms can be detected within the bay (Beltrán-Abaunza et al. 2016), higher Secchi depth values are more frequent in the more transparent, outer bay and towards the open sea. One can also assess inter-annual variability of light attenuation using Hovmöller diagrams (Figs. 19.10 and 19.11). As an example, during summer 2008, an unusual bloom of the phytoplankton species *Prymnesium polylepis* was observed (Hajdu et al. 2015). This bloom caused an anomaly of light attenuation as observed in water bodies 7 and 9 (inside Himmerfjärden bay), where the maximum values in light attenuation shifted by more than 10 weeks from their normal conditions, reaching their peak during June and July in 2008. Furthermore, in 2006, industrial toxins lead to an unexpected malfunctioning of the nitrogen treatment in the local sewage treatment plant at the head of the bay (discharging into water body 7), leading to an increase in phytoplankton abundance (Beltrán-Abaunza et al. 2016).

The spatial and temporal information provided here demonstrates the advantage of using the MERIS time series to assess light availability at a coastal site. It must be noted that this coastal site is optically-complex and highly dominated by CDOM and also influenced by land adjacency effects. It is very unlikely that such high quality data and information could be retrieved by using other available ocean colour sensors, such as MODIS.

19.3 Identification and Monitoring of *Lepidodinium chlorophorum* Harmful Blooms in the Coastal Bay of Biscay

The Bay of Biscay is a gulf of the north-east Atlantic Ocean stretching from the western coast of France from Brest southwards to the Spanish border, and along the northern coast of Spain. The main anthropogenic activities in the region, among others, include tourism, fishing and aquaculture. Thus, the ecological state and its dynamics are of significant importance for the riparian countries. Satellite monitoring as a component of an integrated monitoring system can offer improved spatial and temporal coverage, as exemplified below. The gently sloping shelf zone is an area that is subject to seasonal variations in river run-off, determining the input of suspended minerals and nutrients as well as fresh water. The main rivers flowing into the Bay are the Vilaine, Loire, Charente, and Gironde, and Adour.

Two major phytoplankton blooms occur annually in spring and autumn (Lavender et al. 2008). In spring, diatoms are dominant in the phytoplankton community at the shelf zone. In addition the shelf zone also accommodates blooms of the harmful green dinoflagellate *Lepidodinium chlorophorum* (Elbraechter and Schnepf 1996). Unlike many other species of dinoflagellates, which generate toxic blooms, this alga releases polysaccharides in the form of transparent colloidal biopolymers. This enhances sedimentation, generation of colloidal mass and promotes the accumulation of bacteria and viruses within the bloom, which is located predominantly in coastal waters and bays. Although non-toxic, this alga still has a potentially harmful effect on the ecology as it may cause anoxic conditions, especially in shallow waters. This may cause the death of crustaceans, molluses, and small fish (Claquin et al. 2008). Ecologists as well as fish and shellfish farmers are therefore interested in monitoring the outbursts and spatio-temporal dynamics of this phenomenon, and remote sensing is a cost-effective way to do this.

Data and Methods Satellite OC and SST data for 2002–2009 were obtained from MODIS data. Up to date, *in situ* measurements of *L. chlorophorum* are very scarce, presumably because of the high cost of effective monitoring programs. The only available data were microscopic cell identification and counts by the ‘Institut Français de Recherche pour l’Exploitation de la Mer’, (IFREMER; <http://www.ifremer.fr/>) at two stations accounting for 47 measurements during different months from 2001 to 2008, and from cases of intensive *L. chlorophorum* blooms reported in the press. For detecting the extent of *L. chlorophorum* blooms, two conceptually different techniques were applied, namely a NN and the fuzzy *c*-means classification (Morozov et al. 2010, 2013). The input data needed for the network operation are $R_{rsw}(\lambda)$ in the six MODIS visible bands, i.e. at 412, 443, 488, 531, 551, and 667 nm. Using the available *in situ* data the NN was trained to invert the input spectral sub-surface reflectance values, $R_{rsw}(\lambda)$, in the above six channels into a numerical output characterising whether the analysed pixel belongs to a *L. chlorophorum* bloom or not. Using the available *in situ* data the NN was trained to invert the input spectral

sub-surface reflectance values, $R_{\text{rsw}}(\lambda)$, in the above six channels into a numerical output ranging from 0 to 1. The value 0 indicates the absence of the *L. chlorophorum* bloom; 1 means that the pixel confidently belongs to the bloom. All results in between 0 and 1 can be considered as a transition from non-blooming to blooming areas.

The second algorithm is based on fuzzy c-means classification or clustering, i.e. sorting objects into groups based on the likelihood of features for the objects of one group and the divergence from other groups. An important advantage of such algorithms is that they do not require any training i.e. *in situ* data to be able to classify the pixels in the image. Fuzzy partitioning allows us to easily solve the problem related to objects located at the interface of two clusters by attributing each object its fractional degree of belonging (Zimmermann 2001).

In order to improve algorithm performance, an additional selection criterion was introduced in order to dismiss pixels erroneously attributed to *L. chlorophorum*. The cause of such an erroneous attribution resides in the inherent limitation of the NN interpolation/extrapolation ability (Haykin 1998) or, else, because of noise and errors in the training data set, and the presence of different types and numbers of other phytoplankton species, resulting in a transitional zone between bloom and non-bloom areas. The advantage of the unsupervised classification employing a fuzzy logic is that it does not require any a priori information and relies exclusively on the characteristics of the general inhomogeneity in the spatial distribution of input data (in this case, space-borne water surface reflective characteristics in pixels of the image). Also, the fuzzy c-means classification method easily deals with the transitional zones between *L. chlorophorum* bloom and blooms of other algae. However, areas identified with the fuzzy c-means classification are a result of assigning all pixels in the image towards one of the two classes, and additional, independent information is required. The additional selection criterion that can provide this information resides in the fact that *L. chlorophorum* signals must have a minimum at the 488 nm channel due to the presence of Chl-*b* and peridinin pigments present in this dinoflagellate species (Matsumoto et al. 2011) which result in increased absorption in the spectral range of 450–500 nm in comparison to other phytoplankton species in the Bay (see Fig. 19.12a). Subsequently, spectra with a maximum in this channel are ignored. The actual spectra obtained from remote sensing (see Fig. 19.12b as an example) fully confirmed this assumption.

Application of both algorithms to an independent data set (which was not used for algorithm development) shows their consistency. In order to increase the robustness of bloom identification it is possible to use both algorithms simultaneously, which may help to decrease incidents of false identification (Fig. 19.13).

Along with diatom-dominated phytoplankton blooms, outbursts of the harmful alga *L. chlorophorum* are observed in the coastal zone of the Bay. The occurrence frequency of *L. chlorophorum* blooms proves to be area-specific. As Fig. 19.14 illustrates, there are areas (river estuaries) where the blooms of this alga occur annually; whereas in the Iroise Sea and near the Bailiwick of Guernsey the temporal bloom pattern is remarkably different: in the latter areas, extensive blooms of

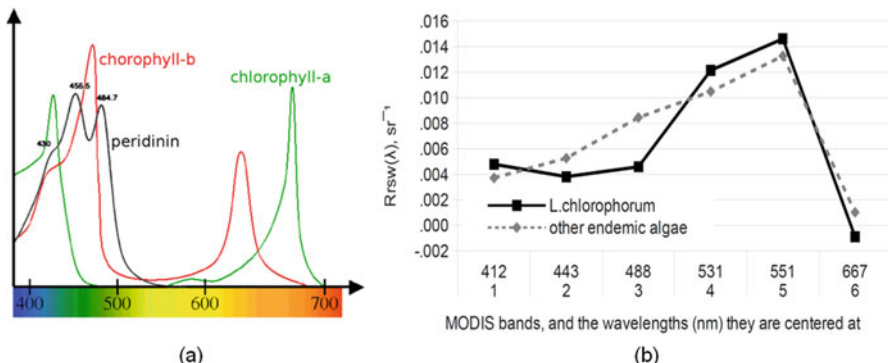


Fig. 19.12 (a) Specific absorption coefficient of Chl-*a* (green line), chlorophyll-*b* (red line), and peridinin (black line); (b) MODIS spectra from pixels of water areas containing *L. chlorophorum* and endemic algae (dominated by diatoms), 24 September 2006, Iroise Sea

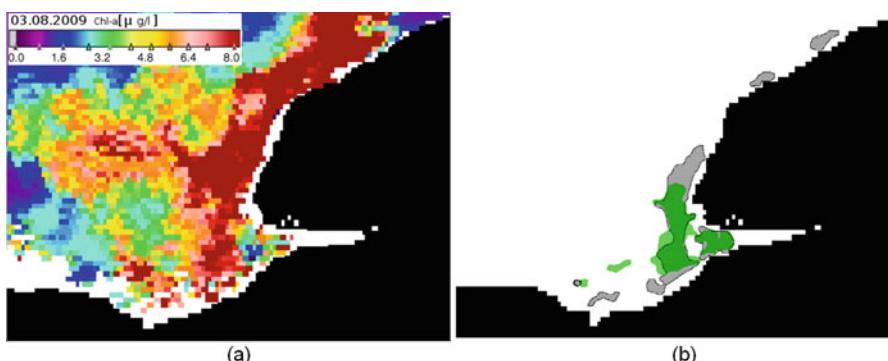


Fig. 19.13 (a) Spatial distribution of chlorophyll-*a* concentration (a) and the *L. chlorophorum* bloom area (b) in the region of the Seine river estuary. The bloom extent identified by the NN algorithm (black dashes) and the fuzzy c-mean algorithm (green). MODIS-Aqua data NASA

L. chlorophorum (covering 5 % or more of the respective area) occurred only in 2003, 2006, 2007, and 2008 (Guernsey) and 2006, 2007, and 2008 (Iroise Sea). The reason for that may be the continuous supply of nutrients by rivers, and therefore, a reduced need for *L. chlorophorum* to compete for nutrients with other species.

Relatively little is known about the ecology of *L. chlorophorum*. However, it is not unreasonable to suppose that in conditions of restricted supply of nutrients (both areas are not recipients of riverine waters), these algal blooms occur when they are preceded by low-level blooms of indigenous diatoms (and hence the nutrient depletion is not significant). In addition, this alga is not only immune to photo-inhibition but also prefers ample illumination by sunlight (Elbraechter and Schnepf 1996). Therefore, *L. chlorophorum* blooms can be spurred on by conditions of scarce cloudiness. As Fig. 19.14 illustrates for the Iroise Sea, it is indeed the

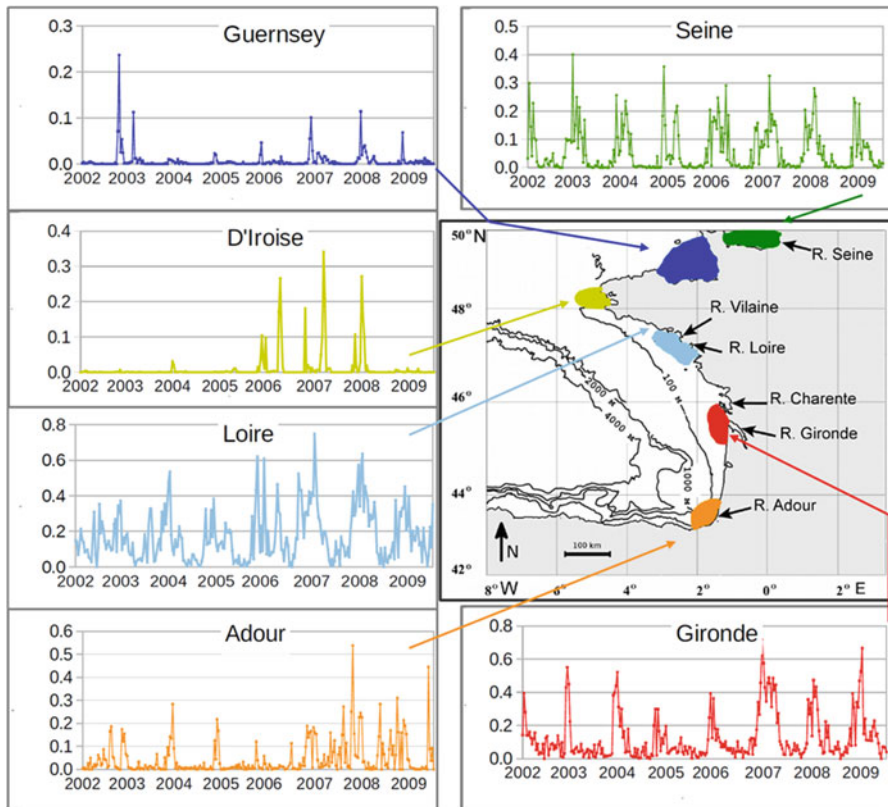


Fig. 19.14 Localization and phenology of *L. chlorophorum* blooms along the coast of the Bay of Biscay and in the areas of the Déroute Strait and the Seine River estuary. On the vertical: relative area covered by the alga bloom in each selected domain

case: the peaks of *L. chlorophorum* emerge during September, August–September, and July of the above-mentioned years when the preceding diatom abundance and degree of cloudiness were low. However, the same Figure indicates that there are exceptions to this regularity. This implies that some other factors may control the growth of this phytoplankton species. SST is likely to be one of the controlling factors, and it can also be derived from space. This assumption seems to be also supported by Fig. 19.15. Thus, it appears that an concurrence of the above three factors - weak preceding diatom blooms, enhanced SST, and availability of sufficient incident light – may control the massive growth of *L. chlorophorum*. However, there might be some other conditions that need to be met, which cannot be detected from space. It must be noted that high concentrations of Chl-a concentrations in April–May, April, and May 2006, 2007, and 2008 respectively should be explained by spring diatom blooms, whereas autumn peaks are mostly due to *L. chlorophorum* blooms.

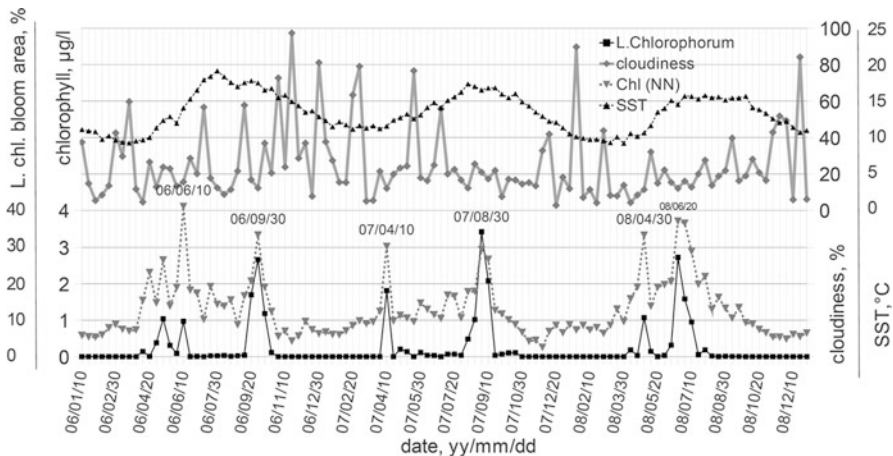


Fig. 19.15 A 10-day averaged time series of *L. chlorophorum* bloom relative area in % (black solid) and contemporaneous variations of possible influencing parameters in the Iroise Sea: diatom Chl-*a* concentration in $\mu\text{g l}^{-1}$ (grey dashed), cloudiness in % (grey solid), and MODIS-derived SST in $^{\circ}\text{C}$ (black dashed)

19.4 Variability of Chlorophyll-*a* and Sea Surface Temperature in the South-Eastern Beaufort Sea (Canadian Arctic) by Remote Sensing (1998–2004)

Introduction Global warming is known to mostly affect the Arctic Ocean where a rapid decrease in thickness and extent of sea-ice, and changes in the marine ecosystem have recently been observed. The transition from thick multi-year ice to a seascape increasingly dominated by thinner, first-year ice (Comiso 2011), has brought discernible modifications to the phenology of the Arctic Ocean region, such as earlier occurrences of the annual phytoplankton blooms (Kahru et al. 2011) and an overall increase in ocean net primary production (NPP) (Arrigo and van Dijken 2011). The Eastern Beaufort Sea (BS) is characterized by the presence of Cape Bathurst and flaw lead polynyas that play a major role in high latitude ecological and biogeochemical processes. These areas are expected to have a higher biological production than offshore waters. In this study we assess the spatial and temporal variability of Chl-*a* in order to evaluate possible impacts of climate-change induced physical processes onto phytoplankton productivity. The aim of this study is to estimate phytoplankton biomass variability using time series of Chl-*a* and SST for a 7 year time series (1998–2004).

Ocean Colour Data SeaWiFS Level 1A (L1A) Merged Local Area Coverage (MLAC, 1.1 km resolution at nadir) data were downloaded from the NASA Ocean Color Web site (www.oceancolor.gsfc.nasa.gov). L1A MLAC data contains raw radiance values for each SeaWiFS band (412, 443, 490, 510, 555, 670, 765, and

865 nm). The images were processed to L2 using the SeaWiFS Data Analysis Software (SeaDAS version 5.2.0). We applied the NASA standard atmospheric correction algorithm, which includes a clear water scheme for open ocean pixels an iteration scheme for moderately turbid waters where the black pixel assumption is violated. The Chl-*a* values from SeaWiFS OC data were corrected by using a SeaWiFS-Adapted regional algorithm (Ben Mustapha et al. 2012). First, monthly composite images of the 5 sub-areas for the 1998–2004 study period were generated. Sub-areas (Fig. 19.2) of size 3 × 3 pixels (27 × 27 km) were then extracted to study the spatio-temporal variability at meso-scale.

Sea Surface Temperature Data Daily mean NOAA (National Oceanic and Atmospheric Administration) AVHRR (Advanced Very High Resolution Radiometer) SST (1.1 km) were used to generate monthly mean averages for the five sub-areas. Individual images (day and night overpasses) covering the Beaufort Sea from 145 W to 115 W and available from the Remote Sensing Laboratory, Department of Fisheries and Oceans Canada, Maurice-Lamontagne Institute were processed and analysed (Table 19.1). After cloud screening, SST data were computed from each overpass using the ‘split window’ Multi-Channel SST algorithm (McClain et al. 1985). After this initial process, image data were compared to ice cover maps generated by the National Snow and Ice Data Center (NSIDC) to eliminate false SST in spring time when the ice surface is melting.

Results Figure 19.16 shows the climatological average values of SST and Chl-*a* concentrations observed in spring (May–June) and summer (July–August–September) from 1980 to 2004. The highest temperatures are observed in the Mackenzie River mouth and on the Mackenzie Shelf both in spring and summer. The Amundsen Gulf is characterized by cold waters in both seasons while Chl-*a* concentration remains low, except along the south coast in summer. This region is characterized by the presence of a persistent thermal front associated with intermediate upwelling supporting increased phytoplankton biomass (Williams and Carmack 2008).

In order to assess the temporal variability, SST and Chl-*a* were extracted in the five sub-regions. It is noted that the availability of data is different for both parameters. This is the result of contamination of the OC radiometric signal by the adjacency of ice and free water mass. Therefore, there is not enough Chl-*a* data available from the offshore region of the Beaufort Sea to analyse the seasonal and inter-annual variability. Table 19.1 shows the seasonal evolution of SST where the peak is usually reached in August. The increase in temperature between June and July is higher than the decrease between August and September. This may be caused by the strong solar irradiance on this region during summer. The sun warms the surface layer faster than in autumn. The seasonal maximum of SST in August seems not to be related to the decrease of ice cover observed over the 7 years. The peak anomalies of this time series occurred in summer 1998, especially during July and August (in all regions). There is a good agreement between these observations and the air temperature measured at Sachs Harbour over the same period of time

Table 19.1 Monthly mean of satellite chlorophyll concentration and SST time series for the 5 sub-areas in the Beaufort Sea. The numbers in the boxes are the monthly mean values. The numbers to the right are the 1998–2004 climatological means and standard deviations. The color coding highlights the corresponding standardized anomaly

		Cape Bathurst		Franklin Bay		McGillivray		Sachs Harbour		Amundsen Gulf		Chukchi Sea		SST		
		J	C	J	C	J	C	J	C	J	C	A	S	J	C	
J	3.2	0.7	0.1	-1.1	0.1	-0.2	0.47°C ± 1.46	J	3.7	0.5	-0.5	-1.5	-0.3	1.5	0.6	
J	8.9	3.3	0.6	4.6	-1.0	-0.5	1.0	J	8.7	2.7	1.3	2.9	-0.6	3.0	2.4	
A	8.8	6.8	2.7	4.2	0.5	1.4	2.6	A	8.1	6.2	1.3	3.2	-0.6	0.9	3.8	
S	5.5	3.9	1.7	2.8	1.3	2.2	1.5	S	5.1	3.8	1.9	-0.6	-0.3	-0.1	1.5°C ± 2.20	
J	0.38	0.10	0.13	0.13	0.13	0.11	0.17 mg m⁻³ ± 0.12	J	0.06	0.07	0.11	0.08	0.08	0.08	0.08 mg m⁻³ ± 0.02	
J	0.06	0.07	0.03	0.09	0.15	0.15	0.08 mg m⁻³ ± 0.04	A	0.10	0.10	0.09	0.12	0.16	0.11	0.11 mg m⁻³ ± 0.03	
A	0.08	0.16	0.09	0.15	0.08	0.14	0.13	S	0.13	0.10	0.07	0.27	0.23	0.08	0.12 mg m⁻³ ± 0.08	
S	0.09	0.12	0.08	0.30	0.53	0.21	0.13	1998	1999	2000	2001	2002	2003	2004		
1998	1999	2000	2001	2002	2003	2004		J	3.1	6.9	1.4	-0.1	0.1	2.5	2.7	
J	2.9	2.1	-0.8	-0.4	0.9	1.3	1.00°C ± 1.42	J	9.0	5.4	3.0	1.9	2.8	6.8	7.5	
J	8.9	2.7	3.3	1.6	3.1	4.7	4.36°C ± 2.49	A	10.7	3.5	2.5	4.9	4.1	3.5	8.5	
A	9.4	6.7	4.6	3.0	2.1	3.6	5.0	4.91°C ± 2.47	S	7.3	0.1	1.6	4.8	2.5	0.3	4.0
S	6.3	4.2	3.1	2.4	1.4	3.3	0.6	3.04°C ± 1.88	J	2.20	1.42	0.70	0.27	1.34	0.68	1.10 mg m⁻³ ± 0.69
J	0.11	0.18	1.54	0.34	0.27	0.46	0.55 mg m⁻³ ± 0.69	J	0.67	1.38	0.80	0.80	2.03	1.15	0.75	
A	0.19	0.44	0.33	0.59	1.68	0.61	0.30	0.59 mg m⁻³ ± 0.50	A	0.95	0.91	1.51	1.26	1.40	1.05	0.98
S	0.32	0.14	0.68	0.56	1.04	0.48	0.31	0.50 mg m⁻³ ± 0.30	S	1.84	0.96	1.08	1.31	1.81	0.82	0.70
1998	1999	2000	2001	2002	2003	2004	1998	1999	2000	2001	2002	2003	2004			
J	2.7	0.1	-0.6	-0.8	1.4	0.7	0.6	0.59°C ± 1.20							2	
J	4.8	1.9	2.7	2.1	3.4	2.3	5.5	3.24°C ± 1.40							1	
A	7.2	5.2	4.6	2.6	2.2	3.4	4.3	4.21°C ± 1.70							0	
S	5.8	1.1	1.6	3.2	3.2	1.7	0.0	2.37°C ± 1.89							-1	
J	1.17		0.24		0.41	0.84	0.51	0.75 mg m⁻³ ± 0.61							-2	
J	1.09		1.44		0.86	0.77	0.68	0.97 mg m⁻³ ± 0.30							0	
A	0.84		0.71		0.83	1.69	0.78	0.55 mg m⁻³ ± 0.40							1	
S	0.73		0.78		0.85	1.66	0.51	0.84 mg m⁻³ ± 0.43								

Standardized anomaly / Anomalie normalisée

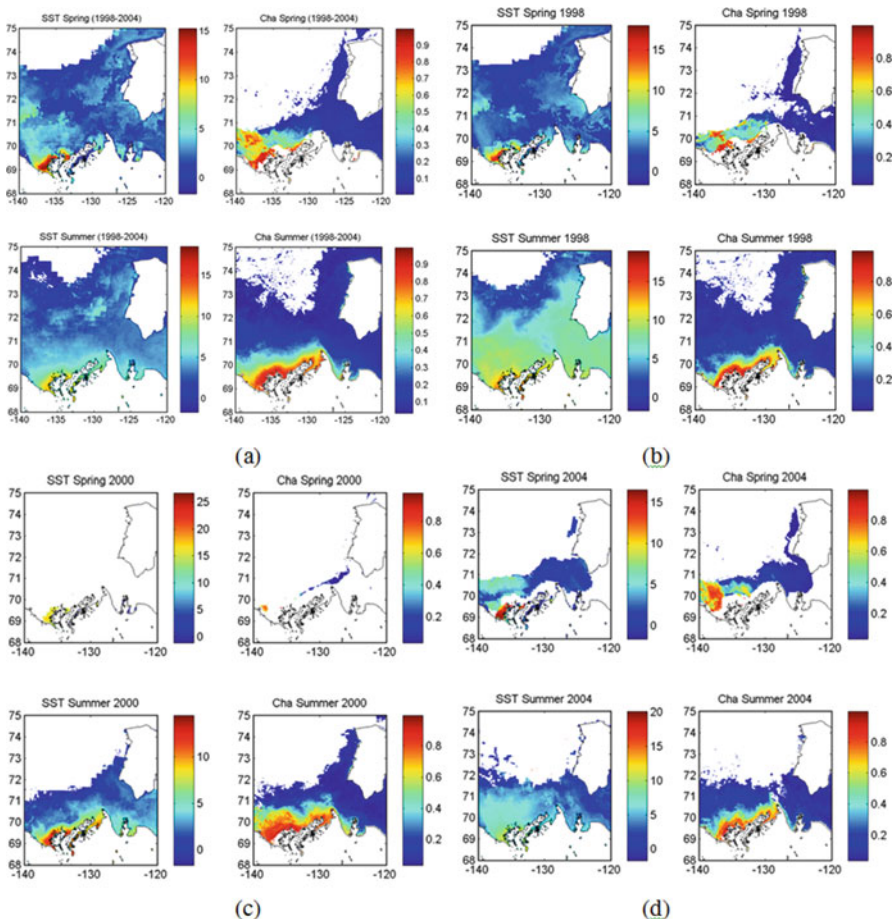


Fig. 19.16 (a) Time series of Chl- a ($\text{mg} \cdot \text{m}^{-3}$) and SST ($^{\circ}\text{C}$) in the Beaufort Sea during spring and summer (average (1998–2004) and monthly means in (b) 1998 (c) 2002 and (d) 2004)

(Ben Mustapha 2013), indicating a strong coupling between the atmosphere and the ocean surface. The influence of El Niño and the Arctic Oscillation seem to have effects on the strong positive anomaly observed in 1998, by means of changing wind patterns in the regions (Maslanik et al. 1999).

Monthly Chl- a show relatively weak seasonal variability in all sub-regions except for the Amundsen Gulf where two phytoplankton biomass maxima are observed in June and September, indicating a phenology different from the other regions. The highest Chl- a concentrations were observed in the Mackenzie region (MK), the Cape Bathurst (CB) and Franklin Bay (FB). Sachs Harbour (SH) and the Amundsen Gulf (AG) have lower concentrations of Chl- a . However, in the Mackenzie plume region, it is likely that the observed values are still overestimated because of CDOM

absorption associated with fluvial freshwater. The seasonal variability observed might therefore rather indicate the impact of river discharge than an increase in phytoplankton production.

The results also show a strong interannual variability of Chl-*a* concentrations. Positive anomalies of chlorophyll were observed in 2002 in the Amundsen Gulf, in Franklin Bay and Cape Bathurst. In the region of Sachs Harbour, positive anomalies of chlorophyll concentration are observed in some months of the years 2001, 2002 and 2003. It is possible that a change in the coupling between primary producers and higher trophic levels (Tremblay et al. 2006) may explain some of the observations during the time series.

Because of the strong stratification of the Beaufort Sea, there is only a limited nutrient replenishment during the winter period. This limits nutrient availability for the phytoplankton bloom. Mixing events are thus very important for the generation of surface phytoplankton blooms during the open water period. The most important mixing factor is the wind, used as a proxy, representative of the mixing (Ben Mustapha 2013). During the open water season (May–October), winds show a dominance of south-easterly winds that cause coastal upwelling along the southern AG coast as indicated by the higher Chl-*a* concentrations observed in FB and CB. The SH region always shows low Chl-*a* values because it is located in a downwelling-prone area. In the AG region, it appears that wind intensity is only rarely strong enough to generate vertical mixing. Winds in the coastal areas (SH) blew primarily along the East-West axis. Strong winds forced the MK plume to expand alongshore. The winds mix nutrients from deeper waters into the surface, resulting in increased Chl-*a* values.

In 1998 an exceptionally early retreat of the sea ice cover occurred, followed by an early phytoplankton bloom. 1998 was also a record year for warm air temperature in the Arctic. Positive anomaly as high as +7 °C in spring was observed. The period of breakup of the sea-ice cover was the longest observed (20 weeks) during the observation period. In 2004, the breakup of the sea ice cover occurred in the end of May in the AG, SH, FB and in early June for the CB and MK while a complete freeze-up occurred within 1 week in late October (Galley et al. 2008).

For all investigated areas the monthly mean Chl-*a* derived from remote sensing has a high interannual variability in the timing, strength and duration of phytoplankton blooms. Recent trends of earlier sea ice break-up and later sea ice formation in the Beaufort Sea have important implications for the biological productivity in the Cape Bathurst polynya at all trophic levels. This study provides mesoscale information about the spatial and temporal variability of phytoplankton in five investigated sub-areas of the Beaufort Sea. Good data coverage was during May to early September; during the other months there was hardly any data available due to ice cover, clouds and the low solar elevation. Monthly and seasonal average images of Chl-*a* were processed over the period 1998–2004, which is the period of availability of mesoscale resolution SeaWiFS data (1 km) over the studied area, while the SeaWiFS data at low spatial resolution (9 km) was available until 2011. For the study presented here, however, mesoscale resolution data was required as a

minimum. It must be noted, however, that the recent decade (2005–2014) has seen remarkable reduction of sea ice cover over the Arctic and might be expected to show even stronger anomalies of SST and Chl-*a* than are revealed here.

19.5 Merging and Fusion of Multi-satellite Datasets to Provide Improved Temporal Coverage

The previous regional examples showed how ocean colour remote sensing improves our understanding of coastal zone dynamics and bloom development. There are efforts to develop merged satellite products on a global scale. The impetus for the merging of global ocean colour data came from the proliferation of polar-orbiting missions and the knowledge that a single polar-orbiting mission does a rather poor job of sampling the ocean on short time scales (IOCCG 2007). The NASA Research, Education and Applications Solutions Network/Making Earth System Data Records for Use in Research Environments (MEaSUREs) (Maritorena et al. 2010) and ESA GlobColour (Pinnock et al. 2007; Fanton d'Andon et al. 2008) projects focused on combining multiple mission observations (MERIS, MODIS-Aqua and SeaWiFS) into a single data product with better spatial and temporal coverage than the individual missions, albeit with a lower spatial resolution. Both projects used the Maritorena & Siegel (2005) GSM bio-optical model to retrieve L2 products and the Level 3 (L3) products (time- or space-binned versions of the L2 products), and are then produced as global products of varying spatial and temporal resolutions. In MEaSUREs, e.g., L3 binned normalised water-leaving radiance data from MERIS and MODIS were converted to 9 km resolution to match the resolution of SeaWiFS before the merging was performed. For GlobColour, the L3 data were processed from L2 with an output resolution of 1/24 degree at the equator which is equivalent to 4.63 km. The ESA Ocean Colour Climate Change Initiative (OC-CCI) project has created 4 km resolution L3 products from L1 data processed using POLYMER (POLYNomial based algorithm applied to MERIS; Steinmetz et al. 2011) for MERIS and the SeaDAS standard processing for SeaWiFS and MODIS, then the remote sensing reflectance is band shifted to fit the SeaWiFS bands before bio-optical products are derived using the algorithms in SeaDAS (OC-CCI 2015). Figure 19.17 shows the similarities in the general Chl-*a* patterns between GlobColour (CHL1 product) and OC-CCI (version 1 dataset release NASA OC4.V6 algorithm product); lower values in the North Eastern Atlantic Ocean and Mediterranean Sea with higher values over the continental shelf, and especially where there is river/estuarine outflows which could represent high Chl-*a* or inorganic SPM affecting the bio-optical models. The differences result from several sources including the atmospheric correction and bio-optical models used, and both products come with estimates of the uncertainties.

The OC-CCI product has a greater number of merged pixels, and hence lower number of missing pixels in the L3 products, as the POLYMER atmospheric correc-

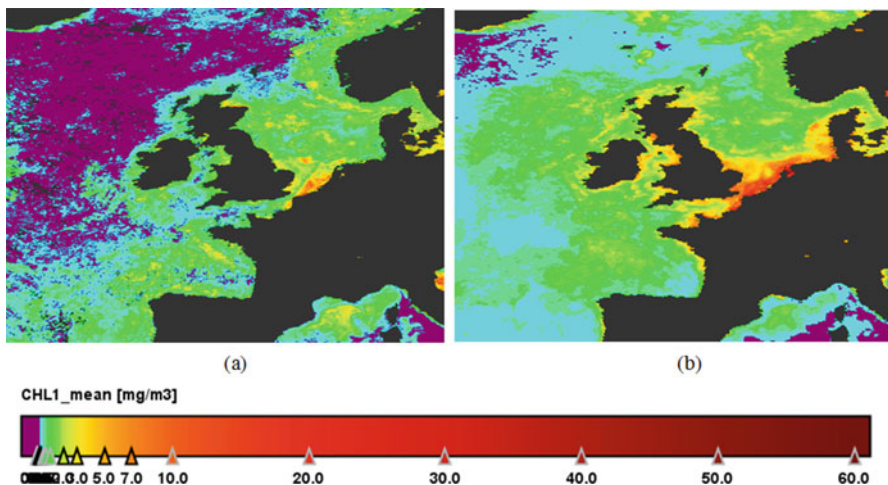


Fig. 19.17 Merged monthly Chlorophyll-a products for April 2003 from (a) Globcolour using the GSM bio-optical model provided as a monthly product with (b) showing the Ocean Colour Climate Change Initiative (OC-CCI) project product where the daily products were provided and then merged using the BEAM Visat binning module by applying simple averaging

tion can be applied within the MERIS sun glint influenced pixels. These efforts, to globally merge ocean colour products, tend to result in products that have a relatively coarse spatial resolution that is not adequate for coastal monitoring. Furthermore, the algorithms used have tended to be optimised for oceanic waters, which often lead to greater uncertainty in the coastal water quality evaluation. However, these issues are well understood and more recently the GlobColour and OC-CCI project activities have transitioned into the Copernicus Marine Environment Monitoring Service products, which have improved resolutions of 1 and 2 km for regional products. Also, OC-CCI is focusing on improving the algorithms for Case-2 waters; the version 3 dataset with optimised bio-optical algorithms is due for release in Spring 2016. The examples shown in Sects. 19.1 and 19.2.2, however, demonstrate that for coastal bays and estuaries, the 1 km resolution is still sub-optimal. But these areas are important for assessing production, as most of the production happens in coastal waters.

Whilst globally merged products remain sub-optimal for coastal waters, alternative regional approaches should also be considered. Kahru et al. (2012) combined over 10 000 Chl- a samples collected by various research programs in the California Current with daily L2 satellite data (OCTS, SeaWiFS, MODIS-Aqua and MERIS) at the highest routinely available resolution using a modification of the Gregg et al. (2009) Empirical Satellite Radiance-In situ Data (ESRID) method to create a 15-year locally optimised time series.

Kahru and Elmgren (2014) describe the compilation of a 35-year-long time series (1979–2013) of cyanobacteria surface accumulations in the Baltic Sea using merged

data from different satellite sensors. The results showed that during the 35 years the timing of the accumulations has been shifted by approximately 20 days earlier during the summer season.

Researchers are also combining ocean colour data with medium resolution sensors, such as the Landsat series, to provide higher resolution coastal products e.g. the Landsat 5 satellite acquired around 28 years of data with its TM instrument at a spatial resolution of 30 m. Approaches have focused on using ocean colour data to aid in the atmospheric correction of Landsat (e.g. Hu et al. 2001) or using the Landsat infrared bands themselves.

References

- Alikas K, Kangro K, Reinart A (2010) Detecting cyanobacterial blooms in large North European lakes using the Maximum Chlorophyll Index. *Oceanologia* 52:237–257
- Alikas K, Kratzer S, Reinart A, Kauer T, Paavel B (2015) Robust remote sensing algorithms to derive the diffuse attenuation coefficient for lakes and coastal waters. *Limnol Oceanogr Methods* 13(8):402–415
- Arrigo KR, van Dijken GL (2011) Secular trends in Arctic Ocean net primary production. *J Geophys Res* 116, C09011
- Austin RW, Petzold TJ (1981) The determination of the diffuse attenuation coefficient of sea water using the Coastal Zone Color Scanner. In: Garver JFR (ed) *Oceanography from space*. Springer, New York, pp 239–256
- Behrenfeld MJ, Falkowski PG (1997) Photosynthetic rates derived from satellite-based chlorophyll concentration. *Limnol Oceanogr* 42(1):1–20
- Beltrán-Abaunza JM, Kratzer S and Höglander H (2016) Using the MERIS archive for the evaluation of spatial-temporal variability of water quality: the Himmerfjärden nitrogen experiment viewed from space. *Int J of Remote Sens* (in print)
- Ben Mustapha S (2013) Etude de la variabilité spatio-temporelle des processus biologiques et physiques dans la mer de Beaufort par télédétection et dans un contexte de changements climatiques en Océan Arctique. PhD thesis Université de Sherbrooke Québec Canada 263 pp
- Ben Mustapha S, Bélanger S, Larouche P (2012) Evaluation of ocean color algorithms in the southeastern Beaufort Sea, Canadian Arctic: new parameterization using SeaWiFS, MODIS, and MERIS spectral bands. *Can J Remote Sens* 38(5):1–22
- Binding CE, Greenberg TA, Jerome JH, Bukata RP, Letourneau G (2011) An assessment of MERIS algal products during an intense bloom in Lake of the Woods. *J Plankton Res* 33:793–806
- CEC (2000) Directive 2000/60/EC of the European Parliament and of the Council of 23 October 2000 establishing a framework for Community action in the field of water policy (Official Journal of the European Communities No. L327, 1.22.12.2000) Brussels
- CEC (2008) Directive 2008/56/EC of the European Parliament and of the Council of 17 June 2008 establishing a framework for Community action in the field of marine environmental policy (Marine Strategy Framework Directive) (Official Journal of the European Communities No. L164/19 25.06.2008) Brussels
- Claquin P, Probert I, Lefebvre S, Veron B (2008) Effects of temperature on photosynthetic parameters and TEP production in eight species of marine microalgae. *Aquat Microb Ecol* 5:1–11
- Comiso JC (2011) Large decadal decline of the Arctic multiyear ice cover. *J Clim* 25(4):1176–1193
- Doerffer R, Sorenson K, Aiken J (1999) MERIS potential for coastal zone applications. *Int J Remote Sens* 20(9):1809–1818

- Donlon C, Berruti B, Buongiorno A, Ferreira MH, Féménias P, Frerick J, Goryl P, Klein U, Laur H, Mavrocordatos C, Nieke J (2012) The global monitoring for environment and security (GMES) sentinel-3 mission. *Remote Sens Environ* 120:37–57
- Elbraechter M, Schepf E (1996) Gymnodinium chlorophorum, a new, green bloom forming Dinoflagellate(Gymnodiniales, Dinophyceae) with a vestigial Prasinophyte endosymbiont. *Phycologia* 35:381–393
- Fanton d'Andon OH, Antoine D, Mangin A, Maritorena S, Durand D, Pradhan Y, Lavender S, Morel A, Demaria J, Barrot G (2008) Ocean colour sensors characterisation and expected error estimates of ocean colour merged products from GlobColour, Ocean Optics XIX, Barga, Italy, 6–10 October 2008, 51 pp
- Ferrari G, Dowell M (1998) CDOM absorption characteristics with relation to fluorescence and salinity in coastal areas of the southern Baltic Sea. *Estuar Coast Shelf Sci* 47:91–105
- Galley RJ, Key E, Barber DG, Hwang BJ, Ehn JK (2008) Spatial and temporal variability of sea ice in the southern Beaufort Sea and Amundsen Gulf: 1980–2004. *J Geophys Res* 113(C5)
- Gower J, King S, Borstad G, Brown L (2008) The importance of band at 709 nm for interpreting water-leaving spectral radiance. *Can J Remote Sens* 34(3):287–295
- Gregg WW, Casey NW, O'Reilly JE, Esaias WE (2009) An empirical approach to ocean color data: reducing bias and the need for post-launch radiometric re-calibration. *Remote Sens Environ* 113:1598–1612
- Guanter L, Ruiz-Verdú A, Odermatt D, Giardino C, Simis S, Estellés V, Heege T, Domínguez-Gómez JA, Moreno J (2010) Atmospheric correction of ENVISAT/MERIS data over inland waters: validation for European lakes. *Remote Sens Environ* 114(3):467–480
- Hajdu S, Gorokhova E, Larsson U (2015) In-depth analysis of an alternate-stage *Prymnesium polylepis* (Haptophyta) bloom and long-term trends in abundance of Prymnesiales species in the Baltic Sea. *Mar Ecol Prog Ser* 526:55–66
- Harvey T, Kratzer S, Philipson P (2015) Satellite-based water quality monitoring for improved spatial and temporal retrieval of chlorophyll-a in coastal waters. *Remote Sens Environ* 158:417–430
- Haykin S (1998) Neural networks. A comprehensive foundation. Upper Saddle River, NJ: Prentice Hall HELCOM, 2007. Baltic Sea Action Plan (HELCOM Ministerial Meeting). Krakow, Poland
- HELCOM (2007) The HELCOM Baltic Sea action plan. Krakow, Poland, p 15
- Hu C, Muller-Karger FE, Andrefouet S, Carder KL (2001) Atmospheric correction and cross-calibration of LANDSAT-7/ETM+ imagery over aquatic environments: a multiplatform approach using SeaWiFS/MODIS. *Remote Sens Environ* 78:99–107
- IOCCG (2000) Remote sensing of ocean colour in coastal, and other optically-complex waters. In: Sathyendranath S (ed) Reports of the International Ocean-Colour Coordinating Group, No. 3. IOCCG, Dartmouth
- IOCCG (2007) Ocean-colour data merging. In: Gregg W (ed) Reports of the International Ocean-Colour Coordinating Group, No. 6. IOCCG, Dartmouth
- Isemer HJ, Rozwadowska A (1999) Solar radiation fluxes at the surface of the Baltic Proper. Part 2. Uncertainties and comparison with simple bulk parametrisations. *Oceanologia* 41(2): 147–185
- Kahru M, Elmgren R (2014) Multidecadal time series of satellite-detected accumulations of cyanobacteria in the Baltic Sea. *Biogeosciences* 11(13):3619–3633
- Kahru M, Savchuk OP, Elmgren R (2007) Satellite measurements of cyanobacterial bloom frequency in the Baltic Sea: interannual and spatial variability. *Mar Ecol Prog Ser* 343:15–23
- Kahru M, Brotas V, Manzano-Sarabia M, Mitchell BG (2011) Are phytoplankton blooms occurring earlier in the Arctic? *Glob Chang Biol* 17(4):1733–1739
- Kahru M, Kudela RM, Manzano-Sarabia M, Mitchell BG (2012) Trends in the surface chlorophyll of the California Current: merging data from multiple ocean color satellites. *Deep-Sea Res II Top Stud Oceanogr* 77(80):89–98
- Kirk JTO (2011) Light and photosynthesis in aquatic ecosystems, 3rd edn. Cambridge University Press, Cambridge, 649 pp

- Kratzer S, Tett P (2009) Using bio-optics to investigate the extent of coastal waters: A Swedish case study. *Hydrobiologia* 629(1):169–186
- Kratzer S, Vinterhav C (2010) Improvement of MERIS level 2 products in Baltic Sea coastal areas by applying the Improved Contrast between Ocean and Land processor (ICOL)-data analysis and validation. *Oceanologia* 52(2):211–236
- Kratzer S, Håkansson B, Sahlin C (2003) Assessing Secchi and photic zone depth in the Baltic Sea from Space. *Ambio* 32(8):577–585
- Kratzer S, Brockmann C, Moore G (2008) Using MERIS full resolution data to monitor coastal waters – a case study from Himmerfjärden, a fjord-like bay in the northwestern Baltic Sea. *Remote Sens Environ* 112:2284–2300
- Kratzer S, Harvey ET, Philipson P (2014) The use of ocean color remote sensing in integrated coastal zone management-a case study from Himmerfjärden, Sweden. *Mar Policy* 43:29–39
- Lavender SJ, Raitsos DE, Pradhan Y (2008) Variations in the phytoplankton of the North-Eastern Atlantic ocean: from the Irish Sea to the Bay of Biscay. In: Barale V, Gade M (eds) *Remote sensing of the European seas*. Springer, Dordrecht, pp 67–78
- Leppäranta M, Myrberg K (2009) Physical oceanography of the Baltic sea. Springer, Berlin/Heidelberg/New York, 378 pp
- Maritorena S, Fanton d'Andon OH, Mangin A, Siegel DA (2010) Merged satellite ocean color data products using a bio-optical model: characteristics, benefits and issues. *Remote Sens Environ* 114:1791–1804
- Maslanik JA, Serreze MC, Agnew T (1999) On the record reduction in 1998 western Arctic sea-ice cover. *Geophys Res Lett* 26:1905–1908
- Matsumoto T, Shinozaki F, Chikuni T, Yabuki A, Takishita K, Kawachi M, Nakayama T, Inouye I (2011) Chlorophyte origin. *Protist* 162:268–276
- McClain CR (2009) A decade of satellite ocean color observations. *Annu Rev Mar Sci* 1(1):19–42
- McClain EP, Pichel WG, Walton CC (1985) Comparative performance of AVHRR-based multi-channel sea surface temperatures. *J Geophys Res* 90:11587–11601
- Morozov EA, Korosov AA, Pozdnyakov DV, Pettersson LH, Sychev VI (2010) A new area-specific bio-optical algorithm for the Bay of Biscay and assessment of its potentials for SeaWiFS and MODIS/Aqua data merging. *Int J Remote Sens* 31(24):6541–6565
- Morozov E, Pozdnyakov D, Smyth T, Sychev V, Grassl H (2013) Space-borne study of seasonal, multi-year, and decadal phytoplankton dynamics in the Bay of Biscay. *Int J Remote Sens* 34(4):1297–1331
- Nazeer M, Nichol JE (2015) Development and application of a remote sensing-based Chlorophyll-a concentration prediction model for complex coastal water of Hong Kong. *J Hydrol* 532:80–89
- Öberg J (2013) Cyanobacterial blooms in the Baltic Sea in 2013. HELCOM Baltic Sea Environment Fact Sheet 2013. <http://helcom.fi/baltic-sea-trends/environment-fact-sheets/eutrophication/cyanobacterial-blooms-in-the-baltic-sea>
- Ocean Colour Climate Change Initiative (2015) Product user guide issue 2.0.5, Retrieved from <http://www.esaoceancolour-cci.org/>
- OSPAR Commission (1992) On the assessment of the quality of the marine environment, Annex IV, OSPAR Convention
- Pierson D, Kratzer S, Strömbeck N, Håkansson B (2008) Relationship between the attenuation of downwelling irradiance at 490 nm with the attenuation of PAR (400 nm- 700 nm) in the Baltic Sea. *Remote Sens Environ* 112(3):668–680
- Pinnock S, D'Andon OF, Lavender S (2007) GlobColour-a precursor to the GMES marine core service ocean Colour. Thematic Assembly Centre. *ESA Bull* 132:42–49
- Preisendorfer RW (1986) Secchi disk science; visual optics of natural waters. *Limnol Oceanogr* 31:906–926
- Robinson IS (2004) Measuring the oceans from space: the principles and methods of satellite oceanography. Springer, Berlin/New York, 670 pp
- Ruddick K, De Cauwer V, Park Y, Moore G (2006) Seaborne measurements of near infrared water-leaving reflectance: the similarity spectrum for turbid waters. *Limnol Oceanogr* 51(2):1167–1179

- Ruddick K, Lacroix G, Park Y, Rousseau V, De Cauwer V, Sterckx S (2008) Overview of ocean colour: theoretical background, sensors and applicability for the detection and monitoring of harmful algae blooms (capabilities and limitations). In: Babin M, Roesler C, Cullen JJ (eds) *Realtime coastal observing systems for ecosystem dynamics and harmful algal blooms*, UNESCO monographs on oceanographic methodology series. UNESCO publishing, Paris
- Ruescas A, Brockmann C, Stelzer K, Tilstone G, Beltrán-Abaunza JM (2014) Coastcolour validation report. Deliverable DEL-27. Version 1.0. Brockmann Consult. Geesthacht
- Santer R, Schmechtig C (2010) Adjacency effects on water surfaces: primary scattering approximation and sensitivity study. *Appl Opt* 39(3):361–375
- Sathyendranath S (ed) (2000) Remote sensing of ocean colour in coastal, and other optically-complex, waters. IOCCG report number 3. MacNab Print, Dartmouth, Canada: International Ocean-Colour Coordinating Group. Retrieved from <http://www.ioccg.org/reports/report3.pdf>
- Schroeder T, Behner I, Schaale M, Fischer J, Doerffer R (2007a) Atmospheric correction algorithm for MERIS above case-2 waters. *Int J Remote Sens* 28:1469–1486
- Schroeder T, Schaale M, Fischer J (2007b) Retrieval of atmospheric and oceanic properties from MERIS measurements: a new Case-2 water processor for BEAM. *Int J Remote Sens* 28:5627–5632
- Siegel H, Gerth M (2013) Sea surface temperature in the Baltic sea in 2012. Baltic Sea Environment Fact Sheet 2013. <http://helcom.fi/baltic-sea-trends/environment-fact-sheets/hydrography/development-of-sea-surface-temperature-in-the-baltic-sea>
- Siegel DA, Maritorena S, Nelson NB, Behrenfeld MJ (2005) Independence and interdependencies among global ocean color properties: reassessing the bio-optical assumption. *J Geophys Res: Oceans* 110(C7)
- Steinmetz F, Deschamps PY, Ramon D (2011) Atmospheric correction in presence of sun glint: application to MERIS. *Opt Express* 19(10):9783–9800
- Sterckx S, Knaeps E, Ruddick K (2011) Detection and correction of adjacency effects in hyperspectral airborne data of coastal and inland waters: the use of the near infrared similarity. *Int J Remote Sens* 32(21):6479–6505
- Sterckx S, Knaeps E, Kratzer S, Ruddick K (2015) SIMilarity Environment Correction (SIMEC) applied to MERIS data over inland and coastal waters. *Remote Sens Environ* 157:96–110
- Tett P (1990) The photic zone. In: Herring PJ, Campbell AK, Whitfield M, Maddock L (eds) *Light and life in the sea*. Cambridge University Press, Cambridge, pp 59–87
- Tremblay J-É, Hattori H, Michel C, Ringuette M, Mei Z-P, Lovejoy C, Fortier L, Hobson KA, Amiel D, Cochran JK (2006) Trophic structure and pathways of biogenic carbon flow in the eastern North Water Polynya. *Prog Oceanogr* 71:402–425
- Wang M, Son S, Harding LW (2009) Retrieval of diffuse attenuation coefficient in the Chesapeake Bay and turbid ocean regions for satellite ocean color applications. *J Geophys Res Oceans* 114(C10), C10011
- Whitehouse BG, Hutt D (2006) Observing coastal waters with spaceborne sensors. In: Richardson LL, LeDrew EF (eds) *Remote sensing of aquatic coastal ecosystem processes*. Springer, Dordrecht, pp 201–215
- Williams WJ, Carmack EC (2008) Combined effect of windforcing and isobath divergence on upwelling at Cape Bathurst, Beaufort Sea. *J Mar Res* 66:645–663
- Zibordi G, Ruddick K, Ansko I, Moore G, Kratzer S, Icely J, Reinart A (2012) In situ determination of the remote sensing reflectance: an inter-comparison. *Ocean Sci* 8:567–586
- Zimmermann HJ (2001) *Fuzzy set theory*. Kluwer Academic Publishers, Boston, 514 pp

Chapter 20

Monitoring Long-Term Disaster Recovery – Space and Ground Views

Tuong-Thuy Vu and Daroonwan Kamthonkiat

Abstract Remote sensing plays a crucial role in post-disaster and emergency responses. For years, it has been a key player in providing invaluable multi-temporal synoptic data for landuse and landcover change detection. Surprisingly, it has not been fully exploited for monitoring long-term disaster recovery due to the involvement of various timeframes and scales in monitoring. This chapter reports our investigation of medium resolution satellite image use in association with ground direct observation, socio-economic field data collection and interviews for monitoring recovery of the tsunami-affected areas in Phanga, Thailand. Multi-temporal landuse/landcover maps of the study area were produced via conventional supervised classification. Socio-economic data was analyzed to obtain information related to the recovery process on the ground. To bridge the gap between the classified maps and the point-based socio-economic data for comparison, landuse/landcover clusters presenting the aggregated level of information were used against buffer regions around the village points. The two data sets presented a good agreement in detection of the recovery of tourism and expansion of agricultural activities. It was not possible to confirm whether a building was newly built but the rehabilitation of mangrove forest could be observed. Overall, ASTER images are sufficient to capture the large landuse/landcover changes induced by human activities. Our study area has been in smooth recovery and some minor decrease in population or slowdown of economic activities could not be observed from the ASTER images. To some extent, the integration of ASTER images and ground data proved useful in providing a clear picture of the recovery process in an area like Phang Nga, Thailand. It would be more effective to have administrative boundaries instead of village points and an enabled-location-awareness interview setting to better link the spatial distribution of socio-economic data with the monitoring context.

T.-T. Vu (✉)

Department of Physics, International University, Vietnam National University HCMC,

Ho Chi Minh City, Vietnam

e-mail: vtthuy@hcni.edu.vn

D. Kamthonkiat

Department of Geography, Faculty of Liberal Arts, Thammasat University, Bangkok, Thailand

20.1 Introduction

In recent decades, the world has experienced more frequently (every few years) large-scale disasters such as the 1995 Kobe-Japan earthquake, the 1999 Kocaeli-Turkey earthquake, the 2001 Gujarat-India earthquake, the 2003 Bourmedes-Algeria earthquake, the 2003 Bam-Iran earthquake, the 2004 Indian Ocean earthquake and tsunami, the 2005 Katrina hurricane, the 2008 Sichuan-China earthquake, the 2011 giant Tohoku earthquake and tsunami, and most recently the 2013 Haiyan typhoon. Numerous other events such as hurricanes, wildfires, drought, and volcanic eruptions are also occurring worldwide. The social and economic impacts of these events continue for years from local to global scales (Huppert and Sparks 2006). The recovery process needs to be carefully monitored, as it is a complex process and involves various stakeholders (Brown et al. 2010).

Much research on the uses of remote sensing and geospatial technologies has been carried out to see how they can really help in the disaster management cycle. It has indicated that satellite remotely sensed imagery is an important data source for disaster management at all stages including *post-disaster responses* (Adams et al. 2004; Eguchi et al. 2000; Vu et al. 2007; Vu and Ban 2010; Acqua and Gamba 2012), *recovery process* (Hill et al. 2006), and *preparedness and mitigation* (Taubenböck et al. 2008; Tralli et al. 2005; Romer et al. 2012). Their wide coverage, huge archives and reasonable-temporal-resolution are significantly valuable in disaster management. They are even the only data source of the hard-hit and difficult-to-access areas at the early stage. The dissemination of such early vital information is improving under the coordination of UN-SPIDER and the activation of the International Charter on Space and Major Disasters. The recent use of satellite images has mainly focused on the response phase, whereas little attention has been paid to its use for monitoring and assessing the recovery phase (Hill et al. 2006).

Following our recent disaster response related research for the tsunami-affected areas in Thailand (Kamthonkiat et al. 2011a, b, 2012; Vu et al. 2007; Vu 2008, 2011), we further investigate the use of medium spatial resolution ASTER imagery in monitoring the long-term recovery of the area. A few relevant studies are discussed in Sect. 20.2 to highlight the need for our study. Our methodology will be described in Sect. 20.3 prior to results and discussion in Sect. 20.4. Finally, concluding remarks and future work are presented in the Sect. 20.5.

20.2 Remote Sensing for Monitoring Disaster Recovery

A few attempts have been made to explore the usability of remote sensing images during recovery processes. Vu (2008) introduced a recovery monitoring system using remote sensing data on a grid-computing platform. It targeted long-term recovery involving a huge data set; hence, grid-based large-scale database and parallel computing were introduced as a suitable approach, which was also

extendable to a sharing platform for continual monitoring. Focusing on remote sensing processing and storage, it did not reveal many issues relevant to real recovery on the ground. Romer et al. (2011) used high-resolution satellite images to assess the recovery of different vegetation types in a tsunami-affected area. The main work was change detection analysis and in interpreting the results, the authors inferred some impact of human activities on vegetation recovery. Likewise, Kamthonkiat et al. (2011a) focused more on monitoring mangrove recovery with medium spatial resolution satellite ASTER images. This work focused more on the usability of satellite remote sensing in monitoring the recovery process. The same research group went a bit further to investigate overall landuse recovery of Phuket after the 2004 tsunami disaster using ASTER images (Kamthonkiat et al. 2011b). Damaged areas were located along the coastline and it was shown that less than 1 m resolution satellite imagery was more appropriate to detect the damage (Vu et al. 2007), which indicates that it is hard to establish a direct link to damage situations when using ASTER imagery in monitoring recovery. The problem of incompatible spatial resolution was mitigated with direct ground observation. In damage mapping and monitoring the recovery of housing areas, the suitability of high-resolution images was illustrated (Vicini et al. 2011). In this study, some attempts were made to develop a quantitative scale for measuring the recovery of a building. The aforementioned studies solved the problem from the remote sensing perspective. However, what should be measured during the recovery period remains unclear.

Brown et al. (2010) reported the outcomes of The Recovery Project, which aimed at identifying the indicators for measuring, monitoring and evaluating post-disaster recovery, both in the short-term and long-term. Remote sensing was proposed as one of the main tools together with ground observation and social audit techniques. Measuring recovery highly depends on timeframe and scale. The project emphasized using very high-resolution satellite images, from which detailed changes can be detected, and recommended investigation of medium resolution satellite imagery to achieve the measurement at a coarser scale. Similarly, the combination of field surveys, ground interviews and remote sensing was proposed in Bevington et al. (2011) to understand the ways of recovery in the aftermath of a disaster.

The recovery stage is the least investigated and still poorly understood (Rubin 1985; Comerio 2005; Bevington et al. 2011) due to the various timeframes and scales that need to be taken into account. Capturing information about the Earth's surface from space, remote sensing techniques would provide both synoptic and detailed (up to half-meter spatial resolution with current satellite platforms) land cover and land use over time. As noted above, remote sensing has been recommended and proved to be a significant source of information to fill the gaps across multiple spatio-temporal scales (Brown et al. 2010; Bevington et al. 2011). To some extent, it can reveal little information about real human activities in the area. For instance, a residential area fully occupied with new buildings (roofs) as can be seen from a satellite image does not imply that life there is getting back to

normal. Change detection applications of remote sensing, so far, are more to report the biophysical changes, which comprise just one aspect of the disaster recovery process.

Among the four periods of the recovery process, i.e. emergency relief, early recovery, reconstruction and on-going development (Brown et al. 2010), the last two seem less investigated due to their longer time-frames and hence have received less attention from international organisations, authorities and media. Looking into these periods, this study aims at further establishing the use of remote sensing in monitoring the recovery process. Using a case study of Phang Nga, Thailand, a tsunami-affected area, this study assessed the feasibility of using medium resolution satellite images for regional monitoring in long-term recovery focusing on human activities and environmental rehabilitation. It subsequently identified the gap between information captured from space and socio-economic data from the ground. Two important questions need to be addressed: “To what extent can medium multi-spectral resolution satellite images reveal the real recovery process on the ground?” “Is it possible to link the captured pixel-based information to ground-based social survey information in an integrated manner?” In attempts to respond to these questions, the study provides a few recommendations for expanding remote sensing uses in monitoring the recovery process.

20.3 Methodology

20.3.1 Study Area

The tsunami impacted provinces in the South of Thailand are Phang Nga, Phuket, Satun, Krabi, Ranong, and Trang. Among these, Phang Nga was the most severely affected by the 2004 Indian Ocean tsunami (Fig. 20.1). Although the tsunami did not strike the area instantly after the Sumatra quake due to the distance, the area was not prepared for such a disaster and hence, the negative impact was intensified, especially on the tourist and fishing activities, which are main contributors to the local economy. Fishing villages are mainly located in the north of Phang Nga whereas tourist resorts are in the central region. It would be very interesting to observe how the area changed after such a devastating event in terms of the physical landscape and its relationship to human life and activities.

20.3.2 Landcover/Landuse (LULC) Change Detection

Previous studies have indicated that high-resolution satellite images are suitable for damage detection and monitoring detailed recovery at the building level. To look into the recovery on a regional scale like the entire Phang Nga province, it would

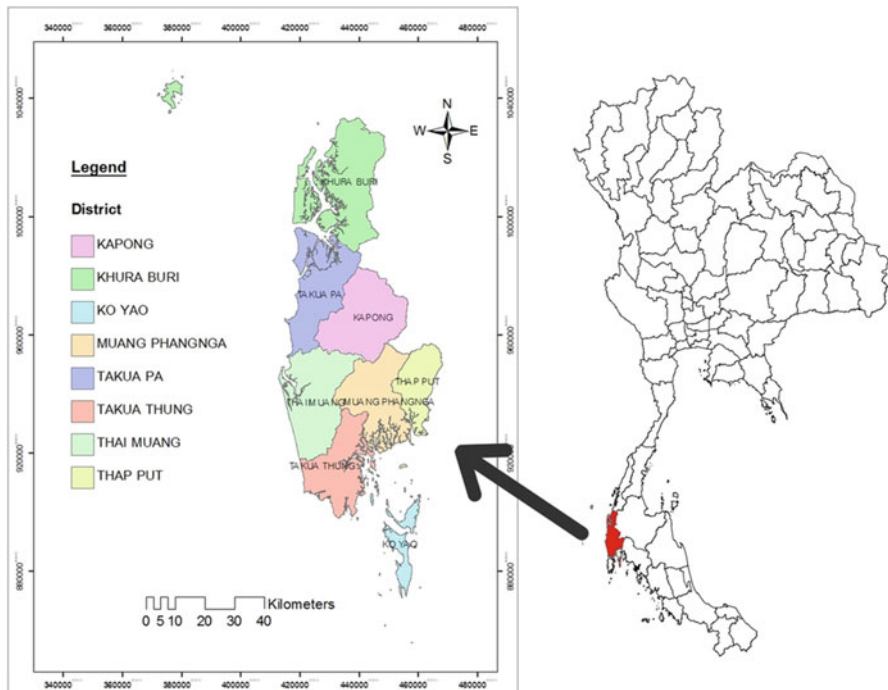


Fig. 20.1 Phang Nga province, Southern Thailand

Table 20.1 Descriptions of ASTER scenes used for mapping LULC changes

Acquisition date	Wavelength and spatial resolution (m)	Remarks
07 March 2003	VNIR, 15 m	About 2 years before the 2004 tsunami
31 December 2004	VNIR, 15 m	5 days after the 2004 tsunami. Cloudy image, only a fraction of mangrove area in Takuapa was observed.
08 February 2005	VNIR, 15 m	43 days after the 2004 tsunami
26 January 2006	VNIR, 15 m	1 year after the 2004 tsunami
6 February 2010	VNIR, 15 m	6 years after the 2004 tsunami

be unnecessarily costly to only use high-resolution satellite images. In observing the changes over a large area, medium resolution ASTER images were acquired at four different times including about 2 years before and three other times after the disaster event in December 2004. As the entire study area can be only fully covered with three scenes, in total 12 scenes were acquired as listed in Table 20.1.

The analysis of land cover and mangroves in this study was performed in the western part of Tai Muang, Takuapa and Kuraburi districts according to the limitation of scene area of the ASTER images presented in Fig. 20.2, which shows the mosaicked ASTER images used for this study. Other ancillary data include:

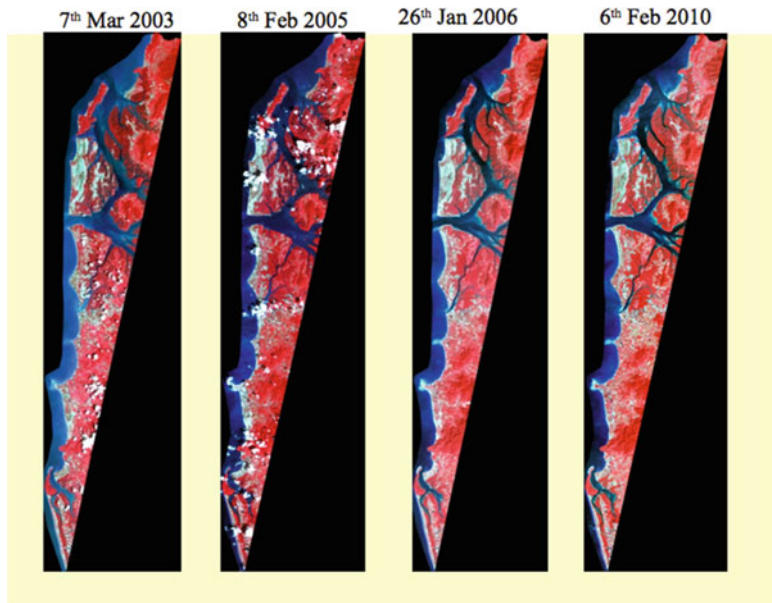


Fig. 20.2 Multi-temporal remote sensing data used in this study

- Landuse Map 2000 (1:50,000) and 2007 (1:25,000) of Phang Nga from the Land Development Department (LDD), Ministry of Agriculture and cooperatives;
- Landuse (Base Map) 1999 of Phang Nga, 1:50,000 from the Pollution Control Department, Ministry of Natural Resources and Environment;
- Landuse and road maps 2006 of Phang Nga Province, 1:50,000 from The Royal Thai Survey Department;
- Mangrove Plantation Sites in Phang Nga, 1:50,000 from Mangrove Administrative Division 2, Krabi Province, Thailand;
- Socio-economic data – Village Profile Data (survey every 2 years) and Family Profile Data (annual survey) of Phang Nga, 2003, 2005, 2006, 2007, 2010 and 2011 from the Ministry of Interior, Thailand;
- Tsunami damage level in Phang Nga from the Department of Disaster Prevention and Mitigation (DDPM), the Ministry of Interior, Thailand.

As illustrated in Fig. 20.3, post-classification change detection was employed for monitoring and mapping LULC changes in the study area. The road network in vector format was used to assist with the precise alignment of ASTER images from different time periods. It is noted that the 2004 tsunami event also caused the displacement of the shoreline (Kamthonkiat et al. 2012). This was also taken into account in image-to-image registration. Intensive field surveying was conducted to guide the supervised classification with the maximum likelihood technique, and only greater than 75 % classification accuracy was accepted to mitigate the possible errors propagated in change detection.

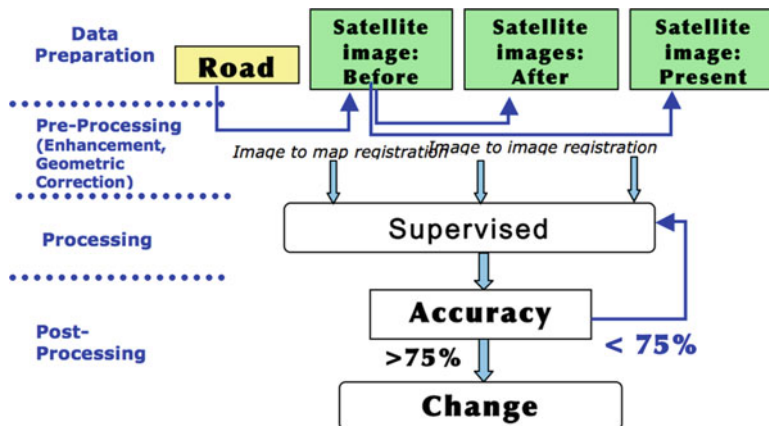


Fig. 20.3 Change detection analysis flowchart

20.3.3 Interpretation of Life Recovery and Environmental Rehabilitation

LULC information derived from satellite image classification provides a synoptic view of geo-biophysical changes over a large area. Remote sensing products have never been a sole data source in any application; careful ground truth and operators' knowledge are required to obtain a reliable outcome. To what extent can medium resolution satellite imagery like ASTER contribute to monitoring the recovery process on the ground?

Based on the outcomes of the image classification, visual interpretation carefully assessed the LULC pattern changes over time with reference to the status before the disaster in March 2003. While the change detection in Sect. 20.3.2 provided overall quantitative information about LULC changes, the assessment here was a step forward. We carefully compared the classified results with ground truth data, including direct observation and interviewing, to reveal the real recovery of mangrove forest and to analyse changes at the village level by checking how the recovery of human activities has been taking place.

Villages in our study areas were categorised into three different groups: North (fishing village and agriculture), Central (tourist hotels, resorts) and South (mangrove forest). Environmental rehabilitation was investigated for villages in the South region whereas detailed assessment of human activities was carried out for heavily impacted villages in the North and Central regions.

Unfortunately, socio-economic data at the village level was provided in the form of attribute tables associated with village point shapefiles, i.e. from socio-economic village profile data. There was an obvious gap between the presenting point-based data and the relevant activities on the ground. Direct comparison of pixel-based LULC information with socio-economic point-based data would not lead to any logical findings.

Table 20.2 Visual interpretation of recovery process

Damage level	Pre-event main activities	Pattern changes from ASTER	Ground observation	Remarks
Very High, High, Moderate, Low	Fishing, Tourism, Forest, Agriculture, Others	e.g. LULC changes	Real activities	Interpreter's comments

To fill the gap between two data sets for a possible comparison, we summarised (based on majority rule) the classified LULC using the clusters formed by mean-shift clustering (Comaniciu and Meer 2002). On the other hand, a buffer with a fixed radius of 500 m was created for an approximate estimation of LULC of a village. Subsequently, visual interpretation was performed on the classified satellite images using socio-economic village profile data in 2003, 2005 and 2007, ground survey photos and fact finding via interviews in local communities. The interpretation results were to fill in the observation table (Table 20.2) to assist the investigation.

20.4 Results and Discussion

An extensive field survey was conducted in the area. We collected ground truth data for training and validation of the LULC classification. In addition to that, interviews with local people provided another aspect of the real situation on the ground for assessing the extent which ASTER can cover. On the other hand, the team was also equipped with a Global Positioning System (GPS), topographic maps and time series satellite images (Fig. 20.4) to confirm the displacement of Phang Nga shorelines after the disaster and observe the environmental rehabilitation, especially of mangrove forest areas. This information was subsequently used to validate the classified ASTER images.

There was a steady rate of erosion in several locations in our study area after the disaster. The inland-shifted positions of the shoreline in 2005 were about 514 m at Pak Ko Village on Kho Khao Island, 85 m at Nam Khem Village, 652 m at Coral Reef Point, and 64 m at Bang Khaya Village. In 2004, the positions of the shoreline at Pak Ko Village had changed while the sand beach was swept. The series of tsunami waves had also re-allocated the sand dune under the sea; this affected the direction of current and thus stronger waves hit the beach as presented in the ASTER 2005 and 2010 (Fig. 20.5). Further details were reported in Kamthonkiat et al. 2012. The field survey also recorded the measures taken for shoreline protection as depicted in Fig. 20.6.

As mentioned in the methodology, the accepted overall accuracy of the classification was at least 75 %. Table 20.3 shows the referenced maps and field data used for accuracy assessment, and the percentages of overall accuracy of each classified image are also presented. The results of the supervised classification of ASTER in

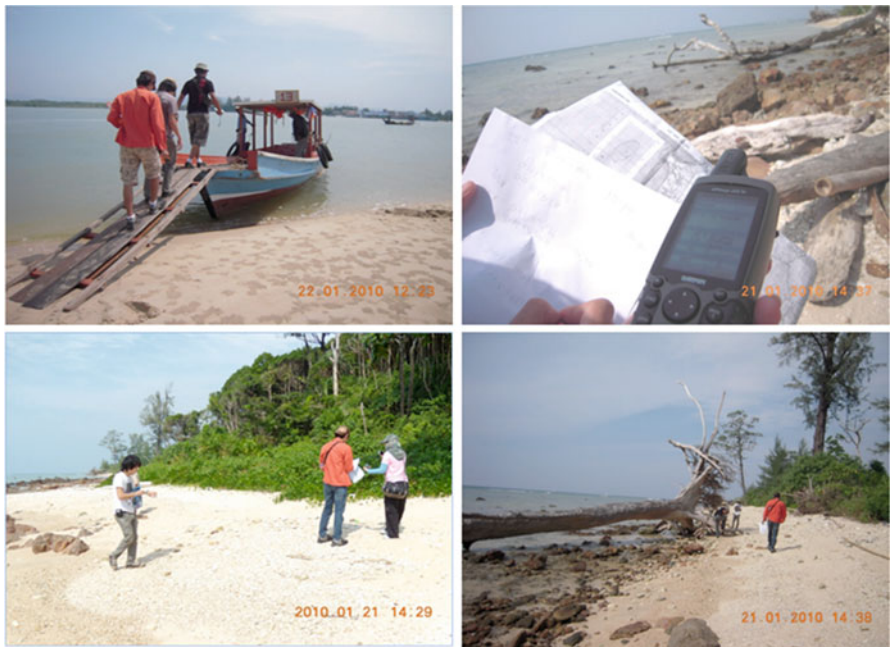


Fig. 20.4 Field survey – beach and shorelines in Phang Nga

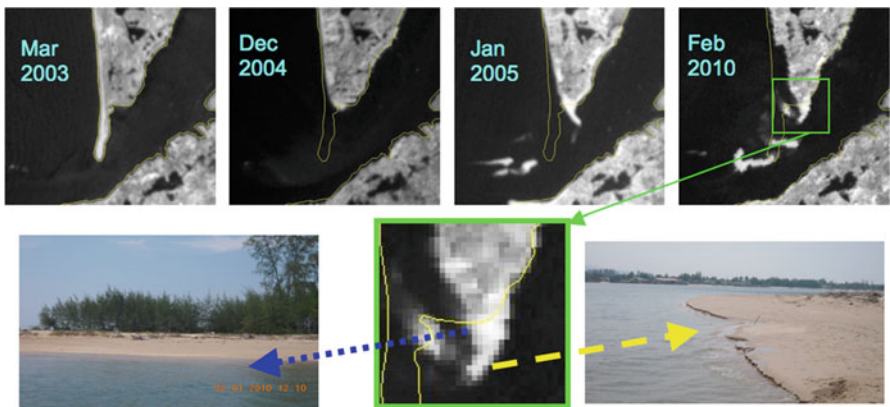


Fig. 20.5 Analysis of shorelines shifting using remote sensing – Pak Ko Village on Kho Khao Island

2003, 2005, 2006 and 2010 (concentrated on the western part of Tai Muang, Takuapa and Kuraburi districts) presented forest, mangrove, agricultural land, built-up, bare land, beach, water bodies and miscellaneous (Fig. 20.7).

Beach, built-up, and mangrove areas in 2003 had changed to bare soil, water bodies and miscellaneous in 2005. One year after the event, about 50 % of beach



Fig. 20.6 Shoreline protection

Table 20.3 Overall accuracy of image classification

Classified image	Source of reference data	Overall accuracy (%)
07 March 2003	Landuse 2000 (Land Development Department)	84.2
08 February 2005	Landuse 2006 (Land Development Department)	77.8
26 January 2006	Landuse 2007 (Land Development Department)	79.9
6 February 2010	Ground truth data (field survey in 2009–2010)	81.6

and built-up (resorts, hotels and shops) areas in Takua Pa, a famous tourist beach, recovered in early 2006 while mangrove had slightly decreased. In 2010, the inland built-up area had increased compared to the area in 2003–2006, mangrove areas presented almost the same extent as in 2003 while forest had been turned into agriculture and built-up.

After the 2004 Indian Ocean tsunami, a 6-year conservation and rehabilitation program for mangrove forests in the tsunami impacted areas was established by the Thai Government. However, information about mangrove restoration or reforestation is limited only to the field scale. The integrated use of remote sensing and field data enabled a regional study of the changes in mangrove areas pre- and post-sunami and its recovery up until 2010. Classified images showed some degree of reforestation in 2005 but the process decreased in 2006. In some locations where the topography and soil structure had changed, only a small number of trees could

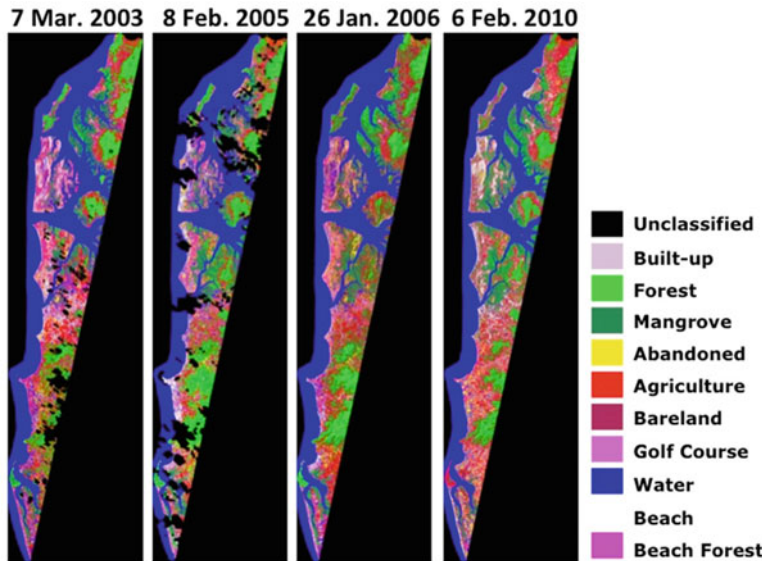


Fig. 20.7 Classified results

survive and hence these areas might be classified as other land cover types like water bodies and bare soil. In addition, the development of shrimp farms, urban recovery and development for tourist activities after the tsunami also disturbed regrowth of the mangroves in the study area, which is outside the tsunami-impacted zone.

Figure 20.8 presents the location of damaged and reforested mangrove near Nam Khem Village, Takua Pa District. The mangrove trees were swept away by the series of tsunami waves and became bare soil in 2004. As aforementioned, the reforestation in 2005 did not succeed in many places, and at this location this was due to degraded soil conditions after the waves carried up salted and sandy soil and deposited it on top. After a few years of mangrove reforestation, the area of mangrove has gradually increased and completely recovered in 2010 as shown in Fig. 20.8. Monitoring of mangrove conditions in the reforested areas is therefore crucial for understanding the progress of recovery (see Fig. 20.9).

The levels of damage were identified by field surveys and the height of wave or inundation level; Low impact (≤ 2 m height of wave/inundation), Moderate (> 2 and ≤ 5 m), High (> 5 and ≤ 10 m) and Very High (> 10 m). Sixty-four villages along the west coast of Phang Nga Province were listed at different damage levels: Low (23 villages), Moderate (14 villages), High (19 villages) and Very High (8 villages) (DDPM 2006). This information was presented in map format for better understanding the tsunami impact: location of villages and damage level as shown in Fig. 20.10. Most of the high and very highly impacted villages were located in Takua Pa District.

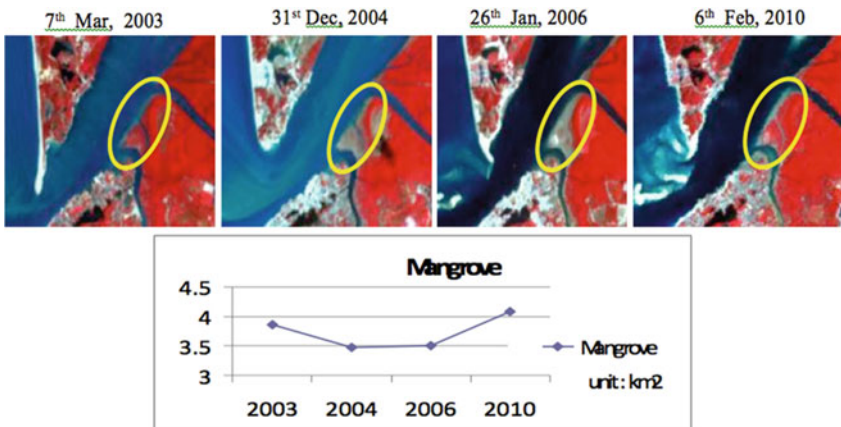


Fig. 20.8 An impacted mangrove area and its recovery



Fig. 20.9 Monitoring of mangrove conditions in the reforested areas in Takua Pa District

The statistical data of population and hired workers in the tsunami-impacted villages were compared using only 3 crucial periods: 2003 (pre-event), 2005 (post-event damage monitoring) and 2007 (post-event recovery monitoring). In addition, the 2010–2011 data was used to identify recovery and assess recent status. Overall, the population changes are depicted in connection with village location in Fig. 20.11. It shows that the population in 2005 of the Low and Moderately impacted villages had slightly decreased in comparison to that in 2003, but it had significantly decreased in the High and Very Highly impacted villages. Only Nam Khem Village has a higher population in 2005 because there were many charities and people who moved into the area for the recovery process. In 2006–2007, most of the impacted villages had recovered physically and in terms of population. In 2010–2011, populations in the Low and Moderately impacted villages were significantly increased (various from 10 to 300 %). The populations in the high and very highly impacted villages had rarely increased while decreased populations (10–50%) were reported for Pak Weep, Pak Jok, Nam Khem and Tab Yang villages in Takua Pa District.

The fluctuation of the amount of hired workers pre- and post-2004 tsunami presented the same trend as the fluctuation of population levels explained above. It

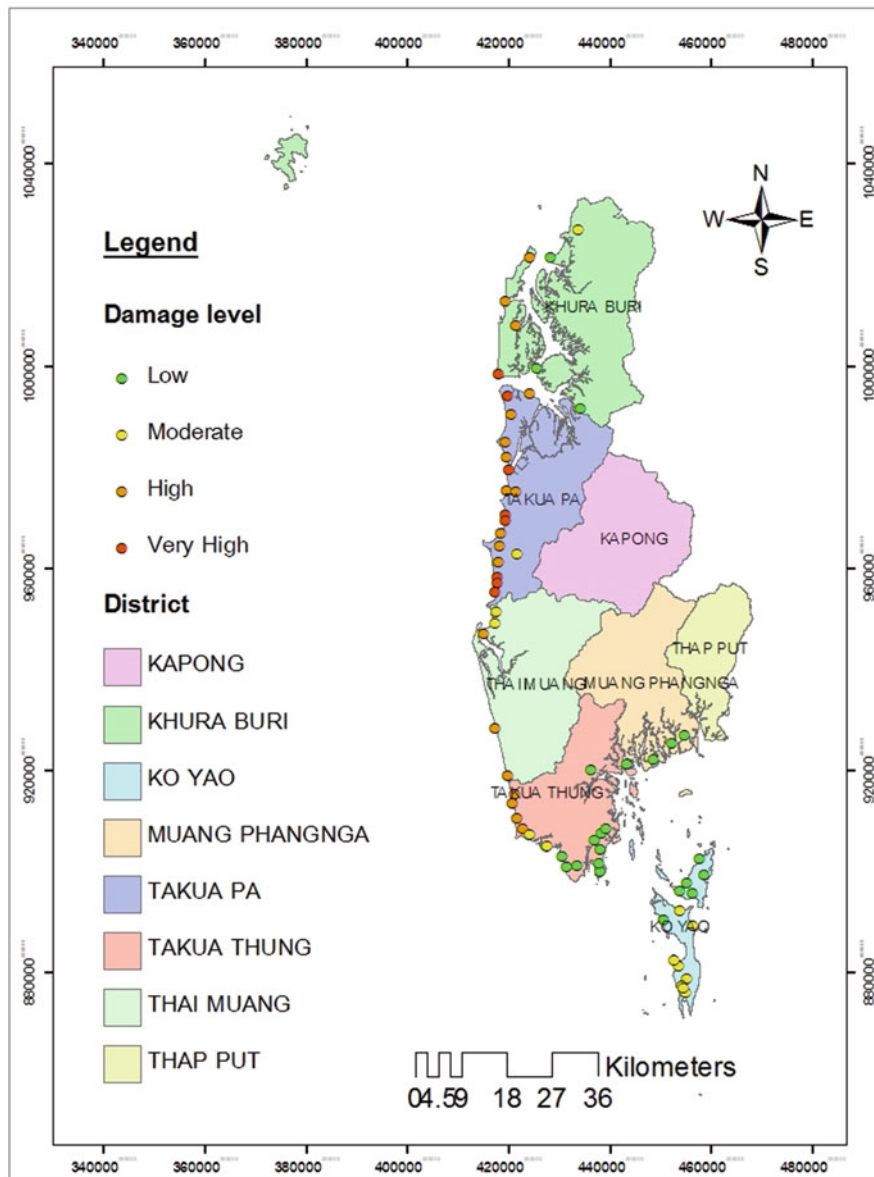


Fig. 20.10 Tsunami impact villages, classed by damage levels

was reported in 2005 that unemployment had increased especially among fishermen and tourist related workers. In 2007 and 2010, the number of hired workers recovered in the field of tourism and increased in the field of agriculture.

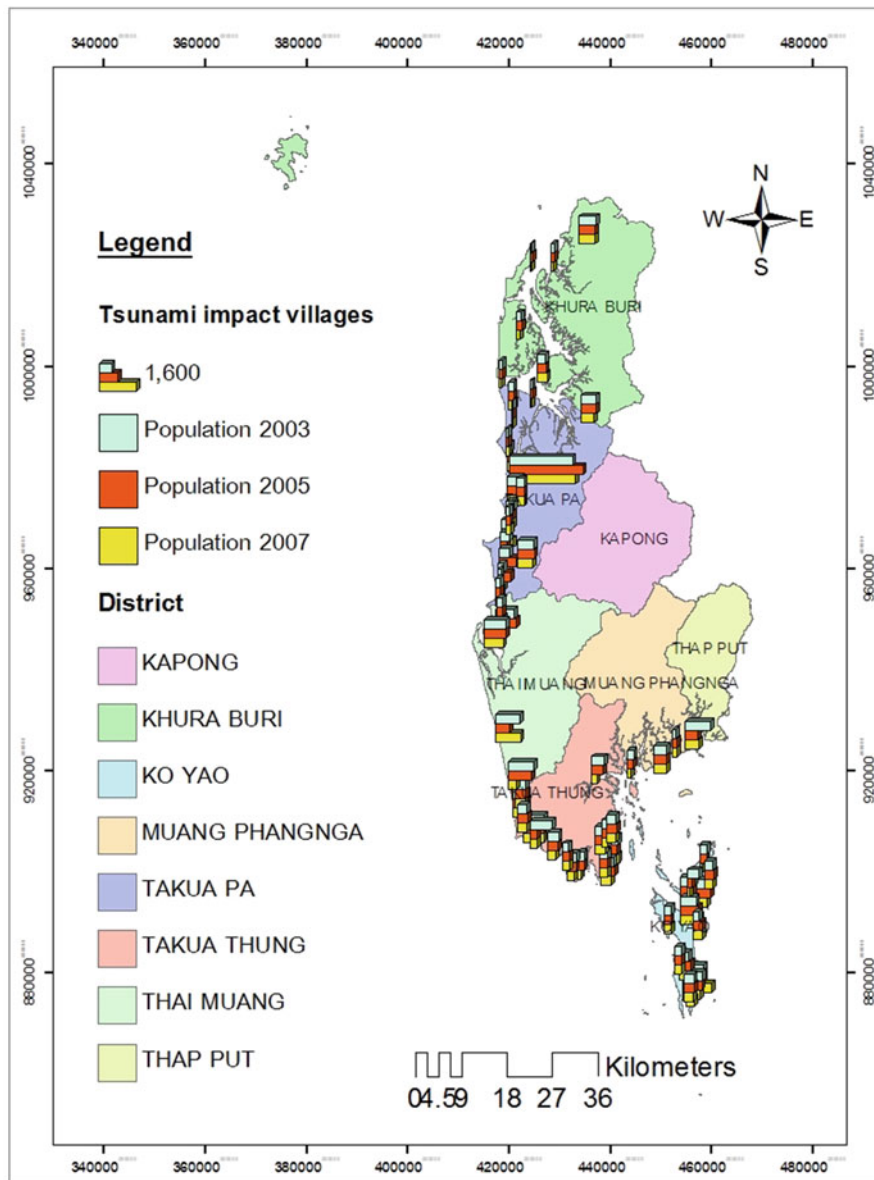


Fig. 20.11 Tsunami impacted villages: population changes in 2003, 2005 and 2007

During the recovery, the changes in population and employment as observed from socio-economic data and field interviews, led to some obvious LULC pattern changes. Recovery of tourism activities and population increase resulted in (and was also a result of) the recovery and expansion of built-up areas including beach resorts

and housing areas. Similarly, the expansion of agricultural land could indicate more people engaged in agricultural activities; we need further detailed analysis of socio-economic data to reveal the ratio between hired workers and residents in the rise of population. It was difficult to observe clearly any evidence related to fishing activities on ASTER images. On the downside, the small decrease of population in some villages could not be captured in classified ASTER images since it did not induce any clear change on a coarse resolution image like ASTER.

In the aftermath of the 2004 tsunami, many international and Thai charities provided for accommodation recovery by fixing or rebuilding new houses at the same location and set up the inland tsunami victim villages. Based on our field survey, accommodation recovery was observed and mapped as shown in Fig. 20.12. We could observe the recovery of built-up areas on ASTER images but were unable to confirm if they were newly built. This would be possible with higher resolution imagery.

The cluster-based classified ASTER images provided an aggregated form of LULC for comparison with socio-economic data. The point-based socio-economic data, in its usual form, provided no spatial distribution. While LULC can reveal the spatial distribution of consequences of human activities, there remains a big gap between the two data sets for monitoring recovery. In this study, we simply tried to improve the information presentation derived from the satellite image and used unrealistic buffer zones around the village points. To better integrate them in a more systematic manner, at least the administrative boundaries in polygon form would be required. The socio-economic and field survey data subsequently would be plotted against the two sets of polygons: clusters from classified ASTER images and administrative boundaries. Moreover, direct observation and field interviews were conducted to provide additional information about the real situation on the ground. To be more effective, the sampling strategy needs to be taken into account so that it enables location-awareness in the process of field data collection and subsequent data analysis. The socio-economic figures associated with each single village point would then be remapped together with field survey clues within the administrative boundary of that village.

Moreover, during the survey, the understanding of tsunamis and the response plan and reactions to unexpected tsunamis in the future were discussed with the villagers (see Fig. 20.13). Since the tragic and catastrophic tsunami in 2004, most of the tsunami victims and Thais had learnt about tsunamis: their source and cause, warning signs before their occurrence, their character and attack style of the series of waves, etc. Since 2005, a preparedness plan and tsunami facilities (barrier, observatory and broadcasting towers, maps and signs of safety zones and routes of evacuation, etc.,) were set up and distributed in the tsunami impacted provinces, especially in Phang Nga and Phuket (Kamthonkiat et al. 2011b). Since then, evacuation activities have been conducted annually.

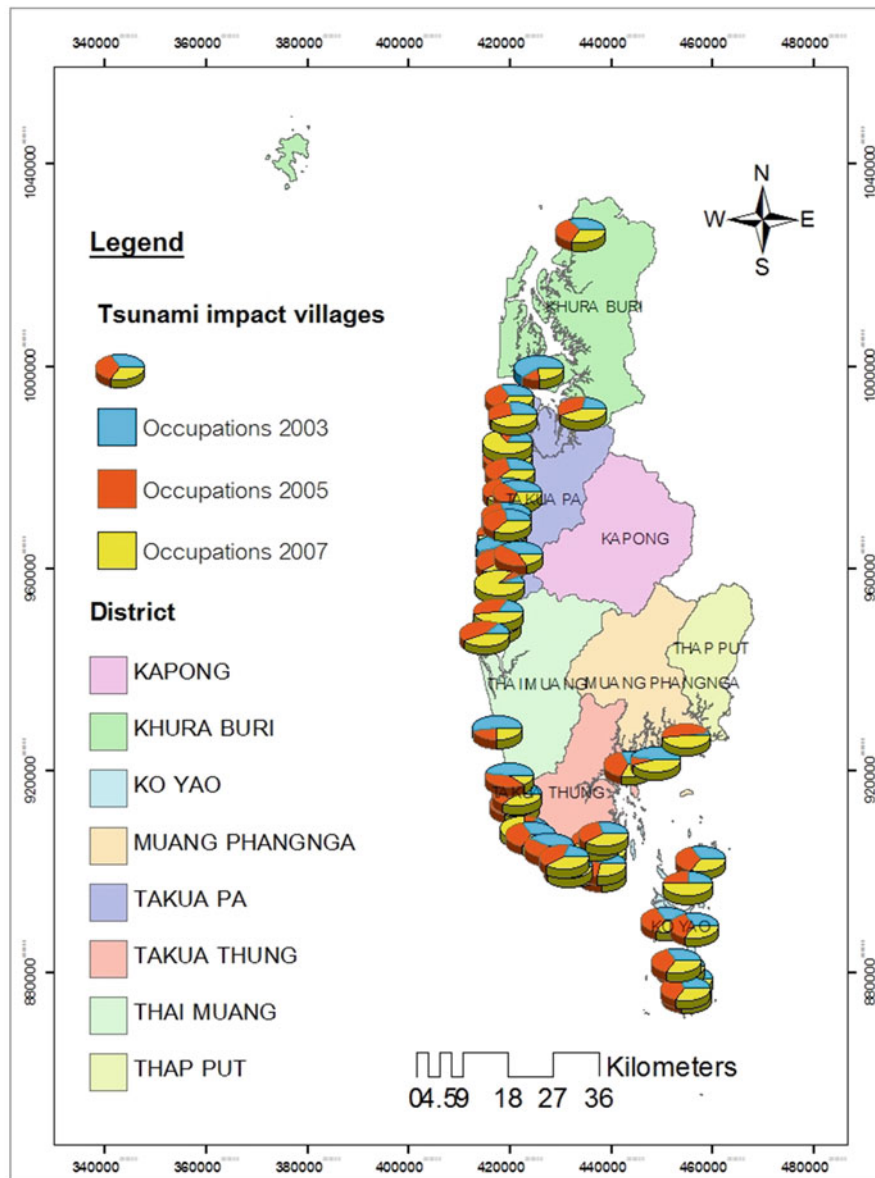


Fig. 20.12 Relocation of houses of tsunami-affected people/villagers based on field survey

Survey – Rebuilt village, interview their tsunami's understanding, information of mangrove area and their activities...



Fig. 20.13 Field survey – rebuilt village and interview with tsunami victims

20.5 Conclusion

In the aftermath of the 2004 Indian Ocean Tsunami, remote sensing has played an important role in mapping impacted areas in Southern Thailand, namely: Phang Nga, Phuket, Krabi, Satun, Ranong and Trang provinces. In this study, monitoring the recovery of environmental rehabilitation and human activities was intensively focused on Phang Nga using ASTER time series data (medium resolution remote sensing) and annual field surveys.

It has been proven clearly that multi-temporal ASTER images or the like are the right data sources for such a regional study of shoreline displacement and mangrove rehabilitation. Interpreting the recovery of human activities faced a tougher challenge due to incompatible data formats. To some extent, information derived from satellite images could help to infer some big changes in human activities in the areas such as recovery of tourism and expansion of agricultural activities. Integration of satellite images, socio-economic data (population, and employment in different sectors) and social survey information are helpful in monitoring physical and living conditions(?) recovery in Phang Nga. In future research, we propose the consideration of a sampling strategy for social interviews and direct observation on the ground, which will help to enable a better connection between conventional socio-economic databases and spatially distributed information derived from satellite images.

Acknowledgements The analysis parts of shoreline anomaly and mangrove recovery after the 2004 Indian Ocean Tsunami were conducted in collaboration with Tohoku University and financially supported by the New Energy and Industrial Technology Development Organization (NEDO) of Japan. The author also appreciates the supply of ASTER data received from the GEO Grid and the National Institute of Advanced Industrial Science and Technology (AIST).

References

- Acqua FD, Gamba P (2012) Remote sensing and earthquake damage assessment: experiences, limits and perspectives. *Proc IEEE* 100(10):2876–2890
- Adams BJ, Huyck CK, Mansouri B, Eguchi RT and Shinouzuka M (2004) Application of high-resolution optical satellite imagery for post-earthquake damage assessment: the 2003 boumerdeas (Algeria) and bam (Iran) earthquakes. *Multidisciplinary Center for Earthquake Engineering Research Progress and Accomplishments 2003–2004*, University of Buffalo. http://mceer.buffalo.edu/publications/resaccom/04-SP01/12_Eguchi.pdf. Accessed 20 Dec 2007
- Bevington JS, Hill AA, Davidson RA, Chang SE, Vicini A, Adams BJ, Eguchi RT (2011) Measuring, monitoring, and evaluating post-disaster recovery: a key element in understanding community resilience. *Proc Struct Congress* 2011:2033–2043
- Brown D, Saito K, Chenvidyakarn T (2010) Monitoring and evaluating post-disaster recovery using high-resolution satellite imagery. In: *Proceedings of the 8th international workshop on remote sensing for disaster management*, Tokyo, Japan, 30 September – 1 October, 2010
- Comanicu D, Meer P (2002) Mean shift: a robust approach toward feature space analysis. *IEEE Trans Pattern Anal Mach Intell* 24:603–619
- Comerio MC (2005) Key elements in a comprehensive theory of disaster recovery. In: *Proceedings of the 1st international conference of urban disaster reduction*. Kobe, Japan, 19 January 2005
- Eguchi RT, Huyck CK, Houshmand B, Mansouri B, Shinouzuka, M, Yamazaki F, Matsuoka M (2000) The Marmara earthquake: a view from space: the Marmara, Turkey earthquake of August17, 1999: Reconnaissance Report. Technical Report MCEER-00-0001 (Buffalo, NY: MCEER): 151–169
- Hill AA, Keys-Mathews LD, Adams BJ, Podolsky D (2006) Remote sensing and recovery: a case study on the Gulf Coast of the United States. In: *Proceeding of the 4th international workshop on remote sensing for post-disaster response*, Cambridge, United Kingdom, CDROM
- Huppert HE, Sparks RS (2006) Extreme natural hazards: population growth, globalization and environmental change. *Phil Trans R Soc A* 364:1875–1888
- Kamthonkiat D, Rodfai C, Saiwanrunrkul A, Koshimura S, Matsuoka M (2011a) Geoinformatics in mangrove monitoring: damages and recovery after the 2004 Indian Ocean Tsunami in Phang Nga, Thailand. *Nat Hazards Earth Syst Sci* 11:1851–1862
- Kamthonkiat D, Koshimura S, Matsuoka M (2011b) Tsunami responses in Phuket Island, Thailand: land uses/land covers and facilities in 2010. *Int J Geoinform* 7(4):55–61
- Kamthonkiat D, Koshimura S, Matsuoka M (2012) Time series analysis of shoreline positions in the pre- and post-2004 Indian Ocean Tsunami in Phang Nga Province, Thailand. *J Earth Sci Eng* 2(1):35–41
- Romer H, Jeewarongkakul J, Kaiser G, Ludwig R, Sterr H (2011) Monitoring post-tsunami vegetation recovery in Phang-Nga province, Thailand based on IKONOS imagery and field investigations – a contribution to the analysis of tsunami vulnerability of coastal ecosystems. *Int J Remote Sens* 33(10):3090–3121
- Romer H, Willroth P, Kaiser G, Vafeidis AT, Ludwig R, Sterr H, Revilla Diez J (2012) Potential of remote sensing techniques for tsunami hazard and vulnerability analysis – a case study from Phang-Nga province, Thailand. *Nat Hazards Earth Syst Sci* 12:2103–2126
- Rubin CB (1985) The community recovery process in the US after a major natural disaster. *Int J Mass Emerg Disasters* 3(2):9–28

- Taubenbock H, Post J, Roth A, Zosseder K, Strunz G, Dech S (2008) A conceptual vulnerability and risk framework as outline to identify capabilities of remote sensing. *Nat Hazards Earth Syst Sci* 8:409–420
- Tralli DM, Blom RG, Zlotnicki V, Donnellan A, Evans DL (2005) Satellite remote sensing of earthquake, volcano, flood, landslide and coastal inundation hazards. *ISPRS J Photogramm Remote Sens* 59(4):185–198
- Vicini A, Bevington J, Davidson R, Hill A (2011) Post-disaster evaluation of community-based housing recovery from aerial imagery: a study of Punta Gorda, Florida following Hurricane Charley. In: Proceeding of the 9th international workshop on remote sensing for post-disaster response, Stanford, USA, CDROM
- Vu TT (2008) Monitoring the recovery process of the disaster-affected areas -scaling context image analysis in GEO grid-based solution. *Int Arch Photogramm Remote Sens Spat Inf Sci* 37(B4):1625–1630
- Vu TT (2011) Building extraction from high-resolution satellite image for tsunami early damage estimation. *Appl Geomatics* 3(2):75–81
- Vu TT, Ban Y (2010) Context-based damage mapping from high-resolution optical satellite images. *Int J Remote Sens* 31(13):3411–3425
- Vu TT, Matsuoka M, Yamazaki F (2007) Dual-scale approach for detection of tsunami-affected areas using optical satellite images. *Int J Remote Sens* 28(13-14):2995–3011